Durham University

Durham E-Theses

Multi-scale assessment of shore platform erosion

ZUZANNA MALGORZATA SWIRAD

How to cite:

SWIRAD, ZUZANNA MALGORZATA (2018) Multi-scale assessment of shore platform erosion. Doctoral thesis, Durham University.

Use policy

The full-text may be used and/or reproduced, and given to third parties in any format or medium, without prior permission or charge, for personal research or study, educational, or not-for-profit purposes provided that:

- a full bibliographic reference is made to the original source
- a https://etheses.durham.ac.uk/id/eprint/12838/ is made to the metadata record in Durham E-Theses
- the full-text is not changed in any way

The full-text must not be sold in any format or medium without the formal permission of the copyright holders.

Please consult the full Durham E-Theses policy for further details.

Academic Support Office, The Palatine Centre, Durham University, Stockton Road, Durham, DH1 3LE
e-mail: e-theses.admin@durham.ac.uk Tel: +44 0191 334 6107
https://etheses.durham.ac.uk

Multi-scale assessment of shore platform erosion

Zuzanna Małgorzata Świrad

Department of Geography

Durham University



Thesis submitted for the degree of Doctor of Philosophy

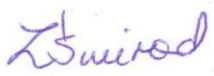
2018

This page is intentionally left blank

Declaration

I confirm that no part of the material presented in this thesis has previously been submitted for a degree in this or any other university. In all cases the words of others, where relevant, have been fully acknowledged.

The copyright of this thesis rests with the author. No quotation from it should be published without prior written consent and information derived from it should be acknowledged.



Zuzanna Swirad

Durham University

August 2018

This page is intentionally left blank

Abstract

The morphology and erosion of shore platforms is a pivotal component of rocky coast evolution as these features control both wave transformation and sediment dynamics. Models that predict coastline evolution and efforts to reconstruct past cliff retreat rates from cosmogenic isotope concentrations are forced to simplify platform morphology and commonly treat erosion only implicitly. The lack of an explicit incorporation of platform dynamics into such models reflects a poor understanding of erosion processes that have conventionally been considered to operate at one of two scales: fine scale abrasion captured by sub-mm precision point measurements of vertical change, and step back-wearing and block removal at metre-scale. Neither approach is well suited to informing a generalised model of foreshore erosion that bridges these two scales or that can be applied more widely. As a result without understanding mechanisms of foreshore erosion models which use these data are limited in their utility to address future coastal change under changing sea level and storminess.

To address this a multi-scale study was undertaken along the North Yorkshire coast (UK) using high-resolution and high-precision monitoring data collected at the spatial and temporal scales relevant to the processes in action. A novel method was developed to monitor mm-scale platform erosion using Structure-from-Motion (SfM) photogrammetry. The average platform down-wearing rate of 0.528 mm yr^{-1} was calculated from 15 individual 0.5×0.5 m sites. The volume frequency and 3D-shape distributions of the detachments suggest that erosion occurs predominantly via detachment of fabric-defined platelets. The erosion rate is faster closer to the cliff toe and at those locations where the tide cycles more frequently. Erosion rates calculated from the 2.6 years of data from 22 km of shore platform using high-resolution airborne LiDAR was 3.45 mm yr^{-1} when derived from individual detachments, or 0.01 mm yr^{-1} when spatially averaged across the platform. Average lowering of the platform sections containing steps was 0.04 mm yr^{-1}, while in areas with no steps 0.01 mm yr^{-1}. Whilst erosion rate cannot be predicted with confidence for any discrete point on the foreshore, systematic trends in across-shore erosion can be shown, with a peak in rate at 10-18 m from the cliff toe, with erosion intensity gradually decreasing seawards.

This new understanding of foreshore erosion has then been used to predict exposure ages from cosmogenic ^{10}Be concentrations at the Hartle Loup platform. This analysis shows that the cliff has been retreating at the steady rate of 0.05 m yr^{-1} cutting the 300 m wide shore platform in the last 6 kyr. This derives rates of retreat comparable to contemporary erosion monitoring. Platform morphology has been shown not to adjust to an equilibrium shape, but it is rather actively modified depending on the interplay between present morphology, sea level and tidal regime. Importantly, this study provides methods to monitor foreshore erosion, enhances our understanding of mechanisms and

controls upon it, whilst the results can be used in models to predict rocky coast evolution by providing an empirically-based assessment of foreshore erosion.

Acknowledgements

This thesis could not be completed without the support of many people. Firstly, I would like to thank my supervisors - Nick Rosser and Matt Brain for giving me the opportunity to work on this unique project, for continuous support, enthusiasm and patience. They have been incredibly generous with their time and supported me at all stages of my PhD. I am grateful to ICL Fertilizers UK Ltd for funding the project. The Department of Geography and Ustinov College supported my training and participation in an international conference. Dylan Rood (Imperial College London) accepted the challenge to work with extremely fine grains with someone who had no experience in geochemistry. His enthusiasm and creativity allowed us push the boundaries of science a bit further. Martin Hurst (Glasgow University) provided his expert knowledge in various aspects of exposure dating using cosmogenic isotopes.

CoBRA team – Emma Vann Jones, Simon Varley, Saskia de Vilder, Jess Benjamin, Sam Waugh, Heather Bell and Dave Hodgson shared long days in the field, technical tips and scientific knowledge. A lot of colleagues helped in data collection: Chris Longley, Clare Bliss, Bev O'Kane, Siobhan Whadcoat, Rob Tomkies, Arminel Lovell, Adam Nichols (who has also been an amazing mentor at Ustinov College), Juliet Sefton, Galane Luo, Callum Pearson, Liz Gleave, Rosie Nelson and Rebecca Smith. Martin West, Amanda Hayton (Durham), Andrew Tye (British Geological Survey), Jens Najorka (Natural History Museum) and Klaus Wilcken (ANSTO) performed laboratory measurements. Merv Brown and Neil Tunstall of Durham University were always at hand when I needed any technical advice. Patrice Carbonneau, Marek Ewertowski, Mike Lim, John Barlow, Jack Williams, Rebecca Hodge, Joel Scheingross, Mark Kinsley, Ed Rollason, Sam Jackson, Victoria Smith and Sarah Dodds provided invaluable input at various stages of the method development, data analysis and/or proof-reading. Alex Seal, Alex Hughes, Anna Caklais and Jenny Shadrick made my long hours of cleaning samples at the Imperial College London enjoyable. I do not think I would have ever ended up at Durham University if not the support of Sebastian Sikora, Piotr Migoń, Gareth Rees, Sophie Weeks and Matt Strzelecki whose love for science has been a great inspiration.

I would also like to thank the postgraduate/post-doc community at the department for sharing ups and downs of academic life in the last four years; my Durham friends: Irene, Smita, Galane, Sam, Stephan, Tharindi, Jing, Zach and Fidel for lots of distractions; and fellow members of Durham Choral Society and Durham Amateur Rowing Club for sharing interests and getting better together.

Finally, I would like to thank my dearest family in Poland and London, as well as friends in Wrocław and Cambridge for their continuous support and patience, for talking and listening, for their optimism and rationality, for being proud of me, for having their door always open, for setting me up to get back to Durham in high spirit, and for assistance to airports/train stations, most likely to double check I was not running away to the other side of the world. Thank you! Dziękuję!

This page is intentionally left blank

Table of contents

List of figures viii
List of tables xviii
Glossary xxi
1. Introduction 1
1.1. Context and rationale 1
1.2. Aims and objectives 2
1.3. Novelty of the study 3
1.4. Structure of the thesis 4
2. Current understanding of shore platform erosion 8
2.1. Introduction 8
2.2. General morphology and evolution of shore platforms 9
2.2.1. Shore platform macro-morphology 9
2.2.2. Controls on the shore platform macro-morphology 9
2.2.3. Theoretical consideration of shore platform evolution 10
2.2.4. Shore platform erosion in existing numerical models of coastal evolution 12
2.3. Monitoring and modelling shore platform erosion 13
2.3.1. Complex nature of shore platform morphology and erosion 14
2.3.2. Platform dynamics at the micro-scale: down-wearing 15
2.3.3. Platform dynamics at the macro-scale: step back-wearing 19
2.4. Consideration of rock resistance 20
2.4.1. Rock control in coastal studies 20
2.4.2. Rock quality assessment 23
2.4.3. Process-based and empirical approaches to rock resistance 25
2.4.3.1. Mechanisms of erosion 25
2.4.3.2. Process-based and empirical studies 26
2.5. Advances in bedrock erosion monitoring 27
2.5.1. Recording bedrock erosion 27
2.5.1.1. Structure-from-Motion: introduction 28
2.5.1.2. Structure-from-Motion: surveying 28
2.5.1.3. Structure-from-Motion: change detection 29
2.5.2. Analysis of erosion 30
2.5.2.1. Event-based analysis of erosion 30
2.5.2.2. Zone-based analysis of erosion 32
2.6. Summary 33
3. Geomorphology of the shore platforms in North Yorkshire, UK 34

3.1. Introduction 34
3.2. Regional settings 34
3.3. Geology 35
3.3.1. Description of the bedrock forming shore platforms in Staithes area 37
3.3.1.1. Methods 37
3.3.1.2. Results 38
3.4. Quaternary history of the area 39
3.5. Current marine conditions 42
3.6. Coastal erosion 43
3.6.1. Cliff retreat 43
3.6.2. Shore platform erosion 45
3.7. GIS mapping of the coastal geomorphology 46
3.7.1. General morphology of the North Yorkshire coast 46
3.7.2. Detailed morphology of Hartle Loup 48
3.7.2.1. Foreshore characteristics 48
3.7.2.2. Field evidence of erosion 52
3.8. Rock control on shore platform morphology at the local scale 55
3.8.1. General morphology of the shore platform 55
3.8.2. Characterising rock strength and structure 58
3.8.3. Representing shore platform in form of coastal cross-sections 63
3.8.4. Relationships between geological variables and shore platform morphology 65
3.8.4.1. Methods 65
3.8.4.2. Results, interpretations and conclusions 67
3.9. Summary 69
4. Developing a new method to monitor bedrock micro-erosion 70
4.1. Introduction 70
4.2. Site selection 70
4.3. Optimisation of the number of photographs 73
4.4. Topographic monitoring 76
4.5. Acquisition of UAV data 78
4.6. Creation of DoDs 79
4.7. 3D positional error 82
4.8. Separation of real detachments from error 83
4.9. Testing performance of the method 96
4.10. Analysis of detachments 98
4.10.1. Creation of detachment inventories 98
4.10.2. Event inventory analysis 99

4.10.3. Spatial analysis of detachments 99
4.10.4. Temporal analysis of detachments 100
4.11. Method suitability to monitor bedrock micro-erosion 102
4.11.1. Method comparison with MEMs 102
4.11.2. Topographic reconstruction and change detection 102
4.11.3. Method validation and importance of the errors 103
4.11.4. Change which is impossible to resolve 103
4.12. Summary 104
5. Mechanisms and controls of shore platform down-wearing 105
5.1. Introduction 105
5.1.1. Potential role of independent controls on the spatial distribution of foreshore detachments and erosion 105
5.2. Results 107
5.2.1. Analysis of the small-scale detachment inventory 107
5.2.1.1. Net erosion rate 107
5.2.1.2. Volume frequency, size and shape of detachments 108
5.2.2. Spatial analysis 113
5.2.2.1. Summary of detachment properties in the monitoring site inventory 113
5.2.2.2. 3D shape of detachments in the monitoring site inventory 114
5.2.2.3. Spatial distribution and character of the foreshore detachments 116
5.2.3. Temporal analysis 121
5.2.3.1. Magnitude and size distribution of detachments throughout the year 121
5.2.3.2. 3D shape distribution throughout the year 123
5.2.3.3. Detachment propagation in time 124
5.2.4. Spatial and temporal distribution of detachments 124
5.3. Discussion 127
5.3.1. Full inventory analysis 127
5.3.1.1. Erosion rates 127
5.3.1.2. Mechanisms of erosion 128
5.3.2. Spatial analysis 132
5.3.2.1. Comparison with previous studies 132
5.3.2.2. 3D shapes of detachments 133
5.3.2.3. Explaining the distribution and character of the foreshore detachments 134
5.3.3. Temporal analysis 135
5.3.3.1. Temporal variability in erosion rates and size and shape distributions 135
5.3.3.2. Detachment propagation in time 136
5.4. Summary 136
6. Developing a new method to monitor bedrock macro-scale shore platform erosion 137

6.1. Introduction 137
6.2. Surveys and data management 137
6.3. Calibration of the method to detect detachments 138
6.3.1. Creation of DEMs 138
6.3.2. Establishing the Level of Detection (*LoD*) 138
6.3.3. Creation of DoDs and selection of the area of interest 139
6.3.4. De-trending the DoDs 140
6.3.5. Separation of the rock detachments from vegetation 142
6.3.6. Identification of boulders and steps 145
6.4. Analysis of detachments 146
6.4.1. Event inventory analysis of detachments 147
6.4.2. Grid cell-based analysis of detachments 149
6.4.3. Modelling the distribution of erosion 151
6.4.4. Temporal distribution of detachments 152
6.5. Method suitability to monitor bedrock macro-erosion 153
6.5.1. Methodical comparison with other studies to detect foreshore erosion 153
6.5.2. Topography reconstruction and change detection 154
6.6. Summary 155
7. Bedrock erosion across the shore platform 156
7.1. Introduction 156
7.1.1. Potential controls on the spatial distribution of erosion 156
7.2. Results 158
7.2.1. Macro-scale detachment inventory 158
7.2.1.1. Summary statistics for the macro-scale detachment inventory 159
7.2.1.2. Volume frequency, size and shape of detachments 159
7.2.1.3. Erosion rates and size distribution of detachments according to the surface class and type of erosion 162
7.2.2. Spatial distribution of the foreshore macro-erosion 164
7.2.2.1. Summary of the grid-cell data content 165
7.2.2.2. Erosion on the non-stepped part of the foreshore 166
7.2.2.3. Erosion on the stepped part of the foreshore 173
7.2.2.4. Across-shore distribution of foreshore erosion 180
7.2.3. Temporal distribution of erosion 184
7.2.3.1. Detachment inventory 184
7.2.3.2. Grid cell inventory 185
7.3. Discussion 187
7.3.1. Putting erosion rates in context 187
7.3.2. Mechanisms of erosion 189

7.3.3. Explaining the spatial distribution of erosion 191
7.3.3.1. Distribution of erosion on a cell-by-cell basis 191
7.3.3.2. Across-shore distribution of erosion as a function of the distance from the cliff 193
7.3.4. Temporal distribution of erosion 194
7.4. Summary 195
8. The importance of shore platform erosion in reconstructing past cliff retreat using cosmogenic ^{10}Be concentrations 196
8.1. Introduction 196
8.1.1. Cosmogenic isotopes: background 198
8.1.2. Exposure dating in rocky coast studies 199
8.2. A conceptual study: modelling ^{10}Be concentrations across the shore platform 202
8.2.1. Model development 202
8.2.1.1. Model assuming negligible platform erosion 202
8.2.1.2. Model including shore platform erosion: theoretical models 207
8.2.1.3. Model including shore platform erosion: empirical model 215
8.2.2. Model results 216
8.2.2.1. Model assuming negligible platform erosion 216
8.2.2.2. Model including shore platform erosion: theoretical models 217
8.2.2.3. Model including shore platform erosion: empirical model 219
8.3. Empirical study: calculating ^{10}Be concentrations 221
8.3.1. Methods 221
8.3.1.1. Study set-up 222
8.3.1.2. Sample collection 223
8.3.1.3. Mechanical sample processing 226
8.3.1.4. Chemical sample processing 227
8.3.1.5. Accelerator mass spectrometry (AMS) 229
8.3.2. Results 230
8.4. Reconstructing rocky coast evolution from cosmogenic ^{10}Be concentrations 232
8.4.1. Methods 232
8.4.1.1. Fitting ^{10}Be concentrations into the constant cliff retreat model 232
8.4.1.2. Using ^{10}Be concentrations and the empirical model to reconstruct past cliff retreat rates 233
8.4.1.3. Additional samples 234
8.4.2. Results 235
8.4.2.1. Fitting ^{10}Be concentrations into the constant cliff retreat model 235
8.4.2.2. Using ^{10}Be concentrations and the process-based model to reconstruct past cliff retreat rates 237
8.4.2.3. Additional samples 244

8.5. Discussion 245
8.5.1. Methodological advances 245
8.5.2. Holocene cliff retreat rates 246
8.5.3. Long-term erosion of shore platforms 248
8.6. Conclusions 249
9. Discussion 251
9.1. What is the dominant mechanism of shore platform erosion? 251
9.1.1. Differences between erosion rates at the two monitoring scales 251
9.1.2. Identifying mechanisms of erosion from the size and shape distribution of detachments 253
9.1.3. Consideration of rock resistance upon the foreshore 255
9.1.4. Identifying controls on the spatial distribution of erosion 256
9.2. What is the relative contribution of the down-wearing and step back-wearing to shore platform erosion? 257
9.2.1. The role of scale in foreshore erosion 257
9.2.2. Separating surface down-wearing and step back-wearing 261
9.3. Does the multi-scale assessment of shore platform erosion enhance our ability to understand millennial-scale coastal evolution? 262
9.3.1. Using the results to reconstruct past cliff retreat rates 262
9.3.2. Implications of results for the evolution of the North Yorkshire coastline 263
9.3.3. Wider implications for modelling coastal evolution 263
9.4. Summary 265
10. Conclusions 266
10.1. Summary of findings 266
10.1.1. Summary of aim 266
10.1.2. Original contribution to knowledge 266
10.1.2.1. What is the dominant mechanism of shore platform erosion? 267
10.1.2.2. What is the relative contribution of the down-wearing and step back-wearing to shore platform erosion? 268
10.1.2.3. Does the multi-scale assessment of shore platform erosion enhance our ability to understand millennial-scale coastal evolution? 269
10.1.3. Thesis weaknesses 270
10.1.4. Wider ramifications 271
10.2. Recommendations for future research 271
References 275
Appendix 1: Swirad et al., 2016 297
Appendix 2: Understanding of erosion 303
Appendix 3: Topographic characteristics of the small-scale monitoring sites at 0.001 m resolution obtained with the SfM in Apr'16. 305

Appendix 4: Monthly distribution of erosion at each micro-erosion monitoring site. 321
Appendix 5: Cumulative distribution of erosion at each micro-erosion monitoring site. 337
Appendix 6: Monthly erosion (depth) at each micro-erosion monitoring site. 353
Appendix 7: Cumulative erosion (depth) at each micro-erosion monitoring site. 369
Appendix 8: Settings to process LiDAR-derived point clouds 385
Appendix 9: Across-shore occurrence of erosion 392
Appendix 10: MATLAB scripts used to predict cosmogenic ^{10}Be concentrations and reconstruct past cliff retreat rates. 397

List of figures

Figure 1.1 Examples of representation of shore platform morphology in coastal evolution models: A) straight inclined surface (Trenhaile, 1983); B) set of sections with equal thickness (Walkden and Hall, 2005); C) two straight inclined sections with different widths and slopes (Kline et al., 2014); D) straight inclined surface and a horizontal bench at the minimum beach level (Limber et al., 2014). 1

Figure 2.1 Key morphometric characteristics of shore platforms. 9

Figure 2.2 Simple geometrical models of the shore platform evolution: A) the parallel coastal retreat, B) the down-wearing is not proportional to the cliff retreat, C) the shore platform widening with the stable seaward edge. 11

Figure 2.3 Shore platform morphology and erosion: A) macro-scale elements of shore platforms, B) controls on the efficiency of platform erosion processes. 14

Figure 2.4 Elements contributing to Fw and Fr in coastal evolution; modified from Sunamura, 1983. 21

Figure 2.5 Block geometry on ternary plots: A) Location of shapes across the plot, B) Division of the plot into ten sectors. Block axes: A – long, B – medium, C – short; based on Williams et al., 2018....32

Figure 3.1 The North Yorkshire coast: A) location within the British Isles (red box); B) coastline outline; C) typical coastal scenery; the photograph was taken from Cowbar facing west (as indicated with the red arrow in B); source: Alamy Stock Photo. 35

Figure 3.2 Cliff composition in west Staithes/Boulby area: A) an example of cliff morphology with clearly visible near-horizontal bedding; B) schematic cross-section of the cliff face; based on Lim, 2006. 36

Figure 3.3 A) coverage of the LiDAR2014 dataset along the North Yorkshire coastline; B) location of the five rock samples used for geochemical analysis on shore platforms (grey surface) in Staithes area....38

Figure 3.4 Landslide complex on cliff face composed of glacial till, Whitby Golf Club (Upgang), North Yorkshire; LiDAR 2016 orthophotograph mosaic. 41

Figure 3.5 Relative sea-level change model for the last ~11 kyr for Tees (ca 25 km north-west of Staithes) with glacio-isostatic adjustment model of Bradley et al. (2011); after Shennan et al. (2018). 42

Figure 3.6 Tidal duration distribution for the Whitby tide gauge based on hourly sea-level data from 2006-2010 binned into 0.1 m elevation range bins; data source: https://www.bodc.ac.uk/. ...43

Figure 3.7 Coastal morphological classes: A) alongshore distribution in Staithes area; B) conceptual cross-shore distribution; C) results of the detailed mapping in Boulby area. 47

Figure 3.8 Morphology of Hartle Loup: A) geomorphological map; B) orthophotograph mosaic; C) DEM; D) slope map; E) roughness map. C, D and E are at 0.1 m resolution; source: LiDAR2016. 49

Figure 3.9 Mean roughness as a function of cell size used to calculate standard deviation of the slope. 50

Figure 3.10 Spatial, marine and geological characteristics of Hartle Loup: A) distance from the cliff; B) distance from the seaward edge; C) tidal duration; D) inundation frequency; E) rock type (based on http://www.southampton.ac.uk/~imw/staithes.htm). A-D are at 0.1 m resolution; source: LiDAR2016....51

Figure 3.11 Morphology of Hartle Loup: A) an outflow channel at the boundary between rock beds; B) a joint network; C) a step with detached boulder; D) a steep slope of the seaward edge; E)

a pedestal rock; F) an ironstone nodule; G) fresh exposure of the shale surface; H) fresh exposure of the barnacle-covered sandstone surface. *53*

Figure 3.12 Example of the shore platform erosion via block removal: A) fresh detachment of blocks; B) concentration of loose material behind the blocks; C) results of rock entrainment during the storm event. *54*

Figure 3.13 Topographic variability along the 4.2 km section of the North Yorkshire coastline in Staithes area: A) elevation; B) slope; C) roughness. The maps are at 0.2 m resolution; source: LiDAR2014. ..... *57*

Figure 3.14 Locations of the rock hardness test sites on the shore platforms along the 4.2 km section of the North Yorkshire coast in Staithes area. *58*

Figure 3.15 Acquisition of the rock hardness data with the Equotip durometer: A) taking readings from a weathered surface; B) removing the weathered surface with the carborundum stone; C) taking readings from an un-weathered surface. *59*

Figure 3.16 Relationships between Schmidt Hammer and Equotip rebound values on the un-weathered and the weathered rock surfaces along the 4.2 km section of the North Yorkshire coast in Staithes area. *60*

Figure 3.17 Geological variability across the shore platforms along the 4.2 km section of the North Yorkshire coast in Staithes area: A) mean rock hardness of 80 rock beds; B) standard deviation of rock hardness of 80 rock beds; C) joint density at 1 m resolution. *62*

Figure 3.18 Automatically extracted coastal cross-sections limited to the shore platform and the cliff along the 4.2 km section of the North Yorkshire coast in Staithes area: A) alongshore distribution; B) cross-shore distribution (colours correspond to A); C) density map of the elevation occurrence for part of the profiles depicted in the inset map of B. *64*

Figure 3.19 Kernel density estimate (normal kernel, default optimal half widths h returned in MATLAB were used) of all variables used in the analysis of the rock control on the shore platform morphology along the 4.2 km section of the North Yorkshire coast in Staithes area: A) Square root of the platform width, Sqrt(pWid) (h = 0.58 m); B) Square root of the platform gradient, Sqrt(pGra) (h = 0.08°); C) Platform elevation, pEle (h = 0.16 m AOD); D) Elevation of the cliff/platform junction, pJun (h = 0.60 m AOD); E) Platform roughness, pRou (h = 0.56°); F) Rock hardness, pHar (h = 9.18 Equotip rebound value); G) Standard deviation of the rock hardness, pStd (h = 5.25 Equotip rebound value); H) Joint density, pJDe (h = 0.05 joints m-2); Y axis: probability density. *66*

Figure 3.20 Residuals of the best-fit multiple regression of the morphology of the shore platforms along the 4.2 km section of the North Yorkshire coast in Staithes: A) Platform width, pWid (m); B) Platform gradient, pGra (°); C) Platform elevation, pEle (m AOD); D) Elevation of the cliff/platform junction, pJun (m AOD); E) Platform roughness, pRou (°); residuals are calculated as observed-predicted. *68*

Figure 4.1 Location of the small-scale monitoring sites and the UAV sites on Hartle Loup. For location along the North Yorkshire coastline see Figure 3.7. Background: the LiDAR2016 DEM at 0.1 m resolution overlaid by a hillshade at 70% transparency. *71*

Figure 4.2 Distribution of the general characteristics of the monitoring sites (the red lines represent single sites) in respect to the range of characteristics across the whole section of the shore platform of 1.26×10^5 m^2 depicted in Figure 4.1 (kernel density estimate: normal kernel, default optimal half widths h returned in MATLAB were used): A) Distance from the cliff, sCli (h = 2.30 m); B) Distance from the seaward edge, sSea (h = 2.42 m); C) Elevation, sEle (h = 0.03 m AOD); D) Slope, sSlo (h = 0.02°); E) Roughness, sRou (h = 0.01°); F) Tidal duration, sTid (h = 0.01%); G) Inundation frequency, sInu (h = 0.74%); Y axis: probability density. *73*

Figure 4.3 Uncertainty of the SfM models as a function of the number of photographs: A) standard deviation of the distances between the points and the best-fit plane for a flat surface with no

objects normalised by the value for three photographs; B) proportion of the points with distance between point clouds with the three objects > 1.5×10^{-3} m high and meshed flat surface with no objects above thresholds normalised with the value for 0.5×10^{-3} m threshold. 75

Figure 4.4 The photographic set-up on the frame: A) the white cloth dissipates the light; B) the distribution of the cameras and the compass in the upper part of the frame; C) the planform distribution of the cameras, compass, GCPs and CPs on the frame. Plot shows the directions of the relative coordinates of the GCPs and the CPs with z facing up. 77

Figure 4.5 Example UAV photograph. Distribution of the GCPs for the UAV survey H. Red box indicates the small-scale monitoring site 13. 79

Figure 4.6 Workflow applied to obtain DoDs from the close-range photogrammetry. 80

Figure 4.7 3D positional error of the point clouds for each survey of the small-scale monitoring: A) the GCP location error; B) the CP location error; C) the number of CPs not included in the models. 83

Figure 4.8 The effect of various factors on generating error on the SfM-derived topography reconstruction. Left panel of distortion (doming effect) represents the situation after having de-trended the surface using the ArcMap Focal Statistics tool. 85

Figure 4.9 Examples of erroneous detection of detachments at the locations with complex geometry (A and B) and at the model edges (C and D): A) DoD3; B) DoD1; C) DoD3; D) DoD2. 85

Figure 4.10 Proportion of objects with at least given size in total count of the objects ≤ 10 pixels. 87

Figure 4.11 Polygon dimensions: A) Minimum Bounding Geometry: Rectangle by Width (blue) created for exemplar erosion polygons (yellow) in ArcMap; B) polygon metrics. 87

Figure 4.12 Examples of clear real detachments (with blue borders) for DoD3 identifiable on the orthophotographs. Background: the orthophotographs before (Nov'16) and after (Dec'16) detachment occurred. Objects with red borders are other objects identified as detachments. 88

Figure 4.13 Dimensions and shape ratios of idealised polygons representing the real and the potentially erroneous detachments; peri = perimeter. 89

Figure 4.14 Kernel density estimate (normal kernel, default optimal half widths h returned in MATLAB were used) of the length and the three shape parameters of 40 real (blue) and 40 erroneous (red) detachments from DoDs1-4: A) Length (h = 0.0034 m); B) Perimeter/area (h = 236.01); C) Length/width (h = 0.20); D) Perimeter/length (h = 0.29); Y axis: probability density. 90

Figure 4.15 Relationships between the length and the three shape parameters of the 40 real (blue) and the 40 erroneous (red) detachments from DoDs1-4: A) length vs perimeter/area; B) length vs length/width; C) length vs perimeter/length; D) perimeter/area vs length/width; E) perimeter/area vs perimeter/length; F) length/width vs perimeter/length. 91

Figure 4.16 The most successful set of filters to separate polygons of real detachments from the error. 93

Figure 4.17 Removal of the polygons while applying the size and shape filters for the four test DoDs: A) DoD1; B) DoD2; C) DoD3; D) DoD4. The arrows indicate north. 94

Figure 4.18 Reduction in detected erosion through applying the filters: A – the originally-identified polygons constitute 100%; B – the remaining proportion of erosion after applying the size filter; C – the remaining proportion of erosion after applying the shape filter. 95

Figure 4.19 The final workflow applied to separate real detachments from error. 96

Figure 4.20 Occurrence of the incorrectly identified 'detachment' events as a function of A) the surface roughness and B) the distance from the centre of the model distributions. The occurrence was normalised by the occurrence across the small-scale monitoring sites. 97

Figure 4.21 The assessment of the propagation of erosion in time based on the random and actual distribution of detachments within the monitoring sites. 101

Figure 5.1 Equivalent cube sizes for the detachment volumetric properties in the detachment inventory. 108

Figure 5.2 Kernel density estimate (normal kernel, half width h = 0.1 $log_{10}(m^3)$) of detachment volume for the entire detachment inventory. Mean volume = 6.96×10^{-8} m^3. 109

Figure 5.3 Relationship between area and volume of detachments across the full inventory on a log-log non-cumulative plot: A) distribution of the sizes of single detachments and the power-law trendline; B) density distribution map with a grid cell size of 0.025 (x) x 0.05 (y). The organisation of events with the smallest area into the vertical stripes is a function of data resolution where the area is rounded to the 10^{-6} m^2 pixel size intervals, while depth, and consequently the volume, adopts the full range of continuous values as it is measured at a higher precision. 110

Figure 5.4 Volume-frequency distribution across the full inventory obtained using SfM methods. Scatter plot (left-hand vertical axis) represents the volume-frequency kernel density distribution curve with the power-law trendline (solid black line) on a log-log scale plot. Additional trendlines were fitted for two sections of volume spectrum (red for Vol 1.12×10^{-8} – 1.26×10^{-6} m^3; blue for Vol > 1.26×10^{-6} m^3) excluding the roll-over at the lowest spectrum of Vol (black data points). The yellow line is the kernel density estimate (normal kernel, half width = 0.08 $log_{10}(m^3)$; right-hand vertical axis) of the individual detachment volumes for the full inventory. Dashed lines indicate the distributions of proposed sub-populations (idealised and manually drawn: see main text). Idealised shapes indicate the equivalent cube sizes for specific volumes, with indicative relative sizes compared to the possible erosion features. . 111

Figure 5.5 Shapes of detached material coloured by the rock type. Block axes: A – long, B – medium, C – short. For sector description see Figure 2.5. The organisation of shapes in diagonal stripes and the concentration of events along the slabs/blocks edge of the ternary plot is explained by high numbers of events with planform size equal to the grid resolution and change precision, or a low multiple thereof. 112

Figure 5.6 Distribution of the erosion variables across the 15 monitoring sites: A) Total area, sArea (m^2); B) Total volume, sVol (m^3); C) Mean volume, sMean (m^3); D) Standard deviation of volumes, sStd (m^3); E) Erosion rate, sEro (mm yr^{-1}); F) Exponent β, sβ; Y axis: number of sites. 114

Figure 5.7 Shapes of detached material coloured by monitoring site, ordered by the distance from the cliff. Block axes: A – long, B – medium, C – short. Sandstone sites are indicated by grey boxes in the lowermost scale; the remaining sites are located on shale sections of the platform. For sector description see Figure 2.5. 115

Figure 5.8 Kernel density estimate (normal kernel, default optimal half widths h returned in MATLAB were used) of the independent and erosion variables at the monitoring sites: A) Distance from the cliff, sCli (h = 17.62 m); B) Distance from the seaward edge, sSea (h = 31.10 m); C) Elevation, sEle (h = 0.62 m AOD); D) Slope, sSlo (h = 2.48°); E) Roughness, sRou (h = 1.12°); F) Tidal duration, sTid (h = 0.23%); G) Inundation frequency, sInu (h = 14.56%); H) Curvature, sCur (h = 1.10×10^{-6}); I) Site roughness, sSRou (h = 2.52°); J) Elevation range, sEleR (h = 0.03 m); K) Number of joints, sJNo (h = 2.74); L) Length of joints, sJLe (h = 0.53 m); M) Erosion rate, sEro (h = 0.23 mm yr^{-1}); N) Mean volume, sMean (h = 1.60×10^{-8} m^3); O) Exponent β, sβ (h = 0.06); Y axis: probability density. 117

Figure 5.9 Matrix of correlation coefficients and best-fit ellipses for all independent variables charactersising the small-scale monitoring sites obtained using the Pearson correlation in R. The colour bar represents the Pearson correlation coefficient (PCC) which describes both the strength of relationship and its sign, '-1' being the strongest negative relationship, '0' expressing no correlation and '1' representing the strongest positive relationship. The sign of

the relationships (positive/negative) is also expressed by the sign of PCC values in the bottom-left part of the plot and the orientation of the oval in the upper-right part, while their strength is represented by the absolute values in the bottom-left part of the plot and the width of the ovals with narrower ovals representing stronger relationships. Significant relationships ($p < 0.05$) are indicated with the thicker oval edge and the bold PCC values. 118

Figure 5.10 Results of the pair-wise least-square regression between the independent variables and erosion..... 119

Figure 5.11 Sequence of input independent variables and resulting R^2 values ($p < 0.05$): A) Erosion rate, sEro (mm yr^{-1}); B) Mean volume, sMean (m^3); C) Exponent β, sβ; dashed lines represent maximum R^2 of full model; accepted models are indicated by the black dot. See Glossary for abbreviation meaning and calculation of the variable values. 120

Figure 5.12 Distribution of residuals for the erosion variables: A) Erosion rate, sEro (mm yr^{-1}); B) Mean volume, sMean (m^3); C) Exponent β, sβ. Points represent the training set, triangles represent the test set; residuals are calculated as observed - predicted values. 121

Figure 5.13 Monthly distribution of the erosion variables as mean values per month: A) Erosion rate, sEro (mm yr^{-1}); B) Mean volume, sMean (m^3); C) Standard deviation of volumes, sStd (m^3); D) Exponent β, sβ. Boxplots contain following information: median (red line), 25-75% interquartile range (blue box), 9-91% quantiles (black lines) and outliers defined as events greater than q3+w(q3-q1) or less than q1-w(q3-q1), where w is the maximum whisker length, i.e. ± 2.7 standard deviation, and q1 and q3 are the 25^{th} and 75^{th} percentiles of the sample data, respectively (red plus symbols). 122

Figure 5.14 Shapes of detached material coloured by month: A) all events; B) mean shape representing each month at each site; C) mean shape representing each month. Block axes: A – long, B – medium, C – short. For sector description see Figure 2.5. 123

Figure 5.15 Reoccurrence of erosion through time: X – pairs of consecutive months; Y – CoR. Black line is the standard deviation of the random distance (section 4.10.4). 124

Figure 5.16 A) Monthly distribution of the detachments at the small-scale monitoring sites ordered by the distance from the cliff. Black polygons within each monitoring plot represent detachments. Sandstone sites are indicated by grey boxes, the remaining sites are located on shale sections of the platform. Grid cells with bold outlines represent example cells showing different modes of detachment. The solid black outline demonstrates an example of a large detachment with multiple smaller detachments. The black dashed outline exemplifies a monitoring plot with multiple small detachments. The red outlined plot provides an example of where minimal erosion occurred during the monitoring period. Plots B, C and D illustrate how observed (black line) and model-predicted (red dashed line) erosion rate (B), mean volume (C) and β (D) vary with distance from the cliff. 126

Figure 5.17 Schematic summary of the process of platelet detachment: A) conceptual model of detachment; B-D: an example of detachment occurred in April-May 2016 at site 9: B) detachment outline with Apr'16 orthophotograph as background; C) detachment outline with May'16 orthophotograph as background; D) detachment thickness (common logarithmic scale) with Apr'16 hillshade as background. 129

Figure 6.1 Kernel density estimate (normal kernel, half width h = 0.002 m) of the change detected on the flat surface of the harbour wall. 139

Figure 6.2 Proposed processes contributing to the detected detachments (red areas) in 2014-2015. Background: LiDAR2014 hillshade at 30% transparency. 140

Figure 6.3 A) The 2015-2016 DoD suggests that there is a systematic surface pattern; B) trend surface as the mean of 101×101 cells; B) trend surface as the mean of 201×201 cells. Red areas in B and C represent change ≥ LoD after DoD de-trending using the adequate trend surfaces. 141

Figure 6.4 Surface cover on Hartle Loup: A) visual inspection of the LiDAR2016 RGB map allows the identification of different types of vegetation, barnacle cover and the bare rock; B) classification of the platform surface.....143

Figure 6.5 Pixels available for change detection 2014-2015: A) data extent after applying the density mask; B) extent of the 'vegetation' class; C) extent of the 'rock' class.....144

Figure 6.6 An example of protrusions automatically-detected on the basis of topography and object shape for the LiDAR2014 survey. Background: LiDAR2014 hillshade at 30% transparency. 145

Figure 6.7 Workflow applied to detect change at the macro-scale from the LiDAR dataset. 146

Figure 6.8 Examples of the removal of beach material detected as single detachments: A) Tile 30, 2014-2015, removal of 86.09 m^3 of material; B) Tile 40, 2016-2017, removal of 310.88 m^3 of material. Background: orthophotographs from surveys preceding events.....148

Figure 6.9 Shapes of detached material > 6 m^3 coloured by the volume (common logarithmic scale). Block axes: A – long, B – medium, C – short. For sector description see Figure 2.5.....149

Figure 6.10 Removal and inclusion of the grid cells into the inventory.....150

Figure 6.11 Assessment of the logistic model performance based on the predicted and observed number (n) of cells with (YES) and without (NO) detachments.....152

Figure 7.1 Proposed processes contributing to the detected detachments (red areas) after DoD de-trending and filtering out detachments which were deemed to represent beach dynamics in 2014-2015. Background: LiDAR2014 hillshade at 30% transparency.....158

Figure 7.2 Kernel density estimate (normal kernel, half width h = 0.02 $\log_{10}(m^3)$) of volume (common logarithmic scale) in the macro-scale detachment inventory. The values in brackets represent volumes in normal (m^3) units. Mean volume = 15.72×10^{-3} m^3.....160

Figure 7.3 Density distribution of the area and volume in the macro-scale detachment inventory across the North Yorkshire foreshore with a grid cell size of 0.02. Events smaller than 1 m^2 are organised into vertical stripes adopting limited number of area values and a full range of volumes, which is caused by the pixel resolution controlling two dimensions.....160

Figure 7.4 Volume-frequency distribution in the macro-scale detachment inventory on a log-log scale plot. The power-law trendlines are presented with the thin lines and described with equations coloured accordingly: black – whole size range, blue – events $\leq 10^0$ m^3 excluding the roll-over, red – events > 10^0 m^3. The thick black line represents kernel density estimate (kernel type: Epanechnikov, half width h = 0.017 $\log_{10}(m^3)$) of the volume.....161

Figure 7.5 Shapes of detached material coloured by the volume (common logarithmic scale). Block axes: A – long, B – medium, C – short. For sector description see Figure 2.5. The smallest events (< 10^{-2} m^3) are organised into diagonal lines including the edges of ternary plot, which is a reflection of the pixel size controlling dimensions of two detachment axes.....162

Figure 7.6 Kernel density estimate (normal kernel, half width h = 0.02 $\log_{10}(m^3)$) of volume for the macro-scale detachment inventory according to the surface class. 163

Figure 7.7 Volume-frequency distribution for the macro-scale detachment inventory according to the surface class with the power-law trendlines on a log-log scale plot.....164

Figure 7.8 Relationship between the distance from the cliff (m) and the average number of pixels per cell.....165

Figure 7.9 Matrix of correlation coefficients and best-fit ellipses for all independent variables of the non-stepped cell inventory obtained using the Pearson correlation in R. The colour bar represents the Pearson correlation coefficient (PCC) which describes both the strength of relationship and its sign, '-1' being the strongest negative relationship, '0' expressing no correlation and '1' representing the strongest positive relationship. The sign of the

relationships (positive/negative) is also expressed by the sign of PCC values in the bottom-left part of the plot and the orientation of the oval in the upper-right part, while their strength is represented by the absolute values in the bottom-left part of the plot and the width of the ovals, with narrower ovals representing stronger relationships. All relationships are significant ($p < 0.05$). 168

Figure 7.10 Sequence of input independent variables into the logistic model of the macro-scale erosion occurrence in the non-stepped cells and resulting proportion of correctly classified cells, P; dashed line represents maximum P of full model; accepted model is indicated by the black dot. See Glossary for abbreviation meaning and calculation of the variable values... 169

Figure 7.11 Performance of the accepted logistic model of the macro-scale erosion occurrence in the non-stepped cells based on the predicted and observed number (n) of cells with (YES) and without (NO) detachments in the test set..... 169

Figure 7.12 Kernel density estimate (normal kernel, default optimal half widths h returned in MATLAB were used) of the erosion and independent variables characterising the non-stepped cells: A) Erosion rate, $lEro_{down}$ ($h = 9.40\times10^{-4}$ mm yr^{-1}); B) Log_{10}(Erosion rate), $log_{10}(lEro_{down})$ ($h = 0.05\ log_{10}$(mm yr^{-1})); C) Distance from the cliff, lCli (h = 3.11 m); D) Distance from the seaward edge, lSea (h = 3.50 m); E) Elevation, lEle (h = 0.08 m AOD); F) Slope, lSlo (h = 0.68°); G) Square root of slope, Sqrt(lSlo) ($h = 11.41°\times10^{-2}$); H) Roughness, lRou (h = 0.34°); I) Square root of roughness, Sqrt(lRou) ($h = 8.00°\times10^{-2}$); J) Curvature, lCur (h = 2.58); K) Tidal duration, lTid (h = 0.02%); L) Joint density, lJDe (h = 0.34 joints m^{-2}); Y axis: probability density. 171

Figure 7.13 Sequence of input independent variables and resulting R^2 values ($p < 0.05$) to predict erosion rate, $lEro_{down}$ (mm yr^{-1}) in the non-stepped cells; accepted model is indicated by black dot. See Glossary for abbreviation meaning and calculation of the variable values. 172

Figure 7.14 Distribution of residuals for the erosion rate, $lEro_{down}$ (mm yr^{-1}) on the test set of the non-stepped cells; residuals are calculated as observed - predicted values..... 173

Figure 7.15 Matrix of correlation coefficients and best-fit ellipses for all variables of the stepped cell inventory obtained using the Pearson correlation in R. The colour bar represents the Pearson correlation coefficient (PCC) which describes both the strength of relationship and its sign, '-1' being the strongest negative relationship, '0' expressing no correlation and '1' representing the strongest positive relationship. The sign of the relationships (positive/negative) is also expressed by the sign of PCC values in the bottom-left part of the plot and the orientation of the oval in the upper-right part, while their strength is represented by the absolute values in the bottom-left part of the plot and the width of the ovals, with narrower ovals representing stronger relationships. All relationships are significant ($p < 0.05$). 175

Figure 7.16 Sequence of the input independent variables into the logistic model of the macro-scale erosion occurrence in the stepped cells and resulting proportion of correctly classified cells, P; dashed line represents maximum P of full model; accepted model is indicated by black dot. See Glossary for abbreviation meaning and calculation of the variable values..... 176

Figure 7.17 Performance of the accepted logistic model of the macro-scale erosion occurrence in the stepped cells based on the predicted and observed number (n) of cells with (YES) and without (NO) detachments in the test set..... 176

Figure 7.18 Kernel density estimate (normal kernel, default optimal half widths h returned in MATLAB were used) of the erosion and independent variables characterising the stepped cells: A) Erosion rate, $lEro_{step}$ ($h = 2.72\times10^{-3}$ mm yr^{-1}); B) Log_{10}(Erosion rate), $log_{10}(lEro_{step})$ ($h = 0.09\ log_{10}$(mm yr^{-1})); C) Distance from the cliff, lCli (h = 4.55 m); D) Distance from the seaward edge, lSea (h = 5.45 m); E) Elevation, lEle (h = 0.14 m AOD); F) Slope, lSlo (h = 1.04°); G) Roughness, lRou (h = 0.45°); H) Curvature, lCur (h = 8.52); I) Tidal duration, lTid (h = 0.03%); J) Joint density, lJDe (h = 0.49 joints m^{-2}); Y axis: probability density... 178

Figure 7.19 Sequence of the input independent variables and resulting R^2 values ($p < 0.05$) to predict the erosion rate, $lEro_{step}$ (mm yr^{-1}) in the stepped cells; accepted model is indicated by black dot. See Glossary for abbreviation meaning and calculation of the variable values. 179

Figure 7.20 Distribution of residuals for the erosion rate, $lEro_{step}$ (mm yr^{-1}), on the test set of the stepped cells; residuals are calculated as observed - predicted values. 180

Figure 7.21 Distribution of cells and erosion across shore platforms binned into 1 m distances from the cliff: A) total number of cells; B) proportion of cells that experienced erosion; C) total detached volume. 181

Figure 7.22 Distribution of the three types of cells and erosion across shore platforms binned into 1 m distances from the cliff: A) contribution of the types of cells to the total number of cells; B) contribution of the types of erosion to the cells that experienced erosion; C) proportion of cells that experienced erosion for the types of erosion; the best-fit trendlines are fit to the sections between 10 and 230 m (dashed lines) from the cliff toe: boulder movement and erosion at steps – linear model, down-wearing – 3rd order polynomial model; D) detached volume. 183

Figure 7.23 Reoccurrence of erosion in the non-stepped, stepped and boulder cells. 187

Figure 7.24 Conceptualised topography of stepped cells with different average slope, which may explain possibility to predict occurrence of erosion on the basis of slope. 192

Figure 8.1 A) Location of the sampling profile across Hartle Loup. Relevant rock beds are labelled. B) Elevation distribution across the profile indicated in A). Background: the LiDAR2016 DEM at 0.1 m resolution overlaid by a hillshade at 70% transparency. 197

Figure 8.2 The distribution of ^{10}Be concentrations across a gently sloping shore platform: A) the apparent hump in concentrations results from the interplay between exposure ages and water shielding; B) an abrupt increase in concentrations for a portion of the platform inherited from the last interglacial; C) a saw-toothed distribution superimposed on the hump due to step back-wearing; based on Regard et al. (2012) and Hurst et al. (2017). 201

Figure 8.3 The topography of Penny Nab (see Figure 8.1 for location) used to calculate topographic shielding, S_{topo}: A) the subtended azimuth angle $\Delta\varphi$; B) the inclination angle ϑ. 204

Figure 8.4 Topographic shielding, S_{topo}, for a 300 m wide shore platform under the assumption of a constant cliff retreat rate of 4.29×10^{-2} m yr^{-1} for the last 7 kyr and a cliff of h = 50 m inclined at $\vartheta = 70°$ and $\Delta\varphi = 102°$: A) S_{topo} for a single point at time t (yr) after exposure; B) cumulative distribution of S_{topo} across the platform. 205

Figure 8.5 Water shielding, S_w: A) tide-dependent $S_{w(t)}$ at any time t; B) change of $S_{w(t)}$ since exposure for the seaward edge of the platform where distance from the cliff d = 300 m and elevation el = -1.49 m AOD; C) cumulative S_w across Hartle Loup (see Figure 8.1B for the profile). 206

Figure 8.6 The geomagnetic scalar for the last 7 kyr; based on Lifton et al., 2014. 207

Figure 8.7 The scaling factor for the ^{10}Be production as a function of depth for the top 3 m under the surface. 208

Figure 8.8 A simplified profile across Hartle Loup to explore the impact of platform down-wearing on cosmogenic ^{10}Be concentrations. 208

Figure 8.9 A conceptual model of the platform down-wearing rate which is relatively fast in respect to the cliff retreat rate. 209

Figure 8.10 A conceptual model of down-wearing when the platform widens and flattens with the stable seaward edge position. 210

Figure 8.11 The distribution of the platform erosion scalar, S_{er}, across shore platforms of diverse width and slope: A) down-wearing proportional to the cliff retreat; B) constant down-wearing

rate of 1.33 mm yr^{-1}; C) constant down-wearing rate of 3.50 mm yr^{-1}; D) platform widening. 211

Figure 8.12 A simplified profile across Hartle Loup to explore the impact of step back-wearing on cosmogenic ^{10}Be concentrations. 212

Figure 8.13 Idealised shore platform profiles to explore the role of step back-wearing in the distribution of platform erosion scalar, S_{er}, across a 300 m wide shore platform; X-axis: distance from the cliff (m); Y-axis: elevation (m). 213

Figure 8.14 The distribution of the platform erosion scalar, S_{er}, across a 300 m wide shore platform where the platform erodes via back-wearing of steps with a range of heights at the same rate as the cliff retreat where A) 1 step; B) 2 steps; C) 3 steps; D) 4 steps; E) 5 steps of the same height exist. 214

Figure 8.15 The distribution of the platform erosion scalar, S_{er}, across a 300 m wide shore platform where the platform erodes via back-wearing of steps with a range of heights at the rate dependent on the contemporary cross-shore step location where A) 1 step; B) 2 steps; C) 3 steps; D) 4 steps; E) 5 steps of the same height exist. 215

Figure 8.16 Results of the model assuming negligible platform erosion on the real sampling profile across Hartle Loup (Figure 8.1): A) distribution of the shielding/scaling factors; B) expected cosmogenic ^{10}Be concentrations. 217

Figure 8.17 Results of the model including platform down-wearing on the profile across Hartle Loup (Figure 8.1): A) distribution of the platform erosion scalar, S_{er}, across simplified platform (Figure 8.8) for different down-wearing scenarios; B) expected cosmogenic ^{10}Be concentrations. 218

Figure 8.18 Results of the model including step back-wearing on the profile across Hartle Loup (Figure 8.1): A) distribution of the platform erosion scalar, S_{er}, across the simplified platform (Figure 8.12) for different step back-wearing scenarios; B) expected cosmogenic ^{10}Be concentrations. 219

Figure 8.19 Results of the model including the platform down-wearing rate developed from the empirical micro-scale data (Eq 8.10) on the profile across Hartle Loup (Figure 8.1): A) Simulation of shore profile evolution in the last 7 kyr; B) distribution of the total platform erosion scalar, S_{er}, across the platform; C) expected cosmogenic ^{10}Be concentrations. 220

Figure 8.20 The workflow used to calculate cosmogenic ^{10}Be concentrations in the rock samples from Hartle Loup. 221

Figure 8.21 Sampling locations: A) LiDAR2016 orthophotograph; B) oblique view on LiDAR2016 point cloud; black lines represent the boundaries of exposed rock beds. 225

Figure 8.22. The contribution of the quartz grains of different sizes to the total volume of a test sample derived from the sandstone bed B1. 226

Figure 8.23 Sample mass loss (mean ± standard deviation) during HF etching as a percentage of the initial mass of the sample. 228

Figure 8.24 The calculation of ^{10}Be concentration in a quartz sample based on the ^{10}Be/^{9}Be ratio measured with the accelerator mass spectrometer. 230

Figure 8.25 The final ^{10}Be concentrations (± standard deviation) for 23 rock samples collected across Hartle Loup (exact locations: Figure 8.21). Distance from the cliff (m) is taken from the sample ID. 232

Figure 8.26 A conceptual model of the cross-shore distribution of exposure ages depending on the cliff retreat mode 233

Figure 8.27 ^{10}Be concentrations in 20 rock samples collected across Hartle Loup measured and predicted under various scenarios of platform erosion. 235

Figure 8.28 ^{10}Be concentrations in 20 rock samples collected across Hartle Loup, measured and predicted under the assumption of platform erosion through combination of the down-wearing where platform widens and flattens in time (Figure 2.2B), and the location-dependent step back-wearing.....237

Figure 8.29 The distribution of exposure ages and the shielding/scaling factors across Hartle Loup under 60 scenarios of cliff retreat rate and pattern: A) exposure age; B) topographic shielding; C) water shielding; D) geomagnetic scalar.....238

Figure 8.30 The distribution of platform erosion scalar across Hartle Loup under 60 scenarios of cliff retreat rate and pattern: A) down-wearing proportional to the cliff retreat rate; B) platform widening; C) empirical model, where the down-wearing rate is a function of the distance from the seaward edge and the tidal duration. 240

Figure 8.31 The distribution of ^{10}Be concentrations across Hartle Loup under 60 scenarios of cliff retreat rate and pattern: A) no platform erosion; B) down-wearing proportional to the cliff retreat rate; C) platform widening; D) empirical model, where the down-wearing rate is a function of the distance from the seaward edge and the tidal duration. White circles depict measured concentrations corrected for the geological inheritance with standard deviation represented by whiskers.....241

Figure 8.32 Goodness-of-fit of the pairwise linear regression models between ^{10}Be concentrations measured and modelled using the combinations of scenarios of cliff retreat rate and pattern (60 columns) and platform down wearing scenarios (0: no platform erosion; 1: down-wearing proportional to the cliff retreat rate; 2: platform widening; 3: empirical model). Grey squares represent scenarios which do not predict concentrations at all 20 sampling locations. Insignificant ($p \geq 0.05$) relationships are crossed out. 242

Figure 8.33 Scenarios which successfully fulfil the conditions to A) predict concentrations ≤ 20% off measured values for samples 20-240; B) expose the whole platform in the last 7 kyr; C) predict > 80% of the measured values for at least seven of samples 241-300 imposed on the combinations of scenarios of cliff retreat rate and pattern (60 columns) and platform down wearing scenarios (0: no platform erosion; 1: down-wearing proportional to the cliff retreat rate; 2: platform widening; 3: empirical model). Grey squares represent scenarios which fulfil the conditions. 243

Figure 8.34 The distribution of measured (circles) ^{10}Be concentrations across Hartle Loup and the most-likely scenario of coastline evolution where the cliff retreats at the steady rate of 0.05 m yr^{-1} and the platform down-wearing rate is a function of the distance from the seaward edge and the tidal duration. 243

Figure 8.35 The platform erosion scalar due to step back-wearing contribution, S_{er_step} (points), at the seaward section of Hartle Loup; the line represents the distribution of elevation.....244

Figure 8.36 The suggested direction of Hartle Loup evolution which may explain relatively low ^{10}Be concentration in samples A) 60 (62.09 m from the cliff toe) and B) 230 (213.11 m). 248

Figure 9.1 Shapes of detached material at the micro- and macro-scales coloured by the volume. Block axes: A – long, B – medium, C – short. For sector description see Figure 2.5. The micro-scale shapes were plotted on the top of the macro-scale shapes. 254

Figure 9.2 Conceptual model of the erosion processes operating on shore platform and rock properties determining resistance across the spatial scales.....259

Figure 9.3 Distribution of erosion across Hartle Loup: A) down-wearing rates predicted using the multiple linear regression model developed at the small-scale (Table 5.4); B) proportion of cells which experienced down-wearing at 1 m interval distance from the cliff.....260

List of tables

Table 2.1 Relationships between shore platform morphology and controlling factors. 10

Table 2.2 Numerical models on the evolution of rocky coast and their consideration of the rock resistance, and foreshore morphology and erosion. 13

*Table 2.3 Shore platform down-wearing reported in literature; referenced by *Dornbusch et al. (2006), **Stephenson and Finlayson (2009). 15*

Table 2.4 Main rock quality assessment systems used in engineering. 24

Table 3.1 Properties of the rocks present in Staithes area; source: Cleveland Potash Ltd. 37

Table 3.2 Characteristics of the rock samples collected from shore platforms in Staithes area (for location refer to Figure 3.3B). 39

Table 3.3 Metals and chloride concentrations (%w/w) in the rock samples. 39

Table 3.4 Information about the Whitby tide gauge station and tidal levels for 2008-2026; modified from https://www.ntslf.org/. 43

Table 3.5 Cliff recession rates (m yr^{-1}) in North Yorkshire based on historical maps: A) by lithology, B) by morphology; modified from Agar, 1960. 44

Table 3.6 The average down-wearing rates of the shore platforms along the North Yorkshire coastline: A) the planar part; B) the ramp; based on Robinson, 1977a. 45

Table 3.7 The morphological classes mapped along the North Yorkshire coast. 47

Table 3.8 The linear features mapped to delimit the major morphological classes along the North Yorkshire coastline. 48

Table 3.9 Mean coefficient of variation (standard deviation/mean) of the Schmidt Hammer and the Equotip readings on the un-weathered and the weathered rock surfaces along the 4.2 km section of the North Yorkshire coast in Staithes area. 60

Table 3.10 Variables used in the profile-based analysis of the geomorphic conditions of the shore platforms along the 4.2 km section of the North Yorkshire coast in Staithes area. Glossary contains the details of the value calculation. 65

Table 3.11 The best-fit multiple linear regression for the shore platform morphology along the 4.2 km section of the North Yorkshire coast in Staithes area. Asterisks (*) indicate significant relationships ($p < 0.05$). For independent variable definitions, see Table 3.10 and Glossary. 67

Table 3.12 The best-fit multiple linear regression for the shore platform morphology along the 4.2 km section of the North Yorkshire coast in Staithes area under the assumption that the wave intensity can be approximated by the platform width. Asterisks (*) indicate significant relationships ($p < 0.05$). For independent variable meaning see Table 3.10 and Glossary. .. 67

Table 4.1 General characteristics of the small-scale monitoring sites. Glossary contains the details of the value calculation. 71

Table 4.2 PhotoScan settings used to process the SfM data. 74

Table 4.3 Surveying timescale. 76

Table 4.4 Relative marker coordinates on the frame (m) calculated using trigonometric functions. 77

Table 4.5 Characteristics of the UAV sites. 78

Table 4.6 Rigid translation of the SfM point cloud coordinates (shifted = original - value from table). 80

Table 4.7 Characteristics of the small-scale monitoring sites based on the SfM-derived DEMs of the Apr'16 survey. Glossary contains the details of the value calculation. *81*

Table 4.8 Proportion of objects ≤ 10 pixels with sizes at 1 pixel interval (%). *86*

Table 4.9 Summary statistics of shape ratios of 40 real and 40 erroneous detachment polygons. *88*

Table 4.10 Correctly classified proportion (%) of the real and the erroneous detachments using single shape filters. *92*

Table 4.11 Success rate (%) of the combination of filters 1-9 (Table 4.10) to separate the real and the erroneous detachments in terms of their number, area and volume. *92*

Table 4.12 Reduction in identified detachments in terms of the polygon number, area and volume while applying the size and the shape filters on the four test DoDs. *94*

Table 4.13 Summary statistics of the 105 modelled £1 coin sizes. Real sizes of the rigid standard body with standard deviation = 0 were precisely measured with callipers. *98*

Table 4.14 Object attributes in the detachment-, site- and month-based inventories of the small-scale monitoring. Glossary contains the details of calculation of the variables per site and month. *99*

Table 4.15 Independent variables characterising the small-scale monitoring sites. Glossary contains the details of the value calculation. *100*

Table 5.1 Summary statistics of the erosion variables across the detachment inventory. *108*

Table 5.2 Summary statistics of the individual detachment sizes across the detachment inventory... *109*

Table 5.3 Summary of the detachment data at the monitoring sites. The largest values are in ***bold****.* *113*

Table 5.4 Accepted numerical models of the erosion variables. See Glossary for abbreviation meaning and calculation of the variable values. *120*

Table 6.1 The information on the LiDAR surveys conducted along the North Yorkshire coastline. *138*

Table 6.2 The summary statistics of the DoD value distribution on the flat surface of the harbour wall. The 95% confidence threshold farthest from 0 is in bold. *139*

Table 6.3 Object attributes in the macro-scale detachment- and the grid cell-based inventories. Glossary contains the calculation details of the grid cell variables. *147*

Table 7.1 Expected relationships between the independent variables and erosion; the sign of relationship is indicated by '+' and '-'. *157*

Table 7.2 Summary statistics of the erosion variables in the macro-scale detachment inventory across the North Yorkshire foreshore. *159*

Table 7.3 Summary statistics of the individual detachment sizes in the macro-scale detachment inventory across the North Yorkshire foreshore. *159*

Table 7.4 Summary statistics of the macro-scale erosion variables according to the surface class. *163*

Table 7.5 Macro-scale detachment count and volume according to the type of erosion. *164*

Table 7.6 Summary of the cells that experienced erosion depending on the type of cell. *166*

Table 7.7 Summary statistics of the independent variables in the training set used to develop a logistic model of the macro-scale detachment occurrence in the non-stepped cells. *167*

Table 7.8 Details of the accepted logistic model of the macro-scale erosion occurrence in the non-stepped cells. *170*

Table 7.9 Summary statistics of the independent variables in the training set used to develop a logistic model of the macro-scale detachment occurrence in the stepped cells. *174*

Table 7.10 Details of the accepted logistic model of the macro-scale erosion occurrence in the stepped cells. 176

Table 7.11 Summary statistics of the erosion variables in the macro-scale detachment inventory excluding boulder movement for the three time periods separately. The actual area and volumes are given while erosion rate is recalculated to a full year using time periods from Table 6.1. 185

Table 7.12 Summary of the total number of non-stepped, stepped and boulder cells and their change for the three time periods separately. 186

Table 8.1 Characteristics of the main cosmogenic nuclides; based on: Darvill (2013) and von Blanckenburg and Willenbring (2014)..... 199

Table 8.2 Characteristics of the sampling locations on Hartle Loup and the rock samples. 223

Table 8.3 The amount of the material at various stages of the mechanical sample processing: total weight (g) and the weight normalised by the initial weight (%). 227

Table 8.4 The calculation of the number of the background ^{10}Be atoms from the blanks based on the ^{9}Be carrier weight and the AMS measurements of ^{10}Be/^{9}Be. 230

Table 8.5 The calculation of ^{10}Be concentrations based on the sample weight and the AMS measurements of ^{10}Be/^{9}Be. 231

Table 8.6 ^{10}Be concentrations measured and predicted under various scenarios of platform erosion for 20 rock samples collected across Hartle Loup..... 236

Table 8.7 The calculation of the step back-wearing rate from the site exposure age and the step height..... 245

Table 8.8 ^{10}Be concentrations corrected for muon production in the samples located within a 3 m radius of the single point with different morphologic/geologic settings. 245

*Table 9.1 Summary of the spatio-temporal scale and erosion variables based on the detachment inventories at the micro- and macro-scales; *excluding boulders. 252*

Table 9.2 Variables used to calculate exposure ages across shore platforms and the input data required. 263

Glossary

Abbreviations used in the thesis:

Abbreviation	Meaning
AMS	Accelerator mass spectrometry
AOD	Above Ordinance Datum
BIS	British Ice Sheet
CoR	Coefficient of Reoccurrence
CP	Check Point
DEM	Digital Elevation Model
DoD	DEM of Difference
dr	Random distance
DXR	Digital X-ray radiogrammetry
Fr	Resisting force of substrate
Fw	Assailing force of waves
GCP	Ground Control Point
HAT	Highest astronomical tide
LAT	Lowest astronomical tide
LoD	Level of Detection
MBG	Minimum Bounding Geometry
MEM	Micro-erosion meter
MHWN	Mean high water level of neap tides
MHWS	Mean high water level of spring tides
MLWN	Mean low water level of neap tides
MLWS	Mean low water level of spring tides
MSA	*Multi-Station Adjustment*
PCC	Pearson correlation coefficient
PLSI	Point Load Strength Index
RMS	Rock Mass Strength
RSL	Relative sea level
S_{er}	Platform erosion scalar
SfM	Structure-from-Motion
TLS	Terrestrial Laser Scanning
TMEM	Traversing micro-erosion meter
UAV	Unmanned Aerial Vehicle
UCS	Unconfined (uniaxial) compressive strength
V_{min}	Minimal detectable volume

Variables used in the thesis:

Variable	Abbreviation	Meaning	Unit
Profile-based dataset to link foreshore morphology to geology (Chapter 3):			
A)	Independent variables:		
Rock hardness	*pHar*	Proxy for *UCS*; each rock bed, i.e. exposure of uniform geology, is represented by the mean hardness. The profiles are represented as the weighted mean based on the proportion of the extent of specific rock beds they cross.	Equotip rebound value
Standard deviation of rock hardness	*pStd*	Weighted standard deviation of the rock hardness in each rock bed crossed by the profiles.	Equotip rebound value
Joint density	*pJDe*	Mean joint density, averaged from the joint density (Figure 3.18C) at points resampled along the profiles at 0.2 m interval, excluding platform sections with sediment cover.	joints m^{-2}
B)	Morphometric variables:		
Platform width	*pWid*	Horizontal distance between the cliff/platform junction and the seaward edge (Figure 2.1).	m
Platform gradient	*pGra*	Dip of a straight line between the cliff/platform junction and the seaward edge calculated as the arctangent of the platform width divided by the elevation difference between the cliff/platform junction and the seaward edge (Figure 2.1).	°
Platform elevation	*pEle*	Mean elevation of the shore platform, averaged from DEM-derived elevations of the points resampled along the profiles at 0.2 m interval.	m AOD
Elevation of the cliff/platform junction	*pJun*	DEM-derived elevation of the seaward-most resampled point classified as the cliff face, i.e. which abuts against the shore platform.	m AOD
Platform roughness	*pRou*	Standard deviation of the slope obtained at points resampled along the profiles at 0.2 m interval.	°
SfM dataset to identify controls on the foreshore micro-erosion based on the 0.5×0.5 m monitoring sites (Chapter 5):			
A)	Independent variables at the macro-scale based on the LiDAR2016 dataset (0.1 m resolution):		
Distance from the cliff	*sCli*	Distance between the monitoring sites and the cliff/platform junction mapped manually using the LiDAR2014 maps (section 3.7.1) calculated using the ArcMap *Near* tool.	m
Distance from the seaward edge	*sSea*	Distance between the monitoring sites and the seaward edge mapped manually using the LiDAR2014 maps, the GoogleEarth orthophotomaps and the historical maps (section 3.7.1) calculated using the ArcMap *Near* tool.	m
Elevation	*sEle*	Obtained for the locations of the survey bolts located at the centre of the monitoring sites.	m AOD
Slope	*sSlo*	Obtained for the locations of the survey bolts located at the centre of the monitoring sites.	°
Roughness	*sRou*	Obtained for the locations of the survey bolts located at the centre of the monitoring sites. It is calculated as standard deviation of slope at 17×17 cell square (Figure 3.9).	°
Tidal duration	*sTid*	The fraction of time when the sea level is at a 0.1 m elevation range which encompasses *sEle*. It is calculated for the Whitby tide gauge from 2006-2010 hourly data from the NERC British Oceanographic Data Centre (https://www.bodc.ac.uk/).	%
Inundation frequency	*sInu*	The fraction of time when the site remains under water. It is calculated for the Whitby tide gauge from 2006-2010 hourly data from the NERC British Oceanographic Data Centre (https://www.bodc.ac.uk/).	%
B)	Independent variables at the micro-scale based on the SfM dataset (0.001 m resolution):		
Curvature	*sCur*	Cumulative effect of profile and surface shape on surface flow. It is calculated as a mean value of the curvature raster created using the ArcMap *Curvature* tool.	n/a
Site roughness	*sSRou*	Standard deviation of the slope map (Appendix 3).	°
Elevation range	*sEleR*	Maximum-minimum value of the DEM (Appendix 3).	m
Number of joints	*sJNo*	Number of polylines representing joints manually digitised from the	n/a

Variable	Abbreviation	Meaning	Unit
		orthophotographs (Appendix 3).	
Length of joints	*sJLe*	Total length of polylines representing joints manually digitised from the orthophotographs (Appendix 3).	m
C)	Erosion variables:		
Total area	*sArea*	The total number of DoD pixels identified as detached at any time multiplied by the pixel size.	m^2
Total volume	*sVol*	The sum of volumes of all detachments.	m^3
Mean volume	*sMean*	The mean volume of all detachments.	m^3
Standard deviation of volumes	*sStd*	Standard deviation of the volumes of all detachments.	m^3
Erosion rate	*sEro*	1,000 × *sVol* (m^3) / 0.25 m^2 / 1.01 yr	mm yr^{-1}
Exponent β	$s\beta$	The power-law exponent of the volume frequency distribution.	n/a
LiDAR dataset to identify controls on erosion at the shore platform level based on the 1×1 m grid cells (Chapter 7):			
A)	Independent variables:		
Distance from the cliff	*lCli*	Distance between the grid cells and the cliff/platform junction mapped manually using the LiDAR2014 maps (section 3.7.1) calculated using the ArcMap *Near* tool.	m
Distance from the seaward edge	*lSea*	Distance between the grid cells and the seaward edge mapped manually using the LiDAR2014 maps, the GoogleEarth orthophotomaps and the historical maps (section 3.7.1) calculated using the ArcMap *Near* tool.	m
Elevation	*lEle*	Mean value of the DEM at the original resolution (0.25 m).	m AOD
Elevation range	*lEleR*	The value range of DEM at the original resolution (0.25 m).	m
Relief	*lRel*	Standard deviation of DEM values at the original resolution (0.25 m).	m
Slope	*lSlo*	Mean value of the slope at the original resolution (0.25 m).	°
Roughness	*lRou*	Standard deviation of slope at the original resolution (0.25 m).	°
Curvature	*lCur*	Cumulative effect of profile and surface shape on surface flow. It is calculated as a mean value of the curvature raster created using the ArcMap *Curvature* tool.	n/a
Tidal duration	*lTid*	The fraction of time when the sea level is at a 0.1 m elevation range which encompasses *lEle*. It is calculated for the Whitby tide gauge from 2006-2010 hourly data from the NERC British Oceanographic Data Centre (https://www.bodc.ac.uk/).	%
Inundation frequency	*lInu*	The fraction of time when the grid cell remains under water based on *lEle*. It is calculated for the Whitby tide gauge from 2006-2010 hourly data from the NERC British Oceanographic Data Centre (https://www.bodc.ac.uk/).	%
Joint density	*lJDe*	Mean value of the join density map based on the manually-digitised joints (section 3.7.1) using the ArcGIS *Line Density* tool at 0.25 m resolution and 0.25 m search radius.	joints m^{-2}
B)	Erosion variables:		
Total area	*lArea*	The number of erosion pixels multiplied by the pixel size (6.25×10^{-2} m^2).	m^2
Total volume	*lVol*	The sum of all detached volumes.	m^3
Mean thickness	*lMean*	*lVol* / *lArea*	m
Erosion rate	*lEro*	1,000 × *lVol* (m^3) / (number of data pixels [1-16] × 6.25×10^{-2} m^2) / 2.62 yr	mm yr^{-1}

This page is intentionally left blank

1. Introduction

1.1. Context and rationale

Shore platforms are sub-horizontal intertidal rock surfaces located at the foot of coastal cliffs; they are wholly erosional landforms (Trenhaile, 1987; Sunamura, 1992). They play a pivotal role in coastline evolution as they control wave energy dissipation, energy delivery to the cliffs and enable or inhibit sediment transport (Stephenson and Kirk, 2000a; Dickson et al., 2013; Ogawa et al., 2015; Poate et al., 2018). Equally, their morphology changes due to erosion by waves and weathering (Stephenson, 2000; Naylor et al., 2010; Moses, 2014).

Most of our knowledge about shore platform erosion comes from morphological evidence such as detached boulders and fresh exposures (Stephenson and Naylor, 2011; Knight and Burningham, 2011; Cullen and Bourke, 2018), and point measurements of micro-erosion, which capture grain-scale changes such as those arising from abrasion (Robinson, 1976, 1977a; Trudgill, 1976 a,b; Kirk, 1977; Stephenson and Kirk, 1998, 2001). Historical maps and aerial photographs also allow the landward retreat of steps to be measured (Cruslock et al., 2010; Dornbusch and Robinson, 2011). In coastline evolution models, platform morphology is conventionally simplified to either a straight inclined surface or a set of sections (Figure 1.1). Foreshore erosion is treated implicitly and represented either by a single value adjusted to fit a model or is derived from monitoring, or as a set of elevation-dependent values which links erosion to wave efficiency (Trenhaile, 1983; 2000; Walkden and Hall, 2005; Kline et al., 2014; Limber et al., 2014).

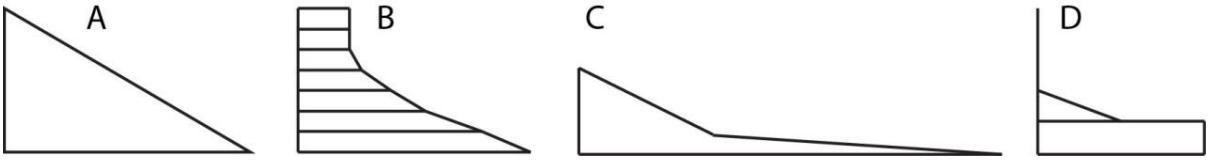


Figure 1.1 Examples of representation of shore platform morphology in coastal evolution models: A) straight inclined surface (Trenhaile, 1983); B) set of sections with equal thickness (Walkden and Hall, 2005); C) two straight inclined sections with different widths and slopes (Kline et al., 2014); D) straight inclined surface and a horizontal bench at the minimum beach level (Limber et al., 2014).

A lot of scientific effort has been made to quantify erosion at the micro-scale and identify the dominating process: wave action or weathering (Trenhaile, 1980; Stephenson, 2000; Taylor, 2003) However, mechanisms of foreshore erosion – understood as a manner of erosion happening (e.g. tensile fracture of the rock) – remain poorly constrained. In consequence, there is gap in understanding and predicting spatial and temporal distribution of erosion events. The advances made

in bedrock river geomorphology and landslide and rockfall studies, notably analysis of the magnitude frequency and 3D shape of detached material, can be adapted to fill this gap (Sklar and Dietrich, 2001; Malamud et al., 2004; Williams et al., 2018).

Abundance of the micro-erosion studies stands in opposition to few attempts to monitor and quantify larger-scale erosion events at the foreshore, such as block removal (Dornbusch and Robinson, 2011; Stephenson and Naylor, 2011). In consequence, it is difficult to assess the relative role of platform down-wearing and step back-wearing, yet this seems pivotal in modelling and reconstructing long-term (centuries to millennia) rocky coast evolution (Matsumoto et al., 2016; Hurst et al., 2017). There exists a need for a multi-scale erosion monitoring in order to understand foreshore dynamics, identify the spatial and temporal scale(s) at which erosion dominates, constrain mechanisms and processes of foreshore erosion which drive long-term coastal evolution, and assess the feasibility of up- and down-scaling measured rates (Naylor et al., 2010; Kennedy et al., 2017).

At present, accuracy of the numerical models of rocky coast evolution is difficult to assess, because of the lack of absolute data on long-term cliff retreat (Trenhaile, 2014). Historical maps are not older than ~150 years and their accuracy is often low (Lim, 2006), while episodic character of cliff failure means that the high-magnitude low-frequency erosion events may be under- or over-represented during the short-term monitoring (Lee et al., 2001). Erosional character of rocky coasts means that they are usually devoid of any datable sediment (Trenhaile, 1987). Exposure dating using cosmogenic isotope concentrations has been recently used to reconstruct past cliff retreat rates (Regard et al., 2012; Hurst et al., 2016, 2017). Further development of the method may allow variability of the past cliff retreat rates and long-term dynamics of the coastal steps to be assessed. Ultimately, exposure dating can help validate existing models of long-term coastline evolution (Kline et al., 2014; Limber et al., 2014; Matsumoto et al., 2016).

1.2. Aims and objectives

This thesis aims to address the gaps in our understanding of shore platform erosion at spatial and temporal scales appropriate to the processes of erosion and the timescales over which they operate. The overall aim of the project is to create a model of multi-scale platform erosion which will allow improved reconstructions and predictions of the evolution of rocky coastlines. The study was conducted along a 22 km stretch of the macro-tidal North Yorkshire coast (UK) built in relatively hard sedimentary rocks. The results of the study are intended to enhance our understanding of erosional mechanisms at the foreshore and provide a set of tools to monitor and model bedrock erosion which can be applied at other sites. Notably, the study focuses on shore platform down-wearing and step erosion, not including local cliff retreat whose dynamics have been presented elsewhere (Lim, 2006; Lim et al., 2005, 2009; Rosser et al., 2007, 2013), and processes preceding

erosion such as swelling (Stephenson and Kirk, 2001), mechanical weathering (Mottershead, 1989; Mayaud et al., 2014) and biological activity (Naylor et al., 2012; Coombes, 2014). Three research questions (RQs) and corresponding objectives (Os) have been set to achieve this goal:

RQ1: What is the dominant mechanism of shore platform erosion?

O1: To answer this question, I aim to: precisely reconstruct platform topography at the micro- (10^{-3} – 10^{-2} m) and macro- (10^{-1} – 10^{0} m) scales; create an inventory of detachments; identify mechanisms of erosion by analysing the size and shape distributions of detachments; and, constrain controls on spatio-temporal patterns of foreshore erosion through analysis of erosion on the basis of equal-size zones.

RQ2: What is the relative contribution of the down-wearing and step back-wearing to shore platform erosion?

O2: Here I will use a high-resolution LiDAR dataset to predict spatially-dependent probability of detachment and magnitude of erosion at the foreshore scale and to compare it with the results of the micro-erosion monitoring in order to understand 1) whether erosion rates can be up- and down-scaled over time and spatially, 2) at which scale the processes dominate erosion and 3) how erosion rates vary at the parts of the foreshore with and without steps, understood as the abrupt slope changes at the limits of exposed rock beds.

RQ3: Does the multi-scale assessment of shore platform erosion enhance our ability to understand millennial-scale coastal evolution?

O3: I will reconstruct dynamics of cliff retreat in the Holocene from cosmogenic ^{10}Be concentrations by applying the empirical foreshore erosion model developed in this study and compare it with existing long-term models of shore platform erosion.

1.3. Novelty of the study

A method to monitor platform down-wearing at the millimetre scale using Structure-from-Motion (SfM) is developed for use over a series of 0.5×0.5 m sites. SfM has only recently been used to perform change detection, in particular at the micro-scale, because of a number of parameters difficult to control which influence its performance (Rock et al., 2011; Nitsche et al., 2013; Gonçalves and Henriques, 2015; Cook, 2017). Here, a method is developed to minimise the influence of factors such as variable lighting conditions, surface reflectivity, and changing camera positions between

surveys. Applying SfM overcomes the multiple limitations of micro-erosion meters (MEMs), such as the need for fixed benchmarks, lack of spatial representability, inability to understand mechanisms of erosion from point measurements, limited vertical reach of the instrument and need to study shore platforms on flat, unjointed rock surfaces (Viles and Trudgill, 1984; Trenhaile, 1987; 2002; Moses, 2014; Turowski and Cook, 2017). DEM-based techniques allow the extraction of single detachments, and permit adaptations of rockfall/landslide event inventory analyses of detachment morphology, and their spatial and temporal distribution (Sneed and Folk, 1958; Malamud et al., 2004; Rosser et al., 2007). These analyses allow the mechanisms of erosion and controls upon its rate to be determined in order to predict erosion rates more widely, which remain problematic with MEM data only.

An annual high-resolution (average 45.22 points m^{-2}) airborne LiDAR dataset is used to systematically analyse erosion at the sub-metre scale across the shore platforms in order to identify and quantify step back-wearing and surface down-wearing, and to assess the relationship and relative role of millimetre and sub-metre scale erosion in platform evolution. This multi-scale understanding of platform erosion is intended to feed into numerical exploratory models of coastline evolution (e.g. Kline et al., 2014; Limber et al., 2014; Matsumoto et al., 2016) and, hence, improve our understanding of long-term coastal dynamics. Here, it is used to reconstruct cliff retreat in the Holocene from cosmogenic ^{10}Be concentrations. The results allow the better representation of the platform erosion coefficient, S_{er}, in improving approaches to modelling exposure ages from cosmogenic ^{10}Be concentrations (Hurst et al., 2017).

Finally, the study bridges the gap between short-term monitoring of erosion and long-term landscape evolution by combining results of the SfM-based micro-erosion study with the cosmogenic ^{10}Be concentrations to reason about cliff retreat rates in the Holocene. It contributes to the application of cosmogenic isotope dating in reconstructing exposure dates by providing a procedure to purify quartz grains of 53-106 μm, one order of magnitude smaller than has previously been achieved. This implies that in the future the technique can be used at locations deemed not feasible due to fine grained rock types. Moreover, the sampling strategy used permits the investigation of not only the average Holocene cliff retreat rates, as in previous studies (Regard et al., 2012; Hurst et al., 2016), but also the short-term (10^1 – 10^2 yr) changes in the rates and dynamics of the coastal steps. The study shows that the cliff backing the Hartle Loup platform has been retreating at a steady rate of 0.05 m yr^{-1} for the last 6 kyr, while the steps located at the seaward portion of the platform have been retreating at the average rate of 0.01 m yr^{-1}.

1.4. Structure of the thesis

The thesis is organised into ten chapters. Bedrock erosion monitoring is organised into four chapters describing separately the methods and then results of the micro- and macro-scale studies. As

the methods development for each was considerable, the decision to split this from the results is intended to provide sufficient explanation and detail should others wish to conduct similar studies. The final chapter of substantive result focusses upon the reconstruction of past cliff dynamics using cosmogenic isotope concentrations, which includes consideration of the related literature, methods and the novel results generated here. In detail, the chapters include:

Chapter 1: Introduction

This chapter puts the project into the context stating the aims and objectives of the study and advocating its original contribution to science.

Chapter 2: Current understanding of shore platform erosion

This chapter summarises the present understanding of the morphology and dynamics of shore platforms by describing both theoretical and empirical considerations of erosion. It highlights issues related to the current lack of techniques available to allow us to constrain the mechanisms of erosion, which results in an inability to accurately reconstruct past cliff dynamics using cosmogenic isotope concentrations and to project future shoreline change. Recent progress in bedrock river geomorphology is referred to to demonstrate the need for the process-based approach to erosion of foreshores. Finally, the techniques to detect change, in particular Structure-from-Motion (SfM) photogrammetry, are described and the methods to analyse erosion on the basis of the detachment inventory and zones of equal sizes are introduced.

Chapter 3: Geomorphology of the shore platforms in North Yorkshire, UK

This chapter provides the context, geology, Quaternary history, marine conditions and current knowledge about coastal erosion in the selected research area: the coast of the North Yorkshire Moors National Park, UK. It describes the mapping of coastal geomorphology which is used in subsequent sections, in addition to a detailed GIS- and field-based description of the Hartle Loup shore platform, which is the area of the small-scale erosion monitoring (Chapter 5) and the exposure dating (Chapter 8). An initial analysis is presented, the findings of which have been published (Appendix 1), which intends to directly link platform morphology to geology, as expressed via measurements of rock hardness and joint density. Results of the study further support the need to understand mechanisms of erosion at the adequate spatial and temporal scales.

Chapter 4: Developing a new method to monitor bedrock micro-erosion

This chapter describes the set-up to monitor, and the procedure to quantify, bedrock micro-erosion (10^{-3} – 10^{-2} m) using SfM. Quantification of erosion rates is based on DEMs of Difference (DoDs). The Level of Detection (*LoD*) is found and detachments are separated. The detachment inventory is used to analyse the size and 3D shape distribution of detachments, while spatial analysis is performed in order to identify controls on erosion rates in order to be able to predict erosion more widely.

Chapter 5: Mechanisms and controls of shore platform down-wearing

This chapter provides the results of the change detection at the small-scale. The average down-wearing rate at the Hartle Loup platform was 0.528 mm yr^{-1} in 2016-2017, but varied between 0.101 and 1.192 mm yr^{-1} between the 15 monitoring sites, and between 0.576 and 0.497 mm yr^{-1} between the periods of April – October and October – April. The volume frequency and 3D shape distribution of the detachments suggest that erosion happens predominantly via detachment of platelets. Erosion rates depend on the location on the shore platform with more erosion happening closer to the cliff, and on the tidal duration with more erosion happening where the tide cycles more frequently. The size distribution of detachments is controlled by the surface micro-topography. The results suggest that platform erosion can be modelled and predicted statistically, and used to model coastal evolution and to assess shore platform exposure ages (Chapter 8).

Chapter 6: Developing a new method to monitor bedrock macro-erosion

This chapter describes the method to extract shore platform erosion at the macro-scale (10^{-1} – 10^{0} m) on the basis of the LiDAR dataset. The approach is similar to that of Chapter 4, with analyses based on DoDs. The distribution of detachment sizes and shapes helps identify mechanisms of erosion. The foreshore is divided into 1 m^2 grid cells which are characterised by a number of parameters including detached volume, location across the platform, topography, tidal characteristics and joint density in order to use a systematic high-resolution empirical dataset to identify controls on the spatial distribution of erosion rates.

Chapter 7: Bedrock erosion across the shore platform

This chapter provides the results of the change detection at the sub-metre scale. 2.6 yr monitoring of foreshore erosion resulted in detection of 2.15×10^{6} detachments of the total 2.77×10^{4} m^3 bedrock from the 3.15×10^{6} m^2 shore platforms in North Yorkshire, which is equivalent to a down-wearing rate of 3.45 mm yr^{-1}. The erosion rate calculated on the basis of 1 m^2 grid cells is of 0.01 mm yr^{-1}. The mean lowering rates of the platform sections containing steps are of 0.04 mm yr^{-1} while of

those with no steps – of 0.01 mm yr^{-1}. Erosion rates could not be predicted on the cell-by-cell basis, but when the cells are collapsed into a single across-shore profile, a clear trend can be seen whereby most erosion occurs at 10-18 m from the cliff and the probability of erosion gradually decreases seawards.

Chapter 8: The importance of shore platform erosion in reconstructing past cliff retreat using cosmogenic ^{10}Be concentrations

This chapter describes the procedure used to calculate cosmogenic ^{10}Be concentrations from 23 sandstone samples collected across the Hartle Loup platform. A model to calculate exposure ages from ^{10}Be concentrations is developed that includes the topographic and seawater shielding, and the platform erosion scalar. The sensitivity of the model to the adopted assumptions is assessed. The results suggest that the cliff has been retreating at the constant rate of 0.05 m yr^{-1}, exposing the entire 300 m wide shore platform in the last 6 kyr. The long-term down-wearing of a site on the platform is a function of changing cross-shore location and tidal duration distribution. This implies that it is pivotal to understand mechanisms and controls on foreshore erosion in order to model the long-term coastline evolution. Over long timescales (centuries to millennia), erosion rates do not average out to fit the geometry-based 'equilibrium' models (Sunamura, 1992; Trenhaile, 1983; 2000).

Chapter 9: Discussion

This chapter provides direct answers to the three research questions (RQs) defined in section 1.2. The results of Chapters 5, 7 and 8 are compared with existing studies and the gaps which the study addresses are highlighted.

Chapter 10: Conclusions

This chapter summarises the main finding of the study and provides suggestions for future research directions.

2. Current understanding of shore platform erosion

2.1. Introduction

This chapter outlines the current understanding of shore platform morphology and dynamics. It presents conceptual understanding of long-term (10^2 – 10^3 yr) foreshore evolution, inclusion of platform erosion into numerical models of rocky coast evolution and existing techniques to monitor foreshore erosion. Recent progress in other disciplines to measure rock resistance, monitor bedrock erosion and analyse detachments is outlined. The overall aim of the chapter is to provide a context for this project, identify knowledge gaps and introduce the methodological basis for the approach developed in this research.

The morphology and erosion of shore platforms is a key component of the rocky coast evolution as these landforms control wave transformation at the foreshore, wave energy at the cliff toe and sediment redistribution (Dickson et al., 2013; Ogawa et al., 2015; Poate et al., 2018). They are included in conceptual (Johnson, 1919; Flemming, 1965; Trenhaile, 1974; Sunamura, 1992) and numerical exploratory (Trenhaile, 1983; 2000; Walkden and Hall, 2005; Kline et al., 2014; Limber et al., 2014) models of coastal evolution. However, the mechanisms of erosion and controls on its spatial distribution are poorly constrained and quantified, which means that the accuracy of existing models is uncertain and it is difficult to model future coastal erosion under predicted sea-level and storminess changes (Slott et al., 2006; IPCC, 2013) and reconstruct past cliff retreat rates using cosmogenic isotope concentrations (Choi et al., 2012; Regard et al., 2012; Hurst et al., 2016; 2017).

This uncertainty of model outcomes is in part due to erosion monitoring techniques used in foreshore studies, which rely on either point measurements at the 10^{-4} – 10^{-3} m scale using micro-erosion meters (MEMs) (Robinson, 1976; 1977a; Stephenson and Kirk, 1998; 2001) or coarse resolution (10^0 m) mapping using cartographic data (Dornbusch and Robinson, 2011). Recent progress in topographic reconstructions based on point clouds: Structure-from-Motion (SfM) photogrammetry and high-resolution LiDAR has a potential to increase spatial representativeness of small-scale (10^{-3} – 10^{-2} m) erosion monitoring and bridge the spatial gap between the MEM- and cartography-based studies (10^0 m) by considering the scale of 10^{-2} – 10^{-1} m (Cook, 2017; Turowski and Cook, 2017). Detachment analyses developed in rockfall/landslide studies, such as analyses of magnitude frequency and 3D shape of detachments, allow the mechanisms of erosion to be identified (Malamud et al., 2004; Guzetti et al., 2009; Williams et al., 2018). Characterising the spatial distribution of erosion on the basis of cells of equal size enables the identification of the controls on the spatial distribution of erosion, and as a consequence, the prediction of erosion outside the studied area and/or timescale (Kritikos et al., 2015; Parker et al., 2015).

The information from the chapter is used throughout the thesis. The methods to monitor foreshore erosion (Chapters 4 and 6) are based on recent progress in topographic reconstructions (section 2.5.1). The size and shape distribution of detachments and the spatial analysis and predictions (Chapters 5 and 7) are based on the rockfall/landslide literature (section 2.5.2). Different theoretical models of platform evolution (section 2.2) form a basis for modelling exposure ages from cosmogenic ^{10}Be concentrations (Chapter 8). In Chapter 9 the results of this project are compared with our current understanding of foreshore erosion at the range of spatial and temporal scales (section 2.3).

2.2. General morphology and evolution of shore platforms

2.2.1. Shore platform macro-morphology

Shore platforms are erosional landforms located in the intertidal zone (Trenhaile, 1987; Sunamura, 1992). Their key morphometric characteristics are: width, gradient (slope), elevation (height) and elevation of the cliff/platform junction (cliff toe). The platforms stretch horizontally between the seaward edge and the cliff/platform junction, and vertically between the platform base and the elevation of the cliff/platform junction (Figure 2.1).

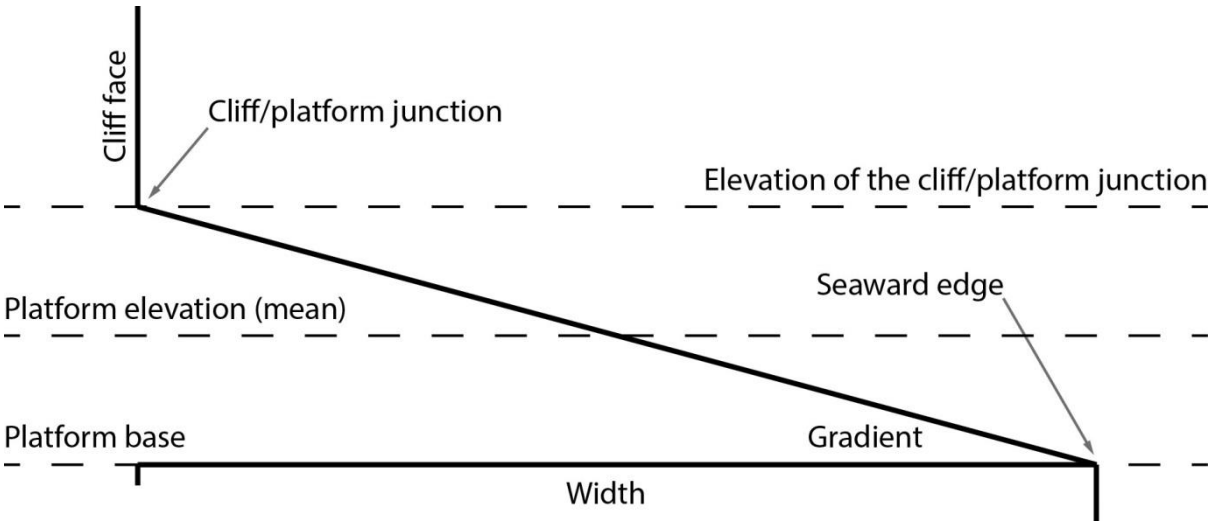


Figure 2.1 Key morphometric characteristics of shore platforms.

2.2.2. Controls on the shore platform macro-morphology

The four measurable characteristics of platforms (Figure 2.1) vary between and within platforms. Previous research has considered the controls on platform morphology in terms of the relationships between morphology and 1) geology: lithology and structure (Wright, 1970; Trenhaile, 1972; 1974; 1978; 1980; 1987; Williams, 1986; Stephenson, 2000; Davies et al., 2006; Kennedy and Dickson, 2006; Thornton and Stephenson, 2006); 2) alongshore coastline amplitude i.e. the location in

the headland/bay sequence (So, 1965; Bird and Dent, 1966; Wood, 1968; Trenhaile, 1972; 1987; Kirk, 1977); 3) tidal regime (Trenhaile, 1978; 1980; 2000); and 4) wave intensity (Trenhaile, 1978; 1980; Kennedy, 2010). These studies have been based on theoretical considerations, qualitative observations and low-resolution quantitative studies consisting of manual topographic surveying along coastal cross-sections. In general, more resistant rocks and low wave-energy locations associate with narrower, steeper and higher shore platforms and more elevated cliff/platform junctions (Table 2.1).

Table 2.1 Relationships between shore platform morphology and controlling factors.

Morphologic element	Controlling factor	Relation	Reference
Platform elevation	Rock strength	The harder rock, the higher platform	Stephenson, 2000; Thornton and Stephenson, 2006
	Joint density	The lower joint density, the higher platform	Kennedy and Dickson, 2006
	Exposure to wave attack	Higher platforms at headlands than in bays	So, 1965; Kirk, 1977
Platform gradient	Rock strength	The harder rock, the steeper platform	Williams, 1986; Trenhaile, 1987
	Exposure to wave attack	Steeper platforms at headlands than in bays	Wood, 1968; Trenhaile, 1972 (So, 1965: the opposite)
	Tidal range	The greater tidal range, the steeper platform	Trenhaile, 1978; 1980
	Wave intensity	The more intensive waves, the flatter platform	Trenhaile, 1980
	Cliff height	The higher cliff, the steeper platform	Edwards, 1941
Platform width	Rock strength	The harder rock, the narrower platform	Davies et al., 2006
	Rock layer dip and strike	Wider platforms when either gently dipping and strike parallel to the cliff or steeply dipping and perpendicular strike	Trenhaile, 1978
	Tidal range	The greater tidal range, the wider platform	Trenhaile, 2000
	Exposure to wave attack	Wider platforms at headlands than in bays	So, 1965; Wood, 1968; Trenhaile, 1987 (Bird and Dent, 1966; Kirk, 1977: the opposite)
	Wave intensity	The more intensive waves, the wider platform	Trenhaile, 1978 (Kennedy, 2010: controversial)
	Cliff height	The higher cliff, the narrower platform	Edwards, 1941; Trenhaile, 1980
Elevation of the cliff/platform junction	Rock strength	The harder rock, the higher junction	Wright, 1970; Trenhaile, 1972; 1974; 1978; 1980
	Exposure to wave attack	Higher junction at headlands than in bays	So, 1965 (Wood, 1968: disagreed)

2.2.3. Theoretical consideration of shore platform evolution

Numerous conceptual and geometry-based models on cross-shore evolution of a planar sloping platform have been formulated (e.g. Johnson, 1919; Challinor, 1949; Flemming, 1965; Trenhaile, 1974; Sunamura, 1992). They form the basis for numerical exploratory models of rocky coast evolution (Trenhaile, 1983; Limber et al., 2014) and models to reconstruct past cliff retreat using cosmogenic isotope concentrations (Choi et al., 2012; Regard et al., 2012; Hurst et al., 2016; 2017). Based on the literature, the models which assume no change in the elevation of the platform

base have been grouped into three types (Figure 2.2). Chapter 8 explores how sensitive our understanding of rocky coast evolution is dependent on which model we accept, which points out the need to understand underlying mechanisms rather than relying on geometry-based 'equilibrium' models.

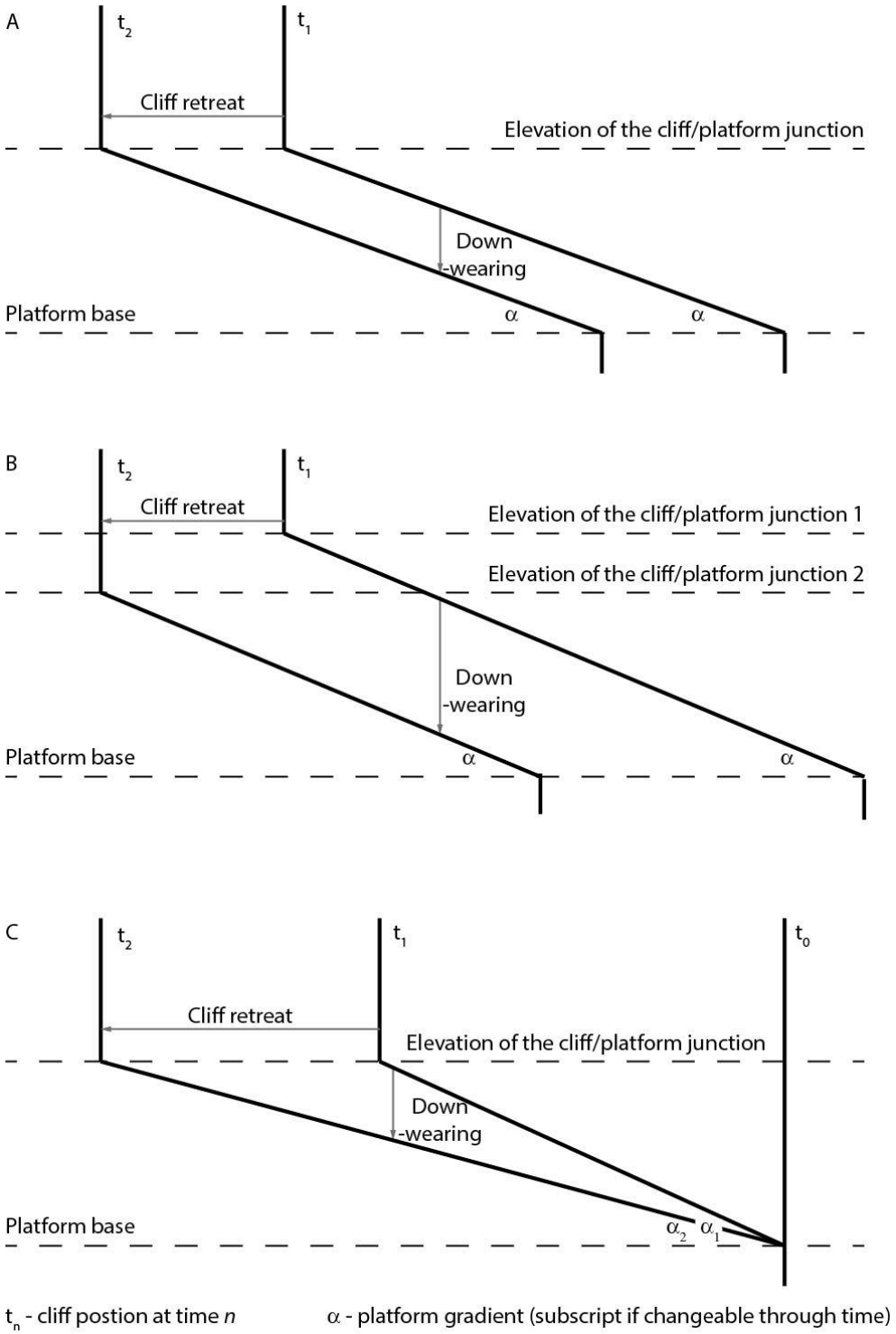


Figure 2.2 Simple geometrical models of the shore platform evolution: A) the parallel coastal retreat, B) the down-wearing is not proportional to the cliff retreat, C) the shore platform widening with the stable seaward edge.

In the first model, once a coast reaches its equilibrium shape, the entire profile migrates landwards (see e.g. Challinor, 1949). Platform down-wearing proceeds proportionally to cliff retreat and can be expressed as (Trenhaile, 1974):

$$w = r\ tan\alpha \qquad \text{Eq 2.1}$$

where w (m yr^{-1}) is the platform down-wearing rate, r (m yr^{-1}) is the cliff retreat rate and α (°) is the platform gradient (Figure 2.2A). The second model assumes that vertical erosion happens at a rate that is not proportional to that of cliff retreat. As the platform gradient remains unchanged, the elevation of the cliff/platform junction changes in time (Figure 2.2B). The third model assumes that the seaward edge does not change its horizontal position as it is located below the wave base (see Johnson, 1919; Flemming, 1965; Sunamura, 1992). Once the sea stabilises at a given level at time t_0, the waves start operating on (eroding) bedrock and a platform develops. The elevations of the platform base and the cliff/platform junction are here dictated by tidal range and remain at the same level through time. The evolving platform widens and flattens. Assuming that the cliff retreats at a constant rate, the gradient α at time n can be calculated as:

$$\alpha_n = \text{atan}\frac{ph}{t \times r} \qquad \text{Eq 2.2}$$

where ph (m) is the vertical range of the platform (the elevation of the cliff/platform junction minus the elevation of the platform base), t (yr) is the time from the start of the cliff retreat, and r (m yr^{-1}) is the cliff retreat rate (Figure 2.2C).

2.2.4. Shore platform erosion in existing numerical models of coastal evolution

Although shore platforms have been included in coastal evolution models (Trenhaile, 1983; 2000; Kline et al., 2014; Limber et al., 2014), their morphology and erosion have inevitably been simplified (Table 2.2). The morphology has been represented by a straight inclined surface or a set of discrete sections (Figure 1.1). Foreshore erosion has been represented either by a single value adjusted to fit the model or derived from monitoring, or a set of values which links it to wave efficiency (Trenhaile, 1983; 2000; Walkden and Hall, 2005; Kline et al., 2014; Limber et al., 2014). The lack of a more refined representation of platform erosion in the models may be a reflection of the reliance upon the geometry-based equilibrium models (section 2.2.3) and/or the poor understanding of the mechanisms which results from limitations of the techniques used in shore platform studies (section 2.3). At present, the lack of systematic quantification of erosion, and the poor understanding of underlying mechanisms and constraint of controls on the spatial distribution of erosion mean that we

are not able to assess how accurate such models are in terms of capturing key patterns and controls on foreshore erosion.

Table 2.2 Numerical models on the evolution of rocky coast and their consideration of the rock resistance, and foreshore morphology and erosion.

Model	Type	Scale	Purpose	Rock resistance	Platform shape	Foreshore erosion
Trenhaile, 1983	Cross-shore, mathematical	10^0-10^2 m, no timescale	To explore effects of wave and tidal regimes on shore platform development at platform end points	Calibrated from the relationship between wave energy and erosion; no physical meaning	A straight between the platform end points	Entirely depends on the back-wearing rate of the platform end points
Trenhaile, 1983; 2000	Cross-shore, mathematical	10^0-10^2 m, no timescale	To explore effects of wave and tidal regimes on shore platform development	Calibrated from the relationship between wave energy and erosion; no physical meaning	Composed of the horizontal layers with pre-defined thickness	Results from the back-wearing of platform sections
Walkden and Hall, 2005 (SCAPE)	2.5D (series of cross-profiles), predictive, process-based	10^1-10^3 m, 10^1-10^3 yr	To explore dynamics of soft rock coasts and to predict future behaviour of a specific study site	Abstract; $R = 1.27\times10^6$ $m^{9/4}$ $s^{3/2}$ calibrated by comparing predictions of recession to observations	Platform development is in the scope of model; it widens and flattens in time.	Erosion of the platform via section back-wearing (easy re-calculation to down-wearing); it entirely depends on the location within the profile relative to the wave forcing.
Limber et al., 2014	Alongshore, exploratory, numerical	10^1-10^3 m, 10^2-10^3 yr	To link the length scales and the physical properties with the cross-shore headland/bay amplitude	Abstract; hard and soft rock; properties implicitly included in the dimensionless sea cliff height and a constant relating wave power to erosion rates	It is composed of two sections: a slope on which a beach rests and a horizontal platform at the minimum beach level	The slope is assumed to erode parallel to the cliff retreat (constant shape), horizontal platform widens as the coastline recedes.
Kline et al., 2014	Cross-shore, exploratory, numerical	10^0-10^1 m, 10^1-10^2 yr	To explore the role of sediments, cliff failure and comminution on cliff retreat	Constant *UCS* = 50 MPa	It is composed of two sectors with different widths and slopes; total width = 1500 m	Exponential decay in the rate from the water surface; it is included to regulate the vertical elevation of the cliff toe
Matsumoto et al., 2016	Cross-shore, exploratory, numerical	10^0-10^1 m, 10^2-10^3 yr	To explore the long-term evolution of shore platforms	Abstract; soft, intermediate and hard with values one order of magnitude apart; tidal-dependent weathering efficacy constant.	It is the result of model runs, characterised by the width, height and slope; input: a vertical cliff.	Explored with the model; happens if *Fw* > *Fr*

2.3. Monitoring and modelling shore platform erosion

Although foreshore erosion needs to be modelled at the timescale relevant to coastal cross-section development (centuries to millennia), it can be directly measured at finer scales. This includes (sub)mm-scale monthly to annual monitoring of platform down-wearing using micro-erosion meters (MEMs) and metre-scale decadal to ~150 yr measurements of step back-wearing using historical

maps and aerial photographs. This section discusses the complexity of the foreshore environment and describes our current understanding of erosion processes based on monitoring.

2.3.1. Complex nature of shore platform morphology and erosion

The shape of shore platforms is much more complex than presented in Figure 2.1. It is often hard to clearly localise the cliff/platform junction as the boundary between the two landforms may be gradual or a niche resulting from the direct wave action carved into the cliff toe (Sunamura, 1992). Vegetation, fauna and sediments are present on platform surface (Coombes, 2014; Moses, 2014). The latter usually occur in bays in the form of the pocket beaches located at the cliff toe, as debris under cliffs and boulders. Some boulders are loose while others are immobile, cemented to the rock surface or formed *in situ* by the selective erosion of the rock mass around them. Boulders may protect the platform surface from erosion (Moses, 2014; Wilson and Lavé, 2014) or abrade it (Cullen and Bourke, 2018) (Figure 2.3A). This suggests that the existing models on platform evolution (sections 2.2.3 and 2.2.4) may be too simplistic and a more explicit understanding of processes/mechanisms and controls upon them is critical in order to model coastal evolution.

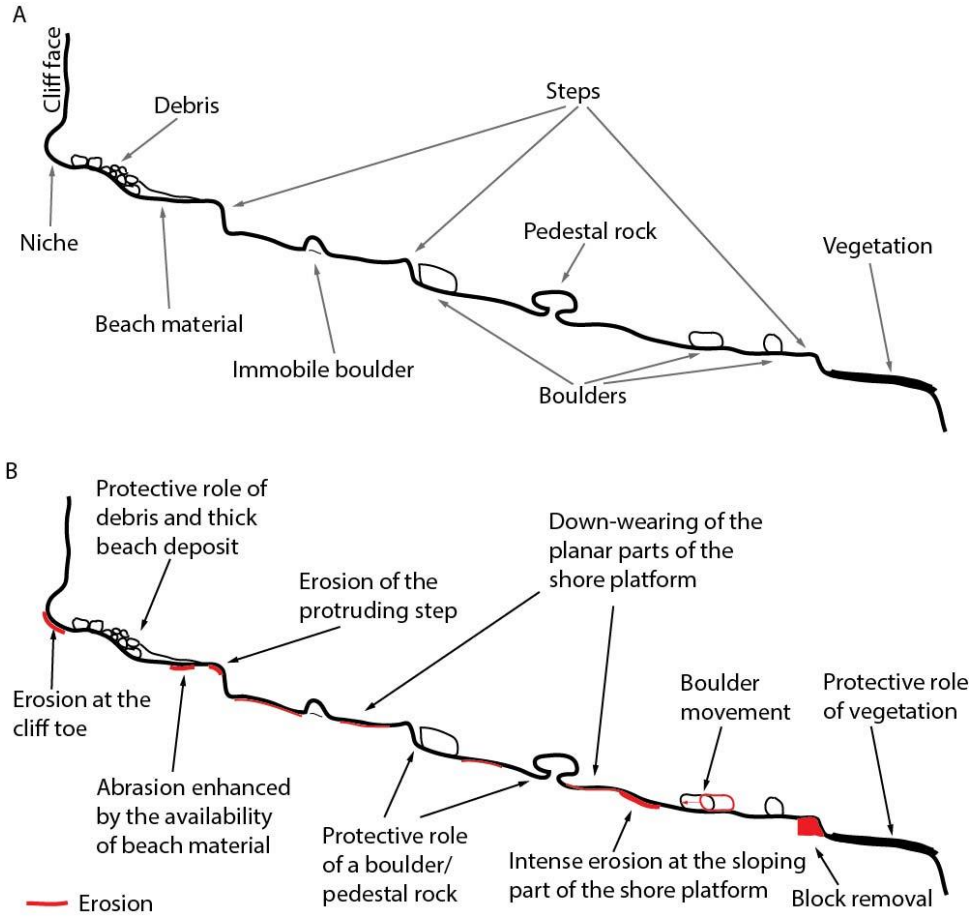


Figure 2.3 Shore platform morphology and erosion: A) macro-scale elements of shore platforms, B) controls on the efficiency of platform erosion processes.

Shore platforms evolve via cliff retreat (platform widening), seaward edge retreat (platform narrowing), down-wearing and step back-wearing which is also referred to as bed stripping and block removal (Stephenson, 2000). However, the complexity of platform morphology suggests that erosion rates and nature, including the size and shape distribution of detachments varies spatially (Figure 2.3B). For instance, sloping sections of the platform may experience more intense erosion than the planar parts due to wave energy concentration at the inclined surfaces (Moses and Robinson, 2011). Vegetation, boulders, debris and thick beach cover may protect the platform surface from erosion, while a thin beach deposit may increase the efficiency of abrasion (Robinson, 1977 a,b; Kline et al., 2014). Existing empirical studies on foreshore erosion (section 2.3.2) attempt to find a spatial pattern in erosion rates, but they may be insufficient to account for the morphological complexity of the foreshore (Figure 2.3).

2.3.2. Platform dynamics at the micro-scale: down-wearing

A micro-erosion meter (MEM) is an instrument designed by High and Hanna (1970) to measure bedrock erosion. It consists of a triangular base and three legs which are placed on bolts fixed to the rock surface. It allows one to take three readings – one at each bolt. The instrument was modified by Trudgill et al. (1981) as the traversing micro-erosion meter (TMEM) which allows up to 170 individual readings from a surface area of 4.50×10^{-3} m^2 (Stephenson and Finlayson, 2009). Both instruments have been widely used in rocky coast geomorphology to quantify platform down-wearing (Robinson, 1976; 1977 a,b,c; Taylor, 2003), assess the relative role of wave action and weathering on foreshore erosion (Robinson, 1977b; Spencer, 1981; 1985 a,b; Stephenson and Kirk, 1998; 2001) and support modelling of platform evolution (Trenhaile, 2001).

The global mean shore platform down-wearing rate is 1.486 mm yr^{-1} (Stephenson and Finlayson, 2009) or 1.148 mm yr^{-1} (Dasgupta, 2010) with the inconsistent values obtained in the two studies due to the use of different datasets. Collation of the results of individual published studies presented in Table 2.3 shows that the average down-wearing rates vary spatially from 0 to 17.5 mm yr^{-1} with the lowest rates recorded where igneous rocks are exposed at the platform surface and the highest rates for clay, chalk and mudstone.

*Table 2.3 Shore platform down-wearing reported in literature; referenced by *Dornbusch et al. (2006), **Stephenson and Finlayson (2009).*

Reference	Location	Rock type	Instrument	Number of sites	Monitoring period (yr)	Down-wearing rate (mm yr^{-1})
Trudgill, 1976 a,b**	Aldabra, Seychelles	Limestone	MEM	NoData	2	1.01-1.25
Kirk, 1977	Kaikoura, New Zealand	Mudstone, limestone	MEM	31	2	1.53 ± 1.45

Reference	Location	Rock type	Instrument	Number of sites	Monitoring period (yr)	Down-wearing rate (mm yr^{-1})
Robinson, 1977a	North Yorkshire, UK	Shale	MEM	70	2	3.21 ± 4.76
Torunski, 1979**	N Adriatic	Limestone	MEM	NoData	1	0.57
Spencer, 1981	Grand Cayman, Caribbean	Limestone	TMEM	3	1.25	0.38
Gill and Lang, 1983	Victoria, Australia	Greywacke	MEM	50	2	0.37
Viles and Trudgill, 1984	Aldabra, Seychelles	Limestone	MEM	27	2	1.92 ± 2.14
	Aldabra, Seychelles	Limestone	MEM	24	11	1.55 ± 0.93
Spencer, 1985a	Grand Cayman, Caribbean	Limestone	TMEM	15	0.66	1.00 ± 1.17
Spencer, 1985b	Grand Cayman, Caribbean	Limestone	TMEM	37	1.25	0.09-1.77
Ellis, 1986*	Sussex, UK	Chalk	MEM	44	3	2.62
Shakesby and Walsh, 1986**	Gower, Wales	Limestone	MEM	NoData	1	0.02-0.14
Mottershead, 1989	Devon, UK	Green schist	MEM	3	7	0.625
Stephenson and Kirk, 1996	Kaikoura, New Zealand	Mudstone, limestone	MEM	15	20	1.43 ± 0.50
Stephenson and Kirk, 1998	Kaikoura, New Zealand	Mudstone, limestone	TMEM	56	2.2	1.13 ± 0.61
Andrews and Williams, 2000*	Sussex, UK	Chalk	TMEM	70	NoData	1.88
Neves et al., 2001	Estremadura, Portugal	Limestone	TMEM	NoData	0.26	0.15
Andrade et al., 2002	Algarve, Portugal	Shale	MEM	NoData	2	0.20-2.80
	Algarve, Portugal	Greywacke	MEM	NoData	2	0.30-3.40
	Estremadura, Portugal	Marl	MEM	NoData	2	2.00-4.00
	Estremadura, Portugal	Limestone	MEM	NoData	2	0.04-1.40
Taylor, 2003	Robinson's Bay Point, New Zealand	Basalt	TMEM	14	2.6	0.27 ± 0.24
	Kaikoura, New Zealand	Mudstone	TMEM	20	6.8-6.9	1.41 ± 1.18
	Kaikoura, New Zealand	Limestone	TMEM	8	6.8	1.12 ± 1.38
	Raramai Arch, New Zealand	Greywacke	TMEM	14	2.5	0.80 ± 1.02
	Lake Waikaremoana, New Zealand	Mudstone	TMEM	9	3.1	14.76 ± 13.54
Stephenson and Thornton, 2005	Victoria, Australia	Greywacke	TMEM	10	3.4	0.30 ± 0.27
Cucchi et al., 2006	W Istria & Gulf of Trieste, Italy	Limestone	MEM	24	1.5	0.13
Dornbusch et al., 2006	Sussex, UK	Chalk	Historical maps	n/a	28	7.00
Foote et al., 2006**	The English Channel, UK & France	Chalk	MEM	NoData	3	3.65

Reference	Location	Rock type	Instrument	Number of sites	Monitoring period (yr)	Down-wearing rate (mm yr^{-1})
Swantesson et al., 2006	Fårö, Sweden	Granite, ortho-gneiss, dolerite	MEM	NoData	3	0-0.93
	Mallorca, Spain	Limestone, dolomite	MEM	NoData	3	0.003-0.94
	Fårö, Sweden	Granite, ortho-gneiss, dolerite	Laser scanner	15	3	0.004
	Mallorca, Spain	Limestone, dolomite	Laser scanner	15	3	0.09
Blanco-Chao et al., 2007	Galicia, Spain	Granite	TMEM	12	1	0.13-1.80
Charman et al., 2007	Kent, UK	Clay	Traversing erosion beam	6	1	17.50
Porter and Trenhaile, 2007	Bay of Fundy, Canada	Sandstone	TMEM	7	10 days	0.94 ± 1.20
		Basalt	TMEM	7	10 days	0.20 ± 0.63
		Argillite	TMEM	8	10 days	0.10 ± 0.33
Porter et al., 2010b	Bay of Fundy, Canada	Sandstone	TMEM	57	3-6	1.25
		Basalt	TMEM	51	3-6	0.72
Stephenson et al., 2010	Kaikoura, New Zealand	Mudstone, limestone	TMEM	52	2.1	1.10 ± 1.61
			TMEM	46	10.1	0.90 ± 0.82
			MEM	12	30	1.09 ± 0.44
Moura et al., 2011	Algarve, Portugal	Limestone, siltstone	TMEM	4	1	0.69 ± 0.69
Moura et al., 2012	Algarve, Portugal	Limestone	TMEM	4	1.5	1.14 ± 1.26
		Siltstone	TMEM	4	1.5	0.15 ± 0.12
Stephenson et al., 2012	Victorial, Australia	Greywacke	TMEM	45	32	0.31 ± 0.23
Moses et al., 2015	Phang Nga Bay, Thailand	Limestone	MEM	16	10	0.23
Mottershead et al., 2016	Devon, UK	Green schist	MEM	3	33	0.40 ± 0.10
	Kaikoura, New Zealand	Mudstone	MEM	2	17.4	2.94 ± 3.05

Field studies at the small scale (10^{-4} – 10^{-2} m) have identified granular abrasion and detachment of rock fragments as key mechanisms of erosion (Kirk, 1977; Robinson, 1977a; Stephenson and Kirk, 1998; 2001; Blanco-Chao et al., 2007). The latter is facilitated by wetting and drying (Robinson, 1977a; Stephenson and Kirk, 1998), warming and cooling (Coombes, 2014; Mayaud et al., 2014), salt crystallisation in rock lattices (Mottershead, 1989; Stephenson and Kirk, 2001) and biological activity (Andrews and Williams, 2000; Naylor et al., 2012), followed by the removal of fragments via hydraulic drag-and-lift force and grain wedging (Kirk, 1977; Stephenson and Kirk, 2001; Blanco-Chao et al., 2007). The rate of platform down-wearing is controlled by: 1) rock type (Kirk, 1977; Stephenson and Kirk, 1998; Taylor, 2003; Dasgupta, 2010; Moura et al., 2011); 2) elevation with respect to tidal duration distribution (frequency of submergence/emergence transitions), which links erosion rate to direct wave action (Robinson, 1977a; Foote et al., 2006), wetting and drying (Kirk, 1977; Robinson, 1977a; Stephenson and Kirk, 1998) and biological activity

(Torunski, 1979); 3) slope (Robinson, 1977a); 4) rock structure (Swantesson et al., 2006); 5) the presence or absence of beach deposits (Robinson, 1977a); and 6) biological cover (Coombes et al., 2017).

Erosion rates change through time, with higher rates observed either in winter or in summer which has been respectively ascribed to the dominant role of wave action and weathering (Robinson, 1977a; Stephenson and Kirk, 1998; 2001). In winter increased storminess and wave energy delivery to the foreshore may increase the efficiency of abrasion and intensify the detachment of rock fragments due to hydraulic forces (Robinson, 1977a; Foote et al., 2006; Moses and Robinson, 2011). In summer higher temperatures increase the efficiency of thermal expansion of salt crystals and of wetting and drying, which leads to the detachment of rock fragments (Robinson, 1977a; Mottershead, 1989; Stephenson and Kirk, 1998; 2001).

Although MEMs allow vertical change at the sub-mm scale to be recorded, they have a number of limitations such as a need for fixed benchmarks (bolts) and a relatively small study area. There are multiple associated sources of error, including the temperature effect on bedrock, the integrity of benchmarks and the instrument, erosion of the rock while surveying, misuse and instrument wear (Turowski and Cook, 2017).

It is uncertain how representative erosion rates measured at a single site are for the whole platform and how to optimise the number and precise location of the monitoring sites (Moses, 2014). It is also challenging to infer mechanisms of erosion from point measurements, and to use MEMs to measure large-scale quarrying of rock fragments and joint blocks (Kirk, 1977; Robinson, 1977a; Trenhaile, 1987; 2002; Cullen et al., in review). Moses (2014) noticed that the effects of spalling and fracturing due to frost weathering, even if operating at the small scale, may not be possible to measure due to the limited vertical reach of MEMs. Viles and Trudgill (1984) questioned the temporal representativeness of results. Mayaud et al. (2014) observed significant intra-tidal expansion and contraction of rocks at MEM sites, pointing out the uncertainties associated with longer-term change detection results. Attempts have been made to use historical maps (Dornbusch et al., 2006), laser scanner (Swantesson et al., 2006) and traversing erosion beam (Charman et al., 2007) to record foreshore down-wearing (Table 2.3), but their utility is limited due to low resolution (maps) and requirement to survey planar surface (laser scanner, beam).

To summarise, although MEMs allow platform erosion at the sub-mm scale to be recorded, they cannot be used to constrain the mechanisms of erosion (the way erosion happens) and systematically analyse the distribution of erosion and controls upon it. Arguably this means that they provide limited input into process-based and empirical coastal evolution models. There is a gap in understanding the relative contribution of different time- and space-variable mechanisms to erosion,

and in identifying which of them need to be explicitly quantified in order to predict coastal change. These points are addressed in this thesis.

2.3.3. Platform dynamics at the macro-scale: step back-wearing

Little scientific attention has been paid to erosion at steps on the foreshore, yet most shore platforms comprise of low-angled surfaces interrupted by near-vertical steps of a few cm to > 1 m (Naylor et al., 2010). The steps are particularly prominent where the platforms are cut in rocks with well-defined horizontal or low-angled bedding planes or major joints (Dornbusch et al., 2007). Because the steps protrude from the platform, they are likely to experience more intense wave attack than planar sections as the wave energy concentrates on the inclined/vertical surfaces. Steps erode via a combination of block removal, abrasion and localised fracturing (Moses and Robinson, 2011). Large, joint-bounded blocks are detached only during occasional severe storms, while localised breakage and fracturing at corners and edges of the steps can occur more frequently during mild storms (Dornbusch and Robinson, 2011).

A number of factors contribute to erosion via block removal at the steps: 1) wave intensity; 2) the rock structure; 3) availability of debris for abrasion, though during severe storms hydraulic force of the waves may be sufficient to detach the blocks; 4) platform morphology below the step; and 5) the impact of waves reflected from the cliff, seawall or groynes (Naylor and Stephenson, 2010; Dornbusch and Robinson, 2011). Angular boulders are produced by the release of joint-bounded blocks at the steps and the platform seaward edge due to the hydraulic compression and the lift-and-drag force, which can be preceded by the weathering along joints and fractures (McKenna et al., 2011). Irregular blocks can be also detached at the step edges when the bedrock gets fractured by the impact of the wave-carried boulders (Knight and Burningham, 2011). In general, boulder geometry reflects the interplay between bedrock properties (joint density) and the nearshore wave climate (Regnauld et al., 2004). Boulders usually become more rounded with residence time on the platform (Moses, 2014). They may be spread across the platform, but small to medium-sized blocks tend to accumulate at the high-tide level. Platform-derived boulders often move landwards and settle at the cliff toe or in front of steps (Paris et al., 2011).

In a quantitative field-based study by Naylor and Stephenson (2010), the authors showed that the rock structure may dictate erosion thresholds, limiting the effectiveness of wave action to either the high-magnitude low-frequency events when the blocks of pre-defined structurally-controlled sizes and shapes are torn away, or the low-magnitude high-frequency micro-scale weathering and erosion processes. Different rock types with similar discontinuity patterns can produce boulders of similar morphology even though the mechanisms of erosion may vary (Cruslock et al., 2010). Stephenson and Naylor (2011) observed that the wave energy necessary to entrain blocks can be estimated from

boulder size unless they are located where repeated entrainment, transport and breakdown occur. Naylor et al. (2016) monitored daily boulder transport during a single storm event but they did not find a relationship between the size and shape of boulders, and the transport mode and distance.

Dornbusch and Robinson (2011) successfully quantified step back-wearing rate on the chalk coast of Sussex, UK. They used 7-11×10^{-2} m ground resolution air photographs from 1973 and 2001 to identify the locations of coastal steps, and measured their height (0.52-0.71 m) in the field. The precision of the study seems low as the total detached volume was approximated from the average step height, step length and average retreat distance, while equivalent down-wearing rate was calculated as the volume lost divided by the area of platform above the step. The erosion measured was 0.60-4.90 mm yr^{-1}.

To conclude, previous studies of the metre-scale foreshore erosion have been unsystematic and/or inaccurate. Although they have characterised step/boulder morphology, the processes of erosion identified and their spatial pattern, previous studies have lacked systematic quantitative analysis which would allow the inclusion of the empirical data on macro-scale foreshore erosion into coastal evolution models. In this research high-resolution LiDAR data (average 45.22 points m^{-2}) are used to systematically look at the foreshore erosion along 22 km of coastline at the (sub)metre scale.

2.4. Consideration of rock resistance

The relationships between geology and coastal morphology remain poorly constrained and quantified (Naylor et al., 2010), and so is the link between rock properties and erosion. A notable paucity in coastal research on the rock resistance comes when comparing the progress made in quantifying the complex interplay between erosive forces and rock resistance in fluvial and bedrock channel geomorphology (Sklar and Dietrich, 2001). From this work, it is clear that the role of geology is multifaceted and is dependent on spatial and temporal scale.

2.4.1. Rock control in coastal studies

Geology has been identified as one of the main controls on coastal form and development, as summarised by Sunamura (1992) in the conceptual model of horizontal cliff erosion (*dx/dt*) as:

$$\frac{dx}{dt} = \ln\frac{Fw}{Fr} \qquad \text{Eq 2.3}$$

where *Fw* is the assailing force of waves and *Fr* is the resistance of the cliff material.

Fw has been quantified and modelled in terms of the deep-water wave parameters and wave transformation in the nearshore (Komar, 1998; Adams et al., 2002; Kline et al., 2014). In contrast, *Fr*

is commonly considered either as a constant and hence has been ignored (Trenhaile, 1983; 2000; Walkden and Hall, 2005), or it is expressed in semi-qualitative sense as 'hard' or 'soft' rock (Limber et al., 2014; Matsumoto et al., 2016). At most *Fr* is represented by a single value, such as unconfined (uniaxial) compressive strength (*UCS*) (Kline et al., 2014), implicitly representing 'resistance' or 'rock strength' (Table 2.2). Importantly, in a dynamic coastal environment, a consideration of rock resistance stands in opposition to a wide variety of processes, including hydraulic fracture, abrasion, and corrosion, at diverse temporal and spatial scales (Trenhaile, 1980), and so it is unlikely that a single value for *Fr* will adequately explain observed behaviour.

The importance of rock resistance in coastal evolution has been acknowledged for many years (Challinor, 1949; Flemming; 1965; King, 1972). Significant progress in conceptual understanding of rock resistance in coastal evolution erosion was made by Sunamura (1977; 1983; 1992) as presented in Figure 2.4. *Fr* is a function of the mechanical properties of rocks such as *UCS*, tensile strength and resistance to abrasion, and structure: jointing, faults and stratification (Sunamura, 1983). *Fr* deteriorates over time due to weathering and fatigue, defined as the result of repeated stress generated in rocks by waves or loading (Adams et al., 2005; Brain et al., 2014). Therefore, erosion may happen even if *Fw* remains unchanged due to the decrease of *Fr*. Sunamura (1992) assumed that *Fr* can be represented by *UCS* in such a way:

$$Fr = B\ Sc \qquad \text{Eq 2.4}$$

where *Sc* is the *UCS* (MPa) at the cliff base and *B* is a non-dimensional constant potentially dependent on discontinuities such as bedding planes, cracks, cleavages, joints and faults.

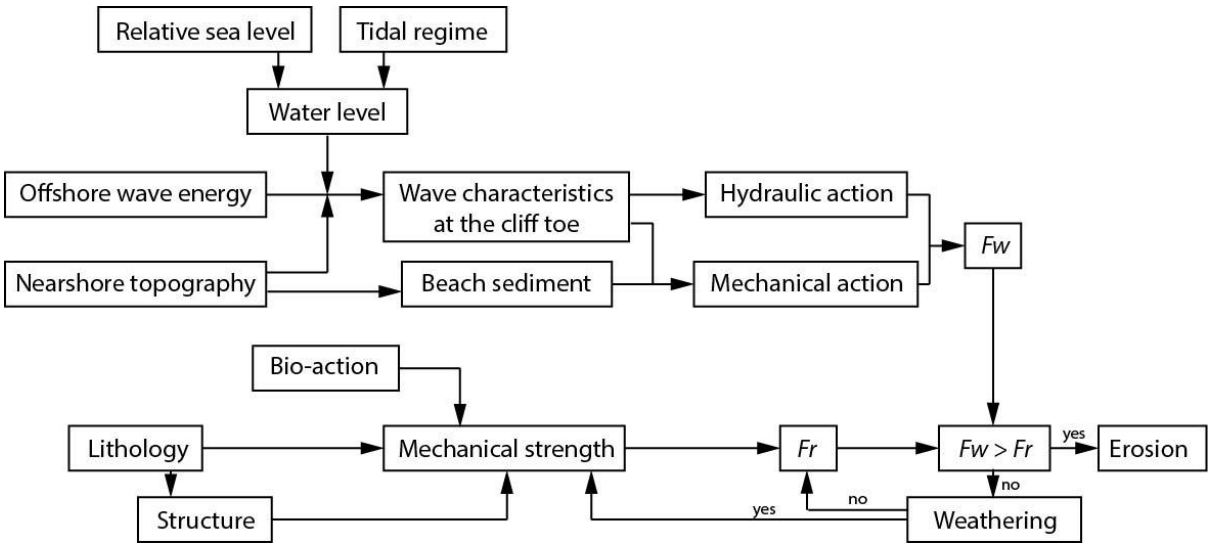


Figure 2.4 Elements contributing to Fw and Fr in coastal evolution; modified from Sunamura, 1983.

Trenhaile (1983) approximated *Fr* by the wave energy needed to cut a notch at the base of a cliff of a unit length. Nairn et al. (1986) and Jones et al. (1993) pointed out the role of shear strength for cohesive coasts and soft glacial tills respectively, while Wilcock et al. (1998) used the cohesive strength when analysing recession of coastal bluffs. Mano and Suzuki (1999) suggested that the combination of cliff height and the Young's Modulus of elasticity is a suitable *Fr* measure for soft rock cliffs. Adams et al. (2005) hypothesised that cyclical loading of rock cliff contributes to flexural fatigue, decreasing the rock strength even before the waves start directly operate at the cliff toe, though Brain et al. (2014) questioned their concept using rock mechanics theory.

Coastal evolution models explore some processes and simplify others, depending on their scope and the spatial and temporal scales considered (Table 2.2). For instance, the model of marine terrace generation and destruction by Anderson et al. (1999) operates at a 10^5 yr scale, at which the sea level is a key control and hence the only explored parameter. Other factors, including geology, are implicitly included in the efficiency factor which relates energy dissipation to erosion rate. In contrast, Kline et al. (2014) explored determinants on coastline evolution over $10^1 – 10^2$ yr timescales, where measured rock strength values were needed to account for *Fr*.

Trenhaile (2000) represented *Fr* by a dimensionless coefficient which linked wave force with horizontal erosion of the cliff and the platform. Subsequently, Trenhaile (2001) added an abstract non-verified reduction factor, which reflected the effect of weathering on the rock strength. For cohesive coasts, Walkden and Hall (2005) set *Fr* as a constant calibrated to match observed erosion rates with a unit ($m^{9/4}\ s^{3/2}$) which does not have a specific physical meaning. By decreasing/increasing the abstract value of *Fr* by one order of magnitude, Carpenter et al. (2014) further explored behaviour of the model with vertical variation in rock strength, observing the importance of vertical location and thickness of layers, in particular around the mean tidal level. Similarly, alongshore coastline diversification was shown to result from the variability in *Fr* (Carpenter et al., 2015).

The alongshore coastline evolution model of Limber et al. (2014) treated *Fr* in an abstract way where sections of coastline were classified as 'hard' or 'soft' and did not represent a specific rock property. The potential role of the rock resistance was implicitly included in the dimensionless sea cliff height coefficient (effect of cliff height and composition) and a constant which related wave power to the cliff retreat. Abstract rock strength was shown not to determine the formation of sea stacks, but it played a role in controlling their size (Limber and Murray, 2015).

Kline et al. (2014) expressed *Fr* by the *UCS* keeping it constant at *Sc* = 50 MPa. Matsumoto et al. (2016) represented *Fr* as 'soft', 'intermediate' and 'hard' with numerical values one order of magnitude apart. They let *Fr* decay over time due to the weathering in to the intertidal zone using the weathering efficacy distribution developed by Porter et al. (2010a), which suggests that the most effective weathering occurs at the high-water level of the neap tides (MHWN).

The lack of systematic empirical analysis of erosion and quantification of rock properties means that the models need to use abstract and/or adjusted values to represent rock resistance. As a result, it is impossible to account for a change of processes through time or spatially, which again points out the uncertainty in these models. In this study a systematic analysis of the relationship between coastal morphology and geology at the local (4.2 km alongshore) scale is undertaken, while rock properties are included in the micro- and macro-scale bedrock erosion analysis.

2.4.2. Rock quality assessment

Physical properties of the rock mass, including mineral composition, structure, texture, density, anisotropy, porosity, water content and stresses, determine the intact rock strength (Augustinus, 1991; Goudie, 2016). Various types of strength have been identified depending on the process the rock is subjected to: *UCS*, tensile strength, shear strength and impact strength (Sunamura, 1992). The mechanics of a particular erosion process, as well as the scale and erosion rate, determine which strength measure best suited (Augustinus, 1991). For instance, as rocks fail in tension by the impact of particles in a low-velocity flow, tensile strength is used for studying fluvial action (Johnson, 1972; Bursztyn et al., 2015).

The Schmidt Hammer rock test, which has been directly related to *UCS* (Deere and Miller, 1966), was designed to carry out *in situ* non-destructive tests on concrete and has been used for engineering purposes to check durability, slope stability and building stone performance (Goudie, 2006). The technique has become common in rocky coast geomorphology to compare rock strength between sites and to account for the reduction in strength due to weathering (Stephenson and Kirk, 2000b; Dickson et al., 2004; Chelli et al., 2010). Recently, the Equotip durometer has gained popularity in geomorphology as it provides similar information as the Schmidt Hammer, but has a lower impact on the rock and deals better with weathered uneven surfaces (Viles et al., 2011; Coombes et al., 2013). In this project the Equotip is used to characterise rock hardness across the foreshore.

Discontinuities such as cracks, cleavage planes, joints, faults, folds and stratifications reduce the overall strength of rock mass (Palmstrøm, 1995). Strength reduction is controlled by opening, interval, continuity, inclination and orientation of the discontinuities (Sunamura, 1992). In engineering, a number of rock quality indicators have been proposed to quantify reduction of rock mass strength due to the presence of discontinuities (Table 2.4). They have been applied to underground excavations: tunnelling, core logging, mines and foundations. The ratings for each parameter can be taken from tables. They either directly express the rock properties, such as *UCS* and joint distance, or are re-classified to a value/factor expressing the average importance of different

parameters. Simplicity of obtaining the suitable numbers for overall rating and possibility to assess rock condition in the field varies from system to system.

Table 2.4 Main rock quality assessment systems used in engineering.

Rock quality indicator	Reference	Equation	Notation
Rock Mass Factor, RMF	Onodera, 1963	$RMF = E_f / E_l$	E – deformation modulus for a rock mass for: (f) *in situ* and (l) intact laboratory specimen
Rock Quality Designation, RQD	Deere, 1963	$RQD = 100\ \Sigma_n^{i=1} x_i/L$	x_i – length of the i-th length ≥ 0.1 m n – number of intact lengths ≥ 0.1 m L – length of scanline/borehole
Rock Mass Rating, RMR	Bieniawski, 1976	$RMR = Si + RQD + Js + Jc + W$	Si – intact rock strength Js - joint spacing Jc – joint condition W – ground water condition
Rock mass quality, Q	Barton et al., 1977	$Q = (RQD/Jn) \cdot (Jr/Ja) \cdot (Jw/SRF)$	Jn – joint set number Jr – joint roughness number Ja – joint alteration number Jw – joint water reduction factor SRF – stress reduction factor
Failure criterion	Hoek and Brown, 1980	$\sigma_{1n} = \sigma_{3n} + sqrt(m\sigma_{3n} + s)$	σ_{1n} – major principal stress at failure normalised with *UCS* σ_{3n} - major principal stress normalised with *UCS* m, s – constants
Geological Strength Index, GSI	Hoek and Brown, 1997	n/a	n/a
Rock Mass index, RMi	Palmstrøm, 1995, 1996 a,b	$RMi = \sigma_c \cdot JP$ $JP = 0.2\ sqrt(jC)\ V_b^D$ $D = 0.37jC^{-0.2}$ $jC = jL\ (jR/jA)$	JP – joint parameter (0: crushed, 1: intact) V_b – block volume (m^3) jC – joint condition factor (most commonly 1:2) jL – joint length and continuity jR – joint wall roughness (smoothness and waviness) jA – joint surface alteration

In order to assess the rock surface condition, Selby (1980) introduced a semi-quantitative field classification, Rock Mass Strength (RMS). Eight parameters of weighted importance are either measured or qualitatively assessed in the field and re-classified from tables. Joint spacing accounts for 30% of the index, the intact strength, joint spacing and orientation make 20% each, while the remaining properties have a marginal importance. RMS is the sum of all re-classified values and can be used to compare strength of the large areas or the rock types rather than to account for the local variability (Taylor, 2003). Brook and Hutchinson (2008) modified the classification for weaker rocks while Cruslock et al. (2010) adapted it to rocky coast environments. Although some foreshore studies include characterisation of rock hardness and discontinuity pattern (e.g. Dickson et al., 2004; Cruslock et al., 2010; Naylor and Stephenson, 2010), these are rarely purely quantitative and systematic and they have not been coupled with numerical modelling.

2.4.3. Process-based and empirical approaches to rock resistance

The scope of geomorphological interest is different from that of the engineering, as in nature a number of forces impact bedrock, eroding it via diverse mechanisms. For instance, on rocky coasts a number of mechanisms link wave action with erosion: breaking-wave shock, water hammer, compression of air in discontinuities, hydrostatic pressure, cavitation and abrasion (Trenhaile, 1980). It is possible that different rock properties dictate rock resistance to marine forces for each individual mechanism. Understanding mechanisms of erosion allows for the identification of a strength measure, which can represent *Fr* (Augustinus, 1991).

Although the quantitative relationships between geology and morphology are still poorly constrained (Suzuki, 2002; Goudie, 2006), in the last 25 years significant progress has been made in bedrock river geomorphology to fill this gap (Sklar and Dietrich, 2001; Wilson et al., 2013; Bursztyn et al., 2015). In this section the main mechanisms of bedrock erosion will be described, followed by a review of recent erosion monitoring studies. Rocky coast geomorphology can build on the knowledge developed in fluvial and bedrock channel studies applying both the methods to quantify erosion and the understanding of the mechanisms.

2.4.3.1. Mechanisms of erosion

There are six primary processes of bedrock erosion: quarrying (plucking, jacking), abrasion (corrasion), fluid stressing (eversion), cavitation, corrosion (dissolution) and physical weathering (Carling et al., 2009). Quarrying can be defined as the removal of whole rock blocks by the lift-and-drag force, while abrasion is the grain-by-grain wearing of a surface by impacts from the sediment particles. Fluid stressing is the particle removal by turbulent stresses by clear water. Cavitation occurs where the instantaneous dynamic fluid pressure causes formation of water vapour bubbles whose rapid collapse leads to erosion due to the pressure-shock wave. Corrosion is the chemical weathering of limestones, marbles and evaporates (Carling et al., 2009).

Abrasion and quarrying are usually the most effective erosional processes (Lamb et al., 2015). Quarrying dominates at locations with exhumed joints, fractures and bedding planes accompanied by angular blocks. Abrasion, on the other hand associates with smooth, polished surfaces and landforms such as ripples, flutes and potholes with simultaneous lack of exhumed planes. The rock determines which of the two processes dominates with the rock strength being of less importance than the structure (Whipple et al., 2000). The threshold between abrasion and quarrying and their respective efficiency depends on the hydraulic forces resulting from channel geometry and discharge, and block geometry: joints and fractures (Dubinski and Wohl, 2013).

The effectiveness of the quarrying and dimensions of detached blocks are controlled by the discontinuity pattern and density (Miller, 1991; Hancock et al., 1998). Blocks are prepared for erosion by the propagation and widening of cracks and loosening by the hydraulic forces, bedload impact, sediment wedging in cracks and weathering (Carling et al., 2009). Depending on the direction of assailing forces and the surface relief (protrusions), blocks can be removed vertically (lifting) or by sliding (Dubinski and Wohl, 2013). Lifting involves a number of forces; the gravity (weight) and the frictional forces along the block side walls form the resisting force, while the shear stress, the form-drag associated with the protrusion and the hydraulic lift contribute to the assailing force. Block dimensions – length, height and protrusion – and the surface slope influence these forces, and hence the effectiveness of erosion process (Lamb et al., 2015).

2.4.3.2. Process-based and empirical studies

Bedrock erosion is difficult to monitor in the field because of the potential importance of high-magnitude low-frequency erosion events. It is also difficult to reconstruct in laboratory settings due to morphological complexity (Miller, 1991; Turowski and Cook, 2017). Instead of relying on historical data and field observations, which show that erosion has happened but does not allow quantitative links between geology and landform evolution to be established, understanding erosional processes provides an alternative to explore interactions between limited number of variables (Carpenter et al., 2014).

Sklar and Dietrich (2001) quantitatively established the link between erosion (in volumetric terms), sediment supply and tensile strength, which importantly is a measurable rock property. Yin et al. (2016) observed suspended-load abrasion in cohesive substrate erosion. Johnson and Finnegan (2015) found that the strength loss resulting from drying and re-wetting (*slaking*) depends on the rock type by subjecting sandstone and mudstone to wetting/drying cycles and quantifying mass loss.

Finnegan et al. (2007) quantitatively showed that the surface roughness causes sediment deposition in shielded areas, local increase of the friction angle for stationary grains on the bed and increased drag on conveyed fluid which progressively reduces shear stress for bed-load transport. Small et al. (2015) exposed bedrock from different locations across river to abrasion mill experiments observing the highest erosion rates at the channel margins where the impact of weathering on rock strength and surface roughness was the highest. In a natural gorge, Beer et al. (2017) observed that abrasion focused on the upstream-facing surfaces, and decreased with increasing height due to temporal flooding.

Wilson et al. (2013) combined a 3D field monitoring and laboratory tests to conceptually model development of diverse morphology of the boulder upstream- and the downstream-facing surfaces in river channels. They concluded that the morphology reflects different mechanisms

operating on the two sides of boulders, with bedload abrasion dominating on the upstream-facing and suspended-load abrasion dominating on the downstream-facing surfaces. Bursztyn et al. (2015) found linear relationships between tensile strength and 1) stream power (positive), 2) gradient (positive) and 3) valley width (negative), establishing direct links between objective rock strength measure and the landform metrics.

In this research, these approaches to monitor erosion at high-resolution and to explore simple relationships between rock properties, erosion and controlling factors are adapted to accurately quantify erosion, and identify the underlying mechanisms and the factors controlling distribution of erosion.

2.5. Advances in bedrock erosion monitoring

Recent progress in detecting bedrock erosion and availability of high-resolution and high-precision data give an opportunity to accurately detect and quantify detachments. Size and 3D shape distributions allow dominant mechanisms of erosion to be constrained, while spatial distribution of erosion helps identify controls on erosion rates. This section describes current techniques adapted from other disciplines which will be applied in this thesis as an alternative to traditionally used MEMs.

2.5.1. Recording bedrock erosion

Bedrock erosion is detected by repeated topographic surveys of a rock surface (Turowski and Cook, 2017). The surveys should 1) be performed with adequate accuracy and precision to detect topographic change; 2) have a reference frame which allows confident comparison; and 3) be repeated with suitable frequency to detect erosion (Cook, 2017). Topographic change detection techniques can be divided into two groups depending on whether benchmarks are present or not. Benchmarks are hammered in or glued objects such as erosion pins, bolts, nails, or engineering structures (e.g. groynes) with negligible erosion rates over the surveying period (Charman, 2001; Turowski and Cook, 2017). The most highly-developed instrument to monitor bedrock erosion with benchmarks is the MEM described in section 2.3.2. Subsequent sections describe Structure-from-Motion (SfM) photogrammetry, which is used in this project as the alternative to the MEM to quantify erosion at the mm to cm scale.

2.5.1.1. Structure-from-Motion: introduction

Topographic change detection techniques that do not require stable benchmarks rely on high-precision GPS which allows data to be put in a spatial reference frame, such as a global coordinate system. Registration of surveys is often refined to match the base survey using adjustment tools in point cloud processing software. For example in Reigl RiSCAN PRO *Multi-Station Adjustment* (MSA) is used or in CloudCompare a *Fine Registration* tool is employed.

The most common techniques make use of LiDAR (Jones et al., 2007; Mallet and Bretar, 2009; Höfle and Rutzinger, 2011; Gallay, 2013; Benjamin et al., in review), Terrestrial Laser Scanning (TLS) (Schürch et al., 2011; Abellán et al., 2014; Smith, 2015), photogrammetry (Lane et al., 1993; Lin and Oguchy, 2002; Lim et al., 2005) and Structure-from-Motion (SfM) (Westoby et al., 2012; Fonstad et al., 2013; Hackney and Clayton, 2015).

SfM, a technique to reconstruct topography from photographs taken from different positions and angles using uncalibrated cameras, has recently gained popularity due to its low cost, fast data acquisition and automated camera calibration and image processing (Westoby et al., 2012). In comparison with traditional photogrammetry it does not require much expertise and makes use of fewer control points (Marteau et al., 2017). Using Unmanned Aerial Vehicles (UAVs) to reconstruct topography has bridged the gap between the field observations and the acquisition of the data from manned aircraft or satellite sensors (d'Oleire-Oltmanns et al., 2012).

The low cost and high automatization of the data processing make SfM an appealing alternative for LiDAR and TLS to reconstruct surface relief. Turowski and Cook (2017) observed that in areas of complex topography UAV data gives better results than TLS. Although Smith and Vericat (2015) observed the overestimation of both positive and negative changes by SfM relative to the LiDAR, Cook (2017) showed similar results for both methods. Smoothening over the smaller-scale roughness can be reduced by including oblique images, increasing the monitoring resolution and decreasing the distance between the cameras and the rock surface (Cook, 2017).

2.5.1.2. Structure-from-Motion: surveying

Photogrammetry and SfM have rarely been used to measure erosion because the reconstruction of the surface is affected by a number of factors that are difficult to control: camera position (distance), light conditions, surface roughness and reflectivity, in particular the presence of water (Rock et al., 2011; Nitsche et al., 2013; Gonçalves and Henriques, 2015; Cook, 2017).

A successful reconstruction of topography requires the presence of Ground Control Points (GCPs) whose coordinates are acquired independently using GPS. Increasing the number of GCPs reduces the errors in representing topography (Turowski and Cook, 2017). Hackney and Clayton

(2015) noticed that the distribution of GCPs throughout the area of interest, particularly at the model edges, minimises a commonly observed doming distortion effect. If the number of GCPs is high enough, some of them may serve as independent Check Points (CPs), and the model performance can be tested by calculating the distance between CP coordinates modelled and measured with GPS (Brasington and Smart, 2003; Marteau et al., 2017).

A limited number of studies have used photogrammetry or SfM to reconstruct surfaces at the small scale. Grennes et al. (2005) reconstructed the surface of tooth replicas at 10^{-5} m scale. Wackrow et al. (2007) observed a decrease of accuracy from the centre to the edges, doming effect and a systematic error pattern on mm-resolution Digital Elevation Models (DEMs) created using SfM. Wackrow and Chandler (2008) developed a method to minimise these errors by applying a mildly convergent configuration of the cameras. Aguilar et al. (2009) compared performance of TLS and photogrammetry in reconstructing soil micro-relief, successfully generating accurate DEMs of 0.001 m with the latter method. Morgan et al. (2017) explored performance of SfM at the cm-scale for flume experiments with varying flume sizes, surface roughness, photography angles and processing software.

2.5.1.3. Structure-from-Motion: change detection

Change detection can be performed directly on the point clouds, by comparison of a triangulated mesh, or by converting point clouds to DEMs (Bell, 2012) and creating DEMs of Difference (DoDs) by subtracting pairs of DEMs (Williams, 2013). Two former methods enable 3D erosion to be explored and change detection to be better performed on complex topography such as overhangs and vertical walls (Lague et al., 2013). However, much more often erosion is quantified based on DoDs. The quality of DEMs controls the uncertainty in detected change and it depends on a number of factors, such as method quality, sampling strategy and relief. The most common technique to separate error from the actual change is by establishing a threshold, called the Level of Detection (*LoD*). If a DoD pixel is represented by values below the *LoD* threshold, it is either ignored or its importance is reduced using a declining weighting function (Wheaton et al., 2010).

If *LoD* is set too low, some error (noise) is classified as erosion, while if it is too high, it implies a loss of information. A number of methods help estimate *LoD*, including repeated observation of control points (Marteau et al., 2017), repeated surveying of unchanging surface (Wheaton, 2008) and statistical analyses (Brasington et al., 2003). For instance, Wheaton (2008) re-surveyed the same surface seven times observing a strong and predictable bias in elevation uncertainty for steeper and rougher areas. The point cloud accuracy deteriorates at the edges of the model because the peripherial areas are included in fewer photographs (Cook, 2017). Therefore, a *LoD* that varies across area of interest can be used instead of a constant value (Wheaton et al., 2010).

LoD determines the minimal detectable volume (V_{min}) of eroded material from one grid cell in such a way (Williams et al., 2018):

$$V_{min} = LoD\ A_c \quad \text{Eq 2.5}$$

where A_c is the cell area.

2.5.2. Analysis of erosion

Creation of DoDs and separation of the actual erosion from no-change are the starting point for a number of analyses which can be performed. In general, the analysis methods can be divided into two groups: 1) the methods based on event (detachment) inventory, and 2) the methods which divide the area of interest into same-size discrete zones characterised by a number of attributes, including erosion variables. Both approaches are undertaken in this project.

2.5.2.1. Event-based analysis of erosion

Analysis of erosion events has been widely performed in the landslide and rockfall studies (Malamud et al., 2004; Guzetti, 2005; Williams et al., 2018). The areas of change above *LoD* are usually converted into polygons representing single detachments. The collection of all events is called the event inventory, in which each detachment is characterised by a number of attributes. Basic attributes include: the identification, time of the survey following event, the location which is usually 2D or 3D coordinates of the centroid, surface area and volume. Depending on the study focus, events may contain additional attributes related to: the topography, such as slope and roughness; geology, such as rock type, affiliation to a specific rock bed and joint density; and conditions, including wetness and tidal duration distribution (Williams et al., 2018).

Detachment size analysis

The analysis of detachment volumes is the basis of the magnitude/frequency distribution curve (Whadcoat, 2017). An inverse power-law relationship commonly exists between the number of events and their size for such phenomena as landslides, rockfalls, volcanic eruptions and earthquakes allowing a probabilistic recurrence of events of given size to be derived (Dussauge-Peisser et al., 2002). The relationship between the non-cumulative frequency (*f*) and volume (*Vol*) of rockfall events is represented by the power law using least-squares fitting (Clauset et al., 2009) as:

$$f = k\ Vol^{-\beta} \quad \text{Eq 2.6}$$

where k is a constant and β is the volume frequency power-law exponent that provides information whether the large or small events dominate erosion which helps assess the dominant mechanisms of erosion (Stark and Guzetti, 2009). A higher exponent β (a steeper slope), suggests the dominance of smaller events (Williams et al., 2018). Hungr et al. (1999) recorded higher exponent values for rockfall in jointed rocks (0.65-0.7) than in the massive rocks (0.4-0.43). The exponent values for landslides are usually higher than 0.6-0.8 (Dussauge-Peisser et al., 2002).

The power-law scaling applies only to a portion of event inventory and the inverse gamma distribution which has a rollover in the frequency of the smallest event sizes (Stark and Hovius, 2001; Malamud et al., 2004). Dussauge-Peisser et al. (2002) suggested that small and shallow rock failures depend on the state of rock surface associated with temperature and weathering, while medium to large detachments are controlled by geometrical and mechanical properties of the rock mass, such as fracturing and friction angle. Guzetti (2005) gave two alternative explanations for the presence of rollover for landslides: the transition from the cohesion to the basal friction as the controlling factor on failure, and the possibility that the deviation from the power-law reflects landslide geometry related to the area/volume ratio.

The rollover may also reflect the limitations of surveying resolution (Dussauge-Peisser et al., 2002). Whadcoat (2017) recorded a power-law β higher than previously observed for similar rock types, suggesting that higher resolution of her study allowed the inclusion of smaller rockfalls into the inventory. Williams et al. (2018) observed the increase in contribution of smaller events with increased surveying frequency. The relationship between detachment area (*Area*) and volume (*Vol*) can be expressed as:

$$Vol = a\, Area^{b} \qquad \text{Eq 2.7}$$

where a is a constant and b is the power-law exponent. The above equation describes how deep events are relative to their planform size. The fit to, and deviation from, the power law can be used to explore the possibility of scale invariant behaviour, or changes in mechanism as a function of volume (Guzetti et al., 2009; Larsen et al., 2010; Williams et al., 2018). If the relationship is strong, the eroded area can serve as a proxy to predict eroded volume. It is important because the effects of erosion can often be seen with naked eye, in photographs or satellite images, and can give an indication about eroded mass without its direct quantification.

A significantly different β exponent has been found by Guzetti et al. (2009) and Williams et al. (2018) with respective values of 1.45 and 1.15, which suggests different underlying failure mechanisms. In the first case (landslides) it is shear stress development along deeper shear planes, while in the second (rockfall) – near-surface tensile stress (Williams et al., 2018).

Detachment shape analysis

Sneed and Folk (1958) developed a ternary plot for sedimentological studies, where the lengths of the three axes of a grain are plotted showing how compact/platy/elongate a grain is. Kalenchuk et al. (2006) adapted the method to rock shape analysis calling respective extreme shapes blocks, slabs and rods (Figure 2.5). The shape of eroded material can indicate erosion mechanism, or can be a reflection of joint spacing. For instance, slabs and rods can be indicative of erosion of the thin rock layers or at the sharp edges via quarrying, while compact blocks can suggest detachment of platelets (Williams et al., 2018).

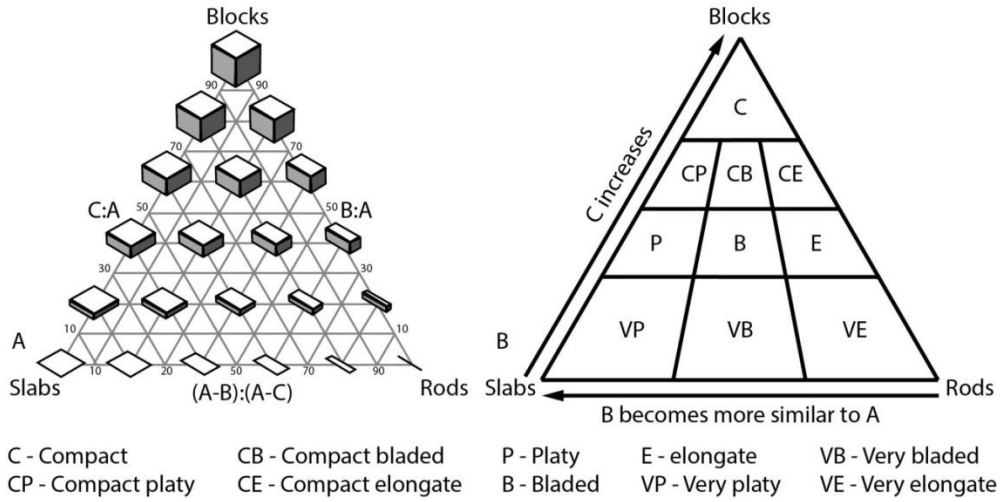


Figure 2.5 Block geometry on ternary plots: A) Location of shapes across the plot, B) Division of the plot into ten sectors. Block axes: A – long, B – medium, C – short; based on Williams et al., 2018.

Spatial relationships between detachments

The analysis of spatial relationships between single events serves to identify areas prone to erosion, such as for example along discontinuities, and enables us to understand whether erosion occurs at random or concentrates or propagates. Rosser et al. (2013) observed that on a coastal cliff face rockfall has random spatial distribution, but that there is a strong clustering in time which suggests failure propagation. Whadcoat (2017) applied Ripley's K-function in clustering analysis, while Williams et al. (2018) observed preceding of larger events by smaller contiguous failures.

2.5.2.2. Zone-based analysis of erosion

The analysis of single detachments may be incorrect if the surveying frequency is too low and recorded events are in fact the sum of multiple smaller detachments (Malamud et al., 2004). Moreover, the rockfall/landslide literature assumes that the distribution of erosion events is random in space (Rosser et al., 2013), which may not be the case for other landforms. Therefore, an alternative

or complimentary approach involves the division of the area of interest into discrete zones of equal sizes, such as a grid. Each zone or cell is characterised by a number of attributes, such as 1) erosion variables, e.g. total detached volume, total detached area, number of events; 2) topographic variables, e.g. elevation, slope and roughness; and 3) site-specific properties, e.g. wetness, rock type, distance from discontinuities. The relationships between erosion and single or multiple independent variables enable prediction of future erosion based on the limited number of variables (Parker et al., 2015). Here, the approach described above is used to predict foreshore erosion at the small- and macro-scales respectively using 0.25 and 1 m^2 zones.

2.6. Summary

Our understanding of foreshore erosion is, in part, limited by the monitoring techniques that have conventionally been used: point measurements of the vertical change using MEMs (e.g. Robinson, 1976; 1977a; Stephenson and Kirk, 1998; 2001) and low-resolution detection of step back-wearing using cartographical sources (Dornbusch and Robinson, 2011). This dual approach to assessment of erosion is reflected in the models to reconstruct (Regard et al., 2012; Hurst et al., 2016; 2017) and predict (Trenhaile, 1983, 2000; Walkden and Hall, 2005; Kline et al., 2014; Limber et al., 2014) coastal evolution where the morphology and erosion of shore platforms are simplified. Many individual processes of platform erosion have been identified, but they are either quantified at low resolution and low precision, or not appropriately quantified, in which case their relative contribution to foreshore erosion is unknown; in turn, this is reflected in the omission of specific processes in existing conceptual and exploratory numerical models. Without understanding the underlying mechanisms and controls on the spatial distribution of erosion, we cannot know how accurate the models are. This limits our ability to predict future geomorphic change in response to anticipated sea-level rise and increased storminess (Slott et al., 2006; IPCC, 2013).

The complexity of foreshore morphology suggests that the current approach may be too simplistic and a number of factors may be important at a variety of scales. The recent progress in fluvial and bedrock channel geomorphology suggests that erosion is multifaceted while different rock properties may represent rock resistance at different scales (e.g. Sklar and Dietrich, 2001; Wilson et al., 2013; Beer et al., 2017). Recent development of 1) high-resolution and high-precision techniques to monitor bedrock erosion, notably SfM and LiDAR (Cook, 2017; Marteau et al., 2017; Turowski and Cook, 2017; Benjamin et al., in review), and 2) detachment size and shape analyses used in rockfall/landslide studies (Malamud et al., 2004; Parker et al., 2015; Williams et al., 2018) give an opportunity to accurately quantify erosion rates and identify mechanisms of erosion and controls on spatio-temporal detachment distribution which is addressed in this project.

3. Geomorphology of the shore platforms in North Yorkshire, UK

3.1. Introduction

This chapter gives the background information on the geology, Quaternary history and current marine conditions of the study area. The introduction to the geomorphologic mapping is provided, which is used in Chapters 6 and 7 to perform change detection on the airborne LiDAR dataset. The detailed GIS- and field characterisation of Hartle Loup gives a background for the micro-erosion monitoring (Chapters 4-5) and exposure dating (Chapter 8).

The North Yorkshire coast is ideal to conduct the present study. The stretch of coastline is long enough to encompass a diverse morphology and geology for statistical spatial analyses. The shore platforms are mostly free from sediment such as beaches and boulder fields, which facilitates bedrock surface reconstruction from remote sensing data. This stretch of coast was also the site of one of the first studies of shore platform micro-erosion (Robinson, 1977 a,b) which gives an opportunity to directly compare recorded erosion rates and interpretations. On the Yorkshire coast, the Hartle Loup platform is selected to undertake detailed micro-erosion and exposure dating studies because of the minimal human intervention, resulting in a pristine character, considerable morphological diversity within a single platform and a suitable rock type (mineralogy and grain size) to calculate cosmogenic isotope concentrations.

The research presented on the relationships between the geology and shore platform morphology at the local scale (4.2 km of the central section of the studied coast) shows that it is not possible to fully explain the observed diversity of platform shape by directly relating it to the typically-used measures of rock hardness and structure. The study advocates the need to understand mechanisms and controls of erosion at relevant scales which is undertaken in subsequent chapters.

3.2. Regional settings

The 27 km stretch of coastline between Skinningrove and Whitby in North Yorkshire, UK exhibits alternating headlands and bays that vary in alongshore length between tens and hundreds of metres. Shore platforms that are 50 to 350 m wide (average: ~140 m) are present along the 22 km stretch between Skinningrove and Sandsend. The average cliff height is 86.5 m and ranges from 20.3 to 206.5 m as calculated from the LiDAR (2014) dataset (details in section 3.7.1). The village of Skinnigrove is at the north-western end of the studied coastline, while the mouth of the River Esk marks its south-eastern limit (Figure 3.1).

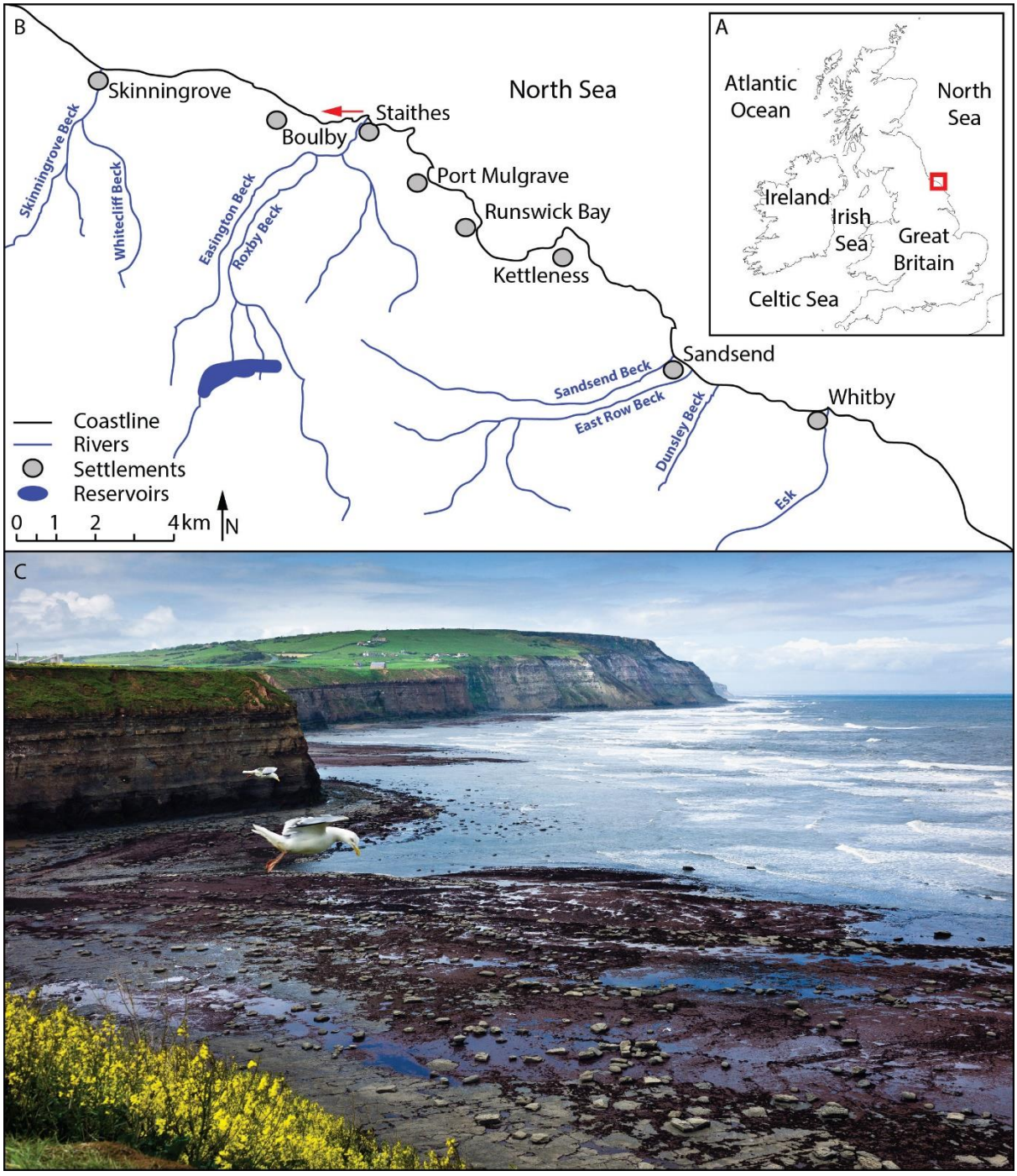


Figure 3.1 The North Yorkshire coast: A) location within the British Isles (red box); B) coastline outline; C) typical coastal scenery; the photograph was taken from Cowbar facing west (as indicated with the red arrow in B); source: Alamy Stock Photo.

3.3. Geology

The study area is located in the Cleveland Basin formed in late Triassic when the Mesozoic strata differentially subsided (Rawson and Wright, 2000; Lim 2006). The basin was inverted due to

tectonic uplift at the transition from the late Cretaceous to the Tertiary resulting in 2° north-south trending dip (Rawson and Wright, 2000). Consequently, there is a continuous sequence of Lower Jurassic (Lower to Upper Lias) lithologies exposed at the coast. Lower Jurassic Staithes Sandstone, Cleveland Ironstone and lower Whitby Mudstone formations are exposed in the vicinity of Staithes (Rawson and Wright, 2000). Figure 3.2 depicts the vertical location of rock beds west of Staithes with interbedded mudstones, shales, siltstones, sandstones and ironstones. The lithologies on the cliff face and shore platforms are characterised by diverse geotechnical properties (Table 3.1) (Lim et al., 2005; Lim, 2006).

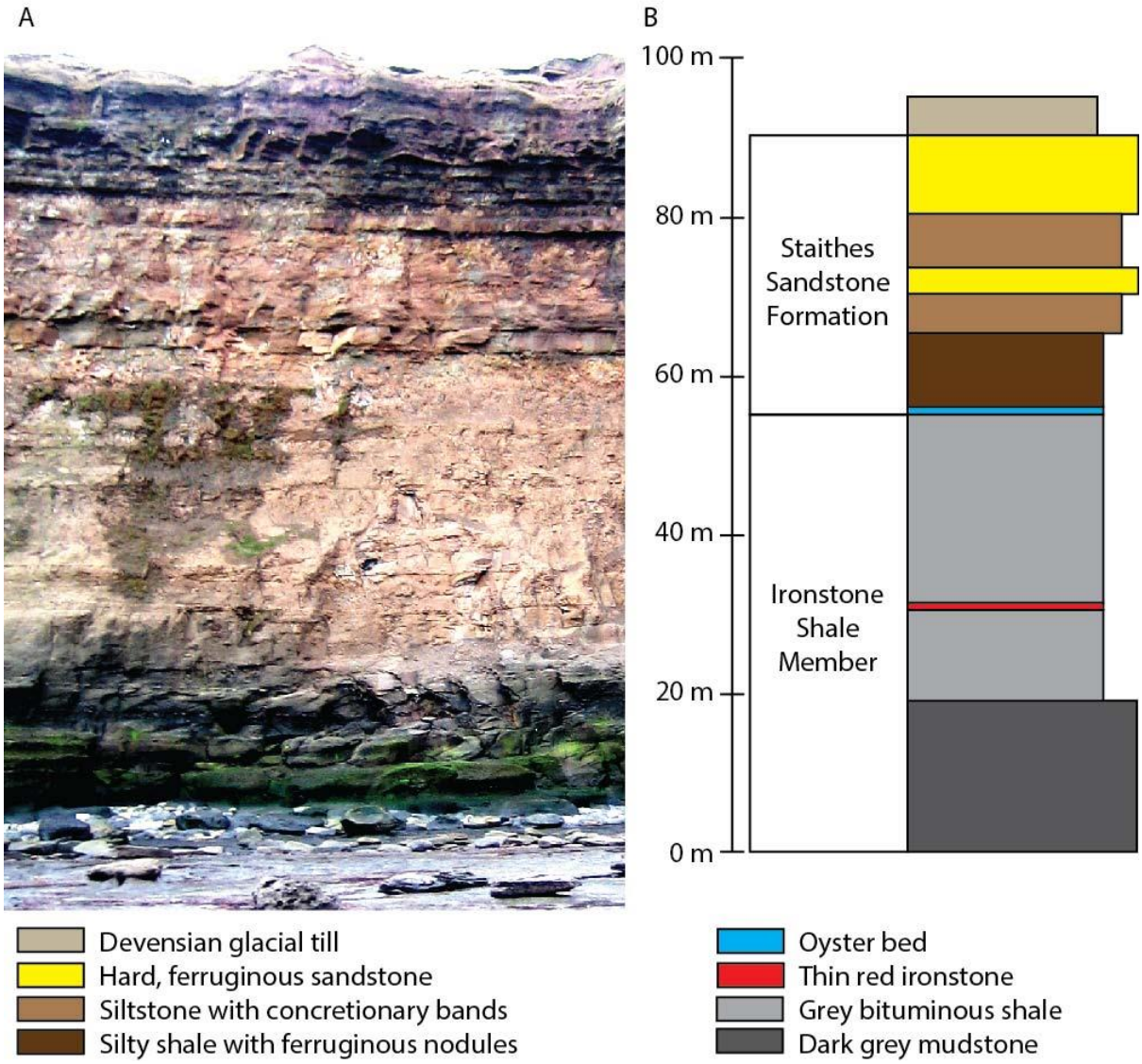


Figure 3.2 Cliff composition in west Staithes/Boulby area: A) an example of cliff morphology with clearly visible near-horizontal bedding; B) schematic cross-section of the cliff face; based on Lim, 2006.

Table 3.1 Properties of the rocks present in Staithes area; source: Cleveland Potash Ltd.

Rock type	Elastic modulus (MPa)	Bulk density (km m^{-3})	Poisson's ratio	Tensile strength (MPa)	Unconfined (uniaxial) compressive strength (MPa)
Sandstone	3480.55	2583	0.30	3.02	34.21
Siltstone	2206.32	2492	0.23	1.72	30.20
Shale	2137.38	2486	0.40	3.03	16.69
Mudstone	4126.33	2513	0.28	3.48	41.54

3.3.1. Description of the bedrock forming shore platforms in Staithes area

Exposure dating using cosmogenic isotope concentrations is currently the only method to validate rocky coast evolution models and reconstruct the long-term cliff retreat rates. This technique is critical to assess the accuracy of the undertaken multi-scale study of foreshore erosion. In order to identify a suitable location for the reconstruction study, petrographic and geochemical characterisation of the rock types exposed around the tidal level in Staithes area were performed. This section presents the methods and results of a study to identify the best lithology in terms of the mineral content and grain size to reconstruct past cliff retreat (Chapter 8).

3.3.1.1. Methods

Five rock samples representing four rock types (2×sandstone, 1×mudstone, 1×shale and 1×siltstone) were collected from shore platform near-surface in the Staithes area (Figure 3.3B). They were described visually and subjected to point load strength tests which can be used to estimate *UCS* (BS, 1999; ASTM, 2008). Dimensions of the samples and the load at the moment of failure allow the point load strength index (PLSI) to be calculated as:

$$Is = \frac{P}{De^2} \quad \text{Eq 3.1}$$

$$Is_{(50)} = F\,Is \quad \text{Eq 3.2}$$

$$F = \left(\frac{De}{50}\right)^{0.45} \quad \text{Eq 3.3}$$

where *Is* (MPa) is the uncorrected PLSI, *P*(N) it the failure load, *De* (mm) is the equivalent core diameter, $Is_{(50)}$ (MPa) is the PLSI corrected to the sample diameter of 50 mm and *F* is the size correction factor (ASTM, 2008). Samples 1-3 were small enough to perform the tests without cutting; the tests were conducted on cores of samples 4 and 5. The PLSI was subsequently converted to a qualitative rock strength class according to the British Standard (BS, 1999).

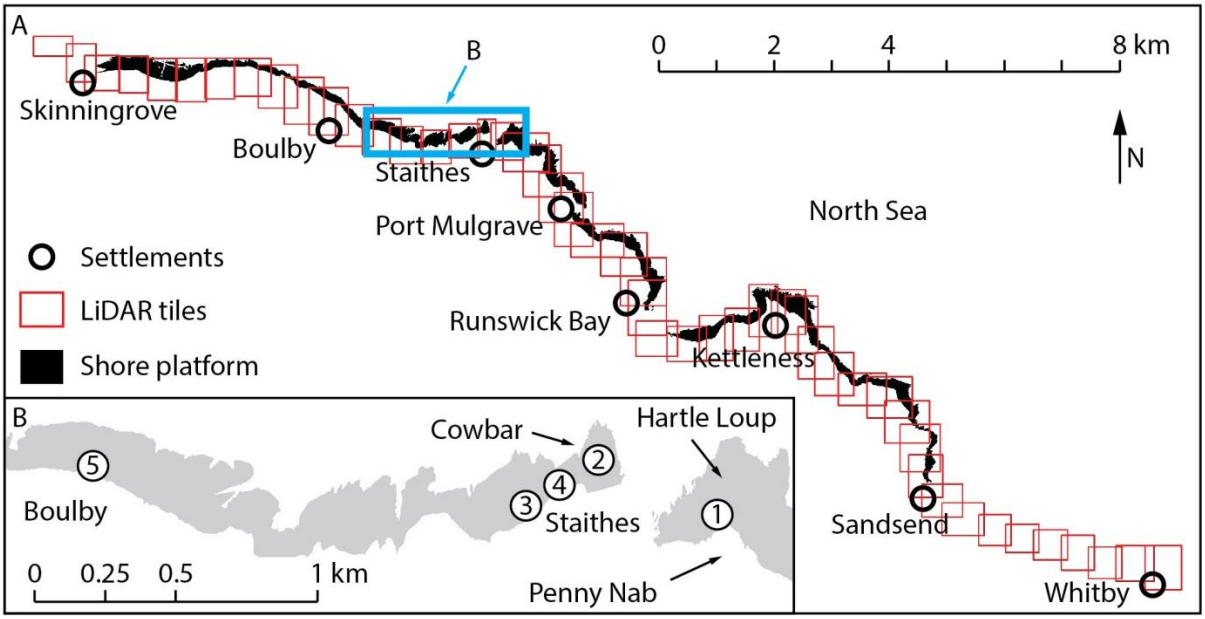


Figure 3.3 A) coverage of the LiDAR2014 dataset along the North Yorkshire coastline; B) location of the five rock samples used for geochemical analysis on shore platforms (grey surface) in Staithes area.

In order to identify the rock type suitable for exposure dating (Chapter 8), the geochemical analyses were performed on the five samples. Potentially weathered outer parts of the samples were removed and the remaining rock material was comminuted into pieces of ~5.00×10^{-3} m diameter using a hammer. To prevent loss of volatiles during the drying process, the samples were freeze dried (McClymont et al., 2007). Ball milling was used in order to obtain ~20 g of the powder from each sample.

Chloride and metal concentrations were measured to identify the target elements for the cosmogenic exposure dating (Dunai, 2010). Three cosmogenic isotopes: ^{10}Be, ^{26}Al and ^{36}Cl are widely used to reconstruct exposure time, and their predominant target elements are: O, Si and Mg for ^{10}Be, Si for ^{26}Al and K, Ca, Cl, Fe and Ti for ^{36}Cl (Dunai, 2010; Darvill, 2013).

Concentrations of chloride were obtained by titration (BS, 1990). Metal concentrations were measured though acid dissolution using an Agilent 5900 ICP-OES instrument. The digestion matrix was made up of 200 mg of milled rock sample, 2 ml of H_2O, 4 ml of HCl, 12 ml of HNO_3, 3 ml of HF and topped up to 50 ml with deionised water (BS, 1990).

3.3.1.2. Results

The analysed samples represent a wide range of rock types present in the area (Table 3.2). The grain size, described visually before the sample comminution, is generally fine, with three

samples (1, 2 and 5) containing sand-size particles and two (3 and 4) with finer grains. This implies that the standard procedures of preparing rock samples for cosmogenic isotope dating (Kohl and Nishiizumi, 1992; Corbett et al., 2016) cannot be used, as these rely on grain sizes ≥ 150 μm, and an alternative method needs to be developed (section 8.3).

Table 3.2 Characteristics of the rock samples collected from shore platforms in Staithes area (for location refer to Figure 3.3B).

Sample	Location	Rock type	Colour	Foliation	Grain size	Sorting	Sand-size particle %	$Is_{(50)}$ (MPa)	Strength (BS, 1999)
1	Hartle Loup	Sandstone	Blue-grey	Thinly-laminated	Fine	Moderate	10-25	2.29	Moderately strong
2	Cowbar	Sandstone	Blue-grey	Thinly-laminated	Fine	Good	10-25	0.46	Weak
3	Cowbar	Mudstone	Dark blue-grey	Thinly-laminated	Fine	-	0	2.10	Moderately strong
4	Cowbar	Shale	Blue-grey	Foliated	Very fine	-	0	2.31	Moderately strong
5	Boulby	Siltstone	Light grey	Thinly-laminated	Fine	Good	10-25	2.07	Moderately strong

Because all samples are rich in Si (Table 3.3) using ^{10}Be concentrations in quartz grains of the sandstone (samples 1 and 2) seems to be a reasonable technique to reconstruct past cliff retreat. The samples contain enough Ca, K and Si (Dunai, 2010) to calculate ^{26}Al or ^{36}Cl concentrations with the addition of or alternative use of ^{10}Be if necessary. The Hartle Loup platform has not been affected by historical industrial and mining activity, unlike the Cowbar platform (Lim, 2006). The morphology of Hartle Loup allows the influence of step back-wearing on cosmogenic isotope concentrations to be accounted for, which previously has only been done conceptually (Hurst et al., 2017). As such, it is a suitable location for the cosmogenic exposure dating study (Chapter 8).

Table 3.3 Metals and chloride concentrations (%w/w) in the rock samples.

Sample	Si	Al	Ca	Fe	K	Mg	Na	Ti	Cl
1	23.75	0.35	5.45	1.90	0.70	0.23	0.96	0.28	0.07
2	30.36	1.50	1.58	1.76	0.58	0.15	0.83	0.25	0.15
3	25.54	2.85	0.04	4.62	1.51	0.03	0.51	0.54	0.11
4	27.93	2.56	0.03	3.95	1.27	0.02	0.70	0.47	0.11
5	24.94	0.52	5.11	2.07	0.63	0.31	0.94	0.24	0.06

3.4. Quaternary history of the area

The aim of this section is to provide a background of the Quaternary history of the North Yorkshire coast in order to 1) explain the abundance of the glacial till on the top of the cliff; 2)

describe the sea-level change in the last 7 kyr which will be used to reconstruct past cliff retreat rate using cosmogenic ^{10}Be concnetrations (Chapter 8); and 3) to introduce the concept of shore platform inheritance from the last interglacial.

The development of the North Yorkshire coastline is strongly related to the evolution of the North Sea basin (Lee et al., 2011). Climate changes throughout the Pleistocene (last ~2.6 Myr), and in particular the magnitude and frequency of the glacial periods, have controlled behaviour of the basin geometry (Lee et al., 2011). The British Ice Sheet (BIS) developed on the British Isles between 1.1-1.8 Myr BP and 11.7 kyr BP (Kelletat, 2005; Lee et al., 2011). Its dynamics controlled terrestrial relief, drainage system evolution and sedimentary infill. Changes in the ice sheet mass caused the isostatic movements as alternating stages of the land uplift and subsidence (Lee et al., 2011). The colder periods (glacials) were accompanied by increased mass and deeper land immersion into the asthenosphere, while the warmer periods (interglacials) were characterised by the ice sheet mass decrease and land uplift (Kelletat, 2005). Eustatic changes relate to the alteration in the volume of water in the oceans and together with isostatic movement dictate the relative sea level (RSL) (Shennan and Horton, 2002). RSL is the main control on the long-term (millennia) coastline evolution as it determines the vertical reach of waves, and hence location of coastal processes (Anderson et al., 1999).

During the Ipswichian (Eemian) Stage 5e (130-118 kyr BP), called 'the last interglacial', the sea stayed at a similar level (± 2 m) to present (Trenhaile, 1987). An interglacial beach (120.84 ± 11.82 kyr BP) was identified at 2 m AOD in Severby, East Yorkshire (Bateman and Catt, 1996). Many hard-rock coasts are believed to have been at least partly developed during the last interglacial because a relatively short time period (3-7 kyr) has been available in the Holocene to explain the formation of shore platforms 10^2 m order of magnitude wide (Trenhaile et al., 1999; Masselink et al., 2011). The shore platforms in North Yorkshire might have been partially exposed during the last interglacial as suggested by Agar (1960). Although, contemporary cliff retreat rates (section 3.6.1) could explain the formation of the platforms in the last 6-7 kyr, we do not know how representative they are over millennial timescales, as the cliff retreat rate might have accelerated in the post-industrial period, as shown on the southern English coast by Hurst et al. (2016). Exposure dating using cosmogenic isotope concentrations (Chapter 8) is the only method to find out whether the platform is inherited or it has been entirely formed in the Holocene (Choi et al., 2012).

The Ipswichian Stage was followed by the Devensian (Weichselian) glaciation (70-11.7 kyr BP) characterised by a dramatic sea-level drop of 100 to 120 m (Kelletat, 2005) and the development of the North Sea Lobe of the BIS (Livingstone et al., 2012). North Yorkshire was covered by ice, which retreated and re-advanced a number of times (Catt, 2007), ultimately retreating from the area by 16 kyr BP (Clark et al., 2012). Erosive and accumulative remnants of glaciation have been identified in the North-eastern England, both on- and offshore: drumlins, erratics, eskers,

glaciolacustrine deposits, meltwater channels and moraines (Clark et al., 2004; Evans et al., 2005). Glacial till overlies the terrestrial sections of the studied area, including the 10-20 m uppermost sections of coastal cliffs. Due to the shore-parallel bedrock dip (2° north-south trending; Rawson and Wright, 2000), at some locations (e.g. Runswick and Upgang) the till is located approximately at the present sea level (Figure 3.4) (Andrews and Smith, 1969; Rawson and Wright, 2000; Lodwick, 2007; Roberts et al., 2013). This dramatic difference in lithology between the hard Jurassic rocks and the glacial diamicton results in significant differences in mechanisms of cliff erosion within the study area (rockfall and landslides) as well as the retreat rates and magnitude frequency patterns.

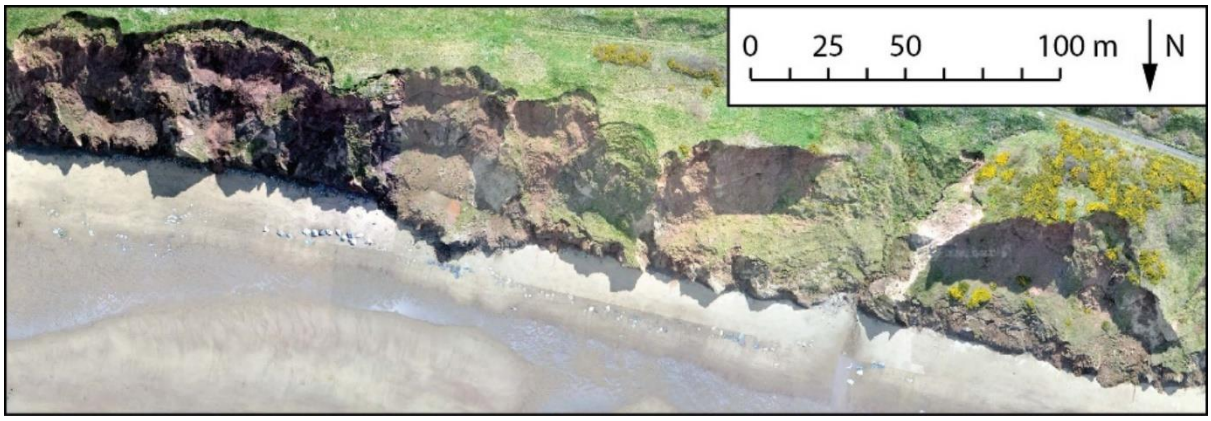


Figure 3.4 Landslide complex on cliff face composed of glacial till, Whitby Golf Club (Upgang), North Yorkshire; LiDAR 2016 orthophotograph mosaic.

Holocene ‘eustatic’ sea-level rise resulted in re-drowning of the North Sea basin up to the present level (Shennan et al., 2000, 2018; Shennan and Horton, 2002). Waves have cut through the glacial deposits and in many places excavated hard-rock cliffs and shore platforms which had been formed during the last interglacial (Trenhaile, 1987). Glacio-isostatic adjustment has resulted in differential relative sea-level (RSL) change across the British Isles in Late Holocene. Figure 3.5 shows the local RSL change curve for Tees mouth, the northern limit of the North Yorkshire coast (Shennan et al., 2018).

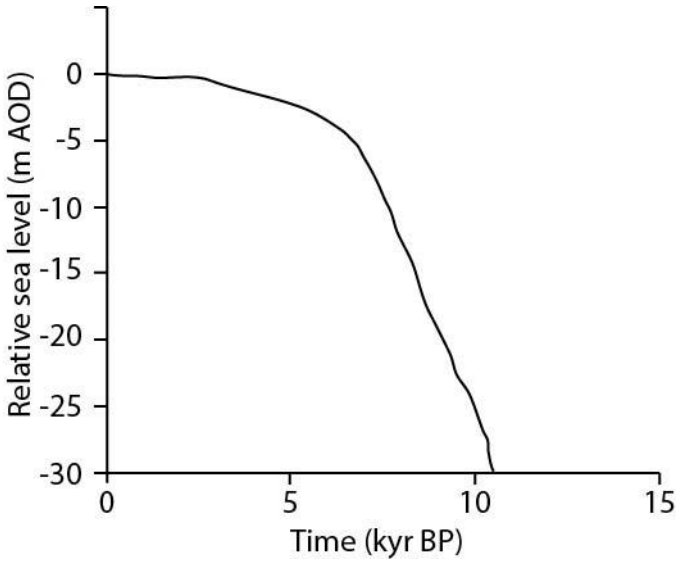


Figure 3.5 Relative sea-level change model for the last ~11 kyr for Tees (ca 25 km north-west of Staithes) with glacio-isostatic adjustment model of Bradley et al. (2011); after Shennan et al. (2018).

3.5. Current marine conditions

Tidal regime is important for foreshore erosion as it delimits the vertical extent of direct wave action and the frequency of submergence/emergence transition which influence the efficiency of mechanical weathering (section 2.4.3.1). In this thesis, when monitoring erosion (Chapters 5 and 7), two quantitative tidal variables – tidal duration and inundation frequency – are considered potential controls on foreshore erosion. The vertical and horizontal distribution of tidal duration is also included in the model to calculate exposure ages from cosmogenic ^{10}Be concentrations because of the impact of water on the reduction of the surface isotope production (Chapter 8).

The North Yorkshire coast is a storm-wave dominated environment at the western part of the North Sea (Rosser et al., 2013). High wave dynamics is reflected in apparent almost absence of beach material, except migrating pocket beaches in bays, and in the fast removal of rockfall-derived debris from the cliff toe. The still water level is located up to 1 m above the cliff toe during high spring tides and offshore from the seaward edge of the platform during low spring tides. The dominant wave direction is from NE (Vann Jones et al., 2018). In 2013-2014 the mean wave height was 0.95 m and the maximum wave height – 9.26 m as reported by Vann Jones et al. (2018) for a location 1.5 km offshore of Staithes.

The closest tide gauge is located in Whitby. Table 3.4 contains the tidal data and calculations for 2008-2026. The coastline, defined as the water/land edge at the mean high water level of spring tides (MHWS) (Oertel, 2005), is located at 2.59 m AOD. The 2006-2010 hourly tidal data of NERC

British Oceanographic Data Centre (https://www.bodc.ac.uk/) was used to calculate tidal duration distribution at the Whitby tide gauge (Figure 3.6).

Table 3.4 Information about the Whitby tide gauge station and tidal levels for 2008-2026; modified from https://www.ntslf.org/.

Latitude	54°29.4'N
Longitude	0°36.9'W
Grid reference	NZ 8986 1140
Highest astronomical tide (HAT)	3.21 m AOD
Mean high water level of spring tides (MHWS)	2.59 m AOD
Mean high water level of neap tides (MHWN)	1.50 m AOD
Mean low water level of neap tides (MLWN)	-0.75 m AOD
Mean low water level of spring tides (MLWS)	-2.01 m AOD
Lowest astronomical tide (LAT)	-2.78 m AOD

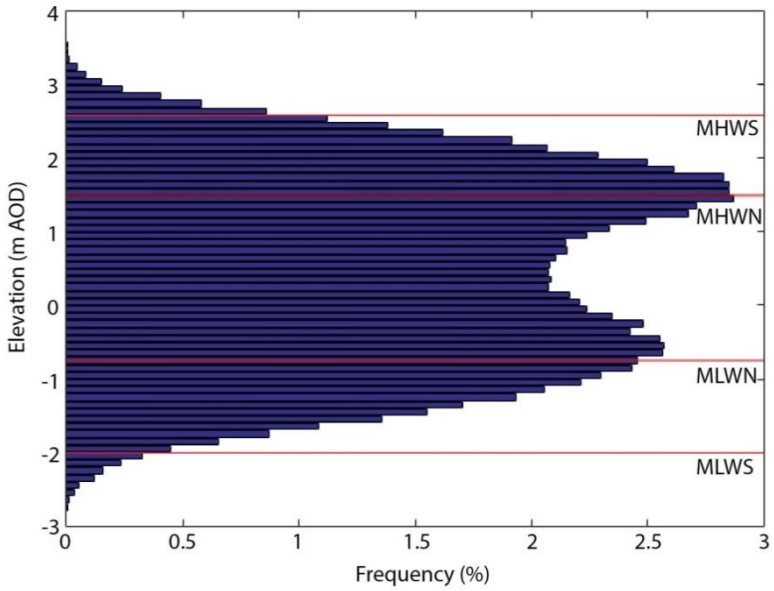


Figure 3.6 Tidal duration distribution for the Whitby tide gauge based on hourly sea-level data from 2006-2010 binned into 0.1 m elevation range bins; data source: https://www.bodc.ac.uk/.

3.6. Coastal erosion

3.6.1. Cliff retreat

Using historical maps, Agar (1960) observed that different lithologies erode at different rates, with one order of magnitude difference between the Lower-Middle Lias and the deltaic series (10^{-2} m yr^{-1}) and the Upper Lias and the glacial till (10^{-1} m yr^{-1}). Moreover, the cliffs in bays seem to retreat faster than at headlands (Table 3.5). Observed differences in erosion rate between the cliff toe and the

cliff top do not have a geomorphological explanation and may indicate the error related to the applied technique, i.e. the mapping inaccuracy relative to the magnitude of erosion (Lim, 2006).

Table 3.5 Cliff recession rates (m yr^{-1}) in North Yorkshire based on historical maps: A) by lithology, B) by morphology; modified from Agar, 1960.

A	Location	Lower Lias	Middle Lias	Upper Lias	Deltaic series	Glacial till
	Huntcliff Station	0.04				
	Staithes, Cowbar		0.05			
	Staithes, Penny Nab		0.1			
	Port Mulgrave, south pier			0.1		
	Runswick Great Ship Rock			0.1		
	Upgang					0.26
	Whitby West Cliff				0.03	
	Whitby East Cliff			0.09		
	Whitby East Cliff			0.19		
	Saltwick Nab			0.04		
	Near Black Nab			0.11		
	Robin Hood's Bay	0.07				
	Robin Hood's Bay					0.31
	Robin Hood's Bay	0.16				
	Low Peak	0.05				
	AVERAGE	0.08	0.075	0.105	0.03	0.285

B	Morphological unit	Cliff top	Cliff toe
	Headlands	0.01	0.04
	Bays	0.04	0.07
	ALL	0.02	0.05

Lim et al. (2009) monitored cliff erosion in the area to the west of Staithes on a monthly basis over a period of 20 months using TLS and digital photogrammetry, observing an average cliff recession rate of 0.065 m yr^{-1}. Using the monthly TLS data for a longer time period of 7 yr resulted in the detection of slower retreat (0.027 ± 0.029 m yr^{-1}) with V_{min} = 1.00×10^{-4} m^3 (Rosser et al., 2013). This observed slow erosion rate combined with a high local standard deviation in rate suggests episodicity in hard rock cliff failure.

In Chapter 8 the results of Rosser et al. (2013) are used to represent the short-term cliff retreat rates which are compared with the millennial-scale erosion rates calculated by cosmogenic isotope concentrations.

3.6.2. Shore platform erosion

Robinson (1977 a,b) monitored the down-wearing of shore platforms between Saltburn and Robin Hood's Bay in North Yorkshire (Table 3.6), setting up 70 MEM stations (see section 2.3.1) at nine locations along the coast taking readings at two-month intervals between November 1970 and July 1972. The average erosion rate calculated based on all stations equalled 3.21 ± 4.76 mm yr^{-1}. Robinson (1977a) divided the shore platforms into two morphological classes – a near-horizontal planar section which occupied a major part of the platforms and an up to 15° steep ramp located closer to the cliff. The down-wearing rates for the two domains were of 1.33 ± 2.17 mm yr^{-1} and 5.20 ± 5.87 mm yr^{-1}, respectively. The erosion was 15-18.5 times faster at the locations covered by the pocket beach deposits. The ramp eroded faster in the winter when more storms occurred, while the planar part experienced more erosion in the summer when the high temperatures enhanced the efficiency of the wetting/drying cycle (Robinson, 1977 a,b). Reliance upon the MEMs had a number of limitations including the inability to: 1) characterise the size and shape distributions of detachments in order to constrain the mechanisms of erosion; 2) establish the quantitative links with factors controlling spatial distribution of erosion rates; and 3) encompass range of morphological situations such as sloping and stepped surfaces (section 2.3.2). Chapter 4 presents an alternative method to monitor foreshore micro-erosion, and in Chapter 5 the results are discussed with the study of Robinson (1977a).

Table 3.6 The average down-wearing rates of the shore platforms along the North Yorkshire coastline: A) the planar part; B) the ramp; based on Robinson, 1977a.

	Location	Erosion rate (mm yr^{-1})
A	Saltwick Bay	2.25
	Whitby Harbour	1.14
	Lingrow A	0.13
	Lingrow B	1.10
	AVERAGE	1.33 ± 2.17
B	White Horse	0.25
	White Stone Hole A	1.25
	White Stone Hole B	7.24
	Fourth Bight	12.27
	Lingrow B	14.66
	AVERAGE	5.20 ± 5.87
	ALL	3.21 ± 4.76

Throughout this thesis, shore platform down-wearing rates are reported in mm yr^{-1} while the cliff retreat rates are reported in m yr^{-1} to keep the results consistent with existing literature.

3.7. GIS mapping of the coastal geomorphology

3.7.1. General morphology of the North Yorkshire coast

Geomorphological mapping was undertaken in order to quantitatively describe geomorphology of the North Yorkshire coast, provide the basis for the sub-metre scale monitoring of foreshore erosion (Chapters 6-7), and to identify the location of the detailed study of direct relationships between foreshore morphology, rock hardness and structure (section 3.8).

A rotary wing airborne LiDAR survey was conducted along a 27 km section of the North Yorkshire coastline between Skinningrove and Whitby on 15 August 2014 (herein referred to as LiDAR2014), which provided a point cloud of 41.78 points m^{-2} density organised in 49 tiles of ~500 m alongshore (Figure 3.3A) and orthophotographs of ~0.03 m pixel resolution (Benjamin et al., in review). The tiles were combined into a single LAS Dataset and a DEM and a slope map were created at 0.2 m resolution. The coastline was found by extraction of the 2.59 m AOD isolines, elevation representing the mean high water level of spring tides (MHWS), and selection of the continuous line parallel to the cliff smoothed with 5 m moving tolerance.

A 400 m wide seaward and landward buffer was applied on the 22 km stretch of the coastline between Skinningrove and Sandsend to delimit the area for the geomorphological mapping. The section between Sandsend and Whitby was omitted in further analysis due to the absence of shore platforms (Figure 3.3A).

Based on the literature and field observations, eight major morphological classes were established at the North Yorkshire coast: sea, shore platform, cliff face, upper slope, hinterland, beach deposit, built infrastructure and river channel with shore platform and cliff face being the most important for this study (Table 3.7; Figure 3.7 A and B). The boundaries between the morphological classes were mapped manually based on the slope map, the orthophotographs and other supporting sources (Table 3.8). When the seaward edge of the shore platform could not be established at the mean low water level of spring tides (MLWS) (Kennedy, 2015) due to an absence of elevation and orthophotographic data, the data were supplemented with GoogleEarth orthophotomaps, the OS 1928 map (1:25,000) and/or the OS 2000 landline based on the OS 1969-72 map. The cliff edge is the interface of the near-vertical hard-rock cliff and the glacial till slope (Table 3.8). At locations where till is present at tide level, the cliff face is < 8 m. Orthophotographs and the slope map were used to manually map the discontinuities on the foreshore including stepped and non-stepped rock bed limits, incised channels, major joints and the sediment cover (Figure 3.7C).

Table 3.7 The morphological classes mapped along the North Yorkshire coast.

Morphological class	Additional information
Sea	Located offshore from the seaward edge of the shore platform and the seaward limit of beach deposit.
Shore platform	A sub-horizontal rock surface located around the tidal level. When the discontinuities are excluded, its slope is of 0-2.5° at the seaward section and of 2.5-15° at the landward section called the ramp (Robinson, 1977a).
Cliff face	A near-vertical hard-rock wall.
Upper slope	Located on the top of the hard-rock cliff. As it is composed of the glacial till, its morphology is shaped by landslides which dominate erosion. Landslide niches are usually clearly visible and the top sets the boundary with the hinterland.
Hinterland	The area behind the cliff not directly exposed to the coastal processes.
Beach deposit	Located at the coastline sections with no shore platforms and at river mouths. Sometimes it covers parts of the platform.
Built infrastructure	Buildings, roads and coastal infrastructure: seawalls, piers and groynes.
River channel	Encompasses the whole channels mapped from the slope maps and the DEM rather than from river extent.

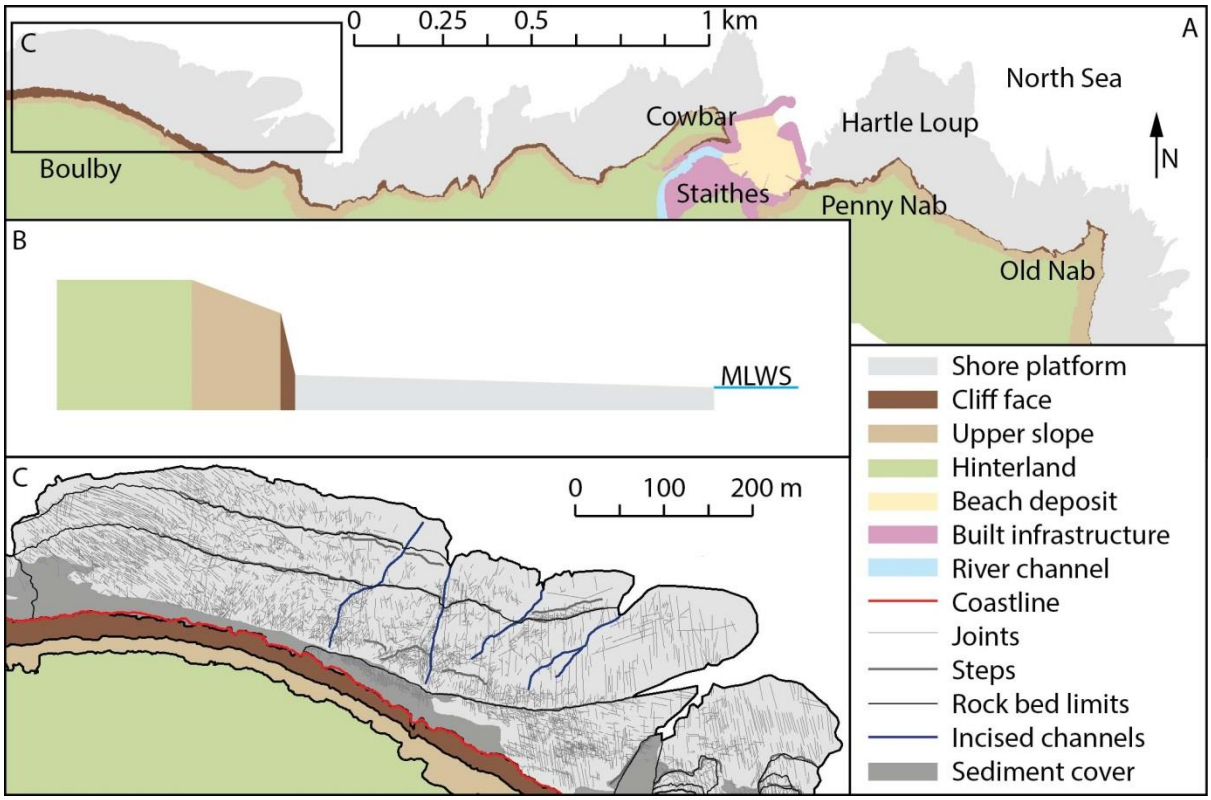


Figure 3.7 Coastal morphological classes: A) alongshore distribution in Staithes area; B) conceptual cross-shore distribution; C) results of the detailed mapping in Boulby area.

Table 3.8 The linear features mapped to delimit the major morphological classes along the North Yorkshire coastline.

Linear feature	Limiting classes (Table 3.7)	Mapping sources
Seaward edge	Sea/Shore platform	DEM (MLWS), slope map, orthophotographs, GoogleEarth orthophotomaps and historical maps (OS 1928 and OS Landline 2000)
Cliff/platform junction	Shore platform/Cliff face	Slope map (usually clear boundary between < 15° and > 65°) and orthophotographs
Cliff edge	Cliff face/Upper slope	Slope map (usually clear boundary between > 65° and < 35°)
Cliff top	Upper slope/Hinterland	Slope map (usually clear boundary between 15-35° and < 15°) and orthophotographs
Beach limit	Beach deposit/Any	Orthophotographs and historical maps (OS 1928 and OS Landline 2000)
Infrastructure limit	Built infrastructure/Any	DEM, slope map and orthophotographs
Channel limit	River channel/Any	DEM, slope map and orthophotographs

3.7.2. Detailed morphology of Hartle Loup

3.7.2.1. Foreshore characteristics

Hartle Loup has been selected for exposure dating using cosmogenic isotope concentration due to the mineral composition and grain sizes of the quartz exposed in the intertidal zone (section 3.3.1). Its morphologic and geologic diversity makes it a suitable location for the micro-erosion monitoring (Chapter 5). This section presents geomorphological characteristics of this platform.

Hartle Loup is located east from Staithes harbour at the foot of the Penny Nab cliffs (Figure 3.7A). Figure 3.8A shows results of the geomorphological mapping of the 1.26×10^5 m^2 of adjacent platform. The platform is composed of rock beds, i.e. exposures of uniform lithology, some of which are divided by steps. Incised channels cut through the platform. A significant part of the platform is highly jointed, while the sediments – pocket beaches and coarser-grain debris from cliff failure – accumulate under the cliff. Elevation varies between -1.8 and over 5 m AOD (Figure 3.8C). Platform topography expressed by the slope and the roughness is highly variable with smoother eastern parts, and more uneven western parts (Figure 3.8 D and E).

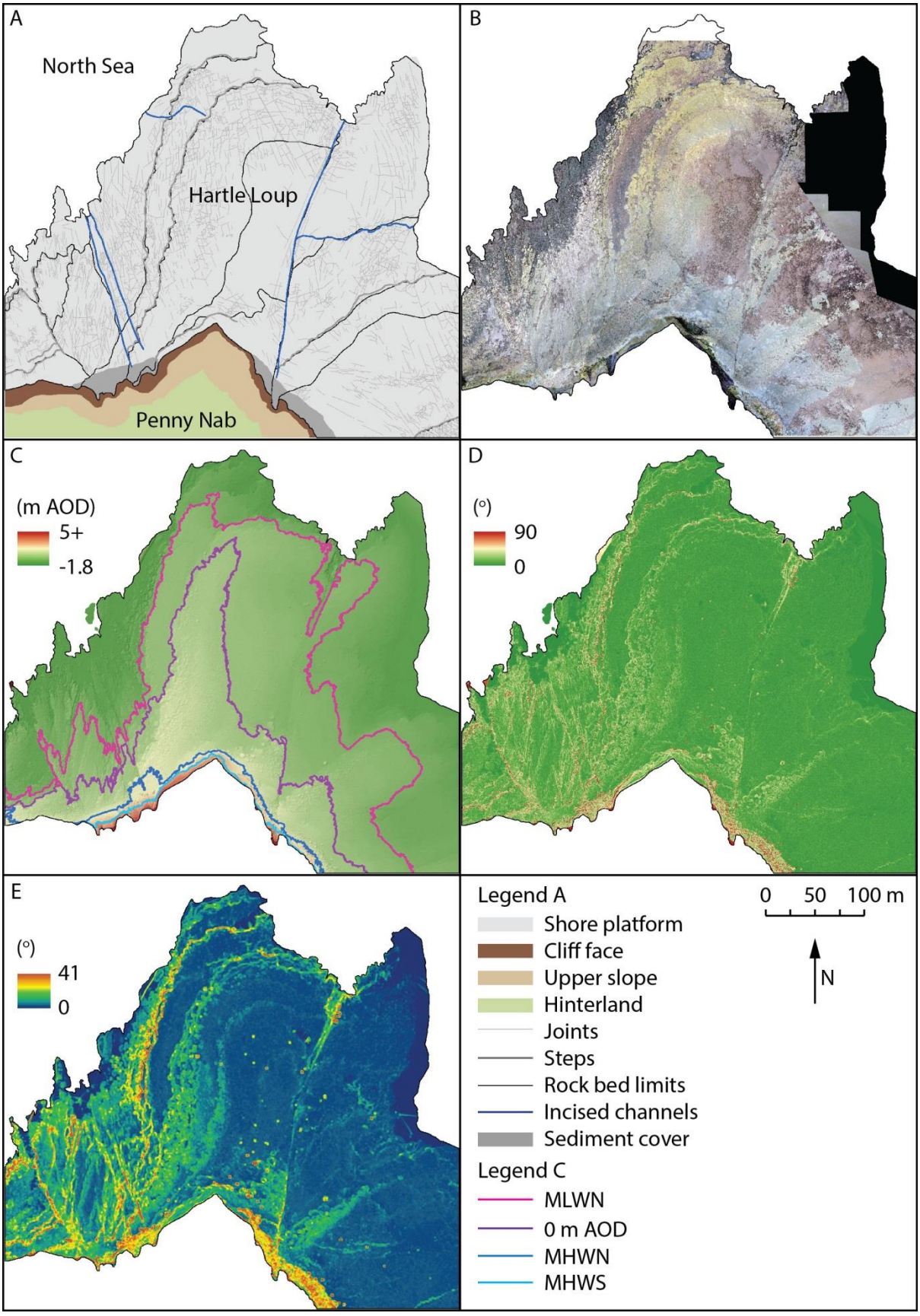


Figure 3.8 Morphology of Hartle Loup: A) geomorphological map; B) orthophotograph mosaic; C) DEM; D) slope map; E) roughness map. C, D and E are at 0.1 m resolution; source: LiDAR2016.

Herein the surface roughness is expressed as standard deviation of the slope (see Smith, 2014). To find the scale, or number of pixels, to create an optimal roughness representation, roughness maps were created with values of standard deviation of the slope at zones (cells) with sizes ranging from 3×3 to 51×51 cells. The mean pixel value from each raster was extracted and the best trendline was fitted between the square size and the value (Figure 3.9). The slope of the trendline decreases with the number of cells and the value stabilises around 5°. 17 cells square was selected as a good representation of the roughness as it in between the value range of an abrupt slope decrease, and of slow decrease, and it is an equivalent of ~75% of the value predicted at 101×101 cell-square (5 m) (Figure 3.8E).

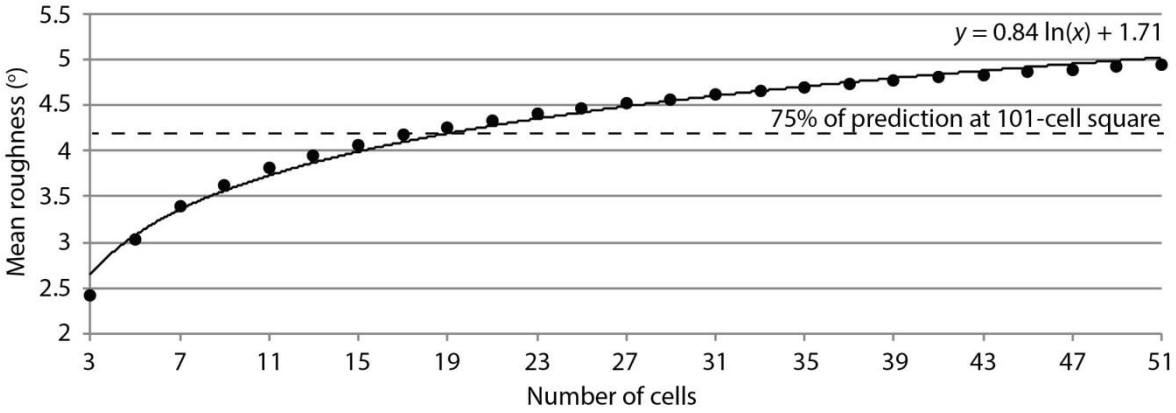


Figure 3.9 Mean roughness as a function of cell size used to calculate standard deviation of the slope.

The distance from the cliff varies between 0 and 330 m, and the distance from the seaward edge – between 0 and 210 m, the two values being different because of the variable platform width (Figure 3.10 A and B). Tidal duration, the fraction of time the sea level is within a 0.1 m elevation bin which encompasses the value of the DEM pixel, varies between 0 and 2.9% with the lowest and the highest parts of the platform hardly ever being at the tidal level (Figure 3.10C). Inundation frequency, the fraction of time the DEM pixel remains under water, varies between 0% (constant exposure) and 97% (near-constant submergence) (Figure 3.10D). The platform is cut in two rock types, sandstone and shale, with the former spreading across the western and the seaward part of the platform (Figure 3.10E).

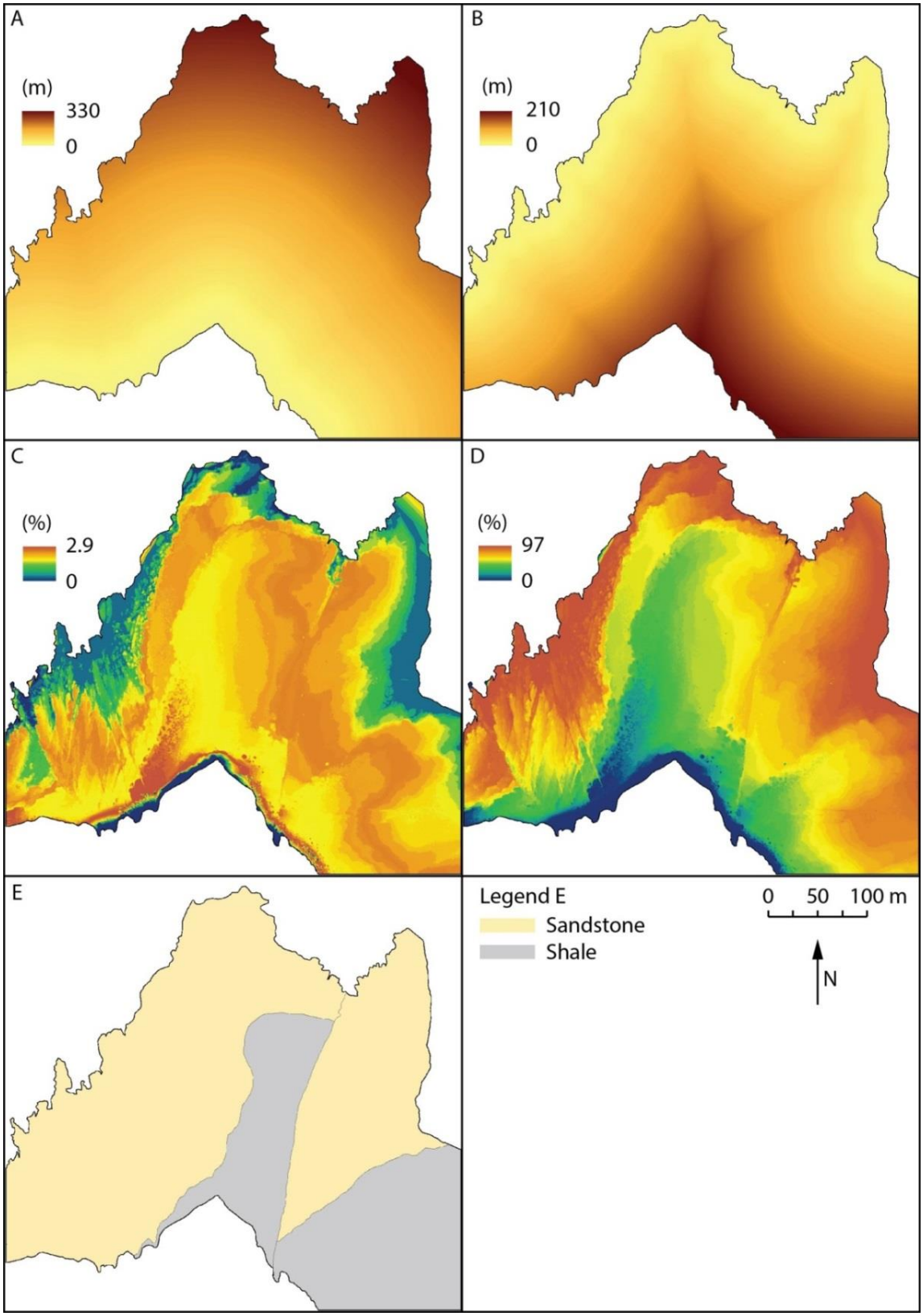


Figure 3.10 Spatial, marine and geological characteristics of Hartle Loup: A) distance from the cliff; B) distance from the seaward edge; C) tidal duration; D) inundation frequency; E) rock type (based on http://www.southampton.ac.uk/~imw/staithes.htm). A-D are at 0.1 m resolution; source: LiDAR2016.

3.7.2.2. Field evidence of erosion

Prior to monitoring foreshore erosion (Chapters 4 and 6), Hartle Loup was visually inspected in order to constrain scales at which processes operate to design suitable monitoring techniques. Meso-scale (10^{-1} – 10^{0} m) discontinuities are present at the boundaries between rock beds and as within-bed joint network (Figure 3.11 A and B). These linear discontinuities are exploited both vertically (deepening) and horizontally (widening), and tend to be densely colonised by organisms due to the sheltering from the intense wave action (Moses, 2014). The platform is cut by a series of steps which seem to retreat via the combination of block removal and abrasion/hydraulic action (see lack of barnacle cover at the step edge in Figure 3.11C). Detached blocks accumulate at the foot of steps (Figure 3.11C), but during the storm events they may be pushed landwards or broken and removed from the foreshore (Paris et al., 2011). Hartle Loup terminates with a steep seaward slope or cliff. Figure 3.11D shows that the waves break farther offshore, which suggests that another bench may be located below the low tidal level (note: the photographs were taken during the lowest tide of the spring tides on 21 July 2016). Resistant ironstones persist on the platform in the form of pedestal rocks or protruding nodules (Figure 3.11 E and F). Ongoing erosion is evidenced by exposures of fresh surfaces (Figure 3.11 G and H). The rock micro-structure – shale platelets and thin sandstone layers, the apparent lack of sediments on the platform except the ephemeral pocket beaches at the cliff toe, and the dense barnacle cover, in particular on the seaward part of the platform, suggest that erosion via detachment of rock fragments rather than grain-by-grain abrasion may be the dominant platform erosion process on Hartle Loup.

Figure 3.12 illustrates an example of platform erosion via block removal. In November 2015 blocks were detached from a small step in the upper part of the platform at the western side of the Penny Nab headland. The breakage resulted in production of two main boulders with structurally-controlled angular morphology, and some smaller blocks (Figure 3.12A). The former remained *in situ* for over a year while the latter were removed by the waves. Smaller material, such as pebbles, gravels and shells, was deposited in the sheltered area between the step and the boulders (Figure 3.12B). During the storm on 13th January 2017 the two blocks were removed. One of them was broken into two pieces which were transported landwards and turned upside-down, while the other was removed completely from the area. After the storm the platform was temporarily covered by sand (Figure 3.12C).

These observations suggest that erosion happens at the millimetre to centimetre and sub-metre to metre scales, and so the monitoring techniques to quantify erosion and identify controls upon it should be able to resolve change at these scales (see Cook, 2017).



Figure 3.11 Morphology of Hartle Loup: A) an outflow channel at the boundary between rock beds; B) a joint network; C) a step with detached boulder; D) a steep slope of the seaward edge; E) a pedestal rock; F) an ironstone nodule; G) fresh exposure of the shale surface; H) fresh exposure of the barnacle-covered sandstone surface.



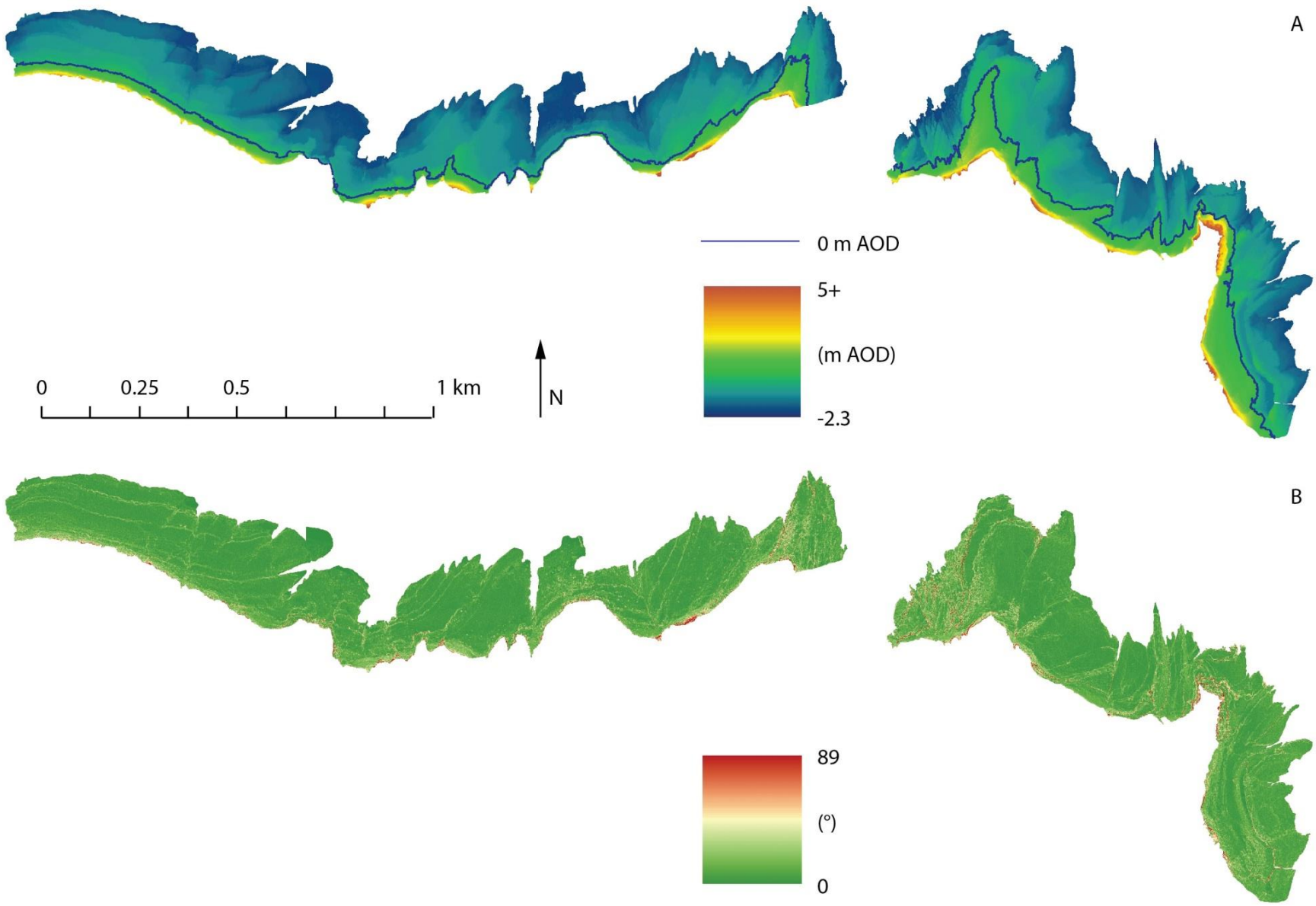
Figure 3.12 Example of the shore platform erosion via block removal: A) fresh detachment of blocks; B) concentration of loose material behind the blocks; C) results of rock entrainment during the storm event.

3.8. Rock control on shore platform morphology at the local scale

Theoretical and low-resolution empirical studies have shown that higher, steeper and narrower platforms coincide with harder and less jointed rock types (Wright, 1970; Trenhaile, 1972; 1974; 1978; 1980; 1987; Williams, 1986; Stephenson, 2000; Davies et al., 2006; Kennedy and Dickson, 2006; Thornton and Stephenson, 2006). In order to verify whether a quantitative relationship can be established between foreshore morphology and geology at the local scale ($10^2 – 10^3$ m) a high-resolution systematic study was undertaken along a 4.2 km section of the coastline in Staithes area, and the multiple linear regression models were built to explain morphology using geologic variables. This area was selected for the study because of considerable diversity in morphology and geology, and the platform size suitable to perform rock hardness tests at the density which allows a representation of all rock beds (80) by the mean hardness and its standard deviation (Figure 3.7A). Geology is represented by the rock hardness and the joint density, the properties which have been typically used in foreshore studies (Dickson et al., 2004; Cruslock et al., 2010). The results were published by Swirad et al. (2016).

3.8.1. General morphology of the shore platform

The results of geomorphological mapping (section 3.7.1) show that analysed section of the coastline is variable in terms of topography (Figure 3.13). Platform elevation varies between -2.3 and over 5 m AOD (Figure 3.13A). Although the surface is predominantly low angled (< 5°) the slope reaches up to 90° at the cliff toe and the boundaries between rock beds (Figure 3.13B). The roughness varies between 0 and 27.8° and its general pattern agrees with the slope map (Figure 3.13C).


A
0 m AOD
5+
(m AOD)
-2.3
0
0.25
0.5
1 km
N
B
89
(°)
0

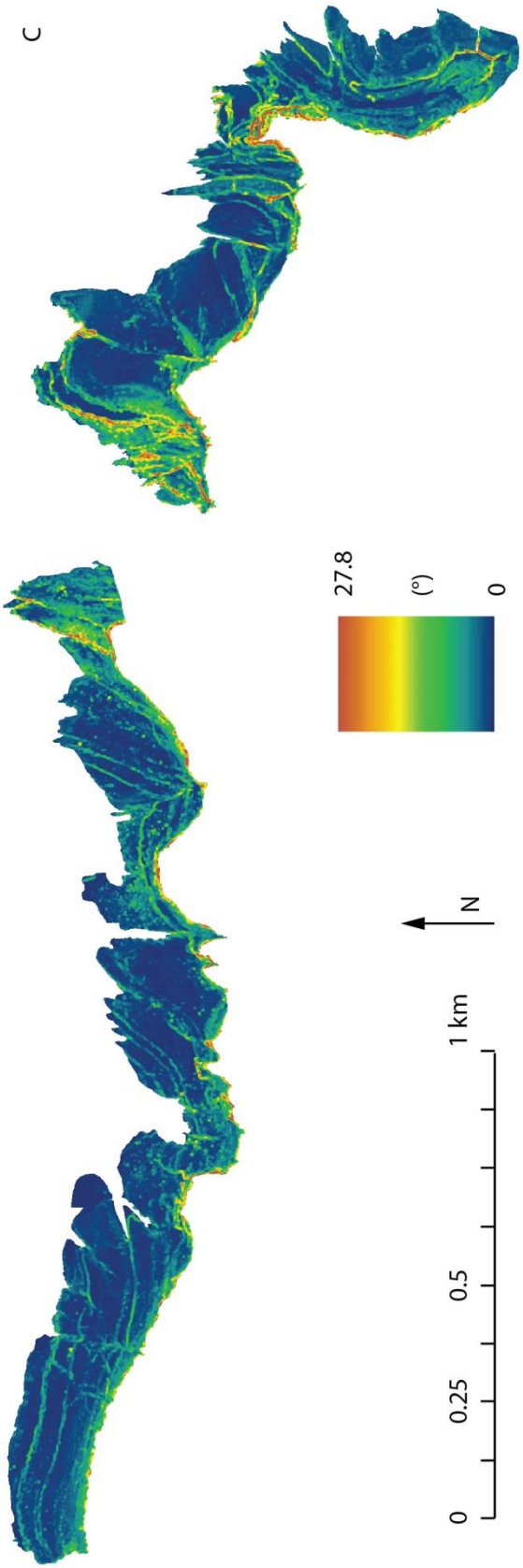


Figure 3.13 Topographic variability along the 4.2 km section of the North Yorkshire coastline in Staithes area: A) elevation; B) slope; C) roughness. The maps are at 0.2 m resolution; source: LiDAR2014.

3.8.2. Characterising rock strength and structure

Rock resistance in shore platform studies is believed to be well represented by the combination of rock hardness and joint density (Dickson et al., 2004). Here, the mapped rock bed limits (section 3.7.1) were used to divide the shore platform into 80 individual beds. Each bed was characterised by its mean hardness and the standard deviation thereof.

The Proceq Equotip 550 Leeb D Type was used to collect the rock hardness readings from 283 sites in May-July 2015 (Figure 3.14). The sampling sites were selected to encompass as many rock beds as possible, but the access to eight beds was prevented due to submergence by water. The number of hardness test sites per bed varied from 0 to 18 with the average of 3.54. Additionally, at 50 sites, readings were taken with the Type N Concrete Test Hammer by Novatest to compare the Equotip and the Schmidt Hammer rebound values as the latter was shown to well represent *UCS* (see Viles et al., 2011). At each sampling site 10 readings were taken before and after removing a millimetre-scale weathered rock layer with the carborundum stone (Figure 3.15). The sites were characterised by the mean weathered and the mean un-weathered hardness with the former representing the fresh surface and the latter its deterioration. At the locations where both the Schmidt Hammer and the Equotip readings were taken, the latter was applied first due to its lower impact.

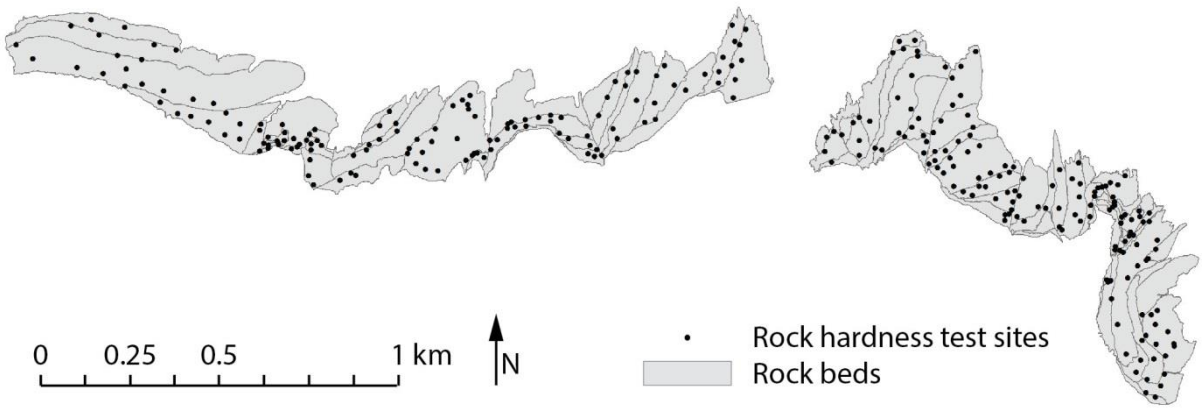


Figure 3.14 Locations of the rock hardness test sites on the shore platforms along the 4.2 km section of the North Yorkshire coast in Staithes area.



Figure 3.15 Acquisition of the rock hardness data with the Equotip durometer: A) taking readings from a weathered surface; B) removing the weathered surface with the carborundum stone; C) taking readings from an un-weathered surface.

Readings taken with the two instruments were compared separately for the weathered and the un-weathered surfaces. A statistically-significant weak to moderate (R^2 = 0.34-0.48, $p < 0.05$) positive correlation was found between the two rock hardness test methods, with a stronger correlation for the un-weathered surface (Figure 3.16). The hardness values were more consistent 1) on the un-weathered surface for both tests and 2) when tested with the Schmidt Hammer (Table 3.9). The latter result may be explained by higher sensitivity of the Equotip and more localised readings (Viles et al., 2011; Coombes et al., 2013).

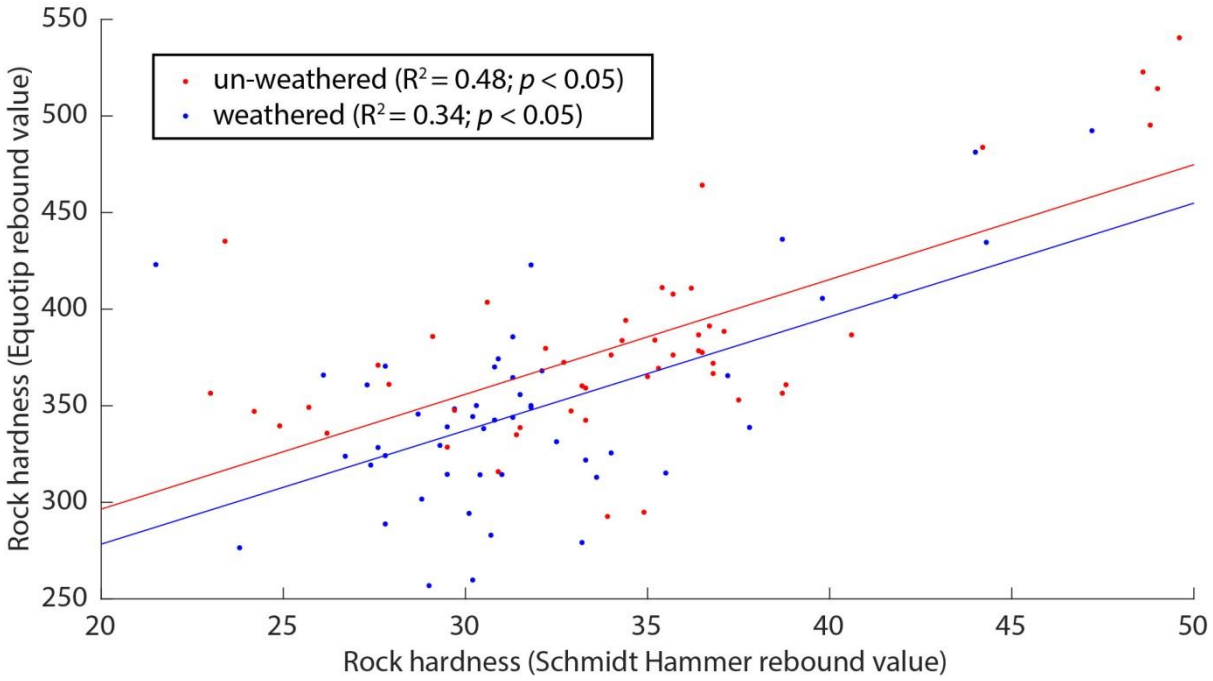


Figure 3.16 Relationships between Schmidt Hammer and Equotip rebound values on the un-weathered and the weathered rock surfaces along the 4.2 km section of the North Yorkshire coast in Staithes area.

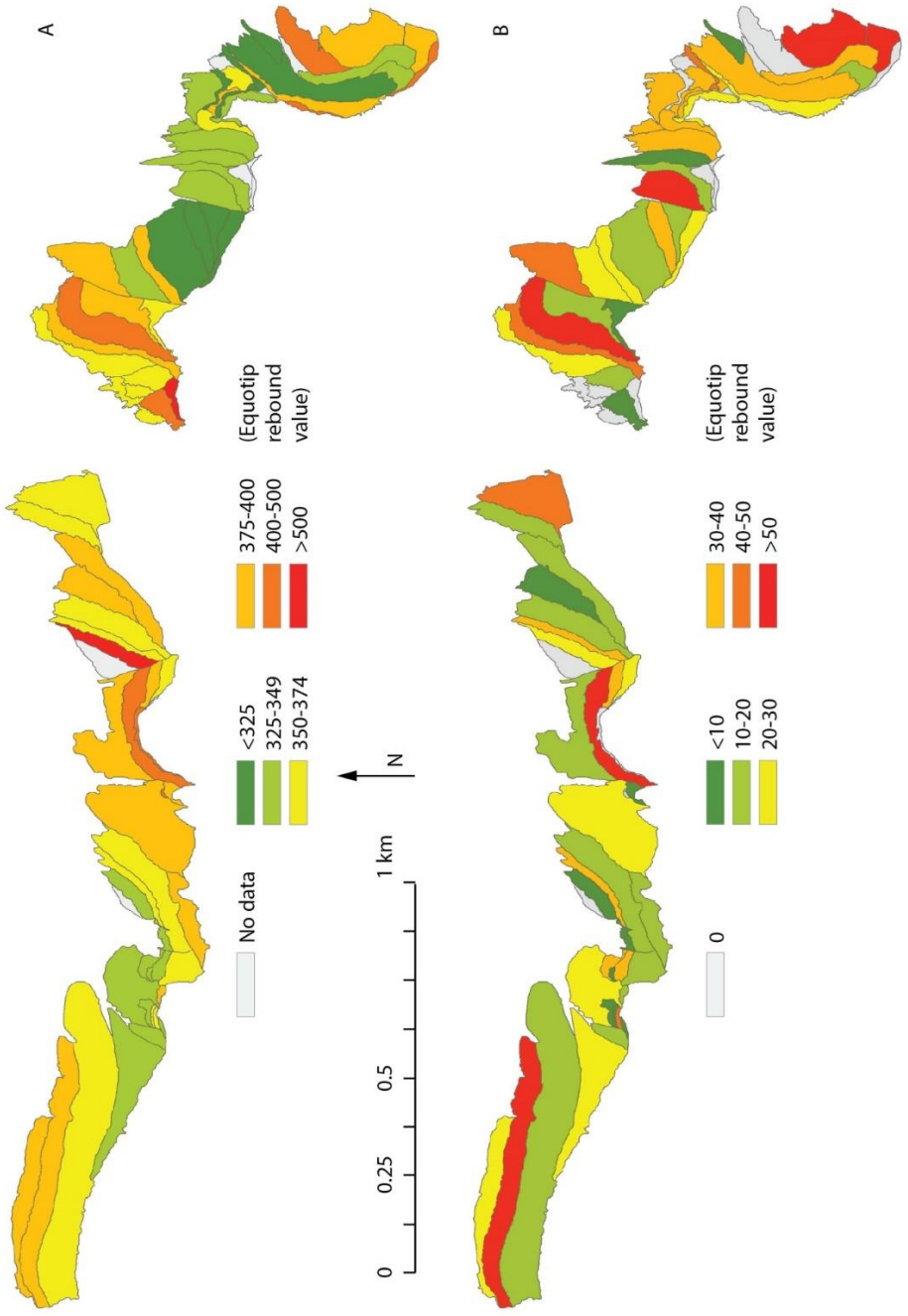
Table 3.9 Mean coefficient of variation (standard deviation/mean) of the Schmidt Hammer and the Equotip readings on the un-weathered and the weathered rock surfaces along the 4.2 km section of the North Yorkshire coast in Staithes area.

	Total	Un-weathered	Weathered
Total	0.14	0.12	0.16
Schmidt Hammer	0.13	0.11	0.14
Equotip	0.15	0.14	0.17

The general reduction of the rock hardness due to weathering was observed at 36 sites (72%). However, at six sites the weathered surface was harder than the un-weathered, which can be explained by the existence of an outer crust (Viles et al., 2011). At four locations the Schmidt Hammer tests indicated that the un-weathered rock was harder, while the Equotip showed the opposite. Where the rock surface is polished due to the dominance of abrasion over weathering, the carborundum treatment, i.e. the operator factor, may result in the increase of micro-roughness (Feal-Pérez and Blanco-Chao, 2012). As the Equotip measures the rock hardness from much smaller volumes than the Schmidt Hammer (Viles et al., 2011), the micro-roughness may strongly impact the hardness readings. At four sites the Equotip readings were higher for the un-weathered rock and the Schmidt

Hammer readings – for the weathered rocks, which was an effect of the carborundum treatment causing the shale platelet loosening and subsequent destruction by the Schmidt Hammer.

Since a positive relationship comparable to that of Viles et al. (2011) was found between the Schmidt Hammer and the Equotip rock hardness readings, the latter were accepted as suitable to represent the rock hardness. 80 rock beds were represented by the mean rock hardness of un-weathered surface and its variability expressed by the standard deviation (Figure 3.17 A and B). Both the mean hardness and its standard deviation vary considerably for different lithologies ranging between 297-526 and 3-89 Equotip rebound value, respectively. The mapped joints (section 3.7.1) were converted into the joint density map using ArcMap *Line Density* tool. Raster resolution and searching radius equal 1 m (Figure 3.17C).



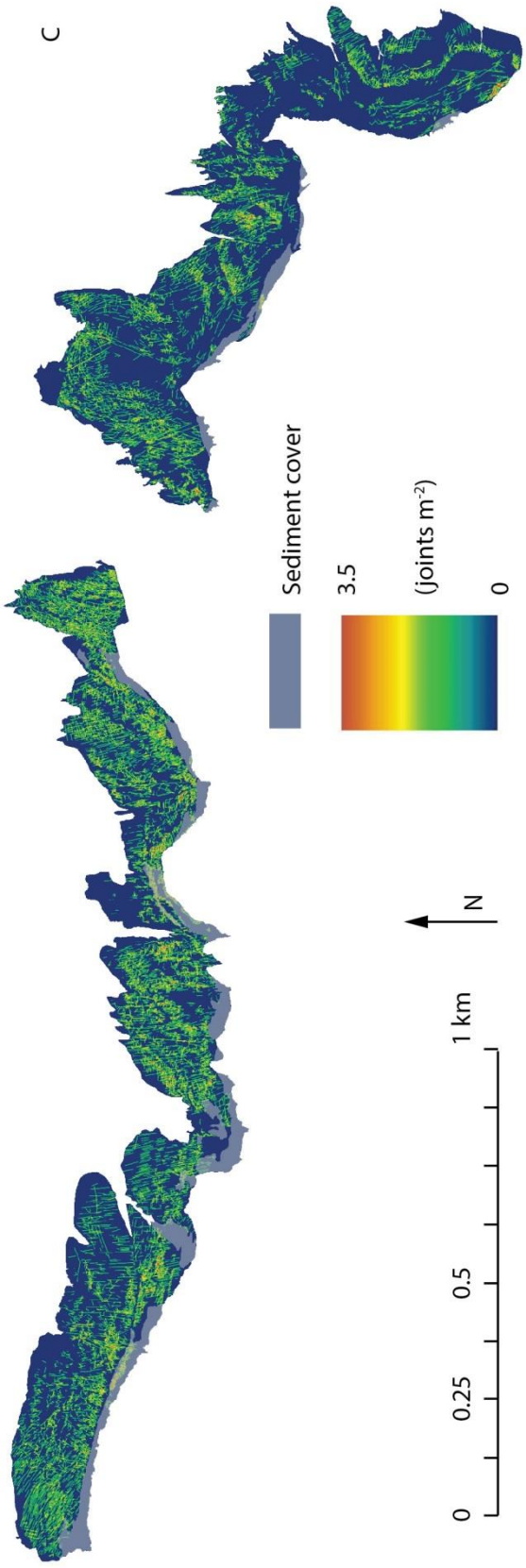


Figure 3.17 Geological variability across the shore platforms along the 4.2 km section of the North Yorkshire coast in Staithes area: A) mean rock hardness of 80 rock beds; B) standard deviation of rock hardness of 80 rock beds; C) joint density at 1 m resolution.

3.8.3. Representing shore platform in form of coastal cross-sections

A series of 169 equally-spaced (every 25 m) station lines perpendicular to the coastline were automatically extracted and spatially-limited to encompass only the shore platform and the cliff (Figure 3.18A; Matsumoto et al., 2017). The lines that were crossing one another were manually rotated. The elevation values were given to the lines at a 0.2 m resampling interval resulting in a series of 2D cross-sections (Figure 3.18B). The coastal cross-profiles vary in morphology with the diverse cliff height, horizontal stretch of the cliff and platform width. Morphology of the platform at the cliff toe is diverse with sections of the platform abruptly decreasing in height and other sections maintaining the high elevation for a larger portion of the width (Figure 3.18 B and C).

The DEM and the slope map were resampled along the cross-sections at 0.2 m interval. The shore platform morphology was represented by the width, the gradient, the elevation, the elevation of the cliff/platform junction (Figure 2.1) and the roughness. The width was measured as the horizontal distance between the cliff/platform junction and the seaward edge. The gradient represents the dip of a straight line between the cliff/platform junction and the seaward edge. The elevation of shore platform is a mean of elevations of the resampled points. The elevation of the cliff/platform junction was extracted from the seaward-most resampled point classified as the cliff face. The roughness was calculated as the standard deviation of the slopes of all resampled points across the platform (note the difference of calculating the roughness in Figure 3.13C).

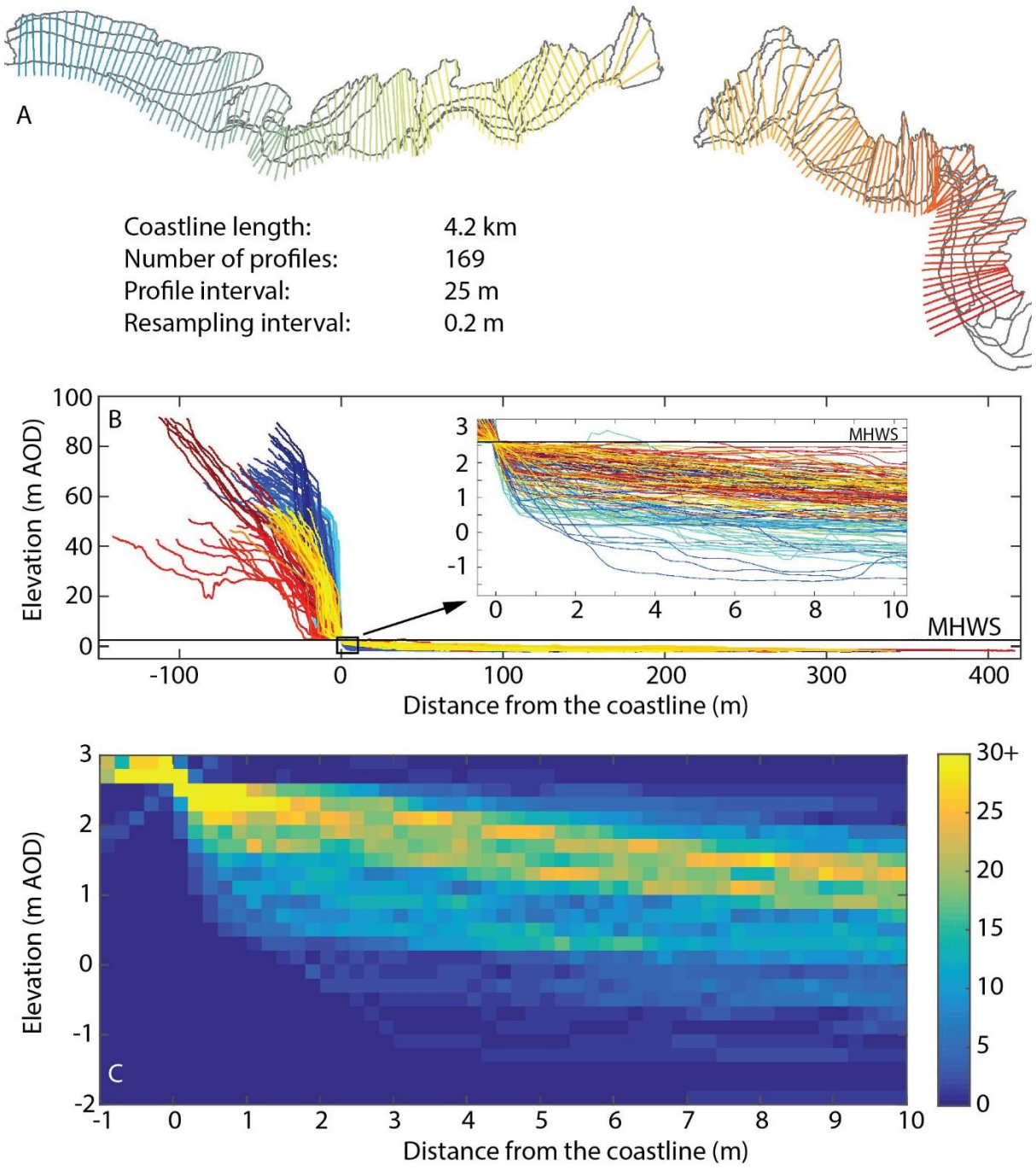


Figure 3.18 Automatically extracted coastal cross-sections limited to the shore platform and the cliff along the 4.2 km section of the North Yorkshire coast in Staithes area: A) alongshore distribution; B) cross-shore distribution (colours correspond to A); C) density map of the elevation occurrence for part of the profiles depicted in the inset map of B.

3.8.4. Relationships between geological variables and shore platform morphology

3.8.4.1. Methods

The 169 profiles across the shore platforms were ascribed three geological and five morphological variables using the methods described in sections 3.8.2 and 3.8.3 (Table 3.10). Platform width and gradient were transformed to the square root scale in which their distribution was closest to normal, which is important for the linear regression modelling (Figure 3.19).

Table 3.10 Variables used in the profile-based analysis of the geomorphic conditions of the shore platforms along the 4.2 km section of the North Yorkshire coast in Staithes area. Glossary contains the details of the value calculation.

Variable	Abbreviation	Unit
Platform width	*pWid*	m
Platform gradient	*pGra*	°
Platform elevation	*pEle*	m AOD
Elevation of the cliff/platform junction	*pJun*	m AOD
Roughness	*pRou*	°
Rock hardness	*pHar*	Equotip rebound value
Standard deviation of the rock hardness	*pStd*	Equotip rebound value
Joint density	*pJDe*	joints m^{-2}

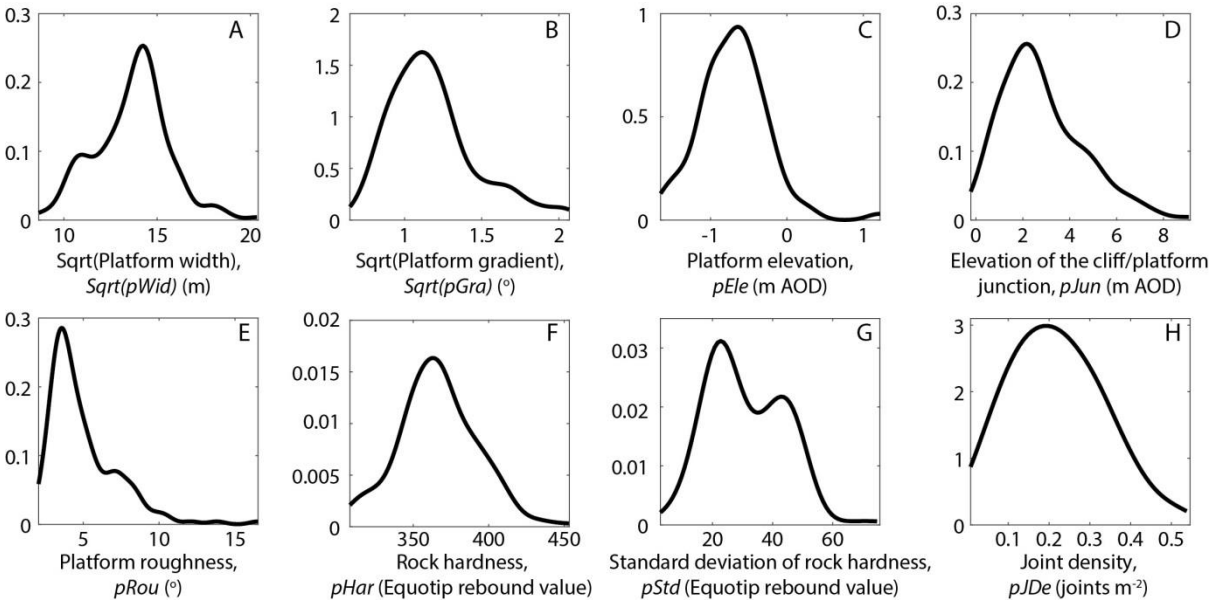


Figure 3.19 Kernel density estimate (normal kernel, default optimal half widths h returned in MATLAB were used) of all variables used in the analysis of the rock control on the shore platform morphology along the 4.2 km section of the North Yorkshire coast in Staithes area: A) Square root of the platform width, Sqrt(pWid) (h = 0.58 m); B) Square root of the platform gradient, Sqrt(pGra) (h = 0.08°); C) Platform elevation, pEle (h = 0.16 m AOD); D) Elevation of the cliff/platform junction, pJun (h = 0.60 m AOD); E) Platform roughness, pRou (h = 0.56°); F) Rock hardness, pHar (h = 9.18 Equotip rebound value); G) Standard deviation of the rock hardness, pStd (h = 5.25 Equotip rebound value); H) Joint density, pJDe (h = 0.05 joints m-2); Y axis: probability density.

Both-way step-wise regression was performed to find the best-fit multiple regression between the geologic and the morphologic variables in order to be able to predict morphology from geology and to find controls on the alongshore diversity in foreshore geometry. The assumption was subsequently tested that the platform width, and hence the wave energy dissipation, is a proxy for wave intensity (see Poate et al., 2018). Over the studied coastline the wave energy delivery to the seaward edge of the platform was assumed to be constant, and so the dissipation of wave energy would vary by the platform width. Wider platforms would associate with less wave energy per platform unit length and so less energy arriving to the cliff toe. Wave action would be more intense for narrower platforms. Step-wise linear regression was performed on the four remaining morphological variables using the three geological variables and the platform width as an independent variable.

3.8.4.2. Results, interpretations and conclusions

Statistically significant relationships ($p < 0.05$) exist between the geology represented as rock hardness, its standard deviation and joint density, and all platform characteristics except the platform gradient, but all relationships are very weak ($R^2 < 0.10$) (Table 3.11). This means that the geology is not able to explain the morphological variation under assumptions of the study and/or following this methodology.

Table 3.11 The best-fit multiple linear regression for the shore platform morphology along the 4.2 km section of the North Yorkshire coast in Staithes area. Asterisks (*) indicate significant relationships ($p < 0.05$). For independent variable definitions, see Table 3.10 and Glossary.

Morphological variable	Equation	R^2	p-value
Platform width (m)	$pWid = (17.331 + 0.026\,pStd - 0.012\,pHar)^2$	0.04	0.011*
Platform gradient (°)	$pGra = (1.257 - 0.353\,pJDe)^2$	0.02	0.062
Platform elevation (m AOD)	$pEle = 1.067 - 0.005\,pHar + 0.004\,pStd$	0.09	<0.001*
Elevation of the cliff/platform junction (m AOD)	$pJun = 5.776 - 0.010\,pHar + 0.020\,pStd$	0.03	0.032*
Platform roughness (°)	$pRou = 6.429 - 0.029\,pStd - 2.611\,pJDe$	0.03	0.027*

Including the platform width into the independent variable set results in an improvement of the best-fit multiple regression for the platform gradient and the platform roughness (Table 3.12). 32% of the variability of the platform gradient can be explained by the platform width and the rock hardness, while 14% of the platform roughness variability can be described by the platform width, the joint density and the standard deviation of the rock hardness.

Table 3.12 The best-fit multiple linear regression for the shore platform morphology along the 4.2 km section of the North Yorkshire coast in Staithes area under the assumption that the wave intensity can be approximated by the platform width. Asterisks (*) indicate significant relationships ($p < 0.05$). For independent variable meaning see Table 3.10 and Glossary.

Morphological variable	Equation	R^2	p-value
Platform gradient (°)	$pGra = (2.909 - 0.083\sqrt{pWid} - 0.002\,pHar)^2$	0.32	<0.001*
Platform elevation (m AOD)	$pEle = 1.067 - 0.005\,pHar + 0.004\,pStd$	0.09	<0.001*
Elevation of the cliff/platform junction (m AOD)	$pJun = 5.776 - 0.010\,pHar + 0.020\,pStd$	0.03	0.032*
Platform roughness (°)	$pRou = 11.381 - 0.392\sqrt{pWid} - 2.235\,pJDe - 0.018\,pStd$	0.14	<0.001*

The statistical analysis of the stretch of coastline undertaken here allowed the identification of the following relationships between shore platform morphology, the geology and the wave intensity approximated by the platform width:

- The platform is wider where rocks are harder.
- The platform is steeper where it is narrower and rocks are weaker.
- The platform and the cliff/platform junction are higher where rocks are weaker.
- The platform roughness is higher where the platform is narrower, the joint density is lower and rock hardness is less variable.

All identified relationships are significant ($p < 0.05$) and weak ($R^2 \leq 0.32$) which suggests that the direct link between rock resistance expressed by the conventionally used rock properties – rock hardness and joint density – and the morphology of the shore platforms at the local scale cannot be established for the coastal cross-profiles following presented procedure despite the very high-resolution topographic information. Figure 3.20 shows that the morphology predicted with the best-fit equations poorly explains observed diversity in foreshore shape.

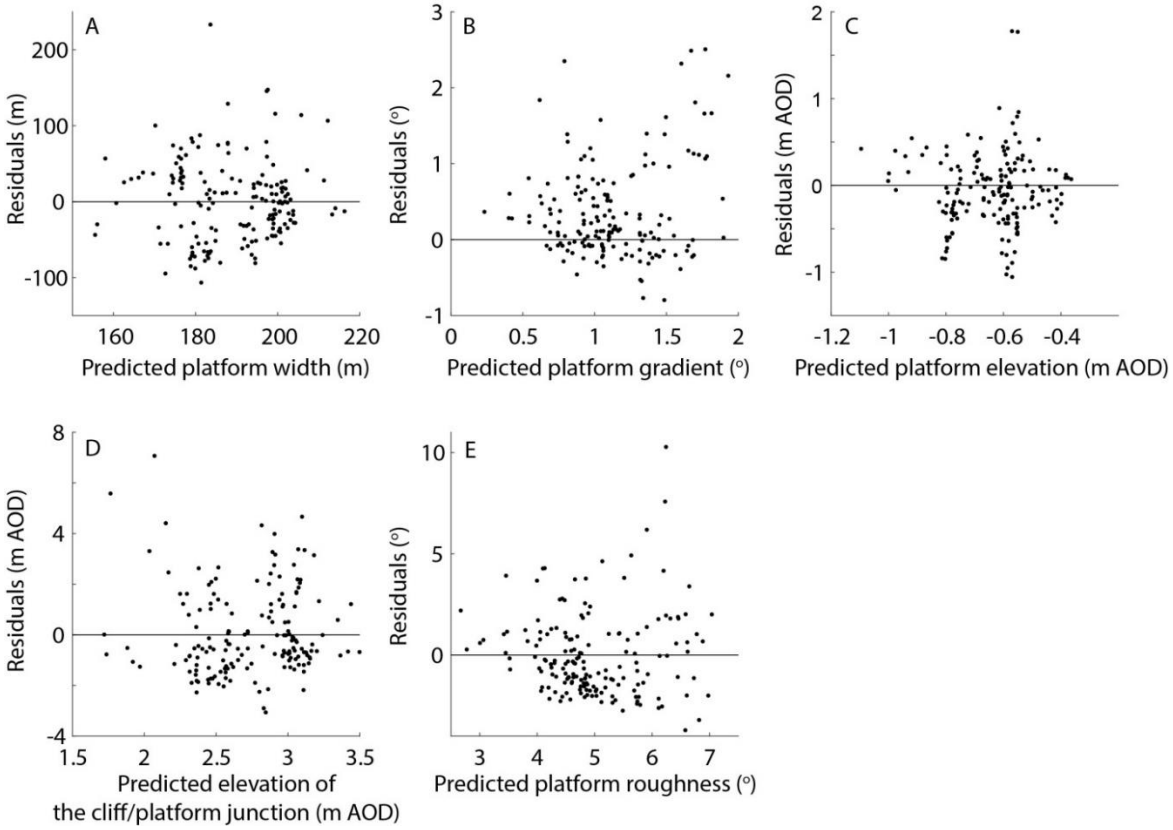


Figure 3.20 Residuals of the best-fit multiple regression of the morphology of the shore platforms along the 4.2 km section of the North Yorkshire coast in Staithes: A) Platform width, pWid (m); B) Platform gradient, pGra (°); C) Platform elevation, pEle (m AOD); D) Elevation of the cliff/platform junction, pJun (m AOD); E) Platform roughness, pRou (°); residuals are calculated as observed-predicted.

There are two possible reasons for the lack of correlation. Firstly, the representation of the shore platform as a series of coastal cross-sections which can be attributed single rock hardness, joint density and morphological values may be incorrect as these vary at smaller scale. For instance, a grid-based approach could be used as an alternative. Secondly, the rock properties used in the study following the standard procedure from the literature may not correctly represent rock resistance. Both cases advocate a need to understand the mechanisms of erosion at the relevant spatio-temporal scales in order to 1) better constrain which measurable rock properties are responsible for rock resistance to specific erosion mechanisms, and 2) define the controls on the shore platform morphology.

3.9. Summary

The North Yorkshire coast is characterised by significant variability in landform morphology, rock type and structure. The average hard-rock cliff retreat rate is 0.027 ± 0.029 m yr^{-1} (Rosser et al., 2013) and for shore platforms, the best-estimate down-wearing rate is 3.21 ± 4.76 mm yr^{-1} (Robinson, 1977a). The morphological evidence suggests that the shore platforms erode primarily via detachments of rock fragments of various sizes (from the millimetre-scale pieces to blocks of > 1 m^3).

Geomorphological mapping was performed along the 27 km stretch of coastline using the high-resolution (~42 points m^{-2}) airborne LiDAR dataset. Detailed mapping was then carried on the shore platforms which span 22 km of the coast and have a total surface area of 3.15×10^6 m^2 that included mapping rock bed limits, joints and sediment cover.

The Hartle Loup shore platform was selected for the micro erosion study (Chapter 5) because of its considerable variability in geology and platform morphology including sloping and stepped surfaces, and for the exposure dating using cosmogenic ^{10}Be concentrations (Chapter 8) due to the mineralogy and grain sizes.

The study of relationships between foreshore morphology – platform width, height, gradient, roughness and elevation of the cliff/platform junction – and geology – rock hardness, its standard deviation and joint density – was conducted along the 4.2 km stretch of coastline in Staithes area. The multiple linear regression modelling shows that geology represented by the rock hardness and the joint density cannot explain the diversity of shore platform morphology at the local scale. It suggests that a study focused on erosion at the relevant spatial and temporal scales is needed to understand the mechanisms and controls of erosion, and to constrain which rock properties express rock resistance to erosion leading to the development of observed topography, which is the scope of subsequent chapters.

4. Developing a new method to monitor bedrock micro-erosion

4.1. Introduction

The aim of this chapter is to describe the procedure to detect bedrock detachments at the small-scale (10^{-3} – 10^{-2} m), which is used to characterise their size and shape, and explain their distribution. The micro-topography is reconstructed using Structure-from-Motion (SfM) photogrammetry. The chapter gives an insight into method optimisation to ensure stable conditions between surveys and development of a set of filters to separate real detachments from error. The method is used in Chapter 5 to quantify and predict shore platform down-wearing. Using SfM allows the reconstruction of topography of a continuous surface and adopting of techniques developed in rockfall/landslide literature. These allow the identification of mechanisms of erosion through analysis of detachment sizes and shapes. Characterising the monitoring sites with a number of independent and erosion variables aims to identify controls on spatial distribution of erosion (section 2.5).

4.2. Site selection

Fifteen sites were selected on Hartle Loup for the small-scale erosion monitoring (Figure 4.1) in order to encompass a wide range of tidal levels, rock types, structure – joint or discontinuity density – and the style of relief: planar, sloping and stepped (Table 4.1). The number of the monitoring sites was optimised to be able to establish quantitative relationships between these variables and erosion rates. This number also enables surveying during a single low-tide window of ca 2 h, which is important because of changeable weather along the North Sea coast (humidity and cloudiness may impact SfM). As the study focuses on mechanisms and controls rather than characterising systematic characterisation of foreshore erosion, which would require a uniform, regular coverage, adding more sites was not considered necessary. The distances from the cliff and the seaward edge were calculated based on the cliff/platform junction and the seaward edge positions (section 3.7.1) using the ArcMap *Near* tool. The topographic and the marine characteristics were obtained for the locations of survey bolts located at the centre of the monitoring sites (Figure 3.8 C-E; Figure 3.10 C and D). The style of relief and the rock type were assessed in the field.

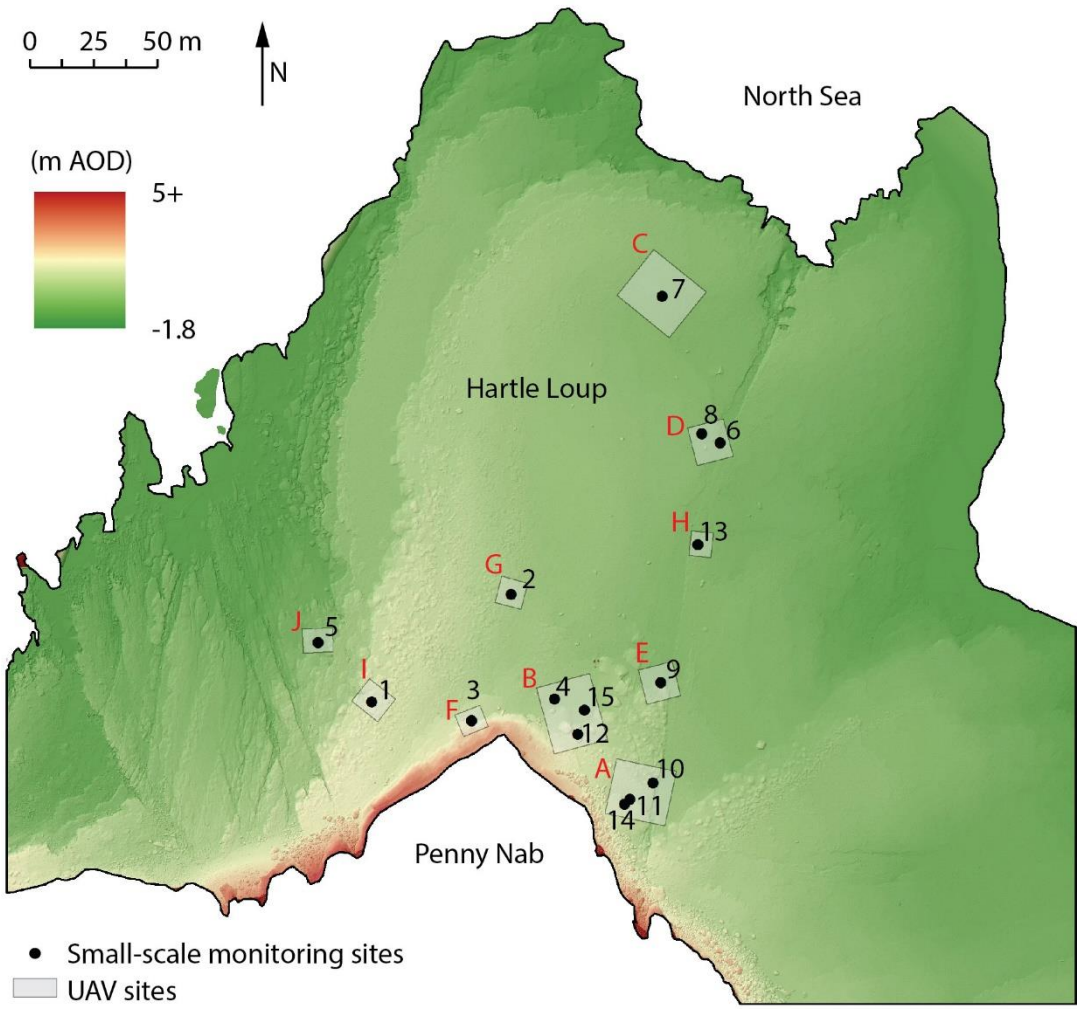


Figure 4.1 Location of the small-scale monitoring sites and the UAV sites on Hartle Loup. For location along the North Yorkshire coastline see Figure 3.7. Background: the LiDAR2016 DEM at 0.1 m resolution overlaid by a hillshade at 70% transparency.

Table 4.1 General characteristics of the small-scale monitoring sites. Glossary contains the details of the value calculation.

Site	Distance from the cliff, *sCli* (m)	Distance from the seaward edge, *sSea* (m)	Elevation, *sEle* (m AOD)	Slope, *sSlo* (°)	Roughness, *sRou* (°)	Tidal duration, *sTid* (%)	Inundation frequency, *sInu* (%)	Rock type	Style of relief
1	42.9	118.5	1.38	29.71	8.33	2.72	29.18	Sandstone	Stepped (15 cm)
2	60.4	135.6	0.22	8.28	3.31	2.07	54.39	Sandstone	Planar
3	12.0	153.7	1.25	14.41	5.37	2.67	32.00	Shale	Stepped (3 cm)
4	26.3	175.7	0.21	3.43	3.39	2.09	54.79	Shale	Planar
5	76.3	84.2	-0.52	8.08	2.90	2.57	72.87	Sandstone	Stepped (1 cm)
6	106.5	86.9	-0.70	1.38	2.47	2.56	75.44	Shale	Planar
7	149.6	51.8	-0.44	3.66	2.33	2.55	70.32	Sandstone	Planar
8	108.8	86.7	-0.49	2.66	1.76	2.55	70.32	Shale	Planar

Site	Distance from the cliff, *sCli* (m)	Distance from the seaward edge, *sSea* (m)	Elevation, *sEle* (m AOD)	Slope, *sSlo* (°)	Roughness, *sRou* (°)	Tidal duration, *sTid* (%)	Inundation frequency, *sInu* (%)	Rock type	Style of relief
9	61.6	143.5	-0.33	17.46	10.41	2.43	67.89	Shale	Sloping (15°)
10	30.7	165.2	0.24	7.87	11.65	2.07	54.39	Shale	Sloping (15°)
11	18.6	177.5	0.75	5.19	7.53	2.16	43.89	Shale	Stepped (6 cm)
12	23.6	184.7	1.09	2.53	17.01	2.35	36.84	Shale	Stepped (2 cm)
13	61.9	117.1	-0.58	2.30	2.63	2.57	72.87	Sandstone	Planar
14	15.6	180.6	0.88	5.02	3.49	2.15	41.74	Shale	Planar
15	33.2	178.5	0.21	2.86	3.26	2.07	54.39	Shale	Planar

In order to be able to survey all of the sites throughout the year (mean spring tidal range: 4.60 m, mean neap tidal range: 2.25 m: http://www.ntslf.org/; Table 3.4), the monitoring sites were located within a narrow elevation range from -0.7 to 1.38 m AOD. This decision limited the full range of conditions that were considered with respect to the full range of conditions on the whole platform, in terms of the elevation range, the tidal duration and the inundation frequency (Figure 4.2 C, F and G). Critically, the elevation equivalent to the lowest sections of the platform could not be included as they remained inaccessible for much of the monitoring period (Figure 4.2 A-C). However, due to the high barnacle cover of the lowest section of the shore platform erosion was assumed to be slower and more episodic.

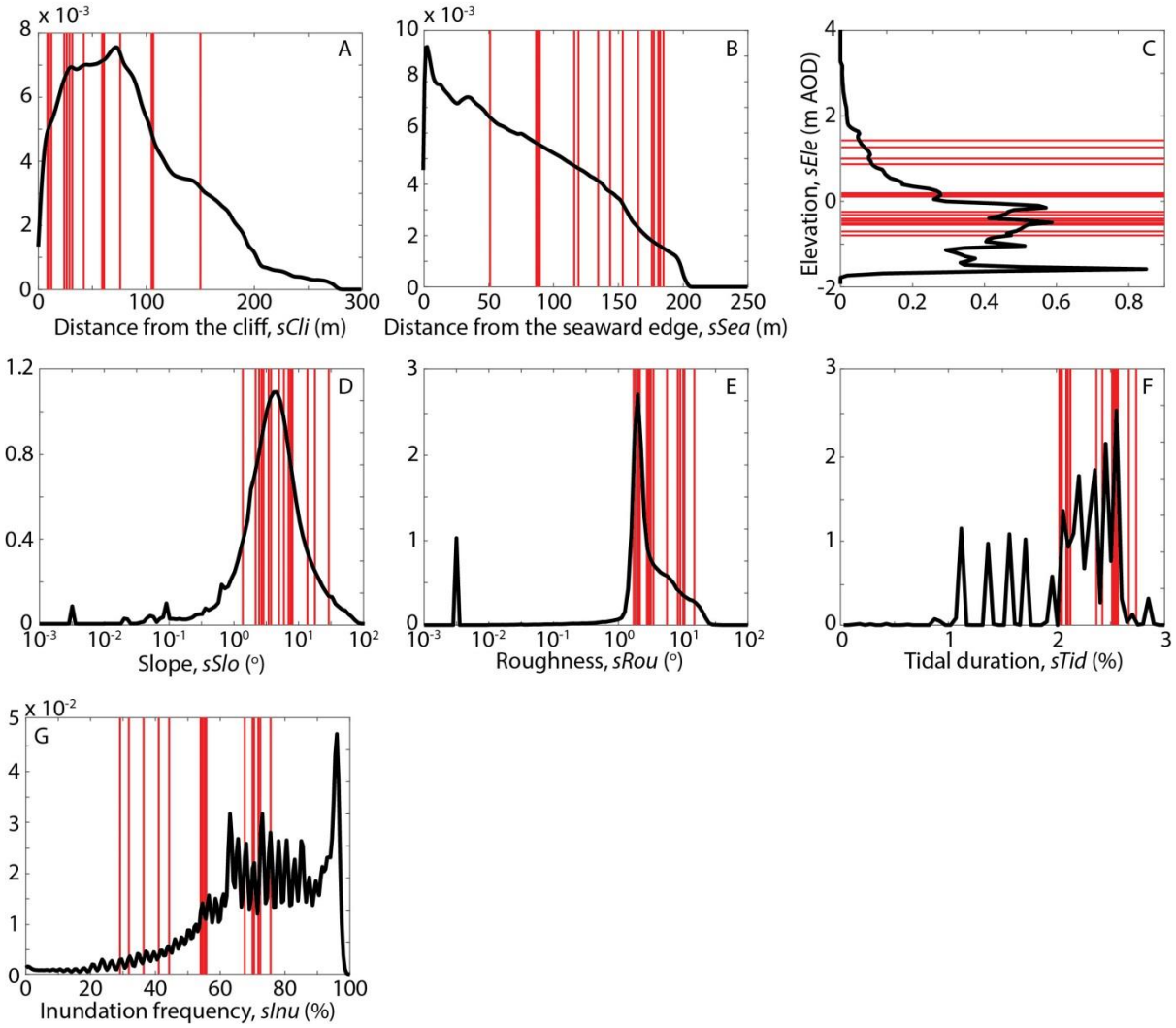


Figure 4.2 Distribution of the general characteristics of the monitoring sites (the red lines represent single sites) in respect to the range of characteristics across the whole section of the shore platform of 1.26×10^5 m^2 depicted in Figure 4.1 (kernel density estimate: normal kernel, default optimal half widths h returned in MATLAB were used): A) Distance from the cliff, sCli (h = 2.30 m); B) Distance from the seaward edge, sSea (h = 2.42 m); C) Elevation, sEle (h = 0.03 m AOD); D) Slope, sSlo (h = 0.02°); E) Roughness, sRou (h = 0.01°); F) Tidal duration, sTid (h = 0.01%); G) Inundation frequency, sInu (h = 0.74%); Y axis: probability density.

4.3. Optimisation of the number of photographs

Because detachment of rock fragments was identified as the dominant mode of erosion on Hartle Loup (section 3.7.2), SfM photogrammetry was used to detect change potentially exceeding the horizontal and vertical range of MEMs, and to provide full 3D shape characteristics (section 2.5.1.1). The method is suitable as it provides continuous rather than point measurements and it has already

been successfully used to reconstruct topography (section 2.5.1.2). However, a new procedure had to be developed to apply the technique to a micro-scale and use it for change detection through time.

The desired single plot size was 0.5×0.5 m to detect detachments smaller than those detectable using airborne LiDAR. Rasters of 0.001 m resolution in plan, with a *LoD* of 0.001 m between subsequent DEMs was specified in the development of the technique. The *LoD* was selected because it was assumed that down-wearing happened primarily through detachment of rock pieces rather than abrasion, and hence detection of lower levels of erosion was not necessary. An assessment of the potential gains in adding camera positions was undertaken to optimise the number of photographs necessary to detect the desirable vertical change.

A 1 m^2 flat linoleum surface was photographed with a Canon EOS 1200D camera (18 MP, 18-55 mm lens) at oblique angles from 12 positions at a height above the surface of ~0.9 m. In order to assess model ability to detect change, three objects of known height were placed on the surface: a £1 coin (height: 3.15×10^{-3} m), an eraser (height: 1.20×10^{-2} m) and a piece of Styrofoam (height: 4.70×10^{-2} m). Point clouds based on the changing number of camera positions between 3 and 12 were built in Agisoft PhotoScan Professional 1.2.4 using the settings from Table 4.2, and analysed in CloudCompare 2.8.

Table 4.2 PhotoScan settings used to process the SfM data.

Align photos		Build dense cloud	Export points
Accuracy	Pair preselection	Quality	Precision
High	Generic	High	6

Two tests were undertaken to calculate model uncertainty as a function of the number of photographs. Firstly, the best-fit plane was created from the point clouds representing the flat surface with no objects and the change of standard deviation of distances between the points and the plane was analysed. The value drops considerably when increasing the number of photographs at the lowest end, but from five photographs and above, the standard deviation remains at 65-70% of the value for three photographs (Figure 4.3A).

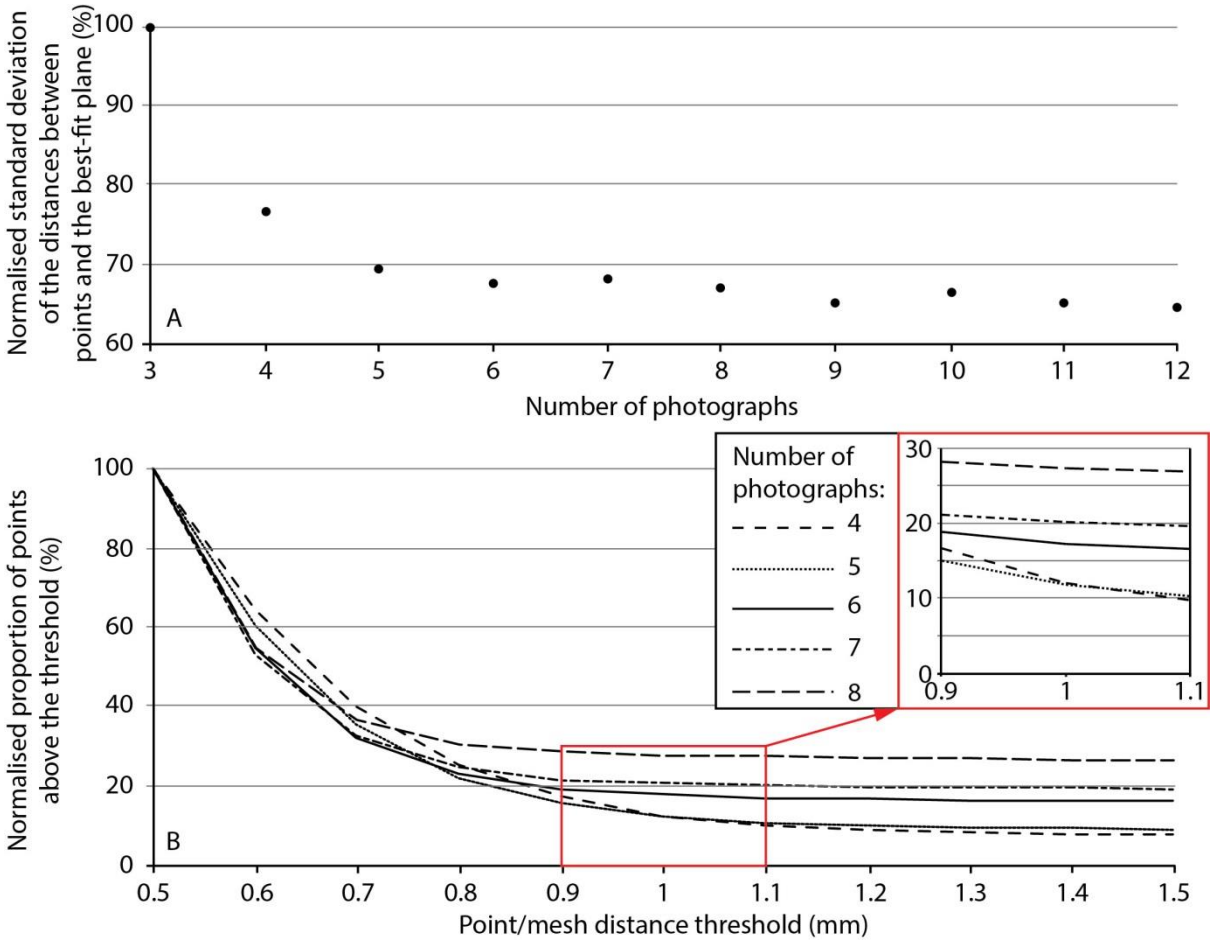


Figure 4.3 Uncertainty of the SfM models as a function of the number of photographs: A) standard deviation of the distances between the points and the best-fit plane for a flat surface with no objects normalised by the value for three photographs; B) proportion of the points with distance between point clouds with the three objects > 1.5×10^{-3} m high and meshed flat surface with no objects above thresholds normalised with the value for 0.5×10^{-3} m threshold.

Subsequently, the flat surface point clouds were meshed and the distances between the mesh and the point clouds with the objects were calculated. The number of points above thresholds between 0.5×10^{-3} and 1.5×10^{-3} m at 0.1×10^{-3} m intervals were calculated for 4-8 photographs and normalised with the number of points above 0.5×10^{-3} m. Two trends can be observed in Figure 4.3B. Firstly, more photographs cause a more abrupt decrease in the proportion of points above threshold for fewer photographs. Secondly, more photographs mean more points remain once the noise is removed. Around the *LoD* the proportion of points still decreases for four and five photographs, whereby not all noise is removed, while for the higher number of photographs it remains stable (inset of Figure 4.3B). The two experiments suggest that the optimal number of photographs is six, to detect a vertical change of 0.001 m.

4.4. Topographic monitoring

All sites were surveyed 13 times between April 2016 and April 2017 (total: 370 days = 1.01 yr) with 24-43 day intervals, with an average monitoring interval of 30.8 days (Table 4.3). The fieldwork was conducted during dry days at the low tide, which maximised the chances of imaging a dry surface. At each site two bolts were installed – one with a concave top and one located towards the centre of the area of interest which served as a benchmark for referencing the point clouds to one another.

Table 4.3 Surveying timescale.

Date	Time from previous survey (days)	Cumulative time (days)	Cumulative time (yr)
2016/04/06	0	0	0
2016/05/09	33	33	0.09
2016/06/07	29	62	0.17
2016/07/08	31	93	0.25
2016/08/01	24	117	0.32
2016/09/02	32	149	0.41
2016/10/02	30	179	0.49
2016/11/01	30	209	0.57
2016/12/14	43	252	0.69
2017/01/14	31	283	0.77
2017/02/15	32	315	0.86
2017/03/15	28	343	0.94
2017/04/11	27	370	1.01

An aluminium frame was constructed to hold the cameras consistently, to enable the rock platform to be photographed from the same positions each month. Keeping the camera position constant was important because using the same viewpoint enabled comparable SfM models to be created. In order to create terrain models of the 0.5×0.5 m surface at 0.001 m resolution, the frame had planform dimensions of 0.6×0.6 m and a height of 1.2 m (Figure 4.4). Two horizontal bars were placed at the bottom of the frame legs to support the construction and to position eight retroreflective markers, six of which served as Ground Control Points (GCPs) and two as independent Check Points (CPs) (Marteau et al., 2017). Assuming that all the markers were at the same level (z) their relative coordinates (x, y) were calculated using trigonometric functions (Table 4.4). A single local coordinate system was established for all sites that ensured all values remained positive throughout the processing.

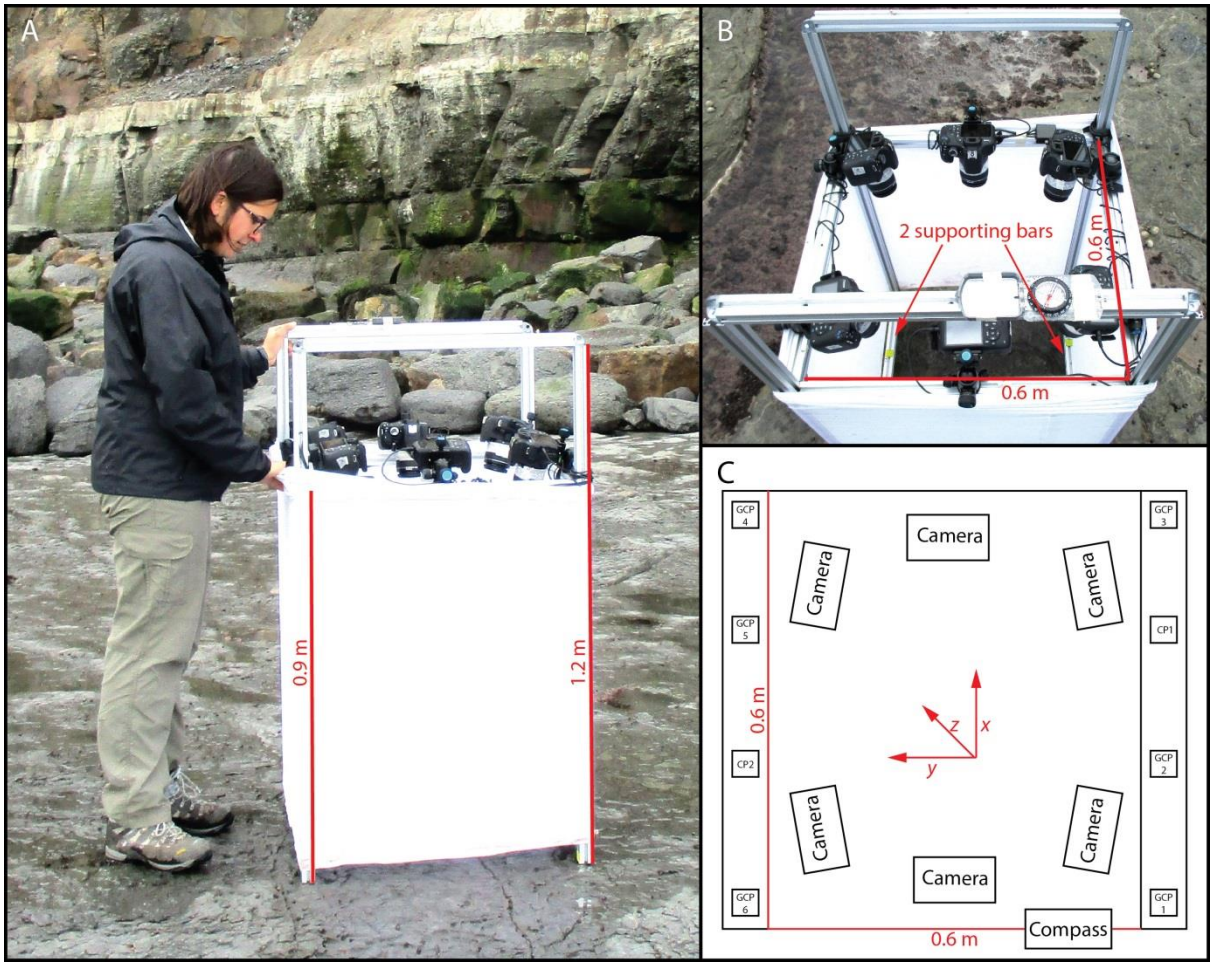


Figure 4.4 The photographic set-up on the frame: A) the white cloth dissipates the light; B) the distribution of the cameras and the compass in the upper part of the frame; C) the planform distribution of the cameras, compass, GCPs and CPs on the frame. Plot shows the directions of the relative coordinates of the GCPs and the CPs with z facing up.

Table 4.4 Relative marker coordinates on the frame (m) calculated using trigonometric functions.

Marker	*x* (m)	*y* (m)	*z* (m)
1	100.0000	100.0000	100.0000
2	100.2017	99.9940	100.0000
3	100.5736	99.9841	100.0000
4	100.5724	100.6190	100.0000
5	100.3691	100.6240	100.0000
6	100.0000	100.6320	100.0000
CP1	100.3954	99.9896	100.0000
CP2	100.1624	100.6256	100.0000

Three frame legs had flat feet, while one had a spike that was placed on the top of the bolt with the concave top. Six Canon EOS 1200D cameras (18 MP, 18-55 mm lens) were attached to the frame at the height of 0.9 m facing downwards at a 10-20° angle relative to the vertical ensuring that all eight markers could be seen from every camera position. A tape fixed the zoom length. The cameras were set to automatic focus, with no flash and their highest resolution in RAW format. Before taking photographs faunal debris, such as winkles, was removed from the area, and excess water was removed with a sponge. A compass attached to the top bar of the frame was used to rotate the frame around the leg supported on the bolt to the same position each month ± 2°. A white elastic tube cloth was put around the frame to scatter the light and to keep the lighting conditions constant throughout the monitoring period. The photographs were taken simultaneously from all six cameras using a single control button.

4.5. Acquisition of UAV data

In order to georeference the SfM data, the topographic information was acquired with UAV imagery captured at a centimetre scale and georeferenced with the LiDAR2016 dataset. Then, the SfM data were georeferenced with the UAV data. Areas of at least 8×10 m^2 that surrounded the small-scale monitoring sites were surveyed in February and March 2017 (Figure 4.1; Table 4.5).

Table 4.5 Characteristics of the UAV sites.

UAV site	Date	Small-scale monitoring sites	Number of photographs	Number of GCPs	Area (m^2)	Number of points	Average point density (points cm^{-2})
A	2017/02/01	10, 11, 14	85	10	624	5,687,602	0.91
B	2017/02/01	4, 12, 15	97	10	720	12,497,112	1.74
C	2017/02/15	7	92	4	700	7,696,981	1.10
D	2017/02/15	6, 8	86	6	256	9,656,144	3.77
E	2017/03/03	9	77	5	225	5,513,768	2.45
F	2017/03/31	3	55	4	110	6,936,575	6.31
G	2017/03/31	2	47	4	132	4,161,686	3.15
H	2017/03/31	13	65	4	80	6,362,693	7.95
I	2017/03/31	1	66	4	168	8,612,690	5.13
J	2017/03/31	5	69	4	130	6,549,310	5.04

At least four GCPs were distributed within each UAV site during the survey. These were A3 laminated sheets of paper with two monochrome triangles conjunct in the centre, secured to the ground (Figure 4.5). The surveys on 1 February 2017, 15 February 2017 and 3 March 2017 were undertaken using a DJI Phantom 2 drone. A GoPro Hero4 camera with a fisheye lens (9-11 mm) was attached to the drone. Due to instrument damage the 31 March 2017 survey was conducted with a DJI

Phantom 3 drone which had a built-in camera with no fisheye effect. At each location at least 100 (Phantom 2) or 50 (Phantom 3) photographs were taken in jpg format. Because of the higher number of photographs and the lower detail required as compared to the small-scale monitoring, RAW images were not critical and the jpg format was used to reduce processing time.

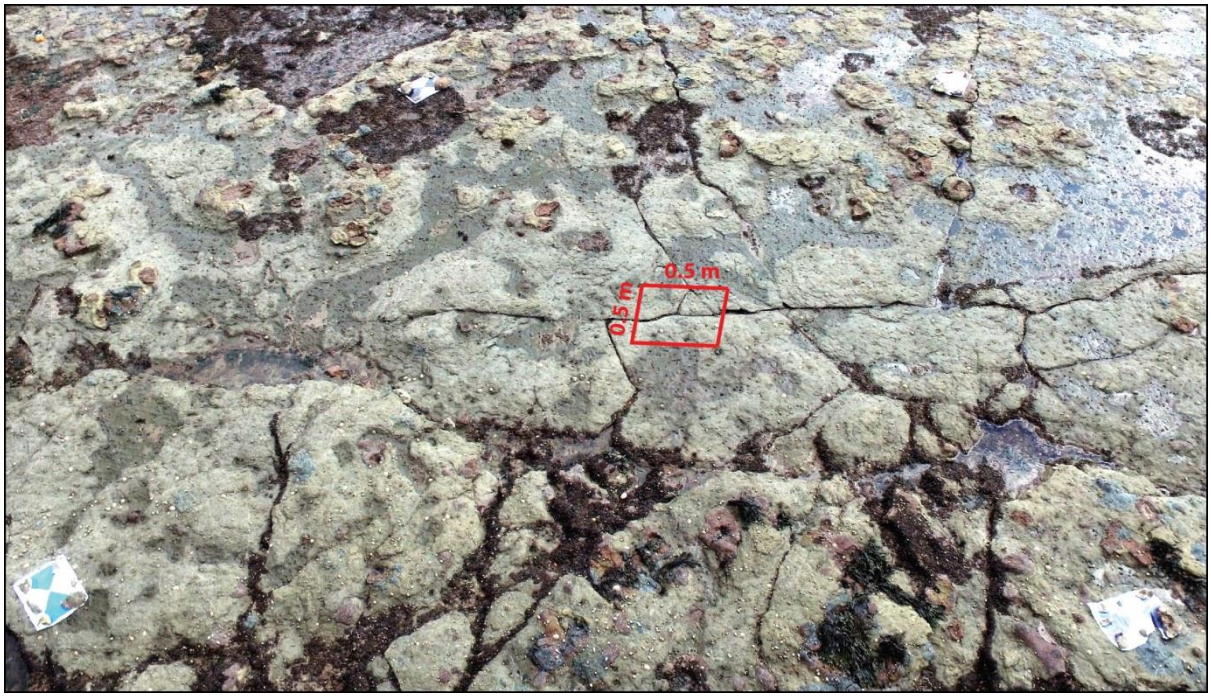


Figure 4.5 Example UAV photograph. Distribution of the GCPs for the UAV survey H. Red box indicates the small-scale monitoring site 13.

Blurred and overexposed photographs, as well as those which did not contain any GCPs were removed. The remaining photographs were processed in PhotoScan using the settings from Table 4.2 to create 3D point clouds of the topography surrounding each small-scale monitoring site. For the Phantom 2 surveys, the camera was automatically calibrated by selecting the 'fisheye' camera type in the PhotoScan *Camera Calibration* tool. For the remaining surveys the camera type was left as 'frame'. The point clouds were imported into CloudCompare and registered to the national coordinate system (OSGB'02) using the high resolution airborne LiDAR2016.

4.6. Creation of DoDs

The SfM technique was used to process the photographs to DEMs of Difference (DoDs) (Figure 4.6). Bit resolution was compressed by converting the RAW images to tiff files using Canon Digital Photo Professional software. The point clouds were built using the PhotoScan settings presented in Table 4.2. Six markers corresponding to the GCPs were placed on every photograph.

Unnecessary points, mainly the white cloth, were trimmed and the point clouds were exported to ASCII files.

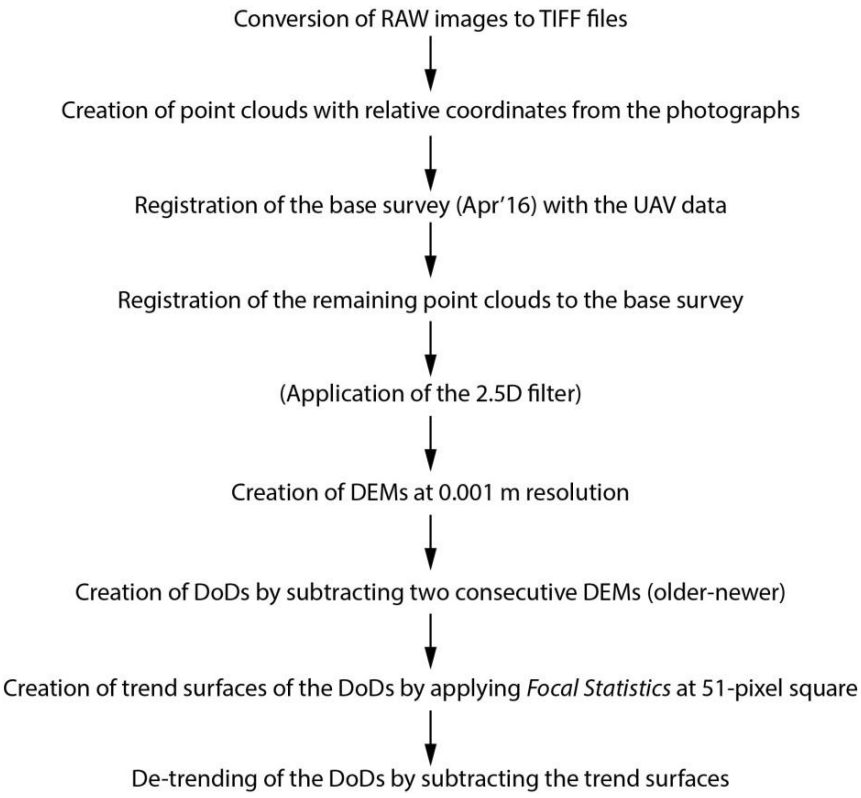


Figure 4.6 Workflow applied to obtain DoDs from the close-range photogrammetry.

The SfM point clouds from the base survey (Apr'16) were registered to the national coordinate system (OSGB'02) in CloudCompare using the UAV-derived topographic data (section 4.5). As the absolute coordinates were not important for further analysis, but the elevation was, the point clouds from each small-scale monitoring site were translated to a position with a 2-digit integer number with 4-digit decimal precision, in order to decrease the point cloud file size (Table 4.6).

Table 4.6 Rigid translation of the SfM point cloud coordinates (shifted = original - value from table).

x (m)	*y* (m)	Small-scale monitoring sites
478600	518900	1, 5
478700	518900	2, 3, 4, 12, 15
478800	519000	6, 8
478800	519100	7
478800	518900	9, 13
478800	518800	10, 11, 14

All point clouds were registered to the base using the coarse registration procedure in CloudCompare. Point cloud scaling was enabled, allowing the model to be stretched or shrunk in *x, y* and *z* axis. This accounted for the potential deformation of the models (see section 2.5.1.3). Registered point clouds with the average density of 7.20 ± 0.31 points mm^{-2} and the orthophotographs (RGB) at 0.001 m resolution were exported. For the sites with a vertical or overhanging topography (sites 1, 3, 8, 11 and 13) the point clouds were imported into RiSCAN PRO and 2.5D filter in *x*, *y* was applied to keep the maximum elevation value within a 0.001 m grid prior to registration. The point clouds were converted into DEMs in ENVI Classic 5.1, where pixels at 0.001 m resolution derived heights based upon the mean *z*-value of the points within 0.001×0.001 m^2 cells. The DEMs were continuous which meant that the *z*-values were interpolated to the *NoData* pixels.

The small-scale monitoring sites varied considerably in terms of their micro-scale characteristics. Appendix 3 shows the DEMs, the DEM-derived slope, roughness and hillshade maps, and the orthophotographs of all sites. Table 4.7 contains the information on the topography and the joint characteristics manually-digitised from the SfM-derived orthophotographs in ArcMap.

Table 4.7 Characteristics of the small-scale monitoring sites based on the SfM-derived DEMs of the Apr'16 survey. Glossary contains the details of the value calculation.

Site	Curvature, *sCur* (×10^{-6})	Site roughness, *sSRou* (°)	Elevation range, *sEleR* (m)	Number of joints, *sJNo*	Length of joints, *sJLe* (m)
1	-7.5	14.27	0.20	3	0.85
2	-0.5	10.25	0.07	11	1.56
3	-1.7	13.31	0.14	0	0
4	-0.1	11.06	0.06	2	0.98
5	0.6	8.04	0.09	1	0.20
6	-1.0	10.93	0.07	9	2.03
7	-2.5	9.95	0.05	1	0.48
8	1.4	9.65	0.04	6	1.63
9	-0.5	15.55	0.18	21	4.57
10	2.3	13.87	0.14	8	1.21
11	4.4	13.81	0.16	4	0.85
12	-2.5	14.87	0.17	2	0.58
13	-3.3	11.27	0.06	3	1.28
14	-0.4	8.26	0.03	9	2.98
15	0.1	7.66	0.04	0	0

To quantify erosion, DoDs were created by subtracting pairs of sequential DEMs in ArcMap (older → newer). Although usually DoDs are obtained by subtracting the DEMs from the first DEM (base), to account for the drift in the results due to systematic and accumulative errors (Williams et al., 2018), here pairs of consecutive DEMs were used. The reason for not using the base DEM was the

presence of flora and fauna – limpets, barnacles and winkles, algae and seaweed – whose activity from month to month could be easily masked out by comparing consecutive orthophotographs. Using the base DEM would imply potential masking out rock erosion at locations covered by the organisms during the first survey and uncovered before experiencing erosion.

To remove the doming effect on DoDs (see section 2.5.1.3), trend surfaces were created, which reflected the general shape of the modelled 3D surfaces. To derive the trend surface for each DoD epoch, the mean pixel value was derived for a kernel of 51 cells, i.e. 10% of the raster length, using each DoD. This was equivalent to a low-pass filter that approximated long length-scale structures in the data, which were here analogous to the doming effects resulting from the photogrammetry. The trend surfaces were then subtracted from DoDs to obtain the de-trended surfaces.

4.7. 3D positional error

Creation of point clouds from the photographs inevitably introduces error. The location error depends on the quality of the photographs, the number of GCPs used to construct the model, the precision of the manual location of the GCPs and the degree of deformation of the model (Marteau et al., 2017). Here, the processing error was assessed in two ways. Firstly, the GCP location error was returned by PhotoScan when the coordinates of control points in the local coordinate system (Table 4.4) were entered into the corresponding marker positions. Secondly, 3D CP coordinates were acquired using the CloudCompare *Point Picking* tool, and their distance from their location in the local coordinate system (Table 4.4) was calculated.

Figure 4.7 shows the locational error of the GCPs and the CPs for each survey, as well as the number of CPs which were not included in the created point clouds making the error impossible to calculate at these positions. Each survey encompassed 30 CPs (2 CPs per 15 sites). In both tests, the error remained stable throughout the year (4-6 mm for GCPs and 2-7 mm for CPs) except Aug'16 survey, when performance of the model was relatively poor, which is expressed by a higher mean error and standard deviation. The impact of the processing error was minimised while re-scaling during the point cloud registration in CloudCompare (section 4.6) and by application of the filters (section 4.8).

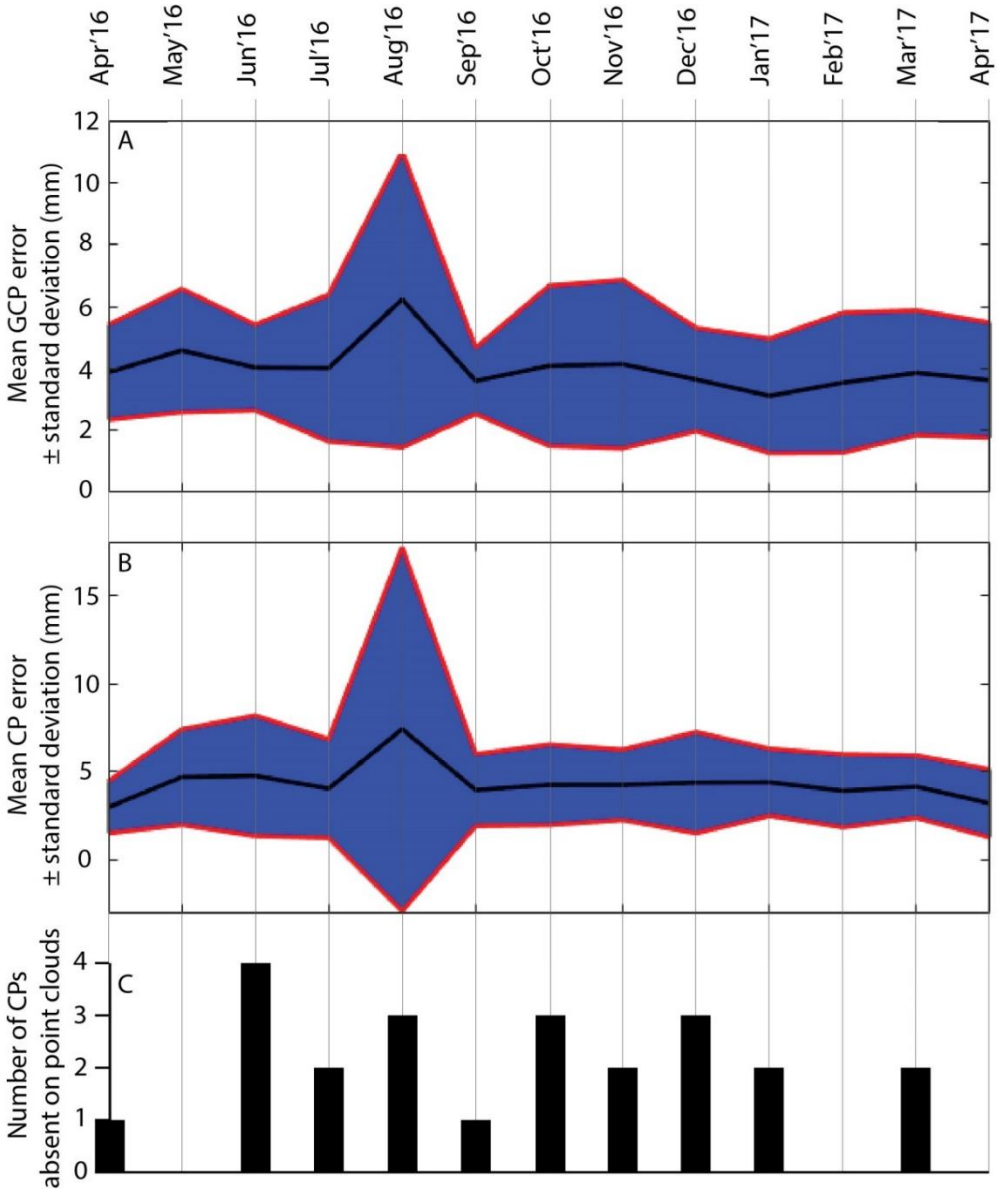


Figure 4.7 3D positional error of the point clouds for each survey of the small-scale monitoring: A) the GCP location error; B) the CP location error; C) the number of CPs not included in the models.

4.8. Separation of real detachments from error

Binary maps of the vertical change ≥ 0.001 m were created for all de-trended DoDs. These were then converted into the polygonal shapefile, where each object represented a single detachment. The orthophotographs were used to remove the polygons whose detected change was coincident with the biological activity. The remaining polygons were deemed to represent rock detachments and errors.

Notably, effects of potential swelling, here understood as negative erosion, were removed by filtering out vertical change < 0.001 m. It was possible to consider swelling by extracting areas of

vertical change ≤ -0.001 m as the method was calibrated to resolve change at or above *LoD* regardless the sign. However, decision was made not to analyse swelling, which was motivated with two arguments. Firstly, the study focuses on quantifying erosion and arguably swelling leads to subsequent erosion (Stephenson and Kirk, 2001). Inclusion of this phenomenon could raise questions about ignoring other 'preparatory' processes such as biological activity (Coombes, 2014). Secondly, erosion is here considered through analysis of separate detachments. Analysis of magnitude frequency and shape distributions of detached rock fragments are crutial to constrain mechanisms and controls on erosion rates. The event-based approach to foreshore erosion stands in opposition to point measurements of vertical change performed using MEMs (see section 5.3.2). The approach of this study does not seem suitable to analysing swelling, because 'event' sizes and shapes would not have any physical meaning.

The most important sources of error present in the study are: incorrect alignment, distortions due to the doming effect, and a lower precision in topographic reconstruction at places of complex topography (Figure 4.8 and section 2.5.1.3). Visual inspection of the orthophotographs suggests that these result in three types of error: noise that could lead to the overrepresentation of very small detachments, errors at sharp edges (Figure 4.9 A and B) and at the edges of the model (Figure 4.9 C and D). The latter error is associated with the lowest point density at the edges of the model and distortions due to the doming effect (Wackrow and Chandler, 2008; Cook, 2017; Marteau et al., 2017), which cannot be completely removed by de-trending due to the lack of surface continuation outside the study area (Figure 4.8).

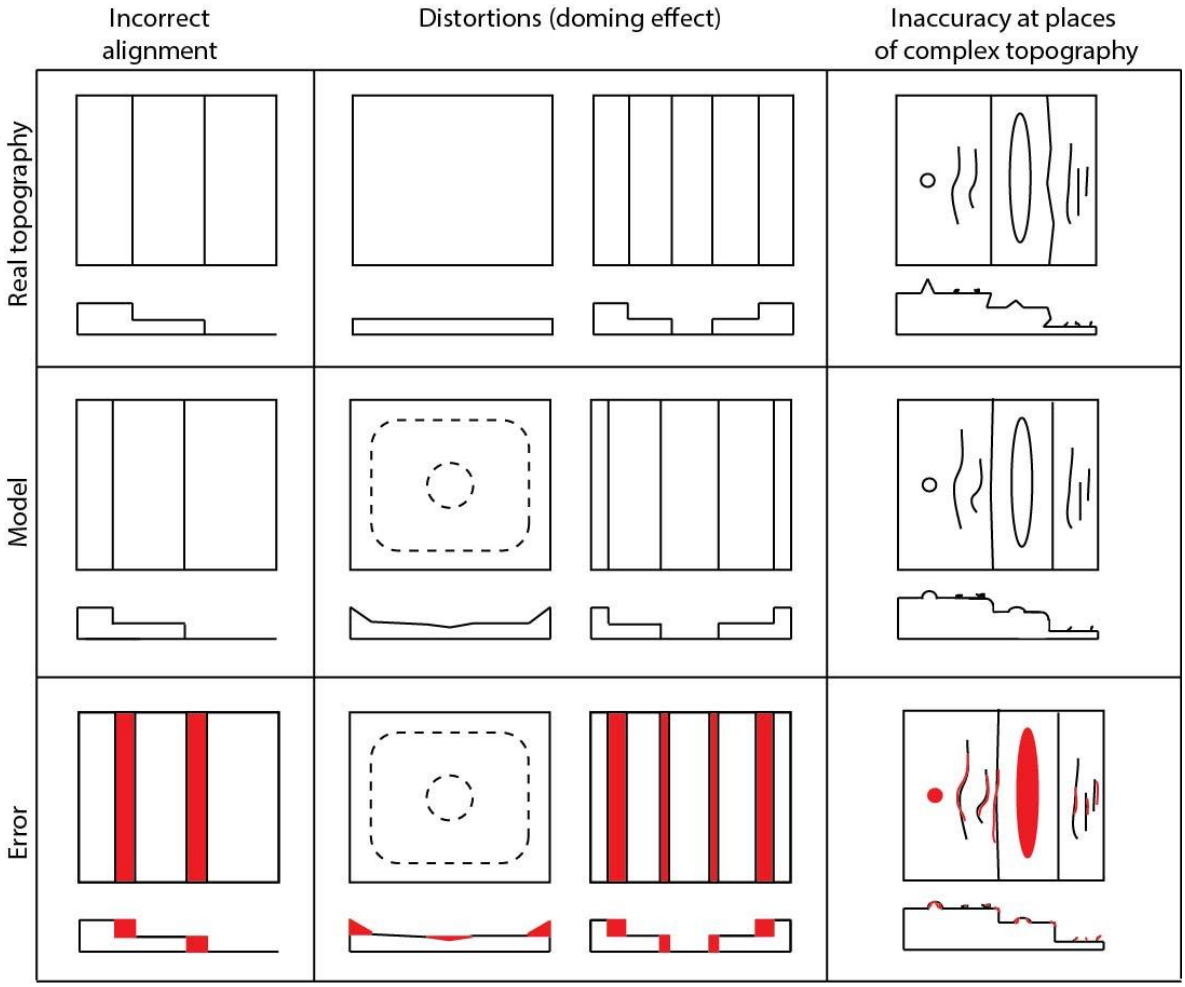


Figure 4.8 The effect of various factors on generating error on the SfM-derived topography reconstruction. Left panel of distortion (doming effect) represents the situation after having de-trended the surface using the ArcMap Focal Statistics tool.

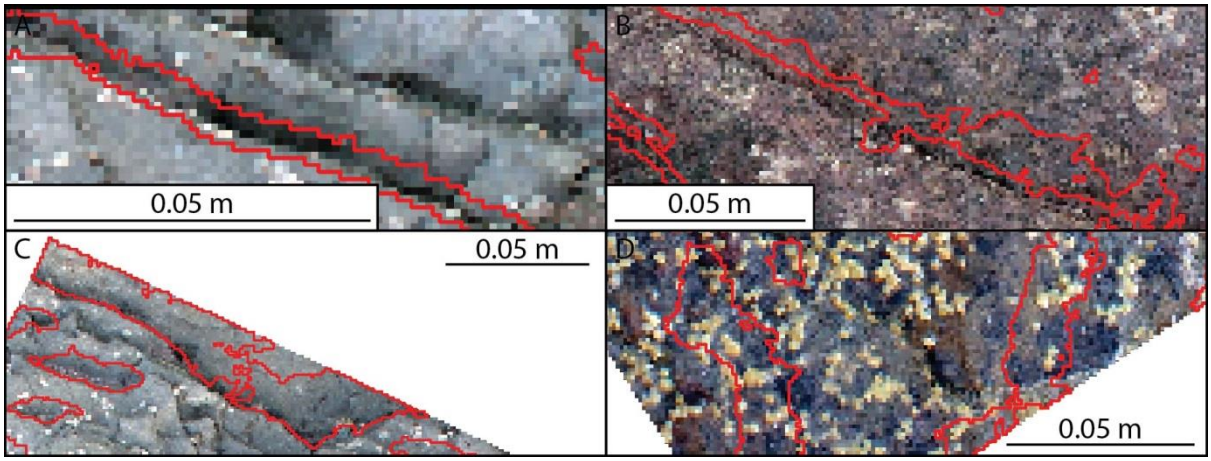


Figure 4.9 Examples of erroneous detection of detachments at the locations with complex geometry (A and B) and at the model edges (C and D): A) DoD3; B) DoD1; C) DoD3; D) DoD2.

To separate real detachments from potentially erroneous detachments, two filters were applied: 1) a size filter to remove the smallest polygons which were deemed to be indistinguishable from the noise, and 2) a shape filter to remove errors at the locations with complex topography and at the model edges. Four DoDs were used to calibrate the filter thresholds that were then applied to all of the models:

- DoD1: site 1 – month 2;
- DoD2: site 7 – month 5;
- DoD3: site 9 – month 8;
- DoD4: site 12 – month 11.

Size filter

In order to remove noise, a polygon-size threshold was established by analysing the number of objects with the surface area of 1-10 pixels normalised by the number of all events ≤ 10 pixels (Table 4.8, Figure 4.10). The value six was selected as a suitable threshold as it allowed the filtering out of > 80% of the smallest objects for all surveys which were deemed to be error.

Table 4.8 Proportion of objects ≤ 10 pixels with sizes at 1 pixel interval (%).

Size (pixels)	DoD1	DoD2	DoD3	DoD4
1	56.30	55.02	50.59	52.51
2	8.15	15.21	16.97	17.99
3	7.41	8.74	9.92	9.62
4	8.15	5.83	6.05	6.28
5	4.44	5.83	3.87	3.97
6	4.81	1.94	3.70	2.09
7	3.33	1.94	1.85	1.05
8	3.33	1.62	2.86	2.51
9	2.96	2.91	2.02	2.51
10	1.11	0.97	2.18	1.46

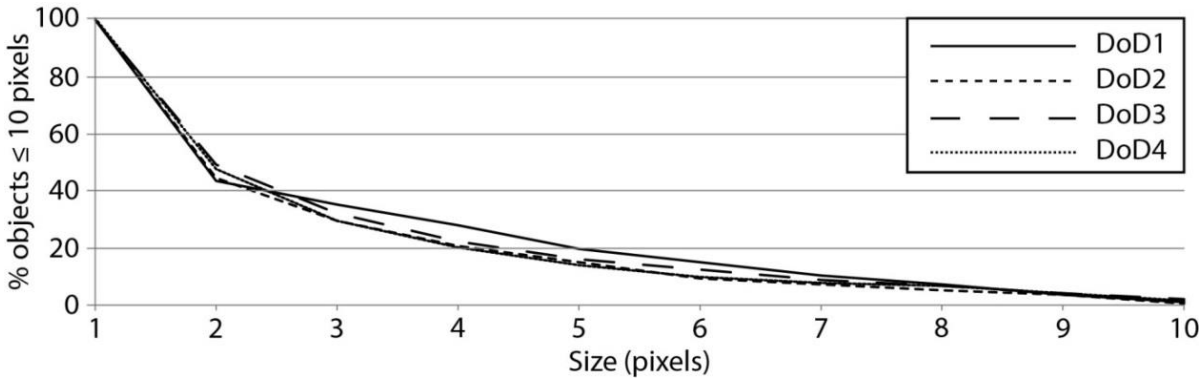


Figure 4.10 Proportion of objects with at least given size in total count of the objects ≤ 10 pixels.

Shape filter

Some objects were of unusual shapes and there was a potential to filter based upon their morphology. To enable this, a set of shape-based descriptive statistics for each object was derived. The Minimum Bounding Geometry (MBG) was created for all polygons in order to calculate their primary (length) and secondary (width) axis dimensions (Figure 4.11A). Consequently, each polygon was characterised by area, perimeter, width and length, as described in Figure 4.11B. These were used to calculate three ratios: perimeter/area, length/width and perimeter/length.

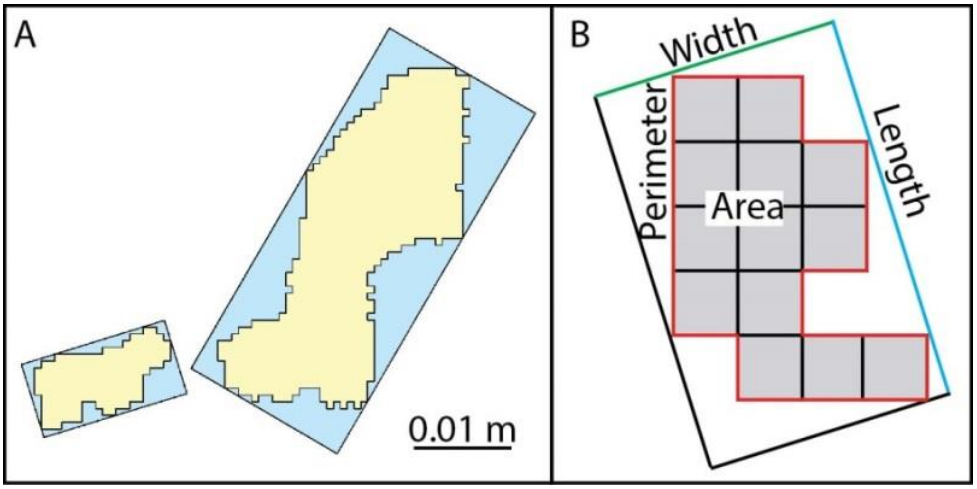


Figure 4.11 Polygon dimensions: A) Minimum Bounding Geometry: Rectangle by Width (blue) created for exemplar erosion polygons (yellow) in ArcMap; B) polygon metrics.

The orthophotographs were used to create an inventory of 40 actual and 40 incorrectly classified detachments, ten of each per DoD. Figure 4.12 shows two examples of clear real detachments. In general, the erroneous objects are elongate with higher length/width ratio and lower perimeter/area ratio (Table 4.9).

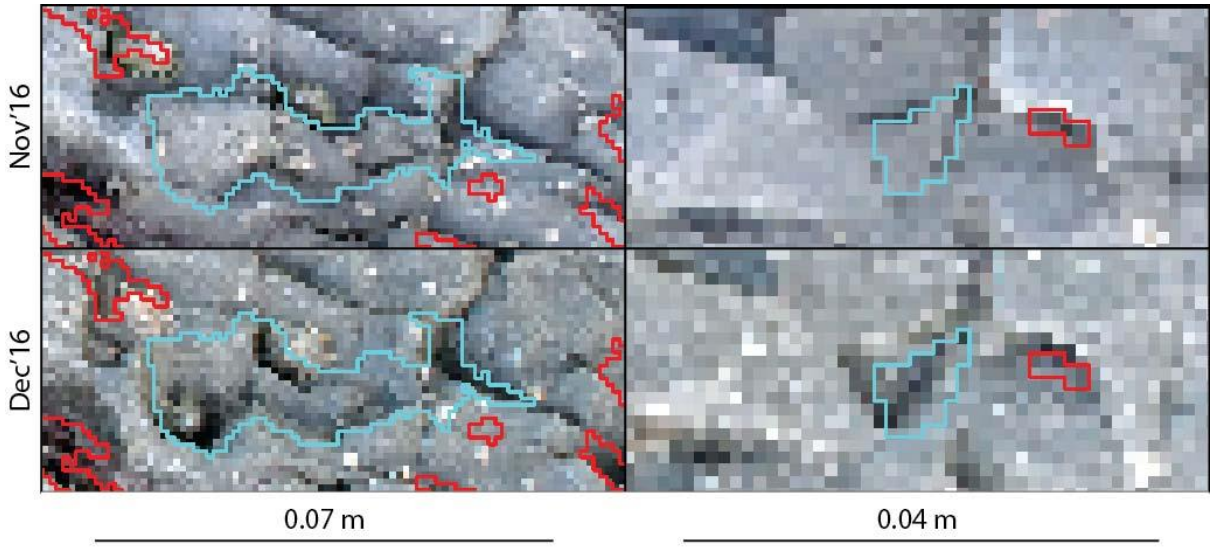


Figure 4.12 Examples of clear real detachments (with blue borders) for DoD3 identifiable on the orthophotographs. Background: the orthophotographs before (Nov'16) and after (Dec'16) detachment occurred. Objects with red borders are other objects identified as detachments.

Table 4.9 Summary statistics of shape ratios of 40 real and 40 erroneous detachment polygons.

		Length (m)	Perimeter/area	Length/width	Perimeter/length
Real change	Min	0.003	333.333	0.750	2.615
	Max	0.058	1818.180	3.250	5.375
	Mean	0.013	997.982	1.730	3.622
Error	Min	0.011	273.848	1.500	2.824
	Max	0.337	1888.890	7.133	6.364
	Mean	0.064	695.640	3.553	3.728

The potentially false detachments are oblong (Figure 4.9) while the real detachments are more compact (Figure 4.12). In order to explore relationships between the object metrics for compact and oblong objects, idealised shapes were created and the four metrics and the three ratios were calculated (Figure 4.13). In general, the oblong geometries have higher perimeter/area and length/width ratios and lower perimeter/length ratio.

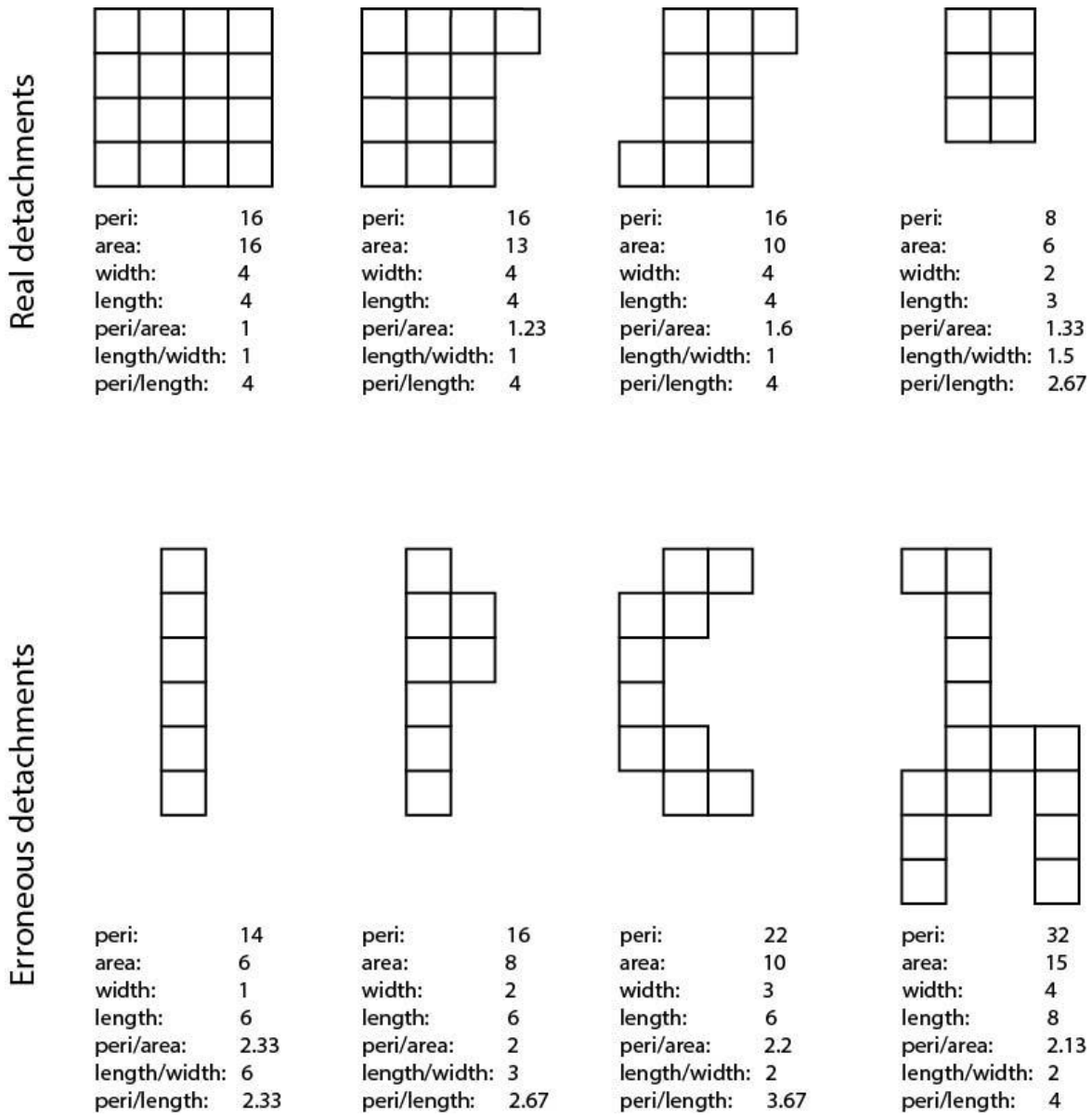


Figure 4.13 Dimensions and shape ratios of idealised polygons representing the real and the potentially erroneous detachments; peri = perimeter.

Because the real detachment geometries are more complex than the falsely identified detachments, including for example variations on their perimeters, the distributions of the values and relationships between different ratios for the objects in the inventory were explored. There is a clear distribution difference between the real and the erroneous objects based upon the length and length/width ratio. Real detachments are no longer than 0.03 m with one exception and the length/width ratio is usually lower than 2. In contrast, the perimeter/area and the perimeter/length ratios are distributed throughout the range of values (Figure 4.14).

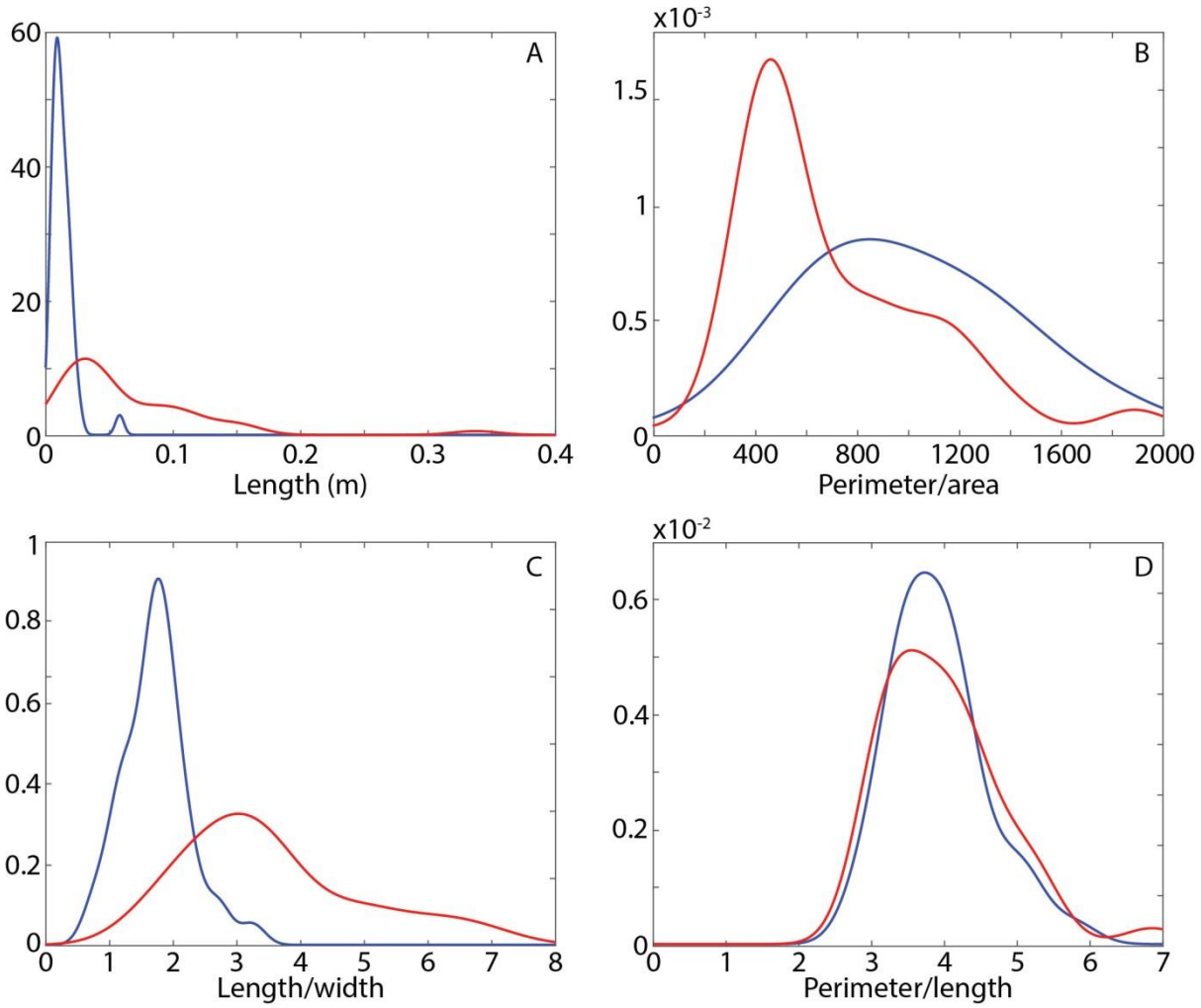


Figure 4.14 Kernel density estimate (normal kernel, default optimal half widths h returned in MATLAB were used) of the length and the three shape parameters of 40 real (blue) and 40 erroneous (red) detachments from DoDs1-4: A) Length (h = 0.0034 m); B) Perimeter/area (h = 236.01); C) Length/width (h = 0.20); D) Perimeter/length (h = 0.29); Y axis: probability density.

Scatter plots with all combinations of the four geometric characteristics were created (Figure 4.15) to see whether real and erroneous detachments could be better separated using the combination of metrics from Figure 4.14. Visual inspection of the histograms and the scatter plots helped choose the optimal metrics that enabled the separation of the real change from error. A set of filters was selected with two thresholds each tested to 1) leave all real change removing as much error as possible, and 2) leave as much real change as possible removing as much error as possible. Table 4.10 summarises how appropriately the polygons were classified in terms of their number, using nine filters to remove polygons if the criteria were met.

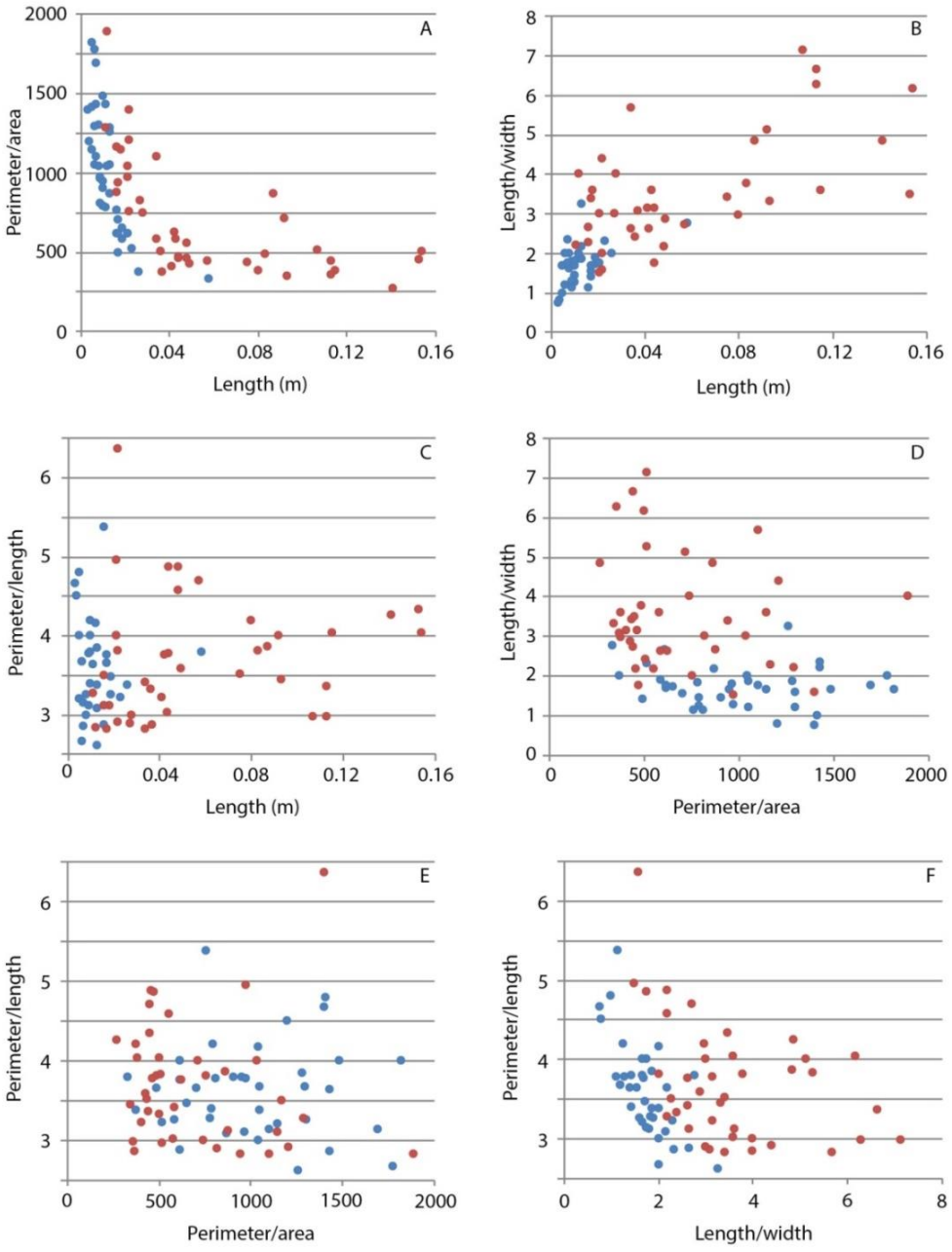


Figure 4.15 Relationships between the length and the three shape parameters of the 40 real (blue) and the 40 erroneous (red) detachments from DoDs1-4: A) length vs perimeter/area; B) length vs length/width; C) length vs perimeter/length; D) perimeter/area vs length/width; E) perimeter/area vs perimeter/length; F) length/width vs perimeter/length.

Table 4.10 Correctly classified proportion (%) of the real and the erroneous detachments using single shape filters.

Filter	Condition (remove if…)	Real	Error
1	Length > 0.03	97.5	67.5
2	Length > 0.06	100.0	35.0
3	Length/width > 2	82.5	90.0
4	Length/width > 3.5	100.0	40.0
5	Length > 0.013 AND perimeter/area > 800	100.0	20.0
6	Length > 0.02 AND perimeter/area > 400	95.0	20.0
7	Length > 0.025 AND perimeter/area > 400	100.0	10.0
8	Perimeter/length > 4 AND length/width > 2	100.0	20.0
9	Perimeter/length > 4 AND length/width > 1.25	97.5	20.0

The filters were considered successful if they correctly classified > 90% of real detachments. These were subsequently combined in order to better separate the real detachments from error (Table 4.11). Filter 9 was excluded because it did not increase the performance on erroneous polygon identification while reducing performance on real change detection in respect to filter 8.

Table 4.11 Success rate (%) of the combination of filters 1-9 (Table 4.10) to separate the real and the erroneous detachments in terms of their number, area and volume.

		1,4,5,7,8	2,4,5,7,8	1,4,5,6,8	2,4,5,6,8	4,5,7,8	4,5,6,8
Real change	%number	97.5	100.0	92.5	95.0	100.0	95.0
	%area	76.8	100.0	67.0	90.2	100.0	90.2
	%volume	45.5	100.0	31.7	86.2	100.0	86.2
Error	%number	62.5	77.5	62.5	77.5	57.5	62.5
	%area	87.6	96.7	87.6	96.7	80.0	87.6
	%volume	95.7	98.7	95.7	98.7	91.6	95.7

Remaining filters were applied in all possible combinations. Because filters 1 and 2, as well as 6 and 7 imposed different thresholds on the same pairs of metrics, they were not used together. Although filter 5 used the same metrics as filters 6 and 7, the threshold was different for both metrics involved (length and perimeter/area) and therefore was applied simultaneously. Combinations were also tested without the length filters (1-2) because they described size rather than shape. This time the number of polygons, area and equivalent of eroded volume extracted using the ArcMap *Zonal Statistics* tool were used. The results suggest that the combination of filters 2, 4, 5, 7 and 8 (Figure 4.16) is the most powerful enabling the detection of all real events, and the removal of 77.5%

erroneous events which contribute to 96.7% of the detachment area and 98.7% of the detachment volume.

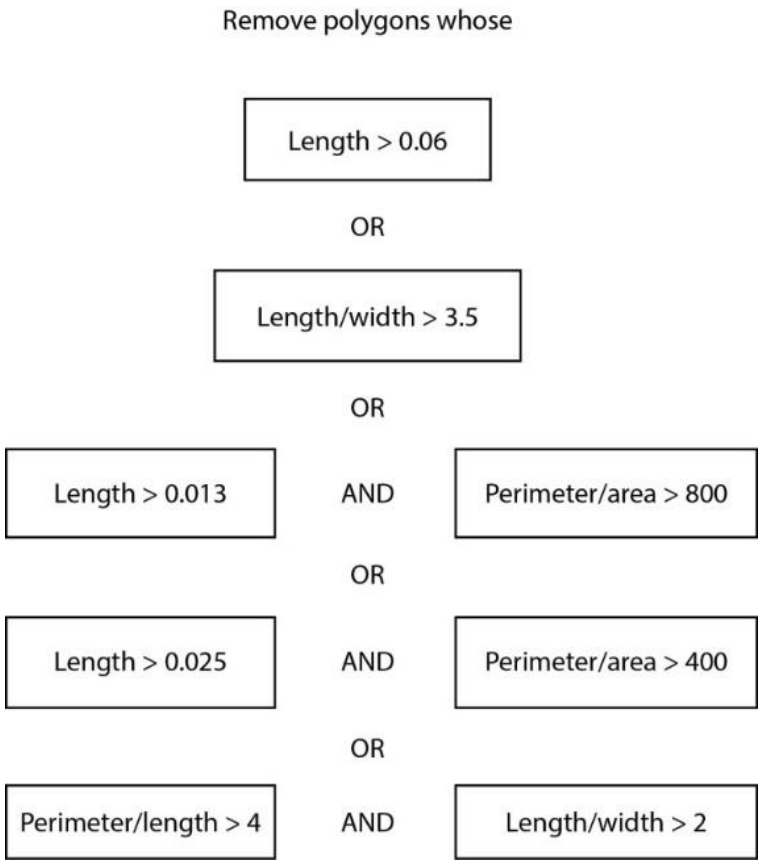


Figure 4.16 The most successful set of filters to separate polygons of real detachments from the error.

Application of the filters

The two filters were subsequently applied to all four test datasets (Figure 4.17), and the summary statistics were extracted to calculate how much of the originally-identified detachments were removed during the filtering process (Table 4.12). Although the removal of the smallest polygons dramatically reduces their number, it does not contribute significantly to the total area and volume loss. In contrast, filtering out the large and oblong polygons has a strong impact on reduction in area and volume (Figure 4.18). DoD4 stands out from the other DoDs because it has the fewest detachments which involve only 1.59% of the total area; here the smallest events contribute more to the area and volume loss. Application of both filters results in leaving only 13.37-27.75% of polygons of 21.70-36.87% area which constitute 4.68-34.50% of the automatically-detected volume.

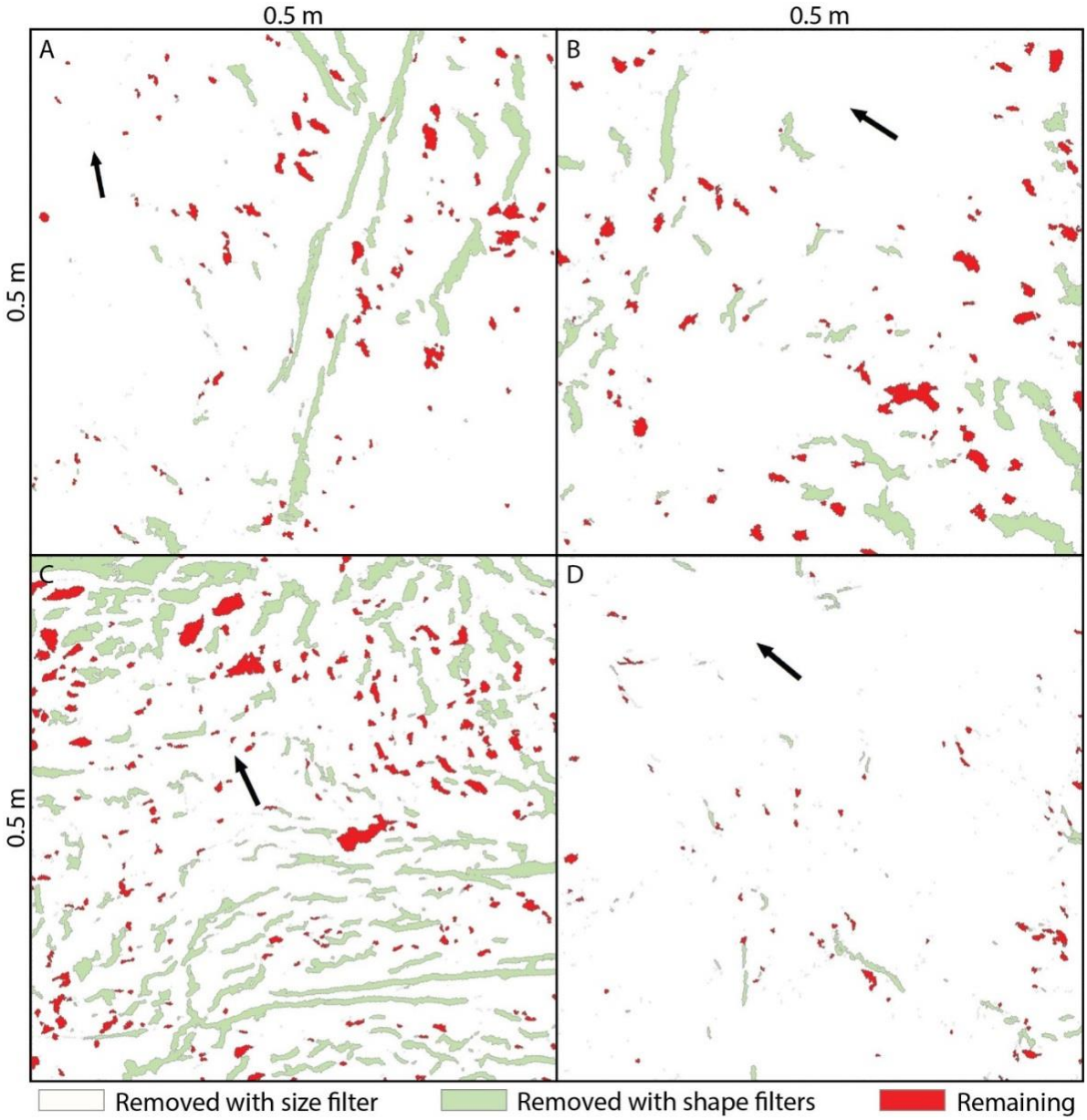


Figure 4.17 Removal of the polygons while applying the size and shape filters for the four test DoDs: A) DoD1; B) DoD2; C) DoD3; D) DoD4. The arrows indicate north.

Table 4.12 Reduction in identified detachments in terms of the polygon number, area and volume while applying the size and the shape filters on the four test DoDs.

	DoD	Polygons		Total area			Eroded volume	
		Number	%	10^{-2} m^2	%	% site area	10^{-4} m^3	%
Total change > 1 mm after removing effects of biological activity	DoD1	382	100	1.51	100	6.03	1.38	100
	DoD2	428	100	1.69	100	6.77	0.30	100
	DoD3	915	100	4.30	100	17.21	1.08	100
	DoD4	546	100	0.40	100	1.59	0.07	100

	DoD	Polygons		Total area			Eroded volume	
		Number	%	10^{-2} m^2	%	% site area	10^{-4} m^3	%
Remaining change after applying size filter	DoD1	161	42.15	1.47	97.55	5.89	1.37	99.36
	DoD2	151	35.28	1.64	97.09	6.58	0.30	98.20
	DoD3	401	43.83	4.21	97.89	16.85	1.07	98.89
	DoD4	123	22.53	0.32	81.61	1.30	0.06	85.95
Remaining change after applying shape filters	DoD1	106	27.75	0.40	26.74	1.61	0.06	4.68
	DoD2	100	23.36	0.59	34.93	2.37	0.10	32.37
	DoD3	223	23.37	0.93	21.70	3.73	0.17	15.96
	DoD4	73	13.37	0.15	36.87	0.59	0.02	34.50

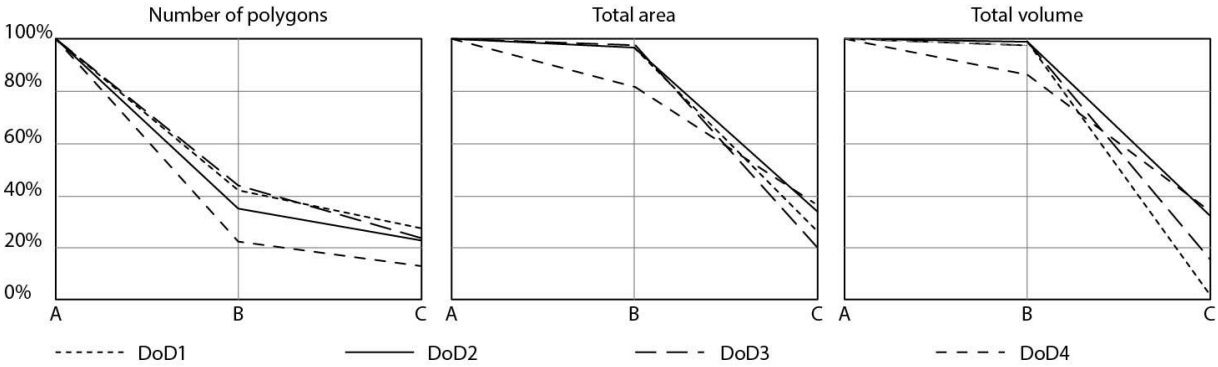


Figure 4.18 Reduction in detected erosion through applying the filters: A – the originally-identified polygons constitute 100%; B – the remaining proportion of erosion after applying the size filter; C – the remaining proportion of erosion after applying the shape filter.

Application of the filters means that potential real detachments that are smaller than six pixels (6×10^{-6} m^2), oblong and/or large are filtered out. This approach has two important implications. Firstly, the magnitude/frequency analysis of rockfall/landslides shows that the smallest events are the most frequent (section 2.5.2.1). If this is the case for platform micro-erosion, low-magnitude high-frequency events will not be included in the detachment inventory. Secondly, the places of complex topography, especially the sharp edges, are where erosion concentrates. Potential real detachments of large/long rock pieces will be filtered out using this procedure. If large but rare detachments are excluded from the inventory, calculated erosion rates may be unrealistically low. However, the visual inspection of the orthophotographs and the understanding the micro-structural properties of the rocks in the study area suggest that more is gained than lost by applying these filters. Therefore, the filters were used to process all datasets following the workflow depicted in Figure 4.19.

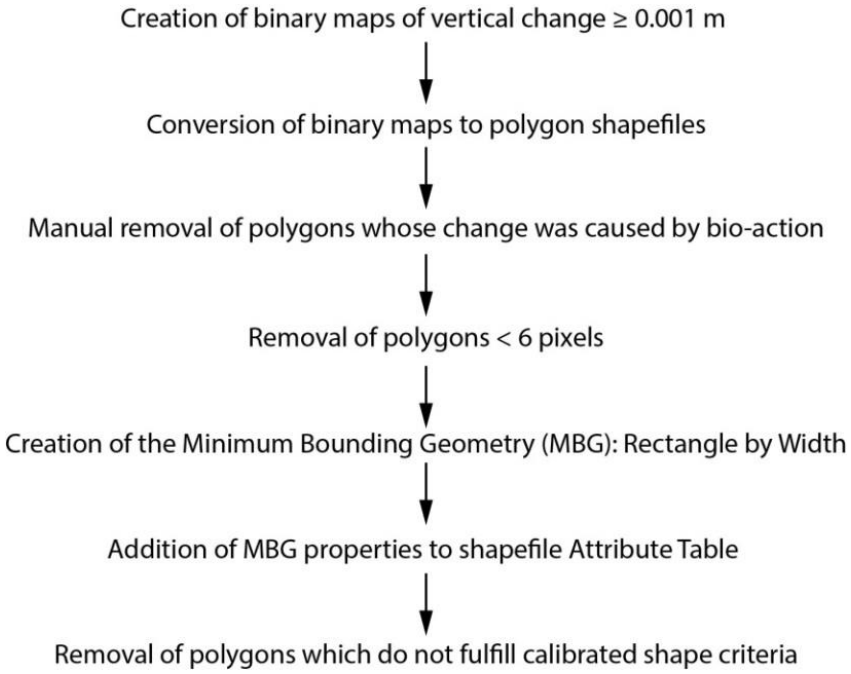


Figure 4.19 The final workflow applied to separate real detachments from error.

4.9. Testing performance of the method

Two independent tests were carried on to assess the performance of the applied method by verifying the reproducibility of the SfM model for situations with no change and the ability to detect changes of known size. During the last survey (Apr'17) two sets of photographs were taken at each small-scale monitoring site, with the camera frame being re-set between image captures to simulate successive surveys with no change to the rock surface. Seven £1 coins were then randomly distributed upon each monitored rock surface, and another set of photographs was taken. In both cases the procedure described in previous sections, including the object filtering, was applied to extract 'detachment' events. The independent check allowed the confidence in the results to be established.

In the reproducibility test 1,610 events were identified on the no-change surface accounting for incorrect detection of 2.83×10^{-2} m^2 of change, or 0.76% of the total area of the 15 monitoring sites. The relationship between the occurrence of the incorrectly identified change and, 1) surface roughness, and 2) distance from the centre point of the model was established, as these two variables have been identified as the major controls on localised model deformation (Cook, 2017). The roughness (Appendix 3) and the distance were extracted for object centroids. Figure 4.20 shows that the error is higher at rougher surfaces and at the edges of the model suggesting that the distortions depicted in Figure 4.8 could not be entirely removed with the size and shape filters.

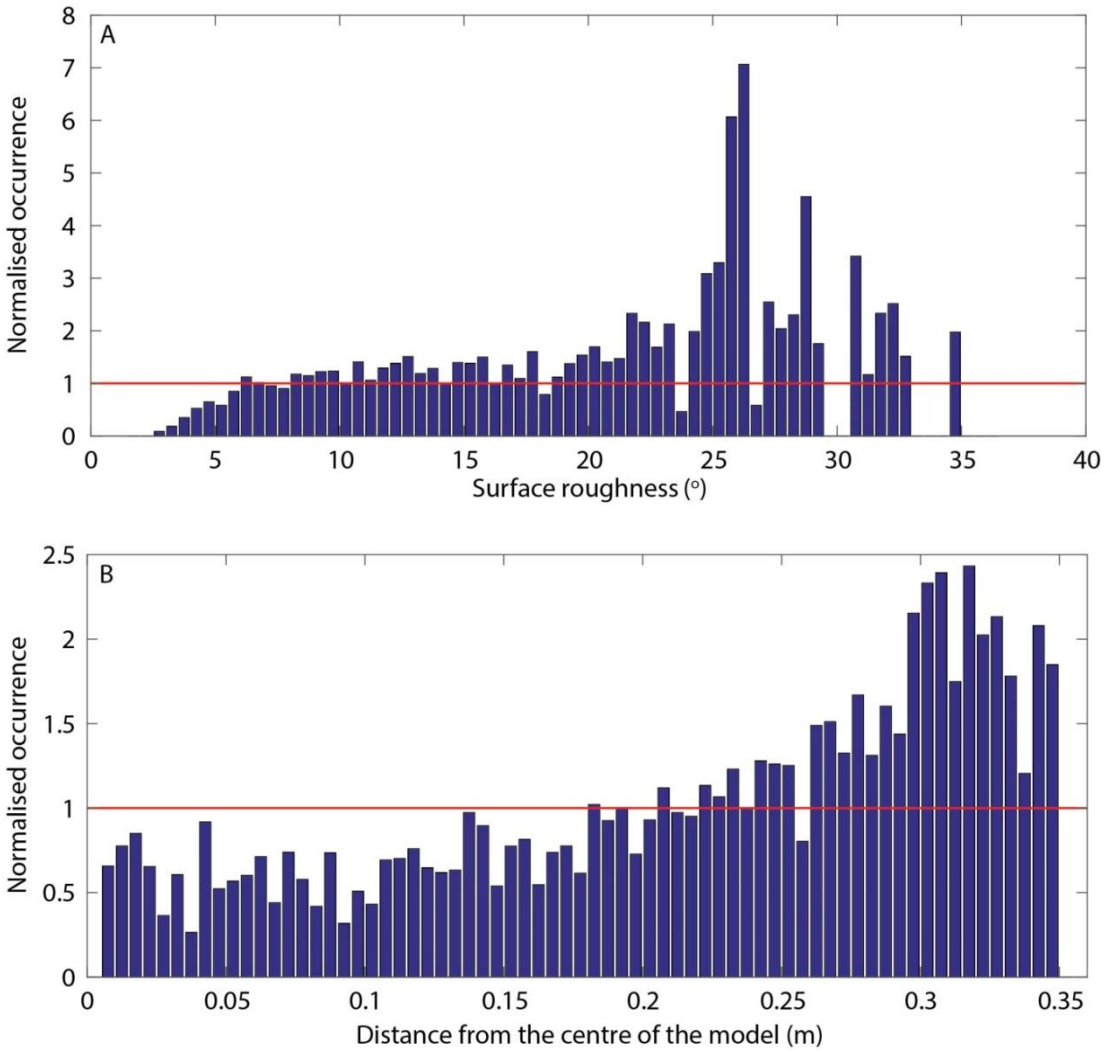


Figure 4.20 Occurrence of the incorrectly identified 'detachment' events as a function of A) the surface roughness and B) the distance from the centre of the model distributions. The occurrence was normalised by the occurrence across the small-scale monitoring sites.

All 105 £1 coins (seven per site) were detected. Table 4.13 contains the information about their size as determined from the SfM DoDs in respect to the real size. The model overestimates both the area and the volume. The overestimation of the area may be due to the terrain smoothing by the model at the abrupt slope changes (Cook, 2017), in this case at the boundaries between the coins and the rock surface. In consequence, the neighbouring areas may be included into change zones contributing to the underestimation of the mean thickness. Alternatively, the overestimation of the area may be caused by the creation of error at the elevation-change zones while de-trending the surface. Overestimation of the volume may be caused by the overestimation of the area and/or placement of the coins at not totally flat locations which would add the void space between the coins and the rock surface to the measured volume.

Table 4.13 Summary statistics of the 105 modelled £1 coin sizes. Real sizes of the rigid standard body with standard deviation = 0 were precisely measured with callipers.

	Real	Mean	Standard deviation
Area (mm^2)	397.61	461.73	32.06
Thickness (mm)	3.15	2.80	0.33
Volume (mm^3)	1,252.50	1,293.00	168.89

Because the volume is used to calculate erosion rates in the study, the distribution of modelled coin volumes was used to assess the confidence in the results. The model overestimates the volume by 3.20% which is equivalent to 40.5 mm^3. The modelled volume is characterised by 13.50% variability of the actual volume (Table 4.13). The results of this test were used to establish the confidence of the method to correctly resolve bedrock erosion at 83.30%.

4.10. Analysis of detachments

Looking at erosion from the event inventory perspective permits the constraint of mechanisms of erosion by finding relationships between detachment area and volume and analysing the volume frequency and 3D shape distributions of detachments (Malamud et al., 2004; Guzetti et al., 2009; Williams et al., 2018). Grouping events by location and monitoring period enables spatial and temporal patterns in detachment distribution to be assessed. Furthermore, the controls on erosion can be identified by linking detachment magnitude and size distribution with external factors (Kritikos et al., 2015; Parker et al., 2015).

4.10.1. Creation of detachment inventories

The identification of detachments using the procedure described above was used to create an inventory of detachment events. Each detachment was characterised by a number of attributes describing its location, time, size and shape. Additional inventories were created which contained detachment characteristics for 1) each monitoring site and 2) each month, i.e. the time period of ~30.8 days between two consecutive surveys, respectively accounting for the spatial and temporal variability in shore platform down-wearing. Table 4.14 summarises attributes included in the three inventories.

Table 4.14 Object attributes in the detachment-, site- and month-based inventories of the small-scale monitoring. Glossary contains the details of calculation of the variables per site and month.

Detachment-based	Site-based	Month-based
Site	Site	Site
Month	Total area, *sArea* (m^2)	Month
Centroid X coordinate (m)	Total volume, *sVol* (m^3)	Total area, *sArea* (m^2)
Centroid Y coordinate (m)	Mean volume, *sMean* (m^3)	Total volume, *sVol* (m^3)
Area (m^2)	Standard deviation of volumes, *sStd* (m^3)	Mean volume, *sMean* (m^3)
Volume (m^3)	Erosion rate, *sEro* (mm yr^{-1})	Standard deviation of volumes, *sStd* (m^3)
Maximum thickness (m)	Exponent β, *sβ*	Erosion rate, *sEro* (mm yr^{-1})
Perimeter (m)		Exponent β, *sβ*
Width (m)		
Length (m)		

4.10.2. Event inventory analysis

The summary statistics of the number of detachments and their volumetric properties was extracted and the erosion rate was calculated as the sum of volumes of all detachments multiplied by 1,000 (m → mm) per total area of the small-scale monitoring (15×0.25 m^2) per 1.01 yr. Relationships between detachment area and volume, and the volume frequency distribution were established (section 2.5.2.1). The 3D shapes of the detachments were plotted, from which the width and the length of MBG and the maximum thickness of events were used.

4.10.3. Spatial analysis of detachments

The small-scale monitoring sites were characterised by 12 independent variables (Table 4.15). The general attributes refer to properties identified from the LiDAR data (Table 4.1), while the micro-scale properties are based on the SfM datasets (Table 4.7). Aspect relative to the sea/coastline was not included due to the complex morphological location of some sites: at site 1 the step does not face the sea while the location of site 12 is protected from the direct impacts of upcoming waves by a boulder.

The Stata *gladder* tool was used to confirm that the distribution of the independent variables (Table 4.15) and the erosion attributes (Table 4.14) approximates a normal distribution and no transformation is needed to explore the explanatory power of the independent variables in predicting the location and nature of detachments using linear regression.

Table 4.15 Independent variables characterising the small-scale monitoring sites. Glossary contains the details of the value calculation.

General variables	Micro-scale variables
Distance from the cliff, *sCli* (m)	Curvature, *sCur*
Distance from the seaward edge, *sSea* (m)	Site roughness, *sSRou* (°)
Elevation, *sEle* (m AOD)	Elevation range, *sEleR* (m)
Slope, *sSlo* (°)	Number of joints, *sJNo*
Roughness, *sRou* (°)	Length of joints, s*JLe* (m)
Tidal duration, *sTid* (%)	
Inundation frequency, *sInu* (%)	

The pair-wise Pearson correlation was performed in R between all pairs of independent variables and between each independent variable-erosion variable pairing in order to 1) identify potential strong relationships between independent variables which could overestimate the role of the overriding factor on erosion, and 2) check whether a single factor can explain the variability of observed erosion. Three erosion variables which when combined represent magnitude and size distribution of detachments – erosion rate, the mean volume and exponent β – were modelled using multiple linear regression. The models were constructed manually, instead of using an automated procedure to select a combination of variables which provides the best-fit linear model in order to account for physical meaning rather than goodness-of-fit only (e.g. Parker et al., 2015).

4.10.4. Temporal analysis of detachments

The magnitude and size distribution of detachments were analysed on a month-by-month basis, because previous studies have shown that there is a seasonal difference in erosion rates and patterns (Robinson, 1977a; Stephenson and Kirk, 1998; Moses and Robinson, 2011). Temporal distribution of erosion rates, the mean volume, standard deviation of volumes and exponent β were analysed, and an assessment of whether subsequent detachments occurred at the locations of previous events was performed.

It is important to understand whether erosion occurred via progressive detachment in order to better understand the patterns of erosion (Rosser et al., 2013). For each DoD (15 sites × 12 months) the number of points equal to the number of objects were randomly distributed across an area equal to the monitoring site (0.5×0.5 m) 100 times. During each iteration the distance between each point from earlier of two consecutive DoDs and the nearest point from later DoD was calculated, and the mean minimal distance, dri_m, between the points was extracted where m = 1:100. After 100 iterations the

total mean minimal distance, *dr*, and its standard deviation were extracted to represent the random distance for each pair of DoDs (Figure 4.21).

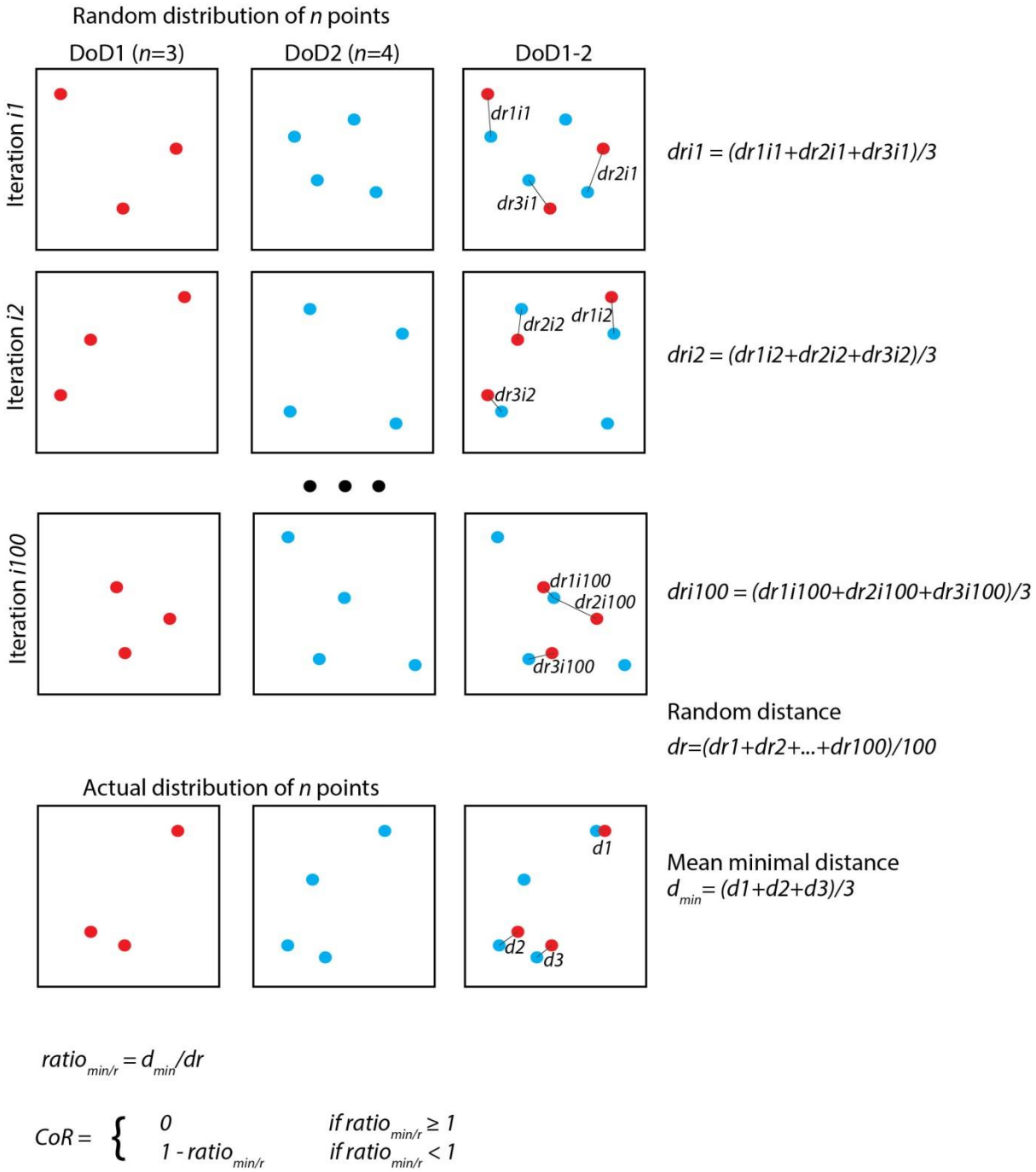


Figure 4.21 The assessment of the propagation of erosion in time based on the random and actual distribution of detachments within the monitoring sites.

The detachments were converted to points located at their centroids and the shortest distance between events from month to month was calculated using the ArcMap *Near* tool. The mean minimal distance, d_{min}, between events was extracted for each pair of months. A coefficient of reoccurrence,

CoR, was calculated as d_{min} normalised by *dr*. If erosion occurred exactly at the same places ($d_{min} = 0$) *CoR* = 1, while *CoR* = 0 if $d_{min} \geq dr$ (Figure 4.21).

4.11. Method suitability to monitor bedrock micro-erosion

4.11.1. Method comparison with MEMs

The method was calibrated to resolve a vertical change of 0.001 m at the horizontal resolution of 0.001 m. This desirable accuracy was chosen because the detachment of rock fragments was assumed to be the primary mechanism of erosion across the studied shore platform. This assumption is based on the scarcity of sediments (abrasive), the shape of fresh exposures (Figure 3.11 G and H), and the micro-structure of the rocks types exposed on the surface. Therefore, the method cannot be used to monitor grain-by-grain abrasion which requires a higher accuracy of measurement. The MEM with the vertical accuracy of 2.5×10^{-5} m remains the best method to quantify effects of abrasion (Robinson, 1977a). There is a potential to use SfM at the sub-millimetre scale by increasing the number of photographs (Grennes et al., 2005).

Independence of the SfM method from the limited vertical range of the MEM needle and larger planform area surveyed enables a study of surfaces of higher relief expressed by horizontal and vertical discontinuities, as well as sloping surfaces. The horizontally-expressed discontinuities include steps at the bedding planes and the micro-layering, while the vertically-expressed features include joints, cracks and fractures. As a consequence, using SfM instead of MEMs allows one to monitor a wider range of geomorphological situations, including the locations with potentially higher erosion rates, which arguably increases the spatial representativeness of the results (Moses, 2014; Cullen et al., in review).

4.11.2. Topographic reconstruction and change detection

Although SfM has recently been more widely used to reconstruct topography, it has been rarely applied to detect change through time. This is due to a number of factors which strongly influence performance of the model but which remain difficult to control: light conditions, shadow, camera positions, surface reflectivity and roughness (Rock et al., 2011; Nitsche et al., 2013; Gonçaves and Henriques, 2015; Cook, 2017). Here, the two former factors were addressed by wrapping the frame in the white cloth to disperse the light, and fastening the cameras at constant positions on the frame, respectively. To minimise the effect of surface reflectivity, the fieldwork was conducted on dry days and at lowest tide which when combined gave the highest chance that the surface was dry at the time of surveying. The study was conducted on a wide range of surface roughness conditions (Table

4.1). The camera positions guaranteed minimal shadowing and occlusions but the effect of edge smoothing (Cook, 2017) could not be entirely removed.

The success of topographic reconstruction with SfM has been often tested with TLS which is believed to very accurately measure the surface (Aguilar et al., 2009; Heng et al., 2010; James and Robson, 2012; Westoby et al., 2012; Micheletti et al., 2015). Using TLS instead of, or in addition to, SfM was considered at the method development stage but it was not used due to the practical difficulties with scanning rough horizontal surfaces with considerable occlusion and, as a consequence, the need for multiple scanning positions, difficulties to always scan from the same positions and hence varied point distribution from survey to survey. The applied SfM method enabled two people to acquire data during the 2 h window of low tide.

4.11.3. Method validation and importance of the errors

Error was controlled at various stages of the processing which provided an understanding of how credible the results were. The errors introduced when creating the point clouds varied between surveys, with the maximal mean GCP error of 6.2 mm and CP error of 7.4 mm for August (Figure 4.7). Their diversity likely depended on the nuances in surveying procedure and the weather and/or surface conditions, such as the wind or surface wetness. For instance, errors could emerge from the shaking of the frame, or from the cloth occluding some of the markers from the camera view. These errors resulted in a systematic error which was addressed through filtering. The filtering showed 98.7% success rate in identifying incorrectly classified detachment volumes (Table 4.11).

Two sets of tests show performance of the technique. Firstly, the change detection performed on surfaces which had not experienced change demonstrated that the filtering did not entirely remove error caused by the surface roughness and the distance from the centre of the model which contributed to errors conceptually presented in Figure 4.8. The test to detect the £1 coins showed that all change 'detachments' were detected, but their area and volume were slightly overestimated while the mean thickness was underestimated (Table 4.13). The method confidence of 83.3% is however satisfactory for the scope of the study, but is considered throughout the discussion of the results.

4.11.4. Change which is impossible to resolve

A number of factors determine the ability to resolve change in the study:

- assumptions about the nature of processes, which determine desirable *LoD*;
- change detection based on DEMs rather than point clouds or triangulated mesh (section 2.5.1.3);

- using SfM rather than TLS or point measurements, which is subjected to the errors which are difficult to control (Figure 4.8);
- filtering out events based on the sizes and shapes (section 4.8).

As a result of these factors some potential real detachments are either impossible to resolve or will be resolved incorrectly, or are resolved with the uncertain success in terms of occurrence or volume. These instances can be classified into six groups:

- the effects of erosion at vertical scale smaller than *LoD*, notably caused by abrasion (impossible);
- detachments with surface area below six pixels (impossible);
- failures of overhanging rocks (incorrect);
- large and/or long detachments (impossible);
- the effect of erosion at sharp edges which were smoothed on the models (incorrect);
- erosion at rougher surfaces and peripheral locations (uncertain).

The method is satisfactory in relation to the scope of the present study and the nature of the shore platform, such as geology, topography and external factors: sediment availability and marine conditions. However, for studies of different environments and/or with different focus the method likely needs re-calibration. Increasing the number of camera positions and diversifying their inclinations (Cook, 2017) could be considered.

4.12. Summary

The chapter describes the procedure used to quantify bedrock erosion at the small-scale (10^{-3} – 10^{-2} m), the results of which are reported in Chapter 5. The surveying, data processing and analysis phases are described.

The SfM photogrammetry is used to build point clouds from six photographs, which are then converted into 0.5×0.5 m DEMs at 0.001 m resolution. The *LoD* = 0.001 m is established and pixels which experience lowering ≥ *LoD* are converted into polygonal shapefile. Filtering based on polygon size and shape allows real detachments to be separated from error. Detachments are analysed on the basis of event inventory which allows the quantification of erosion rates and the identification of mechanisms of erosion. Spatial distribution of erosion is studied by grouping detachments into 0.25 m^2 plots according to their location, while linear regression is used to predict it. Erosion is analysed by month to find seasonality in erosion rates and patterns, and to assess whether erosion propagates in time.

5. Mechanisms and controls of shore platform down-wearing

5.1. Introduction

The main objective of this chapter is to quantify shore platform micro-erosion in order to understand the mechanisms and controls on the spatial and temporal distribution of erosion rates, and on the size and 3D shape of detachments, with the overall goal to predict erosion more widely.

Field evidence shows that detachment of rock fragments at the cm-scale (Figure 3.11 G and H) may be an important contributor to foreshore erosion. However, the monitoring techniques used in shore platform studies to date – point measurements of vertical erosion using MEMs and the coarse-scale step back-wearing calculations using cartographical data (sections 2.3.2 and 2.3.3) – do not provide a resolution capable of detecting these changes. The mechanisms of shore platform erosion are as a result poorly constrained and the relationships between erosion and controlling factors have not been quantified. Without understanding foreshore dynamics, we are not able to assess whether our models on coastal evolution are accurate as the morphology and erosion at the foreshore controls wave energy distribution at the cliff toe (Ogawa et al., 2015; Poate et al., 2018).

The methods used in this study are presented in Chapter 4. In Chapter 7 macro-scale monitoring of the foreshore erosion is undertaken – combining these two scales will help me understand at which scale erosion is the most important for a long-term coastal evolution, how erosion rates calculated for the two scales compare, and what the relative contribution of surface down-wearing and step back-wearing to foreshore erosion is. The results are applied in Chapter 8 to account for shore platform erosion to model past cliff retreat rates from cosmogenic ^{10}Be concentrations. The results can serve as a high-resolution and high-precision empirical dataset to feed numerical models of rocky coast evolution.

5.1.1. Potential role of independent controls on the spatial distribution of foreshore detachments and erosion

Here current knowledge on the controls on the spatial variation in foreshore down-wearing is considered and used to define a set of quantifiable variables that will be tested for the ability to explain the variability in erosion rates observed across the foreshore from high-resolution small-scale (10^{-3} – 10^{-2} m) monitoring. Faster surface down-wearing has been recorded closer to the cliff (Moses and Robinson, 2011), which is in agreement with both theoretical (Flemming, 1965; Sunamura, 1992) and exploratory numerical (Kline et al., 2014; Matsumoto et al., 2016) models of coastal cross-section evolution. This has been attributed to the availability of sediment for abrasion and higher surface

inclination which concentrates wave energy (Moses, 2014). Erosion rates are therefore expected to negatively correlate with the distance from the cliff. The strong negative correlation between the distance from the cliff and the distance from the seaward edge would imply a positive relationship between erosion rate and the distance from the seaward edge. However, the distance from the seaward edge can also serve as a highly simplified proxy for the wave energy where the strongest waves with presumably the highest eroding ability are present at the seaward edge of the shore platform and subsequently dissipate energy when traversing the platform (Poate et al., 2018).

In the alongshore consideration of the shore platforms the higher elevation sections are associated with more resistant rocks and consequently slower erosion rates (Stephenson, 2000; Thornton and Stephenson, 2006). Steeper platform surfaces are associated with faster erosion, mainly because an inclined surface presents a more prominent obstacle to waves (Moses, 2014). Higher platform roughness, from more or larger protrusions and more complex relief (Smith, 2014), increases the potential for wave breaking and energy concentration, and therefore increased erosion (Wilson et al., 2013).

Foreshore erosion has been linked with either direct wave action (Robinson, 1977a; Foote et al., 2006) or mechanical weathering (Kirk, 1977; Robinson, 1977a; Stephenson and Kirk, 1998). If the mechanical wave action rather than weathering dominates the down-wearing, the tidal duration can be a key control on erosion rate because it dictates for how long the waves actively operate at or slightly above given elevation (Trenhaile, 2000; Matsumoto et al., 2016). As tidal duration is related to the frequency of the submergence/emergence transitions, it may also be crucial for defining the efficiency of wetting and drying (mechanical weathering) (Robinson, 1977a).

The platform curvature provides a combined insight into the role of the profile and planform shape of the surface which influences exposure/shading and water flow across it; it was shown to determine the distribution of erosion in fluvial environments (Hurst et al., 2012). The roughness at the 10^{-2} – 10^{-1} m scale is important as it shows whether protrusions are available for lifting from the rock mass (Lamb et al., 2015). The elevation range within a site may reflect either a generally steeper sloping surface or the presence of a step, both of which imply the potential for increased erosion (Moses and Robinson, 2011). Foreshore erosion is also believed to concentrate along discontinuities (Moses, 2014).

Based on the literature, I consider here 12 variables as potential controls on the distribution of erosion across the shore platform. Seven of them refer to the general characteristics of the 0.5×0.5 m monitoring sites: 1) location on the platform: distance from the cliff, distance from the seaward edge and elevation; 2) topography: slope and roughness; and 3) location-dependent marine conditions: tidal duration and inundation frequency (Table 4.1). Five other variables characterise: 1) the cm-scale

topography: curvature, site roughness and elevation range; and 2) the rock structure: number and density of joints (Table 4.7).

Using the methods described in Chapter 4, the data of foreshore erosion captured using SfM on 15 sites at Hartle Loup over 12 months will be presented in this chapter. An analysis is presented that allows the identification of mechanisms of erosion through analysis of detachment size and shape distribution and establish quantitative relationships between erosion rates and controlling factors.

5.2. Results

The full graphical depiction of the recorded detachments is provided in the Appendices 4-7. In total, 720 maps were produced for the 12 months of monitoring across the 15 monitoring sites: Appendix 4 contains the binary information (erosion/no erosion zones) describing the distribution of erosion for each site on a month-by-month basis; Appendix 5 shows the cumulative distribution of erosion, with each month of data overlaid; Appendix 6 presents the magnitude of monthly erosion (depth); and Appendix 7 shows the cumulative magnitude of erosion (depth). The results and discussion sections are organised such that firstly, all detachments are presented together in a single database, then individual monitoring sites are treated separately to explore the spatial variations in foreshore erosion, and finally, erosion is presented by month to consider the seasonal variability of erosion and its development through time.

5.2.1. Analysis of the small-scale detachment inventory

Analysis was performed on the full inventory of detachments in order to identify the mechanisms of erosion on the basis of the area volume, volume frequency and 3D shape distributions. In the rockfall/landslide literature it was shown that the area volume exponent *b*, the magnitude frequency exponent β and the compactness of detachments can be used to understand whether erosion happens due to near-surface tensile stresses or shear stresses, and how important is the state of the bedrock surface (Dussauge-Peisser et al., 2002; Malamud et al., 2004; Guzetti et al., 2009; Williams et al., 2018).

5.2.1.1. Net erosion rate

The one-year monitoring of shore platform erosion resulted in detection of a total of 2.88×10^{4} discrete measurable detachments, which in sum amount to 2.00×10^{-3} m^3 of bedrock removal. This is equivalent to the volume of a 0.126 m cube, or a spatially and temporally averaged erosion rate of 5.28×10^{-4} m yr^{-1} (0.528 mm yr^{-1}) (Table 5.1; Figure 5.1).

Table 5.1 Summary statistics of the erosion variables across the detachment inventory.

Variable	Value	Equivalent cube size (m)
Numer of detachments	28,756	n/a
Total detached area (m^2)	0.82	n/a
Total detached volume (m^3)	2.00×10^{-3}	126.03×10^{-3}
Volume of the smallest detachment (m^3)	5.09×10^{-9}	1.72×10^{-3}
Volume of the largest detachment (m^3)	1.41×10^{-5}	24.13×10^{-3}
Average detachment volume (m^3)	6.96×10^{-8}	4.11×10^{-3}
Standard deviation of detached volumes (m^3)	2.50×10^{-7}	6.30×10^{-3}
Erosion rate (mm yr^{-1})	0.528	n/a

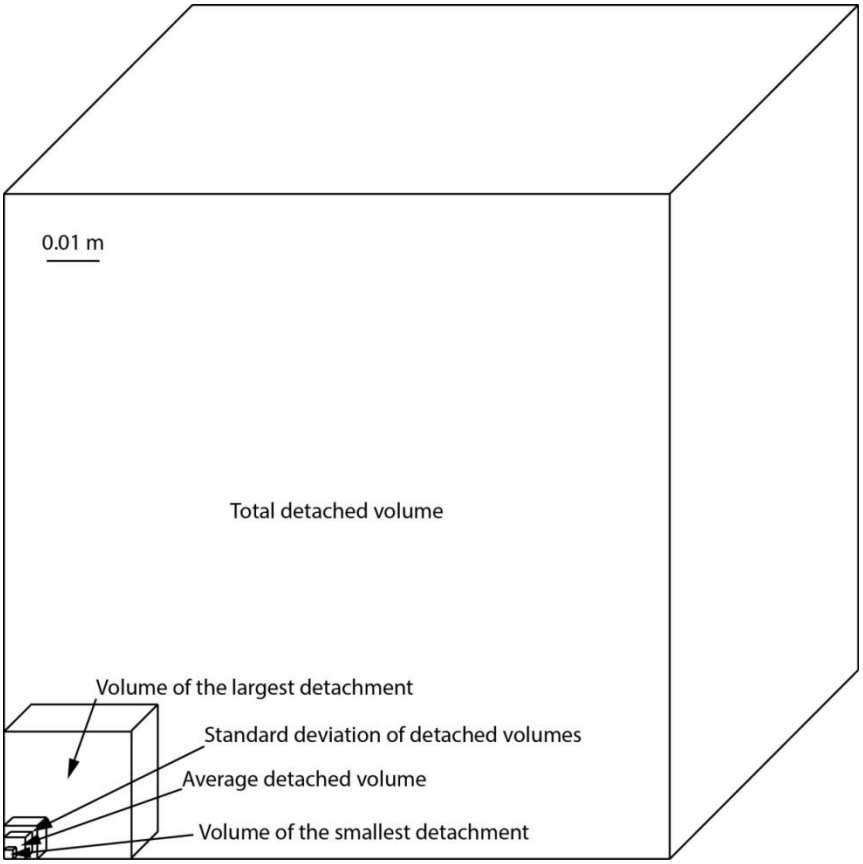


Figure 5.1 Equivalent cube sizes for the detachment volumetric properties in the detachment inventory.

5.2.1.2. Volume frequency, size and shape of detachments

The size of individual detachments varies considerably. The maximum thickness of individual pixels ranges up from a minimum of 1.00×10^{-3} m, equivalent to the *LoD*, to 1.04×10^{-1} m, with volumes of detachments ranging between 5.09×10^{-9} m^3 and 1.41×10^{-5} m^3 (Table 5.2). Detachments of

volume of 10^{-8} to $10^{-7.5}$ m^3 are the most frequent with the abrupt decrease in frequency for the smallest, and the gradual decrease in the frequency of the largest events (Figure 5.2).

Table 5.2 Summary statistics of the individual detachment sizes across the detachment inventory.

Variable	Minimum	Maximum	Mean	Standard deviation
Area (m^2)	6.00×10^{-6}	1.68×10^{-3}	3.44×10^{-5}	7.27×10^{-5}
Volume (m^3)	5.09×10^{-9}	1.41×10^{-5}	6.96×10^{-8}	2.50×10^{-7}
Maximum thickness (m)	1.05×10^{-3}	1.04×10^{-1}	2.39×10^{-3}	3.07×10^{-3}

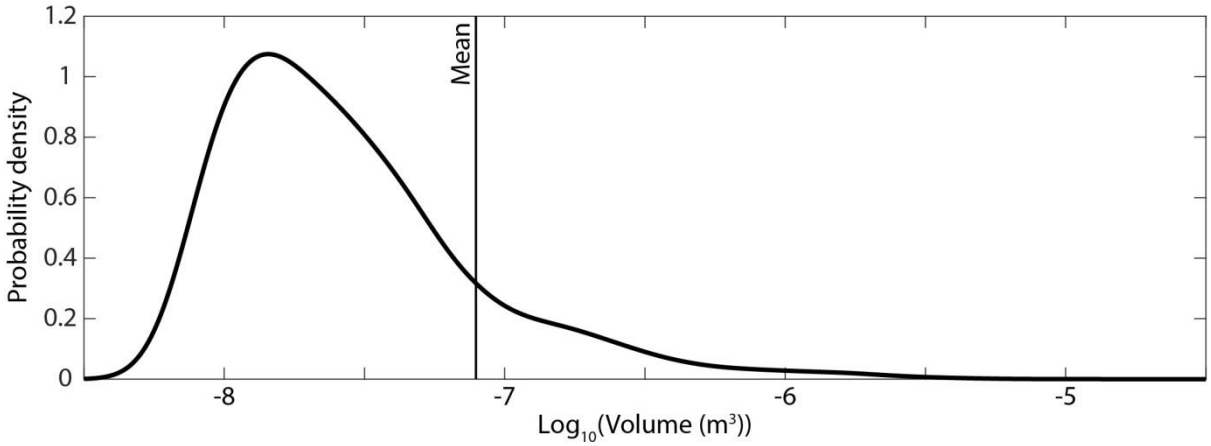


Figure 5.2 Kernel density estimate (normal kernel, half width h = 0.1 $log_{10}(m^3)$) of detachment volume for the entire detachment inventory. Mean volume = 6.96×10^{-8} m^3.

A statistically significant positive relationship (R^2 = 0.925; p < 0.05) is shown between measured detachment planform area and measured 3D volume (Figure 5.3). Although most detachments closely follow a power-law trendline, a sub-population of events exist with planform size of < ~3.98×10^{-5} m^2 (log_{10}(Area) = -4.4) with volume proportionally larger relative to the area (Zone 1 in Figure 5.3). Events with planform > 6.31×10^{-4} m^2 (log_{10}(Area) = -3.2) tend to have larger volumes as a proportion of their area and so there is a deficiency of detachments below the power law (Zone 2 in Figure 5.3). Two detachments are characterised by an anomalously high volume (~1.00×10^{-5} m^3 (Zone 3 in Figure 5.3)).

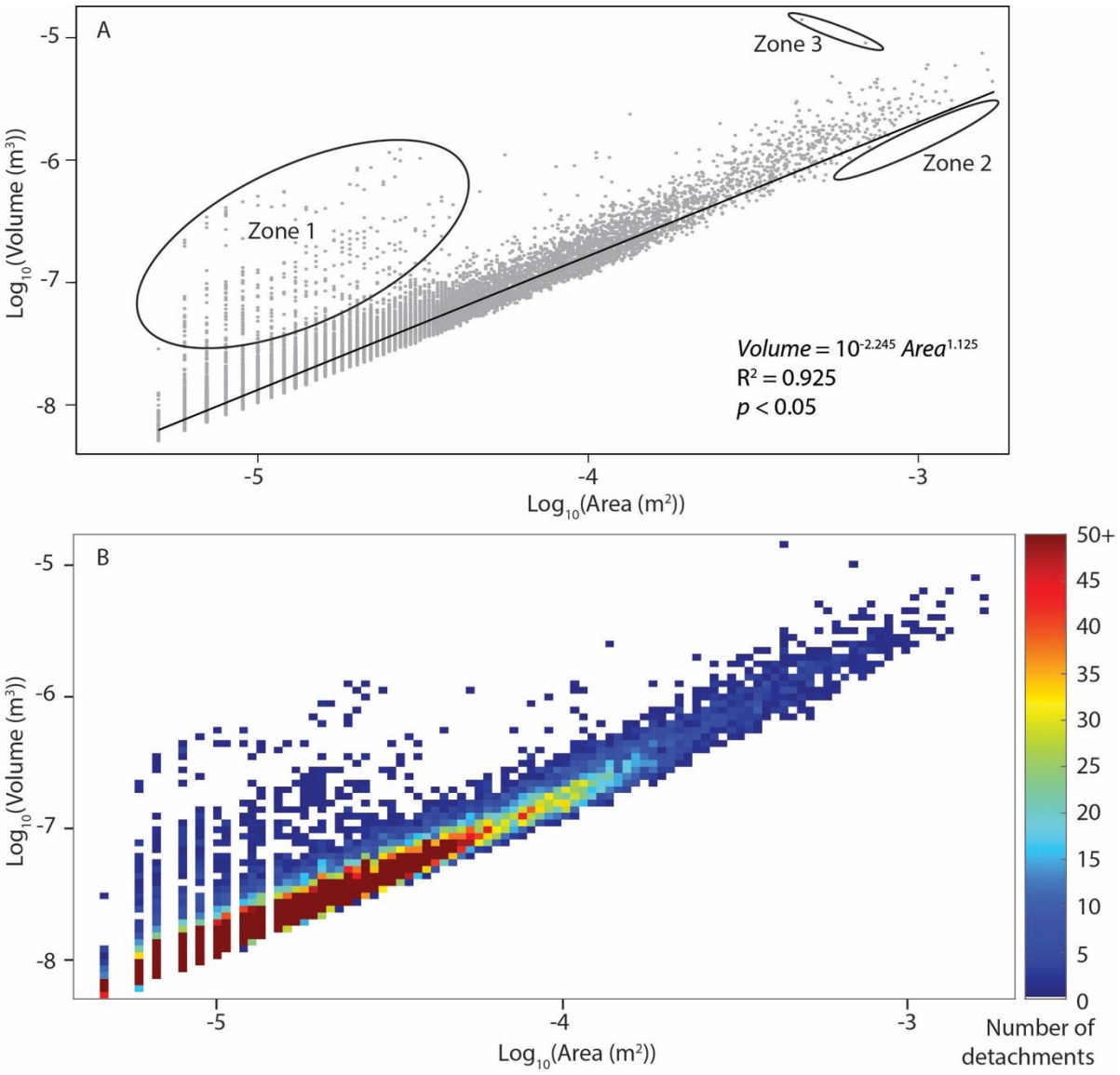


Figure 5.3 Relationship between area and volume of detachments across the full inventory on a log-log non-cumulative plot: A) distribution of the sizes of single detachments and the power-law trendline; B) density distribution map with a grid cell size of 0.025 (x) x 0.05 (y). The organisation of events with the smallest area into the vertical stripes is a function of data resolution where the area is rounded to the 10^{-6} m^2 pixel size intervals, while depth, and consequently the volume, adopts the full range of continuous values as it is measured at a higher precision.

Most events are characterised by low volumes of 10^{-8} to 10^{-7} m^3, and the frequency of detachments decreases with volume (Figure 5.4). The volume-frequency distribution curve fitted using the least-squares method (after Clauset et al., 2009) has a complex shape, but broadly follows a straight line (power law) in log-log space. Minor perturbations away from this trend, and in particular a sharp break in the distribution slope at the detachment size equivalent to a 0.011 m cube, is observed (Figure 5.4). This volume is approximately equivalent to a single shale platelet typically found on the

shore platform (Figure 3.11G). To describe the apparent sub-populations within the volume-frequency distribution, additional trendlines have been fitted for volumes larger and smaller than 1.26×10^{-6} m^3, excluding the roll-over for the smallest volumes (< 1.12×10^{-8} m^3). This gives a power-law fit with β = 0.926 (R^2 = 0.990, p <0.05) for the detachments smaller than the threshold, and β = 2.534 (R^2 = 0.947, p <0.05) for those larger (Figure 5.4). The trendline was not fitted to the roll-over because the section of the magnitude/frequency plot with the smallest events is believed to reflect data resolution and censoring of the smallest events due to superimposition, rather than the actual size distribution (section 2.5.2.1).

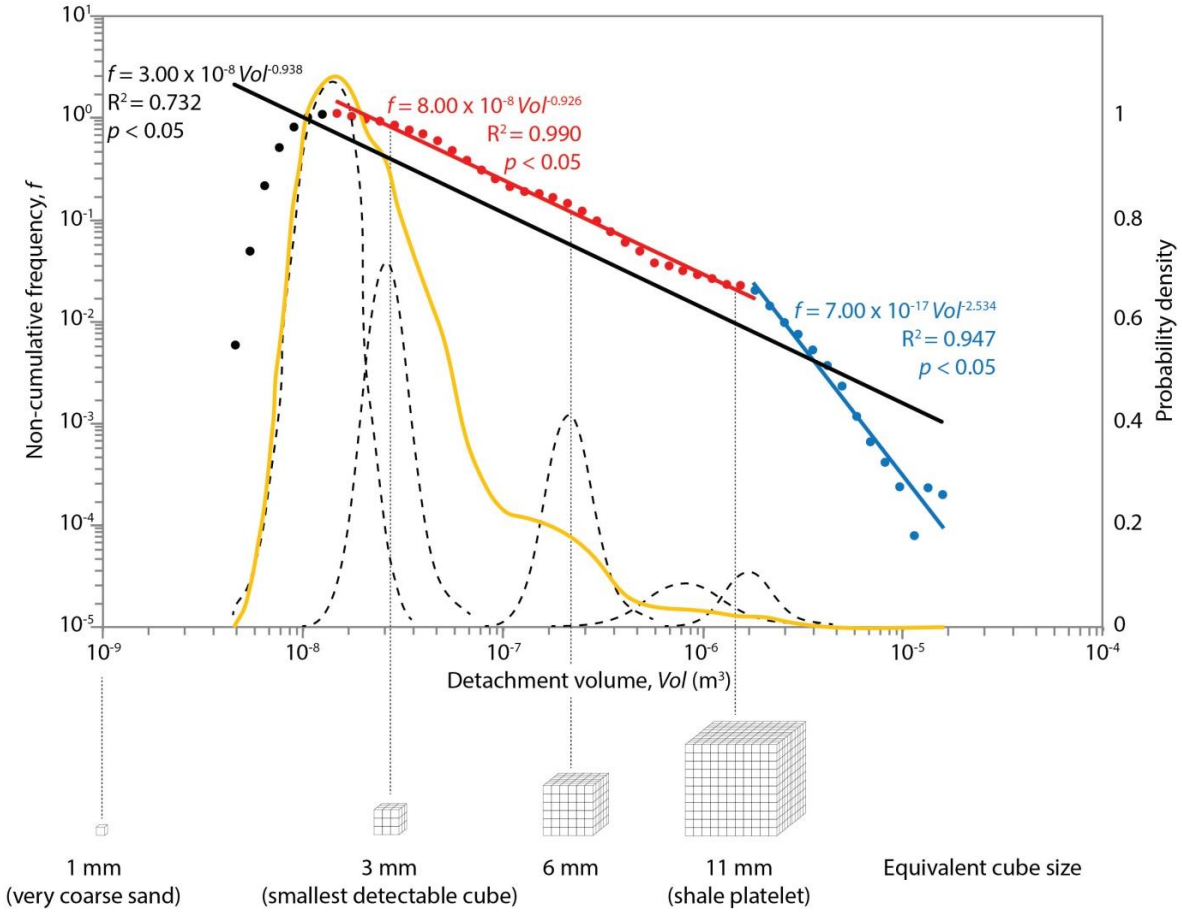


Figure 5.4 Volume-frequency distribution across the full inventory obtained using SfM methods. Scatter plot (left-hand vertical axis) represents the volume-frequency kernel density distribution curve with the power-law trendline (solid black line) on a log-log scale plot. Additional trendlines were fitted for two sections of volume spectrum (red for Vol 1.12×10^{-8} – 1.26×10^{-6} m^3; blue for Vol > 1.26×10^{-6} m^3) excluding the roll-over at the lowest spectrum of Vol (black data points). The yellow line is the kernel density estimate (normal kernel, half width = 0.08 $log_{10}(m^3)$; right-hand vertical axis) of the individual detachment volumes for the full inventory. Dashed lines indicate the distributions of proposed sub-populations (idealised and manually drawn: see main text). Idealised shapes indicate the equivalent cube sizes for specific volumes, with indicative relative sizes compared to the possible erosion features.

The shape of detachments can be indicative of the dominant erosion process (section 2.5.2.1). In the present study, the detached material has a wide spectrum of shapes with the highest frequency in the *very bladed* and *very platy* sectors (Figure 5.5). No detachments are present at the bottom of ternary plot meaning that there are no very thin slab-like forms, which may be due to the censoring caused by pixel resolution or physical inexistence of thin shapes. The shale detachments have a wider range of shapes, in particular the *compact* blocky shapes. The sandstone detachments exclusively occupy the rod corner of the ternary plot (Figure 5.5).

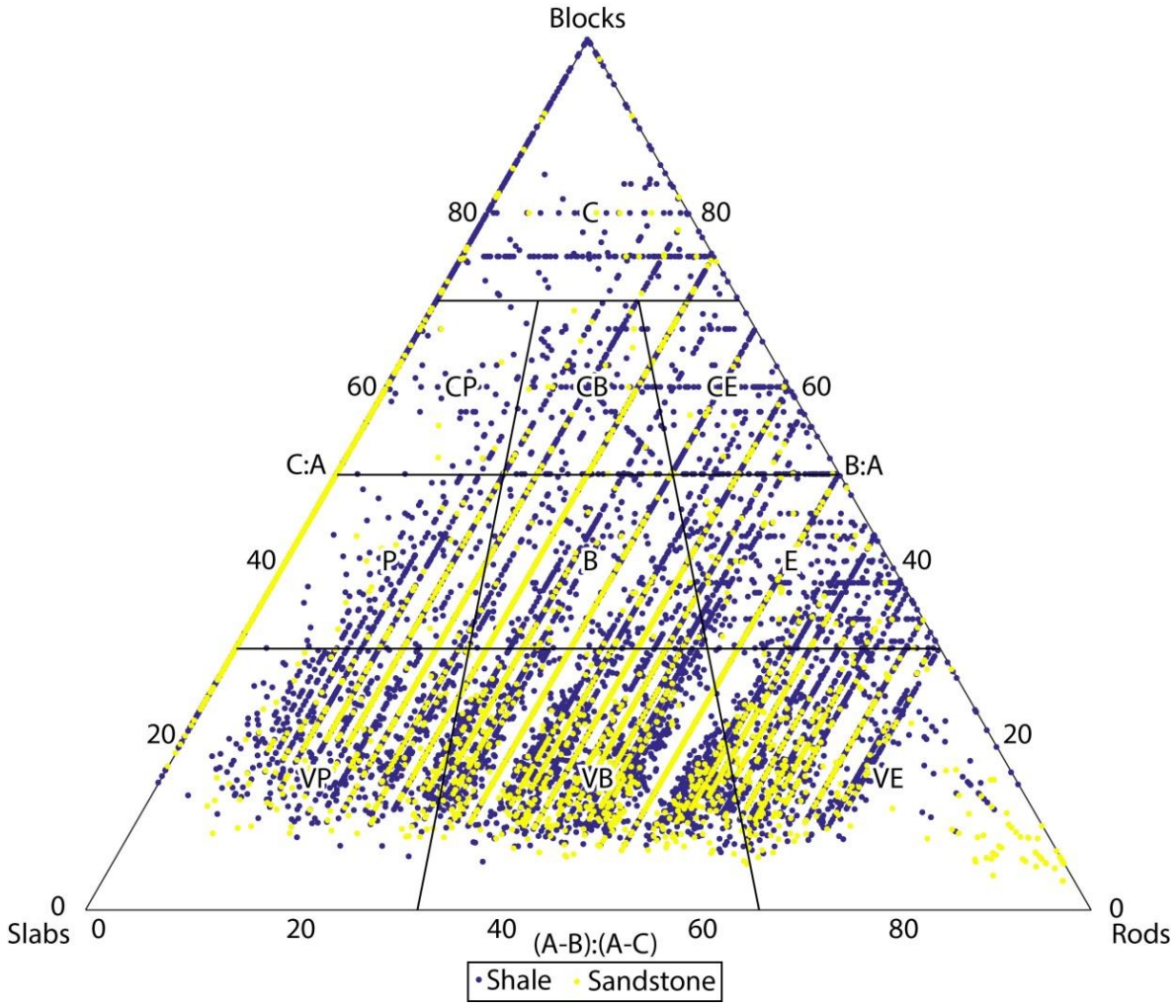


Figure 5.5 Shapes of detached material coloured by the rock type. Block axes: A – long, B – medium, C – short. For sector description see Figure 2.5. The organisation of shapes in diagonal stripes and the concentration of events along the slabs/blocks edge of the ternary plot is explained by high numbers of events with planform size equal to the grid resolution and change precision, or a low multiple thereof.

5.2.2. Spatial analysis

5.2.2.1. Summary of detachment properties in the monitoring site inventory

In order to understand the spatial pattern and controls on the distribution of detachments across the foreshore, the erosion characteristics were summarised per monitoring site (Table 5.3, Figure 5.6). The total area, *sArea*, that has been observed to experience detachments between 0.015 m^2 at site 5 and 0.098 m^2 at site 3, which is equivalent to the erosion of 6.0 to 39.2% of the surface. The total volume, *sVol*, eroded ranges between 2.56×10^{-5} m^3 at site 5 and 3.01×10^{-4} m^3 at site 3, and the erosion rate, *sEro*, between 0.101 mm yr^{-1} at site 5 and 1.192 mm yr^{-1} at site 3, indicating more than an order of magnitude difference in erosion rates between sites. This is also seen in the variability of the mean volume, *sMean*, and the standard deviation of volumes, *sStd*, which span between 3.43×10^{-8} m^3 at site 2 and 1.14×10^{-7} m^3 at site 10, and 5.97×10^{-8} m^3 at site 2 and 4.52×10^{-7} m^3 at site 10, respectively. The volume frequency exponent, *sβ*, varies between 0.555 at site 1 and 0.942 at site 15. Although site 3 is characterised by the highest rate of erosion (*sArea*, *sVol* and *sEro*), detachments are generally the largest (*sMean*) and the volumes are the most variable in size (*sStd*) at site 10. The erosion rate calculated as the mean for all sites is 0.529 ± 0.357 mm yr^{-1}.

*Table 5.3 Summary of the detachment data at the monitoring sites. The largest values are in **bold**.*

Site	Total area, *sArea* (m^2)	Total volume, *sVol* (m^3)	Mean volume, *sMean* (m^3)	Standard deviation of volumes, *sStd* (m^3)	Erosion rate, *sEro* (mm yr^{-1})	Exponent β, *sβ*
1	0.043	9.76×10^{-5}	5.59×10^{-8}	1.15×10^{-7}	0.387	0.555
2	0.020	3.53×10^{-5}	3.43×10^{-8}	5.97×10^{-8}	0.140	0.885
3	**0.098**	**3.01×10^{-4}**	1.07×10^{-7}	3.54×10^{-7}	**1.192**	0.697
4	0.093	2.42×10^{-4}	8.42×10^{-8}	2.30×10^{-7}	0.958	0.589
5	0.015	2.56×10^{-5}	4.55×10^{-8}	1.14×10^{-7}	0.101	0.738
6	0.042	9.29×10^{-5}	7.39×10^{-8}	2.60×10^{-7}	0.368	0.682
7	0.044	7.87×10^{-5}	4.98×10^{-8}	1.24×10^{-7}	0.312	0.785
8	0.037	6.25×10^{-5}	4.58×10^{-8}	1.16×10^{-7}	0.247	0.804
9	0.078	1.94×10^{-4}	8.97×10^{-8}	2.33×10^{-7}	0.770	0.592
10	0.067	2.23×10^{-4}	**1.14×10^{-7}**	**4.52×10^{-7}**	0.881	0.582
11	0.083	2.30×10^{-4}	9.66×10^{-8}	4.07×10^{-7}	0.911	0.746
12	0.024	5.51×10^{-5}	5.60×10^{-8}	2.31×10^{-7}	0.218	0.809
13	0.026	4.26×10^{-5}	6.38×10^{-8}	1.85×10^{-7}	0.169	0.765
14	0.095	2.10×10^{-4}	4.70×10^{-8}	1.48×10^{-7}	0.831	0.901
15	0.058	1.12×10^{-4}	3.85×10^{-8}	9.11×10^{-8}	0.444	**0.942**

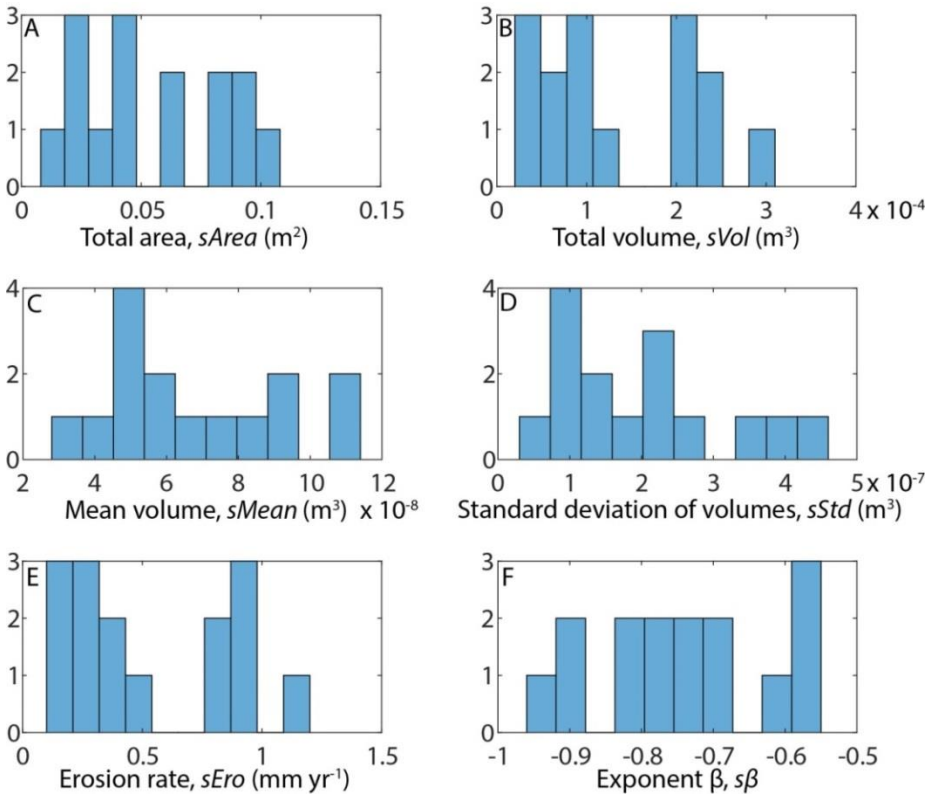


Figure 5.6 Distribution of the erosion variables across the 15 monitoring sites: A) Total area, sArea (m^2); B) Total volume, sVol (m^3); C) Mean volume, sMean (m^3); D) Standard deviation of volumes, sStd (m^3); E) Erosion rate, sEro (mm yr^{-1}); F) Exponent β, sβ; Y axis: number of sites.

5.2.2.2. 3D shape of detachments in the monitoring site inventory

The distribution of detachment shapes based on the spatial location is shown in Figure 5.7. As the events were plotted on the top of each other, the points belonging to the monitoring sites with a higher ID number overlay those of the lower ID numbers, which makes the visual interpretation difficult. Detachment shape shows no clear pattern when aggregated by site, but there is a dominance of detachments at the sandstone sites (1, 5 and 7) of *very platy*, *very bladed* and *very elongate*, with detachments from site 1 concentrating towards the *rods* corner of the ternary plot (Figure 5.7A). In Figure 5.7B the sites are represented by their mean shape, derived from the mean length of the long, the medium and the short axes. There is a visible diversity in shapes with eight sites falling into the *very bladed* sector, four into the *very elongate* and one into the *very platy*, *bladed* and *elongate* sectors.

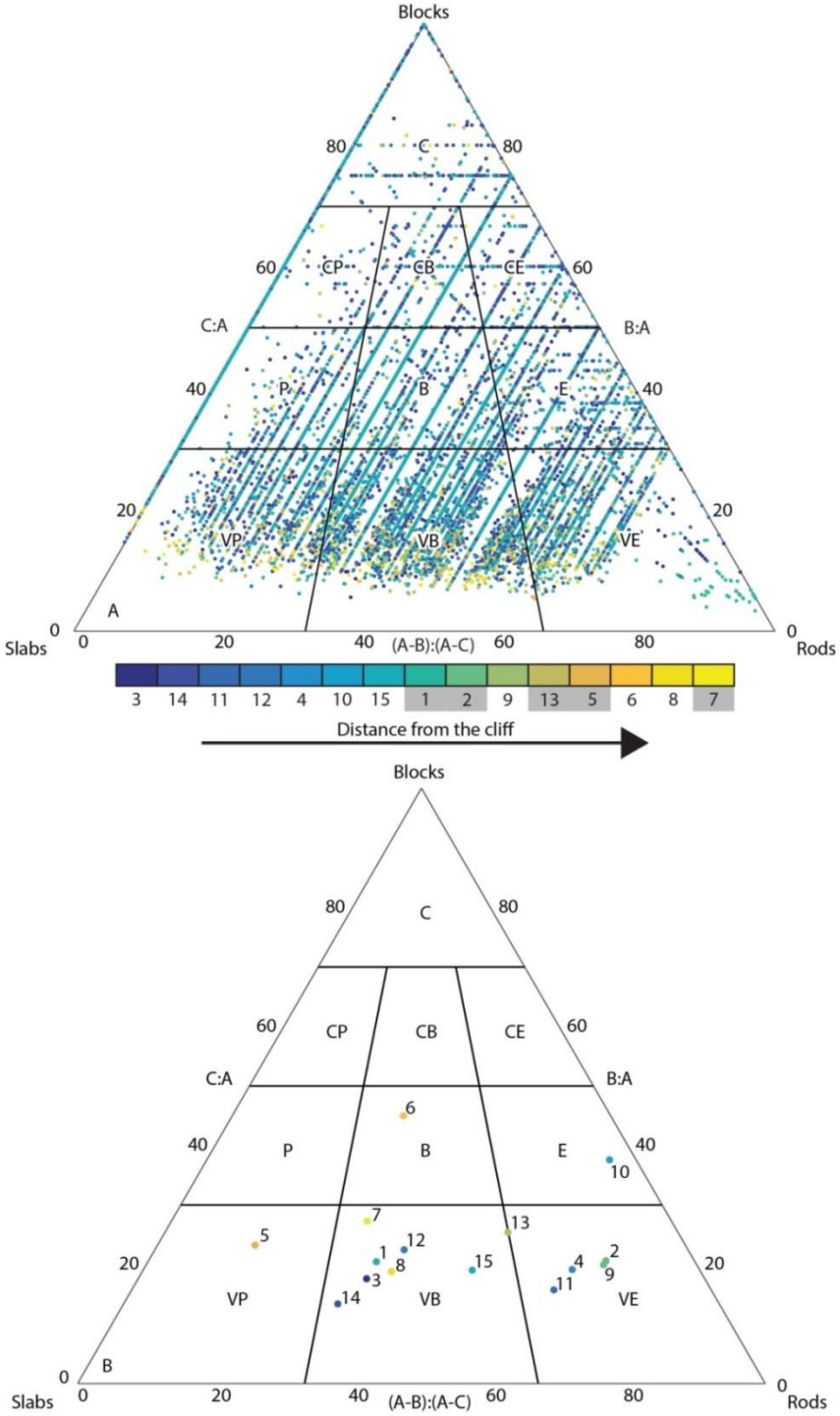


Figure 5.7 Shapes of detached material coloured by monitoring site, ordered by the distance from the cliff. Block axes: A – long, B – medium, C – short. Sandstone sites are indicated by grey boxes in the lowermost scale; the remaining sites are located on shale sections of the platform. For sector description see Figure 2.5.

5.2.2.3. Spatial distribution and character of the foreshore detachments

In order to predict spatial distribution of erosion, the monitoring sites were split into: 1) a training set of 12 sites which was used to develop the model, and 2) a test set of three sites which allowed the performance of the model to be verified. The sites which form the test set (12, 13 and 15) were selected to encompass sufficiently diverse relief and rock types.

Distribution of the variables

Erosion at each site was characterised by six variables, of which three represent the magnitude of erosion: total area, total volume and erosion rate; and three represent the size distribution: mean volume, standard deviation of volumes and exponent β. The erosion rate, *sEro*, is the variable that was modelled because the area and the volume are strongly correlated (Figure 5.3), as are the volume and erosion rate, the latter being calculated from the former. The mean volume, *sMean*, and the exponents β, $s\beta$, provide insight into the size distribution within sites, and so the standard deviation of volumes is also excluded. Figure 5.8 illustrates the distribution of the independent and erosion variables.

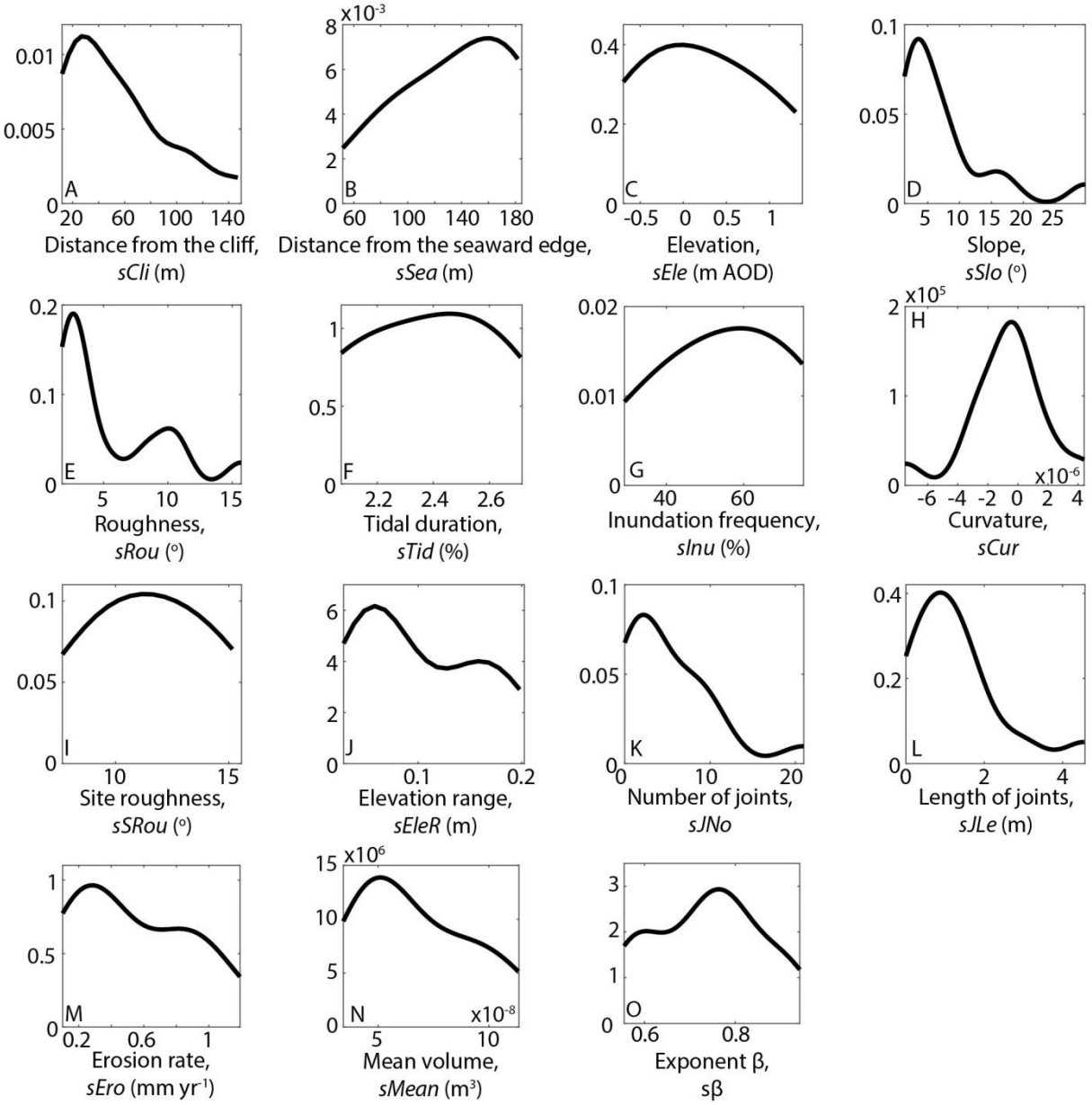


Figure 5.8 Kernel density estimate (normal kernel, default optimal half widths h returned in MATLAB were used) of the independent and erosion variables at the monitoring sites: A) Distance from the cliff, sCli (h = 17.62 m); B) Distance from the seaward edge, sSea (h = 31.10 m); C) Elevation, sEle (h = 0.62 m AOD); D) Slope, sSlo (h = 2.48°); E) Roughness, sRou (h = 1.12°); F) Tidal duration, sTid (h = 0.23%); G) Inundation frequency, sInu (h = 14.56%); H) Curvature, sCur (h = 1.10×10^{-6}); I) Site roughness, sSRou (h = 2.52°); J) Elevation range, sEleR (h = 0.03 m); K) Number of joints, sJNo (h = 2.74); L) Length of joints, sJLe (h = 0.53 m); M) Erosion rate, sEro (h = 0.23 mm yr^{-1}); N) Mean volume, sMean (h = 1.60×10^{-8} m^3); O) Exponent β, sβ (h = 0.06); Y axis: probability density.

Pair-wise correlations between the variables

The variables related to the across-shore location and the monitoring site characteristics, including the distance from the cliff and the seaward edge, elevation and inundation frequency strongly correlate with each other, as do the topographic variables – roughness, site roughness and elevation range (Figure 5.9). The inundation frequency is calculated from the elevation and the tidal duration (section 3.7.2.1) and shows a very strong (PCC = -0.99) and significant correlation with the former variable.

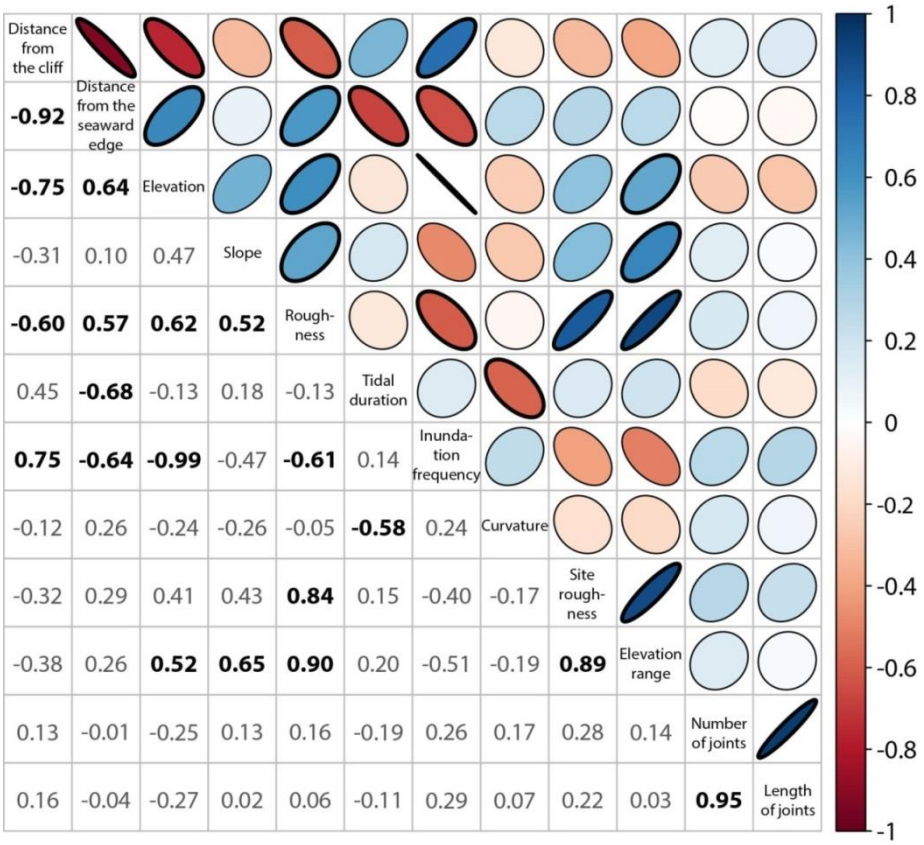


Figure 5.9 Matrix of correlation coefficients and best-fit ellipses for all independent variables characterising the small-scale monitoring sites obtained using the Pearson correlation in R. The colour bar represents the Pearson correlation coefficient (PCC) which describes both the strength of relationship and its sign, '-1' being the strongest negative relationship, '0' expressing no correlation and '1' representing the strongest positive relationship. The sign of the relationships (positive/negative) is also expressed by the sign of PCC values in the bottom-left part of the plot and the orientation of the oval in the upper-right part, while their strength is represented by the absolute values in the bottom-left part of the plot and the width of the ovals with narrower ovals representing stronger relationships. Significant relationships ($p < 0.05$) are indicated with the thicker oval edge and the bold PCC values.

The results from the pair-wise least-squares regression between erosion and the independent variables are presented in Figure 5.10. Most relationships are insignificant ($p \geq 0.05$). In general terms, the erosion rate is higher closer to the cliff and farther from the seaward edge, at locations where elevation, macro- and micro-roughness are higher, and the inundation frequency is lower. Detachments are larger at sites with more rough surfaces and those which have a larger elevation range, which is expressed by both the mean volume and the exponent β (Figure 5.10).

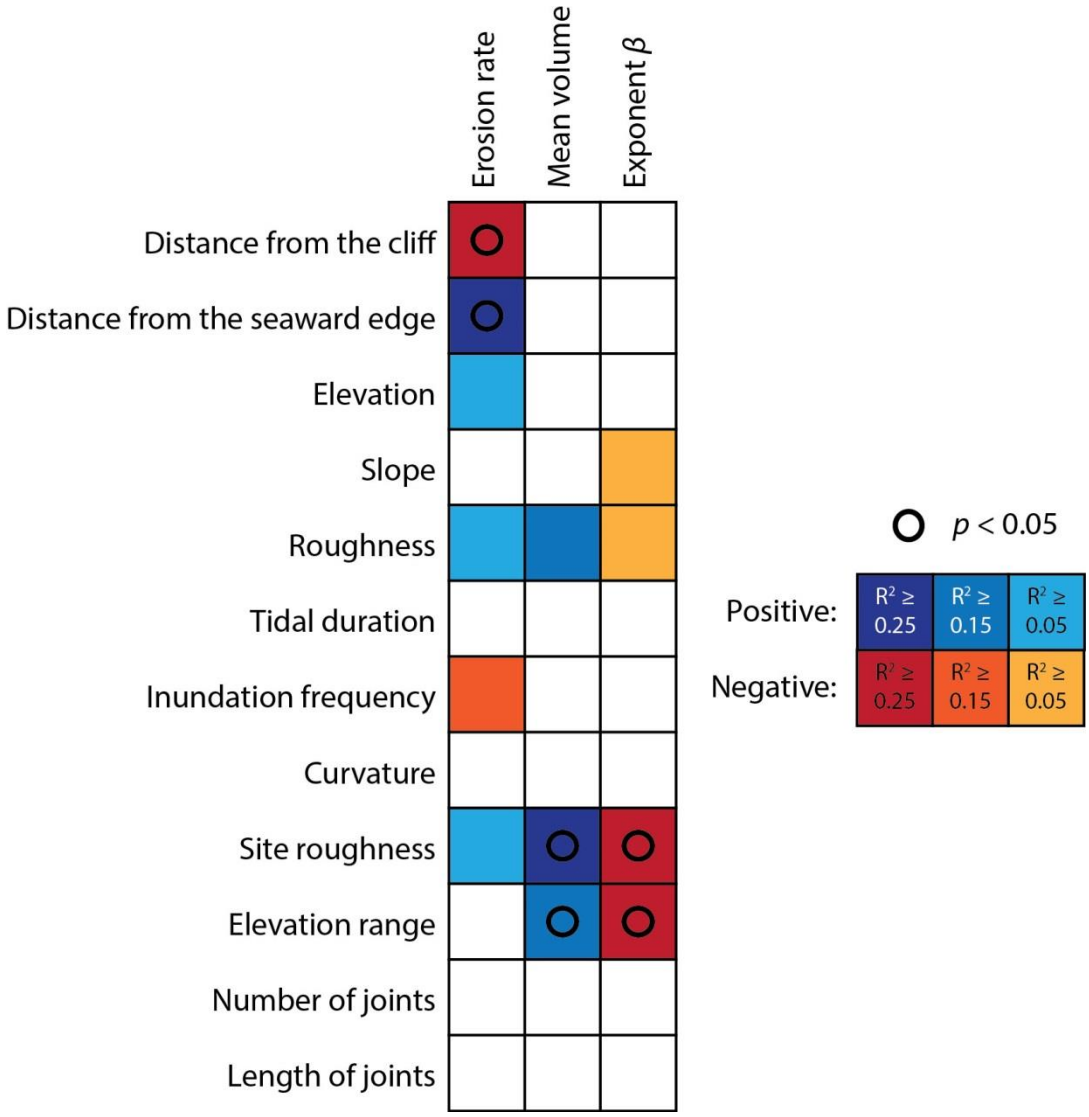


Figure 5.10 Results of the pair-wise least-square regression between the independent variables and erosion.

Modelling the spatial distribution of platform down-wearing

All independent variables except the inundation frequency, the elevation range and the number of joints contribute to best-fit models of erosion (Figure 5.11; Table 5.4). The erosion rate, *sEro*, is controlled by the location on the platform, tidal duration, jointing and elevation which,

excluding the length of joints, *sJLe*, can be obtained from a relatively low-resolution topography dataset and a local tide gauge record. However, because distances from the cliff and from the seaward edge are correlated, the former was excluded from the model so as not to overestimate the importance of the cross-shore location. Also, the length of joints was excluded as it does not increase the performance of the model when the distance from the cliff is excluded. *sEro* is higher farther from the seaward edge (higher *sSea*) and at the locations with higher tidal duration, *sTid*, which is where the tide cycles more frequently (R^2 = 0.648, $p < 0.05$). Detachments are larger (higher *sMean*) at more rough surfaces (higher *sSRou*) with lower gradients (lower *sSlo*) which are located closer to the cliff (lower *sCli*) (R^2 = 0.734, $p < 0.05$). The exponent β negatively correlates with the site roughness, *sSRou*, which means that at more rough surfaces larger detachments dominate, but in comparison to other erosion variables the relationship is weak, yet still significant (R^2 = 0.457, p <0.05). Shapiro-Wilk tests show that the residuals of erosion variables have normal distributions (5% significance level) when the test site 12 is excluded (Figure 5.12).

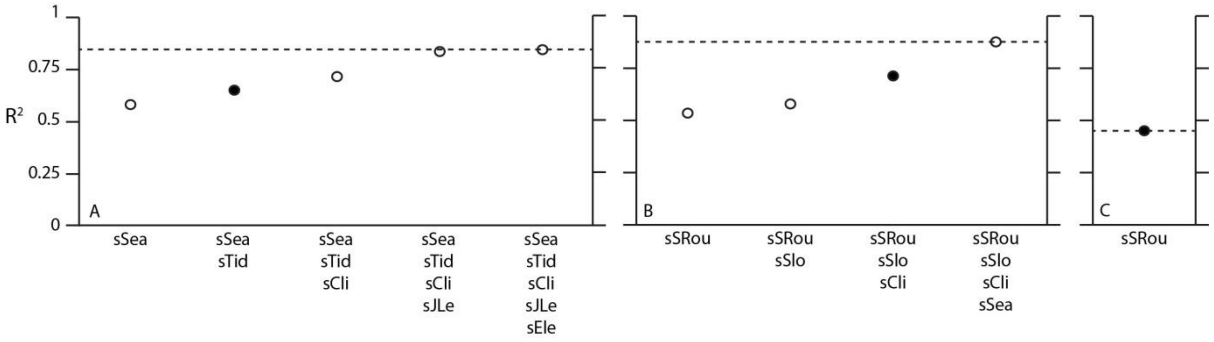


Figure 5.11 Sequence of input independent variables and resulting R^2 values (p <0.05): A) Erosion rate, sEro (mm yr^{-1}); B) Mean volume, sMean (m^3); C) Exponent β, sβ; dashed lines represent maximum R^2 of full model; accepted models are indicated by the black dot. See Glossary for abbreviation meaning and calculation of the variable values.

Table 5.4 Accepted numerical models of the erosion variables. See Glossary for abbreviation meaning and calculation of the variable values.

Erosion variable	Equation	R^2	p-value
Erosion rate (mm yr^{-1})	$sEro = -2.01 + 0.01\ sSea + 0.60\ sTid$	0.648	0.004
Mean volume (m^3)	$sMean = (-215.20 + 105.00\ sSRou - 19.88\ sSlo - 2.03\ sCli) \times 10^{-10}$	0.734	0.003
Exponent β	$s\beta = 1.10 - 33.66 \times 10^{-3}\ sSRou$	0.457	0.009

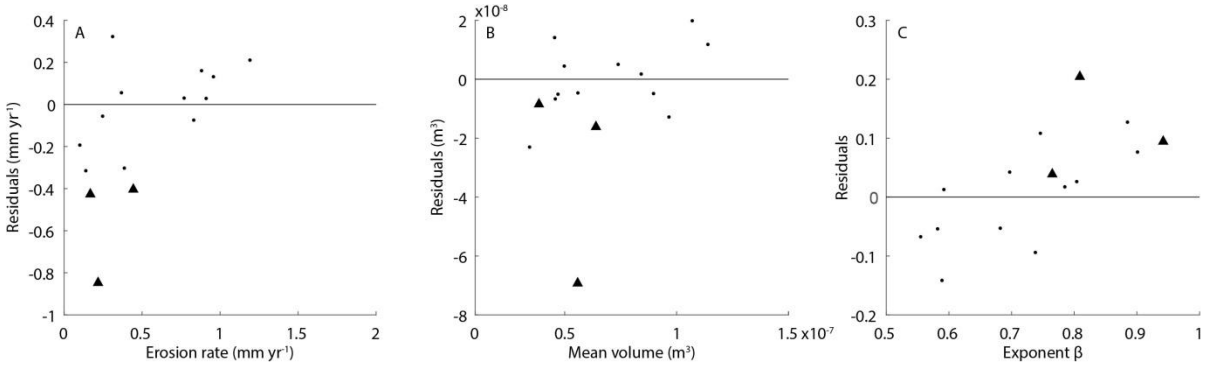


Figure 5.12 Distribution of residuals for the erosion variables: A) Erosion rate, sEro (mm yr^{-1}); B) Mean volume, sMean (m^3); C) Exponent β, sβ. Points represent the training set, triangles represent the test set; residuals are calculated as observed - predicted values.

5.2.3. Temporal analysis

5.2.3.1. Magnitude and size distribution of detachments throughout the year

The detachment monitoring data for each month at each site were used to assess the temporal variability of the erosion. The period between 6th April and 2nd October 2016 was characterised by slightly higher rates of net erosion (0.576 mm yr^{-1}), contributing to 52% of the annual eroded volume from 48% of the total monitored time, as compared to the period of 2nd October 2016 to 11th April 2017 (0.497 mm yr^{-1}) during the remaining 52% of the time (Figure 5.13). There was also greater variability in the erosion rates, *sEro*, the mean volume, *sMean*, and the standard deviation of volumes, *sStd*, between the monitoring sites between April and October, while their highest values fall between July and September. Between October and April, erosion rates averaged from the mean values per site were lower (*sEro* = 0.384 mm yr^{-1}), detachments were smaller (*sMean* = 4.43×10^{-8} m^3) and more consistent in size (*sStd* = 1.11×10^{-7} m^3), and the volume-frequency exponent was higher (*sβ* = 0.667) as compared with the period between April and October. During this period the equivalent averaged values were: *sEro* = 0.495 mm yr^{-1}, *sMean* = 8.40×10^{-8} m^3, *sStd* = 2.16×10^{-7} m^3 and *sβ* = 0.480. The highest frequency of the smallest detachments occurred between December and February (Figure 5.13).

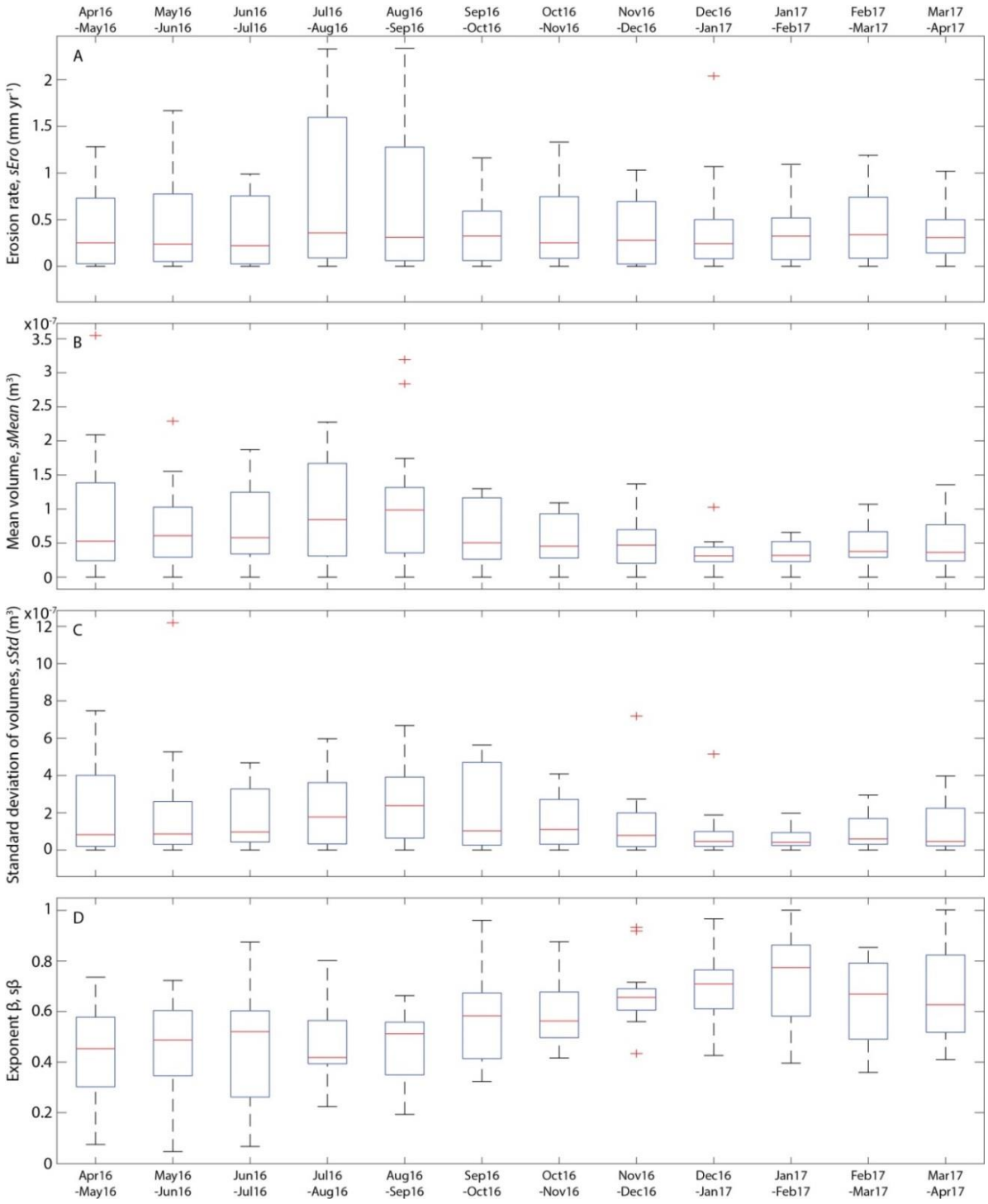


Figure 5.13 Monthly distribution of the erosion variables as mean values per month: A) Erosion rate, sEro (mm yr^{-1}); B) Mean volume, sMean (m^3); C) Standard deviation of volumes, sStd (m^3); D) Exponent β, sβ. Boxplots contain following information: median (red line), 25-75% interquartile range (blue box), 9-91% quantiles (black lines) and outliers defined as events greater than q3+w(q3-q1) or less than q1-w(q3-q1), where w is the maximum whisker length, i.e. ± 2.7 standard deviation, and q1 and q3 are the 25th and 75th percentiles of the sample data, respectively (red plus symbols).

5.2.3.2. 3D shape distribution throughout the year

Detachments in early months of the monitoring period (April to August) dominated the *very platy* and *very bladed* slab-like sectors of the ternary plot (Figure 5.14A). When aggregated by site, nearly all events (175/180) fall into *very bladed* and *bladed* sectors (Figure 5.14B). Additional aggregation by month highlights a subtle but clear pattern which shows that detachments between April and November are generally less compact than those which occurred between November and April (Figure 5.14C).

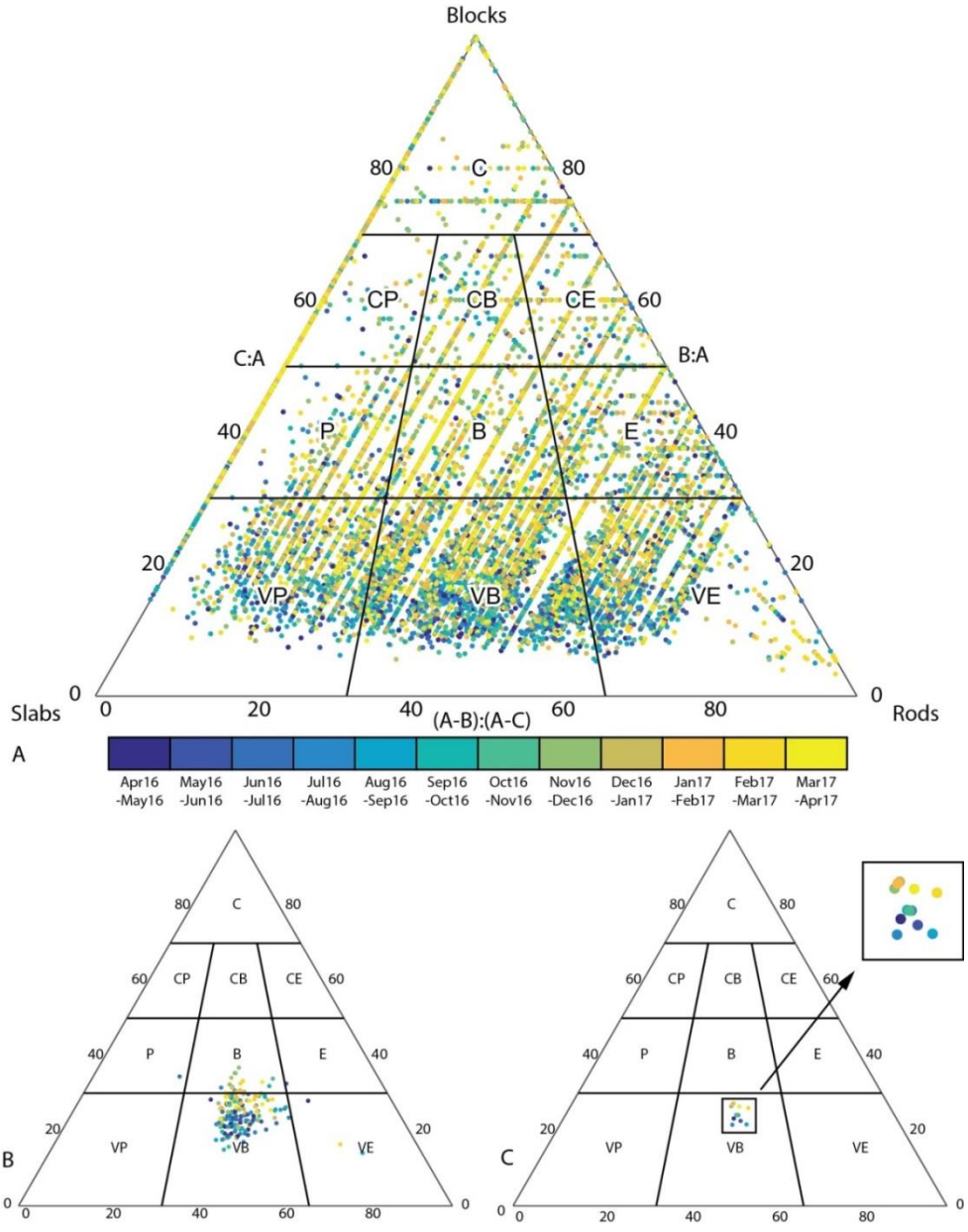


Figure 5.14 Shapes of detached material coloured by month: A) all events; B) mean shape representing each month at each site; C) mean shape representing each month. Block axes: A – long, B – medium, C – short. For sector description see Figure 2.5.

5.2.3.3. Detachment propagation in time

Occurrence of detachments in the same or adjacent areas in successive months varies as a function of space (site) and time (month) (Figure 5.15). While the distribution of erosion at sites 3 and 4 is impossible to discern from a random distance between detachments, *dr* (see Figure 4.21), at other sites detachments occur at the same/nearby locations that in preceding months for at least some portion of the monitoring period. The highest coefficient of reoccurrence, *CoR*, of up to > 0.8 persistent for 9+ pairs of months characterises sites 5 and 13 (Figure 4.21).

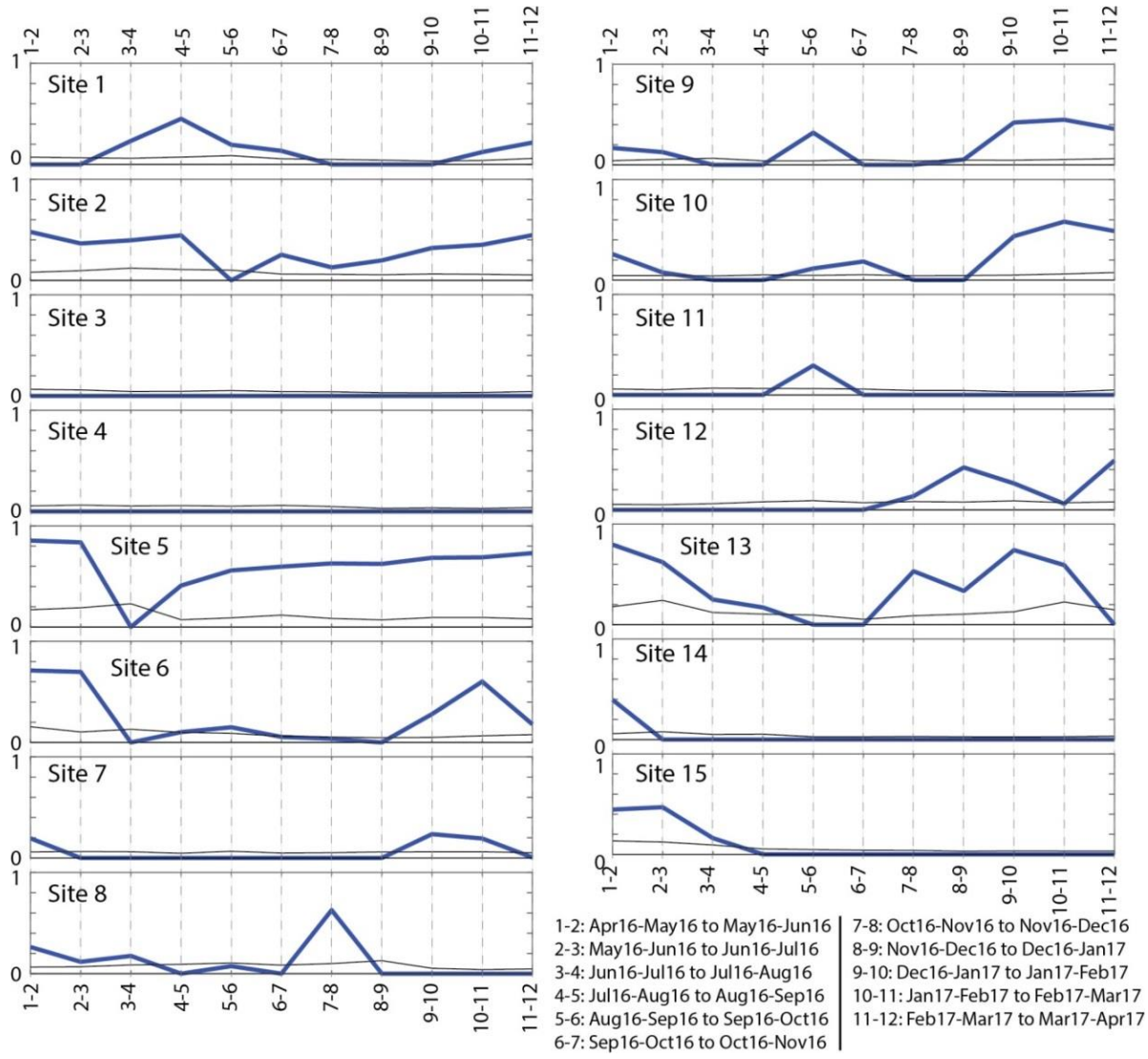


Figure 5.15 Reoccurrence of erosion through time: X – pairs of consecutive months; Y – CoR. Black line is the standard deviation of the random distance (section 4.10.4).

5.2.4. Spatial and temporal distribution of detachments

Figure 5.16 illustrates the spatial and temporal distribution of detachments across Hartle Loup as observed over the one-year monitoring program. Erosion rates are faster at sites closer to the cliff

with the average *sEro* = 0.978 mm yr^{-1} for the three sites closest to the cliff, and *sEro* = 0.309 mm yr^{-1} for the most distil sites. The total volume and the volumes of individual detachments are greater between April and October compared to between October and April. The largest volume, yet lower-frequency detachments tend to concentrate at sites located closer to the cliff toe and occur primarily between April and October. Sandstone erodes slower as compared to shale (0.222 ± 0.122 and 0.682 ± 0.336 mm yr^{-1}, respectively), with rare but occasional large detachments (Figure 5.16).

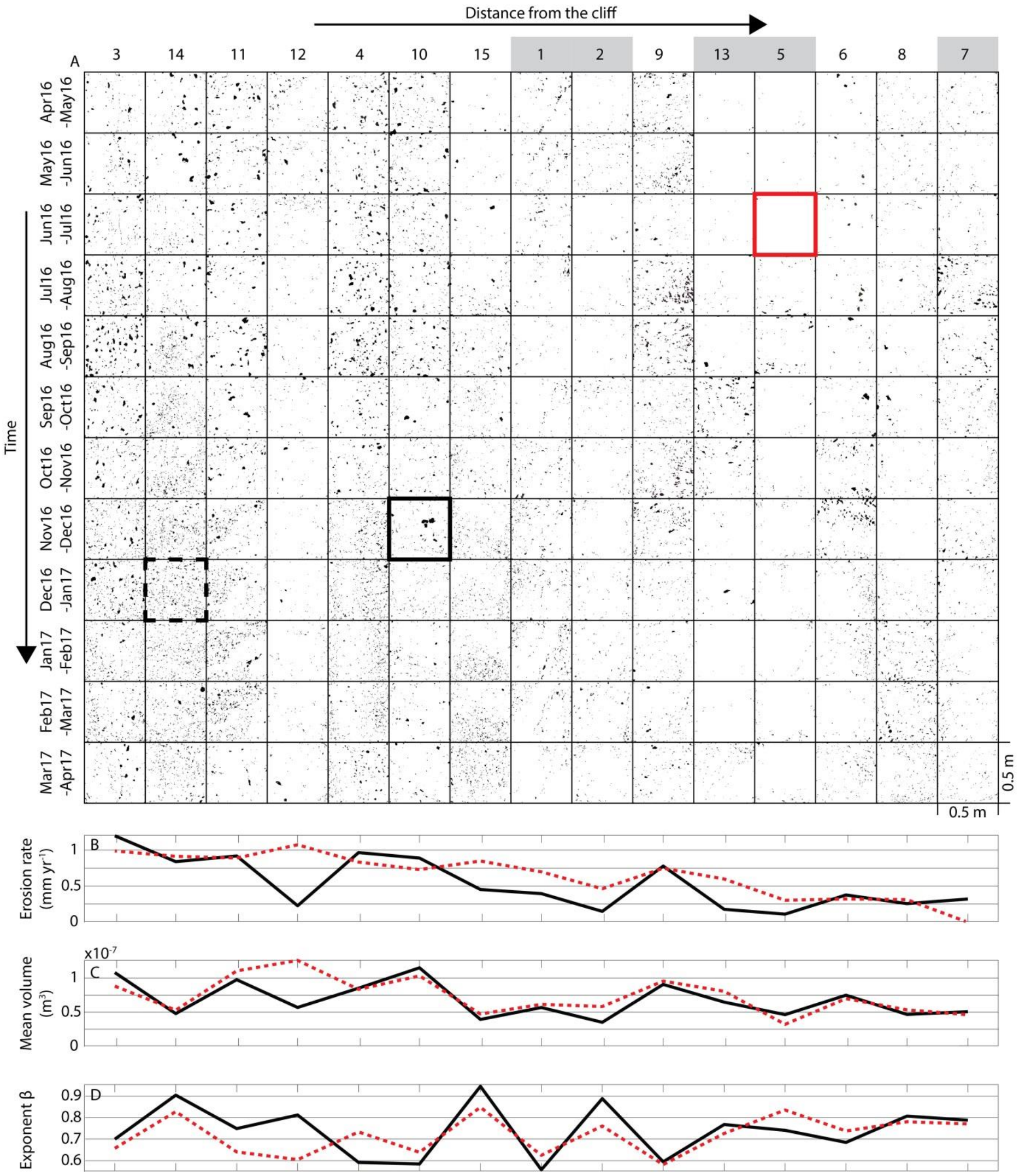


Figure 5.16 A) Monthly distribution of the detachments at the small-scale monitoring sites ordered by the distance from the cliff. Black polygons within each monitoring plot represent detachments. Sandstone sites are indicated by grey boxes, the remaining sites are located on shale sections of the platform. Grid cells with bold outlines represent example cells showing different modes of detachment. The solid black outline demonstrates an example of a large detachment with multiple smaller detachments. The black dashed outline exemplifies a monitoring plot with multiple small detachments. The red outlined plot provides an example of where minimal erosion occurred during the monitoring period. Plots B, C and D illustrate how observed (black line) and model-predicted (red dashed line) erosion rate (B), mean volume (C) and β (D) vary with distance from the cliff.

5.3. Discussion

The overall aim of the research described in this chapter is to identify the dominant mechanisms of erosion, predict the down-wearing rates and the distribution of detached volumes, and understand the controls on foreshore micro-scale erosion. This section follows the structure of the results by approaching the problem from three different perspectives: detachment inventory, and variation in detachments, firstly spatially and then temporarily.

5.3.1. Full inventory analysis

5.3.1.1. Erosion rates

The average erosion rate of 0.528 mm yr^{-1}, based on individual detachment volumes, is lower than the global estimates of mean shore platform erosion rates of 1.486 mm yr^{-1} (Stephenson and Finlayson, 2009) and 1.148 mm yr^{-1} (Dasgupta, 2010). The relatively high global erosion rates may be caused by over-representation of studies focused on quickly-eroding chalk platforms (Andrews and Williams, 2000; Dornbusch et al., 2006; Foote et al., 2006) and the relatively resistant rock of the North Yorkshire coastline studied here. The results are, however, comparable with values of 0.20-2.80 mm yr^{-1} of down-wearing of shale platforms in the Algarve, Portugal (Andrade et al., 2002), and values of 0.94 ± 1.20 mm yr^{-1} of down-wearing of sandstone platforms in Bay of Fundy, Canada (Porter and Trenhaile, 2007). This implies a broader rock control, where erosion rates average out despite different approaches to monitoring in these studies.

The erosion rate observed here is one order of magnitude lower than previously recorded down-wearing of 3.21 mm yr^{-1} for the shore platforms in the Saltburn – Robin Hood's Bay section of the North Yorkshire coast, which includes the area of present research (Robinson, 1977a). The study of Robinson (1977a) encompassed a larger area of interest, and no readings were taken on Hartle Loup. However, the shore platforms examined have broadly equivalent lithology, tidal range and exposure to storm conditions, which suggests that in theory the results should be comparable.

The difference in calculated erosion rates may be in part associated with the method employed to measure erosion. Robinson (1977a) surveyed rock surfaces on nine platforms with a total of 70 MEM stations. At each station, three readings were taken every two months over two years. High variability of change between and within the 0.5×0.5 m sites used in this study (Appendix 6) highlights the subjectivity and potential bias in quantifying erosion rates when sites are represented by three point measurements only. In the present study each site is represented by 500×500 pixels (total 3.75×10^6 pixels) and each pixel is equivalent to one MEM sampling point in the sense that it provides one location of vertical measurement at each monitoring epoch. The present method increases the representativeness of recorded erosion rates for a shore platform at the local scale (within-site) by

including the whole detachment area rather than a point measurement. The challenges of selecting locations for the monitoring site across the shore platform will be further discussed in the following section.

Alternatively, the differences may result from focusing this study on smooth planar platform with near-horizontal bedding, few boulders and little micro-relief. Robinson (1977a) studied sites covered by beach deposits, which may imply more intense abrasion and consequently higher erosion rates.

5.3.1.2. Mechanisms of erosion

A change from a reliance upon point readings to DEM-based monitoring of foreshore down-wearing opens new possibilities in terms of the range of analyses which can be performed. Here, the analyses based on the newly generated detachment inventory, previously absent in the shore platform studies have been adapted from the landslide/rockfall literature (e.g. Dussauge-Peisser et al., 2002; Malamud et al., 2004; Williams et al., 2018). These approaches have the potential to address the gap in understanding mechanisms responsible for erosion and enable the characterisation of larger-scale erosion events which are beyond the scales of those possible to capture with MEMs (Trenhaile, 1987; 2002; Moses, 2014).

The strong relationship between detachment area and volume (Figure 5.3; $R^2 = 0.925$, $p < 0.05$) means that detachments have similar shapes irrespective of volume, which suggests either: 1) a single dominant mechanism of erosion that operates across a range of scales, or 2) a range of erosion mechanisms each resulting in detachment shapes that are themselves pre-defined most probably by rock micro-structure which itself may also scale in a similar manner. The area volume exponent *b* can be indicative of underlying erosion mechanism and is higher (> 1.2-1.3) for relatively deep detachments which in some contexts have been linked to a greater role of shear stresses acting along shear planes or parallel to the surface (Guzetti et al., 2009; Larsen et al., 2010), and lower values where near-surface tensile stresses dominate erosion (Rosser et al., 2007; Williams et al., 2018). On this basis, the results ($b = 1.125$) suggests that tensile failure of the rock micro-structure causes fracture and platelet detachment (Figure 5.17). However, the rock type and water/sediment dynamics at the foreshore (Ogawa et al., 2015; Poate et al., 2018) suggest that the rock micro-structure and the spatially-variant compressive, shear and tensile stresses make the erosion process fundamentally complicated and locally highly heterogeneous. This suggests that a single assessment of rock strength, such as that provided by a Schmidt Hammer or Equotip device (see e.g. Viles et al., 2011), may be insufficient in providing a measurement of rock strength that is appropriate in understanding a range of detachment processes which appear to operate on the foreshore. As such, using a single measurement of rock strength as a predictor of erosion rate is unlikely to be valid in all settings, and a

more detailed consideration of the detachment process is required (Whipple et al., 2000; Wilson and Lavé, 2014; Lamb et al., 2015).

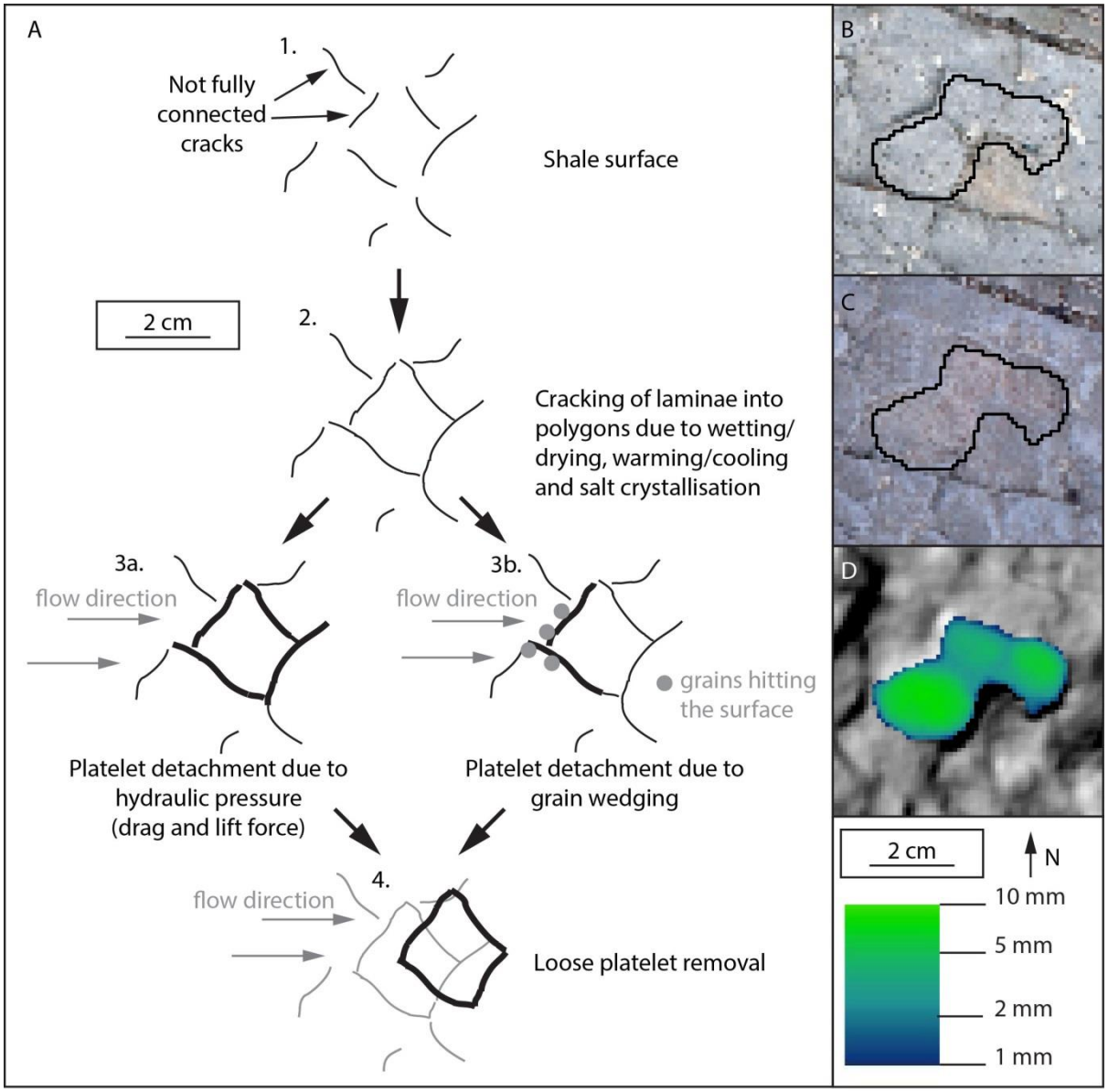


Figure 5.17 Schematic summary of the process of platelet detachment: A) conceptual model of detachment; B-D: an example of detachment occurred in April-May 2016 at site 9: B) detachment outline with Apr'16 orthophotograph as background; C) detachment outline with May'16 orthophotograph as background; D) detachment thickness (common logarithmic scale) with Apr'16 hillshade as background.

The existence of a sub-population of events with relatively small area as compared to the volume (Zone 1 in Figure 5.3) can possibly be explained by detachments at sharp topographic edges, where detachments can be deep, but relatively small in planform. For the rocky coast evolution this may represent a small-scale (mm-scale) equivalent to platform step back-wearing (m-scale) (Moses,

2014), while more generally this process may reflect the preferential erosion of topographic protrusions (Lamb et al., 2015). Alternatively, these events may represent the mean-shape detachments which occur at steep or overhanging foreshore sections, and their real size cannot be resolved with the 2.5 D method applied here (Lague et al., 2013). Existence of the two outliers (Zone 3 in Figure 5.3) can be explained in the same way. Finally, a low number of detachments below the trendline for the largest areas (Zone 2 in Figure 5.3) manifests the likely physical impossibility for detachments with large volumes to have only small areas.

The volume-frequency distribution (Figure 5.4) adheres to the power-law scaling more widely observed in natural and geomorphic phenomena (Malamud et al., 2004). Whilst the scale of investigation is at least five orders of magnitude smaller than that commonly considered, the exponent β falls within that previously documented range for rockfall (β = 0.4-1.1) (Santana et al., 2012), and β = 0.71-2.37 for rockfall for the nearby coastal cliffs formed in the same rock types (Rosser et al., 2007; Barlow et al., 2012; Whadcoat, 2017; Williams et al., 2018). Hungr et al. (1999) identified that high β-values are more common for discontinuous as compared to massive rock masses. Here, the rock micro-structure, dominated by laminations in the shale and sandstone, appears to be exploited by marine action and made more friable or susceptible to 'frittering' due to exposure at the surface (Moon and Healy, 1994). These properties may be critical in generating this high exponent value, indicative of the dominance of smaller detachments in the overall detachment distribution (Malamud et al., 2004).

A rollover, indicated by a reduction in small detachment volume ($< 1.12\times10^{-8}$ m^3) frequency compared to that predicted by the power-law model is evident in the dataset (Figure 5.4), and can be explained by 1) censoring due to the spatial resolution of the monitoring method, 2) by superimposition or coalescence of smaller detachment scars within single monitoring epochs, or 3) as a function of a limit on detachment size imposed by either the erosion processes or rock (micro-) structure (Malamud et al., 2004). Dussauge-Peisser et al. (2002), in a study of rockfall, suggested that the smallest detachment geometry may depend on the condition of rock surface, as affected by the air temperature and the freeze/thaw cycles. Conversely, the characteristics of medium to large events are more dependent on the rock properties, such as the discrete fracture network and the intact rock strength. In this instance, the physical, chemical and biological weathering within the intertidal environment may contribute to promoting the release and erosion of the smallest particles which have volumes comparable to the grain size (Coombes, 2014), while larger-scale rock properties, in particular in this case the laminations, flaking or jointing, likely control the geometry and location of the larger detachments.

The complex shape of the volume-frequency relationship implies that the observed detachments are likely the cumulative result of several superimposed populations that results from discrete processes, as proposed in Figure 5.4. This conclusion was drawn as the sharp inflection in the

slope of the distribution at a detachment size equivalent to a single shale platelet, in combination with the high scaling exponent β for volume > 1.26×10^{-6} m^3, this suggests that platelet detachment is far more frequent, and in sum far more of an effective contributor to erosion of the shore platform, than discrete block (> 0.011 m cube) removal. The subtle peaks at smaller detachment volumes may also have a physical explanation rather than being purely noise in the data, given the high sample numbers in the inventory, and this may reflect different mechanisms dominating at different scales. However, given the dominance of small detachments in the overall distribution, and the concentration of their geometry at dimensions equal to or small multiples of the monitoring resolution, this remains challenging to establish with certainty (Figure 5.4). When upscaling, the understanding of the dominant processes/mechanisms on erosion patterns, and how this is temporally manifest, is more credible than generalised erosion rates, and can feed into coastal evolution models to consider how shore platform change may alter wider hydrodynamic forcing and associated feedbacks on erosion (Kline et al., 2014; Limber et al., 2014; Hurst et al., 2016; Matsumoto et al., 2016).

Most detachments have *very bladed* to *very platy* slab-like shapes (Figure 5.5). Notably, the shapes of events are analysed together irrespective of whether the depth is the shortest axis or otherwise. Therefore, the slabs can represent either deep and narrow, or shallow and wide detachments. The high frequency of slab-like blocks indicates erosion at the edges and/or peeling off thin rock layers. The former is expected to dominate at the locations of high relief manifest with steps and discontinuities, while the latter – on the smooth surfaces. The morphology of fresh exposures on the sandstone platforms (e.g. Figure 3.11H) suggests detachment of layers with relatively large (order of 10^{-4} m) planform area and the thickness controlled by the layer thickness. When testing the rock hardness (section 3.8.2) it was noticed that, irrespective the rock type, the surface was sometimes smoothed and a hollow sound accompanied testing the rock with the Schmidt Hammer or the Equotip. This may suggest presence of an outer layer (crust) separated from the underlying rock mass resulted from the weathering, which is then 'peeled off' (Viles et al., 2011). Events closer to the *block* shape sector of the ternary plot are likely to be related to detachment of the single platelets, as identified by Robinson (1977a) as a major erosion mechanism on the planar parts of the North Yorkshire platforms.

The five sites (33%) that were installed on the sandstone platform account for only 19% of the detachment events and only 14% of the eroded volume, which demonstrates that shale experiences more erosion than sandstone (Figure 5.5). A higher resistance of the sandstone is manifest by the platform-scale topography where sandstone is exposed at the higher sections of the platform and at the headlands. The two rock types vary considerably in terms of *UCS*, but their tensile strength is similar (Table 3.1). It is surprising, because quarrying is known to occur under tension, and tensile strength has been suggested a suitable measure of rock resistance (Whipple et al., 2000). It is possible that on the studied platform, given the diversity of the configurations of rock mass structure such as bedding, jointing, layering, cracking and flaking, the surface topography and the surface orientation relative to

the incoming waves make a single measure of the tensile strength impossible to characterise all situations, and the most important resistive character of the rock changes, depending on the relative combination of forcing factors. For instance, the resistance of both shale and sandstone will be lower on the sloping parts of the platform than on the planar parts because the waves will impact the rock surface at a higher angle relative to the layering which makes cavitation and water hammer more efficient (Moses and Robinson, 2011).

5.3.2. Spatial analysis

5.3.2.1. Comparison with previous studies

Robinson (1977a) recorded erosion rates of 1.33 ± 2.17 mm yr^{-1} on the planar parts of the platform and 5.20 ± 5.87 mm yr^{-1} on the ramps proximal to the cliff toe. When considering his 70 MEM stations separately, the erosion rates vary between -1.50 and 19.31 mm yr^{-1} with the range 19.1 times larger than that observed here. The sites of the slowest erosion observed by Robinson (1977a) are located in pools and under thick beach deposits, whilst negative down-wearing values are related to apparent swelling. Mayaud et al. (2014) pointed out the difficulties associated with intra-tidal rock expansion and contraction for long-term monitoring. Here, the negative erosion was filtered out during the data (raster) processing (section 4.8), while erosion rates, *sEro*, were averaged for the sites rather than taken from point measurements (section 4.10.2), which has two important implications which may explain the differences in results here as compared to Robinson (1977a). Firstly, the range of *sEro* is narrower because very deep and very shallow events are averaged out. If the analysis had been based on the point measurements (the highest DoD pixel value equals 0.10 m), the individual readings could be directly compared. Moreover, herein no monitoring site was located under the beach – considered to be location of the highest erosion rates – due to the scarcity and the ephemeral character of loose sediments on the platform. Secondly, swelling is not taken into account in the current study (Stephenson and Kirk, 2001). However, if swelling had been contributor to the different rates recorded in the two studies, erosion rates calculated by Robinsos (1977a) would be lower than those from this study.

Robinson (1977a) used erosion rates and field observations to identify the dominant mechanisms of erosion across the shore platforms. He suggested that it is contraction and expansion of the rock due to wetting and drying on the planar sections of the platforms, and abrasion on the ramps that dominate. Here, virtually no beach is present which means that there is a limited amount of loose material to abrade the cliff toe when entrained as ‘tools’ when inundated during high tides (Kline et al., 2014). Moreover, the complex geology that includes both rock type and structure, and morphology suggest that it may be too simplistic to divide the platform into two simple sections based on location within the cliff/seaward edge profile and the slope, and to assume operation of the

homogeneous mechanisms within each of these zones. An alternative approach was therefore used in which each site was characterised by a number of independent variables with a range of continuous values, instead of classifying locations into the planar part or the ramp. This method allows the identification of controls on erosion and for these controls to be ordered according to their importance. This information can be used to predict erosion at the locations for which the change detection data are unavailable, allowing erosion to be predicted over wider areas.

5.3.2.2. 3D shapes of detachments

The dominance of detachments located closer to the seaward edge that were slab-like in shape may indicate the failure of laminations at sandstone sites as a primary mechanism of erosion in these locations. Conversely, closer to the cliff, weathering (wetting/drying) likely causes more intense cracking which predefines blocks at platelet scale to release (Figure 5.7). At site 5 (sandstone site at the seaward part of the platform at low elevation: Table 4.1) the eroded pieces are predominantly *very platy*. Small steps with heights in the order of 10^{-3} m reflect presence of the horizontal discontinuities, primarily planes between the thin sandstone layers, which facilitate detachment of the flat, slab-shaped pieces (Appendix 3). Large and shallow detachments are visible in the bottom part of site 5 in Appendix 6. In contrast, at site 6 eroded material is predominantly *bladed*. The slope, roughness and hillshade maps (Appendix 3) show high cm-scale relief while the erosion maps (Appendix 6) suggest detachment of compact pieces. These can be single shale platelets which correspond to the 0.02 m diameter lattices described by Robinson (1977a), which experience desiccation and expansion leading to breakage at discontinuities. The locations characterised by the *elongated* and *very elongated* detachments contain discontinuities. In the case of sites 2, 9 and 11, it is a step at the bed boundary, while at sites 4 and 10 the discontinuities are related to the within-bed structure including jointing and micro-structurally controlled cracking. The detachment of blocks at site 6 may be related to the plucking of protruding platelets and exploitation of discontinuities (see Appendix 6). The rod-shape sector of the ternary plot is populated exclusively by detachments of sandstone at site 1. Although Williams et al. (2018) suggested that the presence of *very elongate* shapes indicates errors at protruding edges in a comparable form of change detection; in this case erosion at the 0.15 m high step is believed to result in the rod-like detected shape. It is therefore not error, but rather the limitation of the DEM-based method which cannot correctly resolve erosion of overhanging rock sections on the foreshore (Lague et al., 2013).

Overall, the characteristic shape of most detachments (*very bladed* and *very platy*) reaffirms the platelets form most detachments, which again supports the mechanisms described above (Figure 5.7).

5.3.2.3. Explaining the distribution and character of the foreshore detachments

The results of the data analysis suggest that, while local erosion is in part a function of position on shore platform, which defines the level of exposure to assailing hydraulic action and wetting, the nature of erosion itself, as represented by the size distribution of detachments, depends on the local micro-relief. Topographic edges and exposed free-to-release platelets provide the surface and micro-structural conditions necessary for enabling detachments to be released.

The observed erosion rate has been shown to be a function of the distances from the foreshore seaward limit and tidal duration. It seems probable that the positive relationship with the distance from the seaward edge reflects the more favourable hydraulic conditions at the cliff toe (usually characterised also by higher values of elevation, slope and roughness), which drive higher rates of erosion in this location, as observed elsewhere (Robinson, 1977a; Stephenson and Kirk, 1998; Foote et al., 2006; Moses and Robinson, 2011). This agrees with modelled wave energy dissipation and erosive force at the foreshore (Flemming, 1965; Sunamura, 1992; Kline et al., 2014; Matsumoto et al., 2016). The observed positive correlation between erosion rates and tidal duration suggests that more erosion happens due to hydraulic force or wedging at locations over which the tide cycles are more frequent (Figure 5.17).

The relationship between site roughness and erosion, including the mean volume and the exponent β (Table 5.4; Figure 5.11), suggests that micro-topography has a profound influence on the size of eroded detachments, with a more diverse range of detachment sizes observed at sites with more irregular surfaces. The micro-topography of the platform is also intimately linked to the rock micro-structure, where shale platelets create higher micro-relief than sandstone, which has near-horizontal micro-layers without protruding rock fragments exposed to release.

The regression analysis allows a reasonable estimation of the local erosion rate across the shore platform based on locational, topographic and tidal controls (Table 5.4). The model preforms well when validated using the test set (Figure 5.12). Site 12 is the only location which shows a significant (at 95% confidence interval) discrepancy between the predicted and observed erosion values. The site is located directly behind a large boulder ($1.5 \times 1.2 \times 0.8$ m^3), which may influence the local hydrodynamics. The boulder may afford this section some protection from assailing waves, which implies that more rough platforms, or platforms with more frequent boulder cover, may experience significant local variability in down-wearing rates (Moses, 2014; Wilson and Lavé, 2014). Therefore, the site is treated as an outlier relative to the other sites.

5.3.3. Temporal analysis

5.3.3.1. Temporal variability in erosion rates and size and shape distributions

There is an apparent increase in erosion during summer months, which concurs with the observations of Robinson (1977a), Mottershead (1989) and Stephenson and Kirk (1998; 2001). Detached rock fragments are more diverse size-wise and tend to be generally larger in the summer months. This observation can perhaps be ascribed to the role of expansion and contraction on platelet detachment which is intensified in summer months when maximum temperatures increase the probability of thermal fatigue, thermal shock and thermal expansion of salt, which each can cause rock breakdown (Coombes, 2014). Intensification of erosion in the summer months is particularly pronounced at locations with high local gradient and may also reflect differences in turbulence when submerged and in flow due to platform drainage as the tide recedes (Robinson, 1977a).

In terms of detachment shapes, the first six months of the monitoring period are characterised by slightly more slab-like (flatter) detachments, and the subsequent months by more blocky detachments (Figure 5.14). Assuming that the rock micro-structure controls detachment morphology, the depth of erosion is likely to depend on the rock layer thickness. Because in the summer months detachments are larger, which is expressed by higher values of $s\beta$, and flatter, the material is likely to be wider in planform rather than deeper. This suggests that the higher efficiency of expansion and contraction between April and October results in detachment of material with larger planform size and the vertical reach restricted by the rock layering.

The spatial and temporal distribution of erosion across the platform and through the year of monitoring provides new insight into the magnitude-frequency distribution of shore platform erosion at the sub-metre scale (Figure 5.16). The differences in the magnitude of erosion and the area and volume of individual detachments across the two rock types suggests that: larger detachments are more likely in shale; the erosion rates vary more as a function of position on the platform than as a function of time of year; and, that whilst individual sites for individual months show variability, there is a general gradient in erosion rate, detachment frequency, and detachment size across the platform which can be modelled and predicted statistically. Hurst et al. (2017) highlighted the differences between parallel erosion and dynamic equilibrium models of foreshore erosion (section 2.2.3) when modelling the long-term rocky coast evolution. Here, it has been shown that different mechanisms have different spatial patterns, and so erosion rate may not necessarily be universal but may reflect the process.

5.3.3.2. Detachment propagation in time

The sites at which erosion appears random through time (3, 4, 11 and 14) are characterised by generally higher erosion rates and are usually located close to the cliff (Figure 5.15). There are two possible explanations for the lack of failure propagation, whereby one failure follows a previous failure. Firstly, a high number of events make *dr* relatively short and the propagation cannot be easily identified within the monthly monitoring interval. The other possibility is that the eroding force is so much higher than the rock resistance at those sites that one detachment does not make a neighbouring area any more susceptible. The highest coefficient of reoccurrence, *CoR*, characterises site 5 at which only once (June-July to July-August) the distance between detachments could not be distinguished from the random distance. At this site erosion was generally low and concentrated at the edges of sandstone layers (Appendix 6). In the warmest months (July to September) there was more erosion, which was likely caused by the temperature-dependent efficiency of rock breakage due to expansion and contraction. Increased erosion in July-August made the preceding monitoring interval have a lower *CoR*, but detachments from this time period subsequently propagated as shown by a later higher value of *CoR*. Site 13 experienced high degree of propagation throughout the year with the exception of three intervals with increased number of events (Appendix 6).

5.4. Summary

The down-wearing rate of the Hartle Loup shore platform was 0.528 mm yr^{-1} in 2016-2017, but varied between 0.101 and 1.192 mm yr^{-1} between the 15 monitoring sites, and between 0.576 and 0.497 mm yr^{-1} between the periods of April to October and October to April. The volume-frequency and 3D-shape distributions of the detachments suggest that erosion happens predominantly via platelet detachment. The size distribution shows that the single shale-platelet size is a threshold size above which the detachments are extremely rare (β = 2.534). Erosion rates are higher farther from the seaward edge and at locations of higher tidal duration. Surface micro-topography controls the size distribution of detachments. Faster erosion and larger and more diverse size-wise detachments occur in the summer months.

The chapter showed the dominant mechanisms of erosion at the small-scale. However, as only 15 0.5×0.5 m sites are studied, the method may be limited in terms of extrapolation and upscaling. Therefore, in the following two chapters the macro-scale foreshore erosion (10^{-1} – 10^{0} m) is considered to quantify erosion rates, analyse the size and shape distributions of detachments and constrain controls on the spatial distribution of erosion at the larger-scale.

6. Developing a new method to monitor bedrock macro-scale shore platform erosion

6.1. Introduction

The aim of this chapter is to describe the procedure to detect the macro-scale (10^{-1} – 10^{0} m) erosion on a continuous shore platform along the 22 km North Yorkshire coast using the airborne LiDAR datasets. The study systematically characterises the area described in section 3.7. Parts of the method mimic the small-scale study (Chapter 4). The methods presented here are used in Chapter 7.

DEMs at 0.25 m resolution were created from four airborne LiDAR point clouds (average 45.22 points m^{-2}). Change detection on a no-change surface of the harbour wall allowed a Level of Detection (*LoD*) to be established. Areas detected as erosion were converted into a polygon shapefile and formed a detachment inventory. In order to separate key types of erosion, boulders and platform steps were extracted by identifying protruding sections of the foreshore and applying a set of size and shape filters.

In order to identify the mechanisms of erosion, analyses based on detachment inventory was conducted including volume frequency and 3D shape distributions. Dividing the foreshore into 1 m^2 grid cells allowed the characterisation of the spatial distribution of erosion, which can then be used to feed coastal evolution models.

6.2. Surveys and data management

The 27 km stretch of the North Yorkshire coastline between Skinningrove and Whitby (Figure 3.3) was selected for the macro-scale monitoring because of the morphological and geological diversity, reflected by a wide range of foreshore geometry, coastal configuration (angles relative to incoming waves and the headland/bay sequence), rock types and joint density. This extensive area provided a wealth of data that enabled a systematic statistical analysis of the nature of foreshore erosion.

Four rotary wing airborne LiDAR surveys took place between August 2014 and March 2017 (Table 6.1), using a 3D Laser Mapping Ltd Robin Wings system (Benjamin et al., in review). The point clouds were organised into 49 tiles each containing ~500 m coastline from the platform edge at low tide to around 50 m inland of the cliff top. The geomorphological mapping (section 3.7) showed that only a portion of coastline included the shore platforms. The 38 tiles of interest (tiles 3-40) which contained the shore platforms were used in the analysis. Each point in these tiles was characterised by *xyz* coordinates in the British National Grid datum, the colour (RGB) and reflectivity.

Table 6.1 The information on the LiDAR surveys conducted along the North Yorkshire coastline.

Survey	Date	Time from previous survey (days/years)	Average point density across the shore platform (points m^{-2})
LiDAR2014	2014/08/15	0/0	41.78
LiDAR2015	2015/06/04	293/0.80	51.00
LiDAR2016	2016/04/08	309/0.85	52.69
LiDAR2017	2017/03/29	355/0.97	35.39

6.3. Calibration of the method to detect detachments

In order to quantify erosion, a similar approach to the one presented in Chapter 4 for the small-scale erosion monitoring was used. This section contains the details about processing the point clouds, creating DEMs and DODs, and detecting detachments. The method was calibrated for Tile 19 (the Hartle Loup area) and then applied to the remaining 37 tiles.

6.3.1. Creation of DEMs

In order to tightly co-register the four point clouds representing the four surveying campaigns a *Multi-Station Adjustment* (MSA) was performed in RiSCAN PRO with the LiDAR2016 point cloud fixed as a base as it has the highest point density across the shore platform (Table 6.1) and because it was also used previously to georeference the smaller-scale monitoring data (section 4.5). Appendix 8 contains the information about the MSA settings and the point cloud modification: rotation and translation, and adjustment performance. The point clouds were exported to ASCII files.

The DEMs were created in ENVI Classic from the four full point clouds representing the four surveys. The spatial resolution of 0.25 m was selected to guarantee that each pixel value would be averaged from 3-4 points based on the average point density of the point clouds across the shore platforms (Table 6.1). Appendix 8 contains the information about the ENVI Classic settings applied for the individual tiles.

6.3.2. Establishing the Level of Detection (*LoD*)

A harbour wall present in Tile 19 includes a flat concrete path which was used to establish a threshold between noise and real change (*LoD*). The DoDs were built by subtracting three consecutive pairs of DEMs (older $\rightarrow$ newer). A polygon was drawn around a flat and smooth section of the harbour wall and the DoDs were clipped with it. The ArcMap *Sample* tool was used to obtain single pixel values and their distribution was analysed (Figure 6.1; Table 6.2). The average of all surveys non-equal to zero suggests that the point clouds were not adjusted perfectly. The thresholds for each

dataset at the confidence level of 95% were calculated showing the value farthest from 0 at -4.91×10^{-2} m. Therefore, the *LoD* was established at 0.05 m.

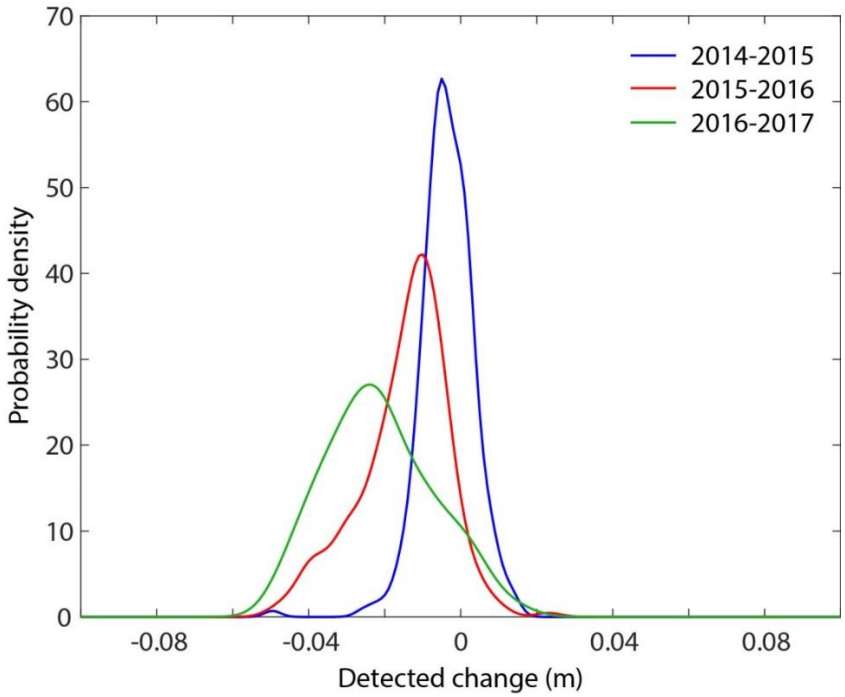


Figure 6.1 Kernel density estimate (normal kernel, half width h = 0.002 m) of the change detected on the flat surface of the harbour wall.

Table 6.2 The summary statistics of the DoD value distribution on the flat surface of the harbour wall. The 95% confidence threshold farthest from 0 is in bold.

	Mean	Standard deviation	Mean – 1.96 standard deviation	Mean + 1.96 standard deviation
2014-2015	-0.0036	0.0069	-0.0172	0.0100
2015-2016	-0.0149	0.0115	-0.0374	0.0077
2016-2017	-0.0214	0.0142	**-0.0491**	0.0064

6.3.3. Creation of DoDs and selection of the area of interest

The DEMs were clipped to the shore platform extent (section 3.7.1) and the pixels with elevation > 3.2 m (highest astronomical tide, HAT) were filtered out using the ArcMap *SetNull* tool. The point density maps and the RGB maps of the foreshore were created in CloudCompare at 0.25 m resolution. The former were converted into the binary masks to remove unreliable pixels, herein assumed to be those which have either 0 or 1 point. DoDs were created by subtracting the consecutive pairs of the DEMs of the platforms below HAT (older → newer). These were subsequently multiplied by the pairs of adequate point density masks.

Visual inspection of the change above *LoD* suggests that different processes contribute to what is detected as 'erosion': surface down-wearing, step back-wearing, boulder movement, removal, redistribution or comminution of debris at the cliff toe, pocket beach dynamics and changes in vegetation cover (Figure 6.2).

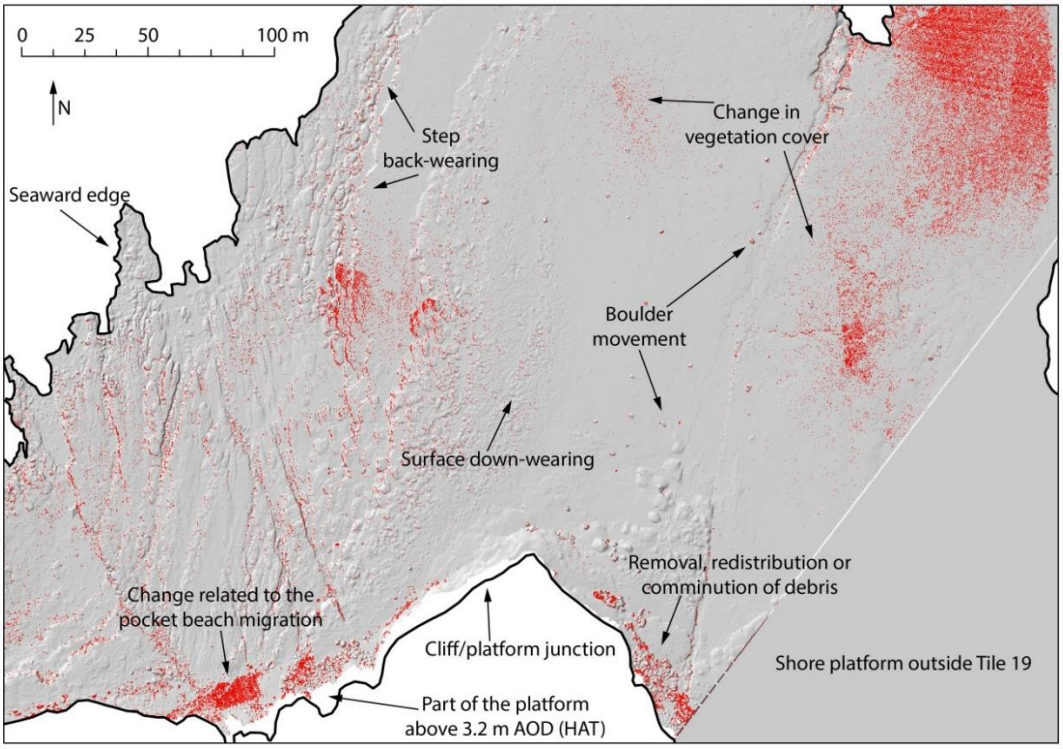


Figure 6.2 Proposed processes contributing to the detected detachments (red areas) in 2014-2015. Background: LiDAR2014 hillshade at 30% transparency.

6.3.4. De-trending the DoDs

Some DoDs included a visible trend surface. For instance, the 2015-2016 DoD has higher values at the seaward part of the platform, lower values at the landward part and a dome in its central part (Figure 6.3A). Change detection performed on 1) DEMs created on raw point clouds (with no MSA); 2) the clouds for which MSA was limited to translation with no rotation; and 3) the shore platforms only, showed that the trend surfaces are not related to the processing method. The offset is likely to be related to the way the point clouds were originally created by merging multiple single flight lines into one point cloud. As the lines could not be separated and re-matched, the DoDs were de-trended.

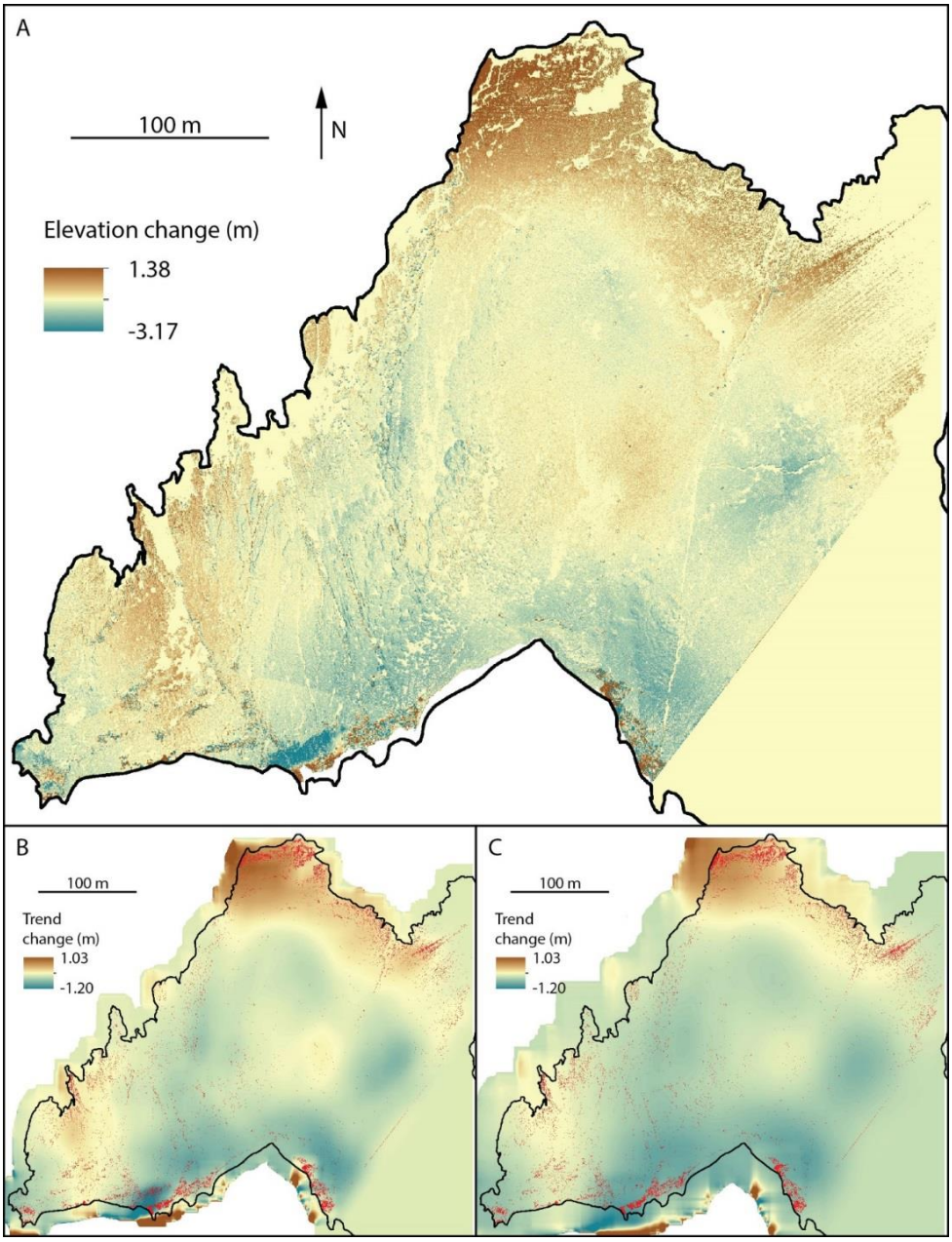


Figure 6.3 A) The 2015-2016 DoD suggests that there is a systematic surface pattern; B) trend surface as the mean of 101×101 cells; B) trend surface as the mean of 201×201 cells. Red areas in B and C represent change ≥ LoD after DoD de-trending using the adequate trend surfaces.

The ArcMap *Focal Statistics* tool was used to find the general DoD surface trend, equivalent to the low pass filter that approximates the long length-scale structures in the data. The mean pixel value was derived for two kernels: of 101 and 201 cells which represented the area of 25×25 and 50×50 m^2, respectively. Visual comparison of the two trend maps suggests that the former includes detail which is deemed to represent topography, while the latter guarantees representation of the large-

scale pattern only (Figure 6.3 B and C). In order not to remove these from the analysis, the trend surfaces at 201×201 cells were subtracted from the DoDs.

6.3.5. Separation of the rock detachments from vegetation

It is likely that a considerable part of detected change is related to vegetation change. An attempt was made to separate it from the change in rock by using the supervised image classification on the RGB maps from the LiDAR2016 dataset with three classes: ‘rock’, ‘vegetation’ and ‘NoData’. The training samples containing various types of vegetation and rock surfaces were used in the ArcMap *Maximum Likelihood Classification* toolset.

Analysis of the orthophotographs suggests that vegetation is localised. The area around the low-tide level, which remains under water for most of the time (Figure 3.10D), is densely colonised by the seaweed. Algae concentrate around the high-tide level at the cliff toe. The vegetation densely covers sections of the planar part of the shore platform and the areas at the foot of the steps whose morphology makes the surface remain wet for a prolonged time after the tidal decrease. The LiDAR point clouds contain no data over pools, which are local topographic indentations filled with water. The areas not classified as ‘vegetation’ were termed ‘rock’. These include: 1) the bare bedrock; 2) the bedrock densely covered by barnacles on the seaward part of the platform, which is expressed in the RGB map by the yellowish colour (Figure 6.4A); and 3) the sediments: beach material, debris and boulders.

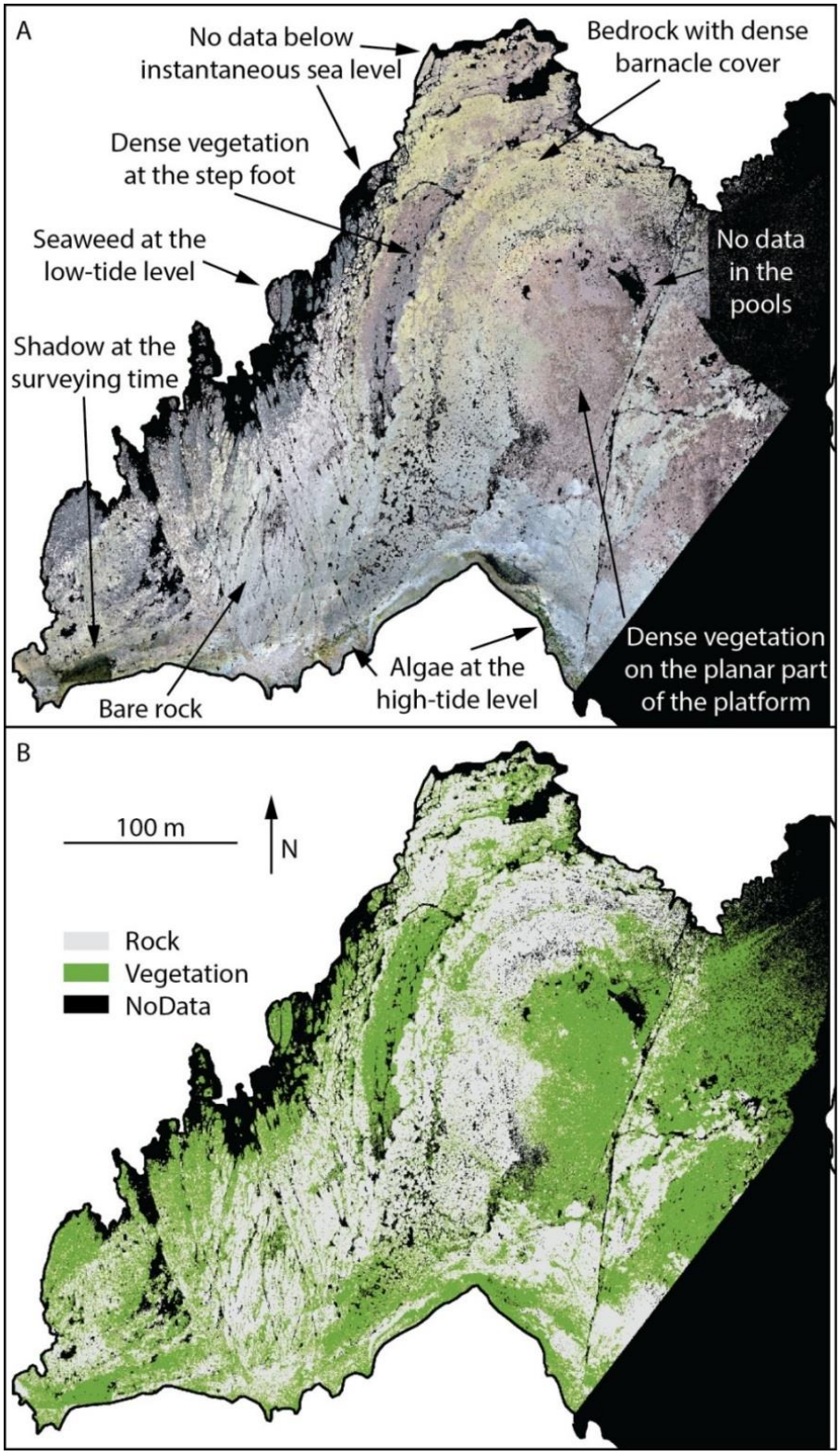


Figure 6.4 Surface cover on Hartle Loup: A) visual inspection of the LiDAR2016 RGB map allows the identification of different types of vegetation, barnacle cover and the bare rock; B) classification of the platform surface.

Visual inspection of the classification results shows that, in general, it was successful. The main areas of error, where the rock detachments may be classified as vegetation dynamics are the sections of platform with thin algae cover at the high-tide level and the zones shadowed by the cliff at the time of the survey (Figure 6.4B).

The signature file – a statistical description of the classes – created from the 2016 training samples was applied on the LiDAR2014 and LiDAR2015 datasets. The 'vegetation' and 'rock' masks were applied separately on the DoDs (Figure 6.5). Because the method does not perfectly separate the rock from vegetation, the change was analysed for both populations and labelled accordingly.

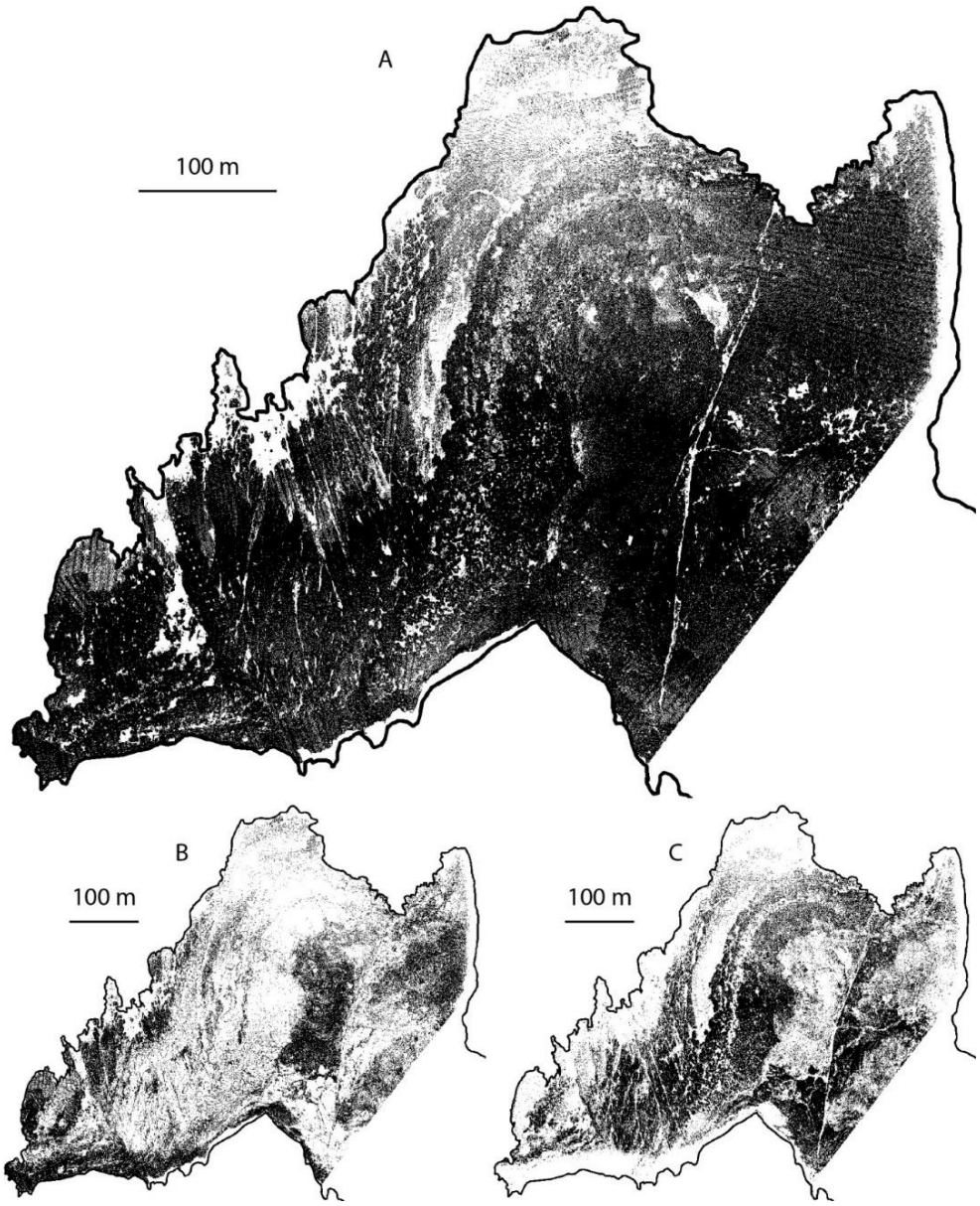


Figure 6.5 Pixels available for change detection 2014-2015: A) data extent after applying the density mask; B) extent of the 'vegetation' class; C) extent of the 'rock' class.

6.3.6. Identification of boulders and steps

As wave energy tends to concentrate on the sloping and protruding surfaces (Moses and Robinson, 2011), erosion rates and underlying mechanisms may be different for planar and inclined sections of the shore platforms. Boulders absorb, reflect or dissipate wave energy, protecting the platform surface from wave erosion (Moses, 2014; Wilson and Lavé, 2014). The approach of this study means that boulder redistribution will be detected as detachments. This section aims to identify protrusions and divide them into steps and boulders using a set of size and shape filters in order to 1) remove boulder dynamics from the detachment inventory and 2) be able to separate erosion at the planar sections of the platform (in here referred to as 'down-wearing') from erosion at steps.

The protrusions were detected for the 2014-2016 surveys. Local protrusions were identified as pixels whose slope > 10°, elevation range at 9×9 cells > 0.3 m and de-trended surface elevation (elevation – mean elevation at 9×9 cells) > 0 m, with the two former conditions identifying areas of the high relief, and the latter, only the positive, or protruding, sections of these areas. The Minimum Bounding Geometry (MBG) attributes of the protrusions: length, width and the length/width ratio were extracted. Based on the field observation the boulders were described as the protrusion polygons whose length/width ratio is < 2.5, length is between 1 and 4 m and width is ≥ 1 m. The steps were defined by the length/width ratio ≥ 2.5 and length > 2 m (Figure 6.6).

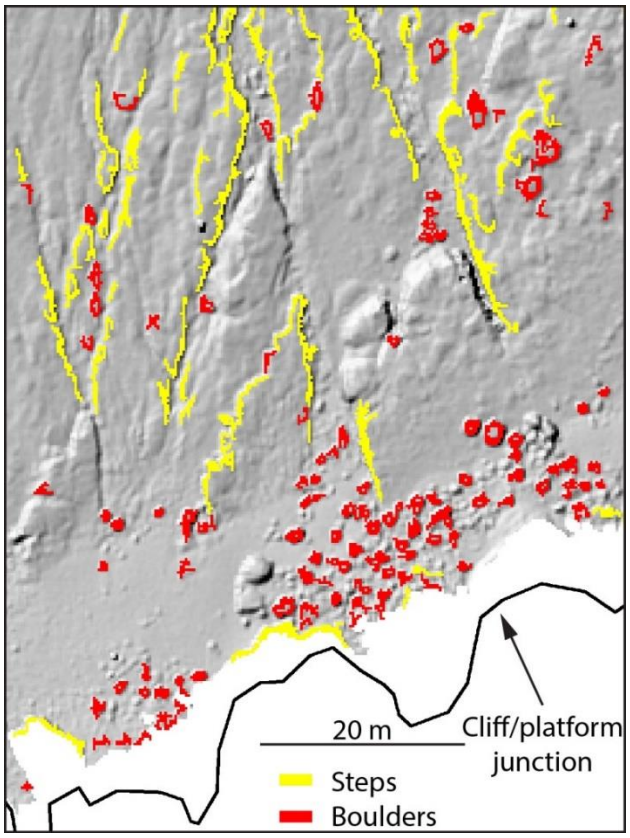


Figure 6.6 An example of protrusions automatically-detected on the basis of topography and object shape for the LiDAR2014 survey. Background: LiDAR2014 hillshade at 30% transparency.

The binary maps of the vertical change ≥ 0.05 m were created for all DoDs, separately for 'rock' and 'vegetation' classes, and converted into a polygon shapefile, where each object represented a single detachment.

The method was applied on all 38 tiles. The DoD de-trending, cover classification and change detection were visually controlled. Figure 6.7 depicts the procedure used to process the LiDAR data.

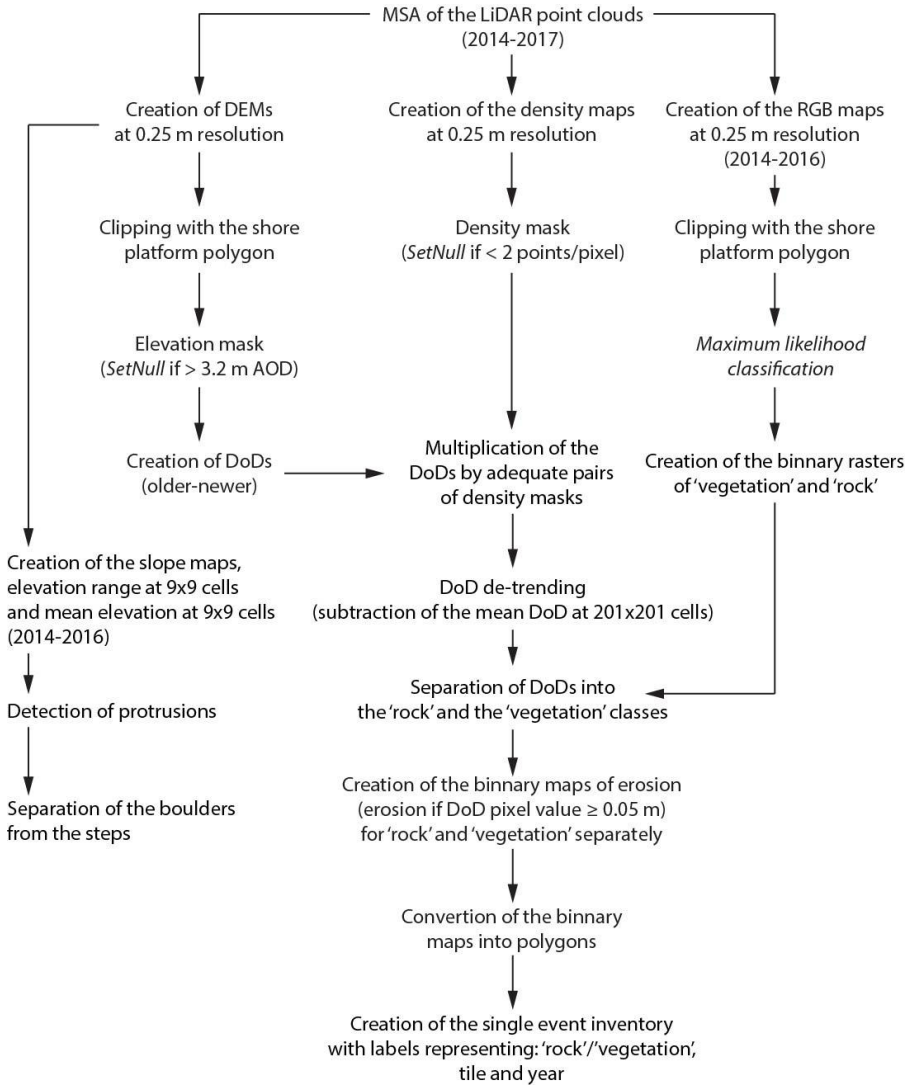


Figure 6.7 Workflow applied to detect change at the macro-scale from the LiDAR dataset.

6.4. Analysis of detachments

The aim of this section is to introduce the method to 1) create a detachment inventory, calculate erosion rates and analyse the size and shape distributions of detachments, in order to identify mechanisms of erosion and to characterise the spatial distribution of detachments, and 2) constrain controls upon erosion to inform foreshore erosion model.

Erosion rate was calculated in two ways. Firstly, based on the detachment inventory it was calculated as the sum of all detachment volumes across the whole platform area (3.15×10^6 m^2; section 3.7.1) per 2.62 yr. Secondly, based on the 1 m^2 grid cell inventory it was averaged from the erosion rates calculated for each grid cell as the detached volume divided by the number of data pixels (n = 1:16; n < 16 if part of a cell is wet and so the LiDAR pulse is not reflected) multiplied by the pixel size (6.25×10^{-2} m^2), and divided by the time between surveys (yr). This value was calculated for all the cells and separately for cells containing a boulder, a step and neither of these. The average platform erosion rate was calculated as weighted erosion from the stepped and the non-stepped cell groups (see Appendix 2). Due to the differences in the surface area by which eroded volume is divided, the calculated erosion rates will be different between the two approaches.

6.4.1. Event inventory analysis of detachments

The analysis mimics the analysis of the detachments at the small-scale (section 4.10). Identified detachments were collated into an event inventory where each object was given 13 attributes describing its location, time, size and shape (Table 6.3). The erosion properties were extracted using the ArcMap *Zonal Statistics* tool. The width and length were calculated for the MBG rectangles. The attributes referring to the distances from landforms were calculated using the *Near* tool.

Table 6.3 Object attributes in the macro-scale detachment- and the grid cell-based inventories. Glossary contains the calculation details of the grid cell variables.

Detachment-based	Grid cell-based
Tile ID	Tile ID
Time period	Time period
Class (1: ‘rock’; 0: ’vegetation’)	ID
Centroid X coordinate (m)	Centroid X coordinate (m) -470,000
Centroid Y coordinate (m)	Centroid Y coordinate (m) -510,000
Area (m^2)	Number of data pixels
Volume (m^3)	Presence of a step (0: N; 1: Y)
Maximum thickness (m)	Presence of a boulder (0: N; 1: Y)
Width (m)	Distance from the cliff, *lCli* (m)
Length (m)	Distance from the seaward edge, *lSea* (m)
Distance from the cliff (m)	Elevation, *lEle* (m AOD)
Distance from a step (m)	Elevation range, *lEleR* (m)
Distance from a boulder (m)	Relief, *lRel* (m)
	Slope, *lSlo* (°)
	Roughness, *lRou* (°)
	Curvature, *lCur*
	Tidal duration, *lTid* (%)

Detachment-based	Grid cell-based
	Inundation frequency, *lInu* (%)
	Joint density, *lJDe* (joints m^{-2})
	Total area, *lArea* (m^2)
	Total volume, *lVol* (m^3)
	Mean thickness, *lMean* (m)
	Erosion rate, *lEro* (mm yr^{-1})

The summary statistics of the number and volumetric properties of detachments were extracted. Erosion rate was calculated as the sum of all detachment volumes across the whole platform area per 2.62 yr. Platform area was calculated as 3.15×10^6 m^2 (section 3.7.1). The pixel size used in the calculation is 0.25×0.25 m. Field observations suggest that block removal is always < 6 m^2 in planform and < 2 m in thickness. Therefore, detachments larger than these threshold values were deemed to represent beach dynamics and they were filtered out (Figure 6.8). The 3D shape distribution of these events shows that they have *very bladed* to *very platy* slab-like morphology typical for beach deposits (Figure 6.9).

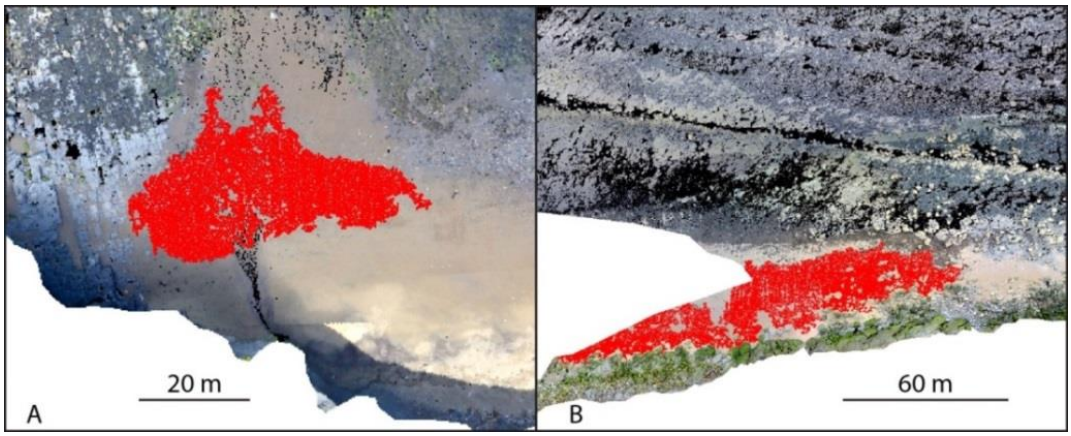


Figure 6.8 Examples of the removal of beach material detected as single detachments: A) Tile 30, 2014-2015, removal of 86.09 m^3 of material; B) Tile 40, 2016-2017, removal of 310.88 m^3 of material. Background: orthophotographs from surveys preceding events.

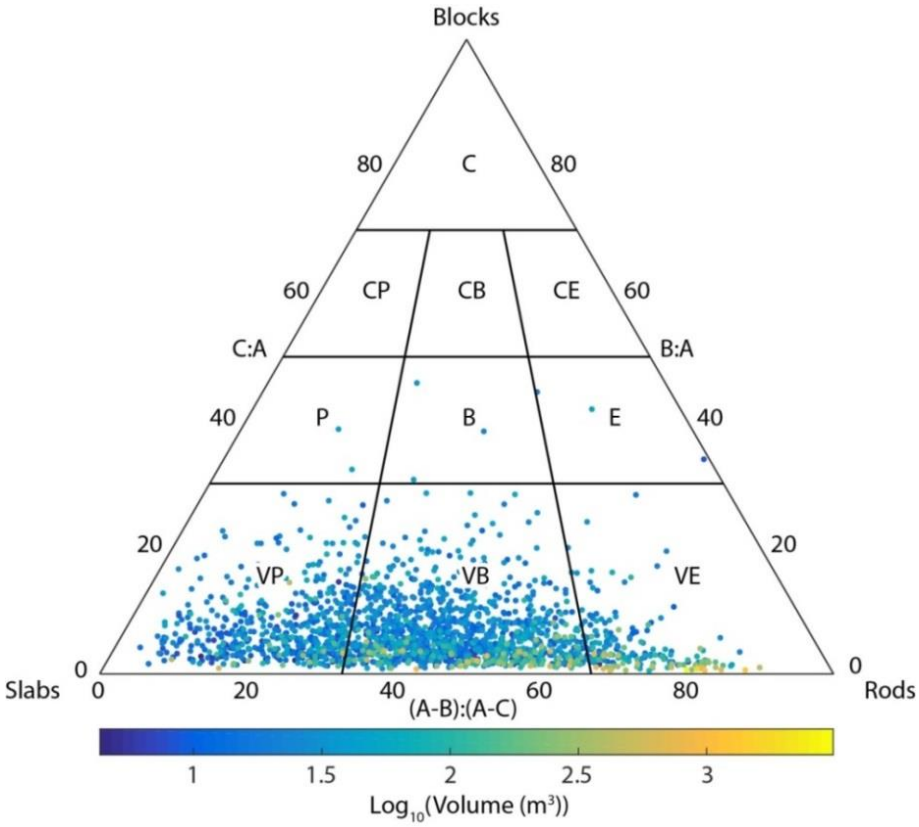


Figure 6.9 Shapes of detached material > 6 m^3 coloured by the volume (common logarithmic scale). Block axes: A – long, B – medium, C – short. For sector description see Figure 2.5.

In order to identify mechanisms of erosion, relationships between detachment area and volume, and the volume-frequency distribution were established (section 2.5.2.1). The 3D shapes of detachments were plotted (Figure 2.5), for which the width and length of Minimum Bounding Geometry (MBG) and the maximum thickness of events were used. The results were presented for the whole inventory and for the 'rock' and the 'vegetation' classes separately. Detachments were divided into three types depending on their location. If the distance from a boulder = 0 m, a detachment is classified as the 'boulder movement'; if the distance from a step = 0 m, a detachment is classified as 'erosion at a step'; and if both distances ≠ 0 m, a detachment is classified as 'down-wearing'.

6.4.2. Grid cell-based analysis of detachments

The shore platform surface within the 38 individual tiles was divided into a 1×1 m grid. The cells which were not fully upon the platform were ignored. The remaining cells were characterised by 23 attributes describing their ID, data content, location, topography, marine conditions, geology and erosion (Table 6.3). Notably, in the inventory the grid cells were extracted separately for the three time periods because of potential changes in topography and boulder movement between the surveys.

The presence of boulders and steps was ascribed to a cell if the distance from a protrusion equalled 0 m. Pocket beaches were mapped from the orthophotographs of the preceding surveys (2014-2016), and the cells which encompassed beach deposits were removed. If a cell contained no data, where the surface was not measured because it was inundated by standing water, it was filtered out (Figure 6.10). Continuous topographic data, including elevation and its derivatives, were taken from the preceding surveys (2014-2016).

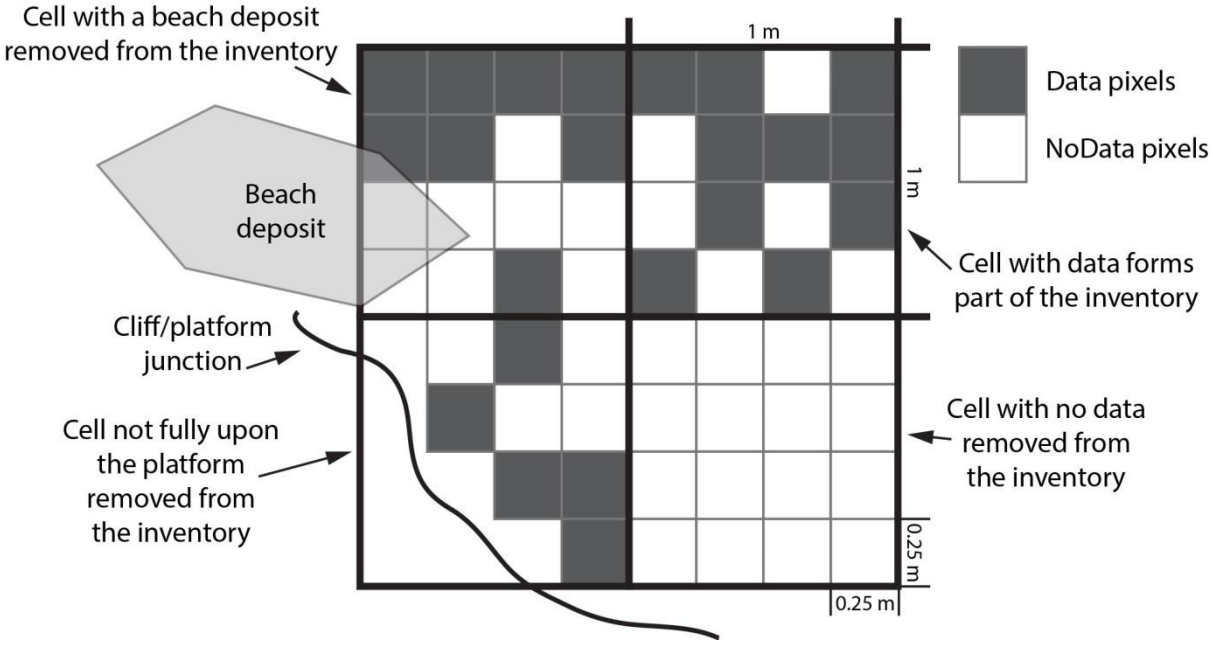


Figure 6.10 Removal and inclusion of the grid cells into the inventory.

Erosion was represented by four variables: 1) total area, *lArea* (m^2) which is the number of detachment pixels (n = 0:16) multiplied by the pixel size (6.25×10^{-2} m^2); 2) total volume, *lVol* (m^3) which is the sum of detachment thickness pixels equivalent to the DoD values (m), multiplied by the pixel size (6.25×10^{-2} m^2); 3) mean thickness, *lMean* (m) which is the average value of the change pixels; and 4) erosion rate, *lEro* (mm yr^{-1}) which is calculated as *lVol* multiplied by 1,000 (m $\rightarrow$ mm) and divided by the number of data pixels (n = 1:16) multiplied by the pixel size (6.25×10^{-2} m^2), and divided by the time (yr) different for the three between-survey periods (Table 6.1). Cells whose *lMean* was greater than 2 m were removed.

The cells were split into three groups – *boulder*, *stepped* and *non-stepped* – which define their location and likely types of erosion which could take place within them. Membership in one of the groups depended on whether a boulder, a step or none of the two was present within them. The aim was 1) to remove the cells where the 'detachment' is related to boulder movement and 2) to separate erosion at steps from the down-wearing. Step back-wearing could be calculated, but because of diverse step heights using the volumetric change seems to be more meaningful, and so the term

'erosion at steps' is used. This approach does not infer a process, as steps erode via combination of block removal, abrasion and localised fracturing (Moses and Robinson, 2011).

In case of cells which contain both a boulder and a step, the cell was classified to the boulder cell inventory to be sure that the developed model of platform erosion does not include boulder dynamics. Erosion rates in the full grid cell inventory, as well as in each of the three groups, were calculated as the mean of erosion rates for each cell. The average platform erosion rate, Ero_{total} (mm yr^{-1}), was calculated as weighted erosion from the stepped and non-stepped cell groups:

$$Ero_{total} = \frac{A_{down}\, Ero_{down} + A_{step}\, Ero_{step}}{A_{down} + A_{step}} \quad \text{Eq 6.1}$$

where A_{down} (%) is the contribution of the non-stepped cells to the total number of cells, A_{step} (%) is the contribution of the stepped cells to the total number of cells and Ero_{down} and Ero_{step} (mm yr^{-1}) represent erosion rates calculated for the respective cell groups.

6.4.3. Modelling the distribution of erosion

The cells were collapsed into across-shore sections at a 1 m interval in order to analyse how the distribution and magnitude of erosion changes with the distance from the cliff, and to assess the spatial pattern in the relative importance of boulder movement, erosion at steps and down-wearing to change of foreshore morphology, which could then be used to account of platform dynamics in coastal evolution models.

In order to verify whether the location and/or magnitude of erosion can be predicted at the cell-by-cell basis two models were developed: a logistic regression model was used to predict whether a detachment is likely to occurs or not in a given cell, while a multiple linear regression model was used to predict erosion rates in the cells more likely to experience erosion. The aim was to understand the distribution and magnitude of erosion across the shore platform and to identify controls upon it.

The models were developed separately for the stepped and the non-stepped cells because of anticipated difference in detachment magnitude and pattern, likely caused by dominance of different mechanisms (Moses, 2014). The inventories were split into training and test sets, the latter consisting of every 100^{th} cell in the inventories. 11 continuous independent variables were used to predict erosion rate, *lEro* (mm yr^{-1}). These included the attributes related to: 1) the location across the platform: distance from the cliff, *lCli* (m), and distance from the seaward edge, *lSea* (m); 2) topography: elevation, *lEle* (m AOD), elevation range, *lEleR* (m), relief, *lRel* (m), slope, *lSlo* (°), roughness, *lRou* (°), and curvature, *lCur*; 3) tidal conditions: tidal duration, *lTid* (%), and inundation frequency, *lInu* (%); and 4) structure: joint density, *lJDe* (joints m^{-2}) (Glossary; Table 6.3).

If the correlation coefficient between independent variables was higher than 0.9 (Tabachnick and Fidell, 2013), a correlated variable, arbitrarily selected based on the physical meaning, was removed. Logistic regression was performed in R to predict the occurrence of erosion in a cell from the independent variables. It was assumed that if the predicted probability > 50% a cell was ascribed 'YES' and a detachment was more likely to have occurred than not. The models were built manually by adding variables one-by-one and assessing performance of the models on the basis of the confusion matrix, which allowed the number of cells correctly or incorrectly classified to be determined (Figure 6.11; James et al., 2013).

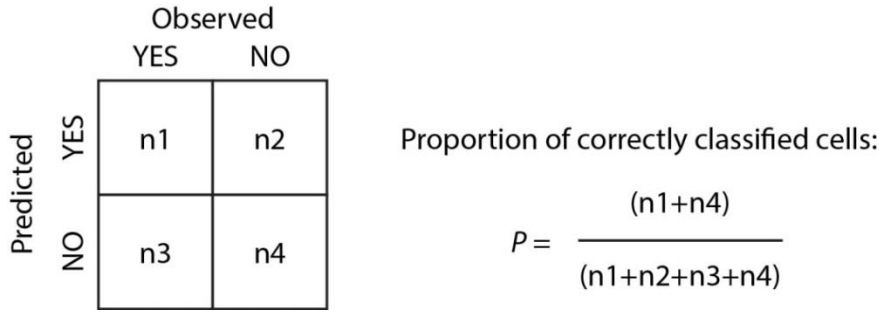


Figure 6.11 Assessment of the logistic model performance based on the predicted and observed number (n) of cells with (YES) and without (NO) detachments.

The magnitude of erosion was predicted only for the cells containing detachments. Mimicking the modelling at the small-scale (section 4.10.3), the best-fit multiple linear model of the erosion rate, *lEro* (mm yr^{-1}), was found manually by adding independent variables one-by-one based on the highest improvement of R^2, with $p < 0.05$, and selecting the model based on the understanding of physical processes and the least input data required to explain erosion (see Parker et al., 2015).

6.4.4. Temporal distribution of detachments

The event inventory was divided into three groups representing the three monitoring periods. The summary statistics of the erosion variables were extracted for each time period in order to assess erosion rate, and size distribution, change through time. Erosion rate was calculated using the time periods from Table 6.1.

The change through time of the spatial distribution and erosion rates in the stepped, the non-stepped and the boulder cells were summarised. The reoccurrence of erosion was assessed by analysing whether cells with the same *xy* coordinates, but different time periods, experienced detachments.

6.5. Method suitability to monitor bedrock macro-erosion

6.5.1. Methodical comparison with other studies to detect foreshore erosion

Bedrock erosion is difficult to observe at the foreshore because it is either small in scale or episodic and localised (Moses, 2014). The localised micro-scale down-wearing rates over 4.50×10^{-3} m^2 surfaces have been monitored with MEMs (e.g. Robinson, 1977a; Stephenson and Kirk, 1998; 2001). Attempts have been made to use a laser scanner (Swantesson et al., 2006) and a traversing erosion beam (Charman et al., 2007), but this has not improved the spatial representativeness of measured erosion rates. Two studies quantified platform erosion at the larger scale. Dornbusch et al. (2006) used historical maps to localise planform position of the high water line along ~20 km of the Sussex chalk coast and calculated platform down-wearing rates averaged for 50 m along-shore sections by dividing the distance between two high water line positions by *tan(α)* under assumption of the uniform platform slope $\alpha = 1.5°$. Calculated down-wearing rate of ~7 mm yr^{-1} was inconsistent with MEM results. Dornbusch et al. (2006) concluded that, because of the high locational error of the high-water line on maps, their method overestimates erosion rates and the MEM results are more reliable. Dornbusch and Robinson (2011) used air photographs to localise horizontal position of ~870 km of steps, measured step height in the field and quantified step back-wearing of 0.6-4.9 mm yr^{-1} as an equivalent down-wearing rate being the removed bedrock volume divided by the platform area landward of the steps.

This chapter describes the procedure to systematically quantify shore platform erosion on the basis of remote sensing data used to generate DEMs of the shore platforms surface along a 22 km stretch of coastline at 0.25 m resolution and detect vertical change ≥ 0.05 m on the ~annual basis (0.80-0.97 yr) over 2.62 yr. The method overcomes limitations of MEMs related to the monitoring site location, the need for benchmarks and a well-trained operator (Moses, 2014; Turowski and Cook, 2017), and a reliance upon historical map accuracy and precision and coarse-scale field measurements of step height and platform slope of the larger-scale studies (Dornbusch and Robinson, 2011). The topographic data are continuous over the area of interest, while elevation is averaged from precise *xyz* coordinates of the points from the clouds.

This approach allows new types of analyses not previously performed in shore platform studies. These are 1) analyses based on the detachment inventory, such as the area volume, magnitude frequency and 3D shape distribution analyses which allow the identification of dominant mechanisms of erosion; and 2) the analyses based on the grid cells, which allow the identification of controls on the spatial distribution of erosion rates in a systematic way. Moreover, erosion is considered across the whole platform and the problem of selecting locations and the number of monitoring sites which would best represent shore platform is irrelevant (Viles and Trudgill, 1984).

The presented method does not consider erosion at steps in terms of the horizontal migration, i.e. step back-wearing, which is the conventional approach (Dornbusch and Robinson, 2011; Knight and Burningham, 2011; Stephenson and Naylor, 2011). Instead it considers erosion vertically and volumetrically (Williams, 2013). Step back-wearing rate could be derived by dividing the volume loss in a cell by step length (~1 m) and step height (~elevation range), but the volume-based approach used instead allows a wide range of analyses to be performed, while step back-wearing rate is not that meaningful as it does not account for diverse step height. Moreover, the volumetric understanding of detachments allows comparison with the rates calculated at the small-scale (Chapter 5), in the macro-scale detachment inventory and in the non-stepped grid cells (this chapter).

6.5.2. Topography reconstruction and change detection

The high resolution of the LiDAR point clouds (35-53 points m^{-2}) allowed creation of DEMs at 0.25 m based on the assumption that the 3D location of 3-4 points can give a representative pixel value. To ensure the highest output quality, the point clouds were adjusted despite being pre-georeferenced on delivery from the supplier. The change detection on the flat section of the harbour wall showed that the average distance of the no-change surface is not equal to 0 (Figure 6.1). This and the presence of an artificial trend surface (Figure 6.3) represent incorrect alignment of the 3D data resulting from different flying paths by the data supplier, which is difficult to remove. As a consequence, the trend surface had to be subtracted before change detection. As this trend surface is averaged from a 201-cell square, equivalent to 50×50 m platform surface, it is unlikely that the DoD de-trending impacts detection of detachments. Filtering out pixels with 0-1 points aims to use only real topography for change detection and not rely on interpolation, which is particularly important at rough and stepped sections of the platform.

Image classification to separate the rock from vegetation aims to filter out detachments likely to represent biological activity. However, the division of the range of RGB values into two classes implies loss of information and imparts a potential over-simplification. It does not allow one to separate bedrock from sediment and rock densely covered by barnacles. It is also unable to take into account variable vegetation thickness – at the seaward part of the platform seaweed growth can be of > 0.05 m thickness but the algae growth and decay at the high tide are of < 0.01 m thickness, so any detected change is likely to represent bedrock erosion. Therefore, the classification should be treated with caution and the magnitude frequency and 3D shape of detachments of the two classes should be compared to see whether a significant difference exists in their morphology which would indicate successful classification. In the future, better methods of surface classification should be developed for shore platforms, such as using the spectral signature of the bedrock and colonizing species (Koetz et al., 2008).

Coarse sediments, namely boulders, are separated from the bedrock erosion by detecting protrusions of specific sizes and shapes (section 6.3.6). These can be then filtered out from the detachment inventory because their movement will tend to overestimate the calculated erosion rates. Detection of steps and the calculation of the distance between them and detachments allow separation of erosion at steps from surface down-wearing on the planar platform sections. To further ensure filtering out events which are not related to bedrock erosion, beach migration is filtered out by removing events with area > 6 m^2 or thickness > 2 m.

Performance of the method was controlled throughout. Firstly, standard deviation of the MSA was recorded to make sure that the final error was below 0.05 m which makes 20% of the pixel size (Appendix 8). The success of detecting protrusions and splitting them into boulders and steps was assessed visually from the DEMs and the slope maps. While modelling the distribution of erosion, 1% of cells were excluded from model development phase to serve as independent test set. Near-even spatial and temporal distribution of the check cells was guaranteed by extracting every 100^{th} event as the test dataset.

6.6. Summary

This chapter describes procedures used to quantify bedrock erosion at the macro-scale (10^{-1} – 10^{0} m), the results of which are reported in Chapter 7.

Four high-resolution LiDAR point clouds (average 45.22 points m^{-2}) were used to create DEMs at 0.25 m resolution and detect change of 0.05 m on the basis of DoDs over the continuous shore platform surface along 22 km of the North Yorkshire coast. The boulders and steps were extracted by identifying protruding sections of the foreshore and applying a set of size and shape filters.

Erosion was analysed on the basis of 1) detachment inventory in order to identify mechanisms of erosion, and 2) 1 m^2 grid cells to characterise spatial distribution of erosion on the foreshore with the aim of providing systematic empirical data to feed coastal evolution models.

7. Bedrock erosion across the shore platform

7.1. Introduction

The objective of this chapter is to use the high quality and high resolution LiDAR data (Chapter 6) to 1) quantify shore platform erosion at the 10^{-1} – 10^{0} m scale; 2) assess how foreshore erosion varies spatially and temporarily; 3) assess the relative contribution of surface down-wearing and erosion at steps to the total foreshore erosion; 4) identify controls on spatial distribution of erosion; and 5) predict location and rates of erosion. The systematic empirical results of this study can feed numerical models to reconstruct past cliff retreat (Choi et al., 2012; Regard et al., 2012; Hurst et al., 2016; 2017) and predict future change (Trenhaile, 2000; Kline et al., 2014; Limber et al., 2014; Matsumoto et al., 2016).

Chapter 5 presents results of monitoring the small-scale (10^{-3} – 10^{-2} m) foreshore erosion based on 15 0.5×0.5 m sites. Despite high-resolution and high-precision of the study, with the monitoring sites located at a limited range of tidal level, two rock types, diverse joint density and the style of relief (planar, stepped and sloping), it is difficult to assess how representative the results are for the whole platform and across spatial scales. In order to understand how foreshore erosion up- and down-scales and which is the dominant scale at which processes operate, the macro-scale study (10^{-1} – 10^{0} m) is undertaken. The analyses are similar to those at the small-scale – firstly the size and shapes of detachments are studied in order to constrain mechanisms of erosion; then spatial distribution of erosion is analysed and the controls upon it are identified; finally, erosion is considered temporarily to see the consistency between monitoring campaigns and establish whether erosion propagates in time.

The results are compared with the small-scale monitoring in Chapter 9, where further implications of the multi-scale approach to foreshore erosion are discussed.

7.1.1. Potential controls on the spatial distribution of erosion

Based on the literature (sections 2.2.2 and 5.1.1) and the results of Chapter 5, the controls on the distribution of foreshore macro-erosion are considered. One of the aims of this chapter is to assess how foreshore erosion varies spatially. If erosion is not uniform in space, the parallel model of coastal evolution, in which the down-wearing is quasi-uniform and proportional in magnitude to the cliff retreat rate (section 2.2.3), is not valid. 11 variables which characterise the 1 m^2 grid cells are considered as potential controls on the distribution of erosion (Table 6.3). They include: 1) position on the platform (distance from the cliff and from the seaward edge); 2) topography at the metre-scale (elevation and slope); 3) variability in topography within grid cells (elevation range, relief, roughness

and curvature); 4) tidal regime (tidal duration and inundation frequency); and 5) the macro-structure (joint density).

Because of potential differences in the mechanisms and rates of erosion, the cells which contain a step are analysed separately to the non-stepped cells. Previous studies of foreshore erosion and the results from Chapter 5 are used here to identify expected relationships, which will be explored in the chapter.

As the steps protrude from the platform they are likely to experience higher rates of erosion (Moses and Robinson, 2011). Previous studies have shown that the joint spacing, orientation and density play a role in step back-wearing, and the excavated discontinuities delimit blocks to be detached from the platform (Naylor and Stephenson, 2010). Blocks with size and shape determined by the macro-scale (order of magnitude 10^{-1} – 10^{0} m^3) discontinuity pattern are detached sporadically during severe storms (Naylor and Stephenson, 2010; Stephenson and Naylor, 2011). Therefore, detected erosion at steps may mainly represent smaller-scale (10^{-3} – 10^{-2} m^3) rock fracturing due to hydraulic pressure and impact of the wave-carried boulders (Moses and Robinson, 2011).

The results of Chapter 5 suggest that erosion rates are higher closer to the cliff and at locations with more frequent submergence/emergence transition (Table 5.4). The former relationship was noticed in previous studies (Robinson, 1977a; Foote et al., 2006; Moses and Robinson, 2011). The highest tidal duration coincides with the mean high water level of neap tides (MHWN = 1.50 m AOD) which is the level of the highest efficiency of weathering (Porter et al., 2010a). The results of mathematical and exploratory numerical models on coastal evolution suggest that the wave energy is highest around or slightly above the mean sea level (Trenhaile, 2000; Matsumoto et al., 2016). Table 7.1 summarises the expected relationships.

Table 7.1 Expected relationships between the independent variables and erosion; the sign of relationship is indicated by '+' and '-'.

Variable	Down-wearing	Erosion at steps	Reference
Distance from the cliff	-	n/a	Robinson, 1977a; Foote et al., 2006; Moses and Robinson, 2011; Chapter 5
Distance from the seaward edge	+	n/a	Robinson, 1977a; Foote et al., 2006; Moses and Robinson, 2011; Chapter 5
Elevation	+/-	+/-	Trenhaile, 2000; Matsumoto et al., 2016
Elevation range	+	+	_
Relief	+	+	Moses and Robinson, 2011
Slope	+	+	Moses and Robinson, 2011
Roughness	+	+	Moses and Robinson, 2011
Curvature	+	n/a	Hurst et al., 2012
Tidal duration	+	+	Porter et al., 2010a
Inundation frequency	+/-	+/-	Trenhaile, 2000; Matsumoto et al., 2016

Variable	Down-wearing	Erosion at steps	Reference
Joint density	n/a	+	Naylor and Stephenson, 2010

7.2. Results

Chapter 6 contains information about acquisition of the LiDAR data, processing and analysis. Organisation of the results and discussion sections in this chapter mirrors that of Chapter 5. First, general observations and summary statistics for all detachments are presented, then the spatial distribution of detachments across the foreshore is analysed at the grid cell basis and finally the temporal distribution of erosion is presented. Erosion rates are calculated separately on the basis of the detachment- and the grid cell inventories (details in section 6.4).

7.2.1. Macro-scale detachment inventory

DEM-based change detection, de-trending of DEMs of Difference (DoDs) and filtering out detachments deemed to represent beach dynamics resulted in identifying events which are believed to represent bedrock erosion and boulder/debris redistribution. Visual comparison of Figures 6.2 and 7.1 suggests that the processing successfully removed erroneous objects.

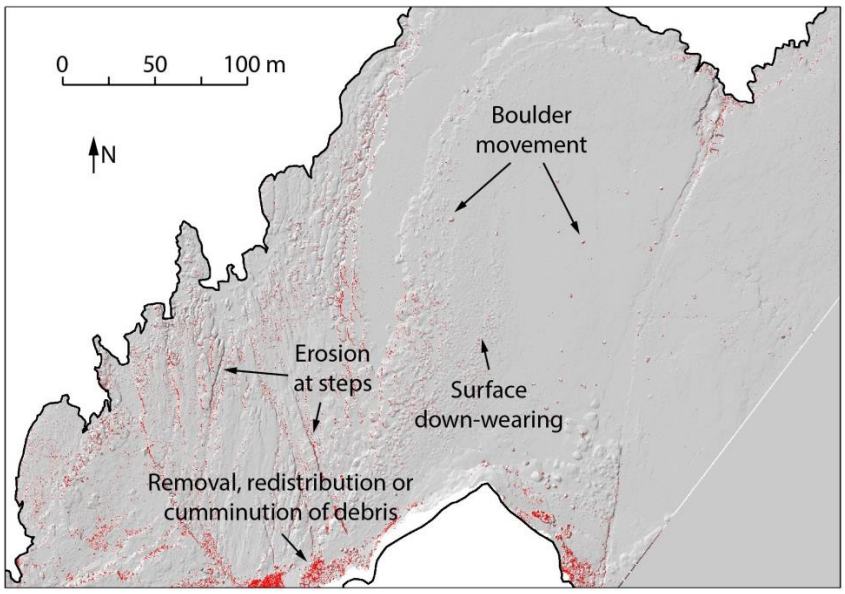


Figure 7.1 Proposed processes contributing to the detected detachments (red areas) after DoD de-trending and filtering out detachments which were deemed to represent beach dynamics in 2014-2015. Background: LiDAR2014 hillshade at 30% transparency.

The aim of this section is to calculate erosion rates on the basis of detachment inventory and to identify mechanisms of erosion from the area volume, volume-frequency and 3D shape distributions of detachments.

7.2.1.1. Summary statistics for the macro-scale detachment inventory

3.34×10^{6} discrete detachments were detected at the ~annual basis between 2014 and 2017, which contribute to removal of 5.25×10^{4} m^3 bedrock volume, equivalent to a 37.44 m cube. The spatially- and temporally-averaged mean erosion rate derived from this is 6.36 mm yr^{-1} (Table 7.2).

Table 7.2 Summary statistics of the erosion variables in the macro-scale detachment inventory across the North Yorkshire foreshore.

Variable	Value	Equivalent cube size (m)
Number of detachments	3,339,766	n/a
Total detached area (m^2)	378,963.13	n/a
Total detached volume (m^3)	52,484.82	37.44
Volume of the smallest detachment (m^3)	3.10×10^{-3}	145.81×10^{-3}
Volume of the largest detachment (m^3)	4.32	1.63
Average detachment volume (m^3)	15.72×10^{-3}	250.48×10^{-3}
Standard deviation of detached volumes (m^3)	41.45×10^{-3}	346.07×10^{-3}
Erosion rate (mm yr^{-1})	6.36	n/a

7.2.1.2. Volume frequency, size and shape of detachments

Detachment area covers three orders of magnitude (10^{-2} – 10^{0} m^2) and detachment volumes across four (10^{-3} – 10^{0} m^3) (Table 7.3; Figure 7.2). The events are from 0.05 m (*LoD*) to 2.00 m deep (normal to the platform surface) and their area ranges between 6.25×10^{-3} m^2 (equivalent to the DEM pixel size) and 6.00 m^2. The upper threshold of thickness and planform was introduced to separate bedrock erosion from beach dynamics (section 6.4.1). A statistically-significant positive relationship (R^2 = 0.647; p < 0.05) exists between the measured planform area and volume of detachments. Detachments are usually smaller than 1 m^2 in planform and 0.2 m^3 in volume (Figure 7.3).

Table 7.3 Summary statistics of the individual detachment sizes in the macro-scale detachment inventory across the North Yorkshire foreshore.

Variable	Min	Max	Mean	Standard deviation
Area (m^2)	6.25×10^{-2}	6.00	11.35×10^{-2}	18.60×10^{-2}
Volume (m^3)	3.10×10^{-3}	4.32	15.72×10^{-3}	41.45×10^{-3}
Maximum thickness (m)	0.05	2.00	0.14	0.12

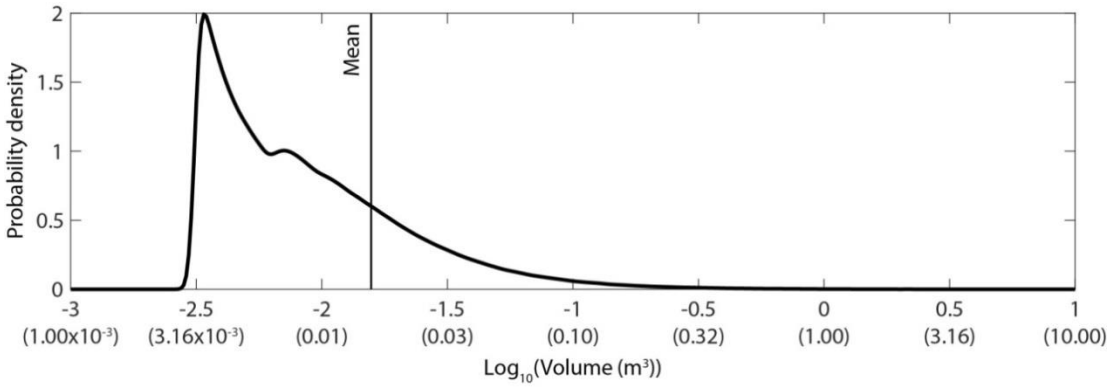


Figure 7.2 Kernel density estimate (normal kernel, half width h = 0.02 $log_{10}(m^3)$) of volume (common logarithmic scale) in the macro-scale detachment inventory. The values in brackets represent volumes in normal (m^3) units. Mean volume = 15.72×10^{-3} m^3.

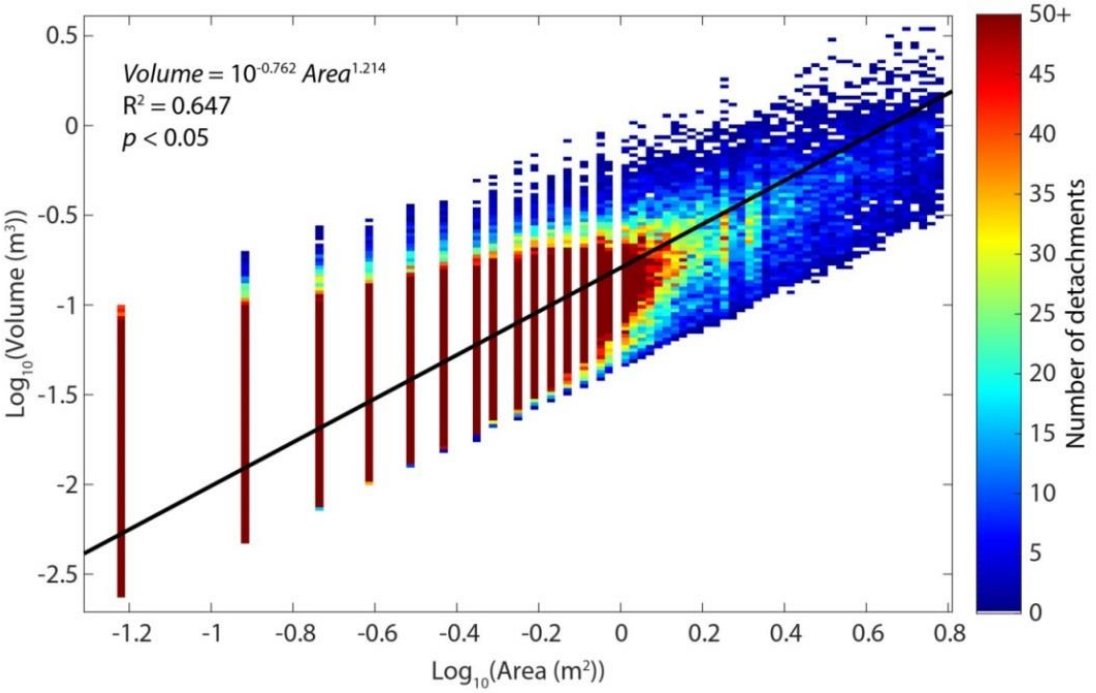


Figure 7.3 Density distribution of the area and volume in the macro-scale detachment inventory across the North Yorkshire foreshore with a grid cell size of 0.02. Events smaller than 1 m^2 are organised into vertical stripes adopting limited number of area values and a full range of volumes, which is caused by the pixel resolution controlling two dimensions.

The number of detachments decreases with size and most detached volumes are < 10^{-2} m^3. The volume-frequency distribution closely follows the power-low trendline fitted using the least-squares method (R^2 = 0.927, p < 0.05) (Clauset et al., 2009). The observed volumes deviate away from the power law for the largest (> 10^0 m^3) detachments. Therefore, additional trendlines were fitted

for two volume sections: ≤ 10^0 m^3 excluding the rollover at the smallest size and > 10^0 m^3, with respective exponent β values of 1.242 and 3.753 (Figure 7.4).

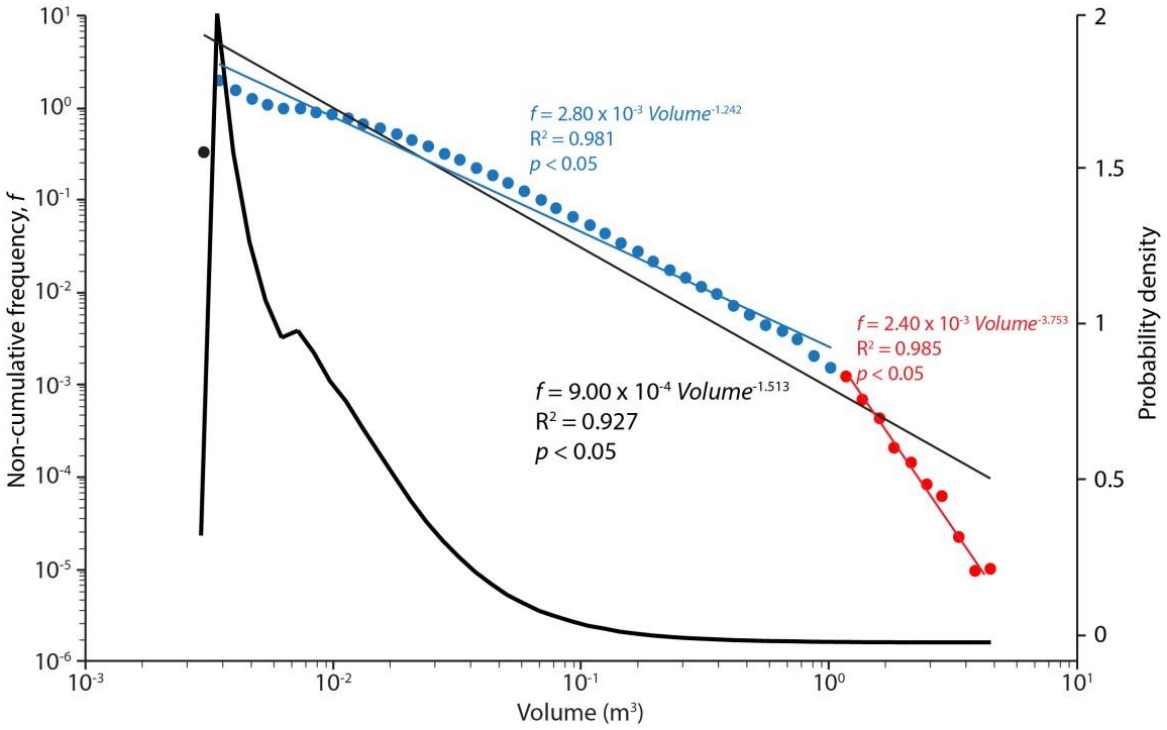


Figure 7.4 Volume-frequency distribution in the macro-scale detachment inventory on a log-log scale plot. The power-law trendlines are presented with the thin lines and described with equations coloured accordingly: black – whole size range, blue – events ≤ 10^0 m^3 excluding the roll-over, red – events > 10^0 m^3. The thick black line represents kernel density estimate (kernel type: Epanechnikov, half width h = 0.017 $log_{10}(m^3)$) of the volume.

Detachments have a wide range of 3D shapes with a concentration in the central bottom of the ternary plot, mainly in the *very bladed* sector. There is a deficiency of detachments of *compact* blocky shape in comparison with the other shape categories (Figure 7.5).

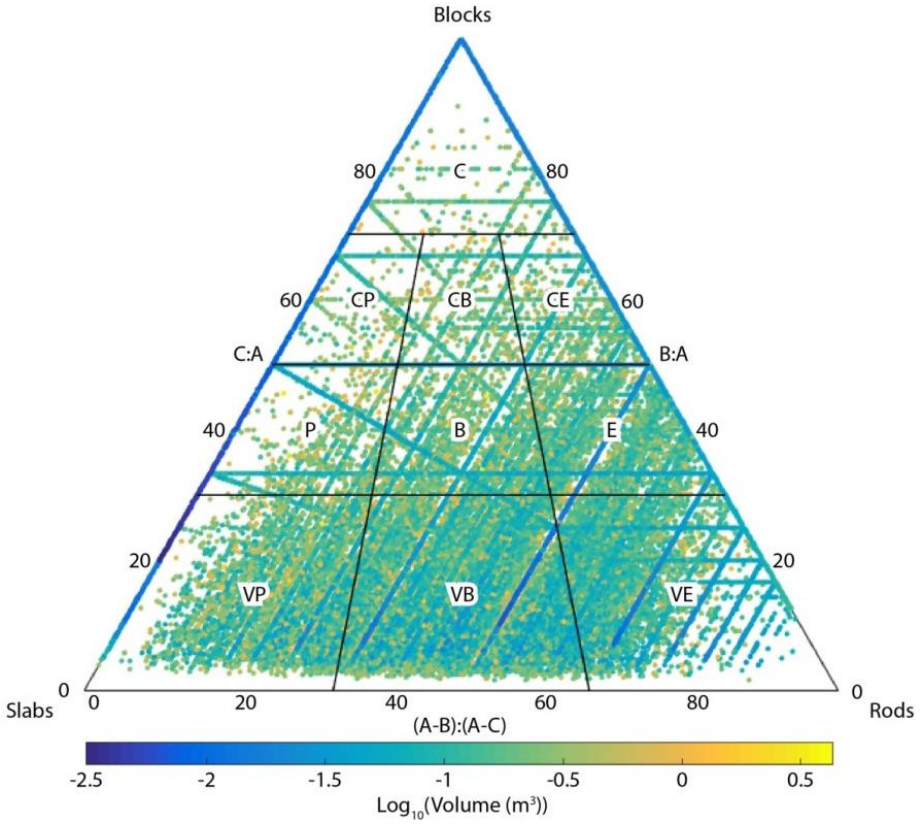


Figure 7.5 Shapes of detached material coloured by the volume (common logarithmic scale). Block axes: A – long, B – medium, C – short. For sector description see Figure 2.5. The smallest events (< 10^{-2} m^3) are organised into diagonal lines including the edges of ternary plot, which is a reflection of the pixel size controlling dimensions of two detachment axes.

7.2.1.3. Erosion rates and size distribution of detachments according to the surface class and type of erosion

In order to separate bedrock erosion from vegetation dynamics, which could be classified as 'detachment' on the basis of DoDs, the *Maximum Likelihood Classification* was performed to separate parts of the foreshore where the bedrock is exposed at the surface from the areas covered by vegetation. The subtle differences in total detached volume, the area volume scaling exponent, volume-frequency distribution and exponent β between the two surface classes suggest that bedrock cannot be simply separated from vegetation based on the RGB imagery (Table 7.4; Figures 7.6 and 7.7). Therefore, in further analysis below, the two surface classes are treated together.

Table 7.4 Summary statistics of the macro-scale erosion variables according to the surface class.

	Rock	Vegetation
Number of detachments	1,436,684	1,903,082
Total detached volume (m^3)	23,061.61	29,423.21
Equivalent cube size (m)	28.46	30.87
Area volume power-law trendline	$Volume = 10^{-0.772} Area^{1.199}$ ($R^2 = 651$; $p < 0.05$)	$Volume = 10^{-0.755} Area^{1.226}$ ($R^2 = 0.644$; $p < 0.05$)

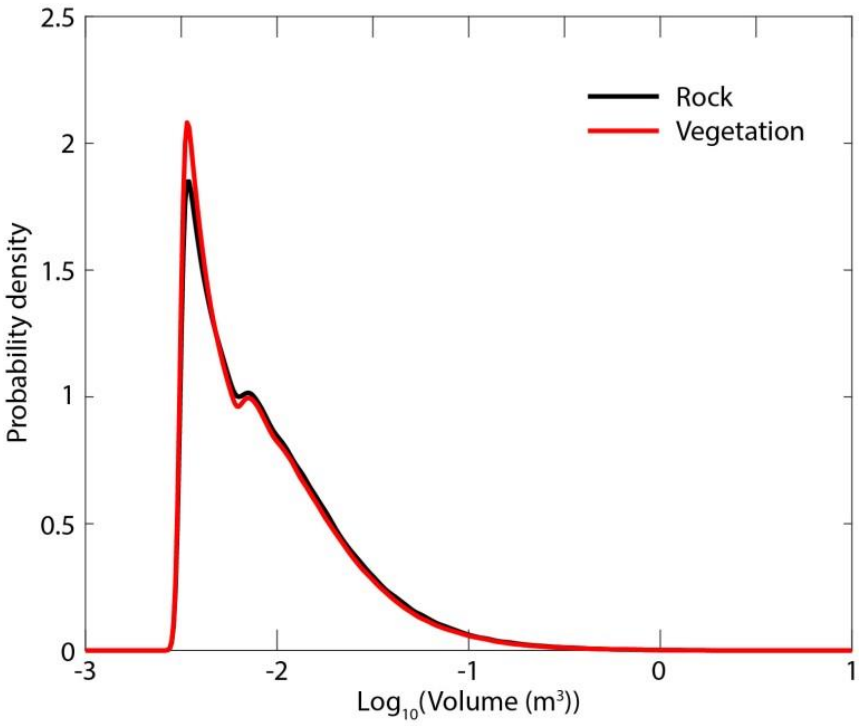


Figure 7.6 Kernel density estimate (normal kernel, half width h = 0.02 $log_{10}(m^3)$) of volume for the macro-scale detachment inventory according to the surface class.

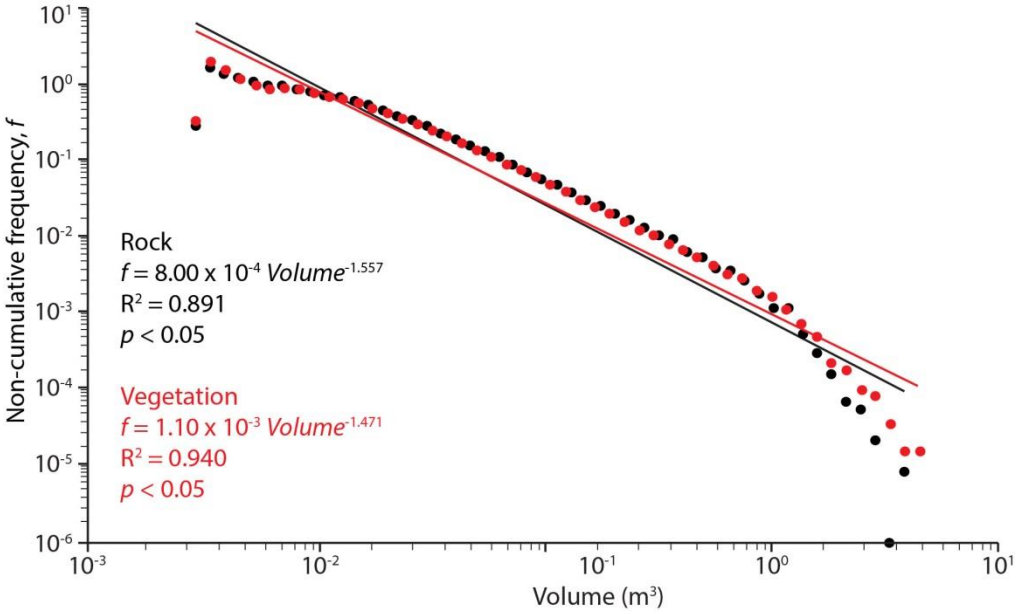


Figure 7.7 Volume-frequency distribution for the macro-scale detachment inventory according to the surface class with the power-law trendlines on a log-log scale plot.

Boulder movement and surface down-wearing contribute approximately equally to the total 93.20% of material loss on the platform surface, whereas erosion at steps accounts for 6.80% of erosion (Table 7.5). Assuming that already detached boulders do not contribute to net bedrock erosion, the erosion rates across the platform resulting from detachments at both stepped and non-stepped sections equals a spatially- and temporally-averaged rate of 3.45 mm yr^{-1}. 2.15×10^{6} discrete detachments resulting from the down-wearing and erosion at steps were identified, which contribute to 2.77×10^{4} m^3 detached bedrock.

Table 7.5 Macro-scale detachment count and volume according to the type of erosion.

Type of erosion	Number of detachments	Detached volume (m^3)	Mean detachment volume (m^3)
Down-wearing	2,000,138	24,104.67	12.05×10^{-3}
Erosion at steps	147,068	3,568.43	24.26×10^{-3}
Boulder movement	1,192,560	24,811.72	20.81×10^{-3}

7.2.2. Spatial distribution of the foreshore macro-erosion

The aim of this section is to assess the feasibility to predict erosion at any point of the foreshore knowing the across-shore location and the topographic, tidal and structural characteristics of the 1 m^2 grid cells. Subsequently, the cells are collapsed into a single cross-section where locations at a 1 m interval distance from the cliff are characterised by the magnitude of erosion. This allows the

relative roles of the three processes of erosion in space to be assessed, which can then be used in coastal evolution models.

7.2.2.1. Summary of the grid-cell data content

In order to understand the spatial pattern and controls on the distribution of detachments on the foreshore, erosion was analysed on the basis of a 1 m grid, with each cell attributed with distances from the cliff and the seaward edge in addition to the topographic, tidal and structural attributes (Table 6.3). The topographic attributes and erosion were calculated on the basis of maps at the original resolution (0.25 m) which means that maximal number of pixels used to derive the attributes was 16. For the cells collapsed to a single across-shore profile and grouped at 1 m intervals, the average number of pixels per cell is always < 12 and decreases with the distance from the cliff (Figure 7.8). The value is never 16 because of the averaging from a large dataset, in which at each 1-m across-shore interval there are cells which contain standing water or vegetation. The value of 11-12 pixels characterises the landward 50 m of the foreshore, and it gradually decreases between 50 and 220 m to increase again at the seaward-most section (Figure 7.8).

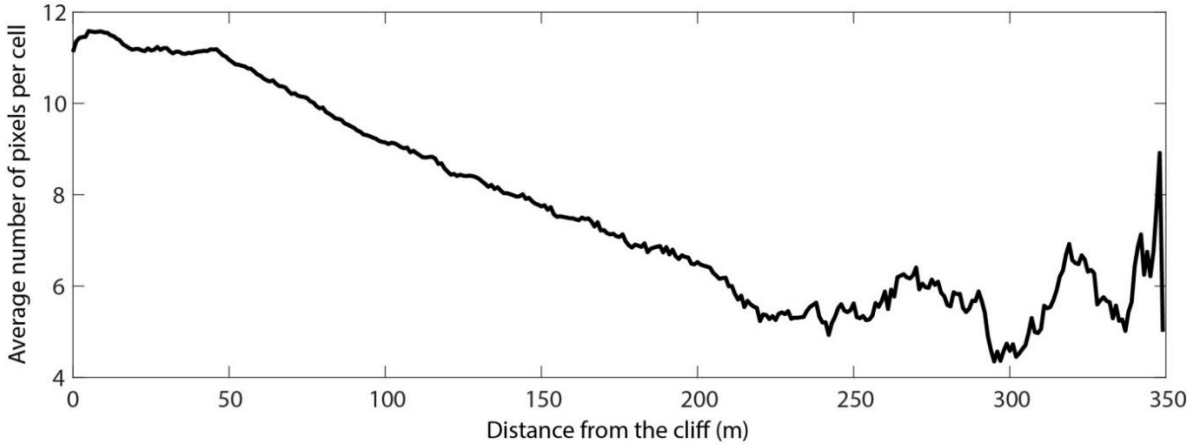


Figure 7.8 Relationship between the distance from the cliff (m) and the average number of pixels per cell.

The total area of shore platforms along the studied coastline equals 3.15×10^6 m^2 with the average width of ~140 m (section 3.7.1). To cover the whole area there should be 9.45×10^6 cells extracted separately for the three time periods. 7.16×10^6 cells were identified through division of the platform surface ≤ HAT for each year into a 1 m grid and removal of the cells located not entirely upon the platform and/or those which do not contain topographic data (Figure 6.10). From these, 6.68×10^6 cells formed the final inventory after removing those which included a beach deposit and/or whose mean change depth > 2 m.

3.43×10^4 cells (0.51% of the total) contained both a boulder and a step, and were classified into the boulder inventory in order not to count boulder dynamics as bedrock erosion. 74.87% of cells contained neither a step nor a boulder, 22.18% contained a boulder, while 2.95% contained a step. The cells were classified into *boulder*, *stepped* and *non-stepped* groups depending on the protrusion present, with such respective types of erosion: *boulder movement*, *erosion at steps* and *down-wearing*. 67.43% of the boulder and 47.72% of the stepped cells experienced detachments, while only 15.50% of the non-stepped cells experienced change. The erosion rate equals 0.01 mm yr^{-1} for the non-stepped, and 0.04 mm yr^{-1} for the stepped cells. The average foreshore erosion rate equals 0.01 mm yr^{-1} (Table 7.6).

Table 7.6 Summary of the cells that experienced erosion depending on the type of cell.

Type of cells	Type of erosion	Total number of cells	% of total platform area (%)	Number of cells that experienced erosion	Proportion of cells that experienced erosion (%)	Total detached volume (m^3)	Erosion rate (mm yr^{-1})
Boulder	Boulder movement	1,482,069	22.18	999,319	67.43	95,928.73	0.06
Stepped	Erosion at steps	197,348	2.95	94,169	47.72	8,519.52	0.04
Non-stepped	Down-wearing	5,003,834	74.87	775,489	15.50	62,819.02	0.01
Total		6,683,251	100.00	1,868,977	27.97	167,267.27	0.02
Total excluding boulders		5,201,182	77.82	869,658	16.72	71,338.54	0.01

7.2.2.2. Erosion on the non-stepped part of the foreshore

As the aim of this study was to model the distribution of foreshore erosion, the non-stepped cells (process of erosion: down-wearing) were split into two sets: 99% of the population formed a training set (4.95×10^6 cells) and 1% – a test set (5.00×10^4 cells). The latter is made of every 100^{th} cell of the inventory to guarantee even distribution on the foreshore. 84.50% of the cells in the training set (4.19×10^6 cells) do not contain any detachment.

Independent variables characterising the non-stepped cells

The cells are characterised by 11 independent variables (Table 7.7). Distance from the cliff ranges between 0 and 348.32 m, with the average of 88.15 m. Distance from the seaward edge adopts values between 0 and 287.92 m, with the mean of 75.72 m. The distance from the cliff and the seaward edge are not identical because of variable platform width. The vertical range varies from -2.08 m AOD, which is similar to MLWS = -2.01 m AOD (Figure 3.4), to 3.18 m AOD which was imposed by filtering out areas > HAT = 3.2 m AOD. The wide range of elevations means a wide spectrum of inundation frequencies (0.00-99.07%). Low relief (mean = 0.03 m) and slope (mean = 5.34°) dominate. Curvature adopts a wide range of values (-1.34×10^3 to 1.58×10^3). Tidal duration

spans between 0.00 and 2.87% with the average of 2.13%. The majority of cells do not contain joints visible within the orthophotographs, but values reach up to 5.07 joints m^2 (Table 7.7).

Table 7.7 Summary statistics of the independent variables in the training set used to develop a logistic model of the macro-scale detachment occurrence in the non-stepped cells.

Independent variable	Min	1st quartile	Median	Mean	3rd quartile	Max
Distance from the cliff, *lCli* (m)	0.00	46.05	80.54	88.15	120.90	348.32
Distance from the seaward edge, *lSea* (m)	0.00	34.64	66.60	75.72	106.90	287.92
Elevation, *lEle* (m AOD)	-2.08	-1.20	-0.75	-0.60	-0.18	3.18
Elevation range, *lEleR* (m)	0.00	0.04	0.06	0.11	0.10	4.99
Relief, *lRel* (m)	0.00	0.01	0.02	0.03	0.03	1.72
Slope, *lSlo* (°)	0.00	1.76	2.81	5.34	5.46	76.61
Roughness, *lRou* (°)	0.00	0.81	1.30	2.65	2.71	40.16
Curvature, *lCur*	-1342.00	-8.25	-0.31	-0.52	7.31	1581.50
Tidal duration, *lTid* (%)	0.00	1.94	2.21	2.13	2.46	2.87
Inundation frequency, *lInu* (%)	0.00	63.06	78.01	73.94	89.46	99.07
Joint density, *lJDe* (joints m^{-2})	0.00	0.00	0.00	0.19	0.00	5.07

The correlation between all pairings of the independent variables shows that the topographic variables – elevation range, relief, slope and roughness – are strongly correlated, as are the elevation and inundation frequency (PCC $\geq$ 0.84, $p < 0.05$). The general correlation pattern agrees with the correlation of variables observed at the small-scale, but the values of PCC are different (Figure 5.10). For instance, the distances from the cliff and from the seaward edge have a stronger correlation at the micro- than macro-scale with respective PCC of -0.92 and -0.46. The reason may be that the location of small-scale monitoring on a single platform versus the diversity of foreshore geometry along the 22 km coastline analysed at the macro-scale. In contrast, the relationship between slope and roughness is stronger at the macro-scale (PCC of 0.89 versus 0.52 at the small-scale), which can be explained by a relatively large sample size which makes outliers less important. The sample size also implies that at the macro-scale all relationships are significant ($p < 0.05$), while at the small-scale this figure is only 28.79% (19) (Figure 7.9). Inundation frequency, elevation range and relief were removed from the predictor list because of the correlation $R^2 > 0.9$ with other variables (Tabachnick and Fidell, 2013) and or direct derivatives, which means that they cannot be considered to be independent.

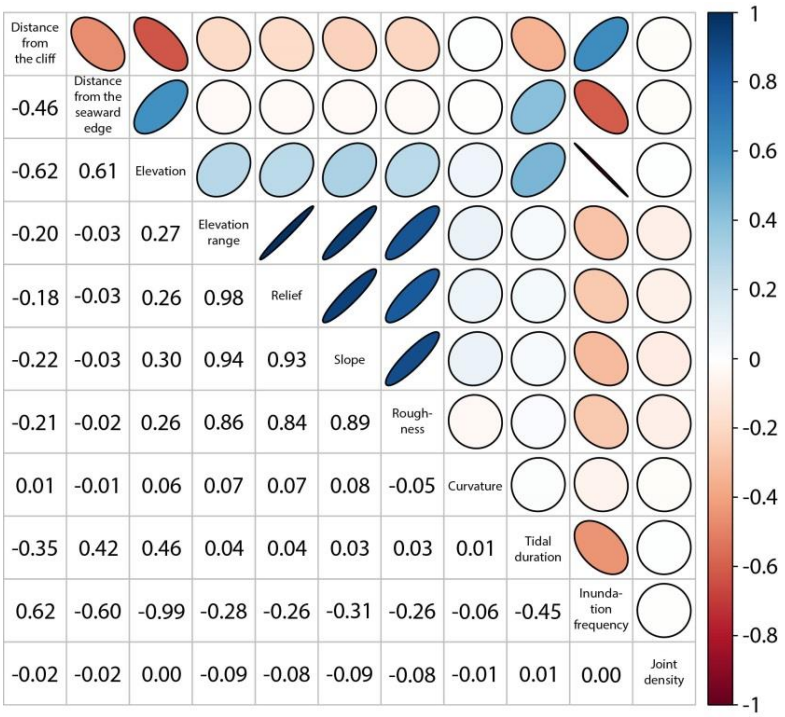


Figure 7.9 Matrix of correlation coefficients and best-fit ellipses for all independent variables of the non-stepped cell inventory obtained using the Pearson correlation in R. The colour bar represents the Pearson correlation coefficient (PCC) which describes both the strength of relationship and its sign, '-1' being the strongest negative relationship, '0' expressing no correlation and '1' representing the strongest positive relationship. The sign of the relationships (positive/negative) is also expressed by the sign of PCC values in the bottom-left part of the plot and the orientation of the oval in the upper-right part, while their strength is represented by the absolute values in the bottom-left part of the plot and the width of the ovals, with narrower ovals representing stronger relationships. All relationships are significant ($p < 0.05$).

Predicting the distribution of the down-wearing

Logistic regression was used to identify whether a detachment occuring in a given cell can be predicted from the remaining eight variables. The performance of models constructed manually by adding the independent variables one-by-one was assessed on the basis of the proportion of correctly classified cells, *P*, on the test set from the confusion matrix (Figure 6.11). The distance from the cliff alone allows correct classification of 84.53% cells; adding the slope to the model increases the success rate to 87.81%; and the joint density to 87.88% (Figure 7.10). Joint density was not included in the final model because of a low gain of *P* in respect to the model constructed using only the distance from the cliff and the slope, and the need of the data that is relatively difficult to collect (joint density map).

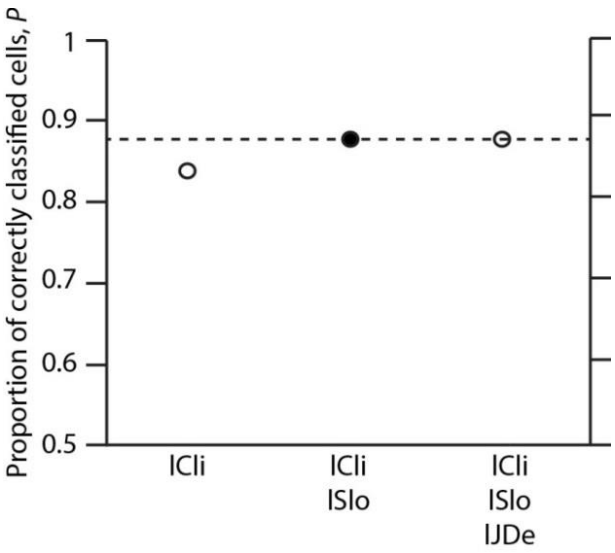


Figure 7.10 Sequence of input independent variables into the logistic model of the macro-scale erosion occurrence in the non-stepped cells and resulting proportion of correctly classified cells, P; dashed line represents maximum P of full model; accepted model is indicated by the black dot. See Glossary for abbreviation meaning and calculation of the variable values.

Figure 7.11 and Table 7.8 provide details of the accepted model of detachment occurrence as a function of the distance from the cliff and the slope. The model successfully predicts the occurrence of erosion in 2,579 cells and the absence of erosion in 41,357 cells. In 5,163 cells erosion occured but the model did not predict it, while 939 cells were wrongly ascribed erosion. 87.81% of erosion locations (cells) can be predicted knowing the distance from the cliff and the slope only (Figure 7.11). The occurrence of erosion decreases with the former and increases with the latter variable (Table 7.8).

		Observed YES	Observed NO
Predicted	YES	2,579	939
Predicted	NO	5,163	41,357

Proportion of correctly classified cells:

$$P = \frac{2{,}579 + 41{,}357}{50{,}038} = 0.8781$$

Figure 7.11 Performance of the accepted logistic model of the macro-scale erosion occurrence in the non-stepped cells based on the predicted and observed number (n) of cells with (YES) and without (NO) detachments in the test set.

Table 7.8 Details of the accepted logistic model of the macro-scale erosion occurrence in the non-stepped cells.

Deviance residuals	Min	1st quartile	Median	3rd quartile	Max
	-4.38	-0.46	-0.39	-0.32	2.90
Coefficients	Estimate	Standard error	*z*-value	*p*-value	
Intercept	-2.42	3.35×10^{-3}	-722.1	< 0.05	
Distance from the cliff, *lCli* (m)	-5.63×10^{-3}	3.07×10^{-5}	-183.5	< 0.05	
Slope, *lSlo* (°)	0.17	2.32×10^{-4}	741.8	< 0.05	
Null deviance	4,272,685 on 4,953,795 degrees of freedom				
Residual deviance	3,198,759 on 4,953,793 degrees of freedom				
AIC	3,198,765				
Number of Fisher Scoring iterations	5				

Variables used to predict the down-wearing rate

15.50% of the training set cells (7.68×10^{5}) experienced erosion, so they were used to assess whether the magnitude of erosion that can be predicted on the cell-by-cell basis using the multiple linear regression. The eight variables which were independent were used to predict erosion rates. These are: distance from the cliff, distance from the seaward edge, elevation, slope, roughness, curvature, tidal duration and joint density. The characteristics of the distribution of each of the variables were analysed. The down-wearing rates are often log-normally distributed. Distances from the cliff and the seaward edge are predominantly < 100 m, while elevations < 0 m AOD characterise most cells. Slope and roughness concentrate towards lower values on the spectrum of values, and they were converted to the square root scale to normalise the distribution. Tidal duration is irregularly distributed across the value spectrum, while the joint density is most frequently represented by 0 and the higher the value it acquires, the lower the respective frequency (Figure 7.12).

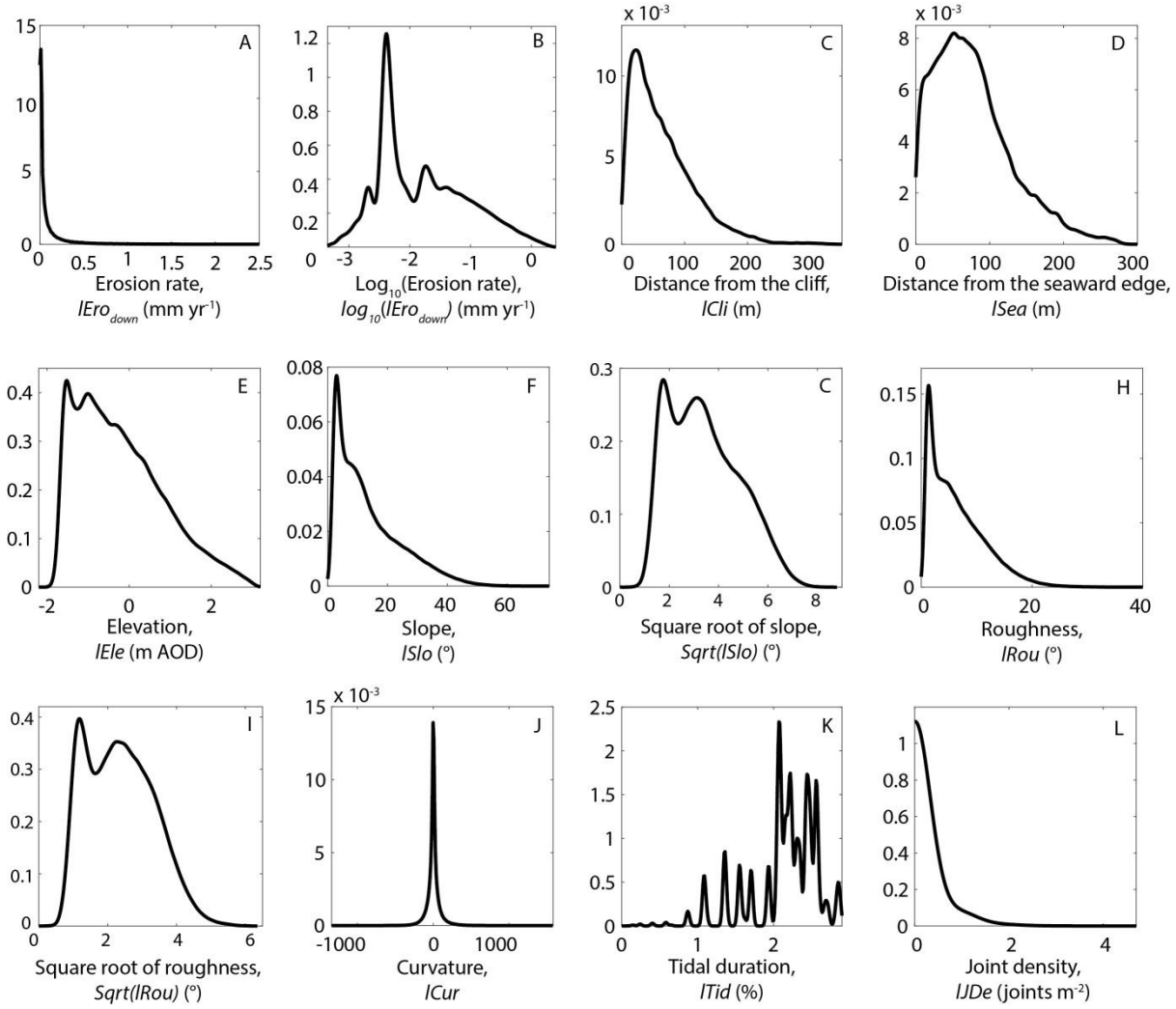


Figure 7.12 Kernel density estimate (normal kernel, default optimal half widths h returned in MATLAB were used) of the erosion and independent variables characterising the non-stepped cells: A) Erosion rate, $lEro_{down}$ ($h = 9.40\times10^{-4}$ mm yr^{-1}); B) Log_{10}(Erosion rate), $log_{10}(lEro_{down})$ ($h = 0.05$ log_{10}(mm yr^{-1})); C) Distance from the cliff, lCli (h = 3.11 m); D) Distance from the seaward edge, lSea (h = 3.50 m); E) Elevation, lEle (h = 0.08 m AOD); F) Slope, lSlo (h = 0.68°); G) Square root of slope, Sqrt(lSlo) ($h = 11.41°\times10^{-2}$); H) Roughness, lRou (h = 0.34°); I) Square root of roughness, Sqrt(lRou) ($h = 8.00°\times10^{-2}$); J) Curvature, lCur (h = 2.58); K) Tidal duration, lTid (h = 0.02%); L) Joint density, lJDe (h = 0.34 joints m^{-2}); Y axis: probability density.

Predicting the down-wearing rate

The variables described were used to build a multiple linear regression model to predict down-wearing rates. The predictors were added manually one-by-one to guarantee the highest improvement in R^2, with $p < 0.05$, and considering the physical meaning rather than goodness-of-fit only (see Parker et al., 2015). Square root of slope allows 11.80% of the variability in erosion rates to

be explained. Adding the elevation improves the performance of the model to 16.70%. The distance from the cliff increases it to 17.30% and subsequently the joint density to 17.40%. The limited success of the model is noted, and discussed further below. As the latter two variables only minimally increase R^2 (by 0.007) the accepted model does not include them (Figure 7.13). The results show that the down-wearing rate, $log_{10}(lEro)$, is higher for steeper (higher *sqrt(lSlo)*) and more elevated (higher *lEle*) surfaces ($R^2 = 0.167$, $p < 0.05$):

$$log_{10}(lEro_{down}) = -2.24 + 0.14\sqrt{lSlo} + 0.16\, lEle \qquad \text{Eq 7.1}$$

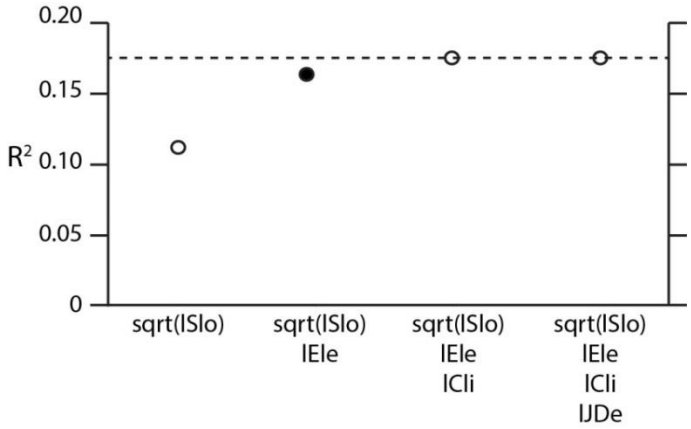


Figure 7.13 Sequence of input independent variables and resulting R^2 values ($p < 0.05$) to predict erosion rate, $lEro_{down}$ (mm yr^{-1}) in the non-stepped cells; accepted model is indicated by black dot. See Glossary for abbreviation meaning and calculation of the variable values.

Testing performance of the model

The weak correlation between erosion and the independent variables ($R^2 = 0.167$, $p < 0.05$) suggests that the model may not be good enough to predict erosion rates. To further explore the results, Eq 7.1 was applied on a test set of 7,742 cells, which is the sub-population of the full test set (5.00×10^4 cells; see beginning of this section) that experienced erosion.

The model is unable to explain the observed erosion rates. There is a clear structure in the distribution of residuals, which suggests that the model should be rejected. The residuals increase gradually; the model overestimates the rates up to 0.01 mm yr^{-1} and underestimates them for faster rates (Figure 7.14).

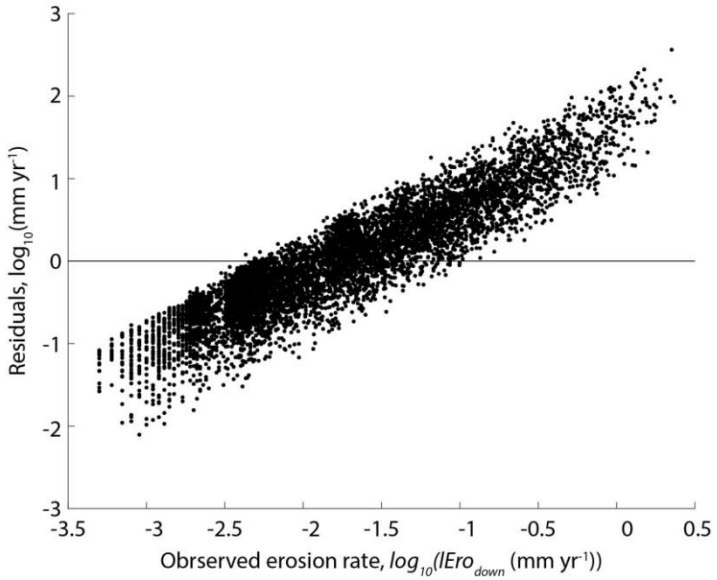


Figure 7.14 Distribution of residuals for the erosion rate, $lEro_{down}$ (mm yr^{-1}) on the test set of the non-stepped cells; residuals are calculated as observed - predicted values.

7.2.2.3. Erosion on the stepped part of the foreshore

The cells containing a step were split into two sets in order to predict the distribution and magnitude of erosion (a training set) and assess performance of the models (a test set). The training set consists of 1.95×10^5 cells (99% of the total), and the test set is made of every 100th cell of the stepped cell inventory (1,973 cells). 52.27% cells from the training set (1.02×10^5) do not contain any detachments. The procedure to predict erosion mimics the procedure used to model it for the non-stepped cells (section 7.2.2.2).

Independent variables characterising the stepped cells

Eleven independent variables were used to predict the occurrence (YES/NO) of erosion at steps (Table 7.9). The distance from the cliff varies between 0.00 and 348.18 m with the mean at 64.95 m, and from the seaward edge – between 0.00 and 287.92 m with the mean at 74.96 m. Because of the differences in morphology, the average values of elevation range, relief, slope and roughness are higher than for the non-stepped cells (Table 7.7). The difference of the mean inundation frequency – 59.94% for the stepped and 73.94% for the non-stepped cells – suggests that the steps tend to occur at higher elevations, which usually coincides with the lower distance from the cliff. Most cells do not contain joints detectable from the orthophotographs (at the 3rd quartile *lJDe* = 0.00 joints m^{-2}) (Table 7.9).

Table 7.9 Summary statistics of the independent variables in the training set used to develop a logistic model of the macro-scale detachment occurrence in the stepped cells.

	Min	1st quartile	Median	Mean	3rd quartile	Max
Distance from the cliff, *lCli* (m)	0.00	17.06	48.49	64.95	93.98	348.18
Distance from the seaward edge, *lSea* (m)	0.00	31.66	66.78	74.96	106.11	287.92
Elevation, *lEle* (m AOD)	-2.03	-0.95	-0.23	0.02	0.77	3.17
Elevation range, *lEleR* (m)	0.00	0.19	0.32	0.38	0.50	4.20
Relief, *lRel* (m)	0.00	0.06	0.10	0.12	0.15	1.66
Slope, *lSlo* (°)	0.69	11.07	16.76	18.51	24.54	73.39
Roughness, *lRou* (°)	0.33	5.30	8.29	8.88	11.71	39.70
Curvature, *lCur*	-1194.30	-37.79	4.43	4.99	42.44	1244.30
Tidal duration, *lTid* (%)	0.00	2.05	2.21	2.14	2.46	2.87
Inundation frequency, *lInu* (%)	0.00	43.89	65.41	59.94	82.90	99.07
Joint density, *lJDe* (joints m^{-2})	0.00	0.00	0.00	0.18	0.00	4.61

Pair-wise correlation between the independent variables (Figure 7.15) shows a similar pattern to that characterising erosion at the non-stepped cells (Figure 7.9). Elevation range, relief and slope are strongly correlated (PCC $\geq$ 0.91, $p < 0.05$), so are elevation and inundation frequency (PCC = -0.99, $p < 0.05$). The correlations between slope and roughness, and elevation range and roughness are weaker than for the non-stepped cells, with the respective PCC values of 0.69 and 0.89 for the former pairing of variables, and 0.69 and 0.86 for the latter. This may reflect the fact that steps may have relatively higher values of elevation range and slope as compared to roughness, for instance when a step delimit two smooth surfaces (see section 7.3.3.1), while for the non-stepped surfaces a change in one variable means a change in the other more often. Inundation frequency, elevation range and relief were excluded from the predictor list because they were co-dependent on other variables (Figure 7.15).

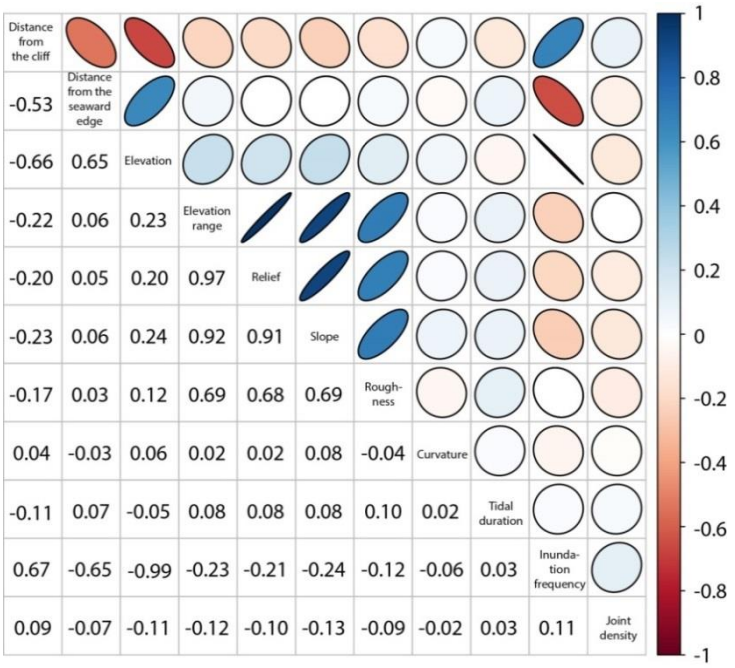


Figure 7.15 Matrix of correlation coefficients and best-fit ellipses for all variables of the stepped cell inventory obtained using the Pearson correlation in R. The colour bar represents the Pearson correlation coefficient (PCC) which describes both the strength of relationship and its sign, '-1' being the strongest negative relationship, '0' expressing no correlation and '1' representing the strongest positive relationship. The sign of the relationships (positive/negative) is also expressed by the sign of PCC values in the bottom-left part of the plot and the orientation of the oval in the upper-right part, while their strength is represented by the absolute values in the bottom-left part of the plot and the width of the ovals, with narrower ovals representing stronger relationships. All relationships are significant ($p < 0.05$).

Predicting distribution of erosion at steps

Eight independent variables were used to predict erosion occurrence across the foreshore using logistic regression. Similar to predicting the occurrence of erosion at the non-stepped parts of the platform, the variables were added one-by-one considering goodness-of-fit (R^2 and *p*-value) and physical meaning. 69.03% of the erosion occurrence can be predicted knowing the slope only. As adding curvature, joint density and roughness only increases *P* by only 0.75%, the accepted logistic model does not include them (Figure 7.16). The accepted model is able to successfully predict occurrence of 69.03% of erosion at steps (Figure 7.17) and suggests that more erosion happens at locations with higher slope (Table 7.10). The model is less successful than the one found for the non-stepped part of the platform ($P = 0.8781$).

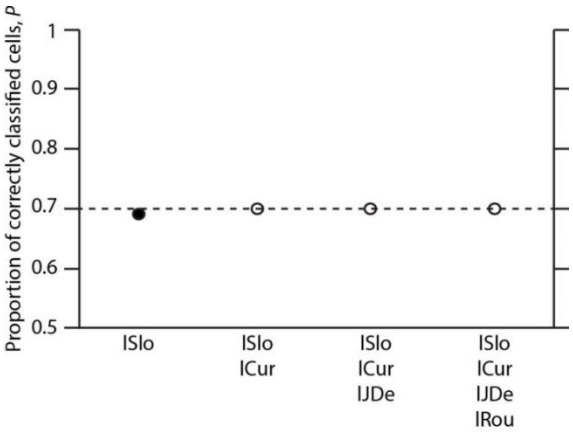


Figure 7.16 Sequence of the input independent variables into the logistic model of the macro-scale erosion occurrence in the stepped cells and resulting proportion of correctly classified cells, P; dashed line represents maximum P of full model; accepted model is indicated by black dot. See Glossary for abbreviation meaning and calculation of the variable values.

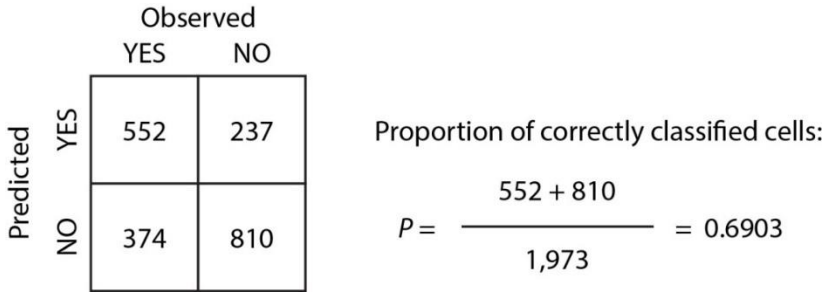


Figure 7.17 Performance of the accepted logistic model of the macro-scale erosion occurrence in the stepped cells based on the predicted and observed number (n) of cells with (YES) and without (NO) detachments in the test set.

Table 7.10 Details of the accepted logistic model of the macro-scale erosion occurrence in the stepped cells.

Deviance residuals	Min	1st quartile	Median	3rd quartile	Max
	-3.07	-0.95	-0.66	1.07	1.93
Coefficients	Estimate	Standard error	*z*-value	*p*-value	
Intercept	-1.81	1.16×10^{-2}	-155.7	< 0.05	
Slope, *lSlo* (°)	0.09	5.92×10^{-4}	159.6	< 0.05	
Null deviance	270,443 on 195,374 degrees of freedom				
Residual deviance	238,210 on 195,373 degrees of freedom				
AIC	238,214				
Number of Fisher Scoring iterations	4				

Variables used to predict erosion rate at steps

A subset of the training set consisting of 9.32×10^4 cells (47.73% of the whole training set) that experienced erosion was used to develop a multiple linear regression model of erosion rates. Analysis of the distribution of the erosion rates and eight independent variables showed that erosion rate is closest to a log-normal distribution, while the other variables did not require transformations (Figure 7.18). Erosion rates of $10^{-2.5}$ – 10^{-1} mm yr^{-1} are the most common. There is a peak in erosion rate at 10-20 m from the cliff, which suggests that the steps concentrate on the landward part of the foreshore perhaps reflecting the dominant foreshore profile. Most stepped cells are located < 100 m from the seaward edge. The cells are characterised by the wide spectrum of elevations (-2 to 2 m AOD). The distribution of slope, roughness and curvature is close to normal. The tidal duration distribution is irregular, which may be an artefact of collapsing elevations into 0.1 m vertical bins (Figure 3.4). The number of cells decreases as the joint density increases (Figure 7.18).

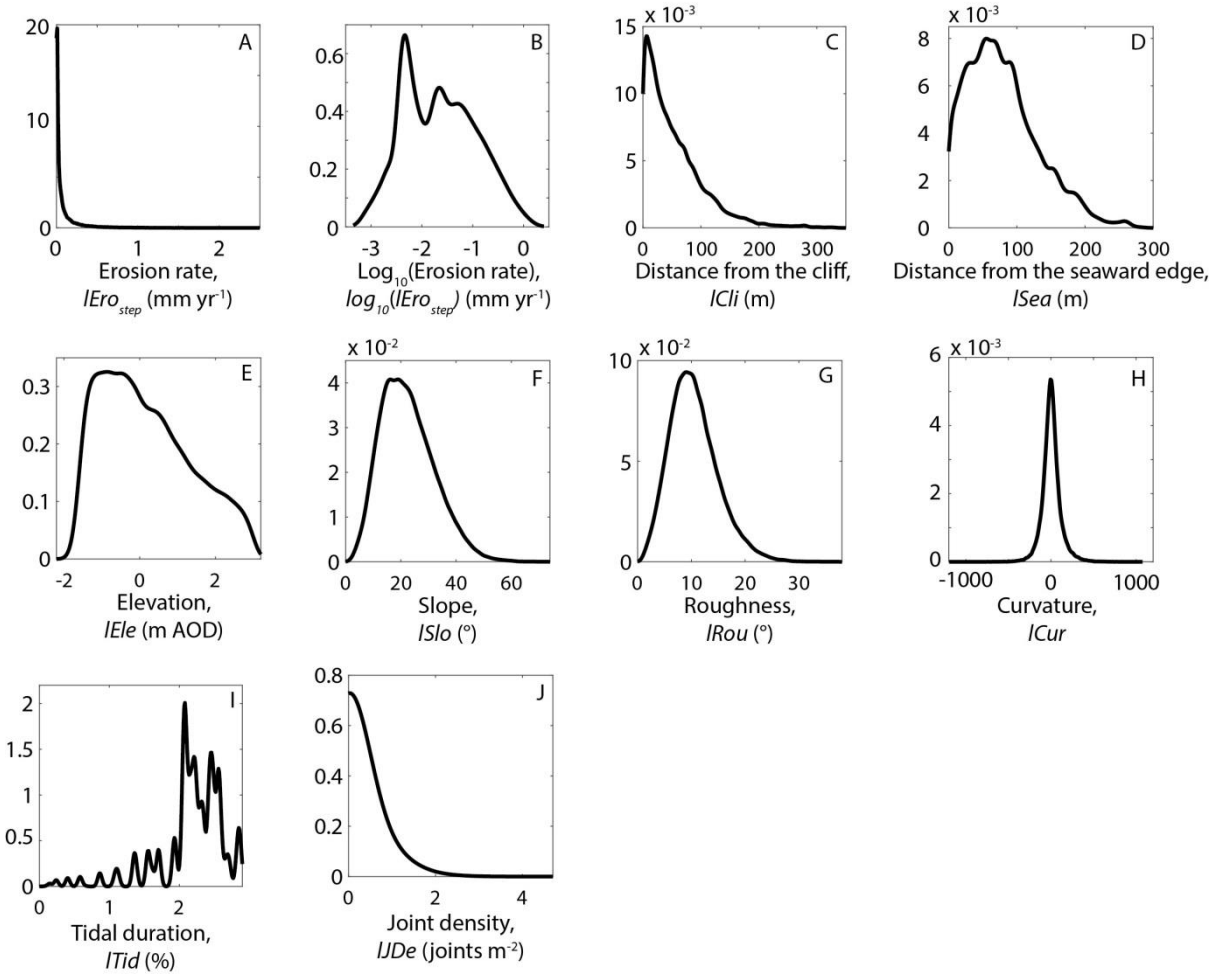


Figure 7.18 Kernel density estimate (normal kernel, default optimal half widths h returned in MATLAB were used) of the erosion and independent variables characterising the stepped cells: A) Erosion rate, $lEro_{step}$ ($h = 2.72\times10^{-3}$ mm yr^{-1}); B) Log_{10}(Erosion rate), $log_{10}(lEro_{step})$ ($h = 0.09$ log_{10}(mm yr^{-1})); C) Distance from the cliff, lCli ($h = 4.55$ m); D) Distance from the seaward edge, lSea ($h = 5.45$ m); E) Elevation, lEle ($h = 0.14$ m AOD); F) Slope, lSlo ($h = 1.04°$); G) Roughness, lRou ($h = 0.45°$); H) Curvature, lCur ($h = 8.52$); I) Tidal duration, lTid ($h = 0.03\%$); J) Joint density, lJDe ($h = 0.49$ joints m^{-2}); Y axis: probability density.

Predicting erosion rates at steps

A multiple linear regression model of erosion rates was built by adding the independent variables described in the previous section one-by-one on the basis of the highest increase of R^2, with $p < 0.05$, and considering the physical meaning. 5.80% of the variability in erosion rates can be predicted from slope alone. Adding elevation improves the prediction to 8.50%. Consecutive inclusion of joint density, distance from the seaward edge and distance from the cliff further improve the mode to 9.00, 9.30 and 9.40% respectively (Figure 7.19). Again, the limited success of the model is noted, and is discussed further below. As the latter three variables improve the model by 0.90%,

they are not included in the accepted model, in which erosion rates in the stepped cells, $lEro_{step}$, are higher for steeper (higher *lSlo*) and more elevated (higher *lEle*) surfaces ($R^2 = 0.085$, $p < 0.05$):

$$log_{10}(lEro_{step}) = -2.00 + 1.49\ x\ 10^{-2} lSlo + 10.42\ x\ 10^{-2} lEle \quad \text{Eq 7.2}$$

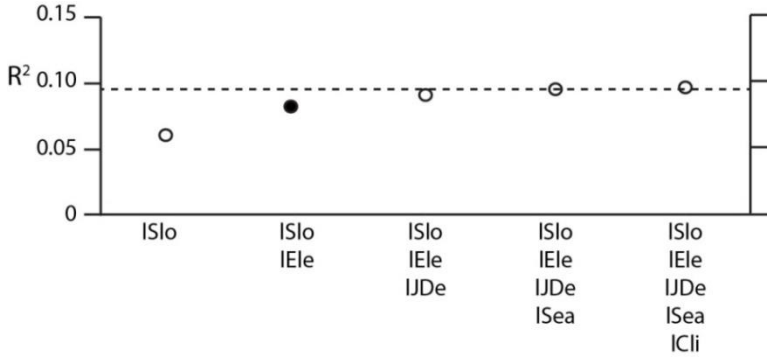


Figure 7.19 Sequence of the input independent variables and resulting R^2 values ($p < 0.05$) to predict the erosion rate, $lEro_{step}$ (mm yr^{-1}) in the stepped cells; accepted model is indicated by black dot. See Glossary for abbreviation meaning and calculation of the variable values.

Testing performance of the model

As the independent variables allowed prediction of only 8.50% of variability in erosion rates ($p < 0.05$), it seemed likely that the model was unsuccessful, similar to the model to predict erosion rates of the non-stepped part of the platform (section 7.2.2.2). To verify this, Eq 7.2 was applied on 926 cells, which is the subset of the original test set of the stepped cells (1,973 cells) which experienced erosion. Erosion rates cannot be predicted using the model as clear structure exists in the distribution of residuals. The residuals increase gradually; the lowest erosion rates (up to ~0.01 mm yr^{-1}) are overestimated, and the highest (from ~0.10 mm yr^{-1}) are underestimated (Figure 7.20).

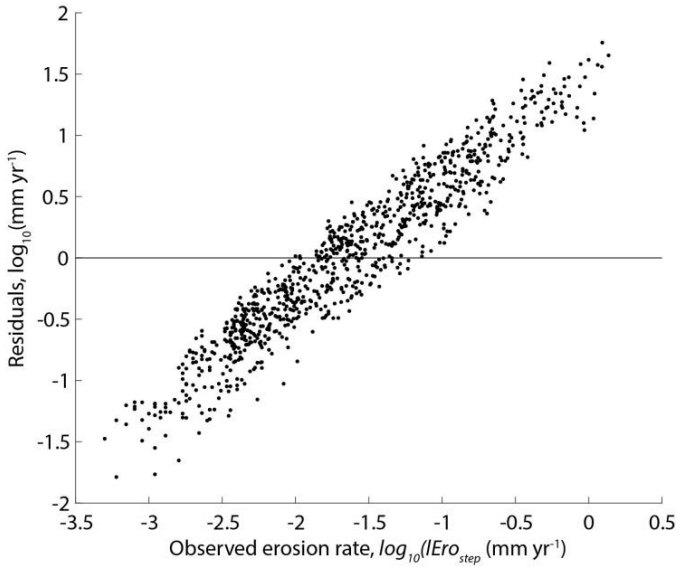


Figure 7.20 Distribution of residuals for the erosion rate, $lEro_{step}$ (mm yr^{-1}), on the test set of the stepped cells; residuals are calculated as observed - predicted values.

7.2.2.4. Across-shore distribution of foreshore erosion

The results of sections 7.2.2.2 and 7.2.2.3 suggest that it is difficult to predict the distribution and magnitude of foreshore erosion on a cell-by-cell basis. Here all cells (6.68×10^6) were collapsed into a 2D model of the across-shore distribution with the distance from the cliff (0-350 m) whereby each observation from along the coast is binned into 1 m interval bins at increasing distance from the cliff toe. The erosion values for each point along the profile are derived from all cells with sufficient data, and the results normalised by the cell frequency in each bin to provide an averaged measure of erosion rate.

The number of cells that included sufficient data generally decreases with the distance from the cliff, with the highest proportion of cells at the distance of 10-100 m (Figure 7.21A). The number of cells located < 10 m from the cliff is lower because of filtering out the pixels > 3.2 m AOD (section 6.3.3) and cells which are either not entirely located upon the platform or those which contain beach deposits (Figure 6.10); these properties characterise locations close to the cliff toe. Cells located closer to the cliff toe experienced erosion more often than cells further seaward (Figure 7.21B). There is a peak in erosion rate at 10-15 m from the cliff toe where 57.15% of cells lost material. The value decreases towards 0.45 moving landwards, and towards < 0.10 moving seawards. The change is gradual between the peak at 10-15 m and the distance of 150 m. The value remains around 0.10 up to ~230 m from the cliff toe. Seawards from this point the distribution of the proportion of cells that experienced erosion is irregular and varies between 0 and 20% (Figure 7.21B).

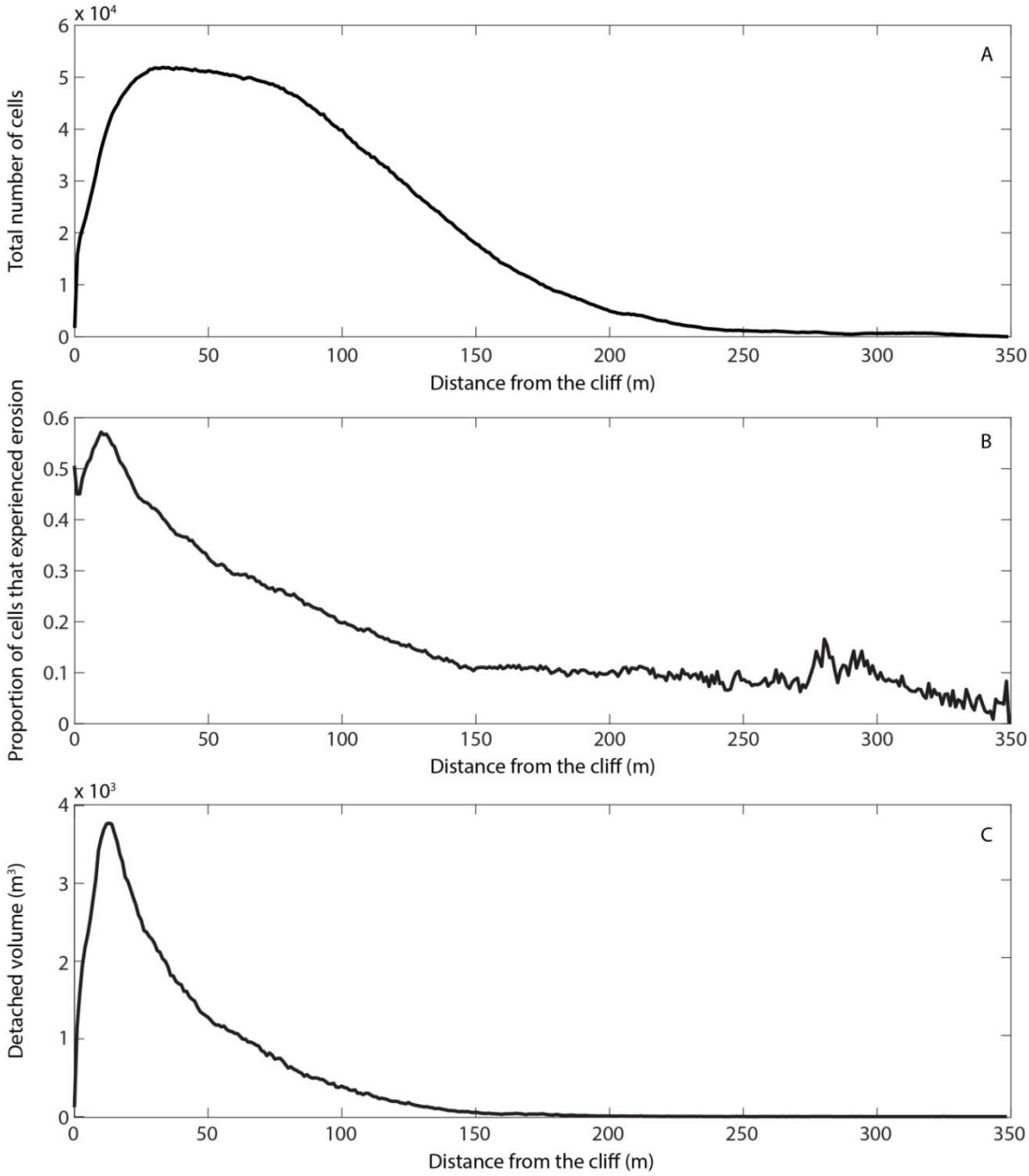


Figure 7.21 Distribution of cells and erosion across shore platforms binned into 1 m distances from the cliff: A) total number of cells; B) proportion of cells that experienced erosion; C) total detached volume.

The detached volume varies in a surprisingly systematic and consistent manner, with the rapid increase in detached volume at the 10 m section closest to the cliff toe, a peak in detached volume of 3.78×10^3 m^3 at 13 m, and a gradual decrease with distance from the cliff, reducing to ≤ 1 m^3 at 250 m (Figure 7.21C).

The contribution of the three types of erosion identified – boulder, stepped and non-stepped – to the total number of cells, and the erosion within them changes as a function of the distance from the cliff (Figure 7.22). At the cliff toe, 59.27% of the cells are stepped, 27.49% are non-stepped and 13.24% contain a boulder. The proportion of boulders increases to 40-41% between 9 and 14 m from the cliff toe and then gradually decreases to 8.33% at 150 m remaining at the low level for the seaward 200 m, excluding the very edge of the platform (16-20%). The proportion of stepped cells falls below 10% at 7 m, below 5% at 14 m and remains at the low level (0-4%) across most of the platform width with the increase to over 10% at 276-281 m and at the seaward-most 6 m. The contribution of the non-stepped cells consistently increases with the distance from the cliff with thresholds of 60% at 21 m, 70% at 49 m and 80% at 98 m. It drops to 75-79% at 277-281 m from the cliff and to 25% at the seaward edge (Figure 7.22A).

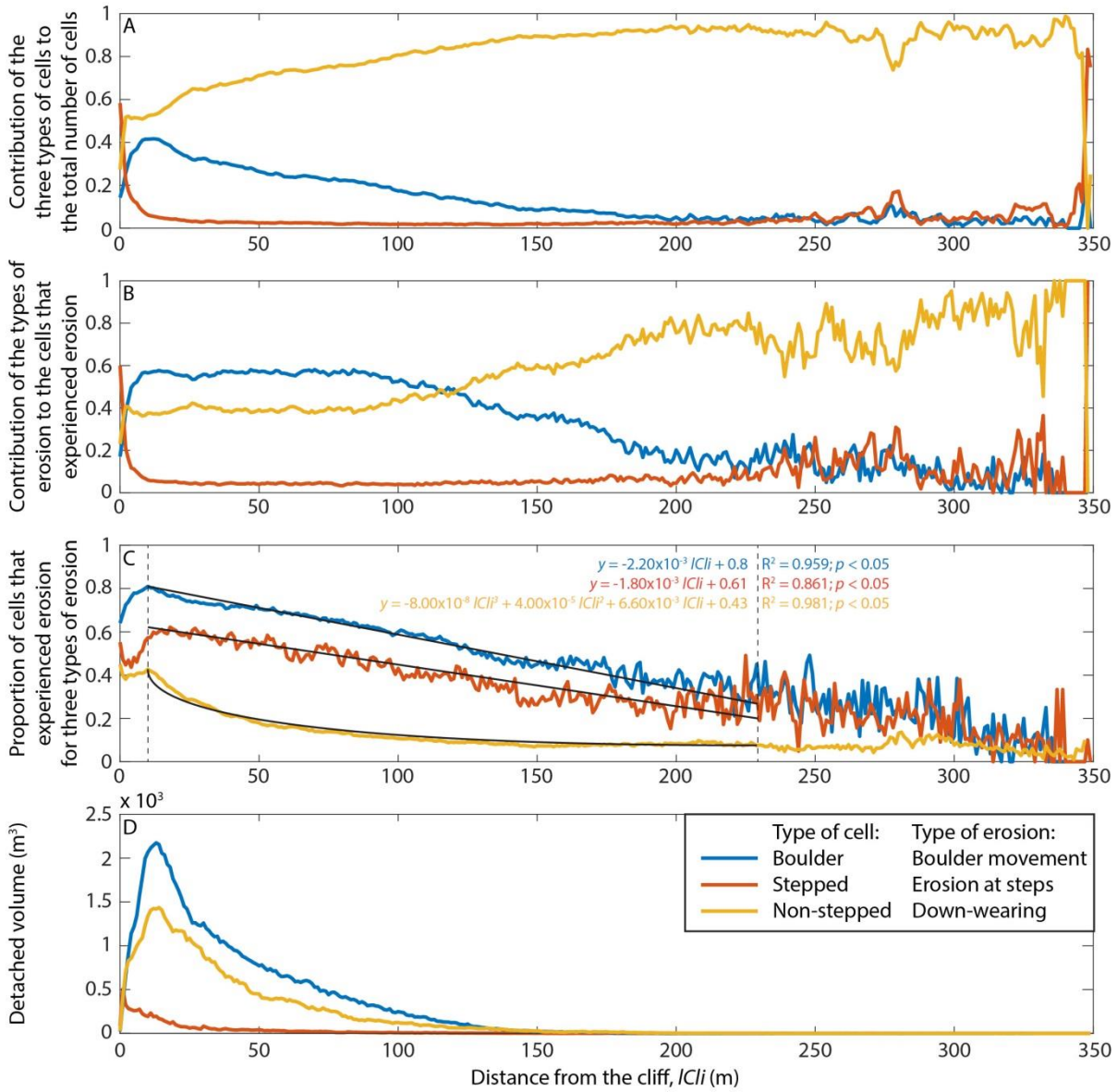


Figure 7.22 Distribution of the three types of cells and erosion across shore platforms binned into 1 m distances from the cliff: A) contribution of the types of cells to the total number of cells; B) contribution of the types of erosion to the cells that experienced erosion; C) proportion of cells that experienced erosion for the types of erosion; the best-fit trendlines are fit to the sections between 10 and 230 m (dashed lines) from the cliff toe: boulder movement and erosion at steps – linear model, down-wearing – 3rd order polynomial model; D) detached volume.

The three types of cells contribute differently to erosion across the platform. At the cliff toe erosion at steps dominates (62.09%), but it drops below 5% 21 m from the cliff. It increases from ~230 m and for the seaward-most 120 m, the value varies between 0 and 40%. Boulder movement is the main component of erosion between 4 and 120 m from the cliff, with 50-60% contribution.

Seawards from 120 m, the down-wearing dominates with a general trend of increased importance with the distance from the cliff (Figure 7.22B).

There is a clear trend that for all three types of erosion the occurrence of erosion decreases with the distance from the cliff (Figure 7.22C). For all types erosion is the highest rates occur between 10 and 18 m from the cliff toe. 78.10% of the boulder cells experience boulder movement at 10 m, 61.30% of stepped cells experience erosion at 18 m and 40.69% of non-stepped cells experienced down-wearing at 10 m from the cliff. Contribution of the cells that experienced erosion is slightly lower or similar (difference of up to 16%) landwards, while seawards this decreases gradually until 230 m. The linear regression trendlines were fitted between 10 and 230 m from the cliff to empirically predict proportion of cells that experienced boulder movement along a coast normal transect (R^2 = 0.959; $p < 0.05$) and erosion at steps (R^2 = 0.861; $p < 0.05$). The third order polynomial model best explains the occurrence of down-wearing (R^2 = 0.981; $p < 0.05$) for the same cross-shore transect. The seaward-most 120 m is characterised by variable rates of all three types of erosion, with the most consistent values of 4-11% for the non-stepped cells (Figure 7.22C). Appendix 9 contains the specific values of the proportion of cells that experienced erosion at the 1 m across-shore intervals.

More material was lost closer to the cliff for all three types of erosion with the peak of the boulder movement at 13 m (2.17×10^3 m^3), the down-wearing at 14 m (1.43×10^3 m^3) and the erosion at steps at 2 m (0.40×10^3 m^3). The volume decreases exponentially with the distance from the cliff and for all types of erosion, it remains under 10 m^3 per 1 m bin for the seaward-most 150 m (Figure 7.22D).

7.2.3. Temporal distribution of erosion

In order to assess how erosion rates vary from year to year, the magnitude of erosion was analysed on the survey-to-survey basis for both the detachment- and the grid cell inventories.

7.2.3.1. Detachment inventory

Total detached volume excluding boulder movement (where the distance between a detachment and a boulder $\neq 0$) in the three epochs varied between 8.58×10^3 m^3 in 2014-2015, and 1.03×10^4 m^3 in 2016-2017. The number of detachments did not vary considerably, with the lowest in 2015-2016 when 9.75% fewer detachments occurred relative to 2016-2017. The erosion rate varied between 3.29 mm yr^{-1} (2015-2016) and 3.40 mm yr^{-1} (2014-2015) (Table 7.11).

Table 7.11 Summary statistics of the erosion variables in the macro-scale detachment inventory excluding boulder movement for the three time periods separately. The actual area and volumes are given while erosion rate is recalculated to a full year using time periods from Table 6.1.

Variable	2014-2015	2015-2016	2016-2017
Total detached area (m^2)	70,710.06	73,522.88	77,675.13
Total detached volume (m^3)	8,581.08	8,820.47	10,271.56
Volume of the smallest detachment (m^3)	3.10×10^{-3}	3.10×10^{-3}	3.10×10^{-3}
Volume of the largest detachment (m^3)	4.21	3.55	2.71
Average detachment volume (m^3)	11.99×10^{-3}	12.99×10^{-3}	13.65×10^{-3}
Standard deviation of detached volumes (m^3)	27.93×10^{-3}	30.25×10^{-3}	33.38×10^{-3}
Number of detachments	715,777	679,046	752,383
Erosion rate (mm yr^{-1})	3.40	3.29	3.36

7.2.3.2. Grid cell inventory

The highest number of analysed cells comes from the 2014-2015 epoch (2.35×10^6 cells). In 2015-2016 the number was lower by 1.59%, and in 2016-2017 by 14.08% (Table 7.12). The average erosion rates of the foreshore were 0.01-0.02 mm yr^{-1} when the boulder movement was excluded. Higher values (0.02 mm yr^{-1}) in 2015-2016 coincides with higher erosion rate at steps of 0.05 mm yr^{-1} as compared to 0.03 m yr^{-1} in 2014-2015, and 0.04 mm yr^{-1} in 2016-2017 (Table 7.12).

Table 7.12 Summary of the total number of non-stepped, stepped and boulder cells and their change for the three time periods separately.

	Non-stepped cells			Stepped cells			Boulder cells			All cells			All excluding boulder cells		
	2014-2015	2015-2016	2016-2017	2014-2015	2015-2016	2016-2017	2014-2015	2015-2016	2016-2017	2014-2015	2015-2016	2016-2017	2014-2015	2015-2016	2016-2017
Total number of cells	1,774,809	1,744,589	1,484,436	68,366	67,389	61,593	507,397	501,162	473,510	2,350,572	2,313,140	2,019,539	1,843,175	1,811,978	1,546,029
Contribution to the total platform area (%)	75.51	75.42	73.50	2.91	2.91	3.05	21.59	21.67	23.45	100.00	100.00	100.00	78.41	78.33	76.55
Number of cells that experienced erosion	248,129	272,249	255,111	32,100	33,304	28,765	334,862	350,188	314,269	615,091	655,741	598,145	280,229	305,553	283,876
Contribution of cells that experienced erosion to the total number of cells (%)	13.98	15.61	17.19	46.95	49.42	46.70	66.00	69.88	66.37	26.17	28.35	29.62	15.20	16.86	18.36
Total detached volume	17,360.23	23,550.22	21,908.56	2,440.42	3,246.20	2,832.91	27,466.12	36,293.31	32,169.31	47,266.77	63,089.72	56,910.78	19,800.65	26,796.41	24,741.48
Erosion rate (mm yr^{-1})	0.01	0.01	0.01	0.03	0.05	0.04	0.05	0.07	0.05	0.02	0.03	0.02	0.01	0.02	0.01

Throughout the monitoring campaign the non-stepped cells contributed to the majority of the platform surface (73.50-75.51%) while the stepped cells formed only 2.91-3.05% of the foreshore. Erosion rates in the non-stepped cells were lower than in the stepped cells with respective average values of 0.01 and 0.03-0.05 mm yr^{-1}

Most stepped and non-stepped cells experienced erosion only during one epoch. Respectively, 15.75% and 20.12% experienced change during two time periods, while 3.17% and 5.48% were eroded during all three intervals. The boulder cells more commonly experienced reoccurrence of the material loss (Figure 7.23).

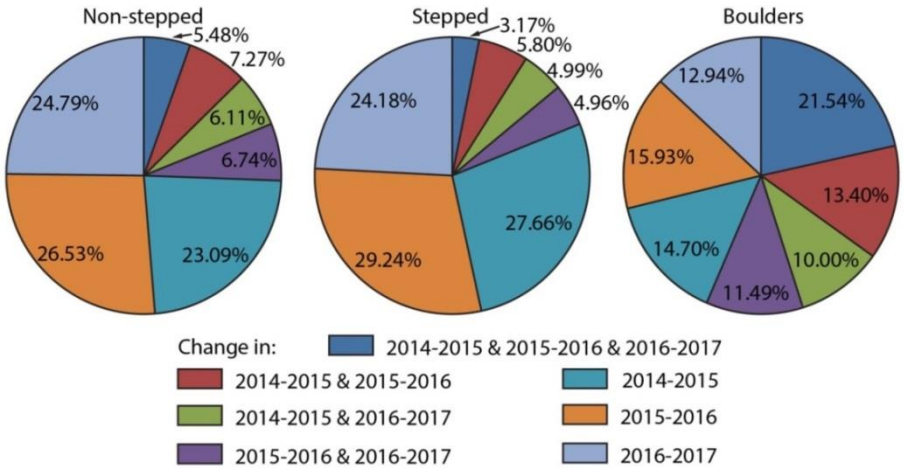


Figure 7.23 Reoccurrence of erosion in the non-stepped, stepped and boulder cells.

7.3. Discussion

7.3.1. Putting erosion rates in context

Erosion rates of 6.36 mm yr^{-1} calculated on the basis of detachment inventory are in the same order of magnitude as the down-wearing rates of 3.21 ± 4.76 mm yr^{-1} measured by Robinson (1977a) along the same stretch of the North Yorkshire coast, and the global platform erosion rates of 1.15-1.49 mm yr^{-1} (Stephenson and Finlayson, 2009; Dasgupta, 2010). Similar rates were obtained in previous studies and in this research, despite both different monitoring techniques and scale. While the previous studies are based on micro-erosion meter (MEM) readings (section 2.3.1), here the LiDAR dataset is used to produce maps at 0.25 m resolution to detect vertical change of < 0.05 m.

Detachments are likely to represent bedrock erosion, biological activity and sediment movement (Figure 6.2). The attempt to separate bare rock from vegetation based on the LiDAR-derived RGB maps was considered unsuccessful because the magnitude frequency and 3D shape distributions of detachments in the two subsets are alike (Table 7.4; Figures 7.6 and 7.7). However, the field evidence shows that dense vegetation is concentrated in the lower sections of the platform

where standing water is more common and so pixels tend to have no elevation data as the LiDAR could not measure over these areas, and so they were filtered out. The change in vegetation around the high-tide level is lower than the monitoring resolution and should not be detected as a change, which is also the case of dynamics of the animals such as barnacles, snails and limpets. This suggests that most of detected change is related to bedrock erosion.

Removing boulders resulted in filtering out 2.48×10^4 m^3 of the apparent detached volume and a corresponding decrease in erosion rate to 3.45 mm yr^{-1}. This rate is of a similar order to the rates of 0.20-2.80 mm yr^{-1} on the shale platform in Algarve, Portugal (Andrade et al., 2002) and of 0.94 ± 1.20 mm yr^{-1} (Porter and Trenhaile, 2007) and 1.25 mm yr^{-1} (Porter et al., 2010b) on the sandstone platform of the Bay of Fundy, Canada, calculated using MEMs. As most studies which consider foreshore erosion at the macro-scale (10^{-1} – 10^1 m) lack quantification of erosion rates (Cruslock et al., 2010; Naylor and Stephenson, 2010; Stephenson and Naylor, 2011), the results are difficult to compare. Dornbusch and Robinson (2011) reported the down-wearing equivalent of step back-wearing of 0.60-4.90 mm yr^{-1} in Sussex, UK. However, their study was conducted on chalk platforms, which are believed to erode faster than siliciclastic sedimentary rocks (Dasgupta, 2010), and they focused only step back-wearing, which is not the case in here.

Erosion rate calculated on the basis of 1 m^2 cells of 0.01 mm yr^{-1} and excluding the boulder cells, is two orders of magnitude lower than that calculated for the detachment inventory (3.45 mm yr^{-1}), which is the reflection of the method used to derive the rates. In case of the detachment inventory, erosion was calculated as the sum of detached volumes divided by the total area of the platform by the total time. In case of the analysis based on the grid cell inventory, the erosion rates were calculated as a mean of erosion rates for each cell. Because erosion rates per cell are calculated by dividing detached volume by the area containing data (based on pixels at 0.25 m resolution) rather than by 1 m^2, they are arguably more credible than the rates obtained for the event inventory (see Appendix 2).

The cells containing boulders are removed even though within such cells both a boulder movement and/or the bedrock erosion may happen, for example through abrasion by clasts (Cullen and Bourke, 2018). The purpose of excluding these cells is to completely exclude boulder dynamics from analysis, as its inclusion could overestimate erosion rates. Because erosion rate is calculated on the grid cell basis rather than from the total foreshore area, exclusion of the boulder cells does not impact calculated rates, while a great deal of cells with no boulders (5.20×10^6) are available to calculate statistically-significant rates. The stepped cells erode at an average rate of 0.04 mm yr^{-1} while the non-stepped cells erode at 0.01 mm yr^{-1}, which supports the statement that the wave energy concentrates on these protruding surfaces locally increasing erosion rates (Moses and Robinson, 2011).

The erosion rates reported in here are much lower than those measured with MEMs (Robinson, 1977a). It is possible that different spatial scales of the studies make the results incomparable, but also perhaps complimentary as at different scales different processes dominate erosion. The effects of grain-by-grain abrasion or detachment of rock pieces at scales less than the present resolution of 0.25×0.25×0.05 m, such as detachment of shale lattices or thin sandstone layers (Chapter 5) cannot be detected. On the other hand, larger-scale detachments or zones of multiple smaller detachments beyond vertical and horizontal reach of MEMs can be identified (Trenhaile, 2002; Moses, 2014), which suggests that total platform erosion (volume and rates) should be calculated as the cumulative contribution of the micro- and macro-scale detachments.

An alternative possibility to explain lower erosion rates at the macro-scale is the fact that larger events occur with a much lower frequency, which was demonstrated for a wide range of physical phenomena such as rockfall (Dussauge Peisser et al., 2002; Malamud et al., 2004; Guzetti et al., 2009). The time period of 2.62 yr between the first and the last LiDAR surveys might not have been long enough to provide a representative magnitude-frequency distribution of detachments at the macro-scale (10^{-1} – 10^{1} m) because the largest events may have a longer reoccurrence period (Lee et al., 2001).

7.3.2. Mechanisms of erosion

The area volume exponent b = 1.214 is within the range recorded for landslides and rockfall (Williams et al., 2018). However, because on slopes gravity plays an important role in generating shear stresses along shear planes (Guzetti et al., 2009; Larsen et al., 2010) and near-surface tensile stresses (Rosser et al., 2007; Williams et al., 2018), it is difficult to directly link results of this research with these previous studies. The diversity of rock type and water/sediment dynamics on the foreshore suggest that the rock micro-structure and the spatially-variant compressive, shear and tensile stresses make the erosion process fundamentally complicated. The relatively low strength of this relationship (R^2 = 0.647; $p < 0.05$) suggests that there may not be a single operating mechanism which can be deduced from the exponent b value.

A volume-frequency exponent β = 1.513 is within the range of 0.71-2.37 documented for rockfall from the nearby coastal cliffs (Rosser et al., 2007; Barlow et al., 2012; Whadcoat, 2017; Williams et al., 2018). The comparison is made because the same rock types build cliffs and platforms in the study area, and so similar values may indicate importance of rock type or structure. High β means a higher proportion of small events, and on hillslopes it is believed to represent structural control (Hungr et al., 1999). However, the planform joint density on the North Yorkshire shore platforms is > 1 joint m^{-2} and if this dominates detachment sizes (Stephenson and Naylor, 2011), the consequence would be a higher proportion of larger volume detachments and, in consequence, a lower

value of β. The dominance of small detachments at the *LoD* and pixel resolution scale (minimal detectable volume V_{min} = 3.13×10^{-3} m^3) may suggest that the smaller-scale discontinuities, such as weathering-induced cracks and within-bed laminations, control the size of detachments. These discontinuities may be opened, widened or excavated during the weathering processes, such as wetting and drying, warming and cooling, and salt crystallisation, or through biological activity or fatigue (Robinson, 1977a; Sunamura, 1992; Stephenson and Kirk, 1998, 2001; Coombes, 2014).

An alternative mechanism is detachment of rock fragments of the order of 10^{-3} m^3, whose morphology does not reflect the discontinuity pattern. Hydraulic action and the impact of wave-carried boulders may cause erosion at locations of higher relief, such as steps, slopes and protrusions (Knight and Burningham, 2011). Non-stepped high-relief locations may be related to local differences in rock hardness, for instance the presence of an ironstone nodule embeddded in the foreshore. Uneven terrain makes flow dynamics complex and a positive feedback may exist where the irregular relatively small blocks are detached and expose new irregular surfaces (Lamb et al., 2015).

Although the volume-frequency distribution closely follows a power-law (R^2 = 0.927, p < 0.05), it seems to be composed of two sections with volumes smaller and larger than 10^0 m^3 (Figure 7.4). This may suggest that different mechanisms dominate erosion at different scales or that there is an underrepresentation for the largest volumes caused by too short a monitoring period. In the former case, the two sub-populations may be detachments of rock fragments at the irregular but non-stepped surfaces and irregular blocks fractured from the step edges by the wave-carried boulder impacts ($\leq 10^0$ m^3) and blocks detached from the steps along pre-existing joints ($> 10^0$ m^3), but this cannot be verified with the present data. A possible way to verify this may be a high-frequency monitoring of erosion during high-magnitude storms (Naylor et al., 2016) using high-resolution techniques to reconstruct topography, such as TLS or UAV-based SfM.

The observed dominance of the *very bladed* slab-like detachments (Figure 7.5) can be indicative of either the erosion of the relatively thin rock layers where the thickness depends on the rock structure and the planform of detachment on the drag-and-lift force, or relatively short, but deep and wide detachments at the step edges.

The division of the cells into those with and without steps was motivated by a need to assess the potential contribution of step back-wearing to overall platform erosion. Detected erosion is unlikely to represent the effect of the grain-by-grain abrasion due to the relatively large *LoD* = 0.05 m. It is probable that splitting the platform into these two groups allows identification of the difference in the magnitude and frequency of erosion, rather than the process itself. The adopted method does not account for different mechanisms at steps such as the removal of blocks with structurally-controlled morphology and localised fracturing due to the impact of wave-carried boulders (Moses and Robinson, 2011). Steps protruding from the platform concentrate wave energy, while the bedding

plane that is commonly at their foot may be exploited via cavitation and weathering prior to detachment, which may facilitate erosion (Moses, 2014). The results confirm this notion as almost half of the cells with a step experience detachment, whilst only 15.50% of the cells with no steps experience erosion (Table 7.6). The intensity of erosion is also reflected by the size of detached material with the mean detachment volume two-times larger in the stepped as compared to non-stepped cells (Table 7.5).

7.3.3. Explaining the spatial distribution of erosion

Spatial distribution of erosion was analysed on the basis of a 1 m grid in order to 1) understand whether erosion rates vary in space or are uniform across the foreshore; 2) identify locations of higher erosion rates; 3) find controls on spatial distribution of erosion; 4) predict occurrence of erosion at any point of the platform on the cell-by-cell basis; 5) predict across-shore probability of erosion as a function of the distance from the cliff; and 6) predict erosion rates.

7.3.3.1. Distribution of erosion on a cell-by-cell basis

Erosion in the non-stepped cells is infrequent at the present resolution, as it is experienced at 15.50% cells only, and its spatial distribution can be successfully predicted (P = 0.8781; Figure 7.11). The decrease in erosion with the distance from the cliff agrees with existing models on shore platform evolution (Flemming, 1965; Sunamura, 1992; Kline et al., 2014; Matsumoto et al., 2016) and the field studies on the micro-erosion (Robinson, 1977a; Stephenson and Kirk, 1998; Foote et al., 2006; Moses and Robinson, 2011). The positive relationship between the occurrence of erosion and slope confirms that protruding and inclined surfaces concentrate and are exploited by wave energy (Moses and Robinson, 2011).

It is more difficult to predict the occurrence of erosion at stepped locations than for a non-stepped surface. 69.03% of cells have been correctly classified using only the local value of slope (Figure 7.17). It is possible that a sub-population of cells which contain an irregular step and a rough surface above and/or below with a high average slope (Figure 7.24). These cells may experience smaller scale detachments at the edges of the step and elsewhere as compared to near-vertical steps which delimit adjacent smooth surfaces.

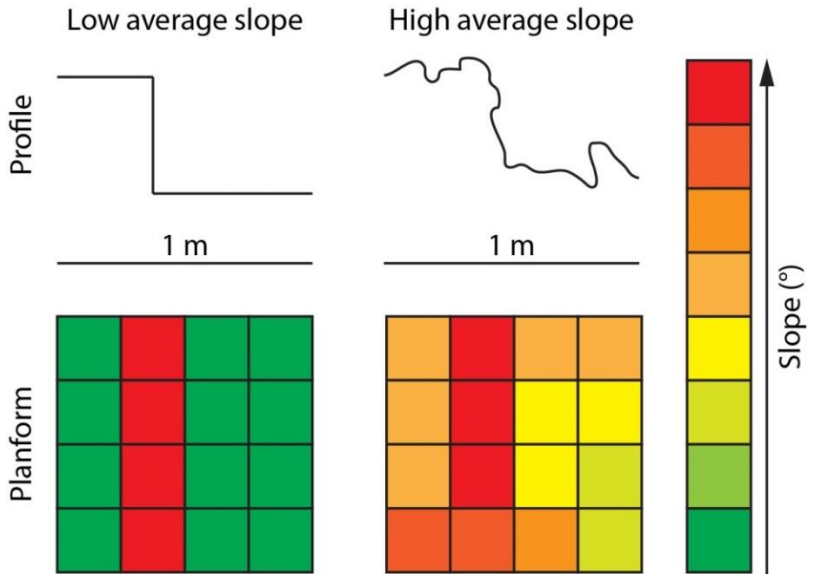


Figure 7.24 Conceptualised topography of stepped cells with different average slope, which may explain possibility to predict occurrence of erosion on the basis of slope.

Alternatively, it is possible that the independent variables considered do not control the distribution of erosion at steps, and other factors should be considered. These may include information about the 3D discontinuity pattern (Cruslock et al., 2010; Naylor and Stephenson, 2010) and wave pressure at different locations at, and adjacent, to the step (Poate et al., 2018).

The multiple linear regression models were unsuccessful in predicting the magnitude of erosion at both the stepped and the non-stepped surfaces. There are two possible explanations for this. Firstly, the 11 independent variables may not control platform erosion in its entirety, and other factors may be important. These may include the smaller-scale discontinuities, rock strength, the morphology of the platform seaward from detachment location, and/or wave conditions (Naylor and Stephenson, 2010). For example, at steps, the depth of detachments may be a function of bed thickness, while the planform dimensions may reflect the interplay between rock structure and wave energy (Regnauld et al., 2004). Secondly, detachments unrelated to block removal along pre-defined joints (e.g. Figure 3.11C) may be the larger-scale equivalent of detachments of clusters of shale platelets and sandstone layers observed previously (see: Chapter 5). Drawing on the general pattern of event frequency decreassing with higher magtniude event observed for other physical phenomena (Malamud et al., 2004; Guzetti et al., 2009), detachments at the scale detectable using the present method (V_{min} = 3.13×10^{-3} m^3) are likely to occur with a lower frequency than for small-scale detachments because more intense waves are needed to detach larger blocks (Dornbusch and Robinson, 2011). The monitoring period of 2.62 yr may be too short to include a full range of erosion events and rates, and so the observed distribution may be censored.

7.3.3.2. Across-shore distribution of erosion as a function of the distance from the cliff

As erosion rates cannot be predicted for any point of the foreshore on a cell-by-cell basis, the cells were collapsed into a single cross-shore transect in order to predict the distribution of erosion as a function of the distance from the cliff. The results provide a systematic and statistically-significant empirical dataset which can be used in numerical models to reconstruct past cliff retreat rates using cosmogenic isotope concentrations (Regard et al., 2012; Hurst et al., 2016; 2017) and to predict coastal evolution (Trenhaile, 2000; Kline et al., 2014; Limber et al., 2014; Matsumoto et al., 2016).

A larger average number of 0.25×0.25 m pixels within each 1 m^2 cell (Figure 7.7 and Figure 7.20A) closer to the cliff toe results from the variable platform width and the submergence or wetness (standing water) of the seaward sections of the platform. The gradual decrease in the number of pixels per cell between 50 and 220 m may be related to the increasing contribution of wet surfaces and unreflective and hence invisible to LiDAR vegetation (Figure 7.9). There are two possible explanations for the observation that both the highest proportion of cells experiencing erosion at 13 m, the largest detached volume at 13 m, and the highest contribution of cells which experienced erosion in each of the three types at 10-18 m from the cliff. Firstly, the filtering out the cells containing a beach deposit may imply recording of lower erosion rates at the landward-most part of platform, as the deposits, which tend to concentrate on the landward-most portion of the foreshore, can serve as an abrasive tool intensifying erosion (Kline et al., 2014). Secondly, this distance from the cliff may coincide with the highest eroding force of waves related to:

- constructive interference of incoming waves and waves reflected from the cliff for waves of ~30 m length may result in the most energetic conditions at some distance form the cliff toe;
- breaking of the most energetic waves as waters shallow (Matsumoto et al., 2016);
- entraining boulders and sediments by breaking waves and their impact on bedrock (Moses and Robinson, 2011); note that at 4-14 m from the cliff the proportion of the boulder cells is at its highest (Figure 7.22A);
- coincidence with MHWN = 1.50 m AOD where the frequency of the submergence/emergence transition is the highest, and so the physical weathering of the foreshore may be the most efficient (Porter et al., 2010a); and
- transition between planar part of the platform and the sloping ramp (Robinson, 1997a).

A clear pattern in cross-shore distribution of the three types of erosion can be seen in Figure 7.22. A higher proportion of the boulders at the high-tide level may be a reflection of the general landward migration of boulders, while their presence at the seaward portion of the platform may link to higher contribution of steps as boulders tend concentrate and become stuck at their foot (Paris et al.,

2011). The highest proportion of the stepped cells at the seaward- and landward-most portions of the foreshore can reflect the large-scale structure of the coast including the bedding and faults (Rawson and Wright, 200). Alternatively, it can be considered in terms of the long-term coastal evolution where steps present below MLWS and above MHWS are subjected to relatively low wave forces as compared to the elevations between these thresholds (Trenhaile, 2000). This scenario implies that the steps would persist as these locations for longer periods while steps at intermediate elevations would back-wear faster. No studies exist on the cross-shore distribution and dynamics of the steps, so this scenario remains speculative. My observations however generally agree with the across-shore distribution of wave energy as reported by Matsumoto et al. (2016).

The dominant contribution of non-stepped cells across the foreshore, and in particular at its seaward portion, is a reflection of platform morphology where majority of the surface is neither stepped, nor covered by boulders (Figure 7.22A). However, although the population of the non-stepped cells is higher than that of the boulder and the stepped cells, the proportion of cells which experience erosion is lower. The underlying reason may be the concentration of wave energy on protruding surfaces (Moses and Robinson, 2011) and physical difficulty of detaching material of detectable sizes ($> V_{min}$) from a planar surface, which restricts detected erosion at the non-stepped cells to parts of the foreshore characterised by higher roughness, for example due to the presence of hard-wearing ironstone nodules (Figure 3.11F).

The proportion of the three types of cells which experience erosion can be predicted for the majority of the foreshore profile as it is linearly (boulder and stepped cells) or polynomially (non-stepped cells) distributed between 10 and 230 m from the cliff (Figure 7.22C). This is an important finding, because the large sample size (order of magnitude = 10^6), and strength model fit (R^2 = 0.861-0.981), makes the relationship highly significant ($p < 0.05$), and so it can be used as an empirical dataset of the across-shore probability of shore platform erosion (Appendix 9).

7.3.4. Temporal distribution of erosion

Erosion rates for the three survey epcohs are similar, within both the event- and the grid cell inventories with respective value ranges of 3.29-3.40 and 0.01-0.02 mm yr^{-1}. Erosion rates are more likely to change at the intra-annual scale, at which either higher storminess and in consequence higher wave energy in winter months, can detach rock fragments (Knight et al., 2009; Naylor et al., 2016) or conversely, the increased of weathering efficiency in summer months can contribute to material loss (section 5.3.3.1). The low reoccurrence of detachments in the stepped and non-stepped cells (Figure 7.23) may suggest that at this relatively large-scale erosion happens episodically, so that the location of the next detachment cannot be predicted from preceding detachment location, or that the monitoring period was not long enough to detect patterns in the reoccurrence of detachments (see

section 7.3.3.1). It has also been suggested elsewhere that the responses of a rocky coast system to erosion can be lagged (Trenhaile, 1987; 2002). Conversely, boulder movement is likely to occur in the same area (Figure 7.23), which may reflect the redistribution of the material within boulder fields, gradual movement of boulders within single cells, and the detachment of fragments of larger boulders (Knight and Burningham, 2011; Naylor et al., 2016).

7.4. Summary

The application of the set of novel methods presented in Chapter 6 on 3.15×10^{6} m^2 of the North Yorkshire shore platform resulted in the detection of 2.15×10^{6} discrete detachments (pixel resolution: 0.25 m), which is equivalent to 2.77×10^{4} m^3 detached bedrock or erosion rate of 3.45 mm yr^{-1}. At this scale (10^{-1} – 10^{0} m), foreshore erosion seems to proceed via detachment of rock fragments. The feasibility to predict erosion at any point on the platform, and then by representing the foreshore as a single across-shore profile, was systematically assessed on the basis of 1 m^2 grid cells, which were divided into three erosion types: the boulder, the stepped and the non-stepped cells. The non-stepped part of the platform erodes at 0.01 mm yr^{-1} via down-wearing, while the stepped area erode at 0.04 mm yr^{-1}, with the average foreshore erosion rate approximately = 0.01 mm yr^{-1}.

Although the location of erosion at the non-stepped part of the foreshore can be successfully predicted (87.81%), knowing distance from the cliff and slope, the attempt to predict both occurrence of erosion at steps and the erosion rates for both types of cells was unsuccessful. Collapsing the cells into a single across-shore profile allows for the prediction of the probability of occurrence of erosion for the three types of erosion with the most erosion occuring 10-18 m from the cliff with a corresponding gradual decrease seawards, the character of which closely follows both a linear and polynomial form (R^2 = 0.861-0.981; $p < 0.05$). The results can serve as a high-resolution systematic empirical dataset to feed coastal evolution models. They should also be directly compared to the model set-up and results of Matsumoto et al. (2016), as a similar pattern of increased erosion around MHWN was assumed in their model and observed in here.

8. The importance of shore platform erosion in reconstructing past cliff retreat using cosmogenic ^{10}Be concentrations

8.1. Introduction

It is important to understand long-term cliff erosion to be able to predict changes anticipated under sea-level rise and increased storminess (Slott et al., 2006; IPCC, 2013). Existing numerical models of long-term rocky coast evolution are based on either theoretical or short-term (up to decades) empirical understanding of cliff dynamics (Trenhaile and Byrne, 1986; Lee et al., 2001; Walkden and Hall, 2005; Dickson et al., 2007; Trenhaile, 2010; Barlow et al., 2012; Kline et al., 2014; Limber et al., 2014; Matsumoto et al., 2016). However, their accuracy cannot be assessed without direct quantification of long-term cliff retreat rates, which implies that their predictive ability remains largely unknown (Trenhaile, 2014). Models must therefore be coupled with absolute dating to identify likely scenarios of cliff retreat over centennial to millennial timescales. A better understanding of past cliff dynamics under known marine conditions can help model future changes under predicted scenarios of sea-level change (IPCC, 2013).

Reconstructing the long-term evolution of rocky coastlines is challenging due to the destruction of geomorphological evidence of past cliff positions and the lack of datable sediments (Trenhaile et al., 1999). As such, our understanding of coastal dynamics is limited to insights gleaned from contemporary field monitoring and cartographic data (Moses and Robinson, 2011; Lim, 2014). The limited duration of these data and monitoring biases our understanding, and prevents us from reliably assessing long-term coastal change (Trenhaile, 2014). In particular, short-term monitoring data are problematic because they may under- or over-represent high-magnitude, low-frequency retreat events (Lee et al., 2001; Recorbet et al., 2010) and cannot provide insight into feedbacks between retreat rates and variable foreshore geometry, notably platform width, elevation and slope (Masselink et al., 2011). Moreover, the responses of rocky coasts to the causes of change, such as sea level and storminess, are often indirect and lagged (Trenhaile, 1987; 2002).

The aim of this chapter is to identify the likely scenarios of long-term cliff retreat rates from cosmogenic ^{10}Be concentrations combined with numerical modelling for a profile across the Hartle Loup platform (Figure 8.1). The role of shore platform erosion in long-term coastal evolution is explicitly explored since these features play a pivotal role in wave transformation and energy delivery to the cliffs (Dickson et al., 2013; Ogawa et al., 2015; Poate et al., 2018), but their morphology and dynamics have commonly been oversimplified in existing coastal models (Trenhaile, 1983; 2000; Walkden and Hall, 2005; Kline et al., 2014; Limber et al., 2014). An assessment is made of the extent to which our understanding of past cliff retreat rates depends on the adopted model of shore platform

erosion. Topographic change detection and morphological evidence suggest that platforms do erode (Robison, 1977a; Stephenson and Kirk, 1998; 2001; Cruslock et al., 2010; Dornbusch and Robinson, 2011) and even if the erosion rate is very low, the millennial time-scales of the exposure dating make it a factor which most likely should not be omitted when modelling exposure ages from ^{10}Be concentrations.

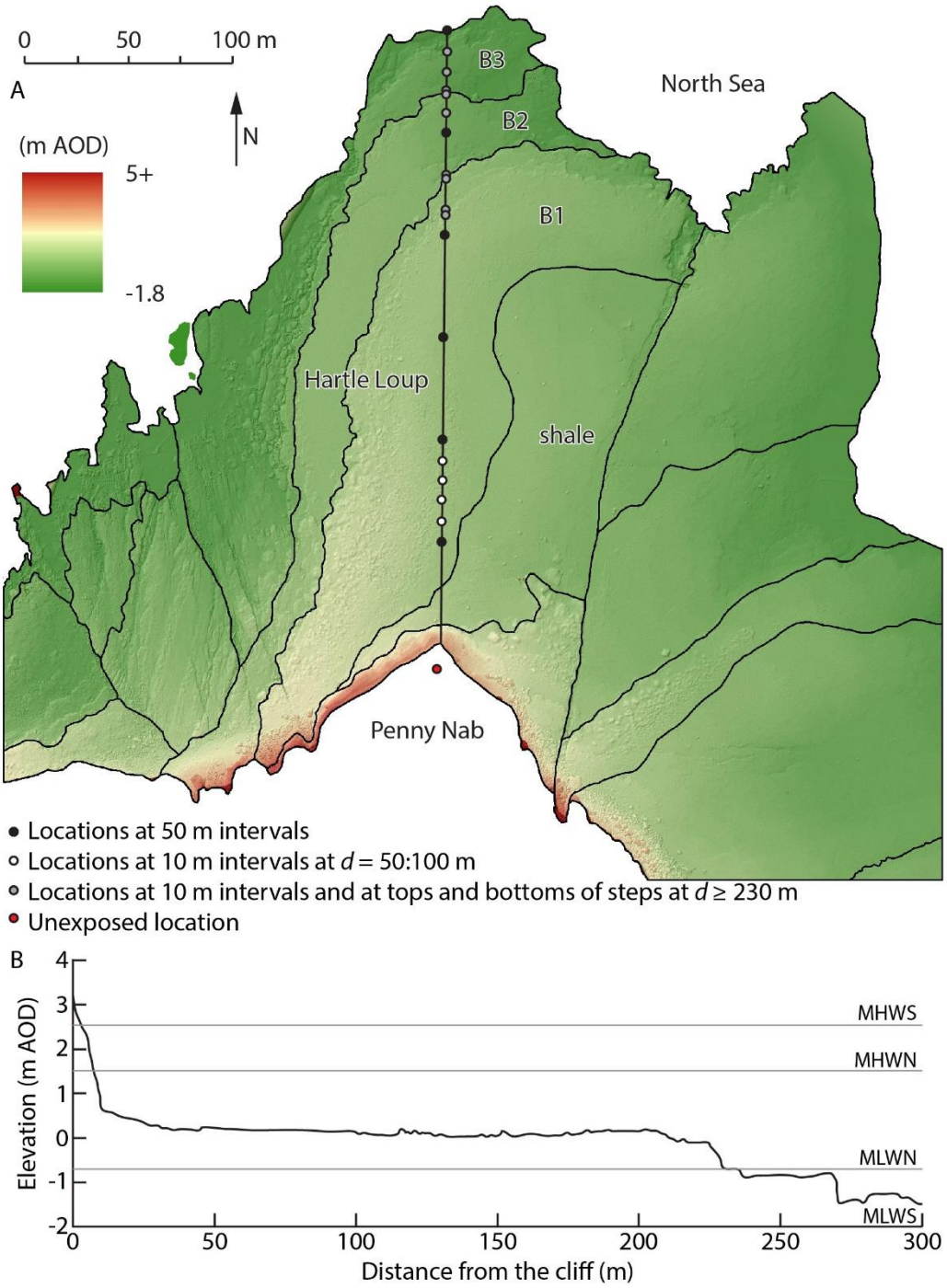


Figure 8.1 A) Location of the sampling profile across Hartle Loup. Relevant rock beds are labelled. B) Elevation distribution across the profile indicated in A). Background: the LiDAR2016 DEM at 0.1 m resolution overlaid by a hillshade at 70% transparency.

The chapter is divided into three parts. Firstly, it describes a set of models developed to calculate expected ^{10}Be concentrations in the foreshore rock samples. The general model includes topographic and water shielding, and a geomagnetic scalar under the assumption of negligible platform erosion. Then different theoretical models of platform down-wearing and step back-wearing are explored to investigate how current understanding of platform erosion determines our understanding of past cliff retreat. Finally, the empirical model of platform erosion based on controls on its spatial distribution (Chapters 5 and 7) is applied.

Secondly, the procedure and results of calculating ^{10}Be concentrations across the Hartle Loup shore platform are described. The sampling strategy is designed to 1) calculate average cliff retreat rates during the Holocene, 2) account for shorter-term (decades to centuries) changes in cliff dynamics, and 3) understand the long-term step back-wearing and the small-scale (metre) variability in ^{10}Be concentrations as a function of rock type and relief. The laboratory procedure to separate beryllium atoms from fine-grain quartz (53-106 μm fraction) and the results of accelerator mass spectrometry (AMS) is described. Finally, the numerical modelling and cosmogenic ^{10}Be concentrations are combined to reconstruct past cliff dynamics by finding the most likely scenarios of platform erosion and cliff retreat.

8.1.1. Cosmogenic isotopes: background

Cosmic rays, high-energy charged particles that bombard the Earth from space, are affected by the Earth's magnetic field (Dunai and Lifton, 2014). In the upper atmosphere, the primary rays react with gas nuclei, such as N, O and Ar, forming secondary cosmic rays. During spallation high-energy nucleons: protons and neutrons (96.4%), and low-mass muons (3.6%) form. When the secondary particles reach the surface of the Earth, they collide with atoms in the rock producing cosmogenic nuclides *in situ*. The main products are the radioactive nuclides ^{10}Be, ^{14}C, ^{26}Al and ^{36}Cl, and the stable noble gases – ^{3}He and ^{21}Ne (Dunai, 2010; von Blanckenburg and Willenbring, 2014).

These nuclides have been used to reconstruct exposure and burial ages, erosion, denudation and uplift rates, and soil dynamics on timescales of hundreds to millions of years. The choice of a specific nuclide depends on the timescale of interest and the rock type available (Alvarez-Marrón et al., 2008; Darvill, 2013). For instance, rocks containing quartz can be analysed using ^{10}Be and/or ^{26}Al, while ^{36}Cl can be used in feldspar- or calcite-rich rocks (Table 8.1). Cosmogenic nuclides are used to analyse such phenomena as glacial advance and retreat, fault movements, lava flows, landslides, meteorite impacts and coastal cliff retreat (Fifield, 1999).

Table 8.1 Characteristics of the main cosmogenic nuclides; based on: Darvill (2013) and von Blanckenburg and Willenbring (2014).

Nuclide	Half-life (kyr)	Production rate (atoms g^{-1} yr^{-1})	Target minerals
^{3}He	Stable	75-120	Olivine, pyroxene
^{10}Be	1,389 ± 14	4-5	Quartz
^{14}C	5.73 ± 0.03	18-20	Quartz
^{21}Ne	Stable	18-21	Quartz, olivine, pyroxene
^{26}Al	708 ± 17	35	Quartz
^{36}Cl	301 ± 2	70 (calcite) / 200 (feldspar)	K-feldspar, calcite

In general, higher concentrations of cosmogenic nuclides characterise surfaces that have been exposed for longer durations. The cosmogenic nuclide production rate is dependent on the altitude, latitude and depth of the sample considered. The cosmic flux and consequently the production rate change through time depending on the geomagnetic field intensity (Kim and Sutherland, 2004). Moreover, in the case of radioactive nuclides, if the surface has been buried the nuclides decay and their concentration decreases. The rate of decay depends on the nuclide half-life (Table 8.1). To calculate burial ages and/or reconstruct the complex exposure/burial history, a combination of two isotopes, ^{26}Al and ^{10}Be or ^{26}Al and ^{21}Ne can be used because of different production and decay rates (Dunai, 2010; Darvill, 2013). Additional important factors to consider while calculating dates from nuclide concentrations are: shielding – partial or total reduction of the cosmic ray flux delivered to the surface due to blocking/absorbtion of the cosmic ray flux – by terrain and water, erosion, inheritance and elevation change (Darvill, 2013).

8.1.2. Exposure dating in rocky coast studies

The first study which used cosmogenic isotopes to date marine terraces was conducted by Stone et al. (1996) who, through the use of ^{36}Cl in calcareous schists, established that the Main Rock Platform in Western Scotland had been entirely formed in the Holocene. Perg et al. (2001) used ^{10}Be and ^{26}Al in vertical profiles of sandy deposits to confirm the interglacial age of raised terraces along the coast of Santa Cruz, California. Kim and Sutherland (2004) used the same pair of isotopes to date uplifted granite platforms and boulders. Combining ^{10}Be, ^{26}Al and ^{21}Ne, Alvarez-Marrón et al. (2008) accounted for periods of burial, expanded the dating time of marine terraces to millions of years, and in consequence established the age of a 100 km long quartzite raised marine terrace in Northern Spain at 1-2 Myr. Depending on the rock type, Recorbet et al. (2010) used ^{10}Be and ^{36}Cl on the coastal cliff face and collapsed blocks in Southern France to date cliff failure events to 3.5-6.7 kyr BP and to establish the average cliff retreat rates to 5.00×10^{-3} m yr^{-1}. Rogers et al. (2012) dated the lag boulders

from a bluff across the shore platform on Whitbey Island, Washington, demonstrating the utility of exposure dating to reconstruct coastline evolution in areas of thick sediment cover.

The first studies to calculate ^{10}Be concentrations in bedrock forming an active shore platform in order to reconstruct past coastline evolution were conducted by Choi et al. (2012) and Regard et al. (2012). Choi et al. (2012) noted that the shore platforms in Western Korea are partly inherited from the last interglacial. Regard et al. (2012) found that up to 600 m wide chalk platforms on the southern coast of the English Channel were entirely formed in the Holocene which means that their minimal average cliff retreat rate is 0.10 m yr^{-1}. Hurst et al. (2016) demonstrated an acceleration of cliff retreat in the last 150 yr in East Sussex, UK, quoting a rate of 0.22-0.32 m yr^{-1} derived from historical maps relative to the average 0.02-0.06 m yr^{-1} in the Holocene obtained using cosmogenic ^{10}Be concentrations.

Modelling exposure ages from the isotope concentrations requires taking into account various factors contributing to the final isotope concentration. The accuracy of results depends on adopted assumptions about isotope production rates, cliff retreat rates and patterns, inheritance, shielding factors and surface vertical erosion. For instance, Kim and Sutherland (2004) assumed no inherited signal and a lack of vertical bedrock erosion. Both assumptions are unlikely (Hurst et al., 2017) yet they strongly affect the modelling results. Rogers et al. (2012) took into account tidal duration distribution and potential gradual and episodic cliff retreat but did not account for potential inheritance of isotope concentrations. Choi et al. (2012) included topographic shielding by the cliff. Assuming that the platform erodes proportionally to cliff retreat (Figure 2.2A), Regard et al. (2012) showed that faster cliff retreat means lower ^{10}Be concentrations. As the cliff retreats, bedrock with the highest ^{10}Be concentrations is gradually removed from the platform surface due to down-wearing, exposing rock mass with lower concentrations. Tides contribute to the reduction of ^{10}Be production in the upper parts of the platforms and its increase in the lower parts. Rising sea level reduces down-wearing rates which results in higher concentrations of ^{10}Be. A ‘hump’ in ^{10}Be concentrations across the platform exists which results from the competition between the duration of exposure and water shielding (Figure 8.2A). A larger tidal range results in a less pronounced ‘hump’ at a more seaward location. Regard et al. (2012) expected an abrupt tenfold change in isotope concentrations at a potential boundary between a section closer to the cliff formed entirely in the Holocene and a section inherited from previous high-stands of the sea, with the latter having higher concentrations (Figure 8.2B). The main premise for this hypothesis is that current rates of coastal retreat are too low to explain the formation of wide shore platforms since 6-10 kyr BP, when the sea reached a level at which it could affect sections of platform exposed today (Trenhaile et al., 1999; Masselink et al., 2011). Regard et al. (2012) could not see this change and so assumed that the platform was entirely formed during the Holocene.

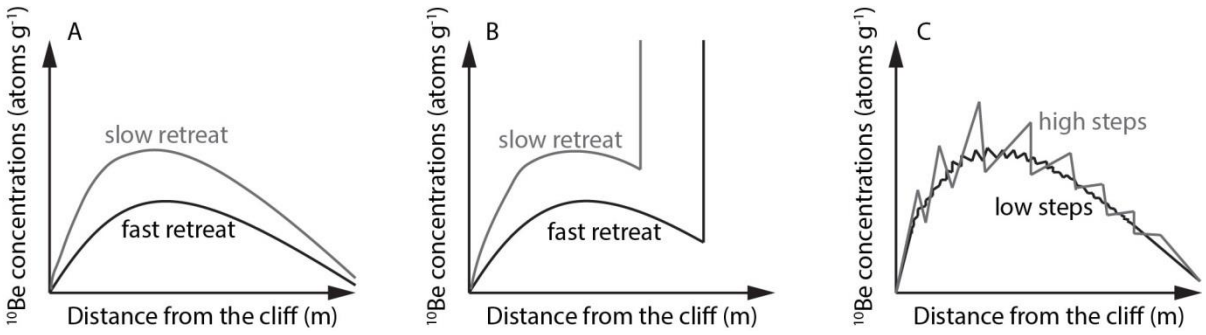


Figure 8.2 The distribution of ^{10}Be concentrations across a gently sloping shore platform: A) the apparent hump in concentrations results from the interplay between exposure ages and water shielding; B) an abrupt increase in concentrations for a portion of the platform inherited from the last interglacial; C) a saw-toothed distribution superimposed on the hump due to step back-wearing; based on Regard et al. (2012) and Hurst et al. (2017).

Hurst et al. (2017) explored factors which affect the across-shore distribution of ^{10}Be. In their model they included topographic and water shielding, mechanisms of platform erosion, the presence or absence of beach deposits and transience in shore platform evolution. They highlighted that the assumption of parallel coastal evolution is not consistent with process-based model predictions and assumed that platform erosion is proportional to the availability of wave energy and is a function of the breaking wave height (see Matsumoto et al., 2016). When a platform erodes via step back-wearing, a 'saw-toothed' distribution of ^{10}Be concentrations is superimposed on the 'humped' distribution, and the size and frequency of steps control the magnitude and frequency of the distribution variability (Figure 8.2C). The presence of beach deposits also affects concentrations but the simulations of Hurst et al. (2017) showed that it is of marginal importance whether the cover is stable or fluctuates in time.

This study builds on the recent progress in understanding long-term cliff dynamics through absolute dating of exposures across shore platforms made by Choi et al. (2012), Regard et al. (2012) and Hurst et al. (2016; 2017). It addresses four main gaps in understanding Holocene cliff retreat rates. Firstly, it is the fourth study which provides absolute exposure dates from across an active shore platform, which is important as cliff dynamics vary worldwide as a function of geology, tidal range and sea-level history (Sunamura, 1992). Exposure dating has never previously been performed on the North Sea coast on a shore platform built in relatively fine-grain sandstone. We do not know whether this hard-rock platform is inherited from previous interglacials or has been entirely formed in the Holocene.

Secondly, different models of shore platform down-wearing are explored to identify which best represents platform erosion to model exposure ages from isotope concentrations. This includes

the empirical model developed in Chapters 5 and 7 based on the understanding of current processes and controls upon erosion rates. Thirdly, the sampling strategy, the spacing of sampling sites across the platform, has been designed to assess shorter-term (decades to centuries) changes in cliff retreat rates as a function of recurrence time between erosion events (Recorbet et al., 2010). Finally, although Hurst et al. (2017) predicted the impact of step back-wearing on cosmogenic ^{10}Be concentrations, their model has not been tested on a real dataset, while the long-term (> 30 yr) step retreat rates have never been calculated. Here, combining the isotope concentration with the most likely scenarios of cliff retreat and platform down-wearing allows the reconstruction of long-term step dynamics.

8.2. A conceptual study: modelling ^{10}Be concentrations across the shore platform

8.2.1. Model development

This section describes a set of models developed to calculate expected ^{10}Be concentrations. First, a model assuming no platform erosion is explored which includes topographic and water shielding, and geomagnetic scalar which vary in across-shore as a function of exposure ages and platform topography, notably the width, slope and elevation. Then different models of platform erosion are explored, including the parallel retreat model (Trenhaile, 1974), extrapolation of the monitoring data (Robinson, 1977a), platform widening and flattening in time (Tenhaile, 2000; Walkden and Hall, 2005) and erosion via step back-wearing (Hurst et al., 2017). Finally, the results from Chapters 5 and 7 are used to build an empirical model of long-term platform erosion. Appendix 10 contains the relevant scripts written in MATLAB R2016b.

8.2.1.1. Model assuming negligible platform erosion

Model assumptions

The concentration of cosmogenic ^{10}Be at any foreshore location can be expressed as:

$$\left[^{10}Be\right] = P\ t_{exp}\ S_{topo}\ S_w\ S_{gm}\ S_{er} \qquad \text{Eq 8.1}$$

where $[^{10}Be]$ (atoms g^{-1}) is the total concentration of ^{10}Be, P (atoms g^{-1} yr^{-1}) is the ^{10}Be production rate at the surface from the unshielded flux, t_{exp} (yr) is the time of exposure, S_{topo} is the topographic shielding, S_w is the water shielding, S_{gm} is the geomagnetic scalar and S_{er} is the platform erosion scalar (Hurst et al., 2017). The scalars are expressed relative to 1, where 1 is the non-shielded value. S_{topo}, S_w and S_{er} adopt values ≤ 1 depending on the importance of the factor (1 means no impact), while S_{gm} can

adopt values higher or lower than 1. In the basic model initiated by John Barlow (previously Durham, now Sussex) and developed here, the following assumptions are made:

A1. Cliff retreat started 7 kyr BP from which point the sea could affect the lowest parts of the contemporary platform (RSL = -5.84 m AOD). This assumption means that the entire shore platform was formed in the Holocene.

A2. There is no inherited ^{10}Be concentration due to deep penetration of muons, herein referred to as 'geological inheritance'.

A3. ^{10}Be production rate at the surface equals 4.009 atoms g^{-1} yr^{-1} (Lifton et al., 2014).

A4. The horizontal position of the seaward edge is constant.

A5. The cliff retreat rate is constant and it entirely depends on the platform width (de Lange and Moon, 2005). For a 300 m wide platform, the rate equals 4.29×10^{-2} m yr^{-1}.

A6. The cliff inclination and subtended azimuth angle are constant.

A7. Once exposed, the platform surface has not been buried by sediments.

A8. There is no beach deposit. This assumption is based on its lack of presence on the historical maps and at present, and more generally at the headland sections of rocky coasts.

A9. The vertical erosion of the shore platform is negligible (S_{er} = 1).

A10. The wave and tidal climates are constant.

Topographic shielding

Dunne et al. (1999) defined the maximum (unshielded) flux F_{max} as:

$$F_{max} = \frac{2\pi I_0}{m+1} \quad \text{Eq 8.2}$$

where I_0 is the incident radiation and m = 2.3 is the scaling coefficient.

The amount of missing flux δF at the time of exposure equals:

$$\delta F = \frac{I_0 \Delta\varphi}{m+1} \, sin^{m+1}\vartheta \quad \text{Eq 8.3}$$

where ϑ is the cliff inclination angle and $\Delta\varphi$ is the subtended azimuth angle (Dunne et al., 1999). These values of ϑ = 70° and $\Delta\varphi$ = 102° for the Penny Nab cliff will be used here to explore

topographic shielding (Figure 8.3). At the time *t* (yr) from the initial exposure, the amount of missing flux, δF_t, equals:

$$\delta F_t = \frac{I_0 \Delta\varphi}{m+1} \, sin^{m+1}(atan\frac{h}{r\,t + d_{cl}}) \qquad \text{Eq 8.4}$$

where *h* (m) is the cliff height, *r* (m yr^{-1}) is the cliff retreat rate and d_{cl} (m) is the horizontal distance between the cliff toe and the cliff top used to calculate ϑ; d_{cl} = 0 for a vertical cliff. Topographic shielding at the time *t* (yr) can be described as:

$$S_{topo(t)} = \frac{F_{max} - \delta F_t}{F_{max}} \qquad \text{Eq 8.5}$$

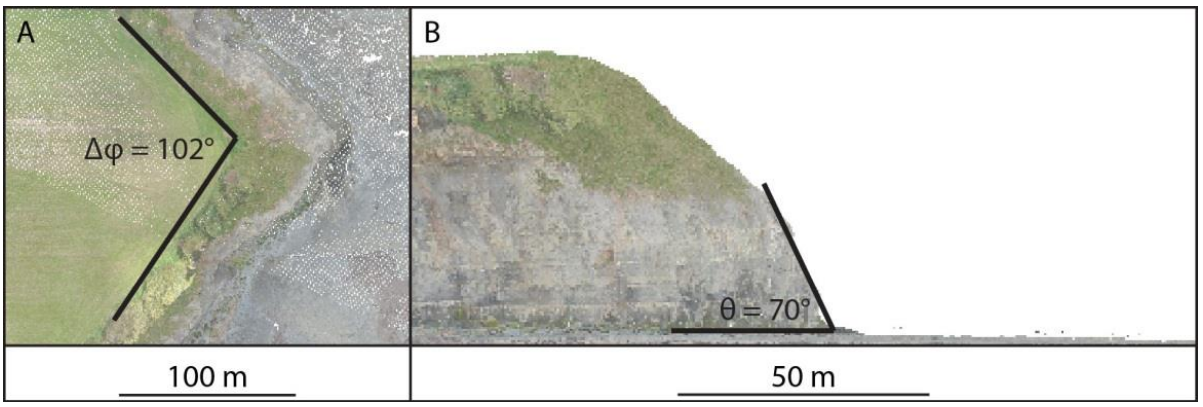


Figure 8.3 The topography of Penny Nab (see Figure 8.1 for location) used to calculate topographic shielding, S_{topo}: A) the subtended azimuth angle $\Delta\varphi$; B) the inclination angle ϑ.

The height of Penny Nab defines *h* = 50 m, and so the topographic shielding adopts the value of 0.7695 for a year of exposure at the cliff toe and increases as time passes (Figure 8.4A).

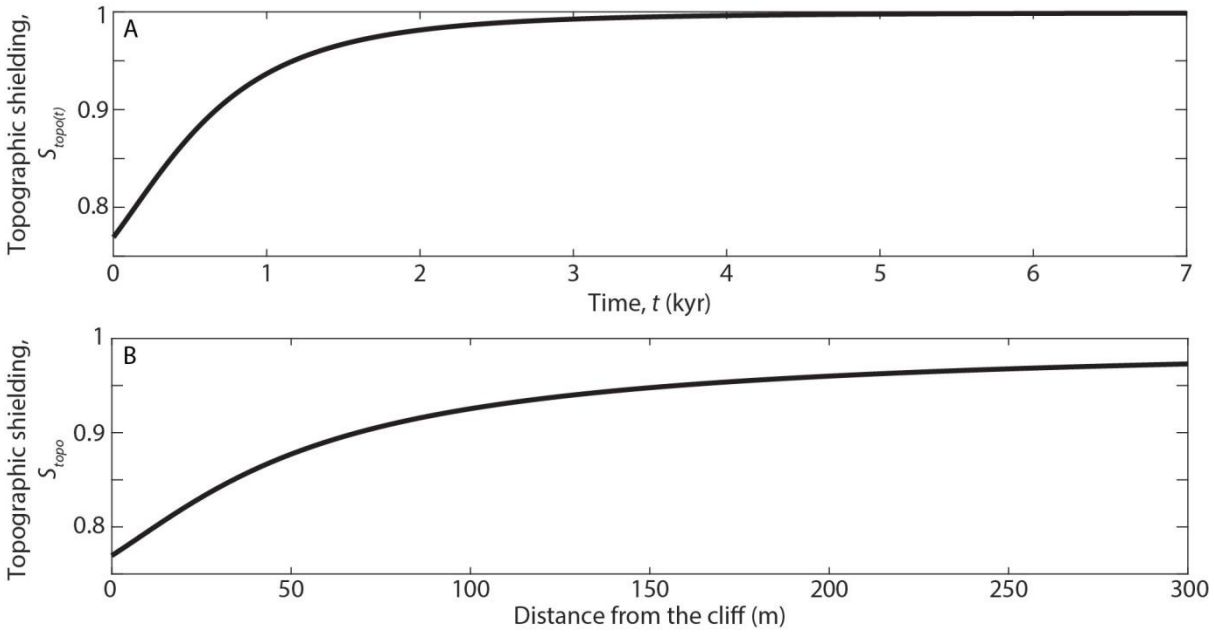


Figure 8.4 Topographic shielding, S_{topo}, for a 300 m wide shore platform under the assumption of a constant cliff retreat rate of 4.29×10^{-2} m yr^{-1} for the last 7 kyr and a cliff of h = 50 m inclined at ϑ = 70° and $\Delta\varphi$ = 102°: A) S_{topo} for a single point at time t (yr) after exposure; B) cumulative distribution of S_{topo} across the platform.

The total topographic shielding, S_{topo}, at a platform location is the cumulative effect of $S_{topo(t)}$ for a period of *n* years, and a time step of 1 yr for the period when the location has been exposed, and can be expressed as (Figure 8.4B):

$$S_{topo} = \sum_{i=1}^{n} S_{topo(t)i} \qquad \text{Eq 8.6}$$

Water shielding

A surface covered by water receives less cosmogenic radiation because a portion of the flux is attenuated while passing through the water column. The ^{10}Be production decreases with increasing water depth. The water shielding, $S_{w(t)}$, at any time *t* depends on the water depth, *x* (m), such that

$$S_{w(t)} = e^{-\rho x/\lambda} \qquad \text{Eq 8.7}$$

where ρ = 1.024 g cm^{-3} is the density of sea water, and λ = 160 g cm^{-2} is the absorption mean free path (Goethals et al., 2009).

Figure 3.5 shows the local RLS curve (Shennan et al., 2018). For simplicity, the sea level over the last 7 kyr was represented as a series of straight sections with inflexion points at every 1 kyr. The RSL for each year was recalculated from the end points for each section. The values are: 7 kyr BP: -5.84 m AOD; 6 kyr BP: -3.42 m AOD; 5 kyr BP: -1.74 m AOD; 4 kyr BP: -1.13 m AOD; 3 kyr BP: -0.53 m AOD; 2 kyr BP: -0.14 m AOD; 1 kyr BP: -0.02 m AOD; 0 kyr BP: 0 m AOD (after Sturt et al., 2013).

Eq 8.7 was combined with the tidal duration distribution curve for the Whitby tide gauge (Figure 3.6) to calculate the tide-dependent S_w (Figure 8.5A). Under the assumption A10, that the tidal duration distribution has been constant for the last 7 kyr, the tide-dependent S_w can be combined with the sea-level curve to calculate S_w for each year for a location with known elevation (Figure 8.5B and C).

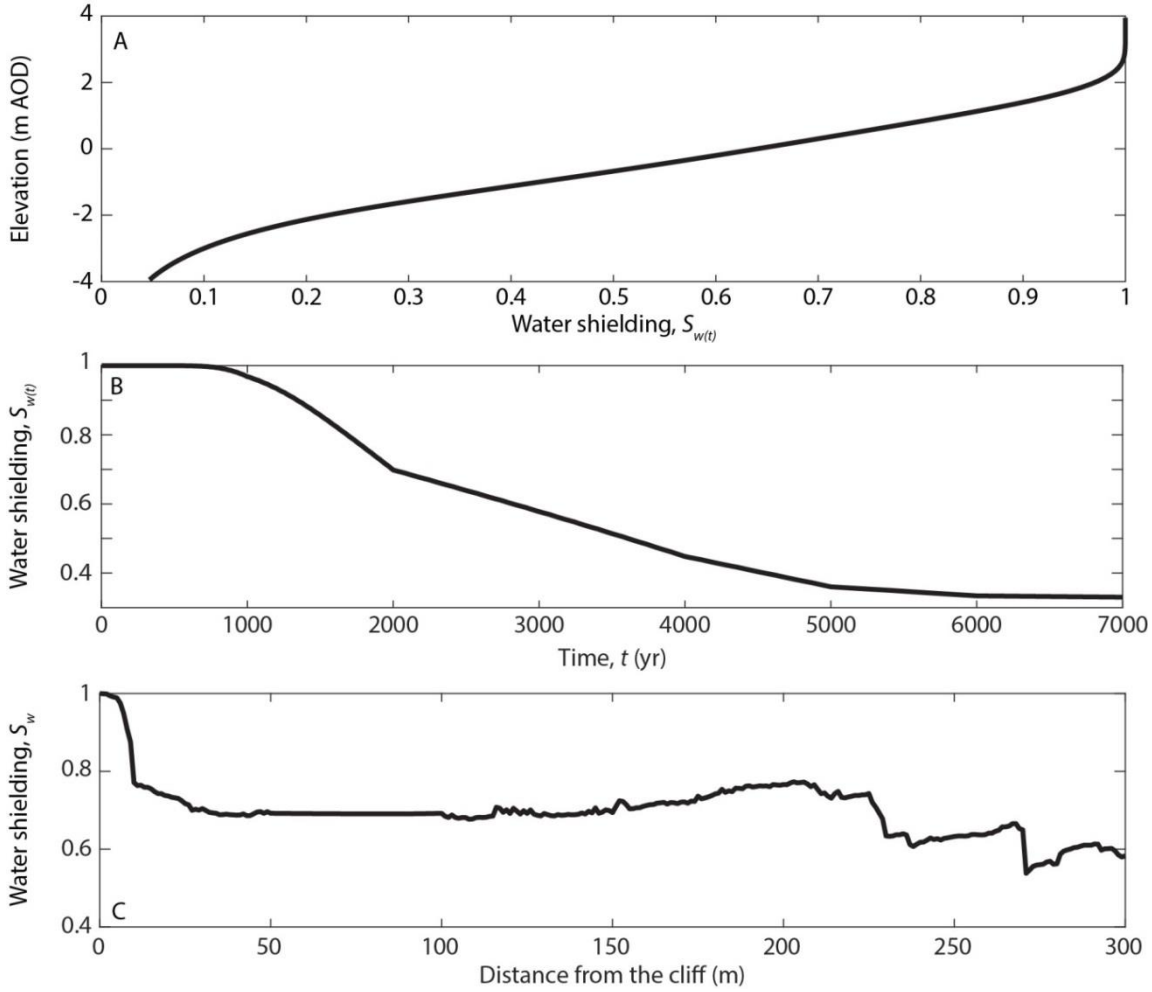


Figure 8.5 Water shielding, S_w: A) tide-dependent $S_{w(t)}$ at any time t; B) change of $S_{w(t)}$ since exposure for the seaward edge of the platform where distance from the cliff d = 300 m and elevation el = -1.49 m AOD; C) cumulative S_w across Hartle Loup (see Figure 8.1B for the profile).

Geomagnetic scalar

Lifton et al. (2014) quantified the variability in geomagnetic and solar modulation effects on the flux of cosmic-ray particles through time. Figure 8.6 shows the variability of the geomagnetic scalar S_{gm} in the last 7 kyr for the latitude 54.5°N, longitude 0.75°W and altitude 0 m AOD.

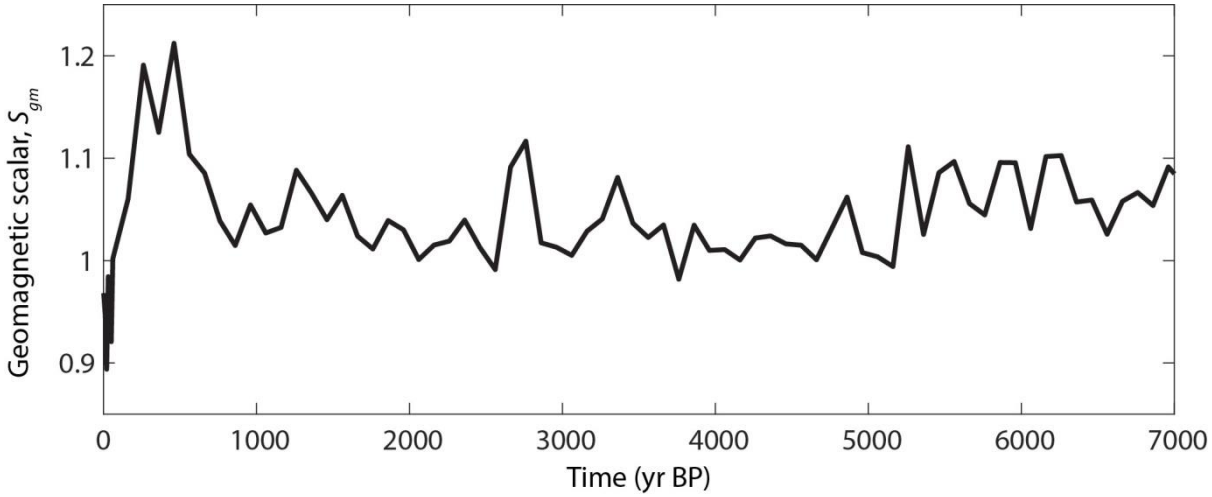


Figure 8.6 The geomagnetic scalar for the last 7 kyr; based on Lifton et al., 2014.

8.2.1.2. Model including shore platform erosion: theoretical models

Modelling platform erosion is important because it links rock samples currently exposed at the surface with specific depths in the past. Attenuation of isotope production with depth is described as:

$$P(z)_t = P(x)_t \, exp^{-z/\lambda} \qquad \text{Eq 8.8}$$

where $P(x)_t$ (atoms g^{-1} yr^{-1}) is the ^{10}Be production corrected with the topographic and the water shielding, z (m) is the depth of the sample at the time t (yr) and $\lambda = 1.3$ is the attenuation length for the particle flux (Dunne et al., 1999; Figure 8.7).

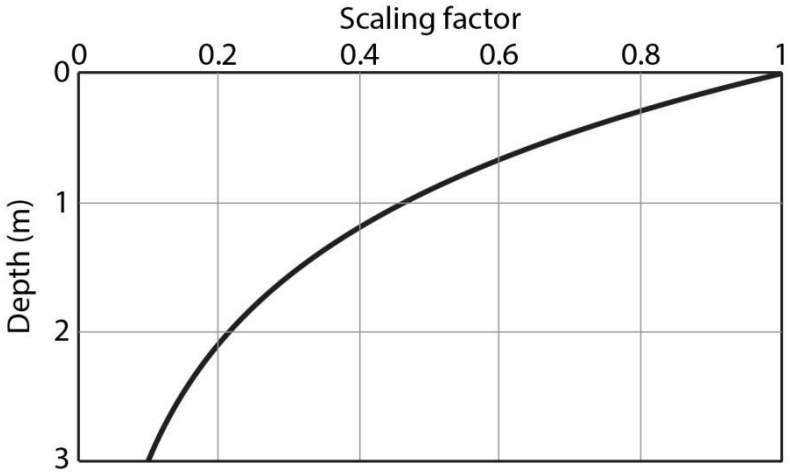


Figure 8.7 The scaling factor for the ^{10}Be production as a function of depth for the top 3 m under the surface.

Platform down-wearing

The shore platform profile presented in Figure 8.1B was simplified to the least-squares regression line. The platform slope is derived from the average cliff retreat rate for the last 7 kyr (4.29×10^{-2} m yr^{-1} under the assumption A5 of the constant cliff retreat rate) and the platform width (300 m), and equals 0.4° (6.981:1000). The cliff/platform junction is at 0.93 m AOD and the seaward edge is at -1.17 m AOD which results in the platform elevation range of 2.1 m. For the low-gradient part of the platform (distance from the cliff d = 13-300 m; Figure 8.1B), the sum of distances between real and simplified elevations is 0.695 m (Figure 8.8).



Figure 8.8 A simplified profile across Hartle Loup to explore the impact of platform down-wearing on cosmogenic ^{10}Be concentrations.

Accounting for the platform erosion means that the assumption A9 of negligible platform erosion is not valid. The importance of three scenarios of platform down-wearing was analysed (section 2.2.3):

Scenario 1: Down-wearing proportional to the cliff retreat

Assuming that the coast retreats in a parallel fashion, whereby A4 suggests the constant seaward edge position is invalid, platform down-wearing can be calculated by multiplying the cliff retreat rate and tangent of the platform slope (Trenhaile, 1974; Regard et al. 2012) (Eq 2.1; Figure 2.2A). For an average cliff retreat rate of 4.29×10^{-2} m yr^{-1} and a platform slope of 0.4°, the platform down-wearing rate equals 0.30 mm yr^{-1}.

Scenario 2: Constant down-wearing extrapolated from the monitoring data

In this scenario the down-wearing rate is uniform across the platform, which implies that the assumption A4, of the constant seaward edge position is again invalid. However, the down-wearing is not proportional to the cliff retreat rate which means that the vertical location of the cliff/platform junction changes in time (Figure 2.2.B), while the erosion rate is calculated from the monitoring data presented in this thesis. The elevation of the seaward edge is assumed to be constant at the wave base level. The down-wearing rates of 1.33 ± 2.17 mm yr^{-1} calculated by Robinson (1977a) for the planar parts of the platform, which here constitute ~287 m of the profile, are used.

Multiplying these rates by the maximum time available for erosion (7 kyr) suggests that the total vertical erosion can reach up to 9.31 ± 24.5 m which is well beyond the platform vertical range. Therefore, the boundary elevations were set at the present elevations of the cliff/platform junction (0.93 m AOD) and the seaward edge (-1.17 m AOD). If at any point in time a location has an elevation beyond the set range, it acquires the boundary value while the profile does not remain a single straight line but a composite of two straight lines (Figure 8.9).

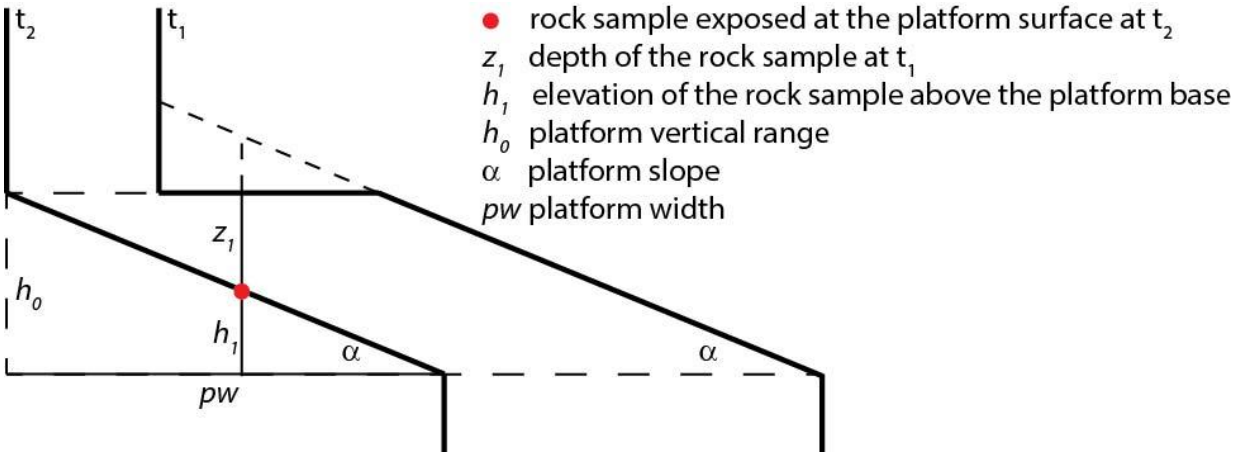


Figure 8.9 A conceptual model of the platform down-wearing rate which is relatively fast in respect to the cliff retreat rate.

Scenario 3: Platform widening

In this scenario the platform widens and flattens through time while the seaward edge remains at a stable position (Figure 2.2C). Building on Eq 2.2, the depth z_t (m) of a rock mass, that is currently exposed at the platform surface, at time t (m) can be calculated as

$$z_t = tan\alpha_t\,(w - dc) - h_{end} \qquad \text{Eq 8.9}$$

where α_t (°) is the platform slope at time t, pw (m) is the platform width, dc (m) is the horizontal distance to the cliff and h_{end} (m) is the elevation difference between the present elevation and the elevation of the platform base (Figure 8.10).

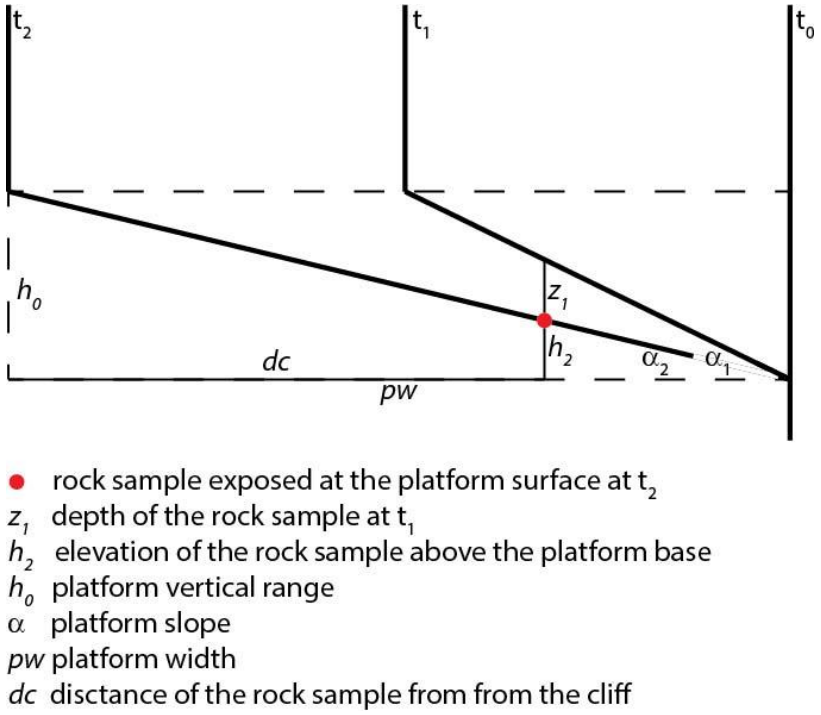


Figure 8.10 A conceptual model of down-wearing when the platform widens and flattens with the stable seaward edge position.

The distribution of S_{er} along the profiles was explored for 16 simplified platform morphologies with the combination of four widths (100, 200, 300 and 400 m) and four slopes (0.5, 1, 1.5 and 2°). The three scenarios of down-wearing were taken into account. For the monitoring-based scenario the mean and maximal (mean + standard deviation) rates were explored, with respective values of 1.33 and 3.50 mm yr^{-1} (Robinson, 1977a). When the platform erodes proportionally to the cliff retreat, the scalar is independent of the width (Figure 8.11A). When the down-wearing rate is constant but non-proportional to the cliff retreat (monitoring-based scenario), the scalar is independent of the slope for down-wearing rates if the platform maintains the single line profile (Figure 8.11B), or

it is dependent on the slope if the down-wearing is relatively fast in respect to the cliff retreat rate (Figures 8.9 and 8.11C). In the platform widening scenario the scalar is lowest in the central part of the profile while its magnitude depends on the slope (Figure 8.11D).

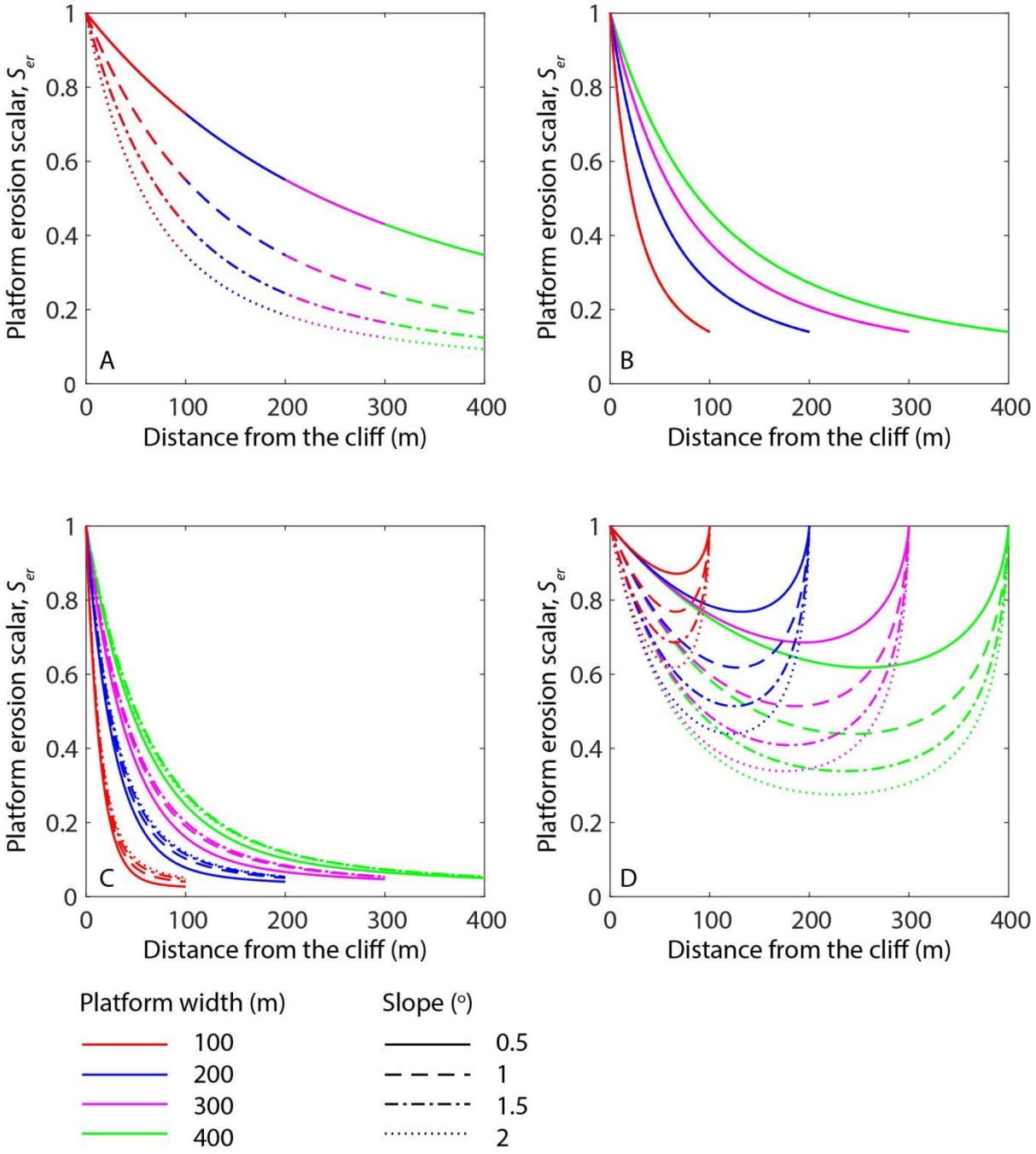


Figure 8.11 The distribution of the platform erosion scalar, S_{er}, across shore platforms of diverse width and slope: A) down-wearing proportional to the cliff retreat; B) constant down-wearing rate of 1.33 mm yr^{-1}; C) constant down-wearing rate of 3.50 mm yr^{-1}; D) platform widening.

Step back-wearing

The shore platform profile presented in Figure 8.1B was simplified to a series of horizontal sections delimited by three steps of: 0.15 m at a distance from the cliff of d = 230 m, 0.7 m at d = 240 m and 0.55 m at d = 270 m (Figure 8.12).

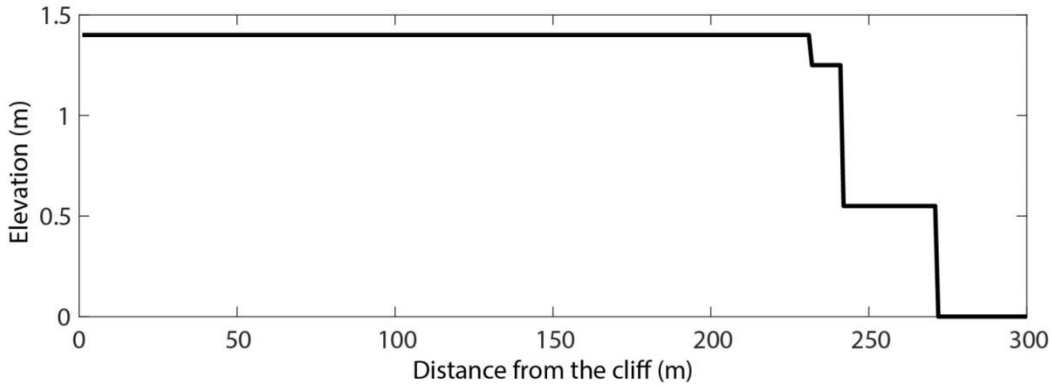


Figure 8.12 A simplified profile across Hartle Loup to explore the impact of step back-wearing on cosmogenic ^{10}Be concentrations.

A set of 20 idealised shore platform profiles was generated to explore the role of the step height and number in the distribution of the platform erosion scalar, S_{er}, across the platform eroding through step back-wearing. The number of steps varied between two and five while step heights were: 0.1, 0.2, 0.5 and 1 m (Figure 8.13).

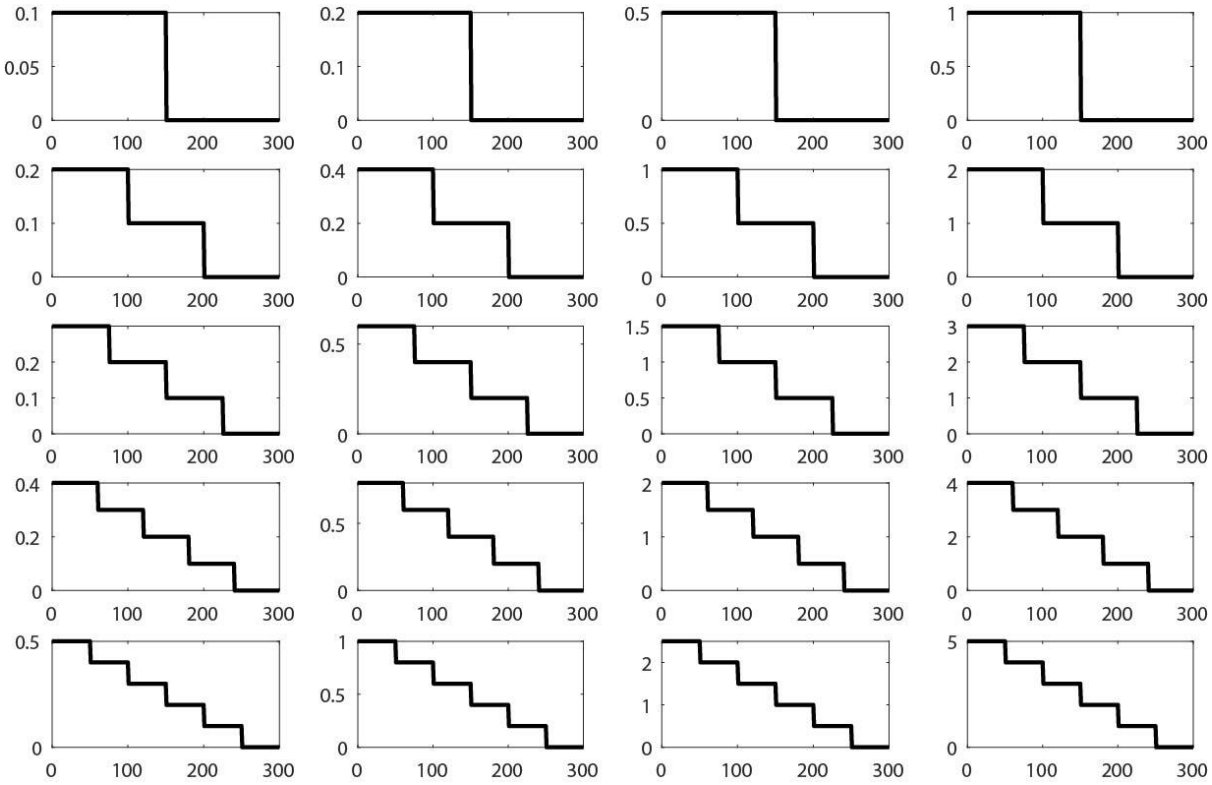


Figure 8.13 Idealised shore platform profiles to explore the role of step back-wearing in the distribution of platform erosion scalar, S_{er}, across a 300 m wide shore platform; X-axis: distance from the cliff (m); Y-axis: elevation (m).

Two scenarios of step back-wearing mode were explored:

Scenario 1: Step back-wearing rate equal to the cliff retreat rate

In this scenario all the steps retreat at a constant pace, which is equal to the cliff retreat rate (Hurst et al., 2017). Moving backwards in time, once a step reaches the seaward edge, it remains static through time (until 7 kyr BP). The section of the platform located landwards from the step closest to the cliff has a scalar value $S_{er} = 1$. At each step the value drops abruptly but increases with the distance from the cliff because of the longer exposure times at a given elevation. The lowest value of S_{er} occurs just under the seaward-most step. The height of the steps has a considerable impact on S_{er} but the distribution of the scalar across the platform also depends on the number and location of the steps (Figure 8.14).

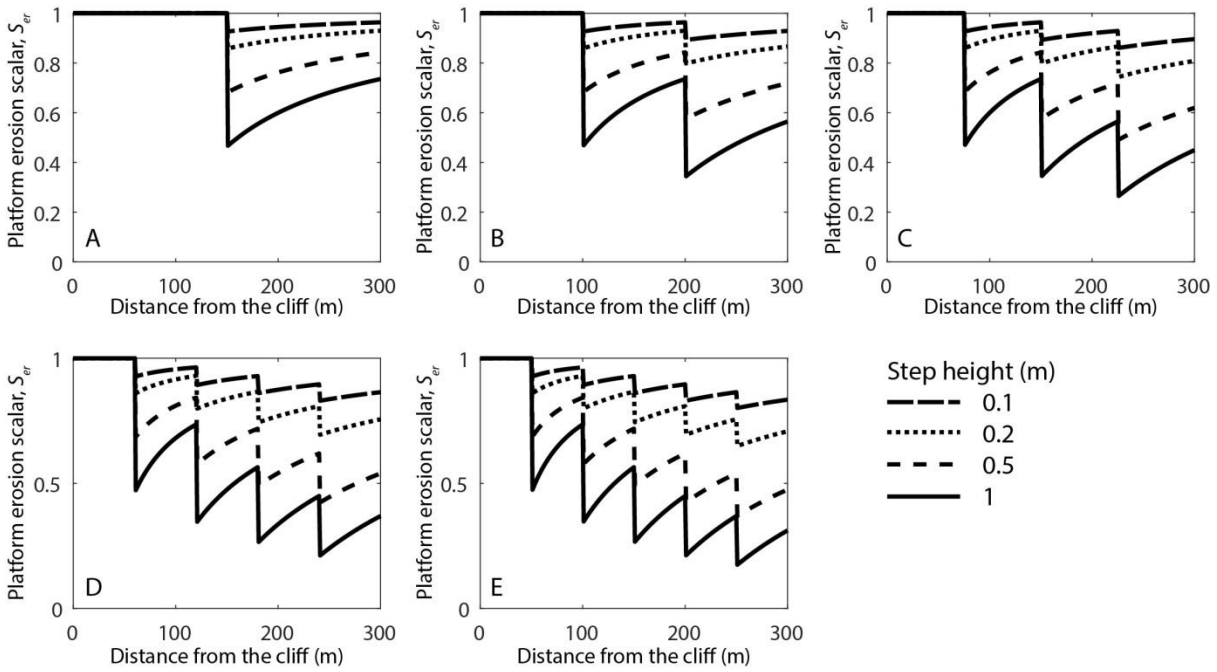


Figure 8.14 The distribution of the platform erosion scalar, S_{er}, across a 300 m wide shore platform where the platform erodes via back-wearing of steps with a range of heights at the same rate as the cliff retreat where A) 1 step; B) 2 steps; C) 3 steps; D) 4 steps; E) 5 steps of the same height exist.

Scenario 2: Location-dependent step back-wearing

In this scenario it is assumed that all steps started to retreat 7 kyr BP and their retreat rates are constant and entirely dependent on the present location along the profile. In this way, retreat of the step located closest to the cliff will be the fastest because its location changed the most in the time period available. In respect to the scenario assuming that step back-wearing is equal to the cliff retreat rate, S_{er} is more diverse within single levels (rock beds) but its values are less diversified between different levels. The seaward-most point along the profile was exposed from under all steps at t = 1 yr which means that S_{er} = 1 at d = 300 m (Figure 8.15).

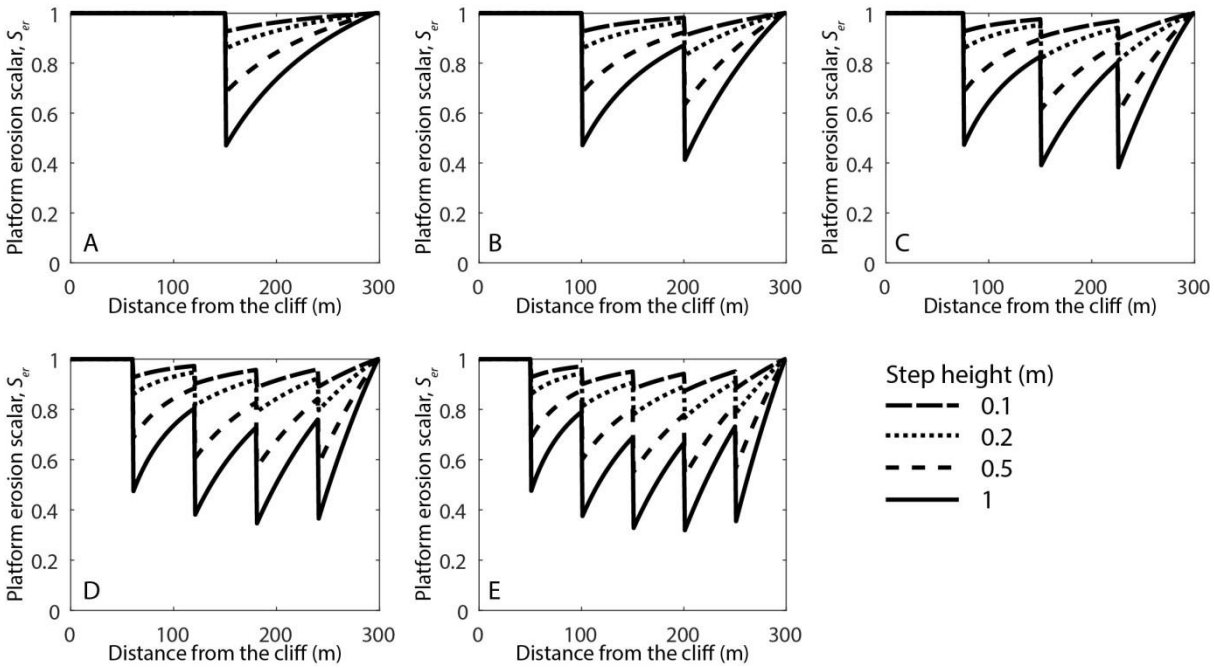


Figure 8.15 The distribution of the platform erosion scalar, S_{er}, across a 300 m wide shore platform where the platform erodes via back-wearing of steps with a range of heights at the rate dependent on the contemporary cross-shore step location where A) 1 step; B) 2 steps; C) 3 steps; D) 4 steps; E) 5 steps of the same height exist.

8.2.1.3. Model including shore platform erosion: empirical model

The results of Chapters 5 and 7 suggest that predicting platform down-wearing rate from across-shore location, topography, structure and tidal data is more successful at the small-scale (uncertainty of the results is ± 16.7%; section 4.9) as compared to the macro-scale. The reason may be the dominance of fine detachments which are below the macro-scale *LoD* of 0.05 m and/or insufficient macro-erosion monitoring period (detailed discussion in Chapter 9). The down-wearing rate, *Ero* (mm yr^{-1}), is a function of the distance from the seaward edge, *Sea* (m), and the tidal duration, *Tid* (%) ($R^2 = 0.648$; $p < 0.05$), in such a way that:

$$Ero = -2.01 + 0.01\,Sea + 0.60\,Tid \qquad \text{Eq 8.10}$$

In time $t = 0$, at zero years since the beginning of platform development (7 kyr BP) the cliff was at a distance $d = 300$ m from its present position and since then it has been retreating at a constant rate of 4.29×10^{-2} m yr^{-1} (A1 and A5). The cliff toe elevation was set to the highest astronomical tide level (HAT = 3.2 m AOD) relative to the sea level at time *t*. At the time of exposure, a point adopted this elevation retaining it until the down-wearing began.

Step back-wearing has been shown to be an episodic process and its distribution and magnitude cannot be predicted using the locational, topographic, tidal and structural variables presented in Chapter 7. Therefore, the importance of step back-wearing will not be modelled but reconstructed from measured ^{10}Be concentrations.

8.2.2. Model results

The results in this section are based on assumption A5, the constant cliff retreat rate which entirely depends on the platform width (de Lange and Moon, 2005). The shielding/scalar factors were applied to the Hartle Loup platform profile (Figure 8.1B) in order to calculate basic concentrations assuming no platform erosion. Subsequently, a series of down-wearing and step back-wearing scenarios were used to assess how sensitive the models to reconstruct exposure ages are to the adopted assumption about foreshore erosion. For these, the idealised morphologies of Hartle Loup profile were used (Figures 8.8 and 8.12). Finally, the empirical platform down-wearing model is explored.

8.2.2.1. Model assuming negligible platform erosion

Total shielding is a result of topographic and water shielding and the geomagnetic scalar. The importance of topographic shielding decreases with distance from the cliff while water shielding is the main determinant of the total shielding, in particular closer to the seaward edge, with abrupt drops of factor values at the steps (Figure 8.16A). Expected cosmogenic ^{10}Be concentrations vary from 3 atoms g^{-1} at the cliff toe to 1.69×10^4 and 1.70×10^4 atoms g^{-1} at 268 and 292 m from the cliff at the top of the two seaward-most steps. Because of the near-horizontal platform morphology, the concentrations are expected to rise gradually up to ca. d = 230 m from the cliff with subsequent variability which results from the distribution and height of steps at the seaward part of the platform (Figure 8.16B).

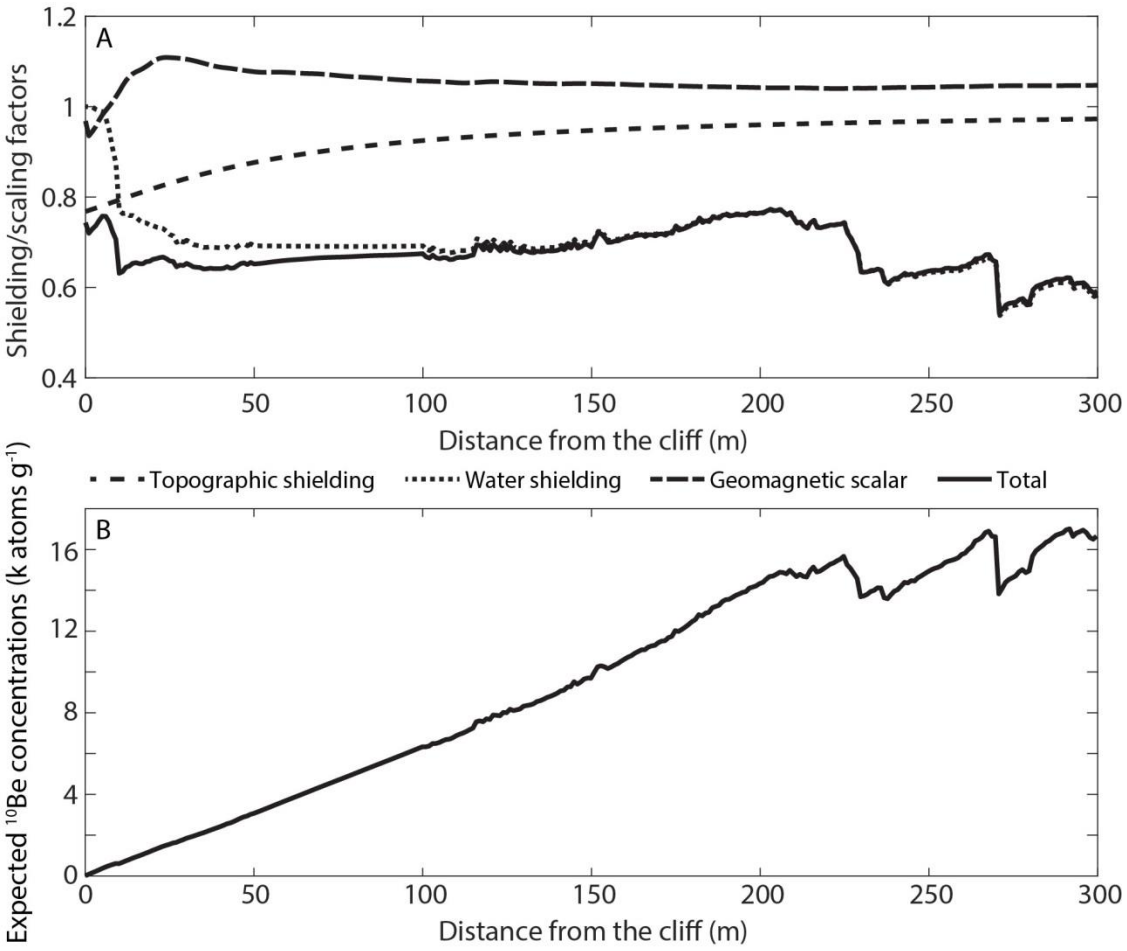


Figure 8.16 Results of the model assuming negligible platform erosion on the real sampling profile across Hartle Loup (Figure 8.1): A) distribution of the shielding/scaling factors; B) expected cosmogenic ^{10}Be concentrations.

8.2.2.2. Model including shore platform erosion: theoretical models

Platform down-wearing

Depending on the scenario of platform down-wearing, the magnitude and distribution of the platform erosion scalar, S_{er}, differs. For the scenario which assumes that the down-wearing is proportional to the cliff retreat rate, it linearly decreases from 1 to 0.5 with the distance from the cliff. For the monitoring-based scenario, it falls abruptly relatively close to the cliff with the slope, depending on the accepted down-wearing rate, and stabilises at a level dependent on the down-wearing rate. For the platform widening scenario the scalar decreases and then increases with the distance from the cliff (Figure 8.17A). The monitoring-based scenarios result in a remarkable decrease in expected ^{10}Be concentrations in respect to the no-erosion model. The two other scenarios contribute to the loss, in particular at the seaward part of the profile, but they still show clear drops in

concentrations at the steps. The difference between them is pronounced at the seaward edge (Figure 8.17B).

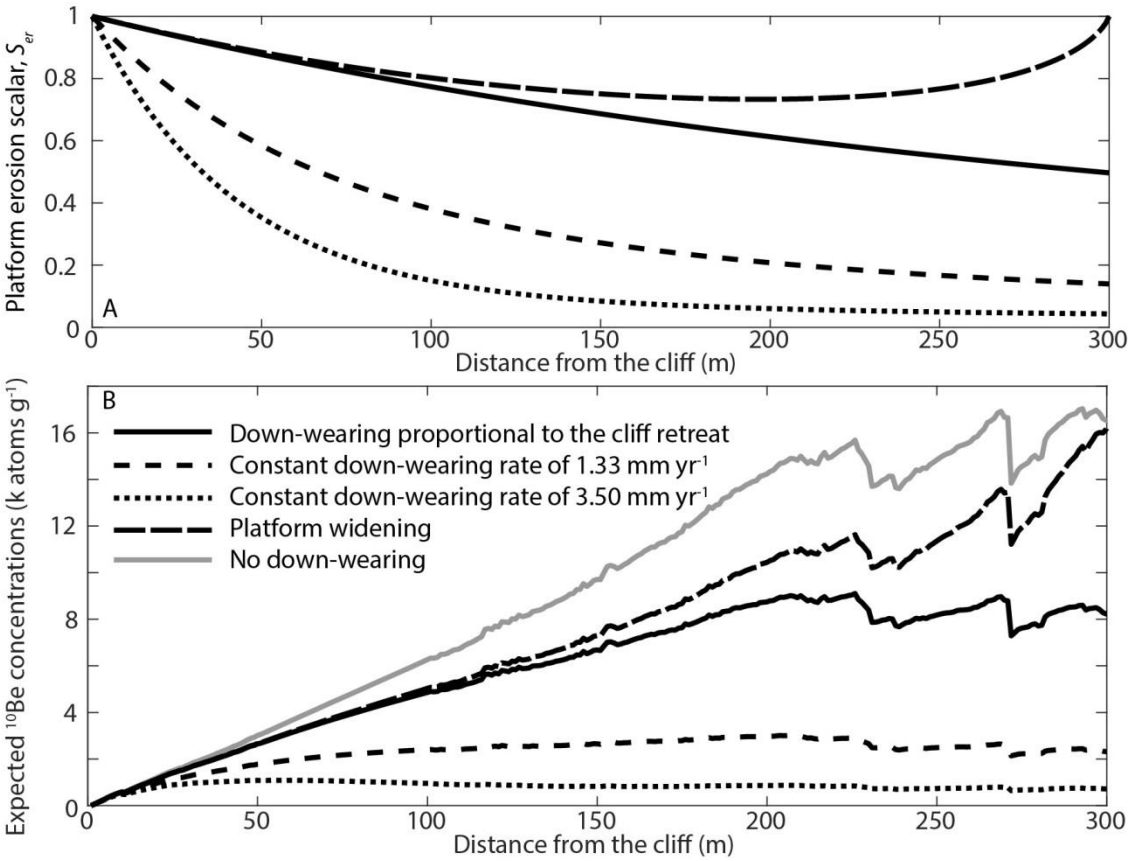


Figure 8.17 Results of the model including platform down-wearing on the profile across Hartle Loup (Figure 8.1): A) distribution of the platform erosion scalar, S_{er}, across simplified platform (Figure 8.8) for different down-wearing scenarios; B) expected cosmogenic ^{10}Be concentrations.

Step back-wearing

If platform erosion proceeds by step back-wearing only, the platform erosion scalar $S_{er} = 1$ up to $d = 230$ m from the cliff and it drops abruptly at the steps. The scalar remains at a similar lower level when the back-wearing is equal to the cliff retreat rate. In the case of the location-dependent back-wearing, it increases with the distance from the cliff (Figure 8.18A). The scalar value is reflected in the expected isotope concentrations which rise in the same way as in the no-erosion model but then fall abruptly. The ^{10}Be concentrations vary by 9.32×10^3 atoms g^{-1} at the seaward edge for the two scenarios (Figure 8.18B).

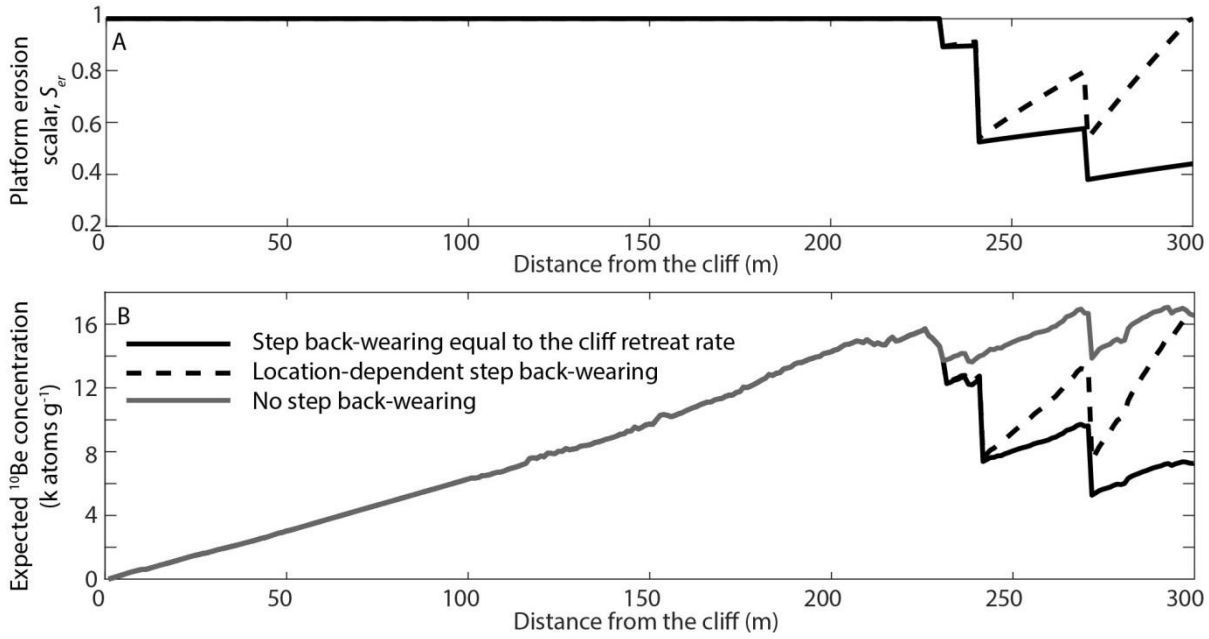


Figure 8.18 Results of the model including step back-wearing on the profile across Hartle Loup (Figure 8.1): A) distribution of the platform erosion scalar, S_{er}, across the simplified platform (Figure 8.12) for different step back-wearing scenarios; B) expected cosmogenic ^{10}Be concentrations.

8.2.2.3. Model including shore platform erosion: empirical model

Because of the 5.84 m RSL rise in the last 7 kyr and its non-linear character combined with the setting up of the cliff toe at 3.2 m relative to the sea level and assumptions A1 (initiation of cliff retreat 7 kyr BP), A4 (constant position of the seaward edge) and A5 (constant cliff retreat rate), the platform down-wearing is entirely controlled by marine factors: the sea level and tidal duration. The distance from the seaward edge which influences erosion rates (Eq 8.10) does not change through time for points along the profile (A4). This makes the seaward-most point of the platform stabilise at -2.64 m AOD in t = 1 yr and remain at this elevation for 7 kyr. The coastal cross-section develops an irregular shape (Figure 8.19A).

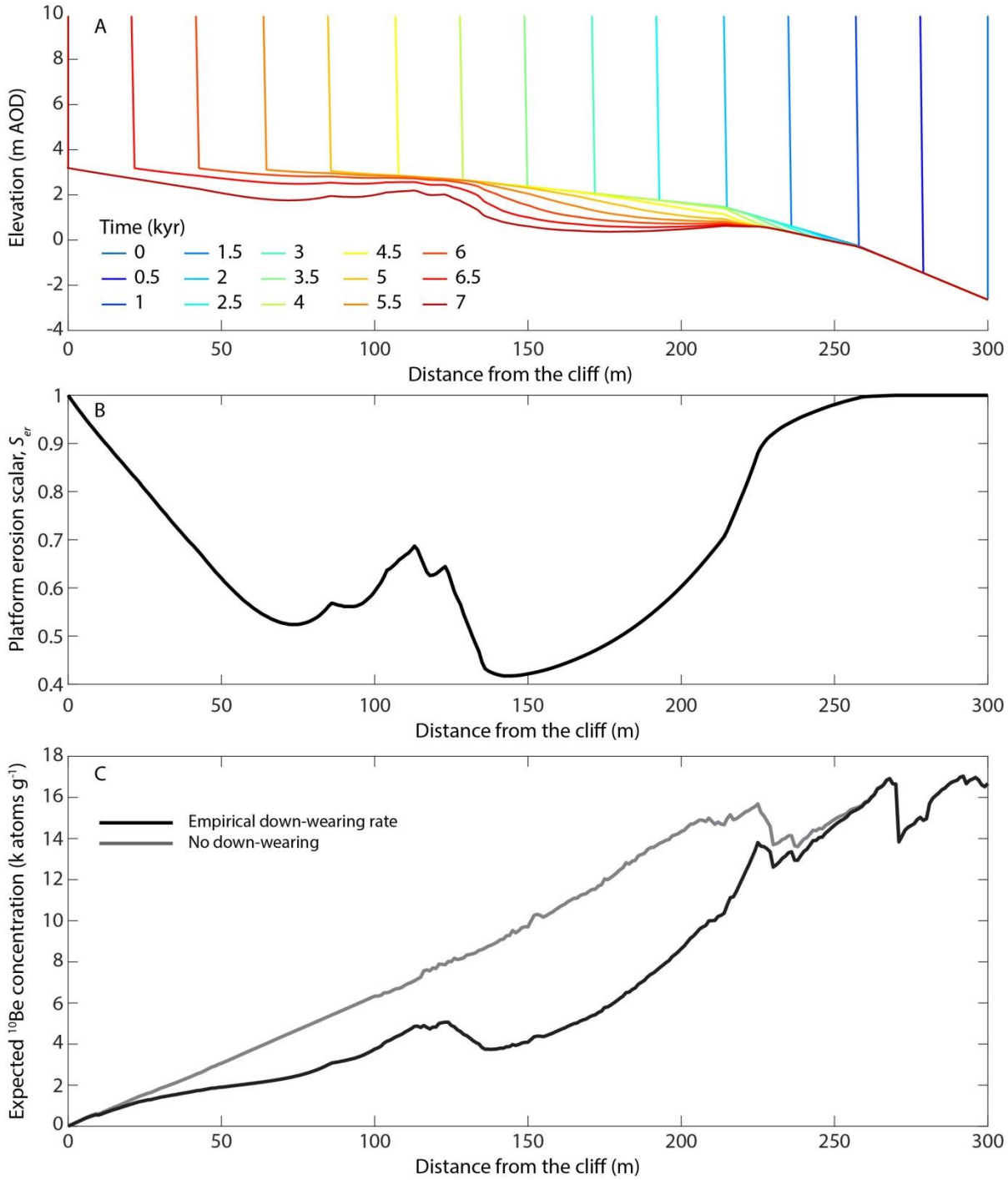


Figure 8.19 Results of the model including the platform down-wearing rate developed from the empirical micro-scale data (Eq 8.10) on the profile across Hartle Loup (Figure 8.1): A) Simulation of shore profile evolution in the last 7 kyr; B) distribution of the total platform erosion scalar, S_{er}, across the platform; C) expected cosmogenic ^{10}Be concentrations.

The platform erosion scalar, S_{er}, has an irregular shape, in particular in the central part of the profile (d = 74-144 m) which results from the tidal duration curve superimposed on the non-linear

sea-level curve. It adopts a value of S_{er} = 1 at the cliff toe and the seaward-most 29 m portion of the platform. The lowest value S_{er} = 0.42 is at d = 144 m. The scalar decreases to S_{er} = 0.52 at 73-74 m (Figure 8.19B). Expected concentration rates follow the results of the modelling assuming no platform erosion at the land- and seaward parts of the profile, but are lower in the central part (Figure 8.19C).

8.3. Empirical study: calculating ^{10}Be concentrations

8.3.1. Methods

This section presents the workflow of sample processing which includes: design of the sampling strategy, collection of the samples on Hartle Loup, mechanical extraction of quartz grains from sandstone, chemical processing to extract ^{10}Be atoms and accelerator mass spectrometry (AMS) to measure ^{10}Be/^{9}Be ratio and calculate ^{10}Be concentrations (Figure 8.20). The laboratory processing was performed at the Department of Earth Science and Engineering, Imperial College London; and AMS – at the Centre for Accelerator Science, Australian Nuclear Science and Technology Organisation, Lucas Heights NSW, Australia.

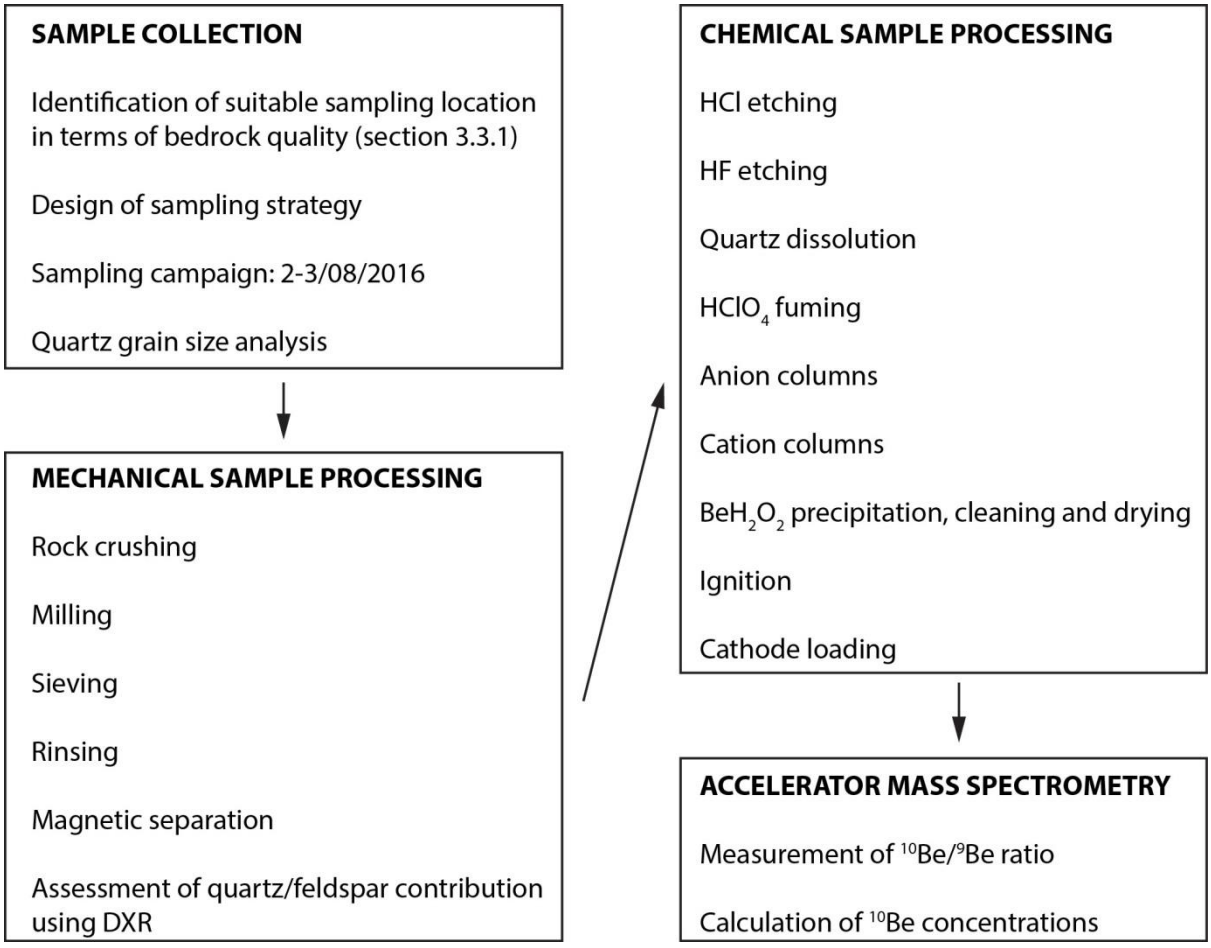


Figure 8.20 The workflow used to calculate cosmogenic ^{10}Be concentrations in the rock samples from Hartle Loup.

8.3.1.1. Study set-up

The Hartle Loup shore platform described in detail in section 3.7.2 was selected for the exposure dating because of the apparent suitability of bedrock, which is a fine-grained sandstone (section 3.3.1). One sampling profile was set up across the platform at the tip of the Penny Nab headland where the platform is 300 m wide (Figure 8.1). Three near-horizontal sandstone rock beds (B1, B2 and B3) are exposed at the platform surface and steps mark the boundaries between them, which has two important implications. Firstly, the inundation frequency and consequently the water shielding do not increase gradually but in a step-like manner. This means that the concentrations are expected to increase gradually in concert with increasing exposure ages moving seaward. The 'hump' in isotope concentrations which results from the interplay between exposure ages and water shielding on the sloping platforms is not expected (Figure 8.2A; Regard et al., 2012). Secondly, the structurally-controlled platform morphology (Sunamura, 1992), i.e. the angular shape of the steps at the exposures of subsequent rock beds and the presence of detached boulders, suggests that step back-wearing may be an important component of platform erosion. The importance of this process was explored by Hurst et al. (2017) in an abstract way, while the empirical exposure dating studies assumed platform erosion occurred only via down-wearing (Regard et al., 2012; Hurst et al., 2016).

A sampling strategy was designed to separate the influence of various factors on ^{10}Be concentrations. 20 locations were selected for sampling. Firstly, six locations were selected at equal intervals of 50 m to calculate the average cliff retreat rate during the Holocene. The results can then be used to 1) improve our understanding of global long-term cliff retreat rates, at present restricted to studies by Choi et al. (2012), Regard et al. (2012) and Hurst et al. (2016); 2) provide empirical values to calibrate coastal evolution models (Kline et al., 2014; Limber et al., 2014; Matsumoto et al., 2016); and 3) compare with short-term (years to decades) monitoring data on cliff erosion (Rosser et al., 2013) to assess whether the short-term cliff dynamics can be extrapolated to centennial to millennial timescales and to understand whether acceleration of coastal erosion due to post-industrial sea-level rise and increased storminess (Kopp et al., 2017), as observed by Hurst et al. (2016), is a universal phenomenon.

Secondly, four sites were located between distances from the cliff d = 50 m and d = 100 m at 10 m intervals to account for a change in cliff retreat rates at shorter time-scales (centuries). This can indicate the recurrence period of erosion events and/or at which timescales erosion rates average out, and so identify the timescales at which it is no longer important whether erosion is gradual or happens through high-magnitude low-frequency events (Lee et al., 2001; Recorbet et al., 2010).

Thirdly, nine locations were set at the seaward-most ($d \geq 230$ m) part of the platform. They were distributed at 10 m intervals to calculate the long-term step back-wearing rates and to quantify their temporal variability. The empirical study described in Chapter 7 showed that erosion at the steps

is episodic and cannot be predicted from the locational, topographic, structural or tidal data. The recurrence period of step back-wearing events may be longer than the monitoring period of < 30 years (Dornbusch and Robinson, 2011), and so numerical modelling coupled with measured ^{10}Be concentrations can help reconstruct step back-wearing over longer (centuries) timescales.

Finally, an unexposed location was included to account for geological inheritance. The subsurface production related to muons which should be subtracted from all concentrations in order not to overestimate exposure ages. In the conceptual study the geological inheritance was assumed to be equal to 0 atoms g^{-1} (A1), but it is likely that the muon production contributes to the total ^{10}Be concentrations (Hurst et al., 2017).

Three factors contributed to selection of the longest profile across Harle Loup for sampling. Firstly, sandstone which is suitable for isotope concentrations measurements is scarse (see Figure 3.10E for the distribution of rock types). Secondly, topography of shorter sections of the foreshore west of the selected profile is complex. This would make separation of the role of cliff retreat and platform erosion – down-wearing and block removal – difficult (see Figure 3.8). Finally, planar character of this profile and presence of steps at its seaward section allows design sampling strategy to consider multiple mechanisms and cliff retreat patterns.

8.3.1.2. Sample collection

The samples were collected along the pre-defined coastal cross-section (Figure 8.1) during the spring tides on 2-3 August 2016. Detailed *xy* coordinates (error < 0.025 m) of the sampling locations were acquired with a Leica 1200 differential GPS and were used to measure distances from the cliff. The LiDAR2016-based DEM at 0.1 m resolution (section 3.7.2.1) was used to measure elevation *z* (Table 8.2).

Table 8.2 Characteristics of the sampling locations on Hartle Loup and the rock samples.

Sample ID	dGPS-based OSGB'02 coordinates (m)			LiDAR-derived *z* (m AOD)	Distance from the cliff (m)	Sample weight (g)	Max depth (cm)
	x	*y*	*z*				
0	478653.72	518856.85	2.46	2.84	0	1283	n/a
20	478748.58	518946.20	0.24	0.32	31.17	1582	1.50
50	478755.04	518965.53	0.16	0.26	50.46	1710	2.00
60	478754.12	518977.23	0.19	0.25	62.09	1433	1.00
70	478755.77	518986.70	0.15	0.23	71.63	2027	2.00
80	478756.76	518997.87	0.14	0.19	82.84	2548	3.00
90	478756.67	519008.03	0.15	0.20	92.98	1454	1.00
99	478754.29	519016.61	0.04	0.09	101.46	1946	1.50
100	478757.14	519016.45	0.09	0.17	101.41	2402	5.00
101	478756.01	519017.32	0.09	0.20	102.23	2699	6.00

Sample ID	dGPS-based OSGB'02 coordinates (m)			LiDAR-derived *z* (m AOD)	Distance from the cliff (m)	Sample weight (g)	Max depth (cm)
	x	*y*	*z*				
150	478755.62	519065.39	-0.19	0.13	150.26	1709	3.00
200	478761.83	519112.75	-0.15	0.17	197.83	1772	2.50
230	478761.43	519127.98	-0.08	0.16	213.02	1098	1.00
231	478760.52	519134.75	-0.26	0.03	219.74	2178	1.50
240	478763.41	519145.99	-0.40	-0.15	231.11	2286	3.00
241	478759.04	519151.16	-1.04	-0.81	236.09	1382	2.50
250	478759.00	519163.15	-1.09	-0.85	248.07	1707	2.00
260	478761.17	519175.32	-1.17	-0.94	260.31	1731	2.50
270	478762.20	519182.37	-1.14	-0.89	267.39	2912	3.00
271	478763.33	519188.94	-1.70	-1.46	274.01	1282	1.00
280	478763.22	519195.04	-1.62	-1.40	280.10	1354	1.50
290	478765.09	519203.37	-1.48	-1.28	288.49	2101	1.50
300	478765.02	519213.47	-1.43	-1.27	298.58	1505	3.00

For consistency, the samples were taken from the highest point within a ~3 m diameter circle around the sample position (Stone et al., 1996; Hurst et al., 2016). Three samples were collected in addition to samples taken from the 20 locations described in section 8.3.1.1. Two of these additional samples were collected at d = 100 m: one from an ironstone nodule to verify whether the ^{10}Be concentrations are independent of the rock composition, here the iron content, and one from a local low point to see how the consistency of sampling at local high points impacts the results and to assess uniformity of the denudation rate. One sample was taken at d = 20 m which is the location along the profile closest to the cliff face where the sandstone bed B1 is exposed under the shale bed. The unexposed sample, which is used to account for the geological inheritance (Hurst et al., 2017), was taken from a low part of the cliff face at ca. 100 m SW of the point where the profile hits the cliff face, where the sandstone bed B1 is exposed at the cliff face (Figure 8.21).

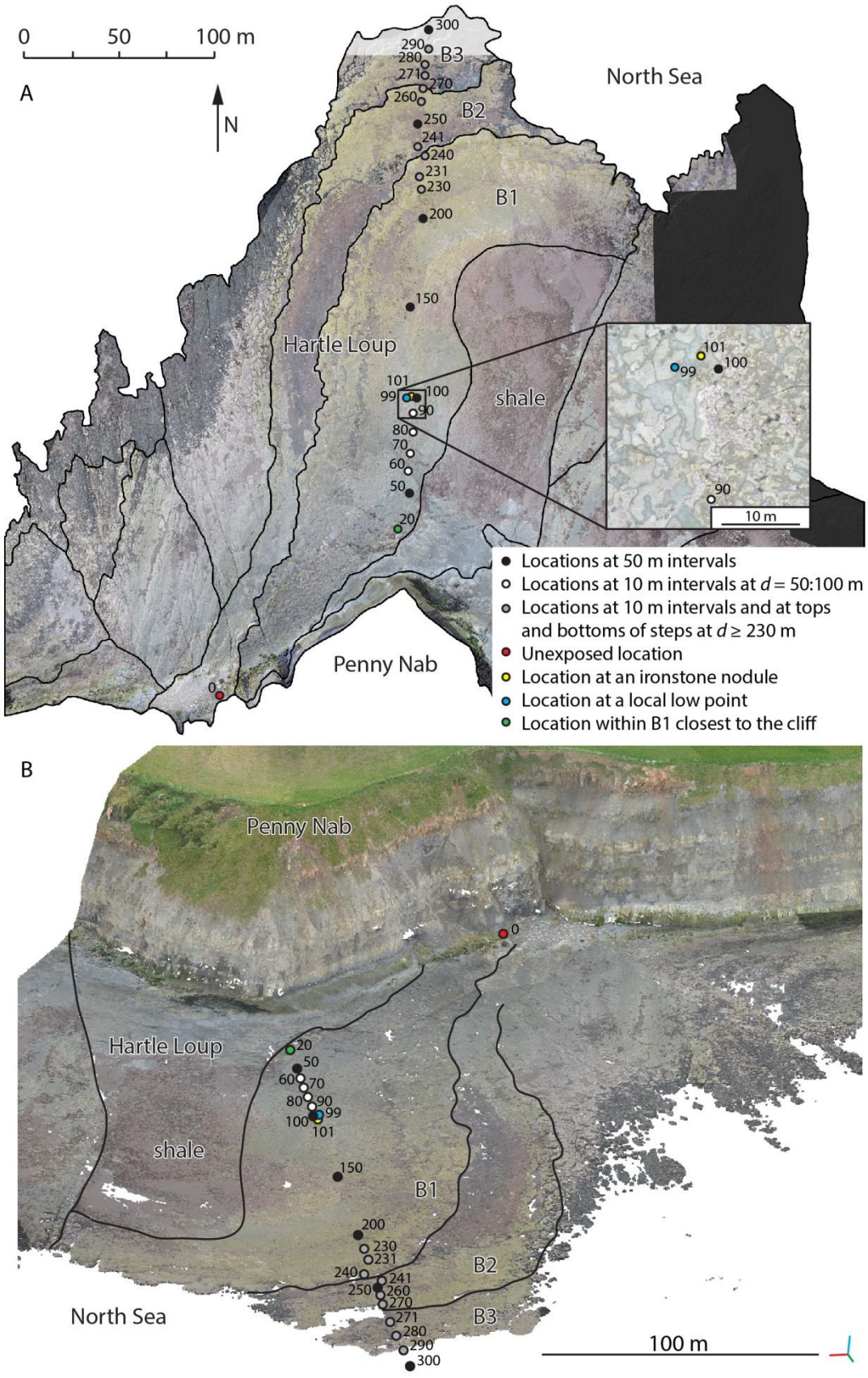


Figure 8.21 Sampling locations: A) LiDAR2016 orthophotograph; B) oblique view on LiDAR2016 point cloud; black lines represent the boundaries of exposed rock beds.

The sampling locations were photographed before, during and after sampling. The bedrock (1 to 2 kg at each site) was sampled following the procedures summarised in Kim and Sutherland (2004) and Choi et al. (2012). The samples were placed in labelled plastic bags to make sure there was no cross-contamination during storage. In the laboratory, the organisms and surficial sediment were removed from the samples. Samples were then air-dried and stored in air-tight plastic bags.

8.3.1.3. Mechanical sample processing

The first stage of laboratory sample processing was to separate quartz grains. The samples were broken into pieces with a maximum diameter of 3-4 cm with a hammer or a Turret Engineering Ltd splitter and crushed into ~0.5 cm pieces using a Fritsch VEM-Antrlebstechnik AG jaw crusher. Each rock sample was then milled using a Pulverisette 13 Fritsch Laboratory Disk Mill and subsequently dry-sieved for > 1 h using three sieves: 53 μm, 106 μm and 150 μm in order to separate the fraction of interest which contains single quartz grains. The sieves were selected based on the grain size distribution of a test sample (Figure 8.22). Microscope observation showed that the 53-106 μm fraction contained single grains while conglomerates were common in the 106-150 μm fraction. Therefore, the material > 106 μm was re-milled to maximise the amount of the desired 53-106 μm fraction.

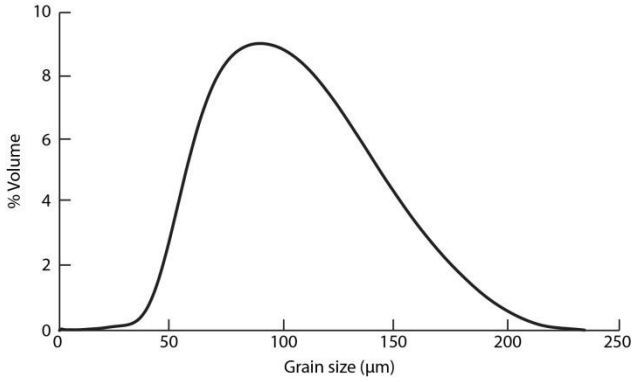


Figure 8.22. The contribution of the quartz grains of different sizes to the total volume of a test sample derived from the sandstone bed B1.

The 53-106 μm fraction was wet-sieved to 53 μm because of the challenges of separating the fine fraction from unwanted dust while rinsing. The material was then rinsed five times with meteoric (tap) water and three times with deionised water, the latter done to rinse out the meteoric water which contains boron (^{10}B) and beryllium (^{10}Be), and it was dried overnight at 70°C. An Outotec Laboratory High Intensity Induced Roll Magnetic Separator MIH(13)111-5 was used to separate non-magnetic grains from unwanted magnetic material. The non-magnetic material was re-run through the separator until < 1% of grains fell onto the magnetic pile. Table 8.3 contains the details of the mass lost during

mechanical sample processing. The digital X-ray radiogrammetry (DXR) facility at the Natural History Museum, London was used to assess the relative contribution of quartz and feldspar in a pulverised 1 g of samples 50 and 99. The samples were mainly composed of quartz which made up 94.5 ± 1.9% and 93.1 ± 1.9% of the weight of the respective samples. Feldspar formed the remainder of the material.

Table 8.3 The amount of the material at various stages of the mechanical sample processing: total weight (g) and the weight normalised by the initial weight (%).

Sample ID	Initial sample weight (g)	53-106 μm fraction after sieving		53-106 μm fraction after rinsing and drying		Non-magnetic material 53-106 μm	
		Weight (g)	Normalised (%)	Weight (g)	Normalised (%)	Weight (g)	Normalised (%)
0	1,272	673	52.91	361	28.38	88	6.92
20	1,567	994	63.43	455	29.04	74	4.72
50	2,929	1,764	60.23	900	30.73	145	4.95
60	1,418	983	69.32	544	38.36	96	6.77
70	2,023	824	40.73	390	19.28	79	3.91
80	2,540	877	34.53	359	14.13	72	2.83
90	1,448	1,060	73.20	512	35.36	102	7.04
99	3,125	1,607	51.42	752	24.06	137	4.38
100	2,394	813	33.96	302	12.61	69	2.88
101	5,169	2,851	55.16	1,178	22.79	75	1.45
150	1,693	565	33.37	310	18.31	86	5.08
200	1,772	1,249	70.49	606	34.20	135	7.62
230	1,902	1,256	66.04	725	38.12	101	5.31
231	2,166	1,393	64.31	652	30.10	93	4.29
240	2,257	691	30.62	344	15.24	80	3.54
241	2,472	1,554	62.86	482	19.50	74	2.99
250	6,844	4,648	67.91	1,288	18.82	109	1.59
260	3,742	2,794	74.67	929	24.83	95	2.54
270	2,901	1,975	68.08	771	26.58	73	2.52
271	10,135	6,216	61.33	399	3.94	69	0.68
280	8,654	6,399	73.94	912	10.54	69	0.80
290	3,952	1,307	33.07	530	13.41	92	2.33
300	7,556	4,110	54.39	850	11.25	228	3.02
Mean	3,475.26	2,026.22	56.35	632.65	22.59	97.43	3.83
Standard deviation	2,493.98	1,716.51	14.85	278.03	9.52	36.08	2.00

8.3.1.4. Chemical sample processing

In order to purify quartz, the samples were etched in HCl and HF. From this stage the Milli-Q water was used exclusively, which is water purified through filtration and deionisation to achieve a resistivity of 18.2 MΩ·cm at 25 °C. Firstly, up to 80 g of material was placed in a glass beaker. 5 ml

of water, 5 ml of 6N HCl and 0.1 ml of H_2O_2 per gram of the sample were added to remove easily dissolved minerals without losing quartz. The solutions were placed on a hot plate for 12 h. The beakers were drained; the samples were rinsed five times and dried at a temperature of 65°C for 24 h (Kohl and Nishiizumi, 1992).

Subsequently, two rounds of HF etching were performed. The samples were weighed and put into 5 l bottles. 64 ml of water, 0.47 ml of nitric acid (HNO_3) and 0.83 ml of HF per gram of sample were added to remove unwanted silicate minerals, maximizing the purity and yield of quartz. The bottles were placed in an ultrasonic bath for 9 h to remove impurities including major elements such as Al, Ca, Fe, K, Mg, Na and Ti (Kohl and Nishiizumi, 1992; Corbett et al., 2016). The excess acid was drained into the acid waste neutraliser, and the samples were rinsed four times, transferred into 125 ml beakers and dried at 60°C. Figure 8.23 shows the decrease in sample mass as a result of HF etching.

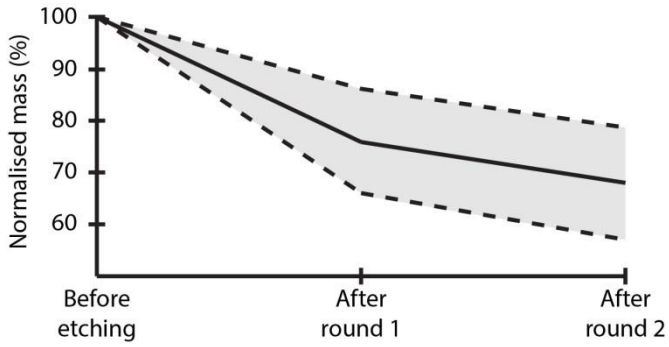


Figure 8.23 Sample mass loss (mean ± standard deviation) during HF etching as a percentage of the initial mass of the sample.

Inductively coupled plasma mass spectrometry (ICP-MS) was used to verify whether the samples were clean enough to proceed with the wet chemistry, as the impurities can overload columns (during the next steps of processing). The etching was considered successful if the concentration of aluminium (Al) was lower than 300 ppm, a value calibrated to confirm that all minerals except quartz were removed (Kohl and Nishiizumi, 1992; Corbett et al., 2016).

Subsequently, 0.334 g of the UMV 17-1 ^{9}Be carrier (759 ± 9 ppm) was added to the quartz. The purpose of this step was to be able to calculate the number of ^{10}Be atoms in samples from the ^{10}Be/^{9}Be ratio measured with AMS knowing the quantity of ^{9}Be atoms. The procedure was performed in three batches, each having a blank, which did not contain quartz. 0.3 ml of HNO_3 and 5 ml of HF per gram of sample were added to dissolve the quartz. The beakers were placed on a hot plate and covered with lids. The temperature was gradually increased from 90° to 190°C. When the quartz dissolved, the lids were taken off and the remaining acid with all silicon (Si) was evaporated. The samples were treated three times with perchloric acid ($HClO_4$) to destroy fluorides and remove boron

(B). In the first round, 10 ml of water, 10 ml of HNO_3 and 4 ml of $HClO_4$ were added and in the second and third rounds, the beaker was rinsed and 2 ml of $HClO_4$ were added. Samples were dried in between the rounds (Dunai, 2010; Corbett et al., 2016).

Anion column chemistry was performed to remove iron (Fe). 20 ml columns were filled with Dowex 1X8 200-400 mesh resin. The columns were conditioned with 60 ml of 9N HCl. The samples were dissolved in 5 ml 9N HCl, transferred to tubes and centrifuged to remove fluorides and a portion of titanium (Ti). Each sample was transferred onto the top of the resin and once it was within the resin, 40 ml of 9N HCl was added. The solution was dried while 80 ml of 0.1N HCl were passed through the columns to collect and reject unwanted minerals (Corbett et al., 2016).

Cation column chemistry served to separate the remaining Ti. 20 ml columns were filled with Dowex 50WX8 200-400 mesh resin. Dried samples were dissolved in 6 ml of 1N sulfuric acid (H_2SO_4) and 1 drop of hydrogen peroxide (H_2O_2), centrifuged and put on the top of the resin. Once the sample was absorbed into the resin, 140 ml of 1N H_2SO_4 mixed with 0.1% of H_2O_2 was added. H_2O_2 was used to detect Ti because the amount of mineral determines the hue of yellow (Clifford, 1999). The obtained fraction was rejected and 100 ml of 1N HCl was poured on the top of the resin. The fraction was collected for further processing while the columns were conditioned with 200 ml of 6N HCl and then with 60 ml of water (Corbett et al., 2016).

The samples were dried and dissolved with 1 ml of 6N HCl. Beryllium hydroxide (BeH_2O_2) was precipitated with ca. 2 ml of ammonium hydroxide (NH_4OH) at pH~8 and cleaned by centrifuging and rinsing. It was transferred into crucibles and dried at 90°C for 6 h. The hydroxide was then burned at 750°C for 5 minutes to produce beryllium oxide (BeO). It was powdered, mixed with niobium (Nb) at a 1:1 ratio and packed into stainless steel cathodes (Hunt et al., 2006; Rood et al., 2010; Corbett et al., 2016).

8.3.1.5. Accelerator mass spectrometry (AMS)

The $^{10}Be/^{9}Be$ ratio was measured using 6MV tandem accelerator at the Australian Nuclear Science and Technology Organisation. To keep the measurement error as close to 5% as possible, ten measurements were performed on each sample. Concentrations of ^{10}Be were calculated from the AMS measurements (Figure 8.24).

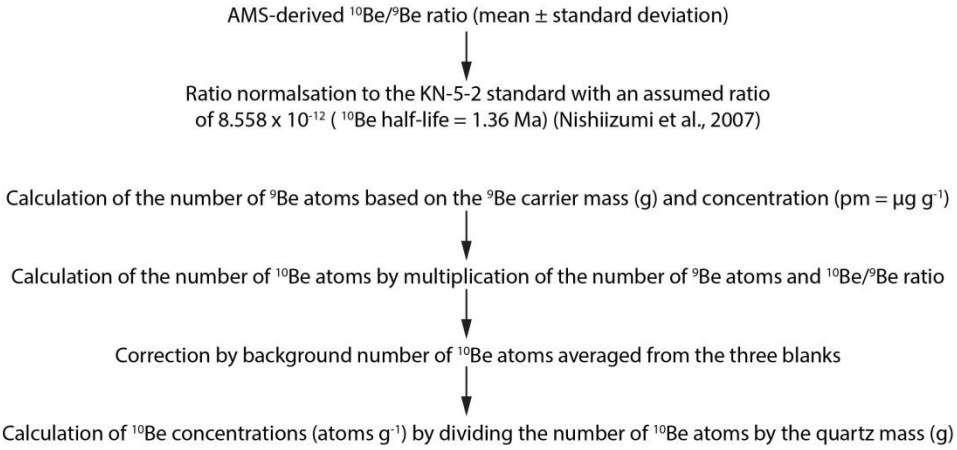


Figure 8.24 The calculation of ^{10}Be concentration in a quartz sample based on the $^{10}Be/^{9}Be$ ratio measured with the accelerator mass spectrometer.

8.3.2. Results

Background ^{10}Be atoms were counted by averaging the number of atoms in three blanks with the ^{9}Be carrier added in the chemical processing phase (section 8.3.1.4). The background quantity of ^{10}Be equals 1.13×10^{4} atoms (Table 8.4). The final concentrations of ^{10}Be vary between 1.30×10^{3} atoms g^{-1} in sample 0 (collected from the cliff face) and 1.36×10^{4} atoms g^{-1} in sample 270 (located 267.39 m from the cliff toe). The error varies between 3.64% (sample 240 – located 231.11 m from the cliff toe) and 11.32% (sample 0), with the average 6.30% (Table 8.5). Generally, the concentrations increase with the distance from the cliff, but there is considerable between-sample variability at the seaward section of the platform, with a 6.13×10^{3} atoms g^{-1} difference between samples 270 and 271 located 267.39 and 274.01 m from the cliff toe, respectively (Figure 8.25). Note that the error (standard deviation) is measured in %. Translating it into the absolute concentrations results in higher error characterising higher-concentration samples (here located more seawards) even though the % error is similar to the lower-concentration samples (Figure 8.25).

Table 8.4 The calculation of the number of the background ^{10}Be atoms from the blanks based on the ^{9}Be carrier weight and the AMS measurements of $^{10}Be/^{9}Be$.

Sample ID	^{9}Be carrier mass (g)	^{9}Be carrier concentration (µg g^{-1})	$^{10}Be/^{9}Be$ ($\times10^{-16}$)	$^{10}Be/^{9}Be$ error ($\times10^{-16}$)	$^{10}Be/^{9}Be$ error (%)	Quantity of ^{9}Be (atoms) ($\times10^{19}$)	Quantity of ^{10}Be (atoms)
BLK120218	0.3396	759	10.28	3.43	33.33	1.72238	17697.46
BLK190218	0.3405	759	3.12	1.18	37.78	1.72694	5379.78
BLK230218	0.3361	759	6.41	1.85	28.86	1.70463	10920.88
						MEAN	11332.70

Table 8.5 The calculation of ^{10}Be concentrations based on the sample weight and the AMS measurements of $^{10}Be/^{9}Be$.

Sample ID	Quartz mass (g)	^{9}Be carrier mass (g)	^{9}Be carrier concentration (μg g^{-1})	^{10}Be/^{9}Be (×10^{-16})	^{10}Be/^{9}Be error (×10^{-16})	^{10}Be/^{9}Be error (%)	Quantity of ^{9}Be (atoms) (×10^{19})	Quantity of ^{10}Be (atoms)	Background-corrected quantity of ^{10}Be (atoms)	^{10}Be concentration (atoms g^{-1})
0	32.177	0.3406	759	30.85	3.49	11.32	1.72745	53,291.89	41,959.19	1,304.01
20	32.327	0.3394	759	57.29	4.93	8.61	1.72137	98,618.77	87,286.07	2,700.10
50	35.214	0.3383	759	72.21	5.05	6.99	1.71579	123,902.12	112,569.41	3,196.72
60	39.680	0.3390	759	67.59	5.91	8.74	1.71934	116,215.15	104,882.45	2,643.21
70	40.151	0.3416	759	88.38	6.00	6.79	1.73252	153,115.25	141,782.55	3,531.23
80	41.861	0.3412	759	124.24	7.62	6.13	1.73050	214,996.71	203,664.00	4,865.24
90	41.673	0.3379	759	140.17	9.21	6.57	1.71376	240,217.48	228,884.78	5,492.40
99	45.911	0.3396	759	142.47	7.13	5.00	1.72238	245,387.51	234,054.80	5,098.01
100	36.196	0.3398	759	140.93	12.98	9.21	1.72339	242,878.00	231,545.29	6,396.99
101	32.453	0.3412	759	106.42	7.18	6.74	1.73050	184,159.29	172,826.58	5,325.44
150	38.327	0.3440	759	208.79	11.26	5.39	1.74470	364,275.10	352,942.39	9,208.71
200	37.511	0.3395	759	234.39	10.68	4.56	1.72187	403,589.82	392,257.11	10,457.12
230	35.434	0.3304	759	221.90	10.27	4.63	1.67572	371,842.21	360,509.50	10,174.11
231	37.401	0.3409	759	266.16	11.12	4.18	1.72897	460,183.60	448,850.89	12,001.04
240	47.375	0.3382	759	325.86	11.85	3.64	1.71528	558,941.04	547,608.34	11,559.02
241	36.832	0.3419	759	196.51	9.35	4.76	1.73405	340,757.25	329,424.54	89,43.98
250	10.924	0.3374	759	76.96	6.75	8.77	1.71122	131,699.09	120,366.38	11,018.53
260	31.897	0.3403	759	205.58	10.03	4.88	1.72593	354,816.78	343,484.08	10,768.54
270	31.713	0.3404	759	256.94	13.00	5.06	1.72644	443,590.89	432,258.18	13,630.32
271	38.961	0.3361	759	178.02	11.45	6.43	1.70463	303,458.04	292,125.34	7,497.89
280	17.468	0.3358	759	93.36	6.69	7.16	1.70311	159,005.51	147,672.81	8,453.90
290	35.771	0.3400	759	221.03	11.70	5.29	1.72441	381,146.10	369,813.40	10,338.36
300	41.129	0.3366	759	312.60	12.31	3.94	1.70716	533,659.73	522,327.02	12,699.73

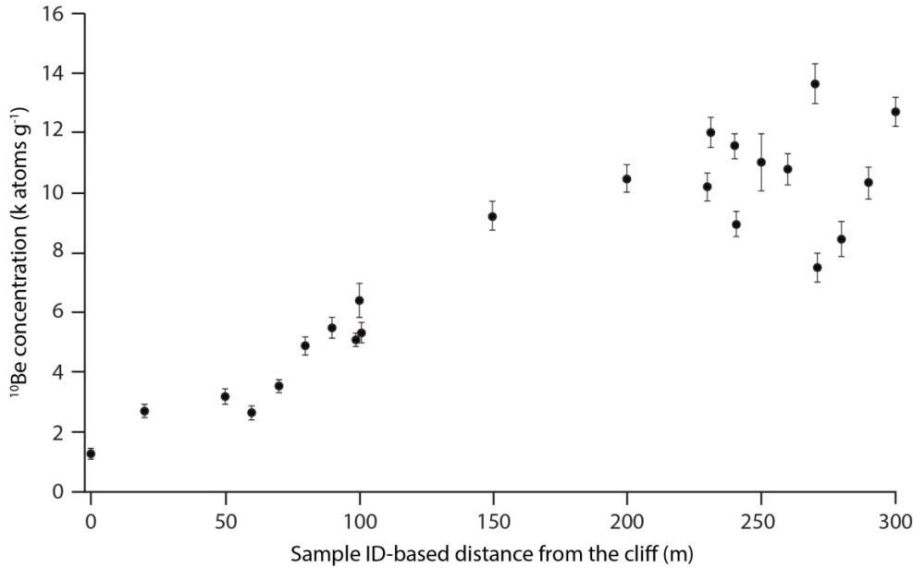


Figure 8.25 The final ^{10}Be concentrations (± standard deviation) for 23 rock samples collected across Hartle Loup (exact locations: Figure 8.21). Distance from the cliff (m) is taken from the sample ID.

8.4. Reconstructing rocky coast evolution from cosmogenic ^{10}Be concentrations

8.4.1. Methods

^{10}Be concentrations were combined with numerical modelling to reconstruct likely scenarios of the evolution of Hartle Loup during the Holocene. The concentration from the sample collected at the bottom of the cliff face (sample 0) was assumed to represent subsurface production related to muons (the geological inheritance), and so its value was subtracted from the remaining sample concentrations (Hurst et al., 2017). Samples 99 and 101 were not included in the profile evolution analysis and they are discussed separately. In all cases, assumptions A3 (P = 4.009 atoms g^{-1} yr^{-1}), A6 (constant cliff geometry), A7 (zero re-burial), A8 (no beach deposit) and A10 (constant wave and tidal climates) were assumed valid, while A1 (initiation of cliff retreat 7 kyr BP), A4 (constant position of the seaward edge), A5 (constant cliff retreat rate) and A9 (no platform erosion) were either valid or not valid.

8.4.1.1. Fitting ^{10}Be concentrations into the constant cliff retreat model

Calculated isotope concentrations were plotted next to the expected concentrations to verify whether the whole 300 m platform could have formed in the Holocene. If it is a feature inherited from previous interglacials (i.e. sea-level high stands), the concentrations should exceed those predicted for the no platform erosion scenario (A9), either for the whole profile or a seaward portion (Regard et al.,

2012). In this model the assumptions about the constant cliff retreat rate initiated at 7 kyr BP, which entirely depends on the platform width and the stable seaward edge position (A1, A4 and A5), were kept valid.

8.4.1.2. Using ^{10}Be concentrations and the empirical model to reconstruct past cliff retreat rates

Potential changes in the cliff retreat rates throughout the Holocene were explored based on the ^{10}Be concentrations and various modes of platform erosion. In this case, A1 (initiation of cliff retreat 7 kyr BP), A4 (constant position of the seaward edge) and A5 (constant cliff retreat rate) were not imposed and 60 scenarios of cliff retreat were analysed. 20 scenarios assumed a constant cliff retreat of 0.25×10^{-2} to 5.00×10^{-2} m yr^{-1} at 0.25×10^{-2} m yr^{-1} intervals which has a similar range to the contemporary retreat rates of the nearby cliffs (Rosser et al., 2013). 20 scenarios assumed a rate deceleration which agrees with coastal evolution models in which wave efficiency at the cliff toe decreases as the platform widens (Johnson, 1919; Flemming, 1965; Sunamura, 1992; Walkden and Hall, 2005). Contemporary erosion rates were set to 0.25×10^{-2} m yr^{-1} with a linear deceleration rate of 5.00×10^{-6} m yr^{-1} to 1.00×10^{-4} m yr^{-1} at 5.00×10^{-6} m yr^{-1} intervals. Finally, 20 scenarios assumed a linear acceleration of the retreat rates of 5.00×10^{-6} m yr^{-1} to 1.00×10^{-4} m yr^{-1} at 5.00×10^{-6} m yr^{-1} intervals with a contemporary retreat rate of 0.05 m yr^{-1} which is within the range recorded by Rosser et al. (2013).

The exposure ages along the 300 m Hartle Loup profile at 1 m intervals with the real elevations (Figure 8.1B) were calculated for the 60 scenarios. If any point experienced exposure over 7 kyr BP it was assumed to be inherited from an interglacial under the assumption A10 of constant wave and tidal climates. In case of retreat acceleration, once a point reached the lowest positive rate moving back in time, the rate stayed stable till 7 kyr BP. Figure 8.26 conceptually explains how exposure ages across the platform change as a function of cliff retreat mode with a steady or linearly changing rate.

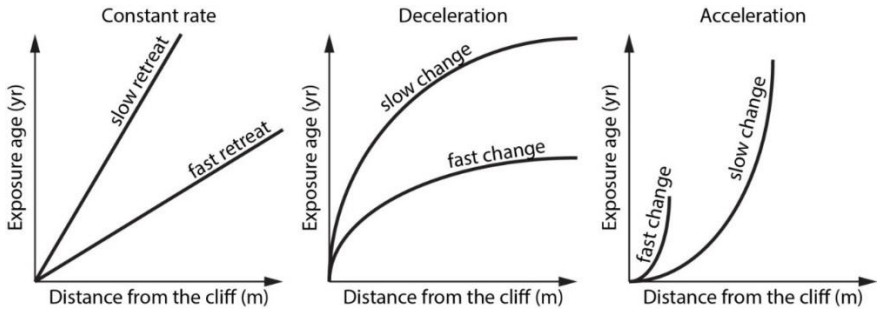


Figure 8.26 A conceptual model of the cross-shore distribution of exposure ages depending on the cliff retreat mode

The topographic and water shielding, and the geomagnetic scalar were calculated from the real profile morphology (Figure 8.1B) for the 60 retreat scenarios.

Three down-wearing scenarios were then explored: 1) the parallel profile evolution with the stable slope of 0.4° (Trenhaile, 1974), 2) the widening of the profile (Trenhaile, 2000; Walkden and Hall, 2005) and 3) the empirical model developed in Chapters 5 and 7. In total 240 scenarios were explored (60 × no platform erosion + 60 × 3 platform erosion scenarios). The expected concentrations were compared with the measured concentrations and the likely scenarios of cliff retreat in the last 7 kyr were identified. Likely scenarios were selected, which fulfilled all of the following conditions:

- Predicted concentrations were within 20% of the measured values for samples located landward from the steps (samples 20-240).
- The whole 300 m platform was formed in the last 7 kyr unless an increase in concentrations of at least one order of magnitude moving seaward is present to account for platform inheritance (Regard et al., 2012).
- For samples located seaward from the landward-most step (samples 241-300), predicted concentrations are higher than 80% of the measured ones for at least seven out of eight samples.

8.4.1.3. Additional samples

The contribution of step back-wearing to platform erosion was explored by comparing expected and measured ^{10}Be concentrations from locations seaward of the landward-most step (samples 241-300). The expected concentrations include exposure ages, topographic and water shielding, the geomagnetic scalar and the platform erosion scalar due to the down-wearing contribution (section 8.4.1.2). The difference between modelled and measured concentrations was assumed to represent the platform erosion scalar due to the step back-wearing contribution, S_{er_step}. Knowing the exposure times of the location where the samples were obtained allows the calculation of exposure time from under the step. This is based on relative contribution of $S_{er_step} < 1$ for the period when the location was exposed from under the cliff but the step had not receded yet, and $S_{er_step} = 1$ for the period when the sample was exposed from under the step. The exact value of $S_{er_step} < 1$ entirely depends on the step height under Eq 8.8.

The concentrations in samples 99, 100, 101 located 101.46, 101.41 and 102.23 m from the cliff toe, respectively, were considered in more detail to understand the pattern of down-wearing at the local (meter) scale rather than along the profile. If surface lowering was spatially uniform, the concentrations would be similar.

8.4.2. Results

8.4.2.1. Fitting ^{10}Be concentrations into the constant cliff retreat model

Measured concentrations are lower than those predicted under the no platform erosion scenario along the whole profile (Figure 8.27; Table 8.6). For the landward 240 m, they are similar to the concentrations modelled using scenarios of the down-wearing both parallel to the cliff retreat rate and when the platform widens, with the respective average difference between modelled and measured concentrations of 18.40% and 21.53% of the measured concentrations when the anomalous sample 60 (located 62.09 m from the cliff toe) is excluded. Inclusion of this sample results in an average difference of 30.82% and 34.22%, respectively. The seaward-most 60 m of the shore platform is characterised by a larger decrease in measured concentrations than when the down-wearing is assumed to be the only erosion process at the foreshore. There is a 25.50% and 49.75% decrease in concentrations in the samples adjacent to the steps (sample pairings 240-241 and 270-271). For scenarios of step back-wearing proportional to the cliff retreat and the location-dependent back-wearing modelled concentrations decreased by 50.68% and 44.26%, respectively, for the step at 240 m and 41.14% and 33.24%, respectively, for the step at 270 m (Figure 8.27).

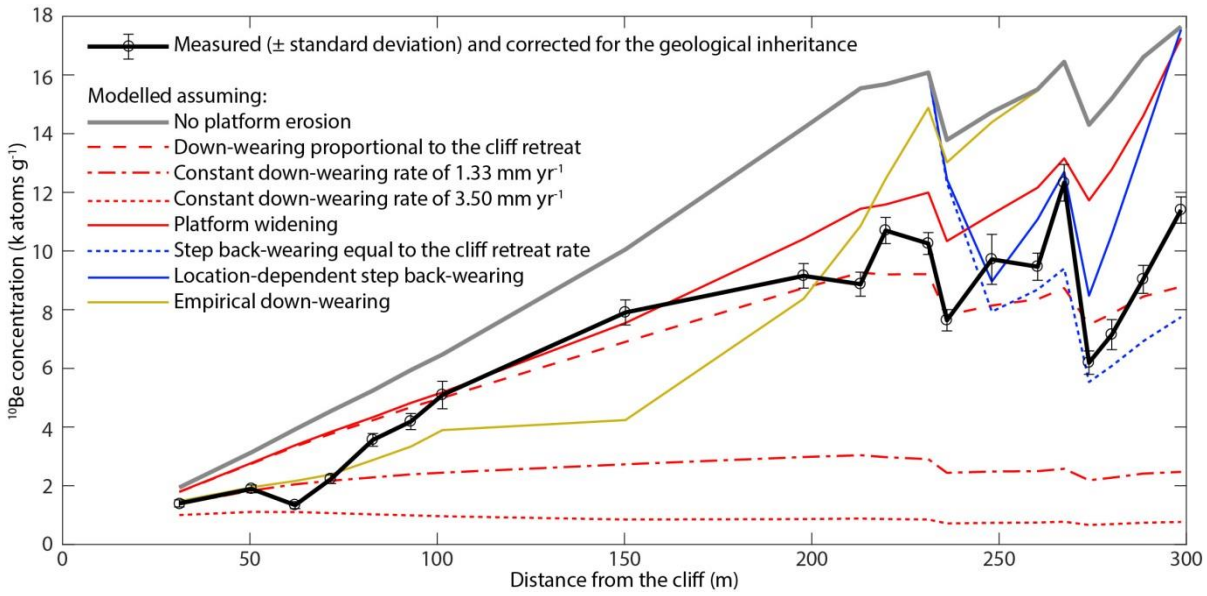


Figure 8.27 ^{10}Be concentrations in 20 rock samples collected across Hartle Loup measured and predicted under various scenarios of platform erosion.

Table 8.6 ^{10}Be concentrations measured and predicted under various scenarios of platform erosion for 20 rock samples collected across Hartle Loup.

Sample ID	Measured and corrected for the geological inheritance	Standard deviation of measured	No platform erosion	Down-wearing proportional to the cliff retreat	Constant down-wearing of 1.33 mm yr^{-1}	Constant down-wearing of 3.50 mm yr^{-1}	Platform widening	Step back-wearing equal to the cliff retreat	Location-dependent step back-wearing	Empirical down-wearing	Platform widening + location-dependent step back-wearing
20	1,396	120	1,941	1,788	1,373	1,001	1,793	1,941	1,941	1,473	1,793
50	1,893	132	3,139	2,753	1,834	1,108	2,776	3,139	3,139	1,947	2,776
60	1,339	117	3,922	3,336	2,048	1,104	3,379	3,922	3,922	2,162	3,379
70	2,227	151	4,544	3,768	2,171	1,068	3,835	4,544	4,544	2,382	3,835
80	3,561	218	5,244	4,231	2,283	1,024	4,333	5,244	5,244	2,876	4,333
90	4,188	275	5,942	4,677	2,387	991	4,822	5,942	5,942	3,335	4,822
100	5,093	469	6,472	4,995	2,445	960	5,182	6,472	6,472	3,896	5,182
150	7,905	426	10,054	6,903	2,731	848	7,548	10,054	10,054	4,238	7,548
200	9,153	417	14,195	8,739	2,978	863	10,410	14,195	14,195	8,374	10,410
230	8,870	411	15,545	9,259	3,040	881	11,440	15,545	15,545	10,854	11,440
231	10,697	447	15,684	9,202	2,974	865	11,585	15,684	15,684	12,462	11,585
240	10,255	373	16,083	9,214	2,906	848	11,992	16,083	16,083	14,883	11,992
241	7,640	364	13,783	7,812	2,440	715	10,336	12,320	12,447	13,021	9,335
250	9,715	852	14,734	8,142	2,484	735	11,254	7,932	8,962	14,390	6,845
260	9,465	462	15,512	8,359	2,496	745	12,162	8,686	11,082	15,468	8,689
270	12,326	624	16,447	8,735	2,577	774	13,156	9,403	12,696	16,436	10,155
271	6,194	398	14,304	7,489	2,186	662	11,725	5,535	8,475	14,304	6,947
280	7,150	512	15,196	7,859	2,273	692	12,782	6,083	10,571	15,196	8,891
290	9,034	478	16,604	8,448	2,414	739	14,602	6,926	13,721	16,604	12,066
300	11,396	449	17,648	8,784	2,472	766	17,259	7,747	17,550	17,648	17,162

To see whether combining the down-wearing and the step back-wearing scenarios provides a better fit between measured and modelled concentrations, the models of platform widening and location-dependent step back-wearing were combined. These two scenarios were chosen as the down-wearing proportional to the cliff retreat rate and/or the step back-wearing equal to the cliff retreat rate underestimate concentrations compared to the measured ones (Figure 8.27). Predicted concentrations are similar to the measured ones with the average difference of 34.22% respective to the measured concentrations for the whole profile. The main difference exists for sample 60 (located 62.09 m from the cliff toe) and at the seaward-most rock bed (Figure 8.28).

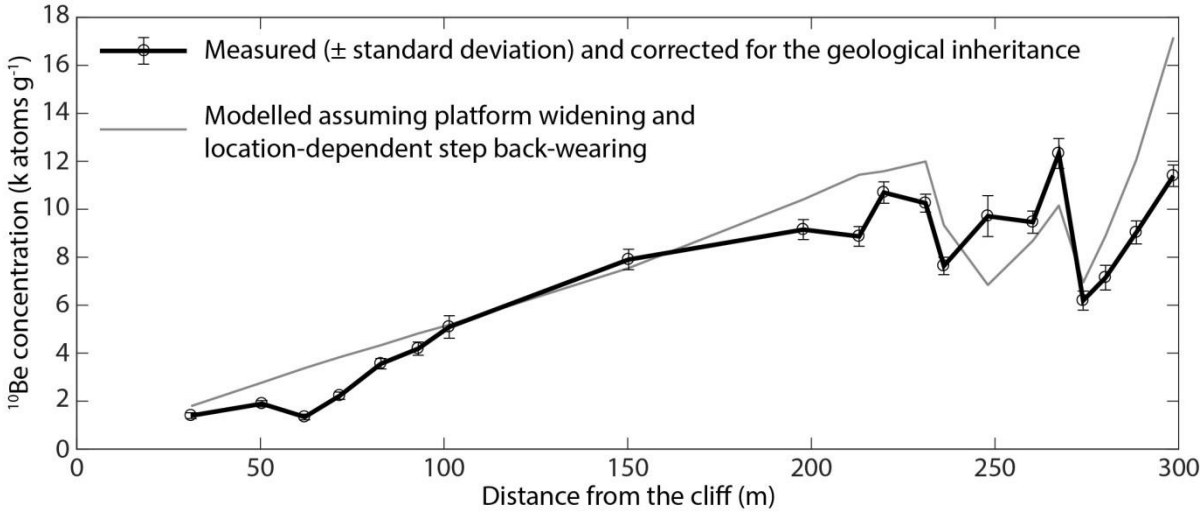


Figure 8.28 ^{10}Be concentrations in 20 rock samples collected across Hartle Loup, measured and predicted under the assumption of platform erosion through combination of the down-wearing where platform widens and flattens in time (Figure 2.2B), and the location-dependent step back-wearing.

8.4.2.2. Using ^{10}Be concentrations and the process-based model to reconstruct past cliff retreat rates

Figure 8.29 depicts modelled exposure ages, the topographic and water shielding and the geomagnetic scalar for 60 scenarios of: stable cliff retreat rates (20), retreat rate acceleration (20) and retreat rate deceleration (20). The simulations end (moving back in time) when 7 kyr BP or the 300 m platform width are reached (section 8.4.1.2). The former is motivated by the lack of abrupt change in measured ^{10}Be concentrations which would suggest platform inheritance from previous high stands of the sea (Regard et al., 2012). The latter is related to the fact that the isotope concentrations have been measured for the contemporary 300 m wide platform, and so locations farther offshore are not within the scope of this study.

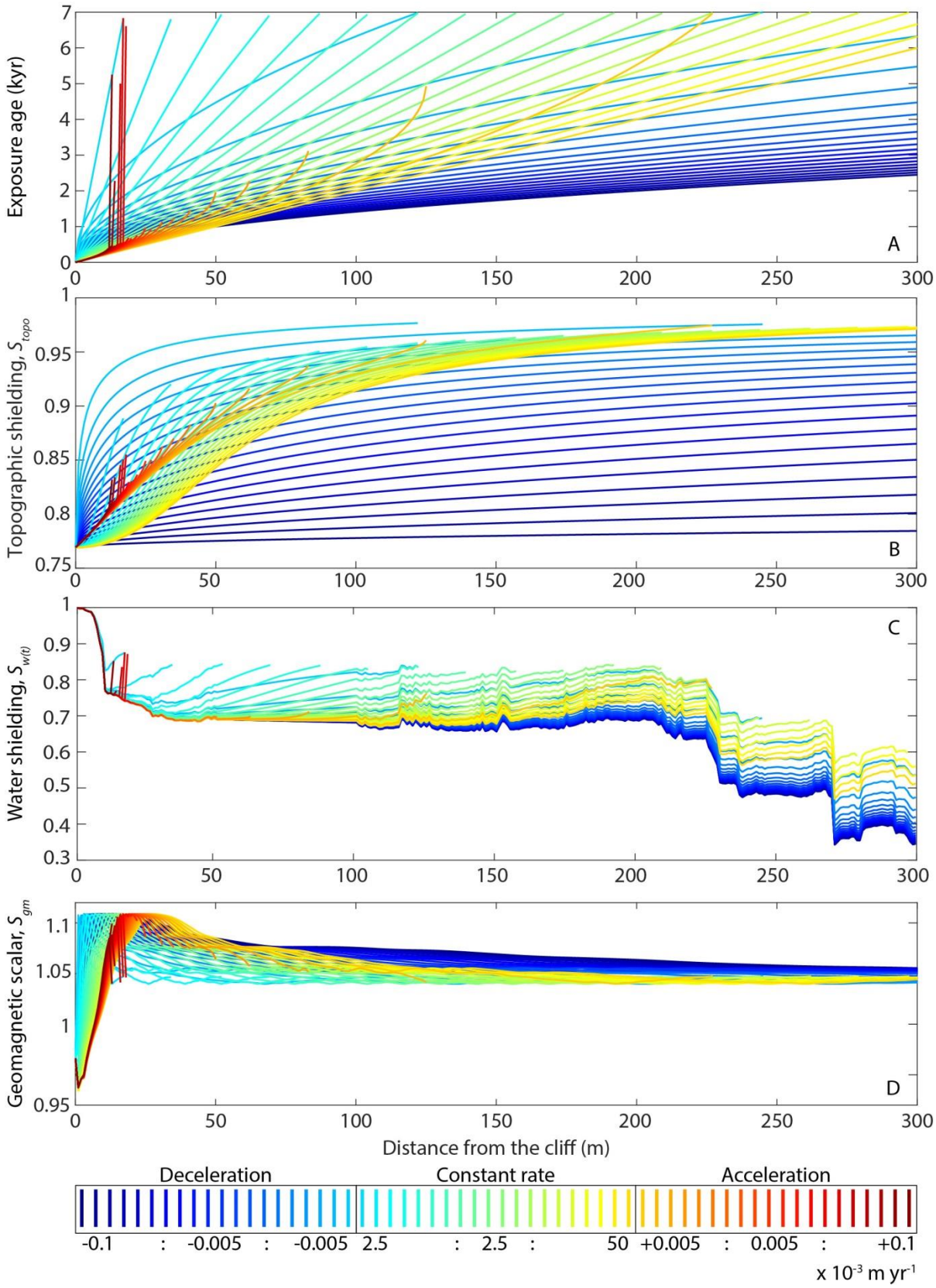


Figure 8.29 The distribution of exposure ages and the shielding/scaling factors across Hartle Loup under 60 scenarios of cliff retreat rate and pattern: A) exposure age; B) topographic shielding; C) water shielding; D) geomagnetic scalar.

The modelled exposure ages across Hartle Loup vary depending on whether the cliff retreat rate is steady or not, and on the rate of retreat, acceleration or deceleration (Figure 8.29A). If the rate is steady, the exposure ages increase linearly. A slower rate means that only a portion of the platform could have been cut in the last 7 kyr. Deceleration of retreat rates means that the landward portion of the cross-section has taken longer to be cut than the seaward portion, with slower deceleration resulting in some portions of the platform being formed before 7 kyr BP. Acceleration of the retreat rate means that the landward portion of the platform has been exposed in a relatively short period while the seaward part was being exposed slowly which often means that the portion of the platform is inherited (Figure 8.29A).

The topographic and the water shielding, and the geomagnetic scalar vary considerably across-shore. The importance of topography decreases with the distance from the cliff for all scenarios, while the water shielding becomes more important moving seawards (Figure 8.29 B and C). For the steady cliff retreat rate, deceleration and slower acceleration scenarios, the water shielding reflects the topography (Figure 8.1B). The geomagnetic scalar is highly changeable for the landward 30 m of the platform (Figure 8.29D).

Depending on the adopted scenario of platform down-wearing, the shape of the cross-shore distribution of the platform erosion scalar varies (Figure 8.30). When the down-wearing is proportional to the cliff retreat rate, the scalar gradually decreases. Platform widening imposes a curved scalar distribution with the lowest values between 150 and 250 m from the cliff toe with the exact location of the lowest values depending on the cliff retreat scenario. For the deceleration rate, it is located more seawards and for the steady retreat rate and the acceleration, more landwards (Figure 8.30B). The empirical down-wearing rate, which increases farther from the seaward edge and at elevations where the tide cycles more frequently, results in the same cross-shore scalar distribution, irrespective of the cliff retreat scenario (Figure 8.30C).

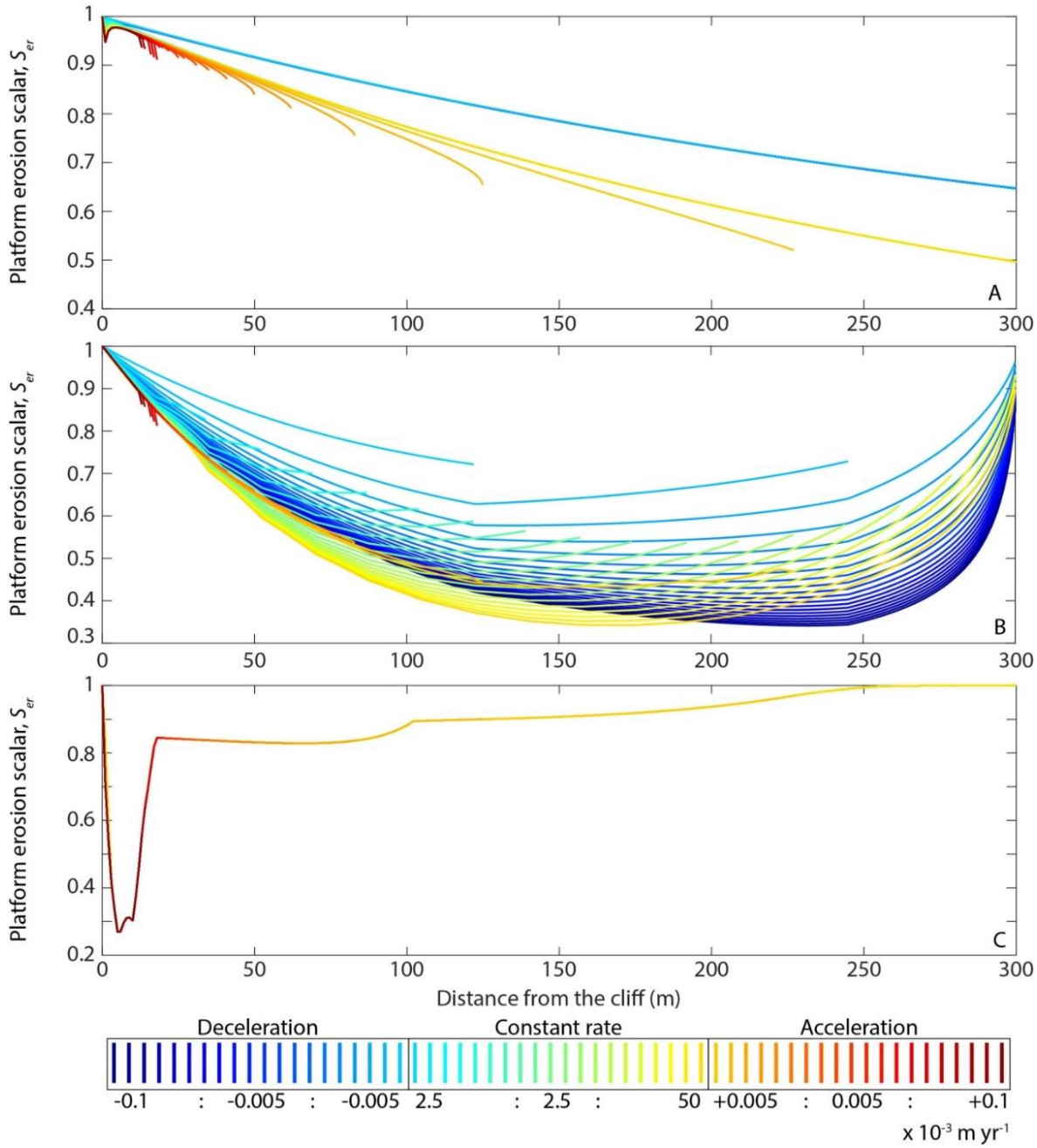


Figure 8.30 The distribution of platform erosion scalar across Hartle Loup under 60 scenarios of cliff retreat rate and pattern: A) down-wearing proportional to the cliff retreat rate; B) platform widening; C) empirical model, where the down-wearing rate is a function of the distance from the seaward edge and the tidal duration.

The 240 scenarios that combine cliff retreat rate and pattern (60) and platform down-wearing (4) result in a variety of predicted ^{10}Be concentrations which span between 0 to 2.40×10^{4} atoms g^{-1} (Figure 8.31). In general, deceleration of the retreat rates means lower concentrations than measured, irrespective of assumptions about platform down-wearing. Slow steady rates and fast retreat acceleration overestimate concentrations, particularly in the landward portion of the platform. They

also suggest inheritance of the platform which is unlikely given relatively consistent and low measured concentrations (Figure 8.31).

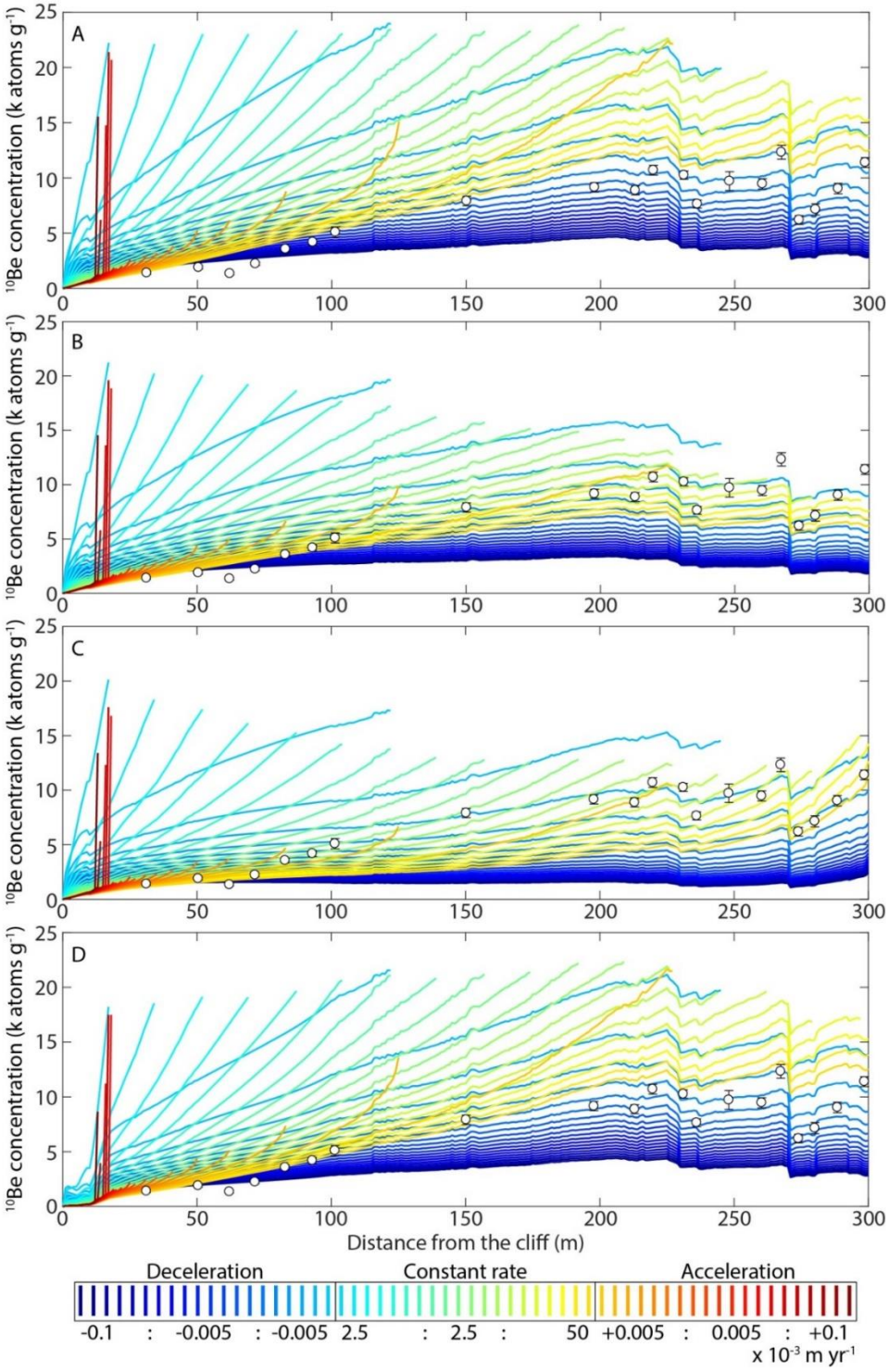


Figure 8.31 The distribution of ^{10}Be concentrations across Hartle Loup under 60 scenarios of cliff retreat rate and pattern: A) no platform erosion; B) down-wearing proportional to the cliff retreat rate; C) platform widening; D) empirical model, where the down-wearing rate is a function of the distance from the seaward edge and the tidal duration. White circles depict measured concentrations corrected for the geological inheritance with standard deviation represented by whiskers.

Results of the pairwise linear regression between measured and modelled ^{10}Be concentrations show that in general there is a strong significant relationships ($R^2 > 0.65$; $p < 0.05$) between scenarios that assume slow deceleration (< 2.00×10^{-5} m yr^{-1}), medium to high constant rates (< 3.50×10^{-3} m yr^{-1}) or slow acceleration (> 2.00×10^{-5} m yr^{-1}), and measured concentrations (Figure 8.32). Scenarios which assume no platform erosion and the empirical model are more successful in predicting ^{10}Be concentrations than the parallel evolution and platform widening models for the cliff deceleration scenarios. Slow constant rate and medium to fast acceleration are unable to explain ^{10}Be concentrations for all 20 sampling locations (Figure 8.32).

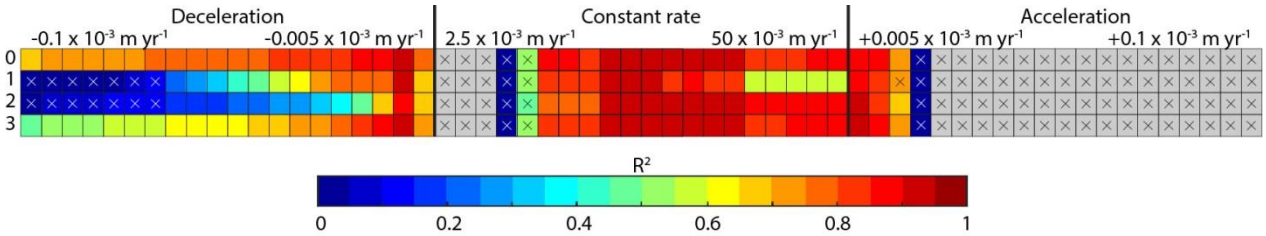


Figure 8.32 Goodness-of-fit of the pairwise linear regression models between ^{10}Be concentrations measured and modelled using the combinations of scenarios of cliff retreat rate and pattern (60 columns) and platform down wearing scenarios (0: no platform erosion; 1: down-wearing proportional to the cliff retreat rate; 2: platform widening; 3: empirical model). Grey squares represent scenarios which do not predict concentrations at all 20 sampling locations. Insignificant ($p \geq 0.05$) relationships are crossed out.

The scenarios were tested for the three conditions described in section 8.1.3.2. These conditions were: 1) the prediction of concentrations ≤ 20% off measured values for samples 20-240 (Figure 8.33A), 2) the exposure of the whole platform in the last 7 kyr or an increase in isotopes of at least one order of magnitude at some across-shore location (Figure 8.33B), and C) the prediction of > 80% of the measured values for at least seven of the samples between 241 and 300 (Figure 8.33C). Scenarios which did not fulfil all three conditions were removed.

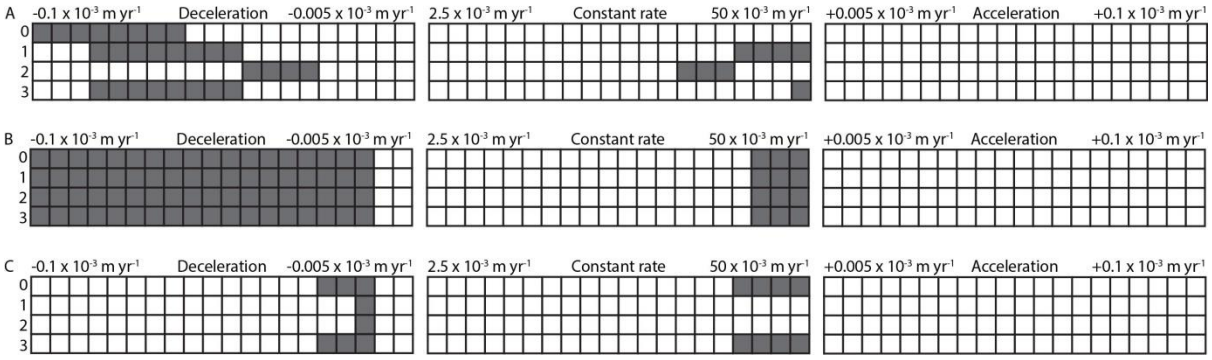


Figure 8.33 Scenarios which successfully fulfil the conditions to A) predict concentrations ≤ 20% off measured values for samples 20-240; B) expose the whole platform in the last 7 kyr; C) predict > 80% of the measured values for at least seven of samples 241-300 imposed on the combinations of scenarios of cliff retreat rate and pattern (60 columns) and platform down wearing scenarios (0: no platform erosion; 1: down-wearing proportional to the cliff retreat rate; 2: platform widening; 3: empirical model). Grey squares represent scenarios which fulfil the conditions.

Only one scenario produces results comparable with the measured concentrations. It is the model which assumes a steady cliff retreat rate of 0.05 m yr^{-1}, which implies that the 300 m of the platform has been formed in the last 6 kyr. The platform erodes as a function of the distance from the seaward edge and the tidal duration (Eq 8.10). The modelled concentrations are on average 15.64% different from those measured for the landward 12 samples, or 8.46% if sample 60 (locate 62.09 m from the cliff toe) is excluded (Figure 8.34). They overestimate concentrations at the stepped seaward part of the platform because the step back-wearing, which was shown to contribute to platform erosion (Chapter 7), has not been included in the model. The importance of the step back-wearing is analysed in the next section.

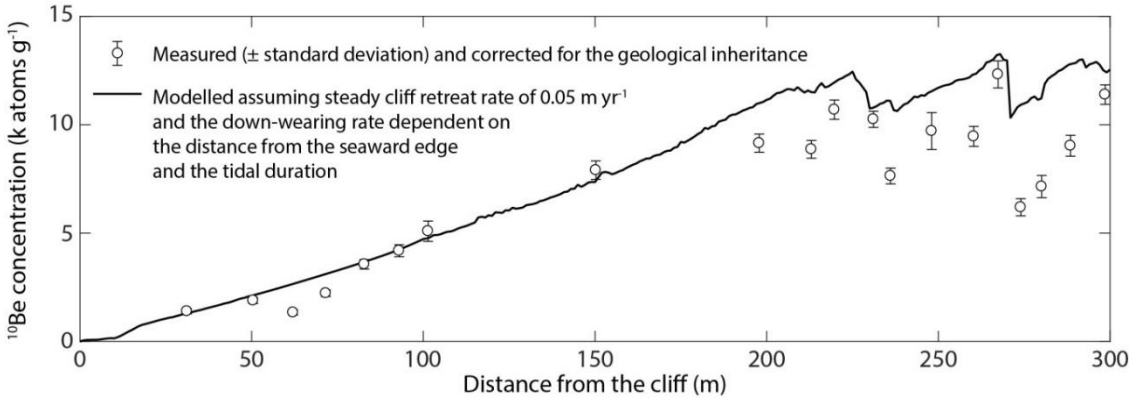


Figure 8.34 The distribution of measured (circles) ^{10}Be concentrations across Hartle Loup and the most-likely scenario of coastline evolution where the cliff retreats at the steady rate of 0.05 m yr^{-1} and the platform down-wearing rate is a function of the distance from the seaward edge and the tidal duration.

8.4.2.3. Additional samples

It is assumed that the difference between measured and modelled ^{10}Be concentrations reflects the platform erosion scalar due to the step back-wearing contribution, S_{er_step} (section 8.4.1.3). The scalar adopts the lowest values immediately at the foot of the steps and gradually increases seaward (Figure 8.35). Sample 260 (located 260.31 m from the cliff toe) has lower concentrations compared to the adjacent samples. The top step (at ~240 m from the cliff) is 0.80 m high, and the bottom one (at ~270 m) is 0.75 m high. For a single year before a location experienced step back-wearing, S_{er_step} equals 0.54 and 0.56 for the respective steps (from Eq 8.8). Knowledge of the exposure ages enables the calculation of the relative contribution of S_{er_step} = 0.54 or 0.56 (before back-wearing event) and S_{er_step} = 1 (after the back-wearing event) in the final S_{er_step} depicted in Figure 8.35.

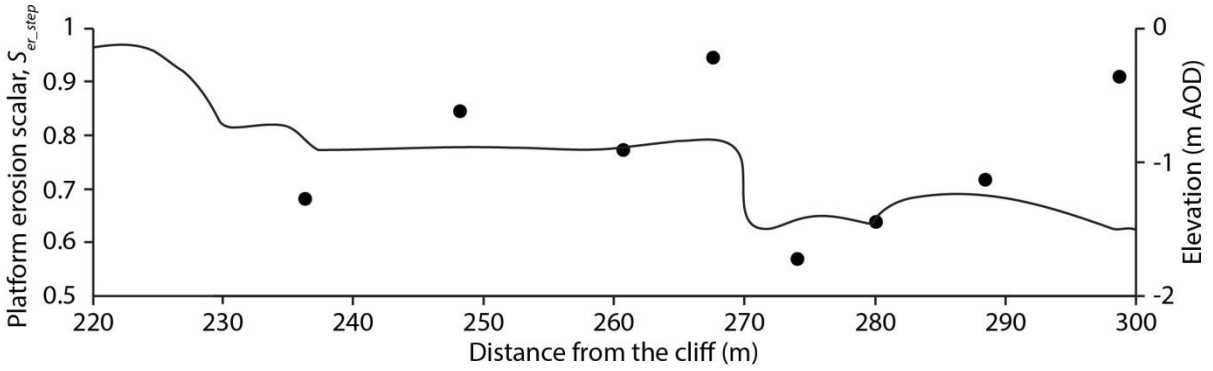


Figure 8.35 The platform erosion scalar due to step back-wearing contribution, S_{er_step} (points), at the seaward section of Hartle Loup; the line represents the distribution of elevation.

The locations adjacent to the steps were exposed from under the steps 1,501 and 142 yr BP for the top and the bottom step, respectively. The step back-wearing rates are $0.92\times10^{-2} \pm 0.29$ m$\times10^{-2}$ m yr^{-1} for the top (i.e. landward) step and $1.12\times10^{-2} \pm 0.68\times10^{-2}$ m yr^{-1} for the bottom (i.e. seaward) step (Table 8.7). Extrapolating these rates shows that the landward-most sampling location of the lowest rock bed B3 (sample 271 located 274.01 m from the cliff toe) could have been under both steps for 112 years since site exposure from under the cliff 5,349 yr BP. However, adding 112 years at the depth of 1.55 m (0.75 + 0.80) does not explain the final S_{er_step} = 0.57, which would suggest that the retreat of the top step is slightly lower than the one calculated by averaging the four samples (241, 250, 260 and 270), which is still within the error. If sample 260 (located 260.31 m from the cliff toe) is excluded, the top step seems to retreat at the relatively stable rate, while the bottom one seems to have accelerated (Table 8.7).

Table 8.7 The calculation of the step back-wearing rate from the site exposure age and the step height.

Sample ID	Distance from the cliff (m)	Exposure age (yr)	Platform erosion scalar due to step back-wearing, S_{er_step}	Distance from the top step (m)	Distance from the bottom step (m)	Exposure time from under the step (yr BP)	Step back-wearing rate (10^{-2} m yr^{-1})
241	236.09	4,701	0.69	11.09	n/a	1,501	0.74
250	248.07	4,941	0.85	23.07	n/a	3,293	0.70
260	260.31	5,181	0.78	35.31	n/a	2,665	1.33
270	267.39	5,321	0.95	42.39	n/a	4,706	0.90
271	274.01	5,461	0.57	49.01	3.01	142	2.12
280	280.10	5,581	0.64	55.10	9.10	1,009	0.90
290	288.49	5,741	0.71	63.49	17.49	1,984	0.88
300	298.58	5,961	0.91	73.58	27.58	4,737	0.58

Samples 99, 100 and 101 (located 101.46, 101.41 and 102.23 m from the cliff toe, respectively), which were taken from three different locations within a 3 m radius, vary considerably in terms of ^{10}Be concentrations (Table 8.8). The isotope concentration in the sample collected for the local low point (0.08 m lower than sample 100) equals 64.49% of the concentration from the local high point, while the ironstone nodule concentration (0.03 m higher than sample 100) is equal to 78.90% of the concentrations from the local high point (Table 8.8).

Table 8.8 ^{10}Be concentrations corrected for muon production in the samples located within a 3 m radius of the single point with different morphologic/geologic settings.

Sample ID	Location	Elevation (m AOD)	Measured ^{10}Be concentrations (atoms g^{-1})	Standard deviation (atoms g^{-1})
99	Local low point	0.09	3,794	190
100	Local high point	0.17	5,093	469
101	Ironstone nodule	0.20	4,021	271

8.5. Discussion

8.5.1. Methodological advances

In this study, sandstone with quartz grains of 53 to106 μm has been analysed. This size is one order of magnitude finer than the grains from which cosmogenic isotopes have been extracted until now. Previous rocky coast studies used the 250-500 μm fraction (Perg et al., 2001; Alvarez-Marrón et al., 2008; Choi et al., 2012; Regard et al., 2012; Hurst et al., 2016). Only Kim and Sutherland (2004) worked on a finer fraction of 150-300 μm. Here the disk mill settings, the long dry sieving, the

subsequent wet sieving and the multiple runs of magnetic separation allowed separation of the fine grain material (section 8.3.1.3).

An attempt to separate quartz from feldspar was made using froth flotation, but the technique was unsuccessful because of the lightness of the fine grains. However, the digital X-ray radiogrammetry (DXR) showed nearly exclusive contribution of quartz to the non-magnetic material, and so the sample processing could be continued without this step. If there had been more feldspar present, using ^{36}Cl instead of ^{10}Be or a different separation method, such as the high-gradient magnetic separation (Hillier and Hodson, 1997), would have been necessary.

The analytical error is low with average 6.30% (3.64-11.32%) which was achieved thanks to the quality of the AMS analysis at ANSTO. The uncertainty is slightly higher than that of Hurst et al. (2016) (2.19-6.96%; average: 4.01%) and lower than the one obtained by Regard et al. (2012) (6.50-11.95%; average 8.63%). This implies that the cliff retreat and step back-wearing rates could be precisely calculated.

8.5.2. Holocene cliff retreat rates

Relatively low ^{10}Be concentrations of up to 1.36×10^4 atoms g^{-1} suggest that Hartle Loup is not inherited from past high stands of the sea, but has been formed entirely in the Holocene. An inherited platform would have an abrupt change in concentrations of at least one order of magnitude at some across-shore locations (Regard et al., 2012). A scenario of exposure during the last interglacial, re-burial by the British Ice Sheet and glacial sediments followed by re-exposure in the last 7 kyr as the sea reached a similar level to the present one seems unlikely because of the gradual increase in concentrations across-shore. Erosion of glacial till would result in faster re-exposure rates as shown in other locations in Yorkshire (Pringle, 1985; Clements, 1994).

The most likely scenario of cliff retreat assumes a steady retreat at a rate of 0.05 m yr^{-1}, which suggests that the whole platform could have been formed in the last 6 kyr. Choi et al. (2012) dated the metamorphosed sandstone platforms in western Korean Peninsula to 148 kyr BP. Regard et al. (2012) calculated that the chalk cliffs of the southern English Channel have been retreating at 0.11-0.13 m yr^{-1} for the last 6 kyr, which agrees with the 30-yr dataset. Hurst et al. (2016) obtained the rates of 0.02-0.06 m yr^{-1} for the chalk cliffs of the northern English Channel. This implies that the whole platform could have been formed within the last 1.5 kyr, while in the last 150 yr, the retreat rate has had an acceleration of one order of magnitude (to 0.22-0.32 m yr^{-1} based on historical maps). The long-term cliff retreat rates calculated in this study are comparable with the results of Hurst et al. (2016) and lower than the results of Regard et al. (2012). Similarity to the results of Hurst et al. (2016) is surprising as this study has been conducted on harder-rock coasts, and so the retreat rates should be lower. This suggest that either the cliff resistance, *Fr*, at the studied coast is not higher than in the

study of Hurst et al. (2016), and so the rock strength (higher for sandstone than for chalk) cannot represent rock resistance to wave action (Sunamura, 1992), or that the assailing force of waves, *Fw*, at the North Sea coast is higher than at the English Channel coast. This can be related to higher storminess, nearshore seabed and/or foreshore geometry but it is impossible to assess from the data available.

The long-term cliff retreat rates calculated in this chapter are within the 0.027 ± 0.029 m yr^{-1} range calculated for the nearby cliffs by Rosser et al. (2013) from the 7 yr monthly monitoring dataset. This implies that erosion rates observed today are representative of, or even slightly underestimate, the long-term (centuries to millennia) retreat rates. The same conclusion was drawn by Regard et al. (2012). It also implies that erosion rates have not increased in the Late Holocene (Kopp et al., 2017). This conclusion is in contrast to the findings of Hurst et al. (2016) on the South English coast. They hypothesised that the tenfold increase in cliff retreat rates in the last 150 yr may be caused by human activity, progressive thinning of beach cover and/or increased storminess. It is possible that changes in one or more of these factors affect soft cliffs to a greater extent than hard-rock cliffs. Alternatively, the difference may be related to relative sea level (RSL). The South English coast is experiencing a faster rate of RSL rise (Shennan et al., 2000, 2018; Shennan and Horton, 2002).

More widely, these results may suggest that anticipated sea-level change in future (IPCC, 2013) may not have a linear influence on erosion rates at different locations because of a number of factors: geology, near- and fore-shore geometry, wave climate, tidal range and sea-level history. Extensive numerical modelling coupled with absolute exposure dating at locations with different geology and marine conditions should be performed in order to understand the long-term cliff dynamics, constrain controls upon cliff retreat rates and predict coastal evolution in future (Trenhaile, 2014; Hurst et al., 2016). The near-linear increase of the concentrations in the samples between 60 and 100 m from the cliff (Figure 8.31) suggests that the retreat proceeds gradually rather than step-wise. The failure may be episodic (Rogers et al., 2012) but it averages out over ~10 m across-shore, the distance equivalent to 200 yr of cliff retreat at the rate of 0.05 m yr^{-1}.

Measured concentrations of samples 60 (located 62.09 m from the cliff toe) and 230 (213.11 m) are lower than concentrations of the adjacent landward samples (50 and 200 respectively), which is counterintuitive because they are believed to be exposed earlier, and so should have accumulated more ^{10}Be. However, if the evolution of Hartle Loup is analysed in planform (2D) rather than as a profile (1D), the tendency of steps to run in NE-SW direction rather than coastline-parallel or perpendicular to the longest cross-profile (E-W) can be observed (Figure 8.1A). It can be related to the direction of upcoming waves or the large-scale ($10^2 – 10^3$ m) structural pattern, but this is difficult to deduce from the data presented herein. Nonetheless, it is possible that sample 50 (50.46 m from the cliff toe) was exposed from under the shale layer before sample 60, while removal of within-bed layers of the sandstone bed B1 contributed to the lower concentrations at sample 230 (Figure 8.36).

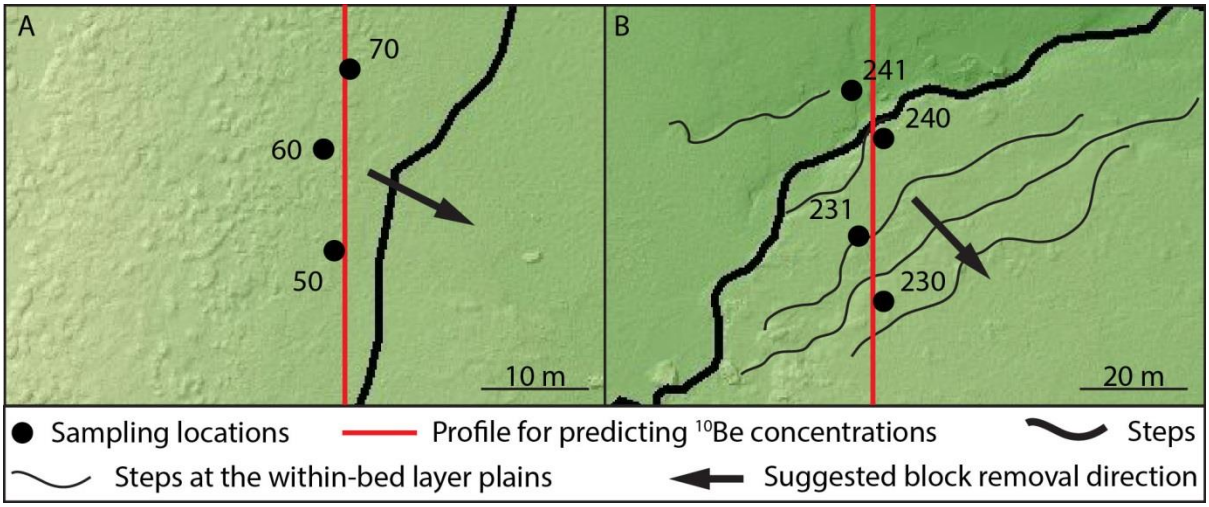


Figure 8.36 The suggested direction of Hartle Loup evolution which may explain relatively low ^{10}Be concentration in samples A) 60 (62.09 m from the cliff toe) and B) 230 (213.11 m).

8.5.3. Long-term erosion of shore platforms

One of the main problems in modelling long-term evolution of rocky coasts is poor understanding of the feedback between cliff retreat and the variable geometry of the foreshore (Masselink et al., 2011). Section 8.1.1.2 explores different scenarios of platform erosion. Depending on which scenario is used, the scalar ranges from < 0.1 to 1 and its cross-shore distribution changes (Figures 8.11, 8.14 and 8.15). Therefore, our understanding of past cliff retreat rates, at least to a certain extent, depends on which scenario of platform erosion we accept. For instance, Kim and Sutherland (2004) assumed no vertical erosion while Regard et al. (2012) assumed that the platform erodes proportionally to the cliff retreat rate. Hurst et al. (2017) explored the models with the parallel evolution and the dynamic evolution in which erosion rate depends on the availability of wave energy (see Dickson et al., 2013; Matsumoto et al., 2016), concluding that different models result in different across-shore distributions of ^{10}Be concentrations. Here the parallel model, the platform widening model, extrapolation of the MEM data and the empirical model are explored in order to identify the ones likely to result in observed concentrations.

The only model which can explain measured concentrations under present assumptions is the empirical model developed in Chapter 5. It assumes that platform down-wearing is a linear function of the distance from the seaward edge with higher rates landwards, and of the tidal duration with higher rates where the tide cycles more frequently (Eq 8.10). This implies that identifying mechanisms of erosion and the controls upon spatial distribution of foreshore erosion is crucial to model long-term platform erosion, and then long-term rocky coast evolution. It also shows that during longer timescales, foreshore erosion does not average out to fit one of the geometrical models and short-term measurements cannot be directly extrapolated to longer timescales. In contrast, localised

down-wearing rates adjust to the changing morphology of the platform and marine conditions – sea-level change coupled with the tidal duration distribution.

The sampling was performed across the widest profile of the Hartle Loup, that is at a 'headland' location. Ideally, three profiles should be sampled in order to understand the along-shore differences in coastline evolution – at a headland, in the middle of a bay and between the two. Here it was impossible because of the scarcity of suitable rock type and its exclusive presence on the foreshore off the Penny Nab headland. If the long-term cliff retreat rates were similar regardless exposure (i.e. at headland and bay locations) it would mean that the whole coastal profile is retreating at the constant pace as described by Challinor (1949) and numerically modelled by Limber et al. (2014). Differences in erosion rates would imply either the lack of an equilibrium coastline shape or that this coast has not reached it, or that headlands are transient features (Limber and Murray, 2014).

Step back-wearing is an important contributor to the distribution of ^{10}Be concentrations across shore platforms (Hurst et al., 2017). The process is difficult to monitor and predict due to its episodic character (Chapter 7). Detachments of large blocks from the steps may be important for further coastal erosion as it may change wave dissipation on the foreshore and, in consequence, the wave eroding power at the cliff toe (Poate et al., 2018). Here, the long-term step back-wearing rate has been calculated for the first time on the basis of cosmogenic isotope concentration (section 8.4.2.3). However, better understanding of controls on step erosion is needed to include it in coastal evolution models.

Finally, the differences in concentrations within a 3 m radius suggest that consistent sampling at the local high points (Stone et al., 1996; Hurst et al., 2016) and preferably consistent rock type may play a major role in reconstructing exposure ages. The causes of the high diversity of isotope concentrations at the local-scale should be further explored to ensure accurate exposure dating.

8.6. Conclusions

The conclusions emerging from this chapter are twofold.

Firstly, successful separation and purification of fine grain quartz (53-106 μm) and subsequent extraction of ^{10}Be is a key methodological advance as it implies that future exposure dating using cosmogenic isotopes may be possible at locations with a wider range of rock types.

Secondly, a contribution to the understanding of coastal processes has been made through the calculation of exposure ages at locations across the Hartle Loup shore platform from cosmogenic ^{10}Be concentrations. The analysis included a range of cliff retreat rates and pattern scenarios: constant rate, acceleration and deceleration, and four scenarios of platform down-wearing: no erosion, erosion parallel to the cliff retreat rate, platform widening and emipirical model.

The results suggest that the cliff at Penny Nab has been retreating at a steady rate of 0.05 m yr^{-1}, exposing the 300 m wide shore platform in the last 6 kyr. As such, Hartle Loup is not inherited from the last interglacial period (130-118 kyr BP). The cosmogenic isotope-derived cliff erosion rates agree with the contemporary annual- to decadal-scale rates of cliff erosion reported by Rosser et al. (2013). On this basis, there has been no acceleration in cliff retreat rates since the mid-Holocene.

Exposure ages calculated for the samples at 10 m intervals between 50 and 100 m from the cliff suggest that the recurrence of failure events is lower than 200 yr, as the retreat rates average out at this timescale. The ^{10}Be concentration change between them is gradual.

The long-term erosion at a location on the shore platform is a function of the distance from the seaward edge and the tidal duration, which changes with sea-level rise. The long-term shore platform down-wearing can be modelled from the short-term empirical data and the understanding of the controls on the distribution of erosion on the foreshore (Chapter 5).

Step back-wearing contributes to platform erosion and in consequence to ^{10}Be concentrations. Two steps at ~240 and ~270 m from the cliff retreat at the respective rates of 0.92×10^{-2} and 1.12×10^{-2} m yr^{-1} with the gradual back-wearing of the landward step and the accelerating back-wearing of the seaward step.

The results can be used to better model coastal evolution as they provide 1) the empirical values to feed the numerical models and 2) the understanding of processes and controls on coastal erosion. The lack of agreement with the results of Hurst et al. (2016) suggests that controls on the long-term coastal erosion in light of the post-industrial sea-level rise and anticipated future sea-level change and increased storminess (Slott et al., 2006; IPCC, 2013; Trenhaile, 2014; Kopp et al., 2017) should be re-considered.

9. Discussion

In this research multi-scale monitoring of shore platform erosion was undertaken in order to 1) quantify erosion rates, 2) identify mechanisms and 3) constrain controls on the magnitude of erosion and distribution of detachment sizes. The results were used to model platform erosion at two scales and were then applied to assess long-term (millennia) coastline evolution. In this chapter the three research questions are discussed using the results from Chapters 5, 7 and 8. The results are compared with existing studies and how these findings address the gaps previously identified are discussed.

9.1. What is the dominant mechanism of shore platform erosion?

9.1.1. Differences between erosion rates at the two monitoring scales

Platform erosion has been monitored at two spatial scales (10^{-3} – 10^{-2} m and 10^{-1} – 10^{0} m), with monthly and annual survey frequencies, respectively (Table 9.1). This approach has broadened the range of spatial scales normally considered by foreshore studies, which until now have relied on MEMs and cartographical data. Existing studies tend to consider platform erosion as purely the vertical change from point measurements at the (sub)mm scale (e.g. Robinson, 1976; 1977a; Stephenson and Kirk, 1998; 2001) and the retreat of protruding edges of rock beds ('steps') at the m scale (Dornbusch and Robinson, 2011). Recent advances in using Structure-from-Motion (SfM) photogrammetry to reconstruct topography (Westoby et al., 2012; Cook, 2017; Turowski and Cook, 2017) and the acquisition of high-resolution and high-precision LiDAR data (Benjamin et al., in review) allow precise quantification of eroded volumes to be monitored over extensive and continuous platform surfaces. Representation of erosion in the form of a detachment inventory allowed a suite of analyses to be adopted from the rockfall and landslide literature to characterise the size and shape distribution of detachments, and suggest mechanisms of erosion (Dussauge-Peisser et al., 2002; Malamud et al., 2004; Williams et al, 2018).

The down-wearing rates calculated on the basis of the detachment inventory at the two scales are of 0.528 mm yr^{-1} (small-scale) and 3.45 mm yr^{-1} (macro-scale), the latter being comparable with the rates of 3.21 ± 4.76 mm yr^{-1} reported by Robinson (1977a) for the same stretch of coast (Table 9.1). Significant here is the observation of an order of magnitude difference between the rates reported at the two scales, which suggests that these results cannot be simply up- or down-scaled. This means that either the dominant observable process changes with the spatio-temporal scale of investigation (section 9.1.2), or that at one of the scales the approach does not capture a representative assessment of erosion rates. The latter is likely to be the artefact of the calculation of the area by which the volume of observed erosion is divided to obtain spatially-averages rates (see Appendix 2).

*Table 9.1 Summary of the spatio-temporal scale and erosion variables based on the detachment inventories at the micro- and macro-scales; *excluding boulders.*

	Micro-scale	Macro-scale
Monitored area (m^2)	3.75	3,150,609.50
Monitoring duration (yr)	1.01	2.62
Average monitoring frequency (yr)	0.08	0.87
Technique	SfM-based change detection on DEMs	LiDAR-based change detection on DEMs
Pixel resolution (m)	0.001	0.25
Level of detection (m)	0.001	0.05
Minimal detectable volume (m^3)	6.00×10^{-9}	31.25×10^{-4}
Number of detachments	28,756	2,147,206*
Total detached volume (m^3)	2.00×10^{-3}	27,673.10*
Erosion rate (mm yr^{-1})	0.528	3.45*
Area/volume exponent *b*	1.125	1.214
Volume frequency exponent β	0.938	1.513

At the micro-scale the plot area of 0.5×0.5 m contains 500×500 pixel-based measurements. In the approach used here at the macro-scale, the total eroded volume is divided by the whole foreshore area (3.15×10^6 m^2). The full platform includes multiple pixels that either do not contain any change measurements beacause 1) the elevation data are missing (e.g. due to standing water), 2) data were sparse (< 1 point per grid cell), or 3) pixels were filtered out if their elevation was > HAT. Representation of the foreshore in the form of 1 m^2 grid cells and the calculation of erosion rates by averaging erosion rates for every cell gave the rates of 0.04 mm yr^{-1} for stepped cells, 0.01 mm yr^{-1} for non-stepped cells and an average foreshore erosion rate of 0.01 mm yr^{-1}. These rates are two orders of magnitude lower than those based on the macro-scale detachment inventory and one order of magnitude lower than that calculated for the small-scale. As the erosion rate for each cell was calculated by dividing volume lost by the area of pixels which actually contained data, rather than by the full cell size (1 m^2), these rates are perhaps more credible than the value of 3.45 mm yr^{-1} based on spatially averaging the detachments observed from the airborne LiDAR data (section 6.4).

The one order of magnitude difference between these rates and those calculated at the small-scale (0.528 mm yr^{-1}), if not explained by a change in the dominant observable process (section 9.1.2), can be ascribed to censoring. Here larger events occur relatively rarely, and so the resultant erosion rate is lower. A short-term monitoring period may be biased towards deriving lower rates of erosion. In this study there are six orders of magnitude of difference in the area monitored with a ~2.5-fold difference in monitoring duration: 3.75 m^2 × 1.01 yr at the small-scale, and 3.15×10^6 m^2 × 2.62 yr at the macro-scale. The standardised results from these two scales derive quite different eroded volumes: 5.09×10^{-9} m^3 – 1.41×10^{-5} m^3 at the small-scale, and 3.10×10^{-3} m^3 – 4.32×10^{0} m^3 at the macro-scale.

The lower precision of the macro-scale study where V_{min} = 31.25×10^{-4} m^3 as compared to the small-scale (V_{min} = 6.00×10^{-9} m^3) means that the results of the fine-scale incremental down-wearing cannot be observed. To see the granular or platelet detachment the study either needs to have the precision to measure changes at the micro-scale (10^{-3} – 10^{-2} m), or the macro-scale monitoring (10^{-1} – 10^{0} m) needs to be conducted for longer.

9.1.2. Identifying mechanisms of erosion from the size and shape distribution of detachments

To explore the possibility of different mechanisms dominating at different scales of observation, the size and shape distributions of detachments were analysed. Morphological evidence of erosion at a range of spatial scales, including the presence of detached boulders at the foot of steps (10^{0} m) and fresh scars from detachments of shale platelets and thin sandstone layers (10^{-2} m) (Figure 3.4), coupled with the scarcity of beach deposits, suggests that the dominant process of foreshore erosion is via the detachment of rock fragments rather than via grain-by-grain abrasion. At the small-scale (10^{-3} – 10^{-2} m) there is an apparent threshold at a size equivalent to a single shale platelet (11 mm cube) with an abrupt decrease in frequency for larger detachments. This suggests that the rock fragments are detached at the sub-platelet scale, most likely due to the impacts of entrained sediments, hydraulic pressure and biological activity (Wilson et al., 2013; Coombes, 2014). The whole platelets are detached when the rock bridges between them break, but larger blocks are only episodically removed (Figure 5.4). A conceptual model of platelet detachment preceded by cracking of shale laminae due to physical weathering and detachment due to hydraulic pressure and/or grain wedging was proposed based upon these observations (Figure 5.17). At the macro-scale (10^{-1} – 10^{0} m) erosion was ascribed to either the detachment of the rock fragments on irregular, but non-stepped surfaces, or at the step edges by enhanced wave impacts (≤ 10^{0} m^3), or via the detachment of blocks from the steps along pre-existing joints (> 10^{0} m^3); however, this remains speculative.

Notably, at both scales of investigation there was a ‘roll-over’ in the magnitude-frequency distribution, explained above in physical terms. However, it is possible that this is also an artefact of censoring, where the largest events occur less frequently than otherwise predicted by power-law behaviour (Figures 5.4 and 7.4). The reason for this censoring may be a too low a monitoring frequency which does not allow the full magnitude-frequency distribution to be captured (Dussauge-Peisser et al., 2002), or some degree of superimposition within the monitoring frequency.

Both datasets show a dominance of *very bladed* to *very platy* slab-like shapes. At the macro-scale, events tend to concentrate around these shape categories (Figure 9.1). There are two possible explanations for this. Firstly, the larger-scale blocks may be, in relative terms, flatter because of the structural controls imposed by the foreshore rock mass. For example, if the horizontal jointing is more

dense than the vertical jointing, platelet detachments at the micro-scale may result in more compact (more blocky) shapes. The former is difficult to verify because I collected no detailed 3D structural data at sub-mm scale. Alternatively, the detection of more plate-like detachments may reflect the resolution limits of this study, where at the macro-scale, the thickness/horizontal axis ratio of the smallest detectable detachments is 1:5 (0.05 m × 0.25 m × 0.25 m), while at the micro-scale it is 1:2 (for a detachment of 0.001 m × 0.002 m × 0.003 m), and so the most frequent smallest events can only have a more blocky shape (Williams et al., 2018).

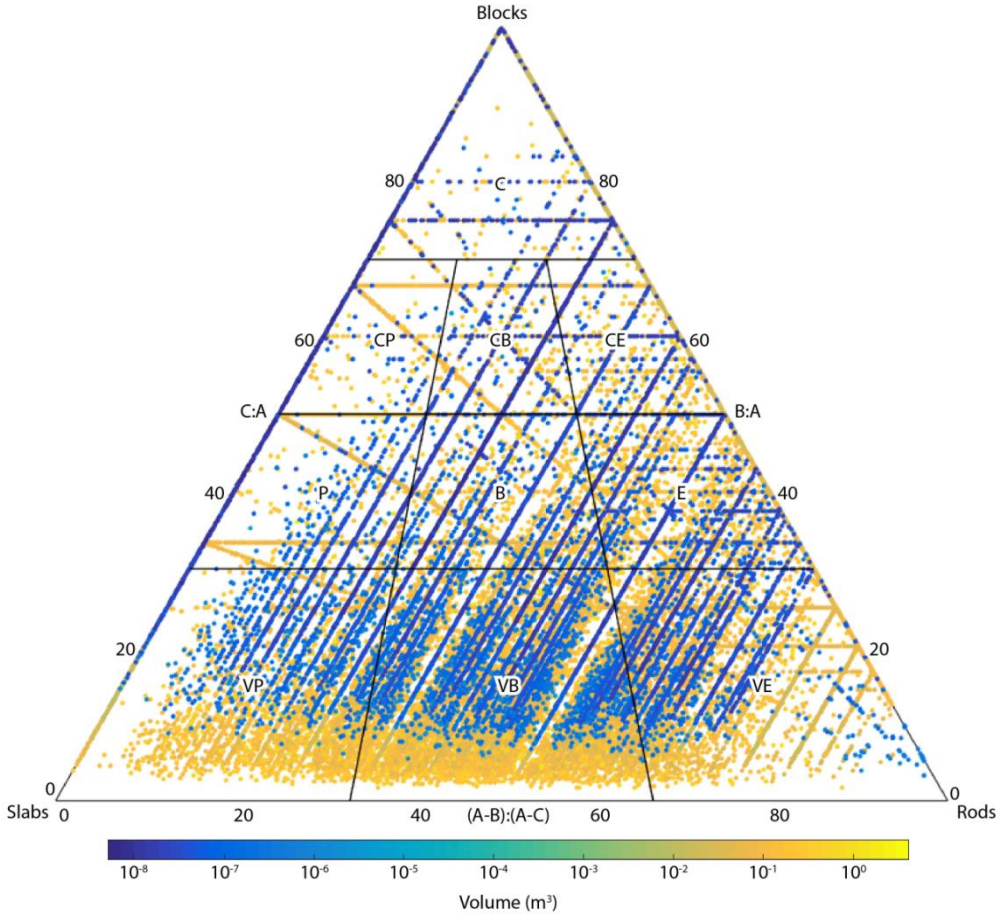


Figure 9.1 Shapes of detached material at the micro- and macro-scales coloured by the volume. Block axes: A – long, B – medium, C – short. For sector description see Figure 2.5. The micro-scale shapes were plotted on the top of the macro-scale shapes.

Knowing whether erosion occurs via granular abrasion or via the detachment of larger pieces can potentially have an impact on how we account for platform erosion when modelling exposure ages from cosmogenic isotope concentrations. The shielding factor that is a function of the depth of material that has eroded from the sample position will change gradually in case of abrasion, and more abruptly or step-wise, in the case of block detachment (Figure 8.7). However, the deterministic model of platform down-wearing, where the continuous range of erosion rates is a function of continuous

values of the distance from the seaward edge and tidal duration, was used for the reconstructions. The observed erosion rates were directly applied to the model (section 8.1.1.3), and so explicit knowledge of the mechanisms was not needed as over long timescales (centuries to millennia) and across large spatial scales (metres), the depth scaling factor which represents erosion averages out. However, the identification of mechanisms and the role of the micro-structure are needed to design an appropriate monitoring technique to resolve change at the scale relevant to operating processes (Cook, 2017).

9.1.3. Consideration of rock resistance upon the foreshore

Previous studies identified grain-by-grain abrasion and detachment of rock fragments as the main mechanisms of shore platform erosion (Kirk, 1977; Robinson, 1977a; Stephenson and Kirk, 1998; Blanco-Chao et al., 2007). Before erosion occurs, the rock mass surface is prepared through wetting and drying, warming and cooling, salt crystallisation in rock lattices and biological activity (Mottershead, 1989; Andrews and Williams, 2000; Stephenson and Kirk, 2001; Naylor et al., 2012; Mayaud et al., 2014; Coombes, 2014). Erosion occurs when the assailing force of waves, *Fw*, is higher than resisting force of the rock, *Fr* (Eq 2.1; Sunamura, 1992). Despite the understanding of processes in action and the wave properties controlling *Fw*, no single measurable rock property has been successfully used to express *Fr* in a manner that is appropriate to both the process and the scale of observation (Augustinus, 1991). In existing models of rocky coast evolution, rock resistance is commonly simplified and described only semi-qualitatively as either 'hard' or 'soft', or is assumed to be a constant (Trenhaile, 1983; 2000; Walkden and Hall, 2005; Kline et al., 2014; Limber et al., 2014; Matsumoto et al., 2016). The complexity of water/sediment dynamics upon the foreshore and the rock micro-structure suggest that multiple mechanisms may operate simultaneously at spatially-variant intensities. No single rock property (compressive, shear and tensile strength) can describe resistance to each of breaking wave shock, water hammer, compression of air in discontinuities, hydrostatic pressure, cavitation and abrasion (Trenhaile, 1980). As a result, the question remains as to whether it is possible to independently quantify *Fr*.

Bedrock river studies have explored relationships between erosion rates and rock properties (e.g. Sklar and Dietrich, 2001; Wilson et al., 2013; Bursztyn et al., 2015). However, water dynamics in rivers are arguably considerably less complex than at the foreshore due to unidirectional and channelized flow, and absence of wave breaking (Ogawa et al., 2015; Poate et al., 2018). For instance, tensile strength has been identified as a rock property which opposes low-velocity sediment impact (Johnson, 1972), and a direct link was established between tensile strength and erosion rate (Sklar and Dietrich, 2001) and river valley morphology (Bursztyn et al., 2015). Wilson et al. (2013) linked the diversity of bedrock morphology with a dominance of different processes at the local (boulder) scale. However, these relationships are fundamentally difficult to identify on a foreshore where morphology,

wave and tidal regime, rock harness and structure, and sediment cover vary through space and change in any given location through time. Similarly, applying one of the various rock quality systems (Bieniawski, 1976; Barton et al., 1977; Hoek and Brown, 1980; 1997; Palmstrøm, 1995; 1996 a,b) seems insufficient as the indices were designed to assess rock resistance at specific conditions (e.g. underground excavations or cut slopes) to specific stresses, and so they are unsuited to resolving the multifaceted character of foreshore processes.

Some studies have looked for rock properties which can explain the diversity in shore platform morphology (Wright, 1970; Trenhaile, 1972; 1974; 1978; 1980; 1987; Williams, 1986; Stephenson, 2000; Davies et al., 2006; Kennedy and Dickson, 2006; Thornton and Stephenson, 2006), but these tend to be qualitative and compare locations with different geologic and/or marine settings. Here, it was shown that rock properties widely used to characterise rock resistance at the foreshore (rock hardness and joint density) cannot explain the variability of coastal morphology at the local (10^1 – 10^2 m) scale, possibly due to the relatively low variability in these properties at such scales (section 3.8.3; Swirad et al., 2016). Therefore, instead of attempting to quantify *Fr* in terms of measurable rock properties, the spatial distribution of erosion at two scales was predicted from a range of continuous locational, topographic, tidal and structural properties, which are believed to influence erosion rate and detachment size (Kirk, 1977; Robinson, 1977a; Stephenson and Kirk, 1998; Foote et al., 2006; Swantesson et al., 2006; Coombes, 2014; Moses, 2014), with some success.

9.1.4. Identifying controls on the spatial distribution of erosion

High-resolution, systematic data provides evidence that allows one to hypothesise on the dominant erosion mechanisms. At the micro-scale, the erosion rate is determined by position on the platform, with higher rates occurring both close to the cliff and at the seaward edge, where the tide cycles between inundated and exposed most frequently at this location. This agrees with the studies by Flemming (1965), Kirk (1977), Robinson (1977a), Torunski (1979), Sunamura (1992), Stephenson and Kirk (1998), Foote et al. (2006), Moses and Robinson (2011) and Matsumoto et al. (2016). This present study is, however, the first to establish quantitative relationships which enable the relative contribution of these controls to be seen, and therefore to be used to predict coastal change (Table 5.4). At the macro-scale, the location of detachments at non-stepped parts of the platform was successfully predicted on a cell-by-cell basis, and were found to concentrate on more rough surfaces (Lamb et al., 2015) and at locations closer to the cliff toe (Robinson, 1977a).

Collapsing all observations from across the entire foreshore into single cross-shore profiles showed that there is an incredibly clear pattern of erosion. This is characterised by an increased probability of boulder movement, down-wearing and erosion at steps around 10-18 m from the cliff toe, and a steady decrease in the probability with distance seaward (R^2 = 0.861-0.981; $p < 0.05$).

Intensification of erosion at such location may be related to 1) constructive interference of incoming and reflected waves; 2) breaking of the most energetic waves; 3) impact of entrained boulders; 4) highest efficiency of physical weathering (wetting and drying); and 5) transition between the planar and sloping parts of the foreshore (section 7.3.3.2).

This is an important finding as the sample size (6.68×10^6 cells) makes it the first systematic empirical dataset to capture the wide area nature of foreshore erosion. It is notable that despite the apparent resistant nature of the platforms studies and the relatively short duration of the study, a clear and physically sensible erosion signal is evident. Building upon this data, a deterministic model of past cliff retreat rates was developed (Eq 8.1) in which an empirical model of platform down-wearing (Table 5.4) was derived. The model was then tested against the concentration of cosmogenic radio-isotopes in a transect across the shore platform. Other foreshore erosion models were considered to explore which best explains the measured concentrations, including: 1) no-erosion; 2) parallel retreat model (Trenhaile, 1974; Regard et al. 2012); 3) extrapolation of rates erosion reported by Robinson (1977a); and 4) platform widening (Johnson, 1919; Flemming, 1965; Sunamura, 1992; Trenhaile, 2000; Walkden and Hall, 2005). An assessment of the ability of 240 scenarios which included combinations of different cliff retreat rates and patterns and platform down-wearing models, was explored to explain the measured ^{10}Be concentrations, and the results suggest that the empirical model based on observed erosion measurements developed in Chapter 5 was the most successful. This confirms the importance of the across-shore location and tidal duration in foreshore down-wearing, which has previously been observed (Trenhaile, 2000; Matsumoto et al., 2016) but not explicitly quantified using high-resolution and high-precision monitoring, as was undertaken in this study.

9.2. What is the relative contribution of the down-wearing and step back-wearing to shore platform erosion?

9.2.1. The role of scale in foreshore erosion

Shore platforms are understood to erode via a combination of incremental down-wearing and lateral erosion or landward transgression of ‘steps’ (Stephenson, 2000). This dichotomy arguably in part reflects the techniques conventionally used to detect geomorphic change on foreshores. Monitoring sub-millimetre down-wearing rates with MEMs captures grain scale changes such as those arising from abrasion (Robinson, 1976, 1977a; Stephenson and Kirk, 1998, 2001), while historical maps and aerial photographs allow the landward retreat of steps to be measured (Dornbusch and Robinson, 2011). However, the erosion of the platform can be seen to occur through a set of concurrent mechanisms that operate across multiple spatial and temporal scales, where the dominance of abrasion or block detachment is a function of rock structure, including joint spacing or micro-layering (Whipple et al., 2000; Dubinski and Wohl, 2013). A two-part understanding of erosion

appears to oversimplify the complexity of these mechanisms, where steps erode in a combination of abrasion, detachments of irregular blocks due to impacts and removal of blocks of structurally pre-defined sizes and shapes (Moses and Robinson, 2011). Equally the non-stepped sections of the platform may experience rock fragmentation in addition to abrasion, for instance through impacts on protruding surfaces and detachment of thin rock layers/platelets (e.g. Cullen and Bourke, 2018).

The results of this study (resolution of 10^{-3} – 10^{0} m or the volume loss of 10^{-9} – 10^{0} m^3) have been used to reflect upon previous research which is generally of a resolution < 10^{-3} – 10^{0} m, to create a conceptual model of processes operating at a range of spatial scales and rock properties which may control *Fr* at these scales (Figure 9.2). At the sub-mm scale, notably a finer scale than that considered here, erosion occurs primarily through grain-by-grain abrasion due to impacts from sand and gravel, and via the activity of micro-organisms (Coombes, 2014). The erosion at the mm-scale was documented here using SfM photogrammetry. At the mm-scale the state of surface, such as temperature and wetness, was identified in literature as important factor on erosion intensity (Dussauge-Peisser et al., 2002; Moura et al., 2011). Although no observations of processes actually in action was undertaken, it was suggested here that in summer months higher temperatures increase effectiveness expansion and contraction on platelet detachment at the cm-scale (section 5.3.3.1). Previous studies suggested that at larger (> cm) scale it is the impacts of coarse material: cobbles and boulders, and hydraulic pressure during stormy conditions which play a key role in block detachment (Naylor and Stephenson, 2011; Naylor et al., 2016).

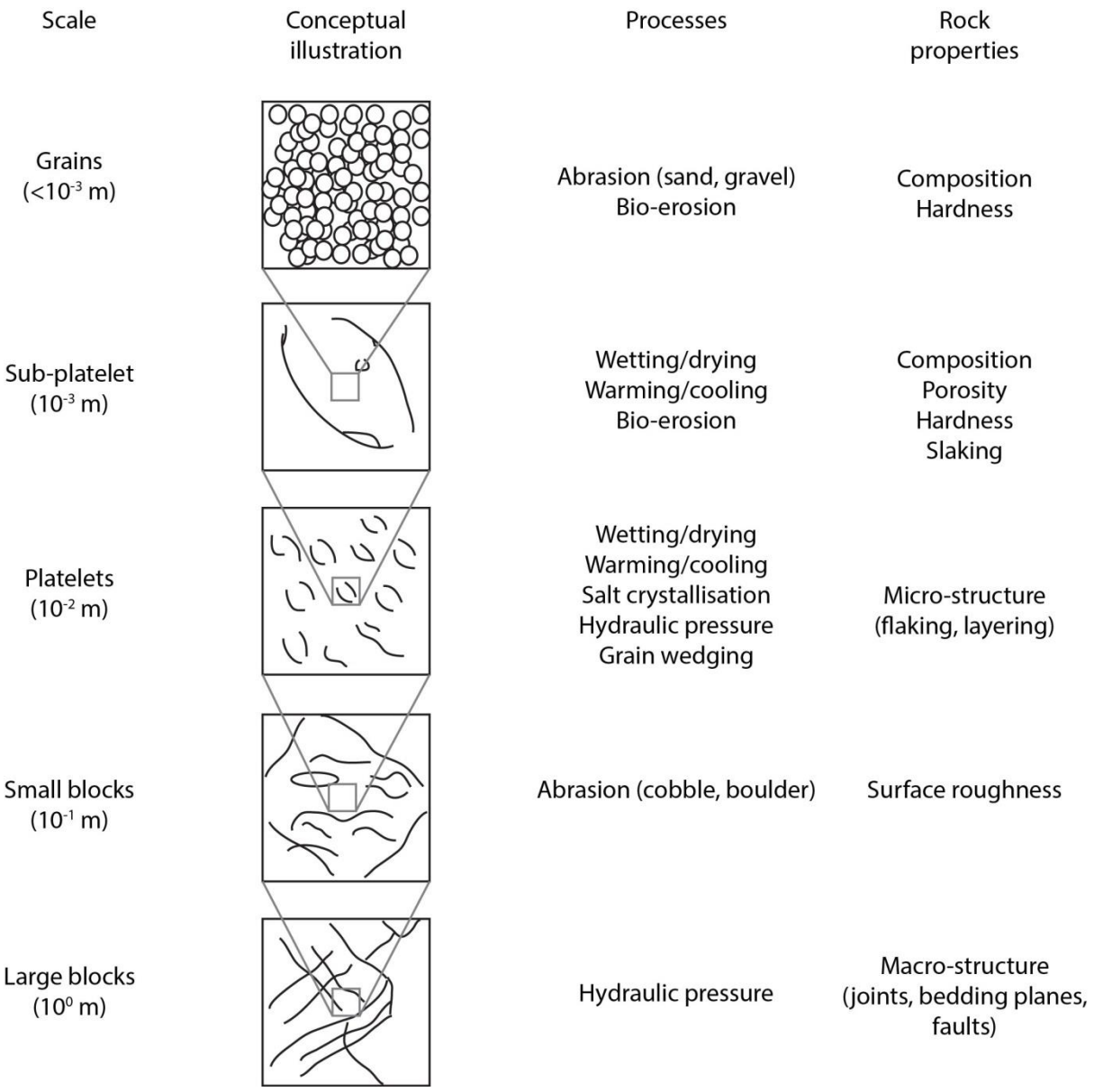


Figure 9.2 Conceptual model of the erosion processes operating on shore platform and rock properties determining resistance across the spatial scales.

Different rock properties provide some resistance to wave forcing at these various scales. At the fine scale, these are likely to be rock composition, porosity, hardness, and slaking (Sunamura, 1992). Micro-structure is a key element for enabling platelet detachments (Figure 5.17), while topography, here considered as surface roughness or the presence of protrusions which concentrate wave energy, is important in detachment of larger and usually irregular shaped blocks (Table 7.8; Knight and Burningham, 2011; Lamb et al., 2015). Finally, the large blocks at the seaward edge of the platform and at steps (Figure 3.11C) depend on the macro-structure with blocks detached when the wave energy is high enough to mobilise blocks of pre-defined sizes (Naylor and Stephenson, 2010) (Figure 9.2).

Although there is a one order of magnitude difference in erosion rates measured at the two scales, the general pattern of the distribution of erosion is similar (Figure 9.3). The 10^{-3} – 10^{-2} m scale of the monthly platform monitoring was successfully used to quantify platform erosion scalar in the model to reconstruct cliff retreat rates using cosmogenic ^{10}Be concentrations. This suggests that the small-scale results can be extrapolated to longer timescales (centuries to millennia) and larger spatial extents (> metres), while erosion at a given point can be predicted from the across-shore location and tidal duration.

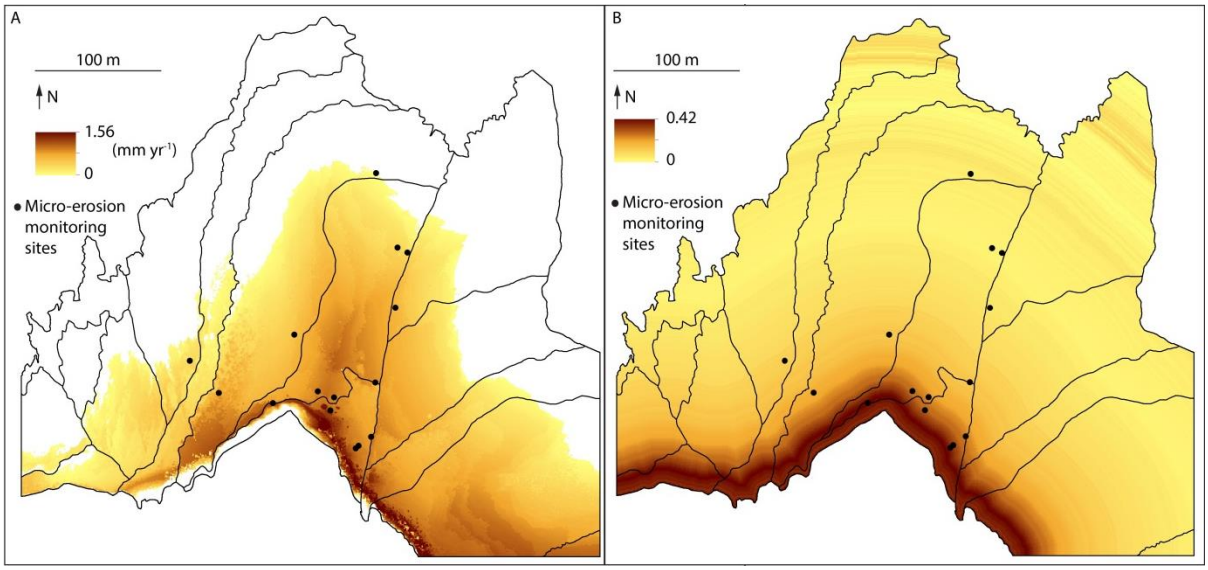


Figure 9.3 Distribution of erosion across Hartle Loup: A) down-wearing rates predicted using the multiple linear regression model developed at the small-scale (Table 5.4); B) proportion of cells which experienced down-wearing at 1 m interval distance from the cliff.

Although erosion rates could not be predicted for any point on the platform at the macro-scale (10^{-1} – 10^{0} m) with any degree of certainty, the occurrence of boulder movement, down-wearing and erosion at steps was shown to have a gradual across-shore change which can be predicted using a linear or a 3rd order polynomial model. The intensity of down-wearing is highest 10 m from the cliff and gradually decreases to ~230 m seaward, and can be observed on the map of the distribution of down-wearing rates on Hartle Loup, using the model developed at the small-scale (Figure 9.3A). There is a clear increase in erosion rates from around 10 m from the cliff toe to 20 m, likely related to the high values of tidal duration around MHWN, and possibly the average location of the point of transition from the cliff toe ramp to the shore platform surface. Erosion cannot be predicted for the landward- and seaward-most portions of the platform as data > HAT was removed, and the combination of the distance from the cliff and tidal duration which makes modelled erosion rates negative (these were also filtered out). Within these zones it is also difficult to predict the probability of erosion based on the macro-scale monitoring as the occurrence of down-wearing does not follow

wider patterns in these areas (Figure 7.22C). These results suggest that there is a general pattern of erosion concentrated closer to the cliff (Figure 9.3), where the submergence/emergence frequency is the highest, which was also shown in the exploratory model of Matsumoto et al. (2016).

9.2.2. Separating surface down-wearing and step back-wearing

There is a gap in the scales of data which would allow the generation of the same format output data across multiple orders of magnitude, such as 3D detachment inventories, to provide a more holistic overview of erosion across the foreshore. The results presented here show that the rate of down-wearing alone varies by one order of magnitude between the two scales of interest, and within these scales, a number of mechanisms potentially contribute to a non-linear distribution of detached volumes (section 9.1). The challenge of up- or down-scaling erosion rates is accentuated when erosion is considered as down-wearing and step back-wearing separately (Stephenson, 2000). Here, a possibility existed to quantify step back-wearing at the macro-scale study as the stepped cells were identified, the step height could be approximated by the local elevation range, and the step length could be assumed to be equal to the grid resolution (1 m). However, it was concluded that reporting erosion in terms of volume, and consequently the down-wearing rate, is more meaningful and comparable as it allows a wide range of sizes and shapes to be analysed and compared to erosion rates from previous studies, which, except the study of Dornbusch and Robinson (2011), were based on MEMs. Moreover, the steps are believed to erode via the combination of abrasion, detachment of irregular blocks due to impacts and quarrying blocks of structurally-predefined morphology (Moses and Robinson, 2011). The monitored section of coastline is relatively extensive (22 km), which would make it difficult to separate these processes with any degree of certainty.

Step back-wearing, the horizontal migration of individual steps that are defined by rock bed contacts was quantified using the cosmogenic ^{10}Be concentrations. A combination of scenarios of cliff and platform down-wearing was used to explain measured isotope concentrations along the foreshore cross-section was found based on the non-stepped part of the platform (section 8.4.2.2). The difference between modelled and measured concentrations along the seaward most 70 m of the platform was used to calculate the contribution of step back-wearing to the decrease in ^{10}Be concentrations. This was then used to calculate long-term step back-wearing rates of $0.92\times10^{-2} \pm 0.29\times10^{-2}$ m yr^{-1} for the step located ~ 240 m from the cliff and $1.12\times10^{-2} \pm 0.68\times10^{-2}$ m yr^{-1} for the one at ~270 m. This is the first study which quantifies step back-wearing over long-time scales (centuries to millennia). As the process is episodic using the field monitoring or cartographical data which only spans up to 150 years before present (Dornbusch and Robinson, 2011) does not seem long enough to obtain representative rates (Lee et al., 2001).

It remains difficult to assess the relative role of down-wearing and step back-wearing as conditions inevitably vary from platform to platform, and closely reflect of the macro-structure relative to the sea level. In this study the across-shore location of the steps determines that the process is important at the seaward section but not the more landwards section. However, the results can be used to consider the long-term evolution of the coastal profile. Combining ^{10}Be concentrations with numerical modelling has shown that the cliff has been retreating at an apparently steady rate of 0.05 m yr^{-1}, while the step back-wearing rate averaged from all eight sampling locations equals 0.01 m yr^{-1}. The non-equal cliff and step retreat is contrary to the exploratory model of Hurst et al. (2017), and suggests that the platform is widening and that step back wearing does not keep pace with cliff retreat, which supports some existing numerical exploratory models (Trenhaile, 2000; Matsumoto et al., 2016), but stands in opposition to the parallel coast profile retreat model (Trenhaile, 1974; 1983; Limber et al., 2014).

9.3. Does the multi-scale assessment of shore platform erosion enhance our ability to understand millennial-scale coastal evolution?

9.3.1. Using the results to reconstruct past cliff retreat rates

Our ability to predict long-term coastline retreat and reconstruct past cliff dynamics depends on assumptions about shore platform erosion in the absence of direct long-term observations (sections 8.2.1.2 and 8.2.1.3) or paleo-environmental records from depositional environments. Poor understanding of the mechanisms of foreshore erosion means that we cannot know how accurate the models of platform erosion and evolution are, which questions their utility to predict future changes under anticipated sea-level rise and increased storminess (Slott et al., 2006; IPCC, 2013). Exposure dating using cosmogenic isotope concentrations is currently the only direct way to validate long-term (10^2 – 10^4 yr) coastline evolution models, and to identify likely scenarios of past cliff retreat rates and platform down-wearing patterns. The results of Chapter 8 suggest that the empirical model based on understanding the mechanisms and controls of platform down-wearing coupled with steady cliff retreat at the rate of 0.05 m yr^{-1} successfully explains measured ^{10}Be concentrations from across the 300 m wide Hartle Loup. Both down-wearing and step back-wearing impact ^{10}Be concentrations, with the former predictable deterministically and the latter possible to quantify if the step height is known (section 8.4.2.3). Table 9.2 depicts the information needed to reconstruct exposure ages using cosmogenic ^{10}Be and numerical modelling.

Table 9.2 Variables used to calculate exposure ages across shore platforms and the input data required.

Variable	Input data
^{10}Be concnetrations	Results of AMS
Topographic shielding	Cliff morphology: -Height -Subtended azimuth Inclination
Water shielding	Sea level Tidal duration
Platform erosion: Down-wearing	Cross-shore location Tidal duration
Platform erosion: Step back-wearing	Step height

9.3.2. Implications of results for the evolution of the North Yorkshire coastline

The results show that the coastline is not inherited from the last interglacial as suggested by Agar (1960), but it has been entirely formed in the Holocene. The calculated long-term (6 kyr) cliff retreat rate of 0.05 m yr^{-1} is similar to that calculated on the basis of the short-term monitoring: 0.065 m yr^{-1} based on monthly monitoring over 20 months using TLS and digital photogrammetry (Lim et al., 2009) and 0.027 ± 0.029 m yr^{-1} based on the monthly monitoring of the 2.71×10^4 m^2 cliff face along 710 m of coastline over 7 yr using TLS (Rosser et al., 2013). This suggests that the high-resolution and high-precision monitoring provides erosion rates that are apparently representative for longer time-scales.

Another important implication of the agreement between long- and short-term erosion rates is the lack of acceleration in erosion rates in the post-industrial period (last ~150 yr) as documented by Hurst et al. (2016) on the southern English coast. Notably, this study is located at the area which is not experiencing RSL rise, unlike the Sussex coast studied by Hurst et al. (2016) which is subsiding (Shennan and Horton, 2002). This observation suggests that either the mode of post-glacial adjustment (uplift, submergence or no vertical movement) is crucial in coastline evolution or the chalk (Sussex) and siliciclastic rock (Yorkshire) coastlines respond differently to the Late Holocene sea-level/storminess change (Hurst et al., 2016). Both options should be considered when predicting coastal change around UK in future (Lim, 2006; Slott et al., 2006; IPCC, 2013; Kopp et al., 2016).

9.3.3. Wider implications for modelling coastal evolution

Existing long-term platform evolution models either assume that an ‘equilibrium’ coastal profile exists to which platform morphology adjusts, or that platform morphology constantly changes

in response to the erosive power of waves and changing external conditions such as sea level. In the former case, the processes observed contemporarily average out over longer timescales, and so they do not have to be explicitly understood to predict general coastal change (Limber and Murray, 2014). In the latter case the interactions between rock resistance and wave force superimposed on the tidal duration distribution are explored and the dynamic model is built (Walkden and Hall, 2005; Kline et al., 2014; Matsumoto et al., 2016). The results of Chapter 8 suggest that the dynamic change of erosion rates across the platform and their adjustment to changing geometry do not 'average out' at long time-scales, and so the geometry-based models, which assume either platform flattening (Johnson, 1919; Flemming, 1965; Sunamura, 1992) or parallel retreat of the profile (Trenhaile, 1974; 1983; Limber et al., 2014) cannot be applied. The model of de Lange and Moon (2005) suggests that the average cliff retreat rates can be calculated by dividing the width of shore platform by the time period in which sea has been at the level which could impact areas presently exposed in the intertidal zone (here 7 kyr the earliest) gives similar rates of 0.04 m yr^{-1} as compared to 0.05 m yr^{-1} calculated in this study.

Based on analysis of 240 scenarios of cliff retreat rates and patterns and down-wearing model, the results presented here suggest that over long timescales platform erosion rates do not 'average out' enabling the platform to acquire a geometry-based equilibrium state. The erosion reflects the interplay between changing sea level, substrate geometry and tidal regime, while platform morphology adjusts to these spatially and temporarily variant controls. The results highlight the importance of the cross-shore location and the tidal duration distribution on erosion rates. The macro-scale monitoring (Chapter 7), although not used in the modelling presented in Chapter 8, supports this pattern showing the highest probability of the occurrence of erosion at the landward part of the foreshore cross-section and its gradual decrease seawards (Figure 7.22C). This understanding agrees with the exploratory numerical model of long-term evolution of shore platforms by Matsumoto et al. (2016). They included a weathering efficacy factor, which reaches its highest values at elevations of the highest tidal duration. Their wave transformation model can be seen as an explicit consideration of the role of location across the platform and tidal duration presented herein. In contrast, results presented here could feed into the model of Matsumoto et al. (2016) to hopefully strengthen it with numerical field-based data. The results can also be used as the empirical statistically-valid foreshore erosion input for the coastline evolution models, and they should be used to re-assess the models which assume direct response of cliff retreat rates to changing sea level without considering complex interactions between foreshore morphology and erosion and wave energy at the cliff toe (Griggs and Trenhaile, 1995; Trenhaile, 2002; 2010).

9.4. Summary

The shore platforms considered here erode mainly via the detachment of rock fragments. The applied techniques, SfM- and LiDAR-based analysis of DEMs, allowed the detection of detachment volumes ranging from 10^{-9} to 10^{0} m^3. The mechanisms operating were interpreted to differ for detachments of different sizes, based on the complex shape of volume frequency distribution curves, including event volumes that were indicative of abrasion, platelet detachment, irregular block detachment and removal of blocks with structurally pre-defined sizes and shapes.

Both surface down-wearing and step back-wearing contribute to platform erosion as evidenced by the distribution of platform erosion across the foreshore and particularly when aggregated into a coast-normal cross-section. The relative importance of these two processes depends on the distribution of steps across the platform, while their erosion rates are different. Therefore, these two processes need to be considered together. The down-wearing rate at the small-scale can be predicted from the location of a point along the shore cross-profile and the tidal duration, while at the macro-scale its location can be successfully predicted from the across-shore location and slope. Collapsing the platform surface into a single cross-profile allows the establishment of a statistically-significant relationship between the distance from the cliff and probability of down-wearing, erosion at steps and boulder movement. The long-term step back-wearing rates can be calculated using cosmogenic ^{10}Be concentrations if the down-wearing rates are known.

Understanding mechanisms of platform erosion at a variety of scales enhances our ability to understand millennial-scale coastline evolution. Combining numerical modelling with measured concentrations of cosmogenic ^{10}Be in bedrock samples collected across a shore platform showed that over long time-scales, foreshore erosion does not adjust to fit a coastal equilibrium shape, either that indicative of parallel retreat or that indicative of platform widening, but rather constantly adjusts to a changing morphology via a positive feedback. The results of present study can be used as an empirical dataset to reconstruct past sea cliff retreat and model future change.

10. Conclusions

10.1. Summary of findings

10.1.1. Summary of aim

Our understanding of shore platform erosion via a combination of incremental down-wearing and the lateral erosion of 'steps' (Stephenson, 2000) is based on morphological evidence and monitoring of erosion generally undertaken at two scales: sub-mm point measurements of the vertical change using MEMs (e.g. Robinson, 1976; 1977a; Stephenson and Kirk, 1998; 2001) and relatively low-resolution detection of step back-wearing using cartographical data (Dornbusch and Robinson, 2011).

The consequences of using these two approaches for monitoring erosion is implicitly reflected in the models to reconstruct (Regard et al., 2012; Hurst et al., 2016; 2017), and predict (Trenhaile, 1983, 2000; Walkden and Hall, 2005; Kline et al., 2014; Limber et al., 2014) coastal evolution. These models necessarily simplify platform morphology and treat erosion tacitly, either by enforcing a single down-wearing rate derived by transposing cliff retreat rates to the platform surface, or by a set of elevation-dependent values related to tidally-dependent wave energy dissipation (Trenhaile, 1983, 2000; Walkden and Hall, 2005; Kline et al., 2014; Limber et al., 2014). The complexity of platform morphology suggests that a number of factors may be important at a variety of scales in driving change. Recent progress in fluvial and bedrock channel geomorphology suggests that erosion is multifaceted while different rock properties may represent key characteristics of rock resistance at different scales (e.g. Sklar and Dietrich, 2001; Wilson et al., 2013; Beer et al., 2017). The explicit understanding of mechanisms and controls on the spatial and temporal distribution of erosion is therefore needed to reconstruct previous erosion and to predict coastline change.

The aim of this thesis was to fill the gap in understanding foreshore erosion and to quantify platform erosion at spatial and temporal scales appropriate to the processes in operation. This was achieved by creating an empirical model of multi-scale platform erosion which allows better reconstruction and prediction of the evolution of rocky coastlines.

10.1.2. Original contribution to knowledge

This section is organised in context of the three research questions outlined in Chapter 1.

10.1.2.1. What is the dominant mechanism of shore platform erosion?

A multi-scale study undertaken along the North Yorkshire coastline derived foreshore erosion rates of 0.528 mm yr^{-1} at the small-scale (resolution of 10^{-3} – 10^{-2} m, detached volumes of 10^{-9} – 10^{-5} m^3) and 0.01 mm yr^{-1} at the macro-scale (resolution of 10^{-1} – 10^{0} m, detached volumes of 10^{-3} – 10^{0} m^3). The high-resolution and high-precision data obtained with SfM photogrammetry and LiDAR were used to detect change, create an inventory of detachments from which the size and 3D shape distributions were analysed, and were then used to predict the distribution of foreshore erosion more widely. None of these analyses has previously been undertaken to study shore platform erosion.

The different erosion rates reported at the small- and macro-scales are believed to represent either 1) censoring where the larger events are underrepresented, which makes the erosion rates derived at the macro-scale apparently lower due to the relatively short monitoring period (2.62 yr); or 2) by a change of dominant observable process with scale. The proposed dominant mechanism that has been observed at the micro-scale is platelet detachment due to the hydraulic action (lift-and-drag force) and/or grain wedging preceded by mechanical weathering, and at the macro-scale, the detachment of rock pieces by the impact of the wave-carried boulders and detachment of blocks of structurally-defined sizes and shapes. However, although erosion was quantified and evidence of detachments were documented in the field, no direct observations of processes actually in operation were made and so the results from previous studies were used to inform my interpretation of processes from the observed erosion patterns.

A deterministic model was built on the basis of the small-scale empirical data, and shows that erosion rates are higher closer to the cliff and at locations where the tide cycles are more frequent; a finding which agrees with both existing models (Flemming, 1965; Sunamura, 1992; Kline et al., 2014; Matsumoto et al., 2016) and previous observations (Ribinson, 1977a; Stephenson and Kirk, 1998; Foote et al., 2006; Moses and Robinson, 2011). The model shows a similarity to the macro-scale distribution of the down-wearing modelled across-shore by collapsing the 1 m^2 grid cells from 22 km long foreshore (average width ~140 m) into a single profile and predicting occurrence of the down-wearing as a function of the distance from the cliff. The highest rates of down-wearing observed at the macro-scale occurred at ~10 m from the cliff toe, which coincides with MHWN where the tidal duration is the highest (Figure 3.6), and also with the highest rates of down-wearing observed at the small-scale. This location may also coincide with a zone of constructive interference of incoming and reflected waves, impact of entrained boulders, or enhanced turbulence due to wave impacts, the highest efficiency of the physical weathering and/or the transition between planar platform and sloping ramp. Whilst there is considerable research on foreshore erosion and cliff face erosion, detailed research that looks at the contact between the two remains sparse.

The model developed here was successfully incorporated into the model to reconstruct past cliff retreat rates from the concentrations of cosmogenic ^{10}Be. The application of the empirical model was more successful in explaining the concentration of cosmogenic ^{10}Be than more simplified models of the parallel coastal retreat (Trenhaile, 1974; Regard et al. 2012) and platform widening model (Johnson, 1919; Flemming, 1965; Sunamura, 1992). This finding confirms that the long-term cliff retreat rates cannot be derived by applying a single empirical erosion rate (Robinson, 1977a). Moreover, the monthly monitoring of the micro-erosion showed that erosion is faster and detachments are larger in summer months, which agrees with observations of Robinson (1977a) and Stephenson and Kirk (1998; 2001) who suggested that in summer the efficiency of mechanical weathering is higher due to the impact of temperature on the state of surface. The implication of this is that monitoring erosion through time needs to account for the potential impact of quite significant seasonal effects.

10.1.2.2. What is the relative contribution of the down-wearing and step back-wearing to shore platform erosion?

The techniques applied here allowed the volumetrical and detachment inventory-based consideration of erosion, rather than as the point measurements of vertical erosion at the (sub)mm scale (e.g. Robinson, 1977a; Stephenson and Kirk, 1998; 2001) and through 2D measurements of the horizontal migration of steps using cartographical data (Dornbusch and Robinson, 2012). This implies that it is difficult to assess the relative importance of the down-wearing and step back-wearing, but erosion rates at the stepped and non-stepped parts of the platform can be compared. The small-scale down-wearing model developed here was successfully extrapolated to the long-term (centuries to millennia) and to a larger spatial scale (metres) for the non-stepped section of Hartle Loup. The macro-scale study conducted here across the 22 km section of coastline had a large enough population of 1 m^2 cells (1.97×10^5) without steps (5.00×10^6) to show statistically-significant patterns of erosion for both sub-populations. The results showed that erosion at steps is faster than that for areas without steps with respective rates of 0.04 and 0.01 mm yr^{-1}.

This study is the first to calculate the long-term (centuries to millennia) step back-wearing rates. The two steps crossing the seaward section of the Hartle Loup profile studied have been retreating at the average rate of 0.01 m yr^{-1}, which is lower than the long-term cliff retreat rate of 0.05 m yr^{-1} (Chapter 8). This suggests platform widening which agrees with the numerical models of Trenhaile (2000) and Matsumoto et al. (2016), but stands in opposition to the parallel retreat model (Trenhaile, 1974; 1983; Limber et al., 2014).

10.1.2.3. Does the multi-scale assessment of shore platform erosion enhance our ability to understand millennial-scale coastal evolution?

This study is the first to provide systematic empirical information on the foreshore erosion across scales (10^{-3} – 10^{0} m) and it has a potential to feed into coastal evolution models based upon directly observed erosion rates. As shore platforms are pivotal in dissipating wave energy and in driving or restricting the redistribution of sediments on the foreshore (Dickson et al., 2013; Ogawa et al., 2015; Poate et al., 2018), assumptions about their morphology and dynamics impact on models which aim to reconstruct past cliff retreat rates (Regard et al., 2012; Hurst et al., 2016; 2017) and predict coastline change (Trenhaile et al., 2000; Walkden and Hall, 2005; Kline et al., 2014; Limber et al., 2014; Matsumoto et al., 2016). Without explicit quantification of foreshore erosion, we are not able to assess the accuracy of these models. Here monitoring of erosion was coupled with measuring cosmogenic ^{10}Be concentrations to identify likely scenarios of past cliff retreat rates. The empirical model developed from the small-scale study was shown to be more successful in explaining measured ^{10}Be concentrations than the geometry-based models which assume equilibrium development of the rocky coasts (Johnson, 1919; Flemming, 1965; Trenhaile, 1974; Sunamura, 1992). One of the main achievements of this study was closing the gap between short-term monitoring of erosion and long-term landscape evolution.

The results of this study increased our understanding of the Quaternary history of the North Yorkshire coast and the rocky coast in general, as only three previous studies attempted to directly measure past cliff dynamics. These include the study of Choi et al. (2012) who only derived the interglacial age of the platforms in Korea, and two studies from the chalk coast of the English Channel (Regard et al., 2012; Hurst et al., 2016) which provided average long-term cliff retreat rates over the Holocene. Here the cliff was shown to have retreated steadily at the rate of 0.05 m yr^{-1} over the last 6 kyr. This has important implications as it shows that 1) the platform is not inherited from previous high stands and 2) the short-term monitoring data are representative for much longer timescales as the 7-year monthly monitoring time series of the nearby cliff retreat using TLS gave similar retreat rates (Rosser at al., 2013).

Densification of the sampling locations along the profile to 10 m between 50 and 100 m from the cliff showed that cliff retreat is, in one sense, gradual. At this sampling resolution it remains impossible to distil whether this rate is steady and incrementally accrued via small events, or if it is dominated by episodic larger-scale events (cliff collapses), the recurrence which is lower than 200 yr (the time equivalent to the across-shore distance of 10 m at these long term erosion rates). The novel sample processing techniques (section 8.3.1) allowed the error to be minimised in calculated concentrations to ~5%, which is much higher-precision that typically possible. This, in turn, means cliff retreat and step back-wearing rates could be more precisely calculated.

10.1.3. Thesis weaknesses

A few conclusions emerge when considering what could have been made differently to increase the quality of the thesis.

Firstly, the imbalance exists between application of the results of Chapters 5 and 7. The former was used in Chapter 8 to represent platform erosion scalar, S_{er}, in the model to reconstruct past cliff retreat using cosmogenic ^{10}Be concentrations. Results of the latter were not subsequently used, even though it was stated that they can feed numerical models on coastline evolution (section 7.4). The motivation not to use them in Chapter 8 was the fact that both the cosmogenic and SfM-based models were deterministic, while the LiDAR-based one was probabilistic, which would make it difficult to incorporate into the exposure dating model. Moreover, the small-scale erosion model represented S_{er} successfully allowing reconstructing cliff retreat rates in the past. However, an attempt could be made to explore potential of the macro-scale model to feed existing numerical models on coastline evolution. Set-up of the models could be explored and the utility of the empirical model presented in here could be assessed.

This point leads to another conclusion that is the impossibility to link between the two scales. At the small-scale platelet detachment was identified as a dominant mechanism of erosion, but at the macro-scale no specific mechanism could be constrained because of the low frequency of surveying. Moreover, although the smallest detectable detachments were four orders of magnitude larger at the macro-scale, the monitoring duration dictated by the project timeframe was only 2.6 times longer. This may be insufficient to detect the full magnitude frequency distribution (see section 9.1.1).

While for the LiDAR study timeframe seems too short to account for the full range of detachment sizes, in the SfM study it is the space that may not fully represent foreshore dynamics at the mm to cm scale. Ideally, the whole surface of the Hartle Loup platform should be surveyed at the 0.001 m resolution. Because it is impossible to do, a set of 15 sites was selected for the micro-erosion monitoring. Visual inspection of the foreshore topography at the 10^{-3} – 10^{-1} m suggests a great variability. The sites were selected to be able to resolve the role of four potential factors on erosion rates and detachment sizes: rock type, tidal level, relief and joint density. However, it is likely that many more factors affect erosion and these were not taken into account. Surveying over two or more years would also help draw more definite conclusions about seasonality in erosion rates and patters.

Although erosion rates at both scales were measured, the processes have not been observed directly. This problem was already noticed for MEM studies (Kirk, 1977; Trenhaile, 1987). In here the problem was addresses by analysing size and shape distributions, which was successfully performed in landslide/rockfall studies to infer the mechanisms. However, even though a range of analyses was wider than ever in foreshore studies, the problem remains about deducing processes from morphology.

10.1.4. Wider ramifications

Although the study was conducted at the specific site characterised by relatively hard rock, steps crossing the platform, micro-tides and high storminess that prevents formation of a beach, some results are transferable to other locations. While erosion rates remain site-specific, identified mechanisms of erosion likely characterise many coasts worldwide, in particular those devoid of beach material. These mechanisms are detachment of: 1) platelets due to hydraulic action and/or grain wedging (Figure 5.17); 2) rock pieces due to impacts (Cullen and Bourke, 2018); and 3) blocks of structurally-controlled morphology (Stephenson and Naylor, 2011). Moreover, the techniques used in here, not used in foreshore studies until now, are transferable and when used in other environments will allow a wide range of size and shape analyses to be performed. Applicability of the results could then be tested by comparing between erosion patterns observed here and elsewhere.

The results of Chapters 5 and 7 can enhance our understanding of foreshore erosion in general. The reason for this is because they do not only provide absolute values of erosion that occurred during the monitoring period, but also show spatial and temporal differences in erosion rates and patterns which allow controls on its distribution to be identified. At the micro-scale erosion is faster closer to the cliff, at the elevations of higher tidal duration and in summer months. At the macro-scale it peaks at 10-18 m from the cliff and gradually decreases seawards. These agree with previous observations elsewhere (Stephenson and Kirk, 1998, 2000b; Moses and Robinson, 2011) and exploratory models (Matsumoto et al., 2016). They also provide a first systematic empirical dataset to evidence the relationships.

The large extent of the macro-scale study means that a wide range of surface topography and structure is included. One of the prominent features of the North Yorkshire foreshore are steps that delimit rock beds exposed in the intertidal zone. The statistical analysis of the distribution of erosion included ca 2×10^5 stepped and 5×10^6 non-stepped 1 m^2 cells (Table 7.6). Both populations are represented by a number of single cells that is sufficient for the relationships found to be statistically significant. This means that the understanding of erosion from this study can be transferred to the shore platforms that are characterised by presence and absence of steps.

10.2. Recommendations for future research

This study addressed the gaps in research which aims to identify mechanisms of foreshore erosion, with the wider aim of constraining the controls on the spatial distribution of erosion rates through the systematic high-resolution and high-precision GIS-based analysis of the topographic data. The results were innovatively used to feed into a model to reconstruct cliff retreat rates using cosmogenic ^{10}Be concentrations, which allowed a new understanding of the long-term coastline

dynamics, and the identification of the likely scenarios of wider shore platform down-wearing and quantify step back-wearing. Future studies of rocky coasts can build on this study both in terms of the applied techniques and the new understandings of foreshore system gained.

Firstly, the small-scale erosion monitoring using SfM seems to be an attractive complementary technique to MEMs. Whilst this approach cannot replicate or replace the ability to characterise granular abrasion, the main advantage is its continuous rather than point-based format and larger surveying area. This implies that more geomorphic situations and possibilities can be monitored, including discontinuous and uneven surfaces, and that erosion can be analysed on the basis of detachments, which allows mechanisms of erosion to be identified. It would be valuable to apply the method in different locations where rock type and marine conditions (tidal regime and storminess) are different. Further optimisation could allow the detection of sub-millimetre change and the quantification of the foreshore clay-rich rock swelling effects observed elsewhere (Stephenson and Kirk, 2001). Volume- rather than point-based approach to erosion could be used to relate magnitude of swelling with specific erosion events I subsequent months. The effect of surface roughness, wetness and lighting should be explicitly addressed as this technique is developed, and approaches for a more efficient removal of the doming effects in SfM models should be found. Detachment size and shape analysis could be performed directly on point clouds in true 3D rather than 2.5D (Lague et al., 2013) which would improve model performance at locations of complex micro-topography, such as overhangs.

Secondly, the study advocates for a transition from considering foreshore erosion either by merely recording change often in an abstract manner, to a more process-based approach as developed here. The recent advances in bedrock river geomorphology provide guidance on how to explore the quantitative interactions between controls, mechanisms and landforms from the relevant-scale field monitoring and laboratory tests (Sklar and Dietrich, 2001; Wilson et al., 2013). In rocky coastal settings, understanding processes in action and controls on the spatial distribution of foreshore erosion can feed the numerical models on coastal evolution to better represent platform morphology, erosion and resistance of the substrate, *Fr* (Trenhaile, 1983; 2000; Walkden and Hall, 2005; Kline et al., 2014; Limber et al., 2014; Matsumoto et al., 2016).

Thirdly, the macro-scale monitoring showed that the diversity in topography, geology and tidal inundation characteristics represented by the set of variables described here does not allow a reliable prediction of the magnitude of erosion at both stepped and non-stepped locations concurrently. Therefore, a consideration of factors relevant to this scale of erosion, that would explain its distribution at sub-metre scale, is necessary to understand the relative importance of various mechanisms. This understanding can then inform coastal evolution models. In previous studies, there is a significant imbalance between the quantification of the micro- versus macro-scale erosion of shore platforms, and the only step back-wearing study by Dornbusch and Robinson (2011) thoroughly

addressing the latter prior to the research presented here. Advances in the acquisition of high-resolution precise topographic data using TLS, SfM and LiDAR may provide a tool to monitor step morphology at sufficient resolution to separate mechanisms that contribute to block removal. Coupling such monitoring with a 3D description of rock structure and detailed monitoring of wave dynamics may allow quantitative relationships between controlling factors and erosion to be described more fully.

Finally, the reliance of this study on direct observations and empirical data provides new insight that can be used in numerical models of coastal evolution which tend to otherwise be quite abstract (Limber et al., 2014; Matsumoto et al., 2016). The results presented here are ideally suited for exploring future coastal change under scenarios with predicted sea-level rise and changes in storminess (Slott et al., 2006; IPCC, 2013). Combining modelling with cosmogenic ^{10}Be concentrations, highlighted the power of multi-scale (space- and time-wise) assessments of platform erosion where a set of control-process-form interactions can be explored and validated using absolute dating. As such techniques become better established, far greater insight into coastal evolution will be developed. Further attempts to link the mechanisms observed here with longer-term assessments of coastal evolution must be one of the priorities in future studies of rocky coast geomorphology, and I hope that this study provides direction and insight for this future work.

This page is intentionally left blank

References

Abellán, A., Oppikofer, T., Jaboyedoff, M., Rosser, N.J., Lim, M., Lato, M.J. 2014. Terrestrial laser scanning of rock slope instabilities. *Earth Surface Processes and Landforms* 39: 80-97.

Adams, P.N., Anderson, R.S., Revenaugh, J. 2002. Microseismic measurement of wave-energy delivery to a rocky coast. *Geology* 30: 895-898.

Adams, P.N., Storlazzi, C.D., Anderson, R.S. 2005. Nearshore wave-induced cyclical flexing of sea cliffs. *Journal of Geophysical Research* 110.

Agar, R. 1960. Post-glacial erosion of the North Yorkshire coast from the Tees Estuary to Ravenscar. *Proceedings of the Yorkshire Geological Society* 32: 409-427.

Aguilar, M.A., Aguilar, F.J., Negreiros, J. 2009. Off-the-shelf laser scanning and close-range digital photogrammetry for measuring agricultural soils microrelief. *Biosystems Engineering* 103: 504-517.

Alvarez-Marrón, J., Hetzel, R., Niedermann, S., Menéndez, R., Marquínez, J. 2008. Origin, structure and exposure history of a wave-cut platform more than 1 Ma in age at the coast of northern Spain: A multiple cosmogenic nuclide approach. *Geomorphology* 93: 316-334.

Anderson, R.S., Densmore, A.L., Ellis, M.A. 1999. The generation and degradation of marine terraces. *Basin Research* 11: 7-19.

Andrade, C., Marques, F., Freitas, M.C., Cardos, R., Madureira, P. 2002. Shore platform downwearing and cliff retreat in the Portuguese west coast. In: Pozar-Domac, A. (ed.) Littoral 2002. The Changing Coast. EUROCOAST/EUCC, Porto: 423-431.

Andrews, C., Williams, R.B.G. 2000. Limpet erosion of chalk shore platforms in southeast England. *Earth Surface Processes and Landforms* 25: 1371-1381.

Andrews, J.T., Smith, D.I. 1969. Statistical analysis of till fabric: methodology, local and regional variability (with particular reference to the north Yorkshire till cliffs). *Quarterly Journal of the Geological Society* 125: 503-542.

ASTM. 2008. Standard test method for determination of the point load strength index of rock and application to rock strength classifications (No. D5731-08). ASTM International, West Conshohocken, PA.

Augustinus, P.C. 1991. Rock resistance to erosion: Some further considerations. *Earth Surface Processes and Landforms* 16: 563-569.

Barlow, J., Lim, M., Rosser, N., Petley, D., Brain, M., Norman, E., Geer, M. 2012. Modeling cliff erosion using negative power law scaling of rockfalls. *Geomorphology* 139-140: 416-424.

Barton, N., Lien, R., Lunde, J. 1977. Estimation of support requirements for underground excavation. *Proceedings of the 16th Symposium on Rock Mechanics*: 163-177.

Bateman, M.D., Catt, J.A. 1996. An absolute chronology for the raised beach and associated deposits at Sewerby, East Yorkshire, England. *Journal of Quaternary Science* 11: 389-395.

Beer, A.R., Turowski, J.M., Kirchner, J.W. 2017. Spatial patterns of erosion in a bedrock gorge. *Journal of Geophysical Research: Earth Surface* 112: 191-214.

Benjamin, J., Rosser, N.J., Brain, M.J. In review. Emergent characteristics of 3D rockfall inventories captured over large spatial extents. *Journal of Geophysical Research: Earth Surface*.

Bieniawski, Z.T. 1976. Rock mass classifications in rock engineering. In: Proceedings on the Symposium on Exploration for Rock Engineering, Rotterdam: 97-106.

Bird, E.C.F., Dent, O.F. 1966. Shore platforms on the South Coast of New South Wales. *Australian Geographer* 10: 71-80.

von Blanckenburg, F., Willenbring, J.K. 2014. Cosmogenic nuclides: dates and rates of Earth-surface change. *Elements* 10: 341-346.

Blanco-Chao, R., Pérez-Alberti, A., Trenhaile, A.S., Costa-Casais, M., Valcárcel-Díaz, M. 2007. Shore platform abrasion in a para-periglacial environment, Galicia, northwestern Spain. *Geomorphology* 83: 136-151.

Bradley, S.L., Milne, G.A., Shennan, I., Edwards, R. 2011. An improved Glacial Isostatic Adjustment model for the British Isles. *Journal of Quaternary Science* 26(5): 541-552.

Brain, M.J., Rosser, N.J., Sutton, J., Snelling, K., Tunstall, N., Petley, D.N. 2014. The effects of normal and shear stress wave phasing on coseismic landslide displacement. *Journal of Geophysical Research: Earth Surface* 120: 1009-1022.

Brasington, J., Langham, J., Rumsby, B. 2003. Methodological sensitivity of morphometric estimates of coarse fluvial sediment transport. *Geomorphology* 53: 299-316.

Brasington, J., Smart, R.M.A. 2003. Close range digital photogrammetric analysis of experimental drainage basin evolution. *Earth Surface Processes and Landforms* 28: 231-247.

Brook, M.S., Hutchinson, E. 2008. Application of rock mass classification techniques to weak rock masses: A case study from the Ruahine Range, North Island, New Zealand. *Canadian Geotechnical Journal* 45: 800-811.

BS 1377-3. 1990. Methods of test for soils for civil engineering purposes. Chemical and electro-chemical tests. British Standards Institution, London.

BS 5930. 1999. Code of practice for site investigations. British Standards Institution, London.

Bursztyn, N., Pederson, J.L., Tressler, C., Mackley, R.D., Mitchell, K.J. 2015. Rock strength along a fluvial transect of the Colorado Plateau – quantifying a fundamental control on geomorphology. *Earth and Planetary Science Letters* 429: 90-100.

Carling, P., Herget, J., Lanz, J.K., Richardson, K., Pacifici, A. 2009. Channel-scale erosional bedforms in bedrock and in loose granula material: character, processes and implications. In: Burr, D.M., Carling, P.., Baker, V.R. (eds.) Megaflooding on Earth and Mars. Cambridge University Press, Cambridge: 13-32.

Carpenter, N.E., Dickson, M.E., Walkden, M.J.A., Nicholls, R.J., Powrie, W. 2014. Effects of varied lithology on soft-cliff recession rates. *Marine Geology* 354: 40-52.

Carpenter, N.E., Dickson, M.E., Walkden, M.J.A., Nicholls, R.J., Powrie, W. 2015. Lithological controls on soft cliff planshape evolution under high and low sediment availability. *Earth Surface Processes and Landforms* 40: 840-852.

Catt, J.A. 2007. The Pleistocene glaciations of eastern Yorkshire: a review. *Proceedings of the Yorkshire Geological Society* 56: 177-207.

Challinor, J. 1949. A principle in coastal geomorphology. *Geography* 34: 212-215.

Charman, R. 2001. Past and present rates of coastal chalk erosion at Peacehaven, Sussex. University of Sussex, Brighton: Undergraduate dissertation.

Charman, R., Cane, R., Moses, C., Williams, R. 2017. A device for measuring downwearing rates on cohesive shore platforms. *Earth Surface Processes and Landforms* 32: 2212-2221.

Chelli, A., Pappalardo, M., Llopis, I.A., Federici, P.R. 2010. The relative influence of lithology and weathering in shaping shore platforms along the coastline of the Gulf of La Spezia (NW Italy) as revealed by rock strength. *Geomorphology* 118: 93-104.

Choi, K.H., Seong, Y.B., Jung, P.M., Lee, S.Y. 2012. Using cosmogenic ^{10}Be dating to unravel the antiquity of a rocky shore platform on the west coast of Korea. *Journal of Coastal Research* 28(3): 641-657.

Clark, C., Evans, D., Khatwa, A., Bradwell, T., Jordan, C., Marsh, S., Mitchell, W., Bateman, M. 2004. Map and GIS database of glacial landforms and features related to the last British Ice Sheet. *Boreas* 33: 359-375.

Clark, C.D., Hughes, A.L.C., Greenwood, S.L., Jordan, C., Sejrup, H.P. 2012. Pattern and timing of retreat of the last British-Irish Ice Sheet. *Quaternary Science Reviews* 44: 112-146.

Clauset, A., Shalizi, C.R., Newman, M.E.J. 2009. Power-law distributions in empirical data. *SIAM Review* 51(4): 661-703.

Clements, M. 1994. The Scarborough experience – Holbeck landslide, 3/4 June 1993. *Proceedings of the Institution of Civil Engineers - Municipal Engineer* 103: 63-70.

Clifford, D. 1999. Ion-exchange and inorganic adsorption. Water quality and treatment: a handbook of community water supplies. American Water Works Association, McGraw-Hill, New York.

Cook, K.L. 2017. An evaluation of the effectiveness of low-cost UAVs and structure from motion for geomorphic change detection. *Geomorphology* 278: 195-08.

Coombes, M.A. 2014. The rock coast of the British Isles: weathering and biogenic processes. *Geological Society, London, Memoirs* 40: 57-76.

Coombes, M.A., Feal-Pérez, A., Naylor, L.A., Wilhelm, K. 2013. A non-destructive tool for detecting changes in the hardness of engineering materials: Application of the Equotip durometer in the coastal zone. *Engineering Geology* 167: 14-19.

Coombes, M.A., Viles, H.A., Naylor, L.A., La Marca, E.C. 2017. Cool barnacles: Do common biogenic structures enhance or retard rates of deterioration of intertidal rocks and concrete? *Science of the Total Environment* 580: 1034-1045.

Corbett, L.B., Bierman, P.R., Rood, D.H. 2016. An approach for optimizing in situ cosmogenic ^{10}Be sample preparation. *Quaternary Geochronology* 33: 24-34.

Cruslock, E.M., Naylor, L.A., Foote, Y.L., Swantesson, J.O.H. 2010. Geomorphologic equifinality: A comparison between shore platforms in Höga Kusten and Fårö, Sweden and the Vale of Glamorgan, South Wales, UK. *Geomorphology* 114: 78-88.

Cucchi, F., Forti, F., Furlani, S. 2006. Lowering rates of limestone along the western Istrian shoreline and the Gulf of Trieste. Geografia Fisica e Dinamica Quaternaria 29: 61-69.

Cullen, N.D., Bourke, M.C. 2018. Clast abrasion of a rock shore platform on the Atlantic coast of Ireland. *Earth Surface Processes and Landforms*.

Cullen, N.D., Verma, A.K., Bourke, M.C. In review. A comparison of Structure from Motion Photogrammetry and the Traversing Micro Erosion Meter for measuring erosion on rock shore platforms. *Earth Surface Dynamics Discussions*.

Darvill, C.M. 2013. Cosmogenic nuclide analysis. In: Clarke, L. (ed.) Geomorphological Techniques. British Society for Geomorphology, London.

Dasgupta, R. 2010. Whither shore platforms? *Progress in Physical Geography* 35(2): 183-209.

Davies, P., Sunamura, T., Takeda, I., Tsujimoto, H., Williams, A.T. 2006. Controls of shore platform width: the role of rock resistance factors at selected sites in Japan and Wales, UK. *Journal of Coastal Research* SI39(1): 160-164.

Deere, D.U. 1963. Technical description of rock cores for engineering purposes. *Felsmechanik und Ingenieurgeologie* 1: 16-22.

Deere, D.U., Miller, R.P. 1966. Engineering classification and index properties for intact rock. *Air Force Weapons Laboratory Technical Report*, AFWL-TR-65-116.

Dickson, M.E., Kennedy, D.M., Woodroffe, C.D. 2004. The influence of rock resistance on coastal morphology around Lord Howe Island, southwest Pacific. *Earth Surface Processes and Landforms* 29: 629-643.

Dickson, M.E., Ogawa, H., Kench, P.S. 2013. Sea-cliff retreat and shore platform widening: steady-state equilibrium? *Earth Surface Processes and Landforms* 38: 1046-1048.

Dickson, M.E., Walkden, M.J.A., Hall, J.W. 2007. Systemic impacts of climate change on an eroding coastal region over the twenty-first century. *Climatic Change* 84: 141-166.

Dornbusch, U., Robinson, D.A. 2011. Block removal and step backwearing as erosion processes on rock shore platforms: a preliminary case study of the chalk shore platforms of south-east England. *Earth Surface Processes and Landforms* 36: 661-671.

Dornbusch, U., Robinson, D.A., Moses, C.A., Williams, R.B.G. 2006. Chalk coast erosion and its contribution to the shingle budget in East Sussex. *Zeitschrift für Geomorphologie* Supplementbände 144: 215-230.

Dornbusch, U., Robinson, D.A., Williams, R.B.G., Moses, C.A. 2007. Chalk shore platform erosion in the vicinity of sea defence structures and the impact of construction methods. *Coastal Engineering* 54: 801-810.

Dubinski, I.M., Wohl, E. 2013. Relationships between block quarrying, bed shear stress, and stream power: A physical model of block quarrying of a jointed bedrock channel. *Geomorphology* 180-181: 66-81.

Dunai, T.J. 2010. Cosmogenic nuclides. Principles, concepts and applications in the Earth surface sciences. Cambridge University Press, Cambridge.

Dunai, T.J., Lifton, N.A. 2014. The nuts and bolts of cosmogenic nuclide production. *Elements* 10: 347-350.

Dunne, J., Elmore, D., Muzikar, P. 1999. Scaling factors for the rates of production of cosmogenic nuclides for geometric shielding and attenuation at depth on sloped surfaces. *Geomorphology* 27: 3-11.

Dussauge-Peisser, C., Helmstetter, A., Grasso, J.-R., Hantz, D., Desvarreux, P., Jeannin, M., Giraud, A., 2002. Probabilistic approach to rock fall hazard assessment: potential of historical data analysis. *Natural Hazards and Earth System Sciences* 2: 15-26.

Edwards, A.B. 1941. Storm-wave platforms. *Journal of Geomorphology* 4: 223-36.

Ellis, N. 1986. Morphology, process and rates of denudation on the chalk shore platforms of East Sussex. Brighton Polytechnic, Brighton: PhD thesis.

Evans, D.J.A., Clark, C.D., Mitchell, W.A. 2005. The last British Ice Sheet: A review of the evidence utilised in the compilation of the Glacial Map of Britain. *Earth-Science Reviews* 70: 253-312.

Feal-Pérez, A., Blanco-Chao, R. 2012. Characterization of abrasion surfaces in rock shore environments of NW Spain. *Geo-Marine Letters* 33: 173-181.

Fifield, L.K. 1999. Accelerator mass spectrometry and its applications. *Reports on Progress in Physics* 62: 1223-1274.

Finnegan, N.J., Sklar, L.S., Fuller, T.K. 2007. Interplay of sediment supply, river incision, and channel morphology revealed by the transient evolution of an experimental bedrock channel. *Journal of Geophysical Research* 112.

Flemming, N.C. 1965. Form and relation to present sea level of Pleistocene marine erosion features. *The Journal of Geology* 73: 799-811.

Fonstad, M.A., Dietrich, J.T., Courville, B.C., Jensen, J.L., Carbonneau, P.E. 2013. Topographic structure from motion: a new development in photogrammetric measurement. *Earth Surface Processes and Landforms* 38: 421-430.

Foote, Y., Plessis, E., Robinson, D.A., Henaff, A., Costa, S. 2006. Rates and patterns of downwearing of chalk shore platforms of the Channel: comparisons between France and England. *Zeitschrift für Geomorphologie* Supplementbände 144: 93-115.

Gill, E.D., Lang, J.G. 1983. Micro-erosion meter measurements of rock wear on the Otway coast of Southeast Australia. *Marine Geology* 52: 141-156.

Goethals, M.M., Hetzel, R., Niedermann, S., Wittmann, H., Fenton, C. R., Kubik, P.W., Christl, M., von Blanckenburg, F. 2009. An improved experimental determination of cosmogenic 10Be/21Ne and 26Al/21Ne production ratios in quartz. *Earth and Planetary Science Letters* 284(1-2): 187-198.

Gonçalves, J.A., Henriques, R. 2015. UAV photogrammetry for topographic monitoring of coastal areas. *ISPRS Journal of Photogrammetry and Remote Sensing* 104: 101-111.

Gosse, J.C., Phillips, F.M. 2001. Terrestrial in situ cosmogenic nuclides: theory and application. *Quaternary Science Reviews* 20: 1475-1560.

Goudie, A.S. 2006. The Schmidt Hammer in geomorphological research. *Progress in Physical Geography* 30: 703-718.

Goudie, A.S. 2016. Quantification of rock control in geomorphology. *Earth-Science Reviews* 159: 374-387.

Grenness, M.J., Osborn, J.E., Tyas, M.J. 2005. Stereo-photogrammetric mapping of tooth replicas incorporating texture. *The Photogrammetric Record* 20: 147-161.

Griggs, G.B., Trenhaile, A.S. 1995. Coastal cliffs and platforms. In: Carter, R.W.G., Woodroffe, C.D. (eds.) Coastal evolution. Late Quaternary shoreline morphodynamics. Cambridge University Press, Cambridge: 425-450.

Guzetti, F. 2005. Landslide hazard and risk assessment. University of Bonn, Bonn: PhD thesis.

Guzzetti, F., Ardizzone, F., Cardinali, M., Rossi, M., Valigi, D. 2009. Landslide volumes and landslide mobilization rates in Umbria, central Italy. *Earth and Planetary Science Letters* 279(3): 222-229.

Hackney, C., Clayton, A.I. 2015. Unmanned Aerial Vehicles (UAVs) and their application in geomorphic mapping. In: Clarke, L. (ed.) Geomorphological Techniques. British Society for Geomorphology, London.

Hancock, G.S., Anderson, R.S., Whipple, K.X. 1998. Beyond power: bedrock river incision process and form. In: Tinkler, K.J., Wohl, E.E. (eds.) Rivers over rock: Fluvial processes in bedrock channels. American Geophysical Union: 35-60.

Heng, B.C.P., Chandler, J.H., Amstrong, A. 2010. Applying close range digital photogrammetry in soil erosion studies. *The Photogrammetric Record* 25(131): 240-265.

High, C.J., Hanna, F.K. 1970. A method for the direct measurement of erosion on rock surfaces. *Geomorphological Research Group Technical Bulletin* 5: 1-25.

Hillier, S., Hodson, M.E. 1997. High-gradient magnetic separation applied to sand-size particles: an example of feldspar separation from mafic minerals. *Journal of Sedimentary Research* 67(5): 975-989.

Hoek, E., Brown, E.T. 1980. Empirical strength criterion for rock masses. *Journal of the Geotechnical Engineering Division* 106: 1013-1035.

Hoek, E., Brown, E.T. 1997. Practical estimates of rock mass strength. *International Journal of Rock Mechanics and Mining Sciences* 34: 1165-1186.

Höfle, B., Rutzinger, M. 2011. Topographic airborne LiDAR in geomorphology: A technological perspective. *Zeitschrift für Geomorphologie* Supplementbände 55: 1-29.

Hungr, O., Evans, S., Hazzard, J. 1999. Magnitude and frequency of rock falls and rock slides along the main transportation corridors of southwestern British Columbia. *Canadian Geotechnical Journal* 36: 224-238.

Hunt, A.L., Petrucci, G.A., Bierman, P.R., Finkel, R.C. 2006. Metal matrices to optimize ion beam currents for accelerator mass spectrometry. *Nuclear Instruments and Methods in Physics Research B* 243: 216-222.

Hurst, M.D., Mudd, S.M., Walcott, R., Attal, M., Yoo, K. 2012. Using hilltop curvature to derive the spatial distribution of erosion rates. *Journal of Geophysical Research* 117.

Hurst, M.D., Rood, D.H., Ellis, M.A. 2017. Controls on the distribution of cosmogenic ^{10}Be across shore platforms. *Earth Surface Dynamics* 5: 67-84.

Hurst, M.D., Rood, D.H., Ellis, M.A., Anderson, R.S., Dornbusch, U. 2016. Recent acceleration in coastal cliff retreat rates on the south coast of Great Britain. *Proceedings of the National Academy of Sciences of the United States of America* 113(47): 13336-13341.

IPCC. 2013. Climate Change 2013. The Physical Science Basis. Working Group I Contribution to the 5th Assessment Report of the International Panel on Climate Change.

James, M.R., Robson, S. 2012. Straightforward reconstruction of 3D surfaces and topography with a camera: Accuracy and geoscience application. *Journal of Geophysical Research* 117.

James, G., Witten, D., Hastie, T., Tibshirani, R. 2013. An introduction to statistical learning with applications in R. Springer, New York.

Johnson, D.W. 1919. Shore processes and shoreline development. Hafner, New York & London.

Johnson, K.N., Finnegan, N.J. 2015. A lithologic control on active meandering in bedrock channels. *Geological Society of America Bulletin* 127: 1766-1776.

Johnson, W. 1972. Impact strength of materials. Edward Arnold, New York.

Jones, A.F., Brewer, P.A., Johnstone, E., Macklin, M.G. 2007. High-resolution interpretative geomorphological mapping of river valley environments using airborne LiDAR data. *Earth Surface Processes and Landforms* 32: 1574-1592.

Jones, J.R., Cameron, B., Fisher, J.J. 1993. Analysis of cliff retreat and shoreline erosion: Thompson Island, Massachusetts, USA. *Journal of Coastal Research* 9: 87-96.

Kalenchuk, K.S., Diederichs, M.S., McKinnon, S. 2006. Characterizing block geometry in jointed rockmasses. *International Journal of Rock Mechanics and Mining Sciences* 43: 1212-1225.

Kelletat, D.H. 2005. Pleistocene epoch. In: Schwartz, M.L. (ed.) Encyclopedia of coastal science. Springer, Dordrecht: 772-773.

Kennedy, D.M. 2010. Geological control on the morphology of estuarine shore platforms: Middle Harbour, Sydney, Australia. *Geomorphology* 114: 71-77.

Kennedy, D.M. 2015. Where is the seaward edge? A review and definition of shore platform morphology. *Earth-Science Reviews* 147: 99-108.

Kennedy, D.M., Coombes, M.A., Mottershead, D.N. 2017. The temporal and spatial scales of rocky coast geomorphology: a commentary. *Earth Surface Processes and Landforms* 42: 1597-1600.

Kennedy, D.M., Dickson, M.E. 2006. Lithological control on the elevation of shore platforms in a microtidal setting. *Earth Surface Processes and Landforms* 31: 1575-1584.

Kim, K.J., Sutherland, R. 2004. Uplift rate and landscape development in southwest Fiordland, New Zealand, determined using ^{10}Be and ^{26}Al exposure dating of marine terraces. *Geochimica et Cosmochimica Acta* 68(10): 2313-2319.

King, C.A.M. 1972. Beaches and coasts. Edward Arnold, London.

Kirk, R.M. 1977. Rates and forms of erosion on intertidal platforms at Kaikoura Peninsula, South Island, New Zealand. *New Zealand Journal of Geology and Geophysics* 20: 571-613.

Kline, S.W., Adams, P.N., Limber, P.W. 2014. The unsteady nature of sea cliff retreat due to mechanical abrasion, failure and comminution feedbacks. *Geomorphology* 219: 53-67.

Knight, J., Burningham, H. 2011. Boulder dynamics on an Atlantic-facing rock coastline, northwest Ireland. *Marine Geology* 283: 56-65.

Knight, J., Burningham, H., Barrett-Mold, C. 2009. The geomorphology and controls on development of a boulder-strewn rock platform, NW Ireland. *Journal of Coastal Research* SI56(2): 1646-1650.

Koetz, B., Morsdorf, F., van der Linden, S., Curt, T., Allgöwer, B. 2008. Multi-source land cover classification for forest fire management based on imaging spectrometry and LiDAR data. *Forest Ecology and Management* 256: 263-271.

Kohl, C.P., Nishiizumi, K. 1992. Chemical isolation of quartz for measurement of in-situ –produced cosmogenic nuclides. *Geochimica et Cosmochimica Acta* 56(9): 3583-3587.

Komar, P.D. 1998. Beach processes and sedimentation (2nd ed.). Prentice Hall, Upper Saddle River, NJ.

Kopp, R.E., DeConto, R.M., Bader, D.A., Hay, C.C., Horton, R.M., Kulp, S., Oppenheimer, M., Pollard, D., Strauss, B.H. 2017. Evolving understanding of Antarctic Ice-Sheet physics and ambiguity in probabilistic sea-level projections. *Earth's Future* 5: 1217-1233.

Kritikos, T., Robinson, T.R., Davies, T.R.H. 2015. Regional coseismic landslide hazard assessment without historical landslide inventories: A new approach. *Journal of Geophysical Research: Earth Surface* 120.

Lague, D., Brodu, N., Leroux, J. 2013. Accurate 3D comparison of complex topography with terrestrial laser scanner: Application to the Rangitikei canyon (N-Z). *ISPRS Journal of Photogrammetry and Remote Sensing* 82: 10-26.

Lal, D. 1991. Cosmic ray labeling of erosion surfaces: *in situ* nuclide production rates and erosion models. *Earth and Planetary Science Letters* 104: 424-439.

Lamb, M.P., Finnegan, N.J., Scheingross, J.S., Sklar, L.S. 2015. New insights into the mechanics of fluvial bedrock erosion through flume experiments and theory. *Geomorphology* 244: 33-55.

Lane, S.N., Richards, K.S., Chandler, J.H. 1993. Developments in photogrammetry; the geomorphological potential. *Progress in Physical Geography* 17: 306-328.

de Lange, W.P., Moon, V.G. 2005. Estimating long-term cliff recession rates from shore platform widths. *Engineering Geology* 80: 292-301.

Larsen, I.J., Montgomery, D.R., Korup, O. 2010. Landslide erosion controlled by hillslope material. *Nature Geoscience* 3(4): 247-251.

Lee, E.M., Hall, J.W., Meadowcroft, I.C. 2001. Coastal cliff recession: the use of probabilistic prediction methods. *Geomorphology* 40: 253-269.

Lee, R.J., Rose, J., Hamblin, R.J.O., Moorlock, B.S.P., Riding, J.B., Phillips, E., Barendregt, R.W., Candy, I. 2011. The glacial history of the British Isles during the Early and Middle Pleistocene: Implications for the long-term development of the British Ice Sheet. In: Ehlers, J., Gibbard, P.L., Hughes, P.D. (eds.) Developments in Quaternary sciences, Quaternary glaciations - extent and chronology, a closer look. Elsevier: 59-74.

Lifton, N., Sato, T., Dunai, T.J. 2014. Scaling *in situ* cosmogenic nuclide production rates using analytical approximations to atmospheric cosmic-ray fluxes. *Earth and Planetary Science Letters* 386: 149-160.

Lim, M. 2006. Coastal cliff evolution with reference to Staithes, North Yorkshire. Durham University, Durham: PhD thesis.

Lim, M. 2014. The rock coast of the British Isles: cliffs. *Geological Society, London, Memoirs* 40: 19-38.

Lim, M., Mills, J., Rosser, N. 2009. Laser scanning surveying of linear features: considerations and applications. In: Heritage, G.L., Large, A.R.G. (eds.) Laser scanning for the environmental sciences. Wiley-Blackwell: 245-261.

Lim, M., Petley, D.N., Rosser, N.J., Allison, R.J., Long, A.J., Pybus, D. 2005. Combined digital photogrammetry and time-of-flight laser scanning for monitoring cliff evolution. *The Photogrammetric Record* 20: 109-129.

Limber, P.W., Murray, A.B. 2014. Unraveling the dynamics that scale cross-shore headland relief on rocky coastlines: 2. Model predictions and initial tests. *Journal of Geophysical Research: Earth Surface* 119.

Limber, P.W., Murray, A.B. 2015. Sea stack formation and the role of abrasion on beach-mantled headlands. *Earth Surface Processes and Landforms* 40: 559-568.

Limber, P.W., Murray, A.B., Adams, P.N., Goldstein, E.B., 2014. Unraveling the dynamics that scale cross-shore headland relief on rocky coastlines: 1. Model development. *Journal of Geophysical Research: Earth Surface* 119.

Lin, Z., Oguchi, T. 2002. Applications of photogrammetry in geomorphology : a review. *Journal of Geography* 111: 1-15.

Livingstone, S.J., Evans, D.J.A., Ó Cofaigh, C., Davies, B.J., Merritt, J.W., Huddart, D., Mitchell, W.A., Roberts, D.H., Yorke, L. 2012. Glaciodynamics of the central sector of the last British–Irish Ice Sheet in Northern England. *Earth-Science Reviews* 111: 25-55.

Lodwick, J. 2007. Reconstructing the glacial history of Upgang, North Yorkshire: a North Sea ice lobe readvance during the termination of the last glacial maximum? Durham University, Durham: Master thesis.

Malamud, B.D., Turcotte, D.L., Guzzetti, F., Reichenbach, P. 2004. Landslide inventories and their statistical properties. *Earth Surface Processes and Landforms* 29: 687-711.

Mallet, C., Bretar, F. 2009. Full-waveform topographic lidar: State-of-the-art. *ISPRS Journal of Photogrammetry and Remote Sensing* 64: 1-16.

Mano, A., Suzuki, S. 1999. Erosion characteristics of sea cliff on the Fukushima coast. *Coastal Engineering Journal* 41: 43-63.

Marteau, B., Vericat, D., Gibbins, C., Batalla, R.J., Green, D.R. 2017. Application of Structure-from-Motion photogrammetry to river restoration. *Earth Surface Processes and Landforms* 42: 503-515.

Masselink, G., Hughes, M., Knight, J. 2011. Introduction to coastal processes and geomorphology. Hodder Education, London.

Matsumoto, H., Dickson, M.E., Kench, P.S. 2016. An exploratory numerical model of rocky shore profile evolution. *Geomorphology* 268: 98-109.

Matsumoto, H., Dickson, M.E., Masselink, G. 2017. Systematic analysis of rocky shore platform morphology at large spatial scale using LiDAR-derived digital elevation models. *Geomorphology* 286: 45-57.

Mayaud, J.R., Viles, H.A., Coombes, M.A. 2014. Exploring the influence of biofilm on short-term expansion and contraction of supratidal rock: an example from the Mediterranean. *Earth Surface Processes and Landforms* 39: 1404-1412.

McClymont, E.L., Martínez-Garcia, A., Rosell-Melé, A. 2007. Benefits of freeze-drying sediments for the analysis of total chlorins and alkenone concentrations in marine sediments. *Organic Geochemistry* 38(6): 1002-1007.

McKenna, J., Jackson, D.W.T., Cooper, J.A.G. 2011. In situ exhumation from bedrock of large rounded boulders at the Giant's Causeway, Northern Ireland: An alternative genesis for large shore boulders (mega-clasts). *Marine Geology* 283: 25-35.

Micheletti, N., Chandler, J.H., Lane, S.N. 2015. Investigating the geomorphological potential of freely available and accessible structure-from-motion photogrammetry using a smartphone. *Earth Surface Processes and Landforms* 40: 473-486.

Miller, J.R. 1991. The influence of bedrock geology on knickpoint development and channel-bed degradation along downcutting streams in South-Central Indiana. *The Journal of Geology* 99: 591-605.

Moon, V.G., Healy, T. 1994. Mechanisms of coastal cliff retreat and hazard zone delineation in soft flysch deposits. *Journal of Coastal Research* 10(3): 663-680.

Morgan, J.A., Brogan, D.J., Nelson, P.A. 2017. Application of Structure-from-Motion photogrammetry in laboratory flumes. *Geomorphology* 276: 125-143.

Moses, C.A., 2014. The rock coast of the British Isles: shore platforms. *Geological Society, London, Memoirs* 40: 39-56.

Moses, C.A., Robinson, D. 2011. Chalk coast dynamics: Implications for understanding rock coast evolution. *Earth-Science Reviews* 109: 63-73.

Moses, C., Robinson, D., Kazmer, M., Williams, R. 2015. Towards an improved understanding of erosion rates and tidal notch development on limestone coasts in the Tropics: 10years of micro-erosion meter measurements, Phang Nga Bay, Thailand. *Earth Surface Processes and Landforms* 40: 771-782.

Mottershead, D.N. 1989. Rates and patterns of bedrock denudation by coastal salt spray weathering: a seven-year record. *Earth Surface Processes and Landforms* 14: 383-398.

Mottershead, D.N., Stephenson, W.J., Hemmingsen, M.A. 2016. Geomorphology and the Law of Unintended Consequences (Locke, 1691): Lessons from coastal weathering and erosion at Prawle (UK) and Kaikoura (NZ). *Geomorphology* 265: 1-11.

Moura, D., Gabriel, S., Gamito, S., Santos, R., Zugasti, E., Naylor, L., Gomes, A., Tavares, A.M., Martins, A.L. 2012. Integrated assessment of bioerosion, biocover and downwearing rates of carbonate rock shore platforms in southern Portugal. *Continental Shelf Research* 38: 79-88.

Moura, D., Gabriel, S., Ramos-Pereira, A., Neves, M., Trindade, J., Viegas, J., Veiga-Pires, C., Ferreira, Ó., Matias, A., Jacob, J., Boski, T., Santana, P. 2011. Downwearing rates on shore platforms of different calcareous lithotypes. *Marine Geology* 286: 112-116.

Nairn, R.B., Pinchin, B.M., Philpott, K.L. 1986. A cohesive coastal development model. In: Proceedings of the Symposium on Cohesive Shores. Burlington, Ontario: 246-261.

Naylor, L.A., Coombes, M.A., Viles, H.A. 2012. Reconceptualising the role of organisms in the erosion of rock coasts: a new model. *Geomorphology* 157-158: 17-30.

Naylor, L.A., Stephenson, W.J. 2010. On the role of discontinuities in mediating shore platform erosion. *Geomorphology* 114: 89-100.

Naylor, L.A, Stephenson, W.J., Smith, H.C.M., Way, O., Mendelssohn, J., Cowley, A. 2016. Geomorphological control on boulder transport and coastal erosion before, during and after an extreme extra-tropical cyclone. *Earth Surface Processes and Landforms* 41: 685-700.

Naylor, L.A., Stephenson, W.J., Trenhaile, A.S. 2010. Rock coast geomorphology: Recent advances and future research directions. *Geomorphology* 114: 3-11.

Neves, M., Pereira, A.R., Laranjeira, M., Trindade, J. 2001. Desenvolvimento de um microerosómetro do tipo TMEM para aplicação em plataformas rocosas litorais. Finisterra XXXVI(71): 83-101 [in Portuguese].

Nishiizumi, K., Imamura, M., Caffee, M., Southon, J., Finkel, R., McAninch, J. 2007. Absolute calibration of ^{10}Be AMS standards. *Nuclear Instruments and Methods in Physics Research Section B: Beam Interactions with Materials and Atoms* 258: 403-413.

Nitsche, M., Turowski, J.M., Badoux, A., Rickenmann, D., Kohoutek, T.K., Pauli, M., Kirchner, J.W. 2013. Range imaging: a new method for high-resolution topographic measurements in small- and medium-scale field sites. *Earth Surface Processes and Landforms* 38: 810-825.

Oertel, G.F. 2005. Coasts, coastlines, shores and shorelines. In: Schwartz, M.L. (ed.) Encyclopedia of coastal science. Springer, Dordrecht: 323-327.

Ogawa, H., Dickson, M.E., Kench, P.S. 2015. Hydrodynamic constraints and storm wave characteristics on a sub-horizontal shore platform. *Earth Surface Processes and Landforms* 40: 65-77.

d'Oleire-Oltmanns, S., Marzolff, I., Peter, K.D., Ries, J.B. 2012. Unmanned Aerial Vehicle (UAV) for Monitoring Soil Erosion in Morocco. *Remote Sensing* 4: 3390-3416.

Onodera, T.F. 1963. Dynamic investigation of foundation rocks. In: Proceedings of the 5th Symposium on Rock Mechanics. Pergamon Press, Minnesota: 517-533.

Palmstrøm, A. 1995. RMi – a rock mass characterization system for rock engineering purposes. Oslo University, Oslo: PhD thesis.

Palmstrøm, A. 1996a. Characterizing rock masses by the RMi for use in practical rock engineering: Part 1: The development of the Rock Mass index (RMi). *Tunnelling and Underground Space Technology* 11: 175-188.

Palmstrøm, A. 1996b. Characterizing rock masses by the RMi for use in practical rock engineering, part 2: Some practical applications of the rock mass index (RMi). *Tunnelling and Underground Space Technology* 11: 287-303.

Paris, R., Naylor, L.A., Stephenson, W.J. 2011. Boulders as a signature of storms on rock coasts. *Marine Geology* 283: 1-11.

Parker, R.N., Hancox, G.T., Petley, D.N., Massey, C.I., Densmore, A.L., Rosser, N.J. 2015. Spatial distributions of earthquake-induced landslides and hillslope preconditioning in northwest South Island, New Zealand. *Earth Surface Dynamics* 3: 1-52.

Perg, L.A., Anderson, R.S., Finkel, R.C. 2001. Use of a new ^{10}Be and ^{26}Al inventory method to date marine terraces, Santa Cruz, California, USA. *Geology* 29(10): 879-882.

Poate, T., Masselink, G., Austin, M. J., Dickson, M., McCall, R. 2018. The role of bed roughness in wave transformation across sloping rock shore platforms. *Journal of Geophysical Research: Earth Surface* 123: 97-123.

Porter, N.J., Trenhaile, A.S. 2007. Short-term rock surface expansion and contraction in the intertidal zone. *Earth Surface Processes and Landforms* 32: 1379-1397.

Porter, N.J., Trenhaile, A.S., Prestanski, K., Kanyaya, J.I., 2010a. Patterns of surface downwearing on shore platforms in eastern Canada. *Earth Surface Processes and Landforms* 35: 1793-1810.

Porter, N.J., Trenhaile, A.S., Prestanski, K.J., Kanyaya, J.I. 2010b. Shore platform downwearing in eastern Canada: The mega-tidal Bay of Fundy. *Geomorphology* 118: 1-12.

Pringle, A.W. 1985. Holderness coast erosion and the significance of ords. *Earth Surface Processes and Landforms* 10: 107-124.

Rawson, P., F., Wright, J., K. 2000. The Yorkshire coast. The Geologists' Asssociation.

Recorbet, F., Rochette, P., Braucher, R., Bourlès, D., Benedetti, L., Hantz, D., Finkel, R.C. 2010. Evidence for active retreat of a coastal cliff between 3.5 and 12 ka in Cassis (South East France). *Geomorphology* 115: 1-10.

Regard, V., Dewez, T., Bourlès, D.L., Anderson, R.S., Duperret, A., Costa, S., Leanni, L., Lasseur, E., Pedoja, K., Maillet, G.M. 2012. Late Holocene seacliff retreat recorded by ^{10}Be profiles across a coastal platform: Theory and example from the English Channel. *Quaternary Geochronology* 11: 87-97.

Regnauld, H., Pirazzoli, P.A., Morvan, G., Ruz, M. 2004. Impacts of storms and evolution of the coastline in western France. *Marine Geology* 210: 325-337.

Roberts, D.H., Evans, D.J.A., Lodwick, J., Cox, N.J. 2013. The subglacial and ice-marginal signature of the North Sea Lobe of the British–Irish Ice Sheet during the Last Glacial Maximum at Upgang, North Yorkshire, UK. *Proceedings of the Geologists' Association* 124: 503-519.

Robinson, L.A. 1976. The micro-erosion meter technique in a littoral environment. *Marine Geology* 22: M51-M58.

Robinson, L.A. 1977a. Erosive processes on the shore platform of northeast Yorkshire, England. *Marine Geology* 23: 339-361.

Robinson, L.A. 1977b. Marine erosive processes at the cliff foot. *Marine Geology* 23: 257-271.

Robinson, L.A. 1977c. The morphology and development of the northeast Yorkshire shore platform. *Marine Geology* 23: 237-255.

Rock, G., Ries, J.B., Udelhoven, T. 2011. Sensitivity analysis of UAV-photogrammetry for creating Digital Elevation Models (DEM). In: Proceedings of Conference on Unmanned Aerial Vehicle in Geomatics. Zurich, Switzerland.

Rogers, H.E., Swanson, T.W., Stone, J.O. 2012. Long-term shoreline retreat rates on Whidbey Island, Washington, USA. *Quaternary Research* 78: 315-322.

Rood, D.H., Hall, S., Guiderson, T.P., Finkel, R.C., Brown, T.A. 2010. Challenges and opportunities in high-precision Be-10 measurements at CAMS. *Nuclear Instruments and Methods in Physics Research B* 268: 730-732.

Rosser, N.J., Brain, M.J., Petley, D.N., Lim, M., Norman, E.C. 2013. Coastline retreat via progressive failure of rocky coastal cliffs. *Geology* 41: 939-942.

Rosser, N., Lim, M., Petley, D., Dunning, S., Allison, R. 2007. Patterns of precursory rockfall prior to slope failure. *Journal of Geophysical Research* 112.

Santana, D., Corominas, J., Mavrouli, O., Garcia-Sellés, D. 2012. Magnitude-frequency relation for rockfall scars using a Terrestrial Laser Scanner. *Engineering Geology* 145: 50-64.

Schürch, P., Densmore, A.L., Rosser, N.J., Lim, M., McArdell, B.W. 2011. Detection of surface change in complex topography using terrestrial laser scanning: application to the Illgraben debris-flow channel. *Earth Surface Processes and Landforms* 36: 1847-1859.

Selby, M. 1980. A rock mass strength classification for geomorphic purposes: with tests from Antarctica and New Zealand. *Zeitschrift für Geomorphologie* 24: 31-51.

Shakesby, R.A., Walsh, R.P.D. 1986. Micro erosion meter measurements of erosion on limestone, Oxwich Point, Gower: Some technical considerations and preliminary results. *Cambria* 13: 213-224.

Shennan, I., Horton, B. 2002. Holocene land- and sea-level changes in Great Britain. *Journal of Quaternary Science* 17: 511-526.

Shennan, I., Bradley, S.L., Edwards, R. 2018. Relative sea-level changes and crustal movements in Britain and Ireland since the Last Glacial Maximum. *Quaternary Science Reviews* 188:143-159.

Shennan, I., Lambeck, K., Horton, B., Innes, J., Lloyd, J., McArthur, J., Rutherford, M. 2000. Holocene isostasy and relative sea-level changes on the east coast of England. *Geological Society London* SI166: 275-298.

Sklar, L.S., Dietrich, W.E. 2001. Sediment and rock strength controls on river incision into bedrock. *Geology* 29: 1087-1090.

Slott, J.M., Murray, A.B., Ashton, A.D., Crowley, T.J. 2006. Coastline responses to changing storm patterns. *Geophysical Research Letters* 33.

Small, E.E., Blom, T., Hancock, G.S., Hynek, B.M., Wobus, C.W. 2015. Variability of rock erodibility in bedrock-floored stream channels based on abrasion mill experiments. *Journal of Geophysical Research: Earth Surface* 120.

Smith, M.W. 2014. Roughness in the Earth Sciences. *Earth-Science Reviews* 136: 202-225.

Smith, M.W. 2015. Direct acquisition of elevation data: Terrestrial Laser Scanning. In: Clarke, L. (ed.) Geomorphological Techniques. British Society for Geomorphology, London.

Smith, M.W., Vericat, D. 2015. From experimental plots to experimental landscapes: topography, erosion and deposition in sub-humid badlands from Structure-from-Motion photogrammetry. *Earth Surface Processes and Landforms* 40: 1656-1671.

Sneed, E.D., Folk, R.L. 1958. Pebbles in the lower Colorado River, Texas a study in particle morphogenesis. *The Journal of Geology* 66: 114-150.

So, C.L. 1965. Coastal platforms of the Isle of Thanet, Kent. *Transactions of the Institute of British Geographers* 147-156.

Spencer, T. 1981. Micro-topographic change on calcarenites, grand Cayman Island, West Indies. *Earth Surface Processes and Landforms* 6: 85-94.

Spencer, T. 1985a. Weathering rates on a Caribbean reef limestone: results and implications. *Marine Geology* 69: 195-201.

Spencer, T. 1985b. Marine erosion rates and coastal morphology of reef limestones on Grand-Cayman Island, West-Indies. *Coral Reefs* 4: 59-70.

Stark, C.P., Guzzetti, F. 2009. Landslide rupture and the probability distribution of mobilized debris volumes. *Journal of Geophysical Research* 114.

Stark, C.P., Hovius, N. 2001. The characterization of landslide size distributions. *Geophysical Research Letters* 28: 1091-1094.

Stephenson, W.J. 2000. Shore platforms: a neglected coastal feature? *Progress in Physical Geography* 24: 311-327.

Stephenson, W.J., Finlayson, B.L. 2009. Measuring erosion with the micro-erosion meter – Contributions to understanding landform evolution. *Earth-Science Reviews* 95: 53-62.

Stephenson, W.J., Kirk, R.M. 1996. Measuring erosion rates using the micro-erosion meter: 20 years of data from shore platforms, Kaikoura Peninsula, South Island New Zealand. *Marine Geology* 131: 209-218.

Stephenson, W.J., Kirk, R.M. 1998. Rates and patterns of erosion on inter-tidal shore platforms, Kaikoura Peninsula, South Island, New Zealand. *Earth Surface Processes and Landforms* 23: 1071-1085.

Stephenson, W.J, Kirk, R.M. 2000a. Development of shore platforms on Kaikoura Peninsula, South Island, New Zealand: Part one: The role of waves. *Geomorphology* 32: 21-41.

Stephenson, W.J, Kirk, R.M. 2000b. Development of shore platforms on Kaikoura Peninsula, South Island, New Zealand: II: The role of subaerial weathering. *Geomorphology* 32: 43-56.

Stephenson, W.J., Kirk, R.M. 2001. Surface swelling of coastal bedrock on inter-tidal shore platforms, Kaikoura Peninsula, South Island, New Zealand. *Geomorphology* 41: 5-21.

Stephenson, W.J., Kirk, R.M., Hemmingsen, S.A., Hemmingsen, M.A. 2010. Decadal scale micro erosion rates on shore platforms. *Geomorphology* 114: 22-29.

Stephenson, W.J., Kirk, R.M., Kennedy, D.M., Finlayson, B.L., Chen, Z. 2012. Long term shore platform surface lowering rates: revisiting Gill and Lang after 32 years. *Marine Geology* 299: 90-95.

Stephenson, W.J., Naylor, L.A. 2011. Geological controls on boulder production in a rock coast setting: Insights from South Wales, UK. *Marine Geology* 283: 12-24.

Stephenson, W.J., Thornton, L.E. 2005. Australian rock coasts: review and prospects. *Australian Geographer* 36(1): 95-115.

Stone, J., Lambeck, K., Fifield, L.K., Evans, J.M., Cresswell, R.G. 1996. A Lateglacial age for the Main Rock Platform, western Scotland. *Geology* 24(8): 707-710.

Sturt, F., Garrow, D., Bradley, S. 2013. New models of North West European Holocene palaeogeography and inundation. *Journal of Archaeological Science* 40: 3963-3976.

Sunamura, T. 1977. A relationship between wave-induced cliff erosion and erosive force of waves. *The Journal of Geology* 85: 613-618.

Sunamura, T. 1983. Processes of sea cliff and platform erosion. In: Komar, P.D. (ed.) Handbook of coastal processes and erosion. CRC Press, Boca Raton, Florida: 233-265.

Sunamura, T. 1992. Geomorphology of rocky coasts. John Wiley & Sons Ltd, Chichester.

Suzuki, T. 2002. Rock control in geomorphological processes: Research history in Japan and perspective. *Chikei* 23: 161-199.

Swantesson, J.O.H., Gómez-Pujol, L., Cruslock, E.M., Fornós, J.J., Balaguer, P. 2006. Processes and patterns of erosion and downwearing on micro-tidal rock coasts in Sweden and western Mediterranean. *Zeitschrift für Geomorphologie Supplementbände* 144: 137-160.

Swirad, Z.M., Rosser, N.J., Brain, M.J., Vann Jones, E.C. 2016. What controls geometry of rocky coasts at the local scale? *Journal of Coastal Research* SI75: 612-616.

Tabachnick, B.G., Fidell, L.S. 2013. Using multivariate statistics (6^{th} ed.). Pearson: London.

Taylor, A.N. 2003. Change and Processes of change on shore platforms. University of Canterbury, Christchurch: PhD thesis.

Thornton, L.E., Stephenson, W.J. 2006. Rock strength: a control of shore platform elevation. *Journal of Coastal Research* 22: 224-231.

Torunski, H. 1979. Biological erosion and its significance for the morphogenesis of limestone coasts and for nearshore sedimentation. *Senckenbergiana Maritima* 11: 193-265.

Trenhaile, A.S. 1972. The shore platforms of the Vale of Glamorgan, Wales. *Transactions of the Institute of British Geographers*: 127-144.

Trenhaile, A.S. 1974. The geometry of shore platforms in England and Wales. *Transactions of the Institute of British Geographers*: 129-142.

Trenhaile, A.S. 1978. The shore platforms of Gaspe, Quebec. *Annals of the Association of American Geographers* 68: 95-114.

Trenhaile, A.S. 1980. Shore platforms: a neglected coastal feature. *Progress in Physical Geography* 4: 1-23.

Trenhaile, A.S. 1983. The width of shore platforms; a theoretical approach. *Geografiska Annaler. Series A, Physical Geography* 65: 147-158.

Trenhaile, A.S. 1987. The geomorphology of rock coasts. Clarendon Press, Oxford.

Trenhaile, A.S. 2000. Modeling the development of wave-cut shore platforms. *Marine Geology* 166: 163-178.

Trenhaile, A.S. 2001. Modeling the effect of late Quaternary interglacial sea levels on wave-cut shore platforms. *Marine Geology* 172: 205-223.

Trenhaile, A.S. 2002. Rock coasts, with particular emphasis on shore platforms. *Geomorphology* 48: 7-22.

Trenhaile, A.S. 2014. Climate change and its impact on rock coasts. *Geological Society, London, Memoirs* 40: 7-17.

Trenhaile, A.S., Byrne M.-L. 1986. A theoretical investigation of the Holocene development of rock coasts, with particular reference to shore platforms. *Geografiska Annaler* 68A: 1-14.

Trenhaile, A.S., Pérez Alberti, A., Martínez Cortizas, A., Costa Casais, M., Blanco Chao, R. 1999. Rock coast inheritance: an example from Galicia, Northwestern Spain. *Earth Surface Processes and Landforms* 24: 605-621.

Trudgill, S.T. 1976a. The marine erosion of limestones on Aldabra Atoll, Indian Ocean. *Zeitschrift für Geomorphologie* Supplementbände 26: 164-200.

Trudgill, S.T. 1976b. The subaerial and subsoil erosion of limestone on Aldabra Atoll, Indian Ocean. *Zeitschrift für Geomorphologie* Supplementbände 26: 201-210.

Trudgill, S., High, C.J., Hanna, F.K. 1981. Improvements to the micro-erosion meter. *British Geomorphological Research Group Technical Bulletin* 29: 3-17.

Turowski, J.M., Cook, K.L. 2017. Field techniques for measuring bedrock erosion and denudation. *Earth Surface Processes and Landforms* 42: 109-127.

Vann Jones, E.C., Rosser, N.J., Brain, M.J. 2018. Alongshore variability in wave energy transfer to coastal cliffs. *Geomorphology* 322: 1-14.

Vidyadhar, A., Hanumantha Rao, K., Forssberg, K.S.E. 2002. Separation of feldspar from quartz: mechanism of mixed cationic/anionic collector adsorption on minerals and flotation selectivity. *Minerals & Metallurgical Processing* 19(3): 128-136.

Viles, H., Goudie, A., Grab, S., Lalley, J. 2011. The use of the Schmidt Hammer and Equotip for rock hardness assessment in geomorphology and heritage science: a comparative analysis. *Earth Surface Processes and Landforms* 36: 320-333.

Viles, H.A., Trudgill, S.T. 1984. Long term remeasurements of micro-erosion meter rates, Aldabra Atoll, Indian Ocean. *Earth Surface Processes and Landforms* 9: 89-94.

Wackrow, R., Chandler, J.H. 2008. A convergent image configuration for DEM extraction that minimises the systematic effects caused by an inaccurate lens model. *The Photogrammetric Record* 23: 6-18.

Wackrow, R., Chandler, J.H., Bryan, P. 2007. Geometric consistency and stability of consumer-grade digital cameras for accurate spatial measurement. *The Photogrammetric Record* 22: 121-134.

Walkden, M.J.A., Hall, J.W. 2005. A predictive Mesoscale model of the erosion and profile development of soft rock shores. *Coastal Engineering* 52: 535-563.

Westoby, M.J., Brasington, J., Glasser, N.F., Hambrey, M.J., Reynolds, J.M. 2012. "Structure-from-Motion" photogrammetry: A low-cost, effective tool for geoscience applications. *Geomorphology* 179: 300-314.

Whadcoat, S.K., 2017. Numerical modelling of rockfall evolution in hard rock slopes. Durham University, Durham: PhD thesis.

Wheaton, J.M. 2008. Monitoring and modelling morphological change in a braided gravel-bed river using high resolution GPS-based survey. University of Southampton, Southampton: PhD thesis.

Wheaton, J.M., Brasington, J., Darby, S.E., Sear, D.A. 2010. Accounting for uncertainty in DEMs from repeat topographic surveys: improved sediment budgets. *Earth Surface Processes and Landforms* 35: 136-156.

Whipple, K.X., Hancock, G.S., Anderson, R.S. 2000. River incision into bedrock: Mechanics and relative efficacy of plucking, abrasion, and cavitation. *Geological Society of America Bulletin* 112: 490-503.

Wilcock, P.R., Miller, D.S., Shea, R.H., Kerkin, R.T. 1998. Frequency of effective wave activity and the recession of coastal bluffs: Calvert Cliffs, Maryland. *Journal of Coastal Research* 14: 256-268.

Williams, J.G., Rosser, N.J., Hardy, R.J., Brain, M.J., Afana, A.A. 2018. Optimising 4-D surface change detection: an approach for capturing rockfall magnitude-frequency. *Earth Surface Dynamics* 6: 101-119.

Williams, R.B.G. 1986. Intermediate statistics for geographers and earth scientists. Macmillian, London.

Williams, R.D. 2013. DEMs of Difference. In: Clarke, L. (ed.) Geomorphological Techniques. British Society for Geomorphology, London.

Wilson, A., Hovius, N., Turowski, J.M. 2013. Upstream-facing convex surfaces: Bedrock bedforms produced by fluvial bedload abrasion. *Geomorphology* 180-181: 187-204.

Wilson, A., Lavé, J. 2014. Convergent evolution of abrading flow obstacles: Insights from analogue modelling of fluvial bedrock abrasion by coarse bedload. *Geomorphology* 208: 207-224.

Wood, A. 1968. Beach platforms in the chalk of Kent, England. *Zeitschrift für Geomorphologie* 12: 107-113.

Wright, L.W. 1970. Variation in the level of the cliff/shore platform junction along the south coast of Great Britain. *Marine Geology* 9: 347-353.

Yin, D., Peakall, J., Parsons, D., Chen, Z., Averill, H.M., Wignall, P., Best, J. 2016. Bedform genesis in bedrock substrates: Insights into formative processes from a new experimental approach and the importance of suspension-dominated abrasion. *Geomorphology* 255: 26-38.

This page is intentionally left blank

Appendix 1: Swirad et al., 2016

Swirad, Z.M., Rosser, N.J., Brain, M.J., Vann Jones, E.C. 2016. What controls the geometry of rocky coasts at the local scale? *Journal of Coastal Research* SI75: 612-616.

What controls the geometry of rocky coasts at the local scale?

Zuzanna M. Swirad, Nick J. Rosser, Matthew J. Brian and Emma C. Vann Jones
Department of Gepgraphy
Durham University
Durham, United Kingdom

ABSTRACT
There is a need to understand the controls on rocky coastal form in order to predict the likely response to climate changes and sea-level rise. Spatial variations in coastal geometry result from inheritance and contemporary processes, notably erosive wave intensity and rock resistance. We studied a 4.2 km long section of coastline (Staithes, North Yorkshire, UK) using LiDAR point cloud data and ortho-photographs. We represented the coast as a series of densely-spaced (25 m) and resampled (0.2 m) 2D cross-sections. GIS-based statistical analysis allowed us to identify relationships between coastal morphology, geology (lithology and rock structure) and wave intensity. We found the following statistically-significant relationships: 1) more intensive waves and weaker rocks are associated with steeper shore platforms, 2) higher platforms and cliff toes are associated with weaker and more variable rocks, and 3) surface roughness increases with greater wave intensity, decreased density of discontinuities and decreased variability of intact rock hardness. However, these relationships are weak, which suggests the potential role of coastal inheritance and/or the need to better represent rock resistance in coastal models.

ADDITIONAL INDEX WORDS: *Rocky coasts, shore platforms, rock control, rock resistance, GIS.*

INTRODUCTION

There is a pressing need to constrain the geomorphic sensitivity of rocky coasts to changes in marine conditions, notably those relating to sea level and wave conditions. Numerous studies have identified controls on coastal geometry based on relationships between shore platform width, gradient and elevation, rock properties and marine action (Trenhaile, 1978; Davies et al., 2006; Kennedy and Dickson, 2006). However, attempts to explain controlling processes and, hence, better constrain future changes have often been based on simplified conceptual models of the relationships between marine conditions, shore platforms and cliffs and the potential feedbacks in their co-evolution. Existing studies lack sufficient spatial resolution and coverage to identify key relationships that may aid simple predictive analysis.

Using a GIS approach and a dataset obtained using airborne LiDAR and ortho-photographs we undertook a systematic analysis of a rocky coast (North Yorkshire, UK) to determine the relationships between coastal shape, geology and wave intensity at a local scale. Our approach helps to understand which rock characteristics (resistance to abrasive and/or structurally-defined erosion) represent 'rock resistance' (Sunamura, 1992) in specific morphologic elements of shore platforms. Potential controls on coastal geometry have been identified previously, but the relationships are still poorly quantified and understood:

1. Higher, steeper and narrower shore platforms form in harder rocks (Trenhaile, 1987; Stephenson, 2000; Davies et al., 2006).
2. Higher joint density associates with lower platforms (Kennedy and Dickson, 2006).
3. More intensive wave action generates flatter platforms (Trenhaile, 1980).

The central aim of our study is to consider the controls on geometry of hard-rock shore platforms by linking morphology to geology. As the variation in coastal morphology reflects variation in alongshore erosion rate, this may provide insight into long-term coastal evolution to better assess future changes in sea-level rise and intensification of wave action as a result of climate change.

Research area

The 4 km long section of the coast around Staithes in North Yorkshire, UK is a storm-wave dominated coast, characterised by tidal range of 4.6 m (http://www.ntslf.org/, accessed: 12/10/2015). Gently sloping (~2°) shore platforms up to 400 m wide are composed of Jurassic bedrock of 16.7-41.5 MPa unconfined compressive strength (Lim, 2006). The lithologies exposed at the sea level are shale (80.6%), sandstone (14.1%), mudstone (3.9%), ironstone (1.1%) and siltstone (0.3%). The platform is backed by hard-rock cliffs up to 90 m high, which are topped by 10-20 m thick layer of glacial till. The platform is partly covered by boulders, ephemeral pocket beaches and intertidal flora (Figure 1).

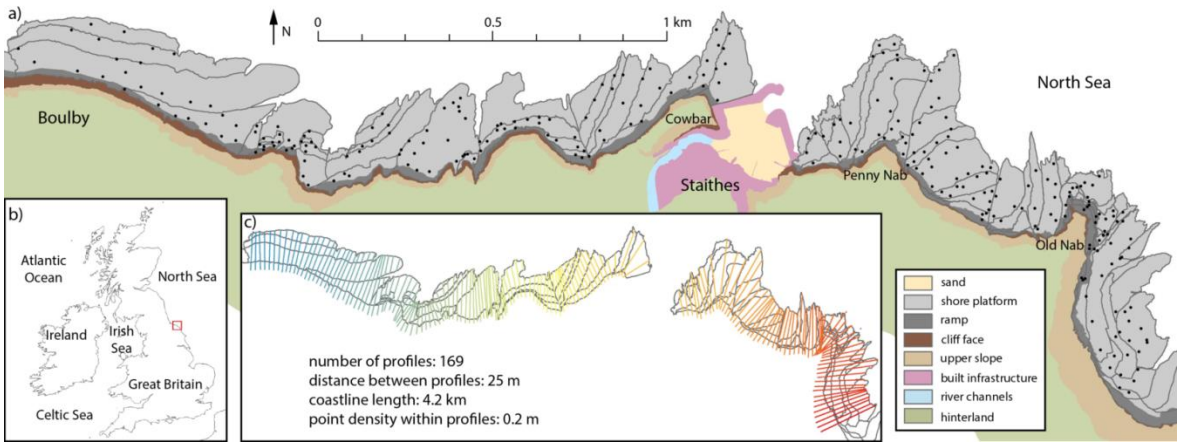


Figure 1. Coast of Staithes, North Yorkshire, England: a) analysed shore platforms and backing cliffs. Zones within platforms represent single rock beds, i.e. exposures of uniform geology limited by apparent altitude/colour change. Dots represent sites of rock hardness measurements; b) location of the North Yorkshire coast in British Isles; c) location of coastal cross-sections. Profiles correspond to coloured profiles in Figure 3.

METHODS

We processed the data and created all layers in ArcGIS 10.2. We used airborne LiDAR-derived point clouds (ca. 100 points/m^2) obtained on 15/08/2014 during a low spring tide to create a Digital Elevation Model (DEM) and slope map at 0.2x0.2 m pixel resolution. We combined these with ortho-photographs (ca. 0.03 m pixel) to divide our study area into morphological classes, including: foreshore platform (seaward limit: mean low water level of spring tides), foreshore ramp (upper part of platform, < 15°), cliff face (near-vertical), upper cliff slope (usually ca. 30°, formed in glacial till), built infrastructure, river channels, hinterland and beach deposits (Figure 2). We divided the platform on the basis of exposed geology (Figure 1). We mapped major (i.e. visible on the ortho-photographs) joints and interpolated them into a joint density raster (resolution: 1 m, ArcGIS Line Density tool). At 283 sites, which were selected to cover all types of geology, we measured fresh rock hardness (after having removed the weathered outer layer with carborundum stone) with a Proceq Equotip 550 Leeb D Type (Viles et al., 2011) and calculated mean rock hardness (Equotip rebound values) and its variation for each rock bed from 1-18 samples (in average: 3.54). We used rock hardness as a proxy for unconfined compressive strength, which has been previously considered as a good descriptor of the resistance of rock to erosion (Sunamura, 1992; Naylor and Stephenson, 2010).

Table 1. Variables used in the analysis of geomorphic conditions of the shore platform at Staithes

Variable	Unit	Calculation
Platform width (w)	m	Horizontal distance between cliff toe and platform seaward edge, i.e. the first and the last points classified as 'platform/ramp'. Proxy for wave intensity on the basis that energy attenuation increases with width.
Platform gradient (α)	°	Dip of a straight line between cliff toe and platform seaward edge; arctangent of platform width divided by DEM-derived elevation difference between the first and the last points classified as 'platform/ramp'.
Platform elevation (z)	m AOD	Mean elevation of platform and ramp, averaged from DEM-derived elevations of points resampled along the cross-sections (0.2 m interval).
Cliff toe elevation (tz)	m AOD	DEM-derived elevation of the first point classified as a cliff face, which abuts against platform/ramp.
Platform roughness (r)		Standard deviation of slope obtained at all points across platform and ramp at 0.2 m interval.
Rock hardness (Sc)	Equotip rebound value	Proxy for uniaxial rock strength. Each rock bed (exposure of uniform geology) is represented as a mean of point readings within it (Figure 1). Profiles are represented as weighted mean based on the proportion of extent of specific rock beds it crosses.
Rock hardness variation (Sc_v)		Weighted mean of square root of variance in Sc in each rock bed which are crossed by profiles.
Joint density (j)	joints/m^2	Interpolated from linear data using ArcGIS Line Density tool. Used only on platform sections not covered by sediments. This is based on the assumption that joint density is the same for covered and exposed sections of platform.

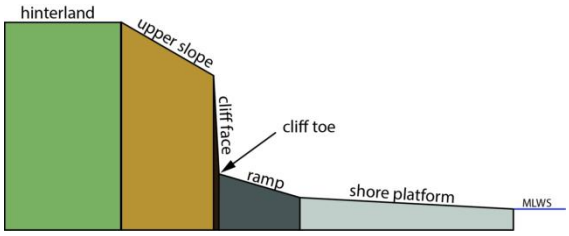


Figure 2. Conceptual model of location of the morphological classes along coastal cross-sections

We automatically extracted equally-spaced (every 25 m) 2D cross-sections as station lines perpendicular to the coastline, along the line defined by the mean water level of spring tides (2.59 m AOD). Along each cross-section, we extracted altitude and morphological data at 0.2 m horizontal intervals (Figure 3), to determine the platform characteristics described in Table 1.

We analysed kernel density plots for each variable across whole dataset, and identified mostly quasi-normal distributions, which are suitable for use in regression analysis. Platform width and gradient are, however, better represented by their square root. We performed pairwise and stepwise regression between morphologic variables and potential controlling factors: geological, marine and combined.

RESULTS

Geology

Lithological variation is expressed by the rock hardness *Sc* and the variablity therein, Sc_v, while structure is expressed by joint density *j*. The best fit of stepwise regression for each morphologic variable is presented in Table 2. Significant relationships (p-value < 0.05) exist between geology and all platform characteristics except gradient, but none of the relationships is strong (R^2 < 0.1). Wider and lower platforms and lower cliff toe elevations weakly coincide with harder and less variable rocks. Platform roughness is negatively correlated with variation of rock hardness and joint density.

Table 2. Relationships between geology and shore platform morphology. Asterisks (*) indicate significant relationships (p-value < 0.05); w – platform width, α – platform gradient, z – platform elevation, tz – cliff toe elevation, r – platform roughness, Sc – rock hardness, Sc_v – viariation in rock hardness, j – joint density.

Relationship	Adjusted R^2	p-value
$w = (17.331 + 0.026\ Sc_v - 0.012\ Sc)^2$	0.042	0.011*
$\alpha = (1.257 - 0.353\ j)^2$	0.015	0.062
$z = 1.067 - 0.005\ Sc + 0.004\ Sc_v$	0.09	0.0002 *
$tz = 5.776 - 0.01\ Sc + 0.02\ Sc_v$	0.029	0.032*
$r = 6.429 - 0.029\ Sc_v - 2.611\ j$	0.031	0.0269 *

Wave intensity

We were not able to express variations in wave intensity across the platform and at the cliff toe in terms of tide gauge-derived deep-water wave characteristics and wave transformation in the nearshore zone because: 1) the studied coastline is relatively short (4 km) and so does not contain a fully representative population of headlands and embayments which limits the inclusion of areas with refraction effects in the analysis, 2) we analysed a single site with no monitoring data on variations in tidal and wave climate, and 3) nearshore bathymetry is only poorly constrained at a resolution suitable to elucidate differences between the profiles considered here, and so wave transformation models cannot be applied.

We test the assumption that platform width, and hence wave energy dissipation, is a proxy for wave intensity. Over the studied coastline we assume that wave energy delivery to the toe of the platform is constant, and so the dissipation of wave energy must vary by platform width. Therefore, wider platforms mean less wave energy per platform unit length and so less energy arriving to the cliff toe. Therefore, we assume more intensive wave action when the platform is narrower.

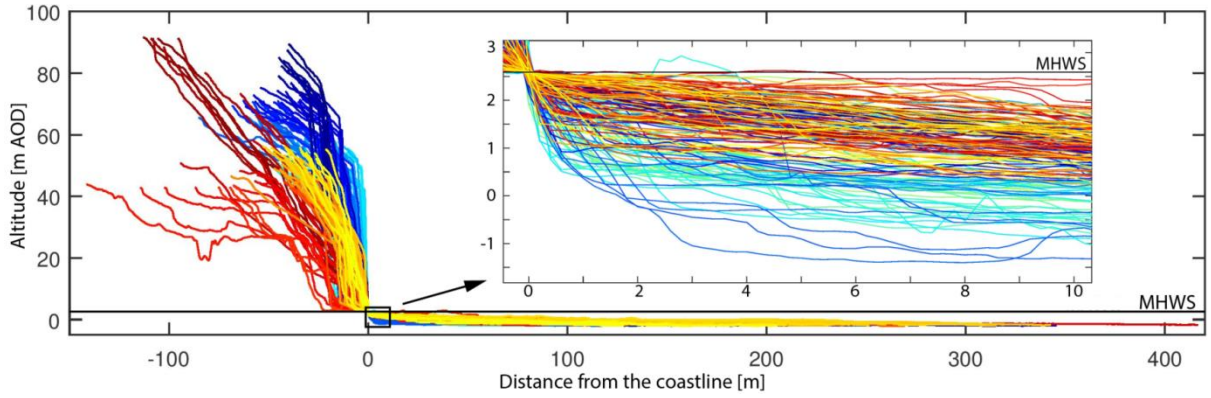


Figure 3. Cross-sections of the Staithes coast including shore platform, ramp, cliff face and upper slope only. Horizontal axis: negative values represent onshore and positive – offshore section. Profile colour corresponds to that displayed in Figure 1.

Pairwise regression between platform width and other morphological characteristics presented in Table 3 shows that significant negative relationships exist between platform width and gradient and platform roughness, while elevations of platform and cliff toe are independent of platform width.

Table 3. Relationships between shore platform width and other morphological characteristics. Asterisks (*) indicate significant relationships (p-value < 0.05); α – platform gradient, z – platform elevation, tz – cliff toe elevation, r – platform roughness, w – platform width.

Relationship	Adjusted R^2	p-value
$\alpha = (2.273 - 0.08\ sqrt(w))^2$	0.306	<0.0001*
$z = -0.731 + 0.002\ sqrt(w)$	-0.006	0.8987
$tz = 1.712 + 0.08\ sqrt(w)$	0.002	0.236
$r = 10.681 - 0.418\ sqrt(w)$	0.129	<0.0001*

Geology and wave intensity

In order to understand the interplay between geologic and marine factors in shaping rocky coasts we performed a stepwise regression including all above independent variables. The best fit relationships are presented in Table 4 and Figure 4. As we use platform width as a proxy for wave intensity it is ignored as a morphometric parameter.

Table 4. Relationships between geologic and marine factors and shore platform morphology. Asterisks (*) indicate significant relationships (p-value < 0.05); α – platform gradient, z – platform elevation, tz – cliff toe elevation, r – platform roughness, w – platform width, Sc – rock hardness, Sc_v – viariation in rock hardness, j – joint density.

Relationship	Adj. R^2	p-value
$\alpha = (2.909 - 0.083\ sqrt(w) - 0.002\ Sc)^2$	0.323	<0.0001*
$z = 1.067 - 0.005\ Sc + 0.004\ Sc_v$	0.09	0.0002*
$tz = 5.776 - 0.01\ Sc + 0.02\ Sc_v$	0.029	0.032*
$r = 11.381 - 0.392\ sqrt(w) - 2.235\ j - 0.018\ Sc_v$	0.142	<0.0001*

Significant relationships exist for all morphologic variables. Platform gradient is moderately (R^2 = 0.323) correlated to platform width and rock hardness. The gradient is higher when platforms are narrower and rocks are harder. Rougher surfaces associate with narrower platforms, lower joint density and less variable rock hardness. Platform and cliff toe elevations do not correlate with platform width, but only with rock hardness.

DISCUSSION

Statistical analysis of morphologic conditions of the Staithes shore platform enabled us to find only weak relationships between coastal geometry, geology and wave intensity. We found the best fit regression for each morphometric variable resolving the role of lithology, structure and marine action in a local-scale coastal morphological setting.

Coastal erosion is likely to increase with wave intensity increase and rock resistance decrease (Sunamura, 1992). Rock resistance depends on both lithology and structure and is higher if a rock is stronger (unconfined compressive strength) and less discontinuous. At localities more intensively eroded platforms should be lower (mean and cliff toe) and flatter (e.g. Trenhaile, 1987). We also expect surface roughness to be larger where the wave action is lower (waves abrade the rocks), but also where rocks are less resistant, discontinuous and weathered.

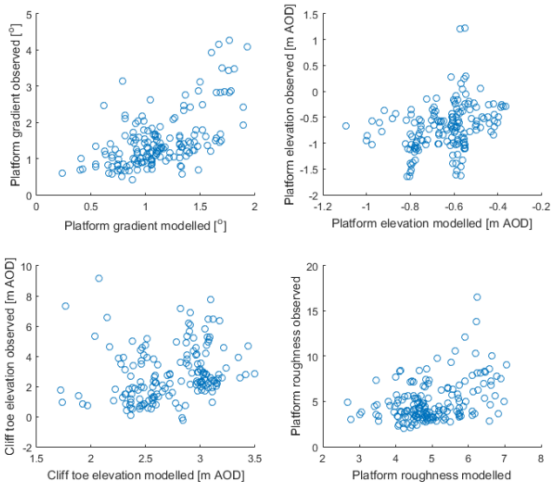


Figure 4. Relation between shore platform geometry modelled through best fit relationships with geology and platform width (x-axis) and observed (y-axis).

We observed that wider platforms are cut in weaker lithologies (lower Equotip readings and more variation within single rock beds), which supports the finding of Davies et al. (2006). Platform gradient is moderately correlated to wave intensity (positively) and rock resistance (negatively). On the contrary, Trenhaile (1980) demonstrated that more intensive waves generate flatter platforms. The reason for discrepancies may relate to the fact that steeper (and narrower) platforms are more intensively eroded by waves, as suggested here, in consequence leading to reduction of platform gradient (Trenhaile, 1980). Elevations of platform and cliff toe weakly correlate with rock hardness only. Higher platforms associate with weaker and more variable lithologies. This is contrary to previous assessments (e.g. Stephenson, 2000), which related harder rocks to higher platforms and cliff toes. Lack of expected relation may suggest little variation in rock hardness. An alternative explanation has been proposed by Gill (1972) who suggested that regardless of the elevation a platform occurs at, while it evolves, it is lowered to the low tidal level. Therefore, the more developed the platform, the less important rock type. The results support So's (1965) statement that platform elevation and gradient are independent from rock structure.

Surface roughness is the only morphological element which seems to be partly controlled by all lithology, structure and marine action. It increases with increase of wave action (narrower platform) and decrease in joint density and rock hardness variation. Positive correlation between roughness and wave intensity is counter-intuitive but can be explained in terms of wave action along the lithological boundaries, where intensive waves work on steps in the foreshore. Moreover, more wave action may coincide with more intensive cliff erosion and presence of debris (high surface roughness) on the upper part of the platform. Potentially, the role of abrasion on roughness could be observed in smaller (<0.1 m) scale. The negative relationship between surface roughness and joint density may suggest that strongly jointed rocks are structurally controlled and are prone to erosion along predefined planes while more massive rocks erode in more randomly distributed manner.

The study demonstrated that a re-thinking of numerical expression of rock resistance in coastal geomorphology

is necessary depending on the processes studied. Different rock properties (rock hardness, its variability, structure) control different parameters of shore platform. Moreover, the role of wave action suggests that significant changes in wave climate may have an impact on a long-term (millennial timescales) coastal evolution by controlling platform gradient and roughness.

The results show that relationships with geology and marine action are not strong enough to explain morphology of rocky coasts in terms of parameters easily-obtained in field and GIS. We suggest two possible explanations of the observed weak relationship. Firstly, included variables may not best represent rock resistance. Despite existing correlations between Equotip and Schmidt Hammer rebound values (Viles et al., 2011) and between the latter and unconfined compressive strength (Sunamura, 1992), other rock properties (such as tensile strength, shear strength, grain size, composition, abrasion resistance) may better represent rock resistance to wave action. Alternatively, weak dependence of coastal form on contemporary processes may suggest inherited nature of the coast (Masselink et al., 2011). Current erosion rates of hard-rock coasts are often too slow to account for formation of wide shore platforms in the last 6 kyr when sea has been at the level similar to todays (Trenhaile et al., 1999). Our statistical analysis demonstrated that the caution should be taken while defining controls on rocky coasts, as existing relationships do not fully explain coastal geometry, and key controls are yet to be found.

CONCLUSIONS

Our method of systematic statistical analysis of a stretch of coastline based on densely-spaced along shore (25 m) and resampled across shore (0.2 m) coastal cross-sections enabled us to find relationships between coastal form, geology (lithology and structure) and wave intensity:

1. More intensive waves and weaker rocks are associated with steeper shore platforms.
2. Higher platforms and cliff toes are associated with weaker and more variable rocks.
3. Surface roughness increases with increase of wave intensity, decrease of joint density and decrease of rock hardness variation.

Identified relationships are weak which suggests that key controls on coastal geometry are still poorly understood. Re-thinking of the numerical expression of rock resistance at different spatial and temporal scales and quantification of potential role of inheritance are crucial to understand geomorphic conditions of rocky coasts and to model their evolution.

ACKNOWLEDGEMENTS

The study is part of Coastal Behaviour and Rates of Activity (CoBRA) project supported by ICL Fertilizers UK Ltd.

LITERATURE CITED

Davies, P.; Sunamura, T.; Takeda, I.; Tsujimoto, H., and Williams, A.T., 2006. Controls of shore platform width: the role of rock resistance factors at selected sites in Japan and Wales, UK. Journal of Coastal Research, Special Issue No. 39, 160-164.

Gill, E.D., 1972. The relationship of present shore platforms to past sea levels. Boreas 1, 1-25.

Kennedy, D.M. and Dickson, M.E., 2006. Lithological control on the elevation of shore platforms in a microtidal setting. Earth Surface Processes and Landforms 31, 1575-1584.

Lim, M., 2006. Coastal cliff evolution with reference to Staithes, North Yorkshire. Durham, UK: Durham University, Ph.D. thesis, 378p.

Masselink, G.; Hughes, M., and Knight, J., 2011. Introduction to coastal processes and geomorphology. London: Hodder Education, 416p.

Naylor, L.A. and Stephenson, W.J., 2010. On the role of discontinuities in mediating shore platform erosion. Geomorphology 114, 89-100.

So, C.L., 1965. Coastal platforms of the Isle of Thanet, Kent. Transactions of the Institute of British Geographers, 147-156.

Stephenson, W.J., 2000. Shore platforms: a neglected coastal feature? Progress in Physical Geography 24, 311-327.

Sunamura, T., 1992. Geomorphology of rocky coasts. Chichester: Wiley, 302p.

Trenhaile, A.S., 1987. The geomorphology of rock coasts. Oxford: Clarendon Press, 384p.

Trenhaile, A.S., 1980. Shore platforms: a neglected coastal feature. Progress in Physical Geography 4, 1-23.

Trenhaile, A.S., 1978. The shore platforms of Gaspe, Quebec. Annals of the Association of American Geographers 68, 95-114.

Trenhaile, A.S.; Pérez Alberti, A.; Martínez Cortizas, A.; Costa Casais, M., and Blanco Chao, R., 1999. Rock coast inheritance: an example from Galicia, northwestern Spain. Earth Surface Processes and Landforms 24, 605-621.

Viles, H.; Goudie, A.; Grab, S., and Lalley, J., 2011. The use of the Schmidt Hammer and Equotip for rock hardness assessment in geomorphology and heritage science: a comparative analysis. Earth Surface Processes and Landforms 36, 320-333.

This page is intentionally left blank

Appendix 2: Understanding of erosion

In this study, shore platform (or foreshore) erosion is understood as the removal of *in situ* bedrock, which importantly does not include the removal of lose sediments such as sand, gravel and boulders. Only at the macro-scale (detachment size > 0.25×0.25×0.05 m) is boulder movement analysed, but in this instance it is treated separately from the bedrock erosion (Chapter 7).

Erosion is considered at two scales: at the small-scale pixel, with a resolution of 0.001 m, and a minimum detectable volume V_{min} = 6.00×10^{-9} m^3, with detachment volumes spanning across five orders of magnitude (10^{-9} – 10^{-5} m^3); and second, at the macro-scale, with a pixel resolution of 0.25 m, V_{min} = 3.13×10^{-3} m^3 and detachment volumes in the order of 10^{-3} to 10^{0} m^3.

At the small-scale, erosion rates (mm yr^{-1}) are quantified as:

$$\frac{1{,}000 \times Vol}{(\frac{AOI}{t})} \quad \text{Eq 1}$$

where *Vol* (m^3) is the total detached volume, area of interest - *AOI* (m^2) is the total analysed area and *t* (yr) is time. *AOI* represents either the cumulative surface area of all monitoring sites (15×0.25 m^2) or the single site area (0.25 m^2) depending on whether the average foreshore erosion rates or their spatial variability are analysed; *t* = 1.01 yr for the whole monitoring period, or is considered equal to the time periods between pairs of consecutive surveys where the temporal analysis of erosion rates is undertaken (Chapters 4-5).

At the macro-scale, erosion rates are calculated in two ways: on the basis of detachment inventory, and, on the basis of grid cell inventory.

In the first case erosion rates (mm yr^{-1}) are calculated as:

$$\frac{1{,}000 \times Vol}{(\frac{Platform\ area}{t})} \quad \text{Eq 2}$$

where *Vol* (m^3) is the total detached volume, *Platform area* = 3.15×10^{6} m^2 is the total surface area of the studied North Yorkshire foreshore and *t* = 2.62 yr is the total monitoring time. When temporal variability of erosion rates is analysed, *t* is represented by the time periods between pairs of consecutive surveys.

When the foreshore is divided into 1 m^2 grid cells, erosion rates are calculated separately for the sub-populations of cells with and without steps, and are expressed as:

$$\frac{1{,}000 \times Vol}{\left(\frac{6.25 \times 10^{-2} \times Pixels}{t}\right)} \quad \text{Eq 3}$$

where *Vol* (m^3) is the total detached volume, *Pixels* = [1:16] is the number of pixels at original resolution of DEMs (0.25 m) that contain data, 6.25×10^{-2} m^2 is the pixel size, t = 2.62 yr is the total monitoring time. When temporal variability of erosion rates is analysed, t is represented by the time periods between pairs of consecutive surveys.

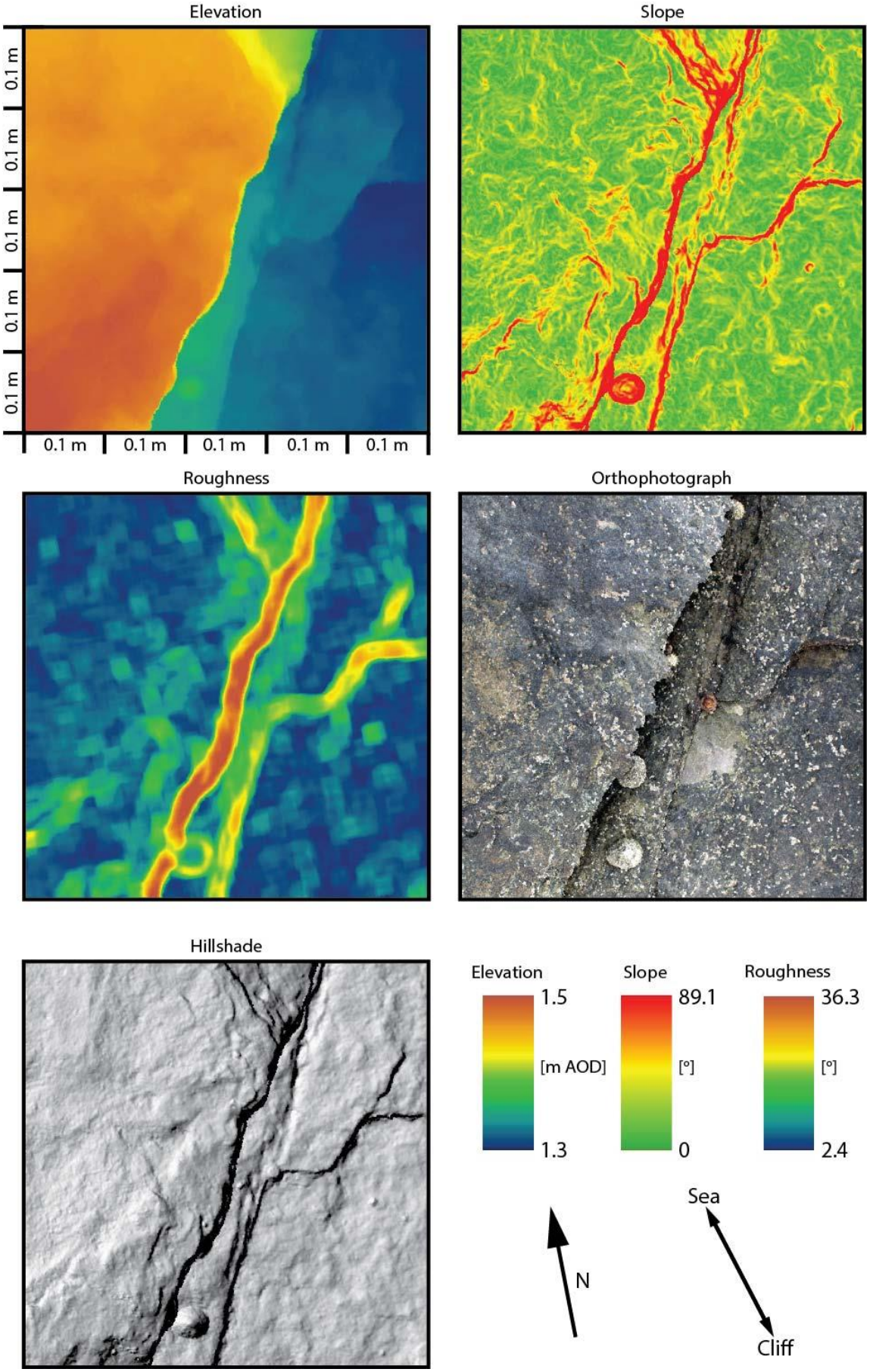
Total foreshore erosion (mm yr^{-1}), is calculated as weighted erosion from the stepped and non-stepped cells:

$$\frac{A_{down} \times Ero_{down} + A_{step} Ero_{step}}{A_{down} + A_{step}} \quad \text{Eq 4}$$

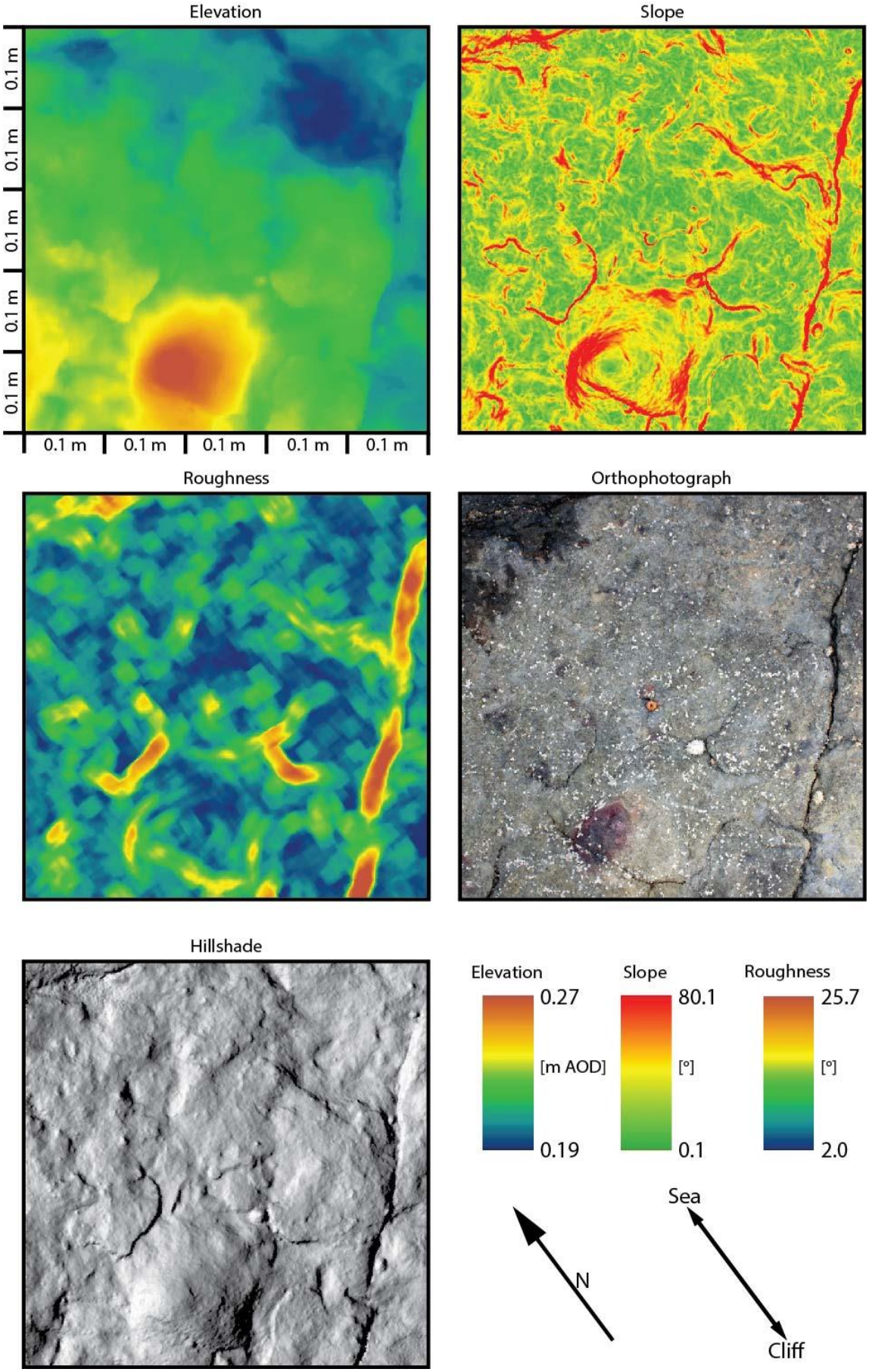
where A_{down} (%) is the contribution of the non-stepped cells to the total number of cells, A_{step} (%) is the contribution of the stepped cells to the total number of cells, and Ero_{down} and Ero_{step} (mm yr^{-1}) represent erosion rates calculated for the respective cell groups.

Appendix 3: Topographic characteristics of the small-scale monitoring sites at 0.001 m resolution obtained with the SfM in Apr'16.

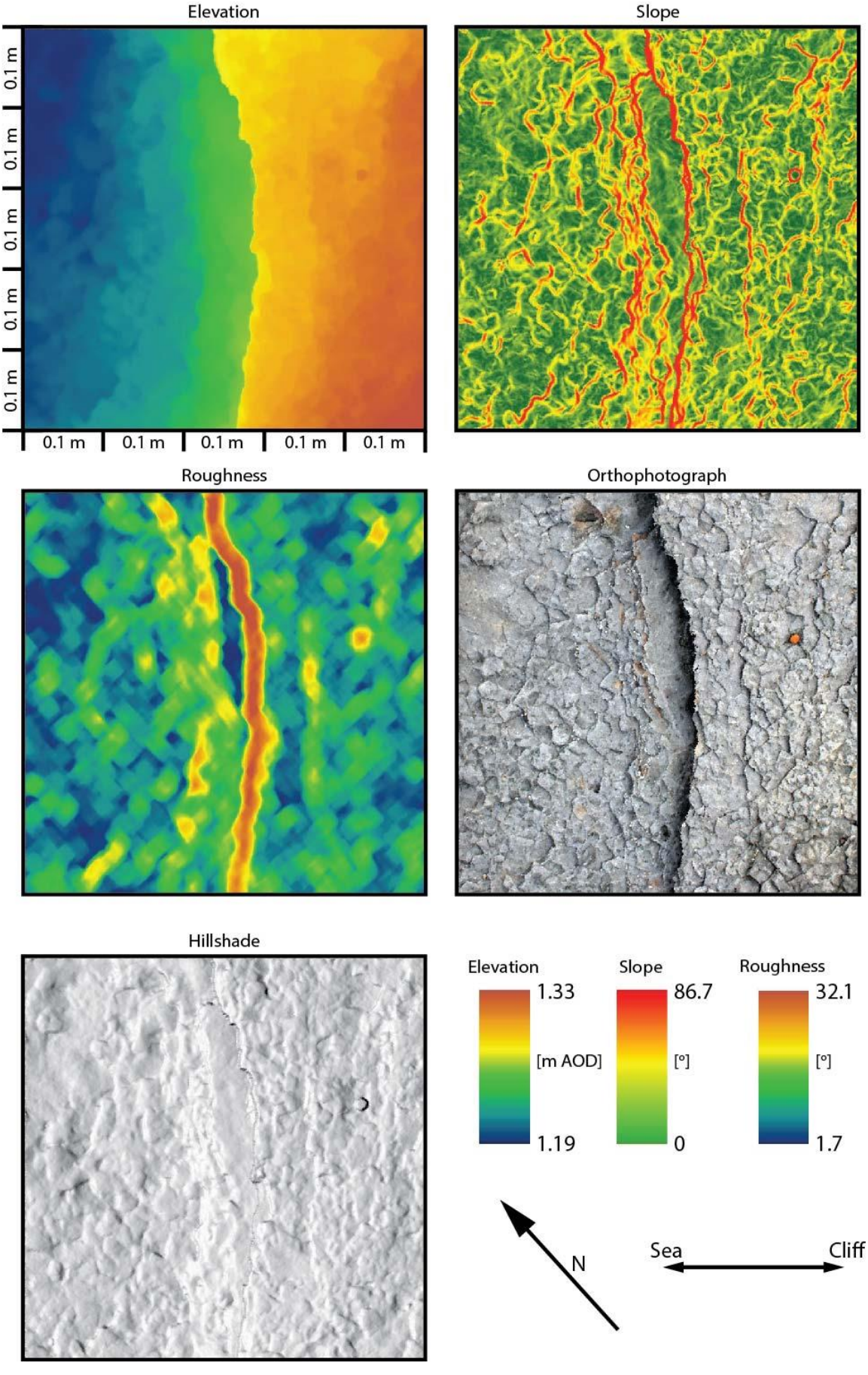
Site 1: Topographic characteristics (Apr16)



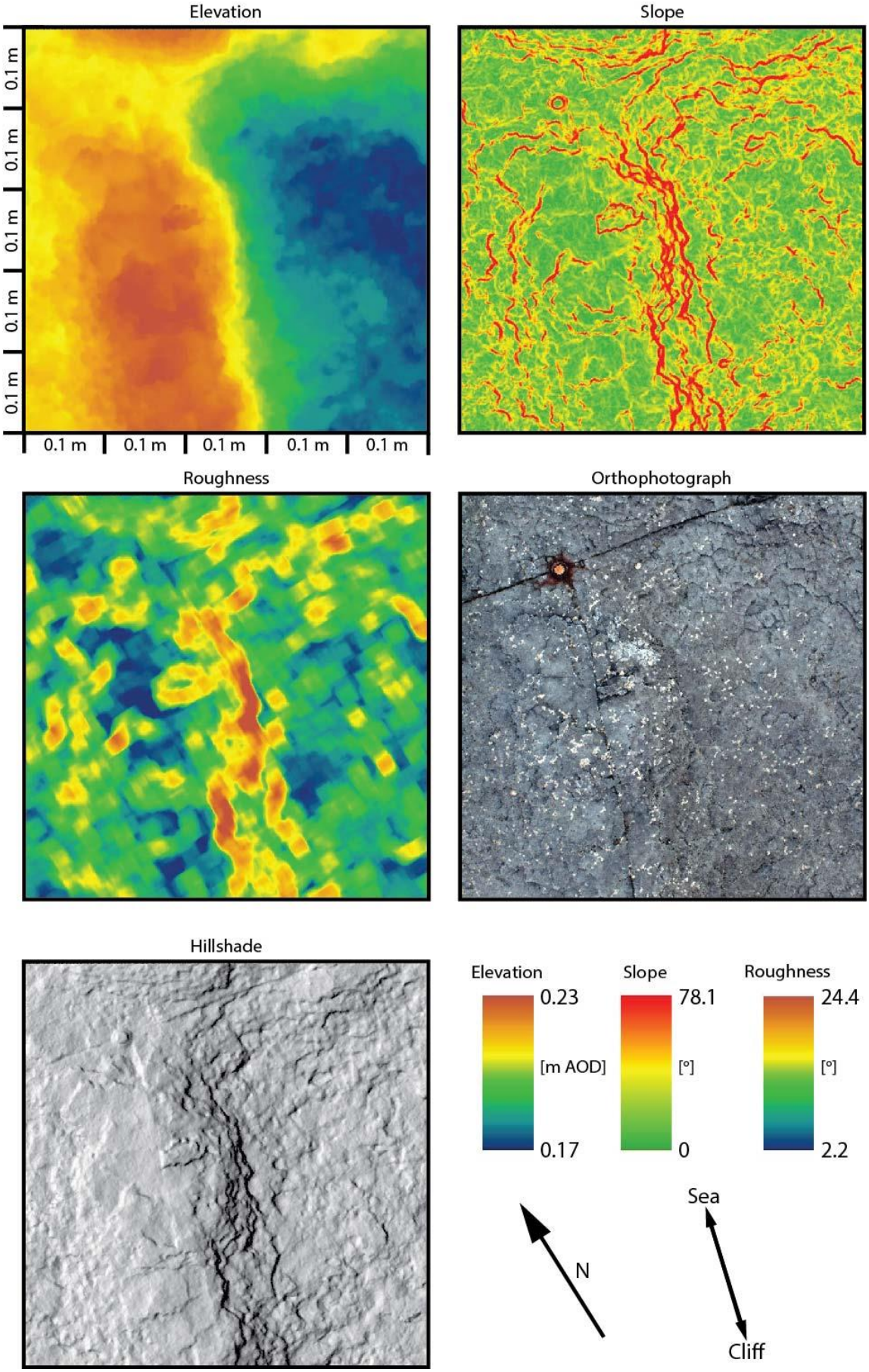
Site 2: Topographic characteristics (Apr16)



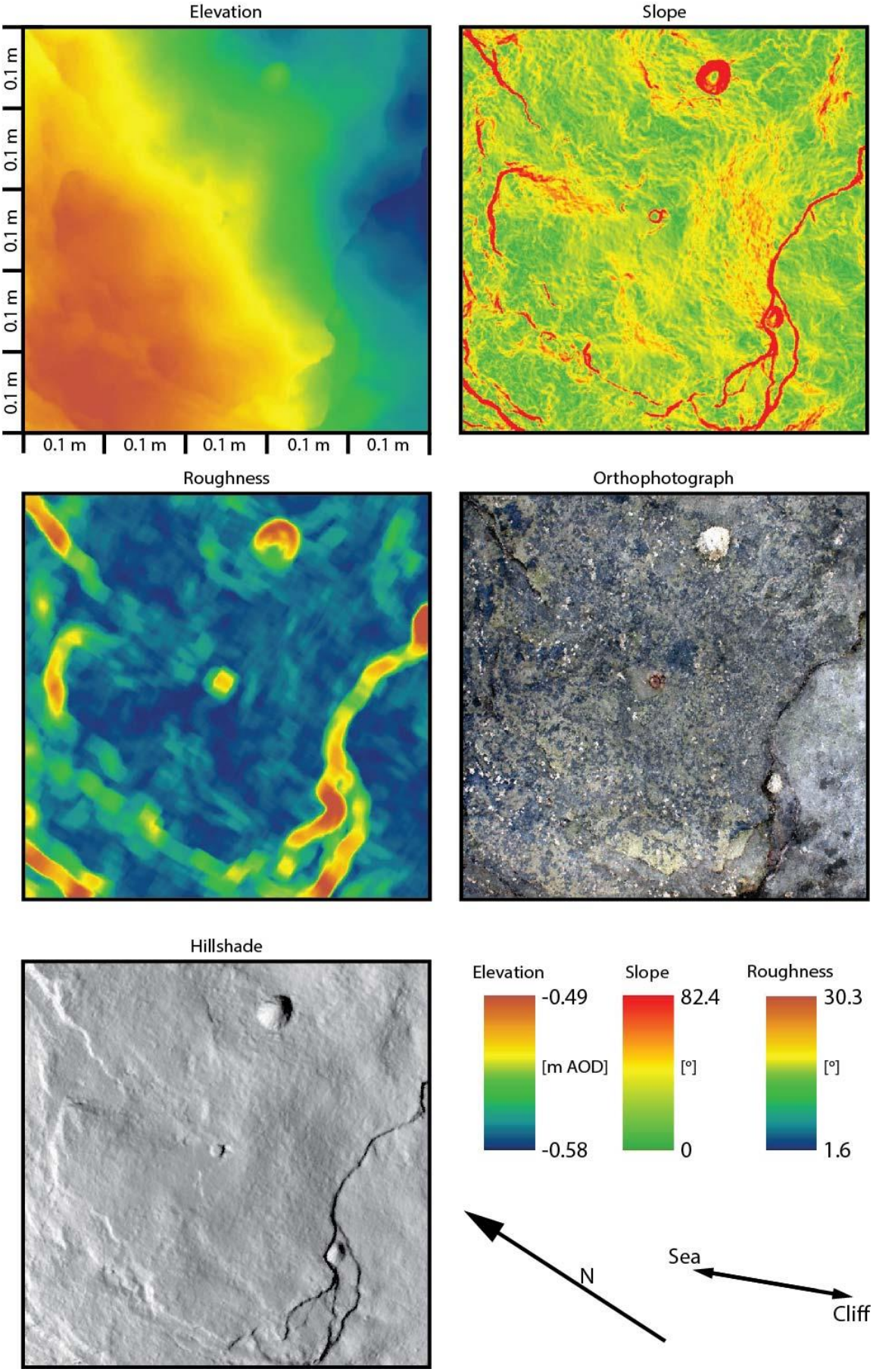
Site 3: Topographic characteristics (Apr16)



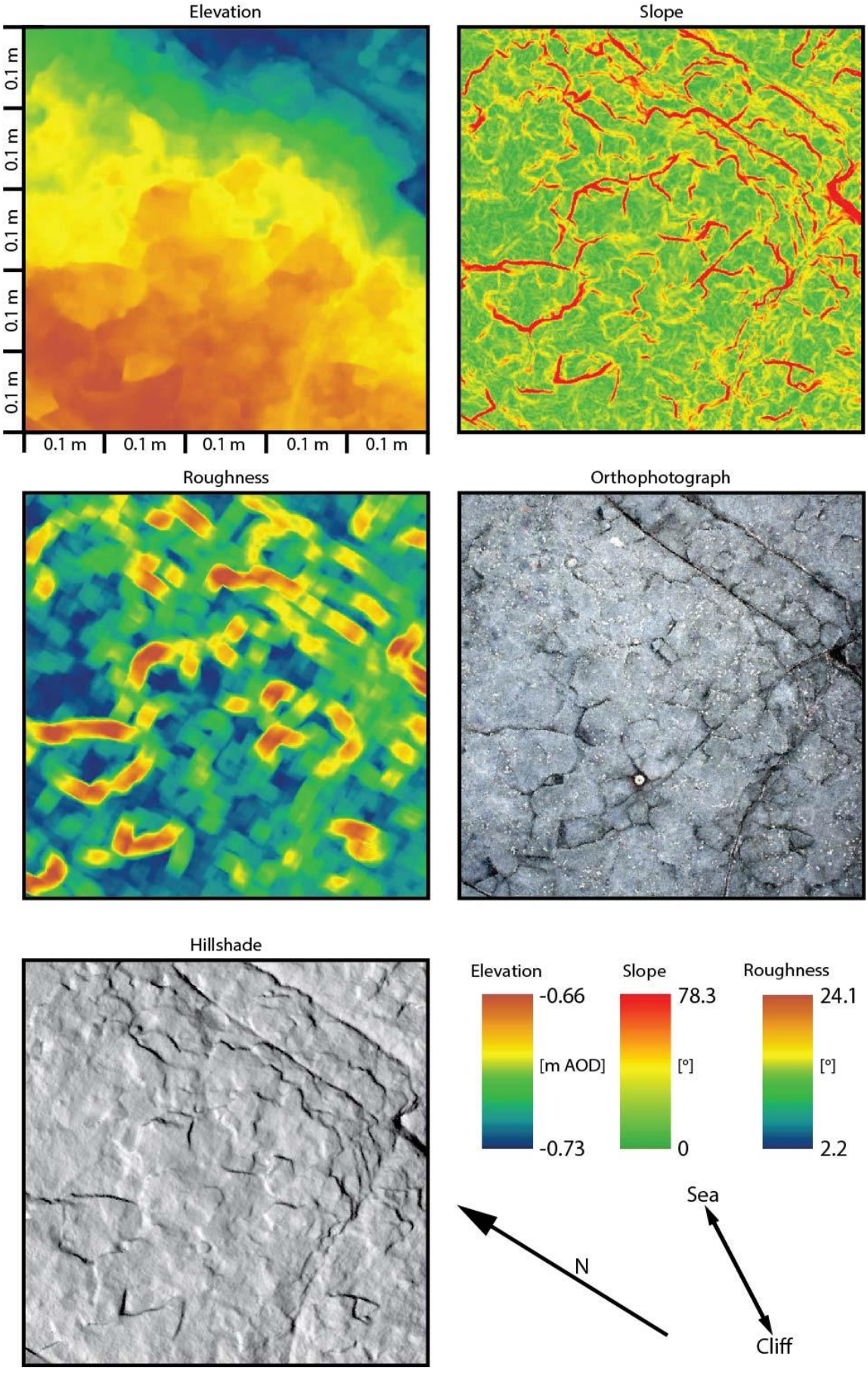
Site 4: Topographic characteristics (Apr16)



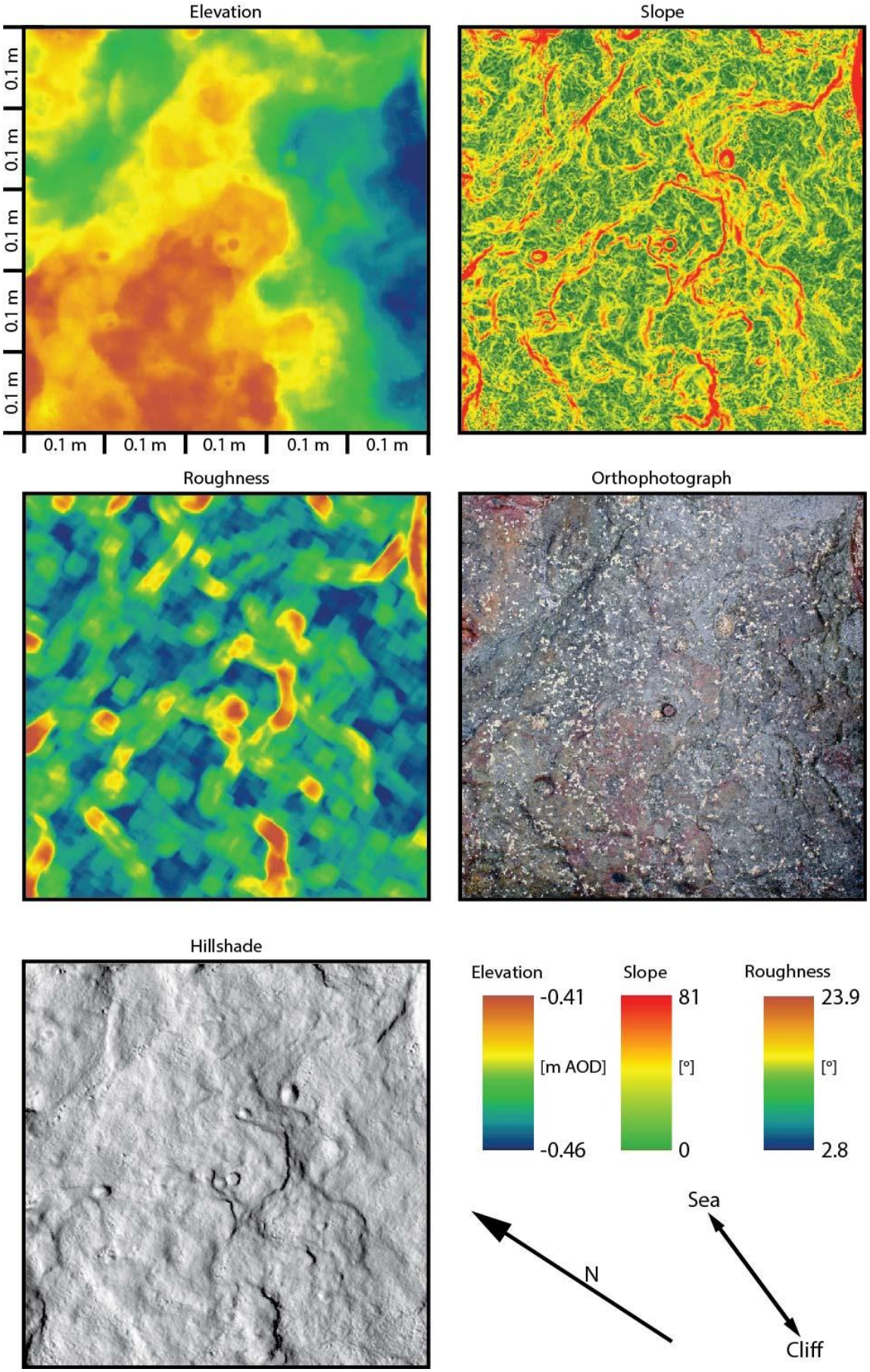
Site 5: Topographic characteristics (Apr16)



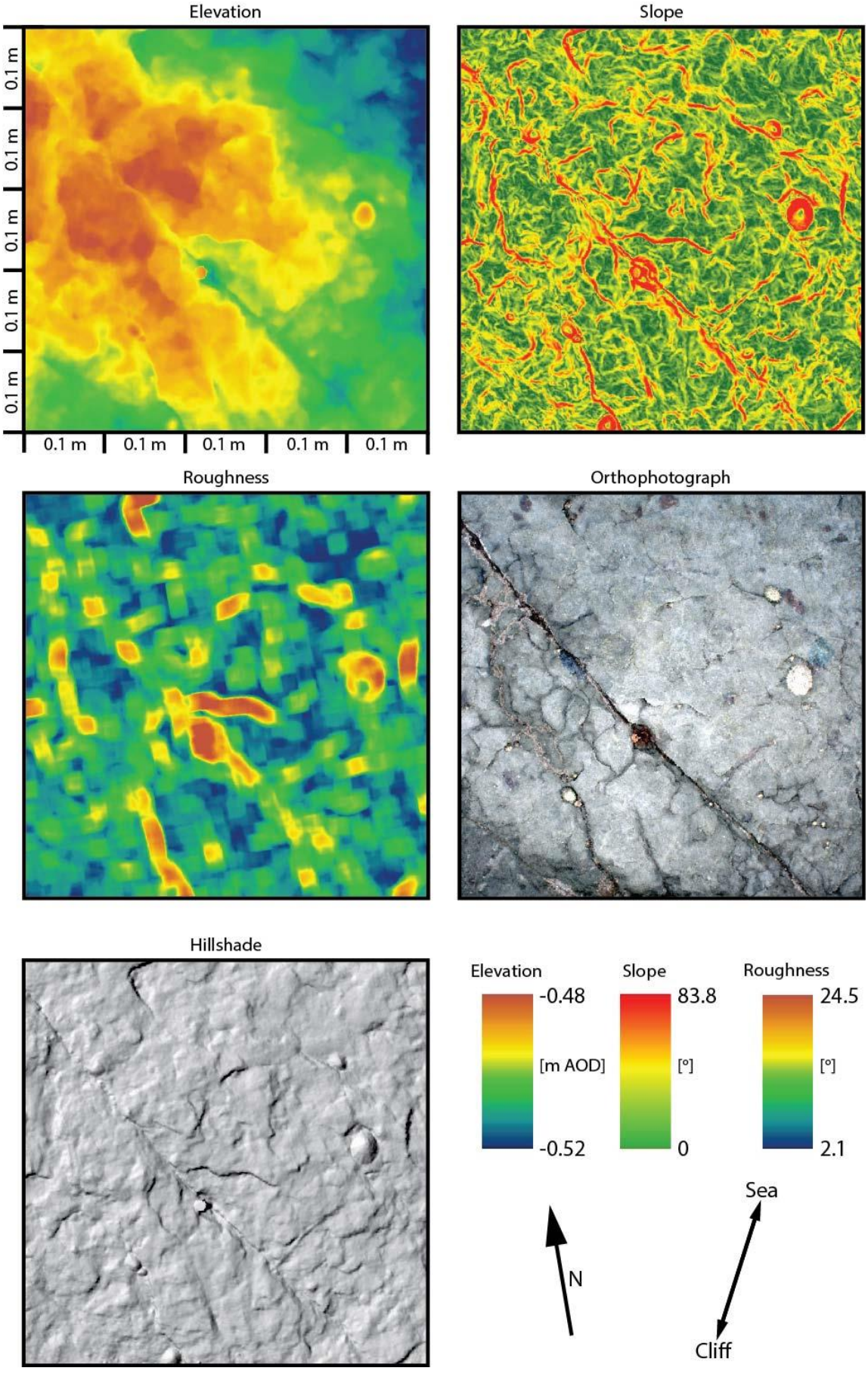
Site 6: Topographic characteristics (Apr16)



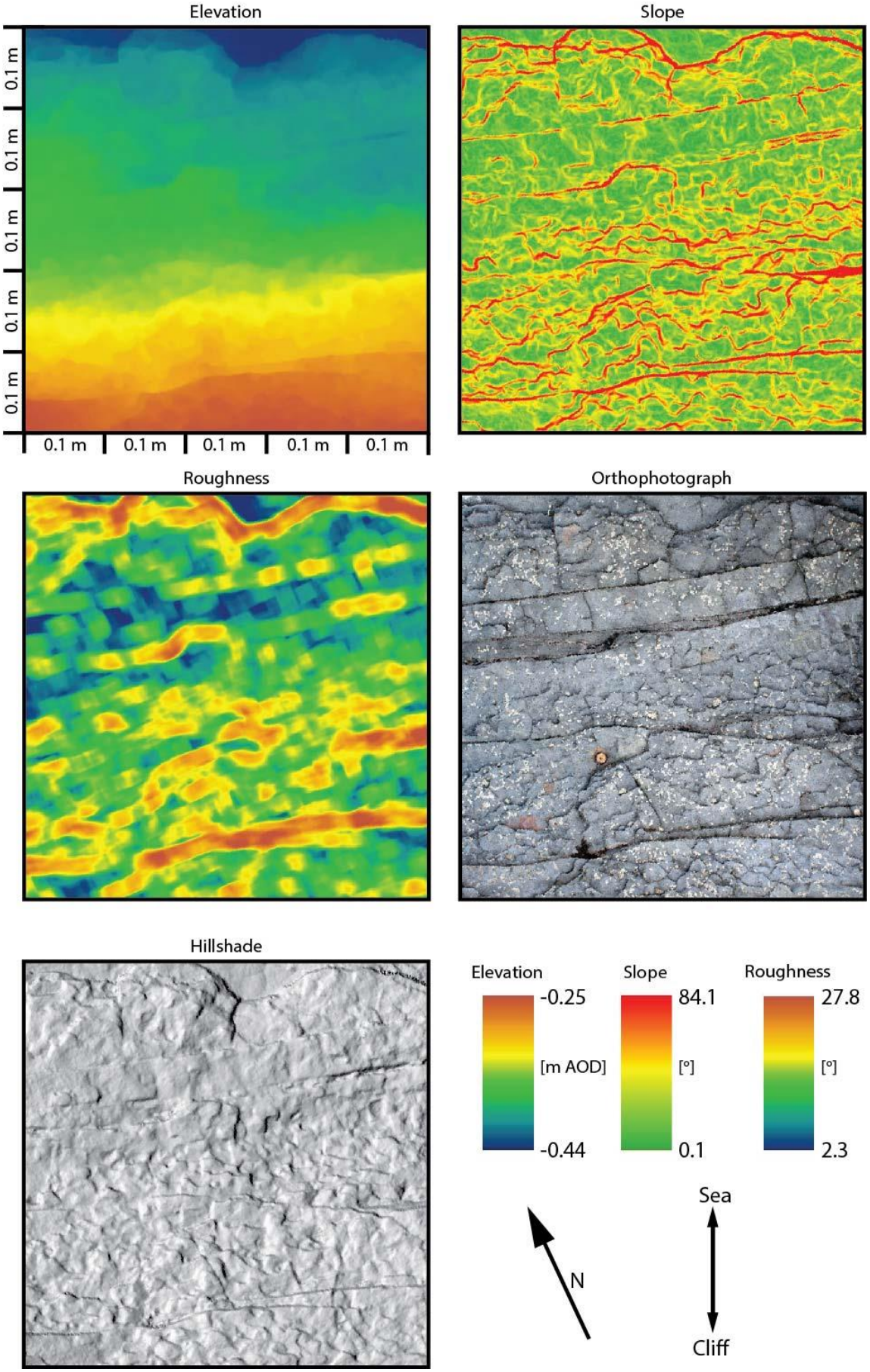
Site 7: Topographic characteristics (Apr16)



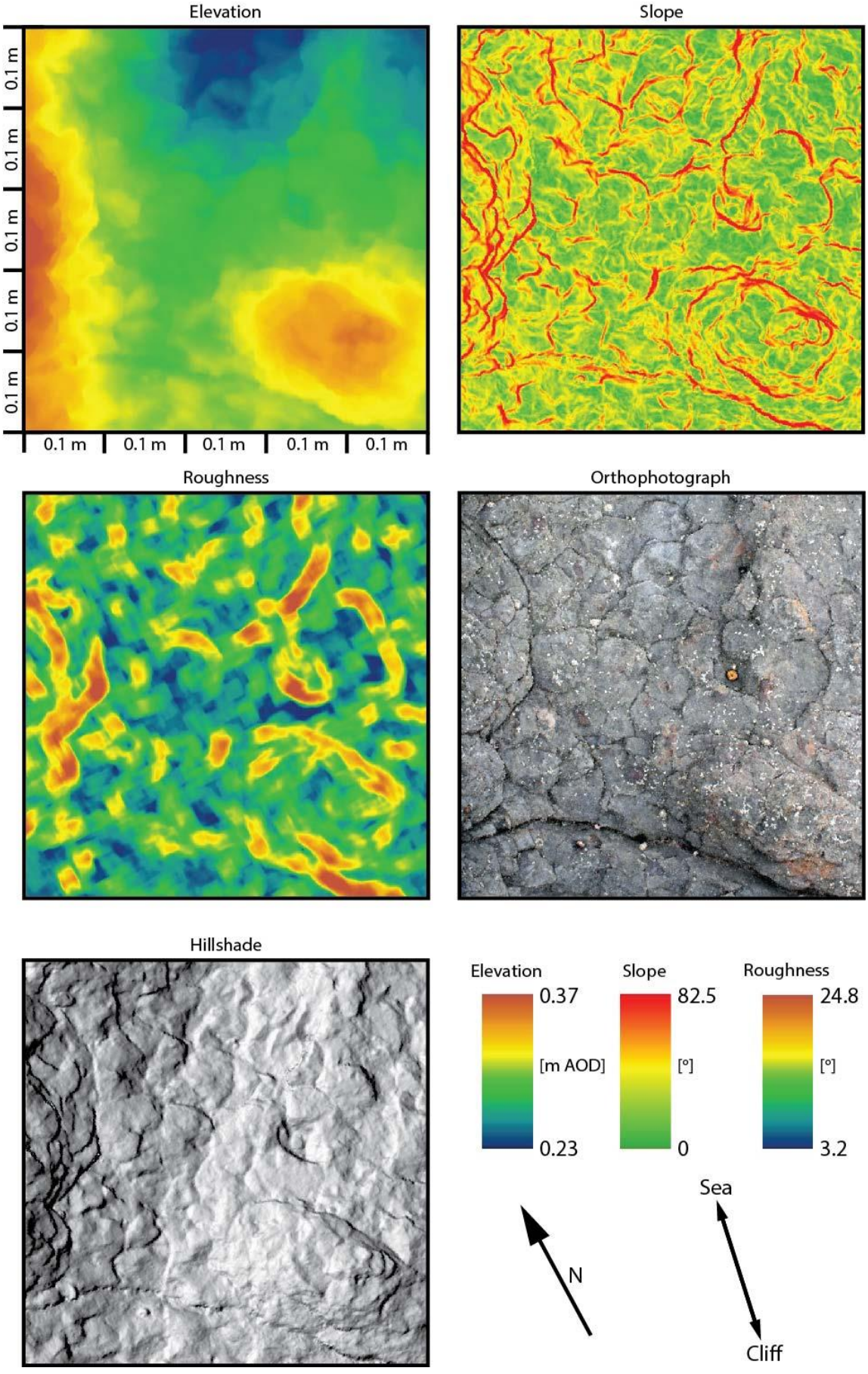
Site 8: Topographic characteristics (Apr16)



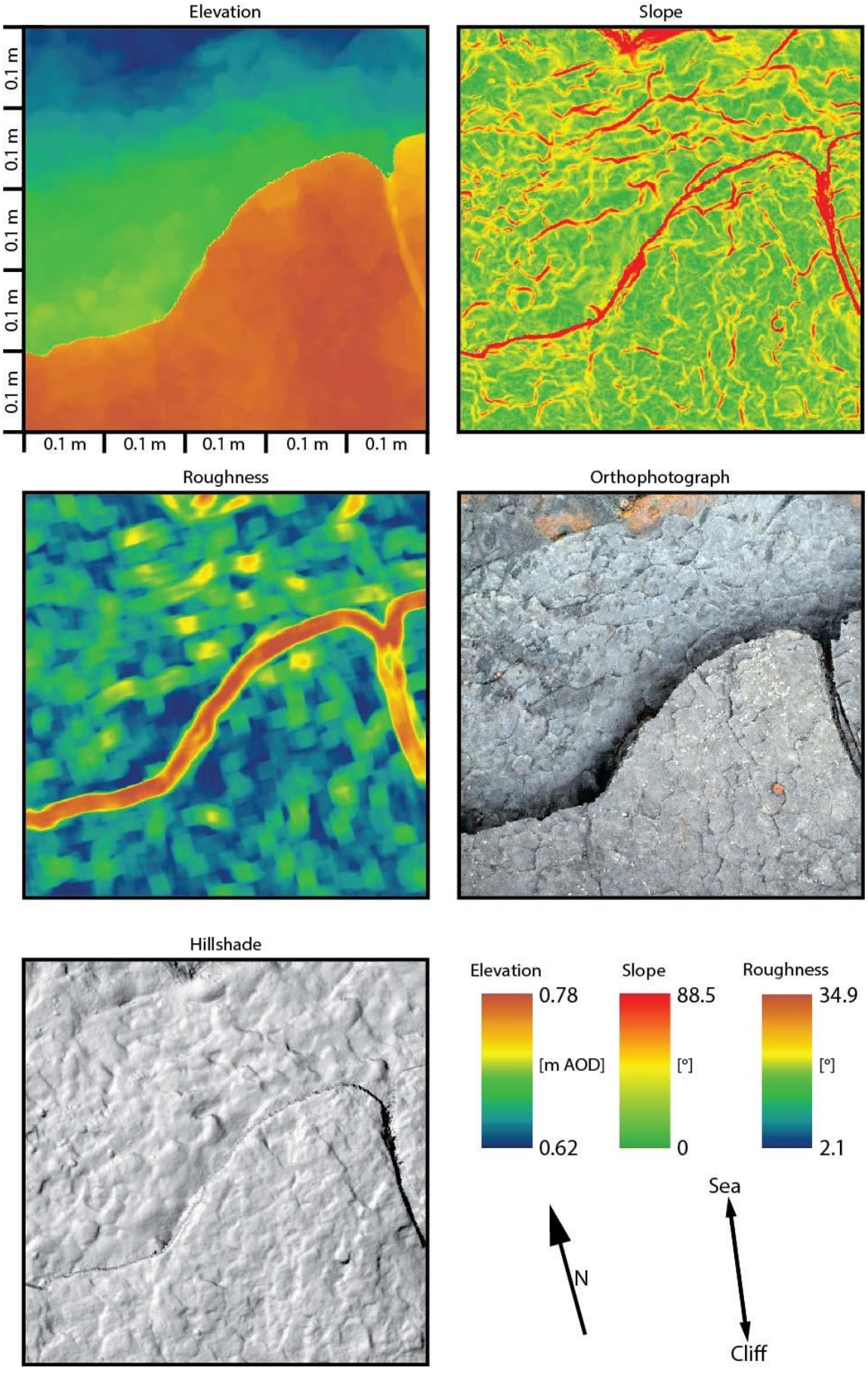
Site 9: Topographic characteristics (Apr16)



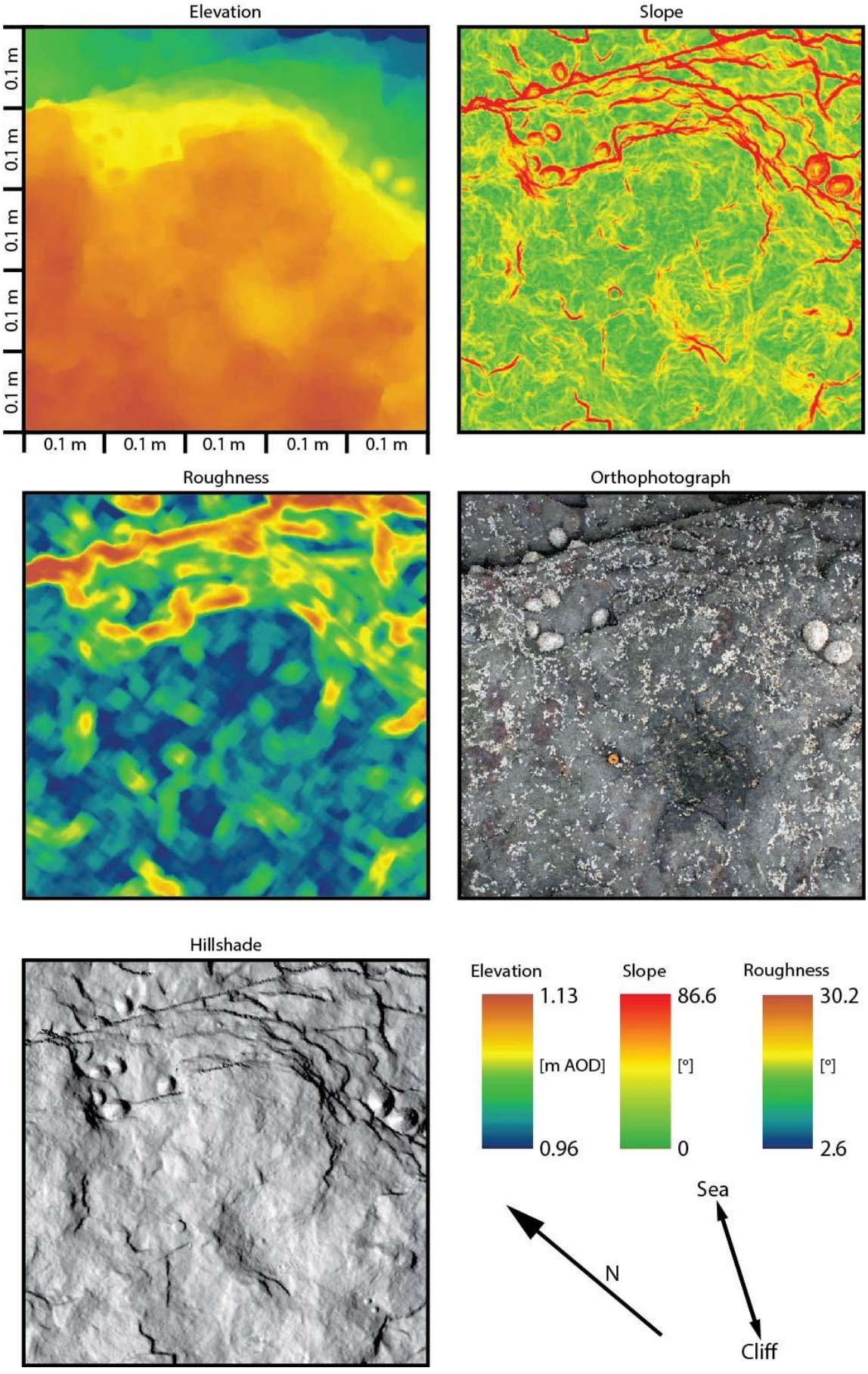
Site 10: Topographic characteristics (Apr16)



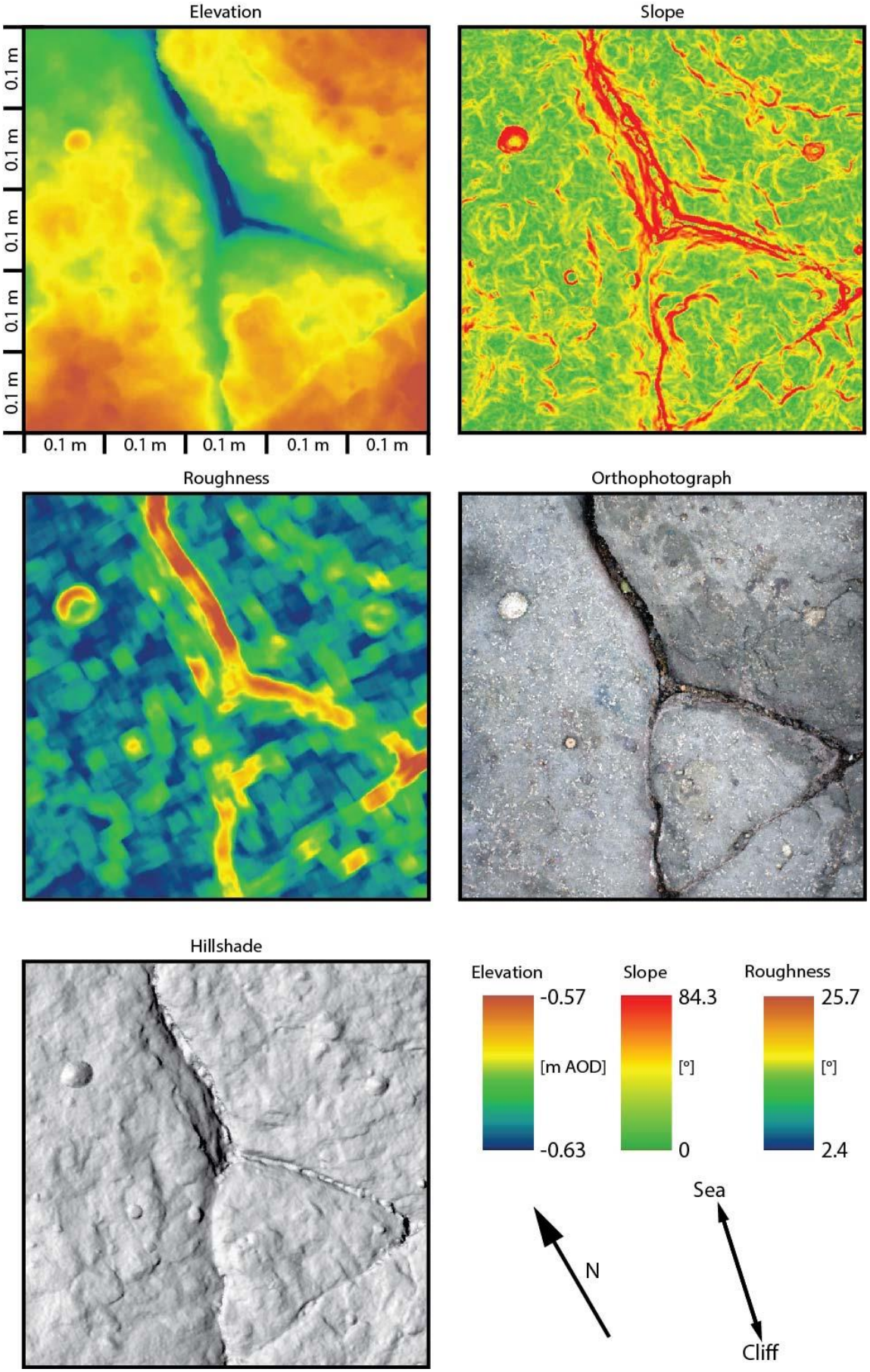
Site 11: Topographic characteristics (Apr16)



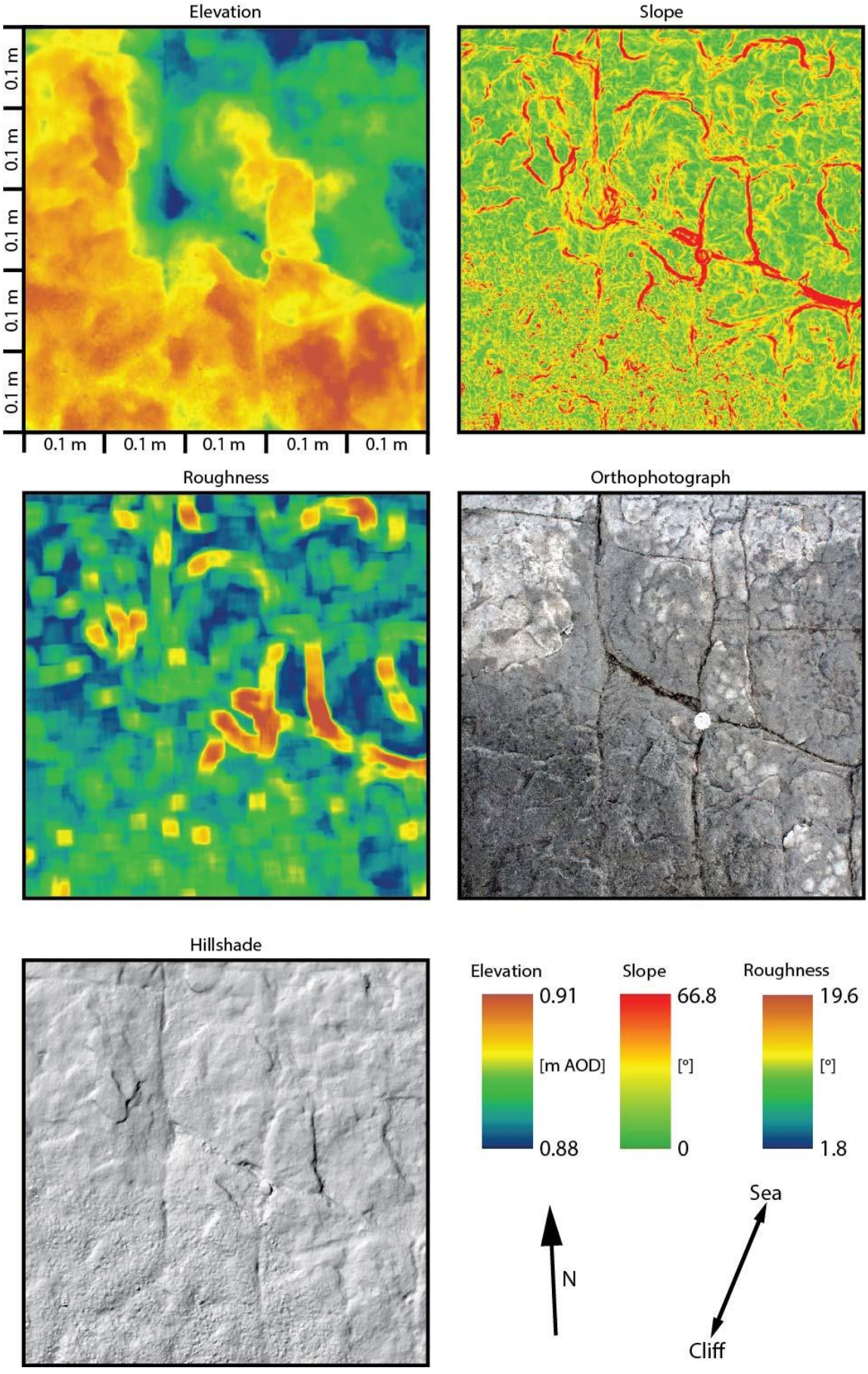
Site 12: Topographic characteristics (Apr16)



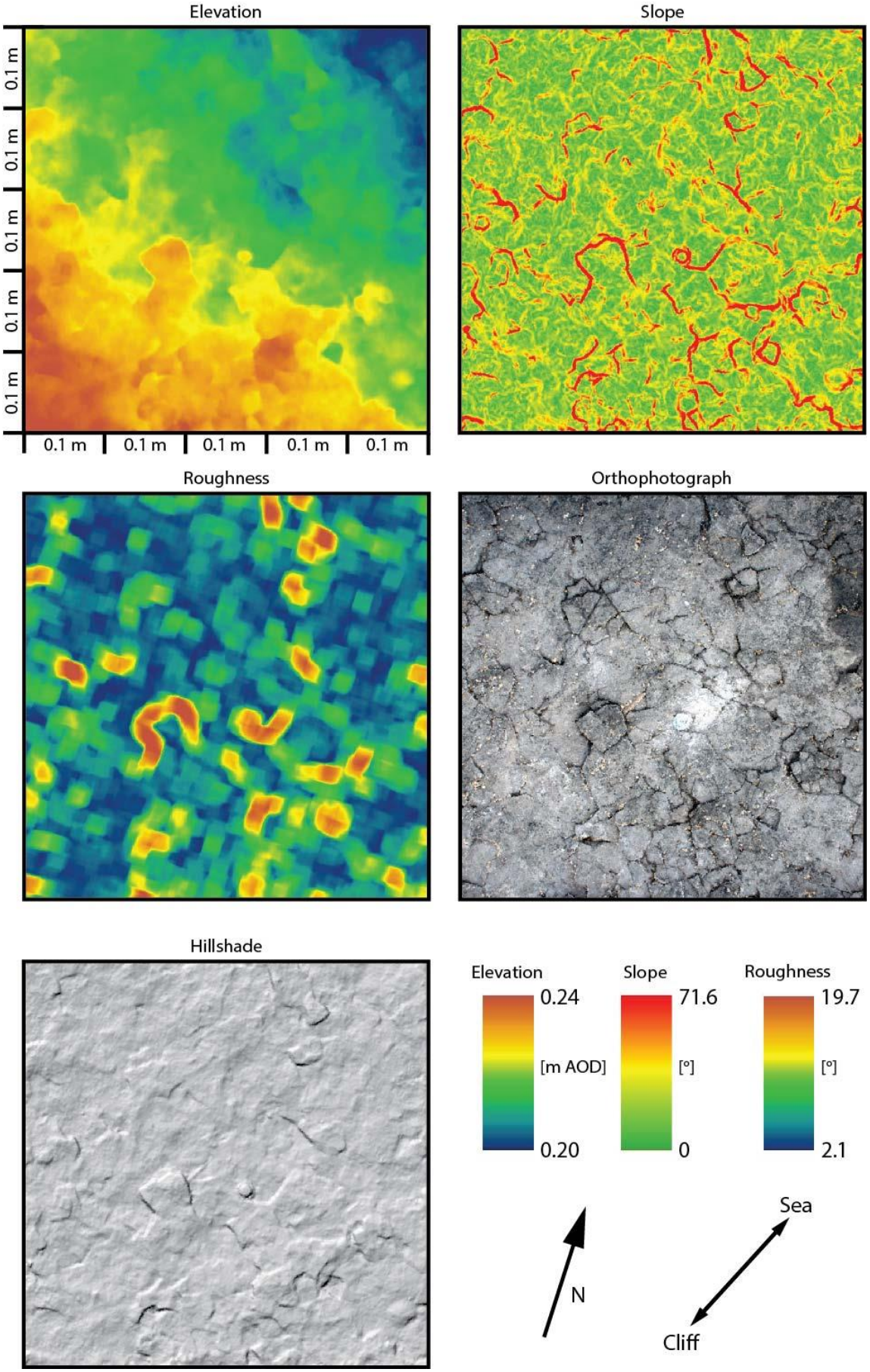
Site 13: Topographic characteristics (Apr16)



Site 14: Topographic characteristics (Apr16)



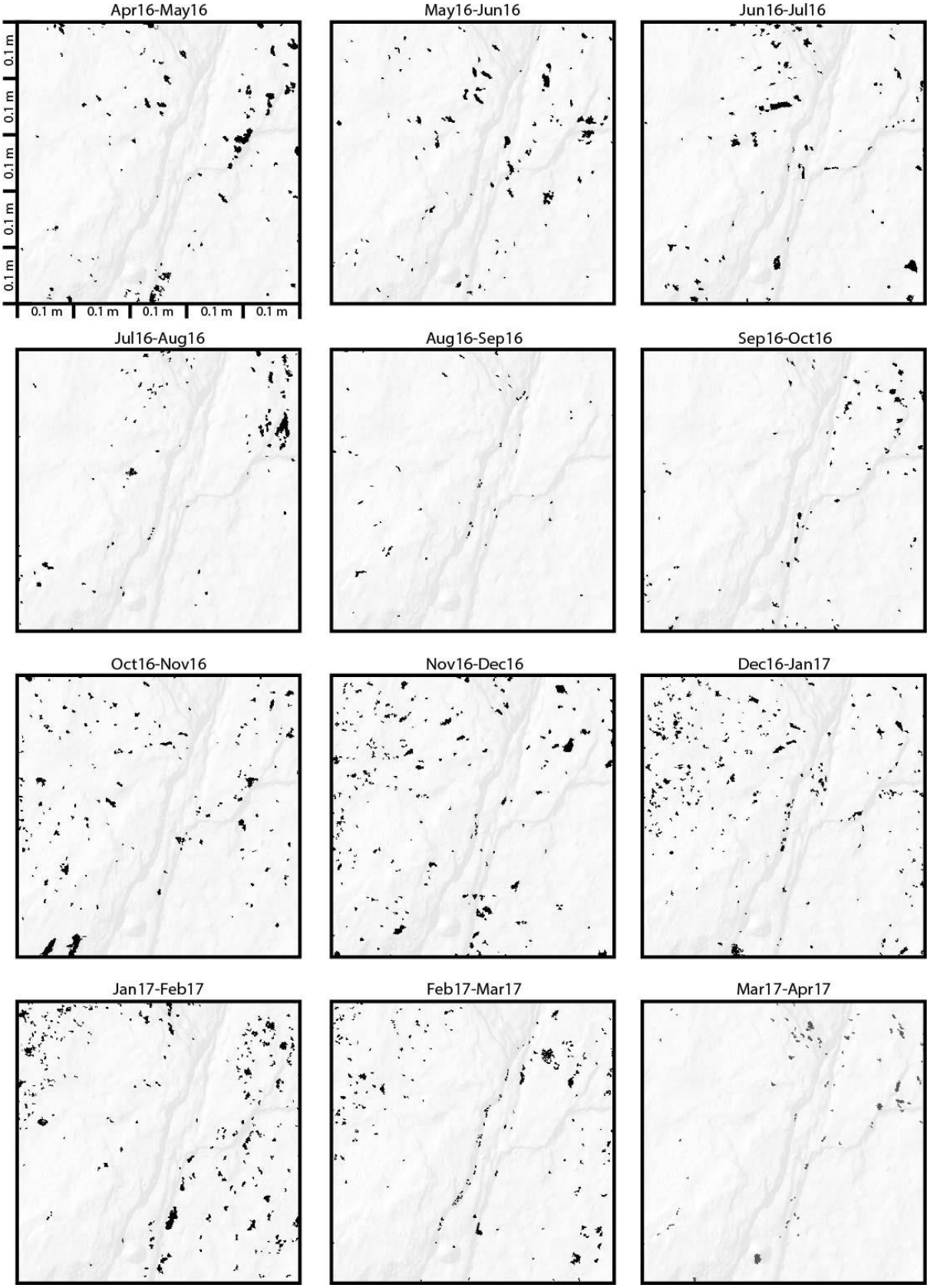
Site 15: Topographic characteristics (Apr16)



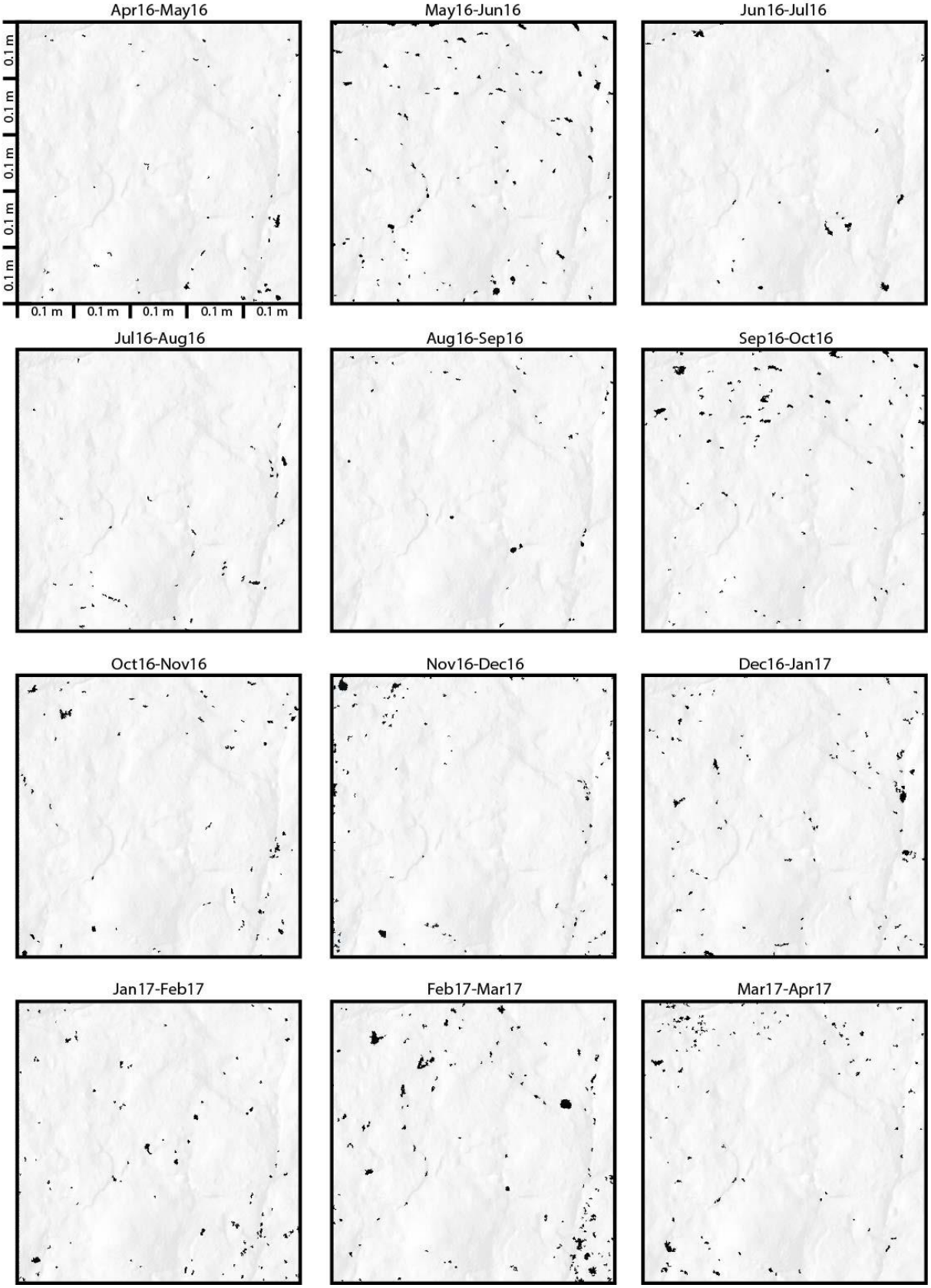
Appendix 4: Monthly distribution of erosion at each micro-erosion monitoring site.

Black polygons within each monitoring plot represent detachments. The background is hillshade at 90% transparency created from the Apr'16 DEM.

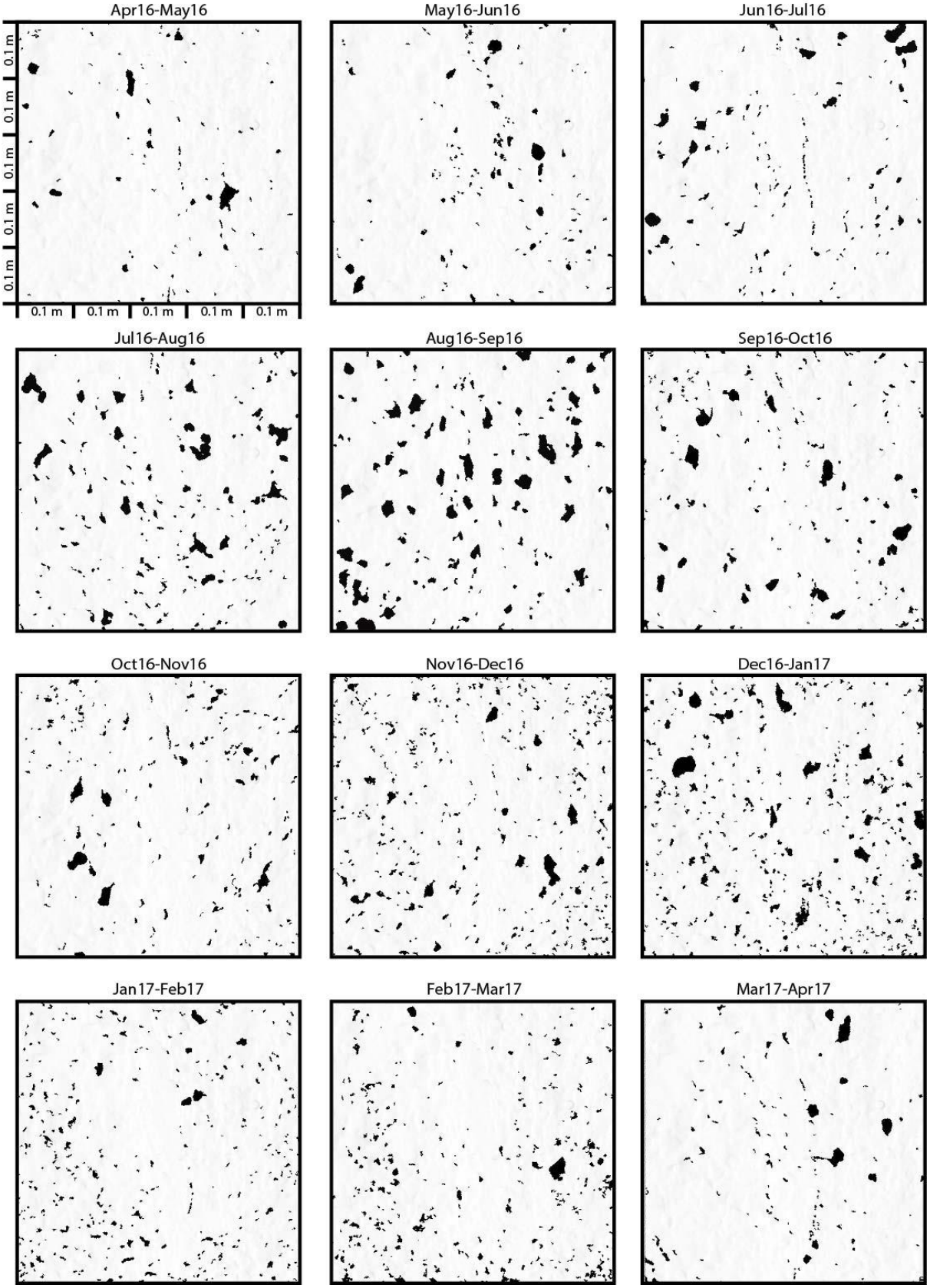
Site 1: Monthly distribution of erosion



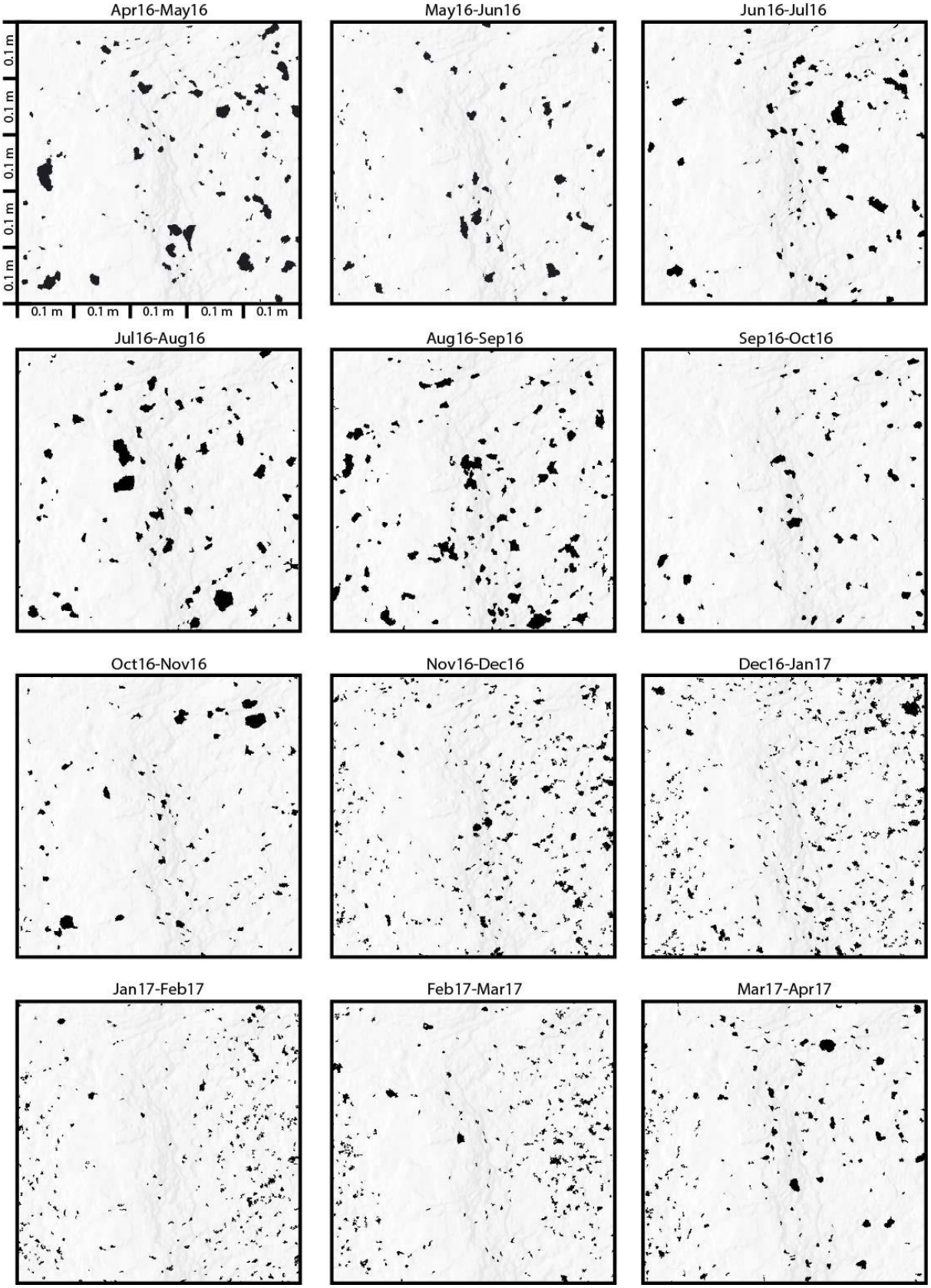
Site 2: Monthly distribution of erosion



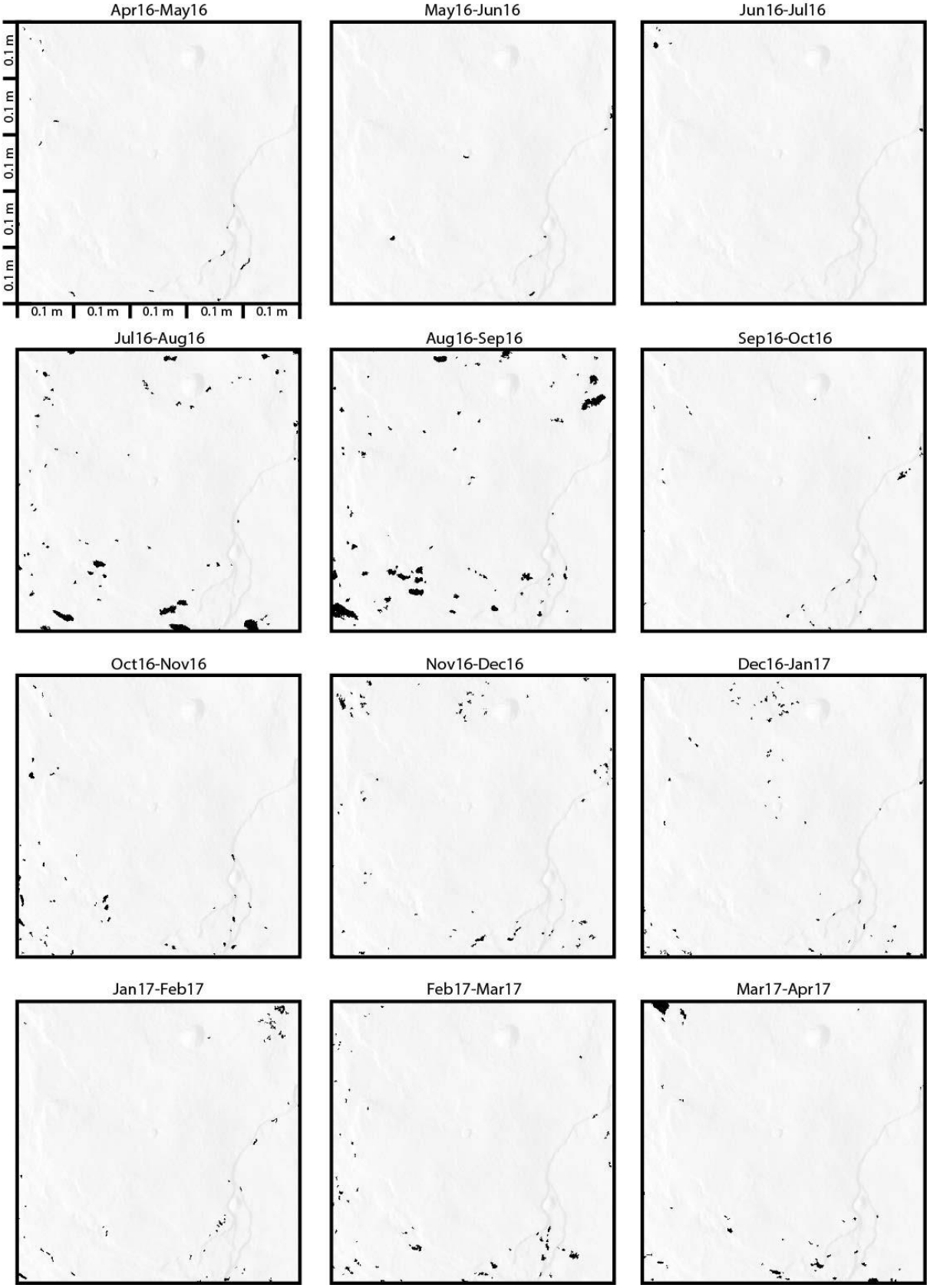
Site 3: Monthly distribution of erosion



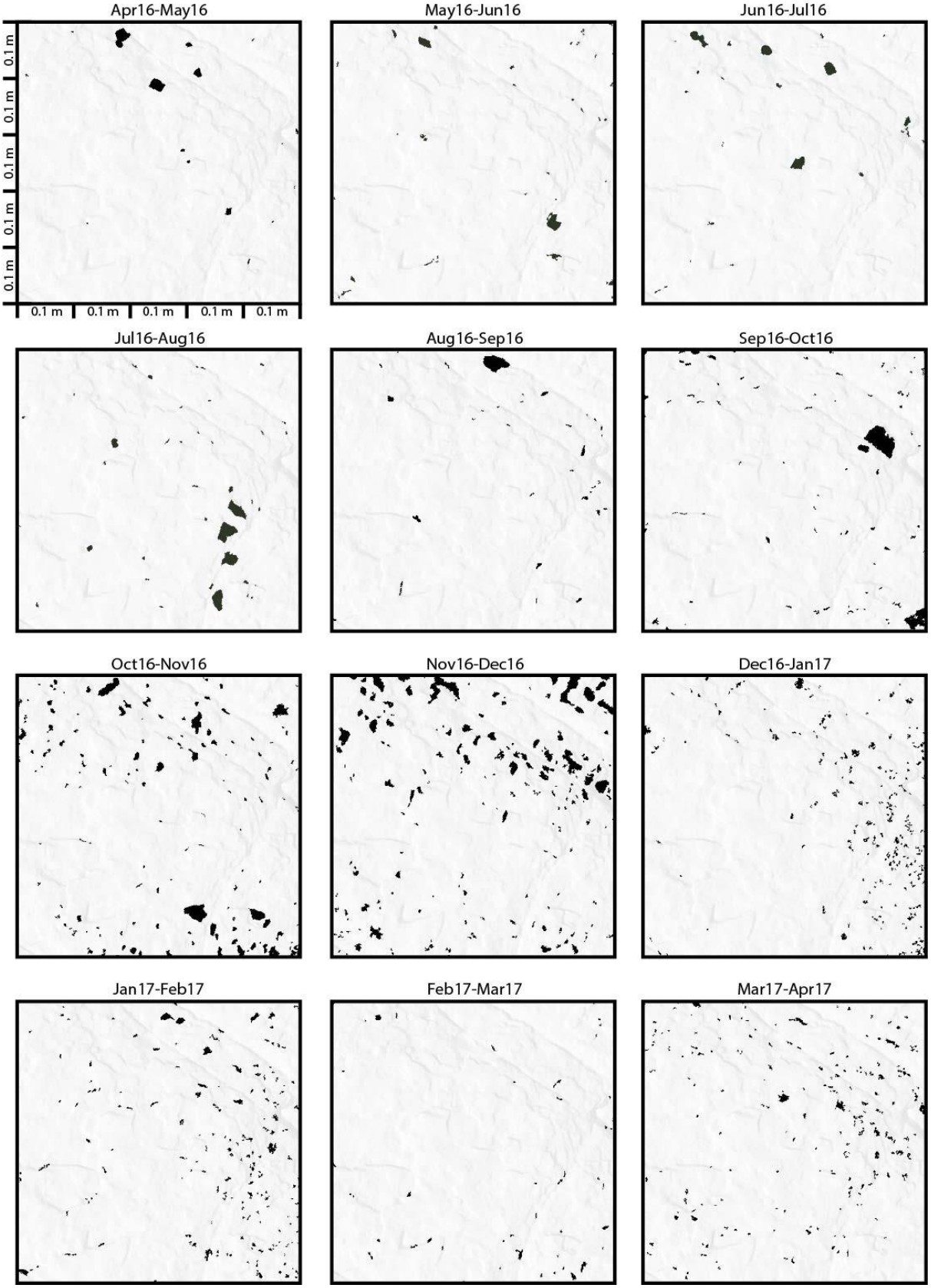
Site 4: Monthly distribution of erosion



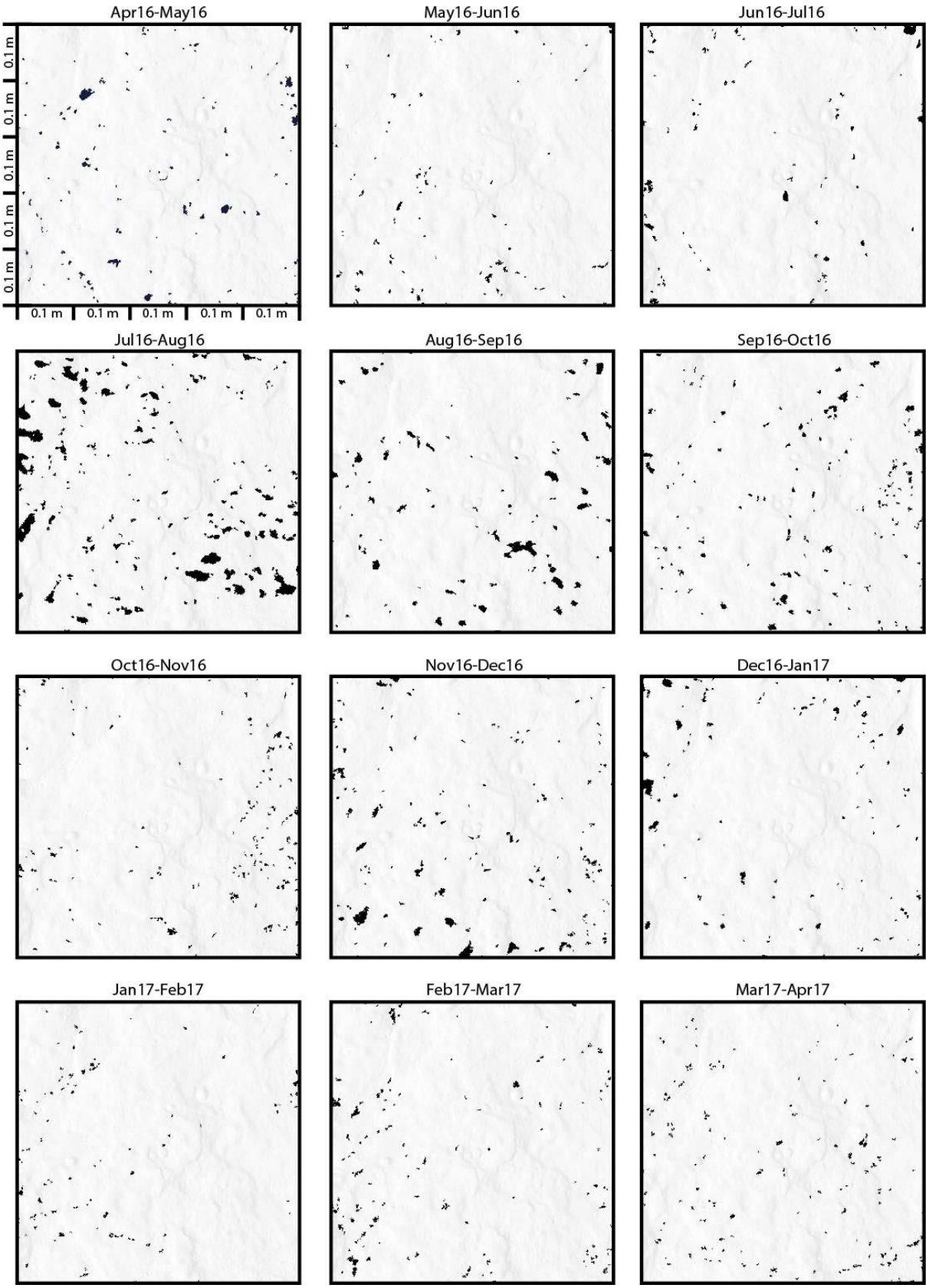
Site 5: Monthly distribution of erosion



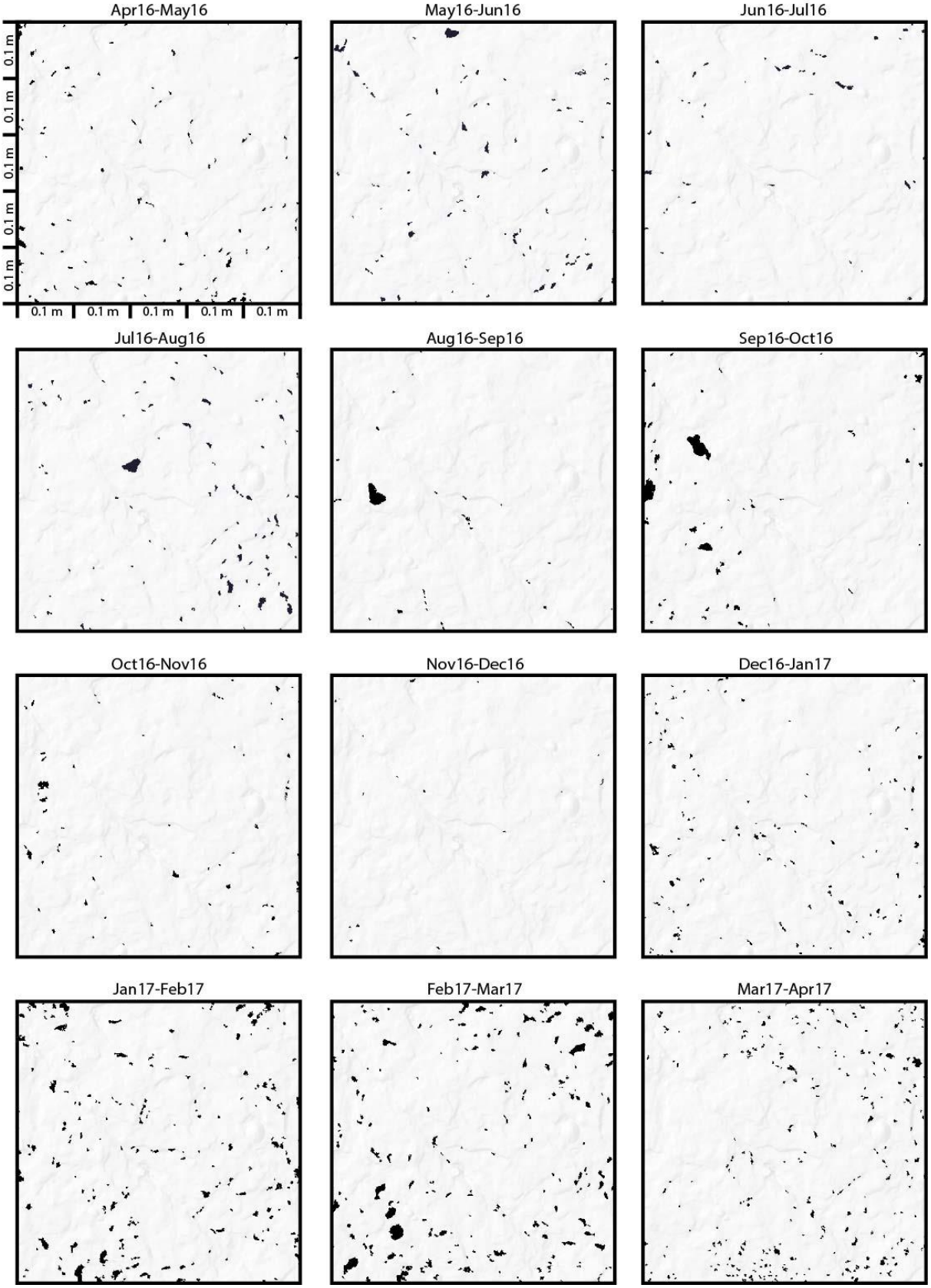
Site 6: Monthly distribution of erosion



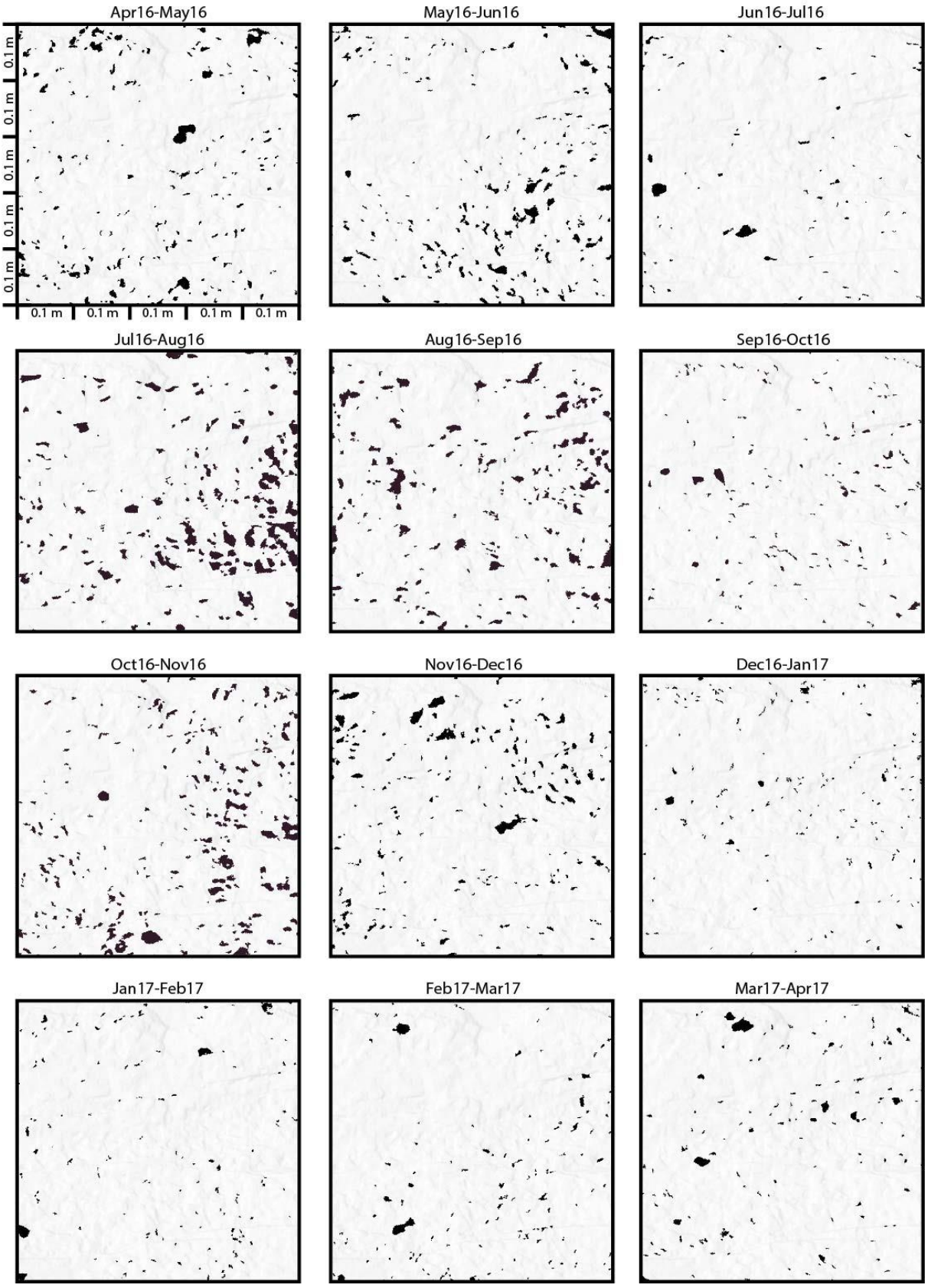
Site 7: Monthly distribution of erosion



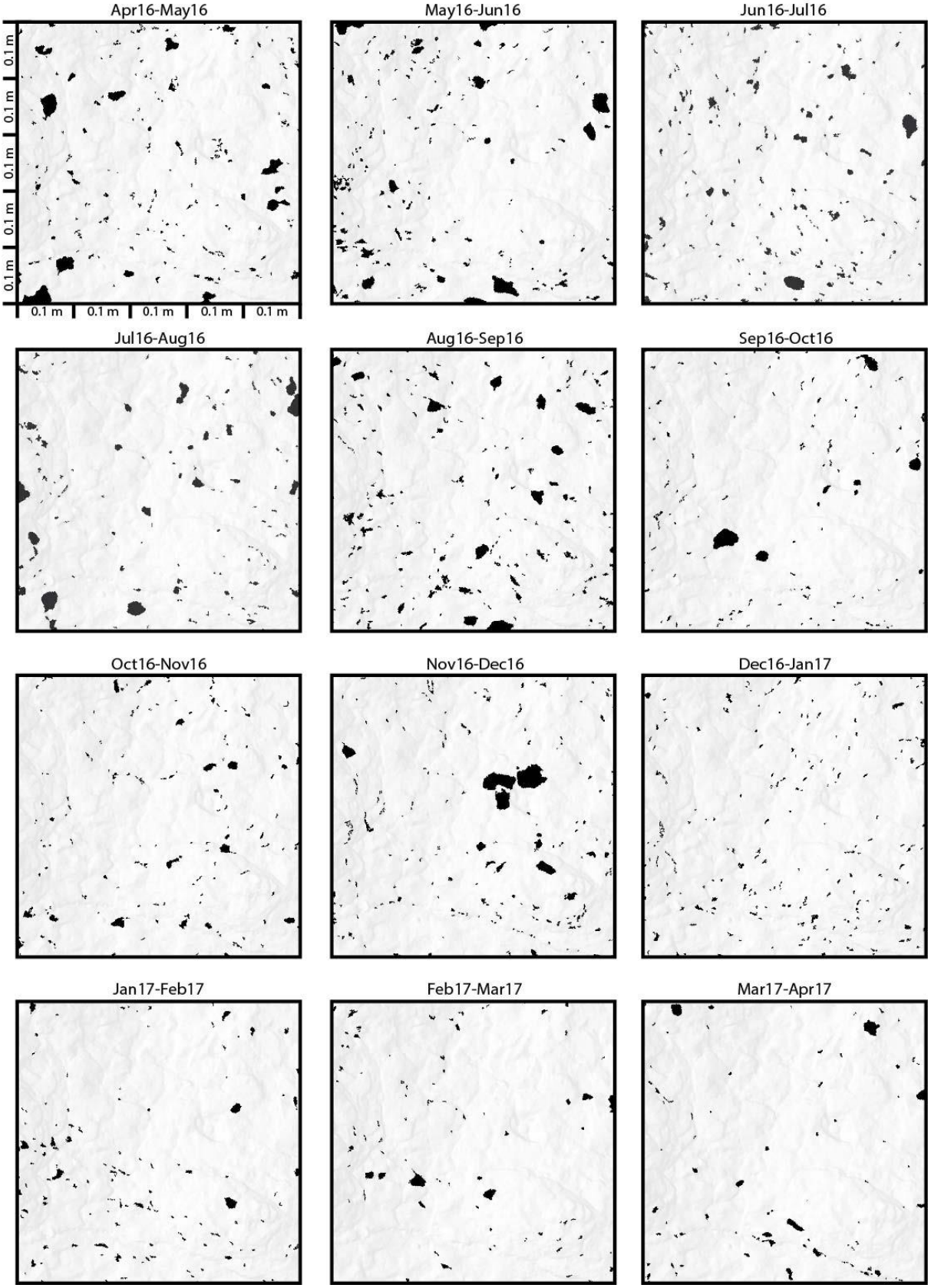
Site 8: Monthly distribution of erosion



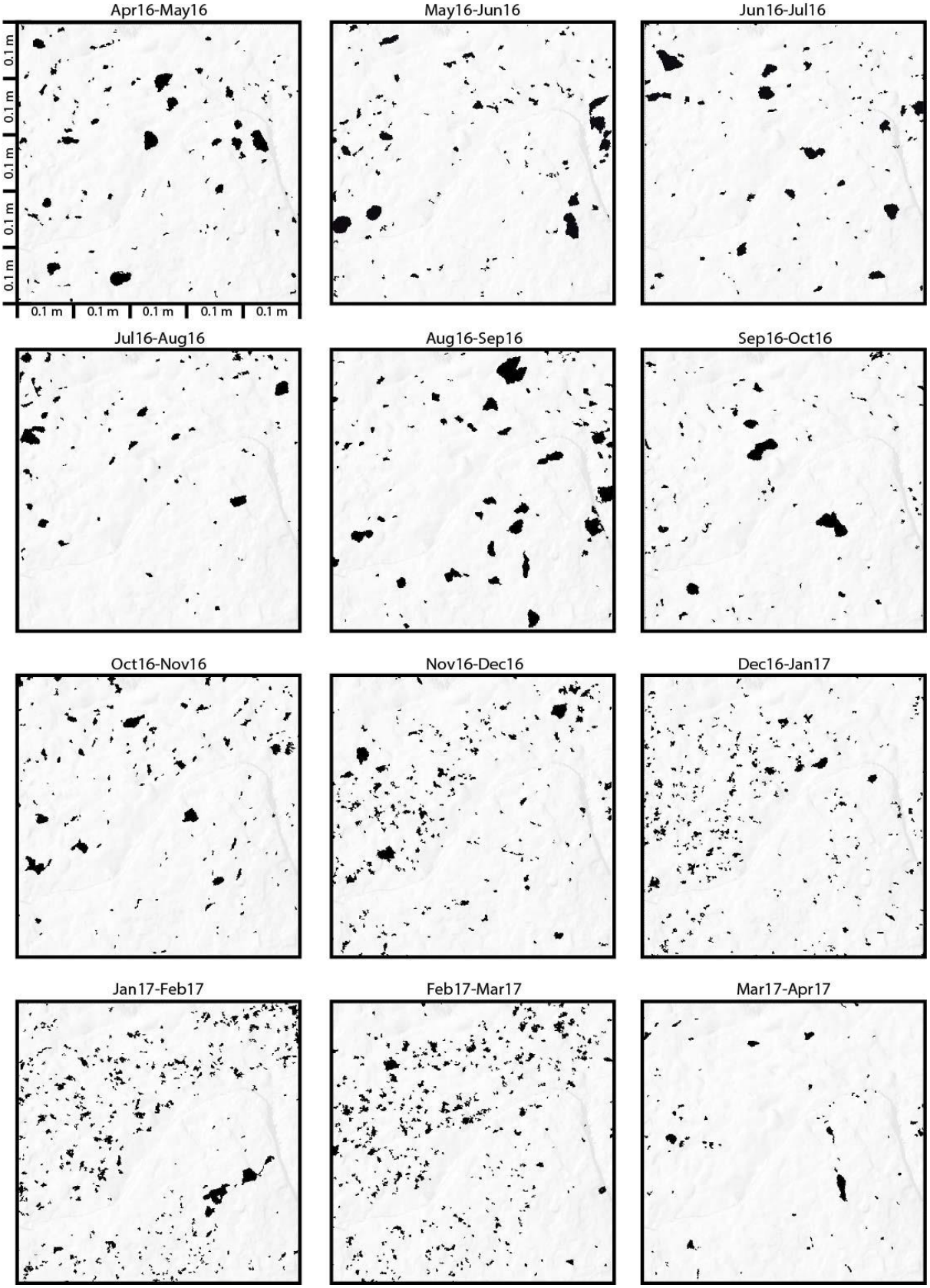
Site 9: Monthly distribution of erosion



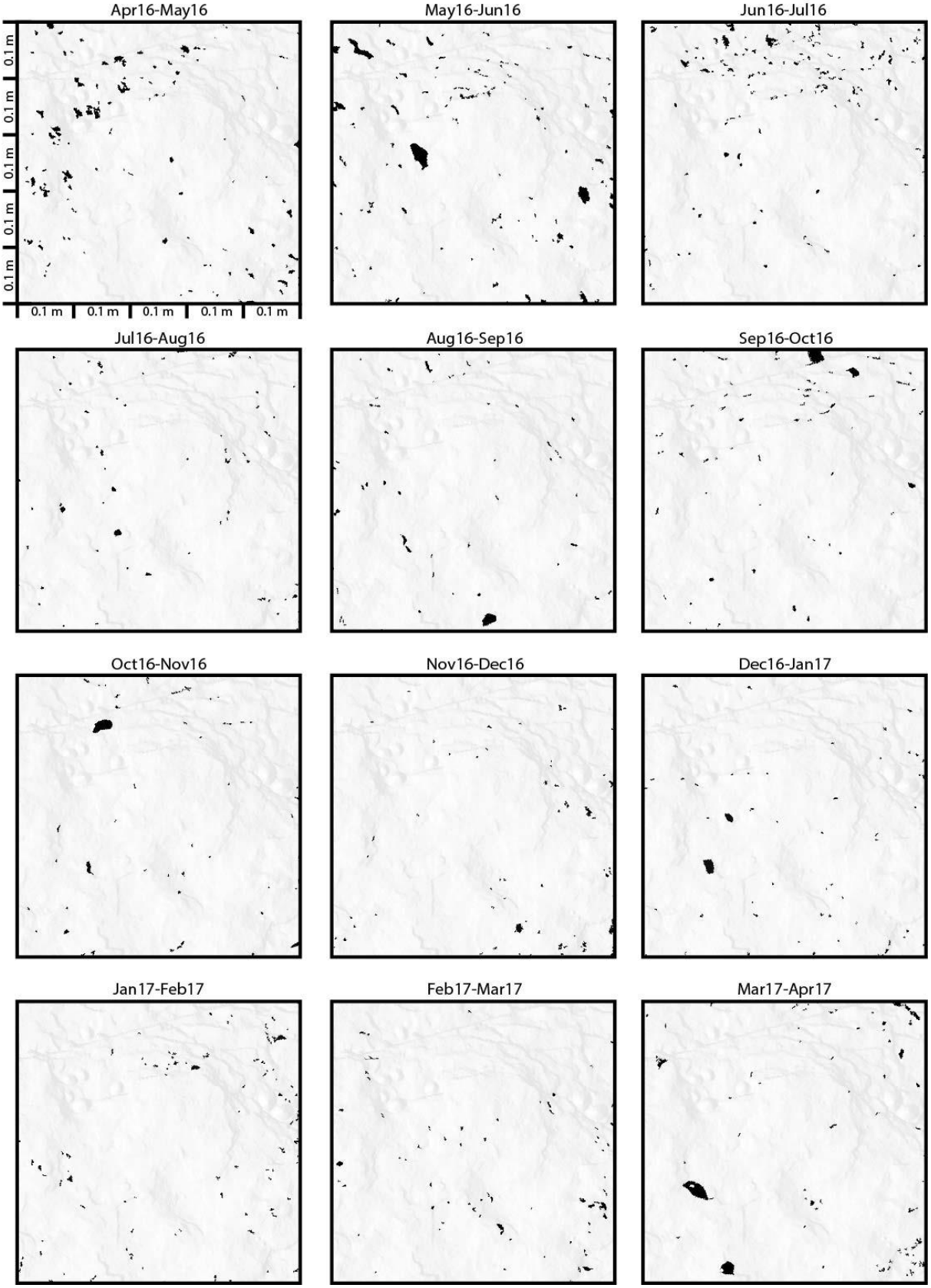
Site 10: Monthly distribution of erosion



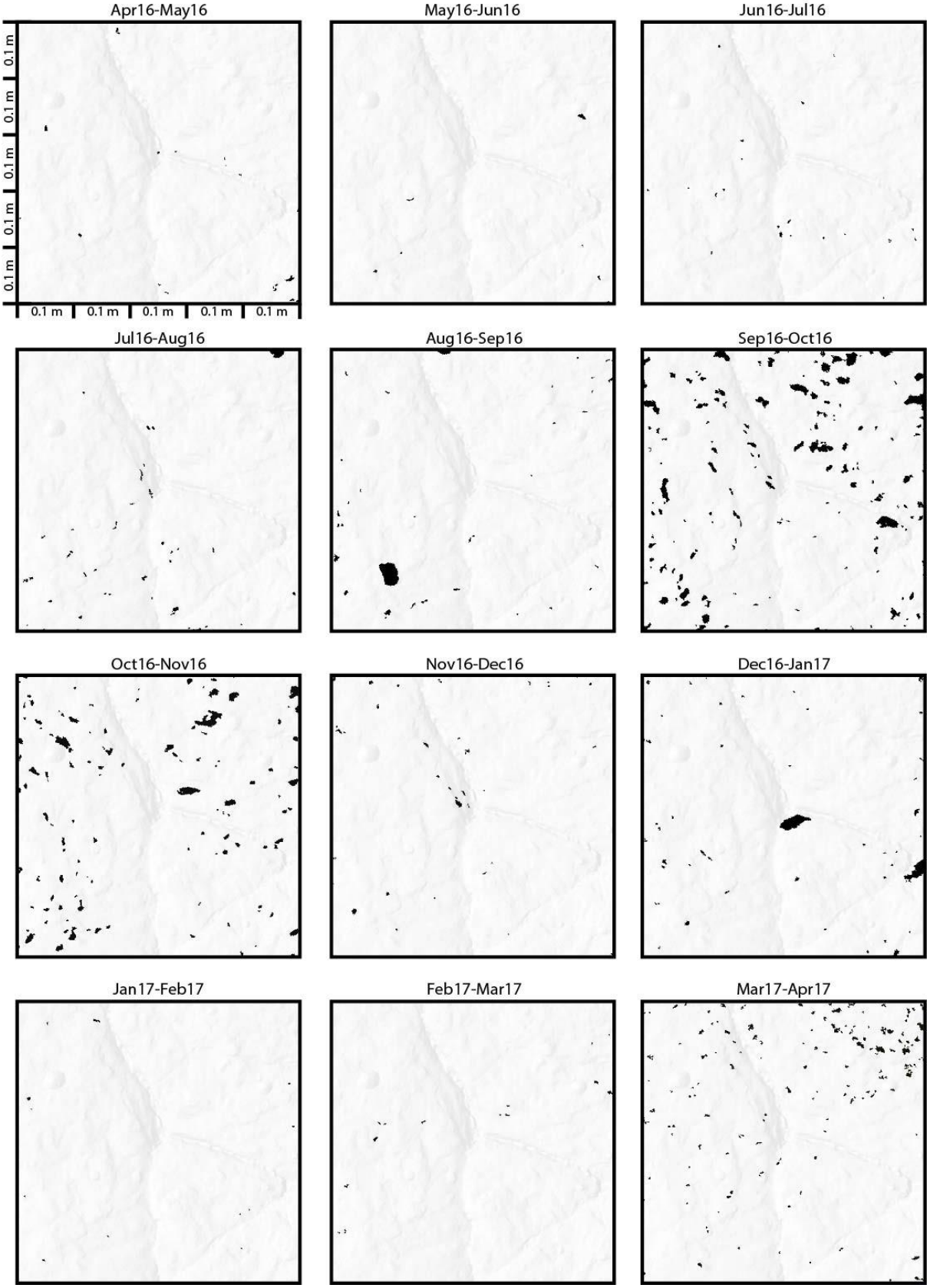
Site 11: Monthly distribution of erosion



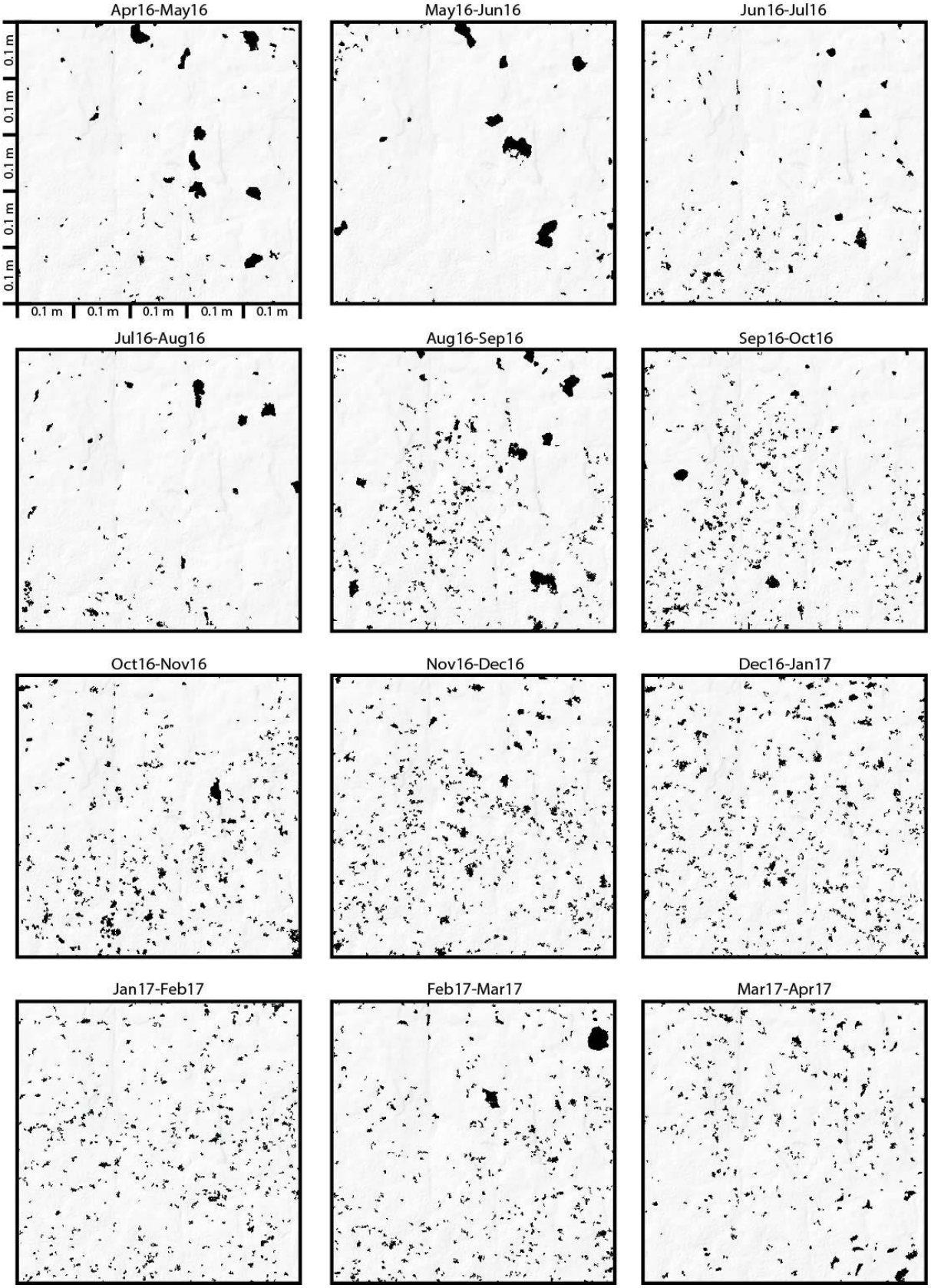
Site 12: Monthly distribution of erosion



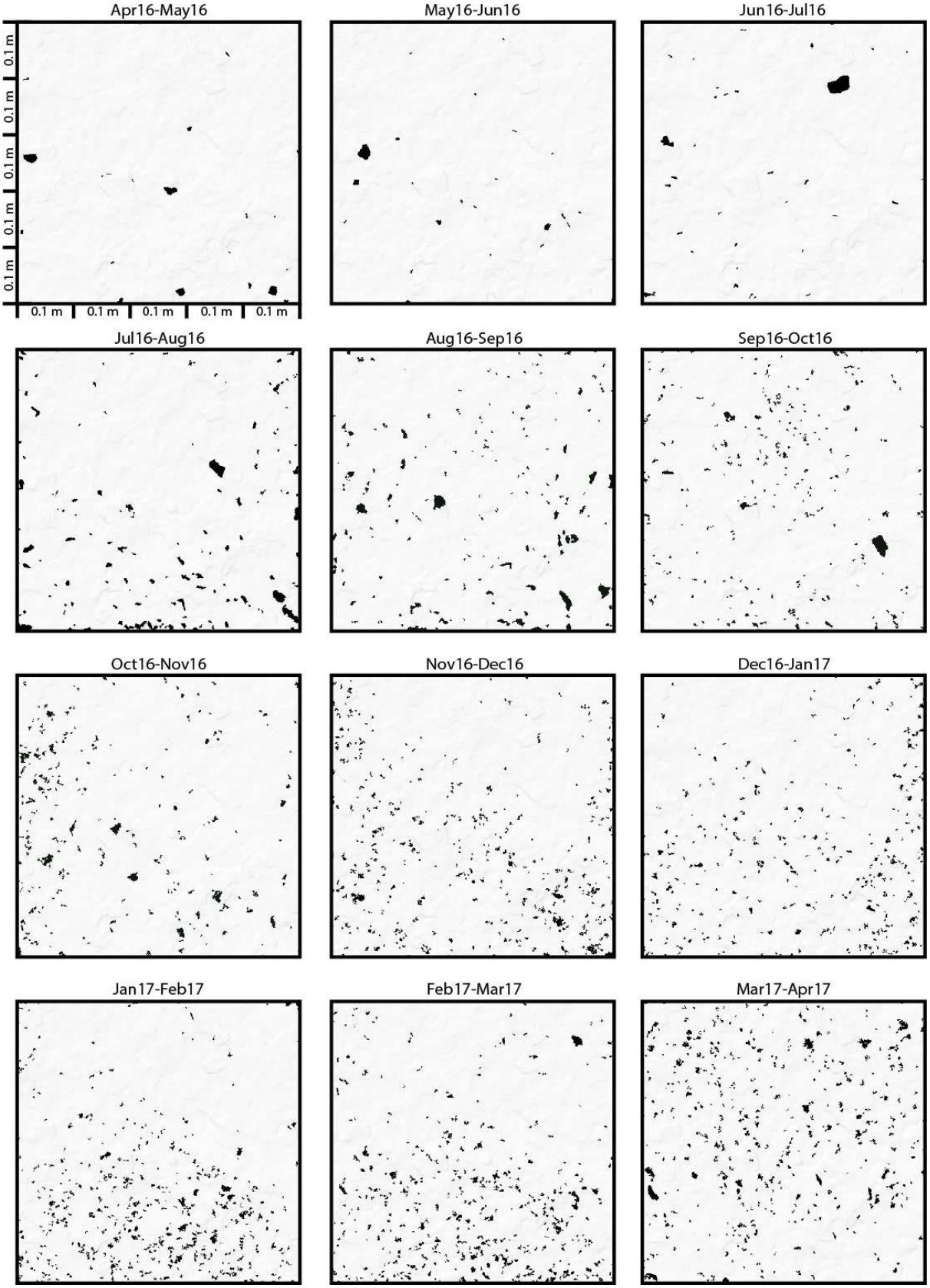
Site 13: Monthly distribution of erosion



Site 14: Monthly distribution of erosion



Site 15: Monthly distribution of erosion

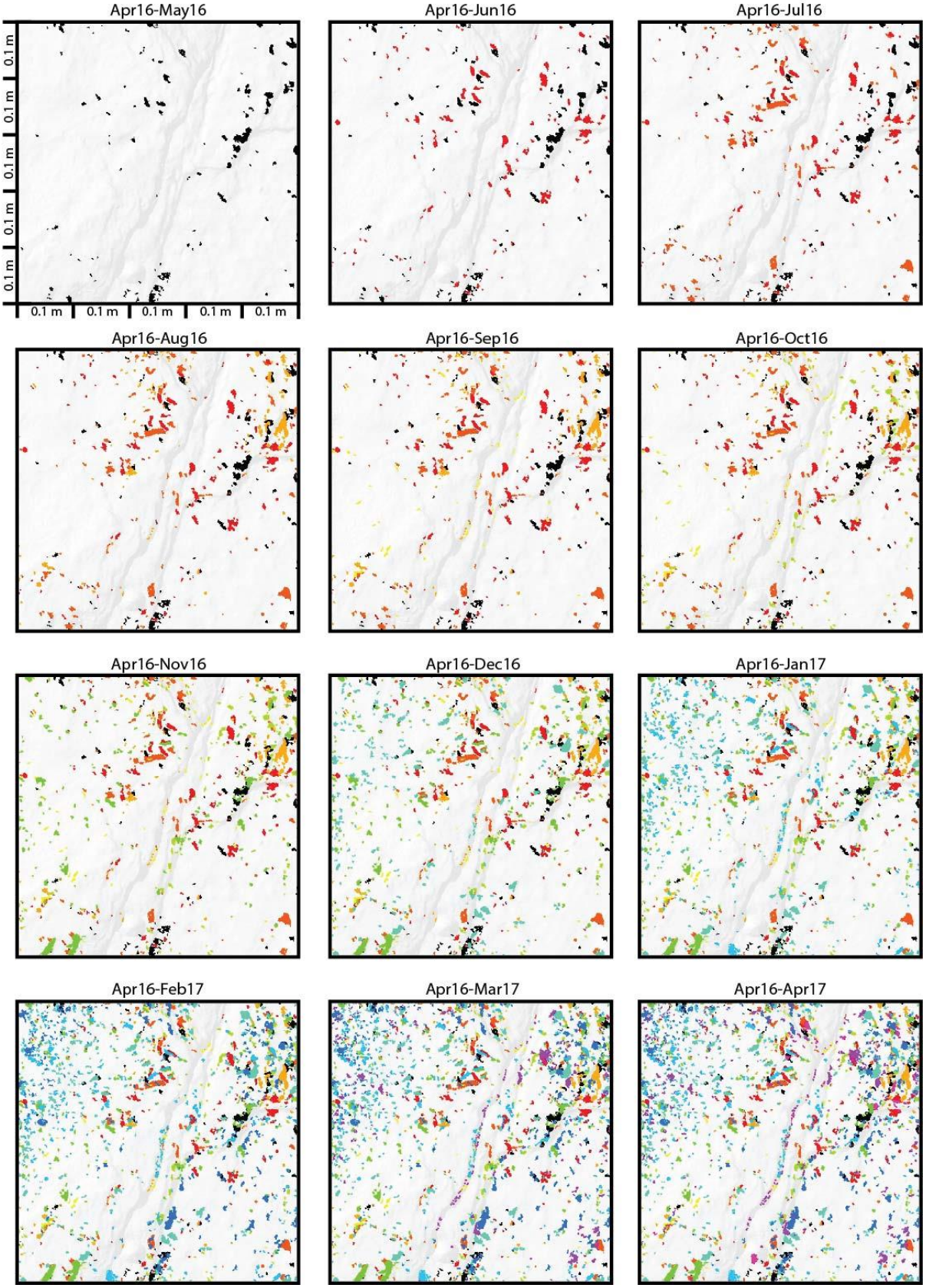


Appendix 5: Cumulative distribution of erosion at each micro-erosion monitoring site.

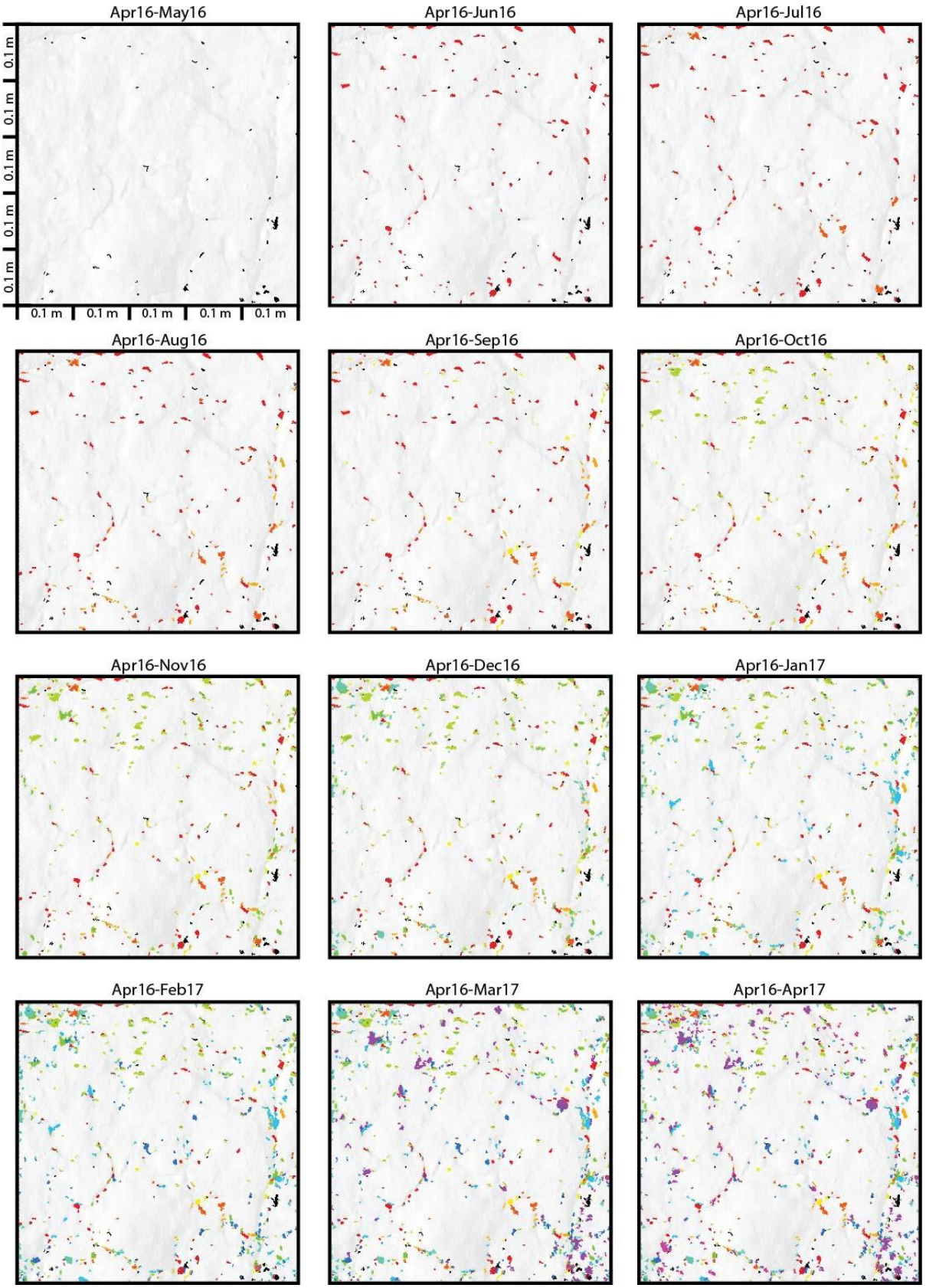
The polygons represent detachments, adhering to the key displayed immediately below. The background image is a hillshade at 90% transparency created from the Apr'16 DEM.



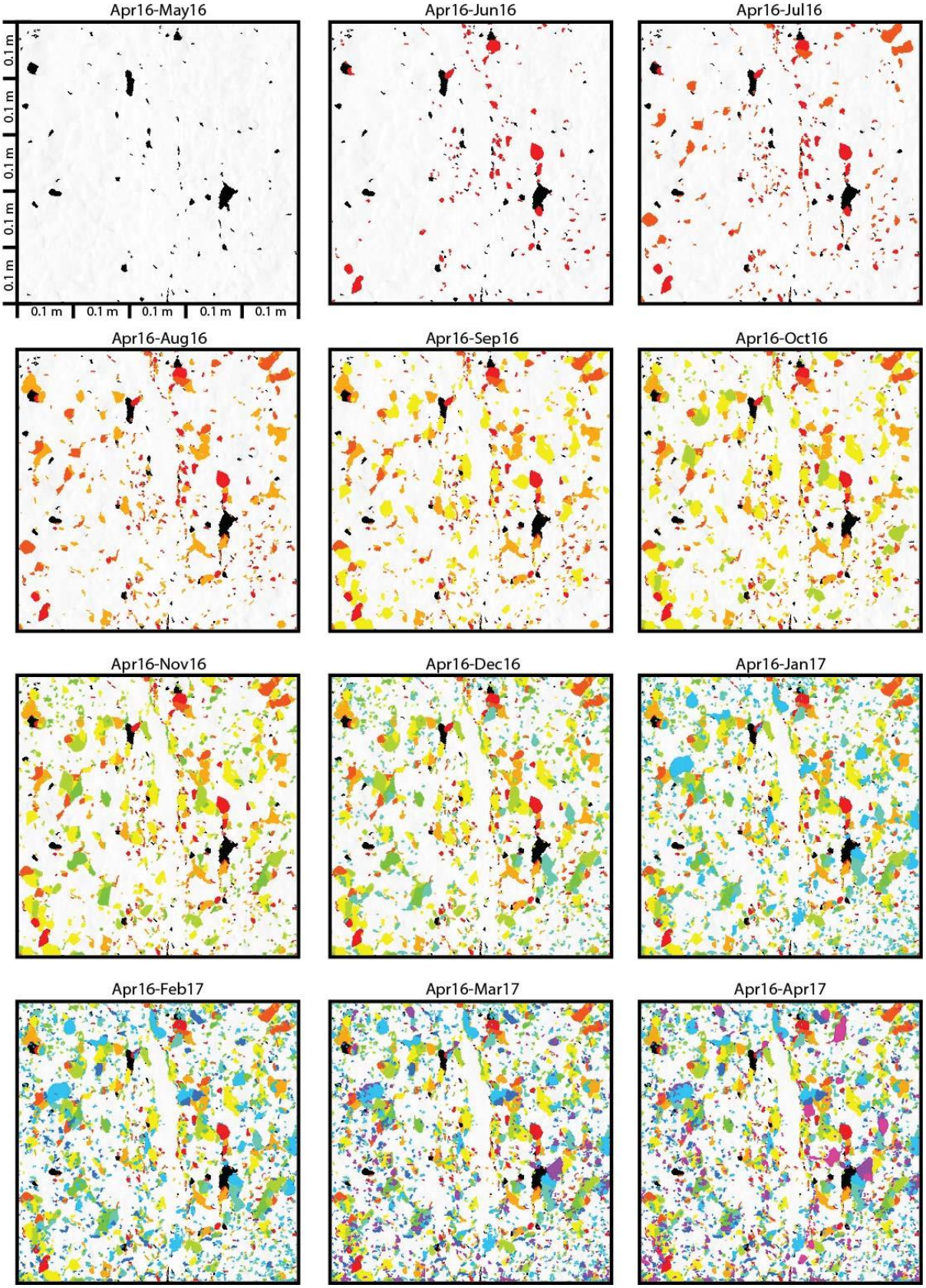
Site 1: Cumulative distribution of erosion



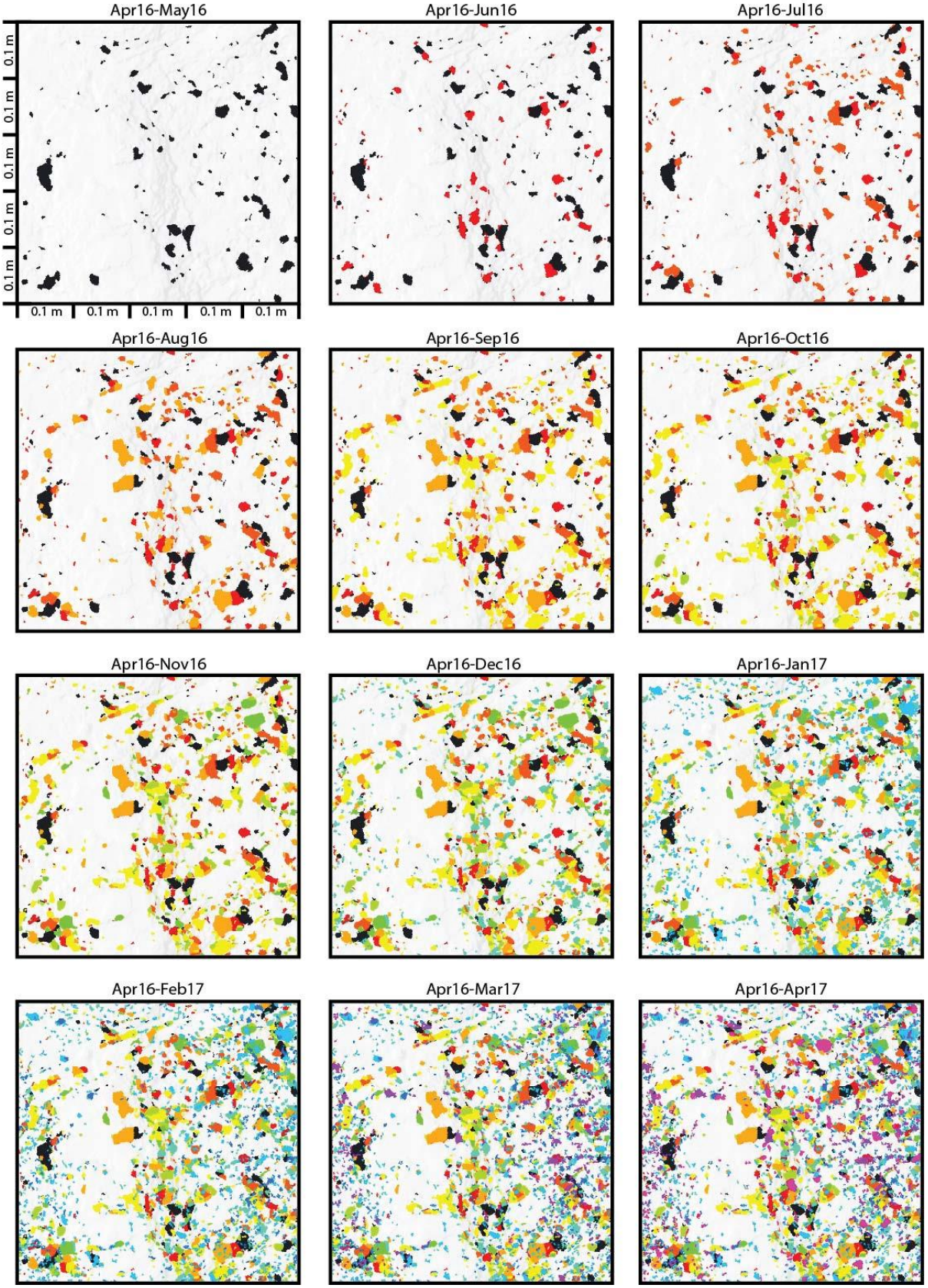
Site 2: Cumulative distribution of erosion



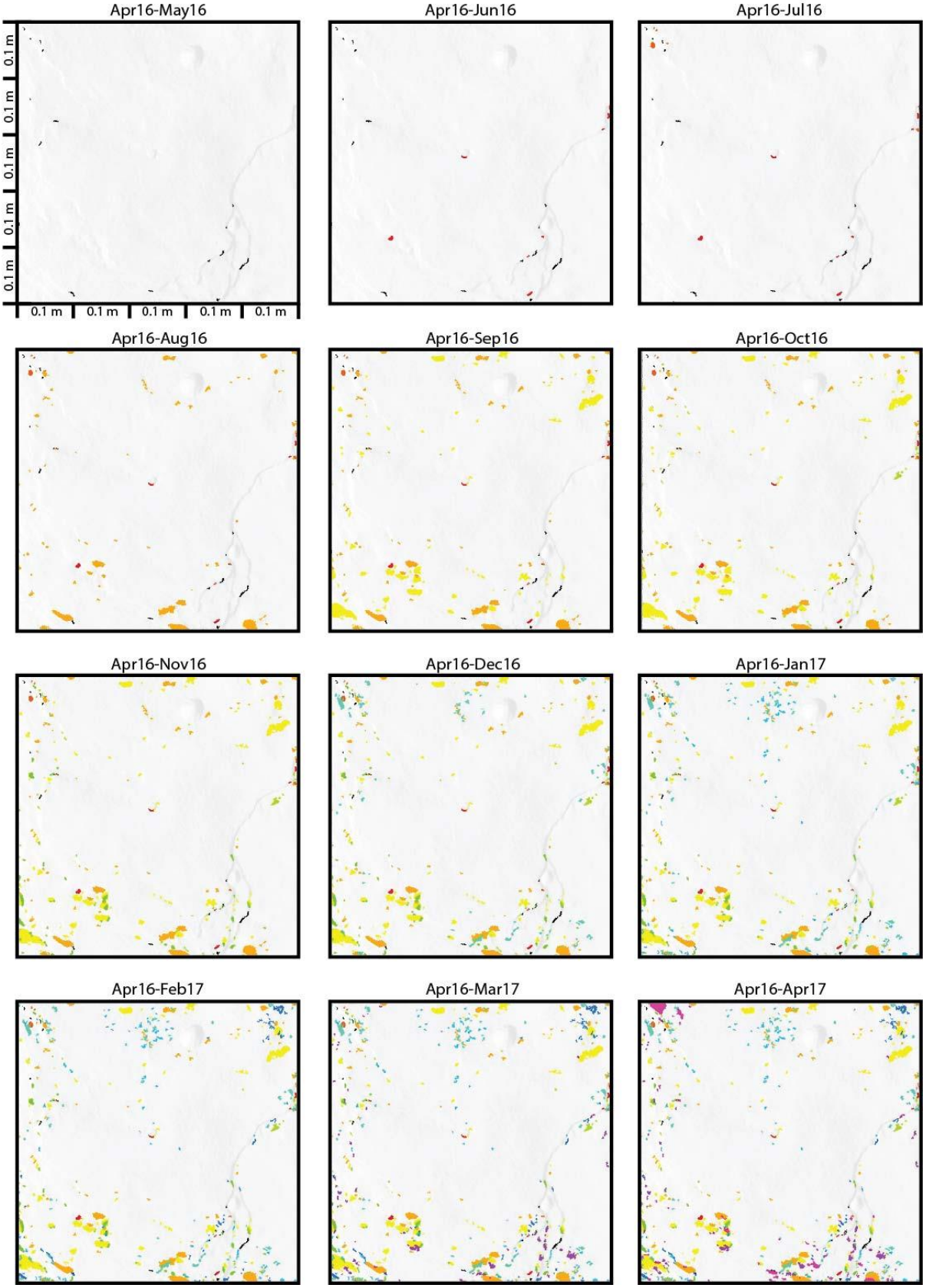
Site 3: Cumulative distribution of erosion



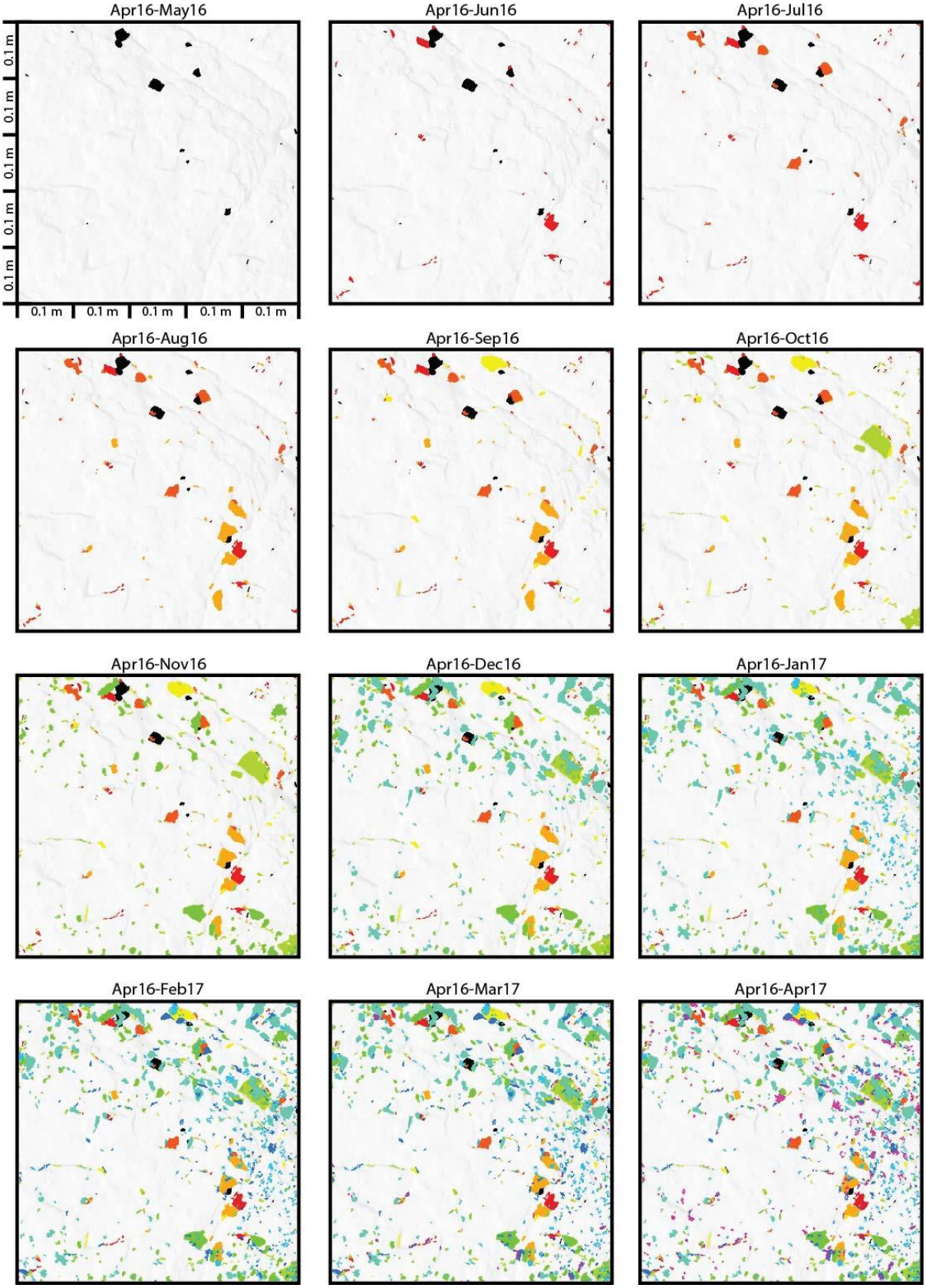
Site 4: Cumulative distribution of erosion



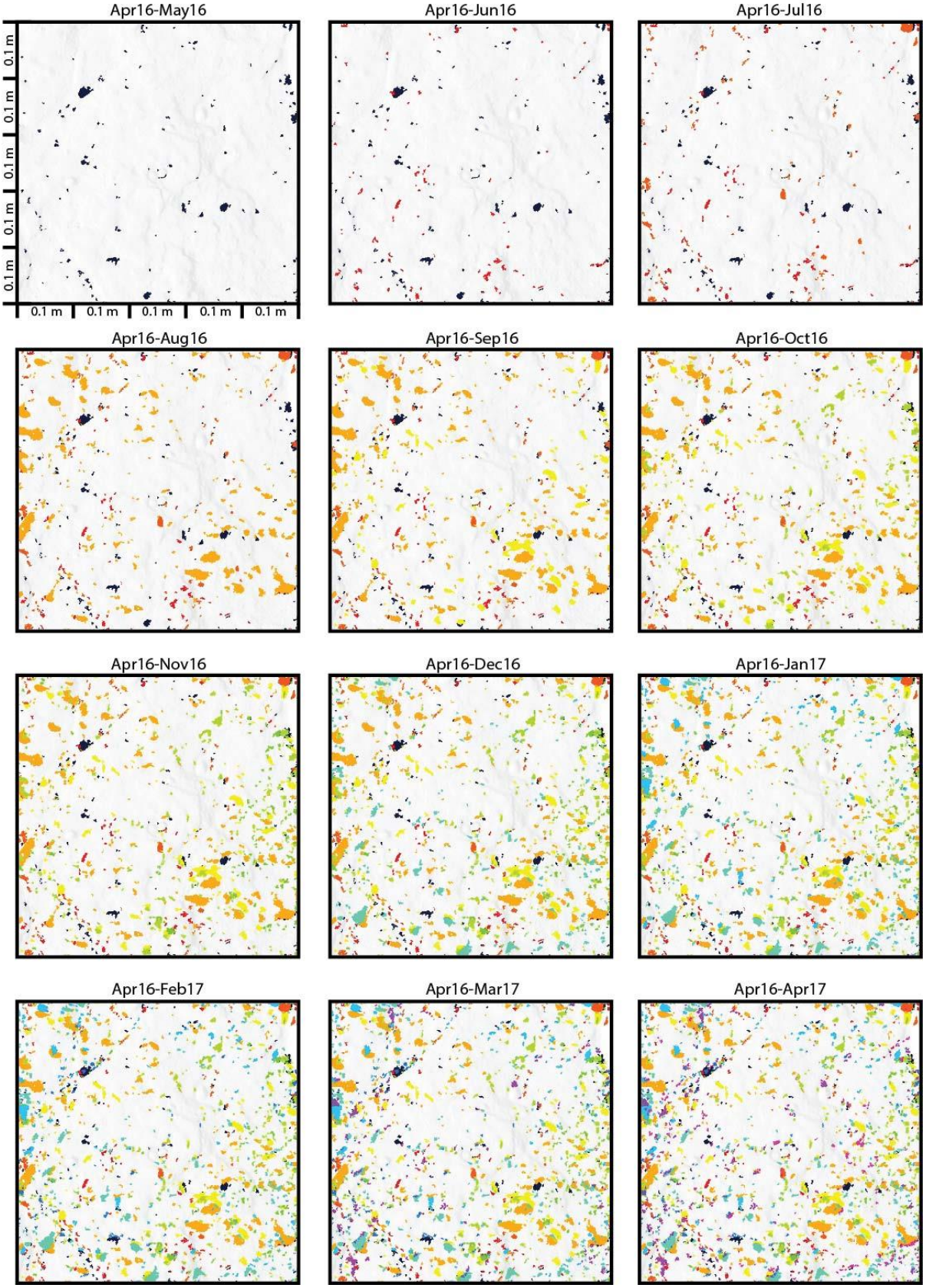
Site 5: Cumulative distribution of erosion



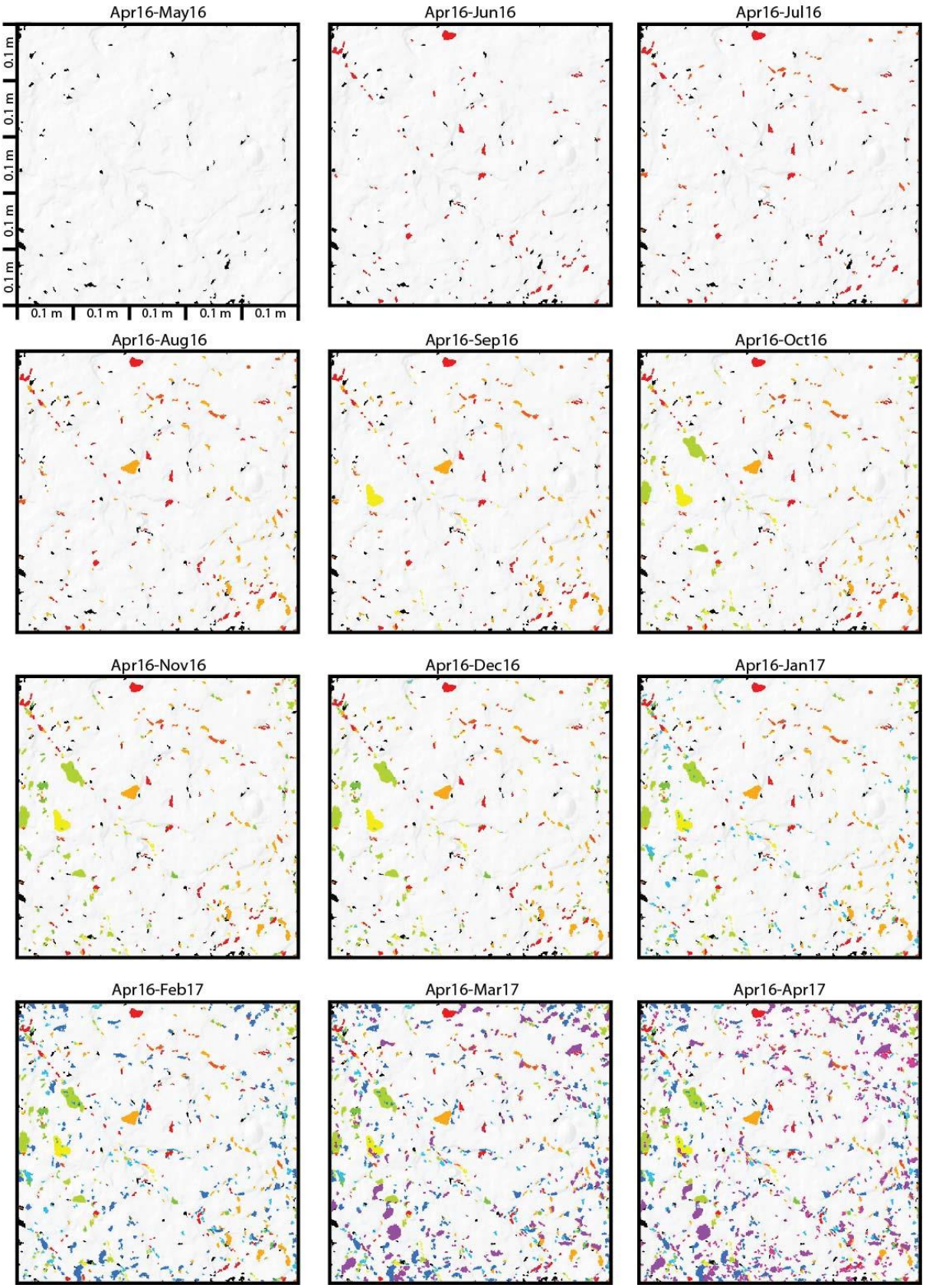
Site 6: Cumulative distribution of erosion



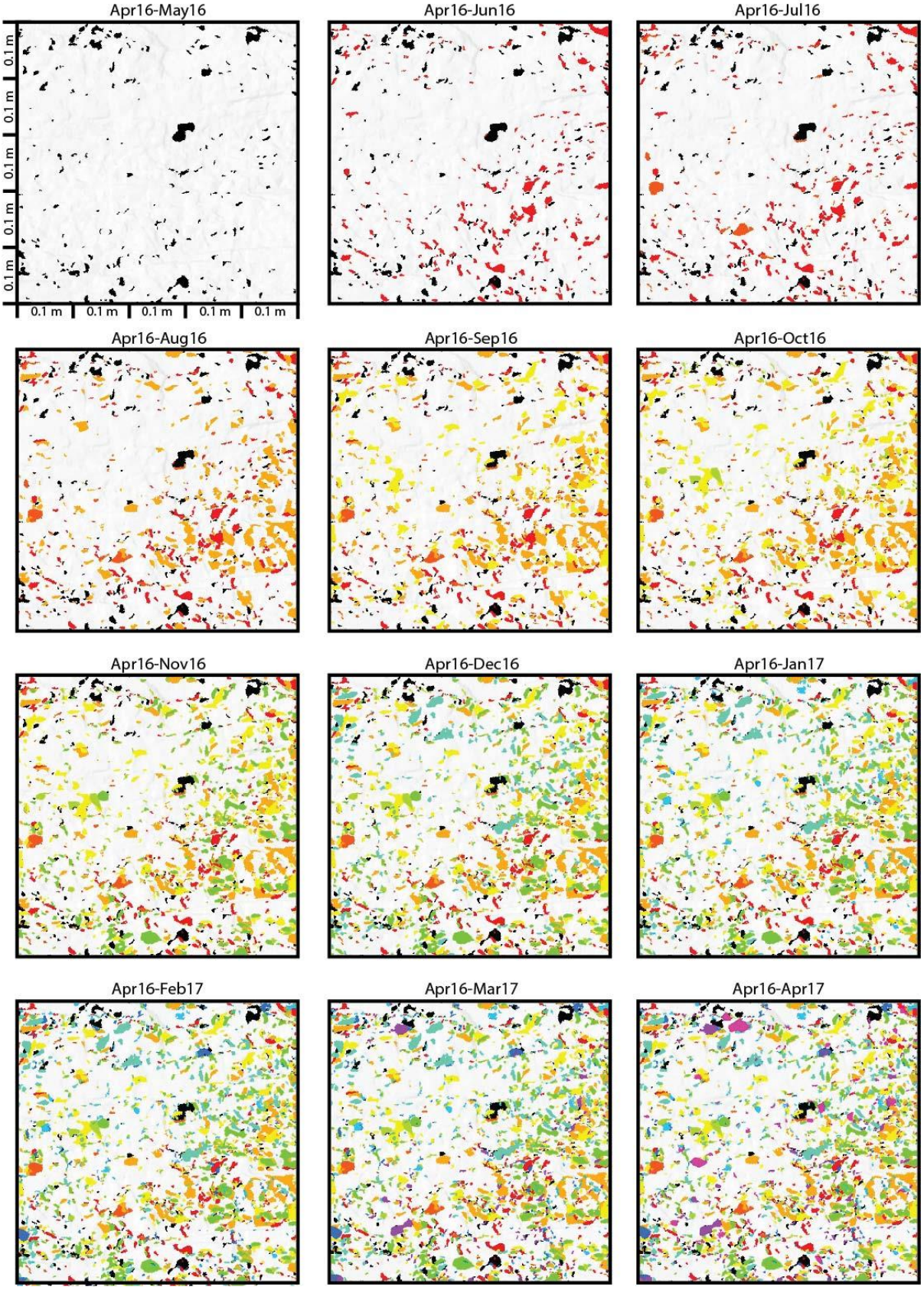
Site 7: Cumulative distribution of erosion



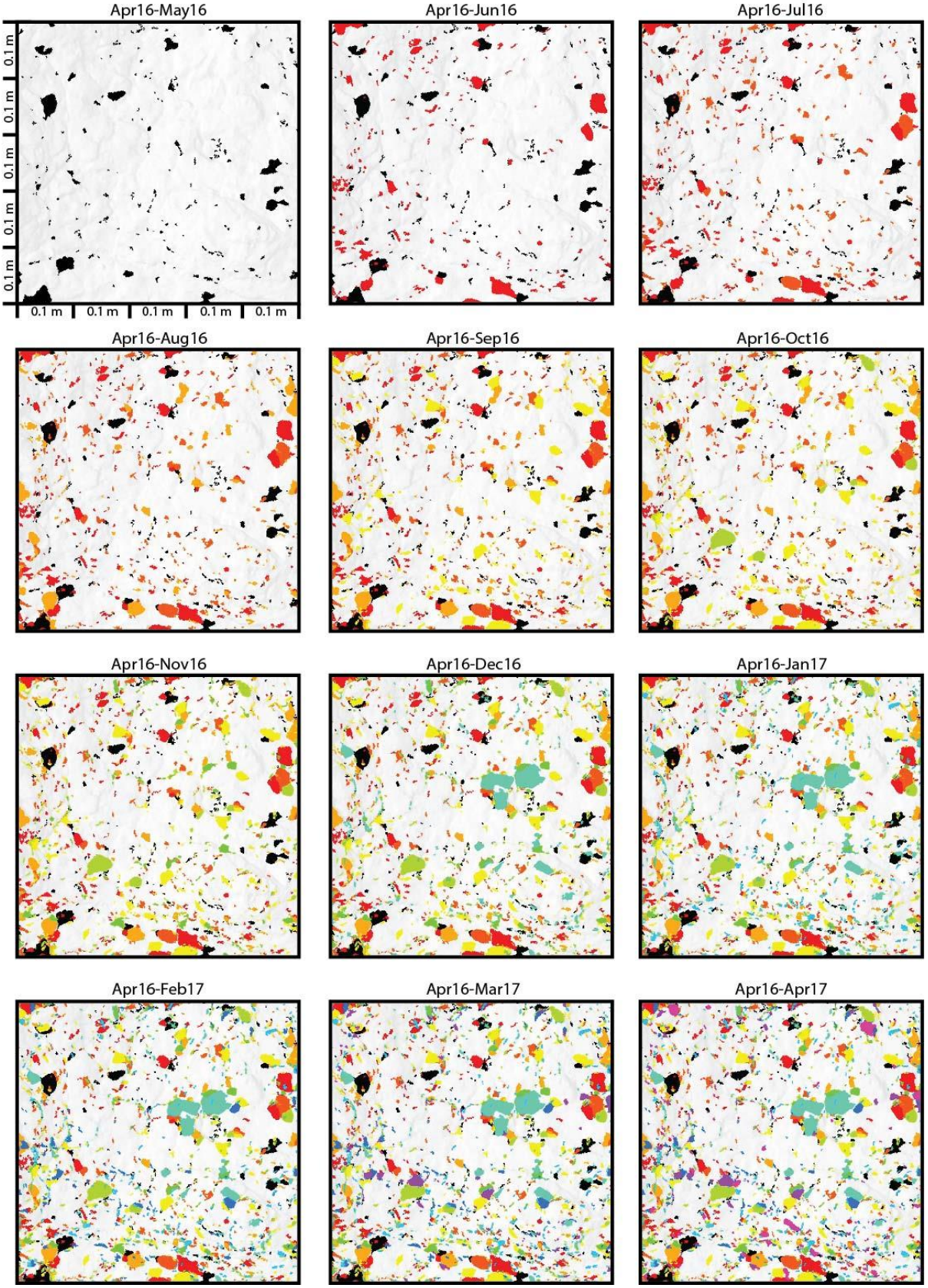
Site 8: Cumulative distribution of erosion



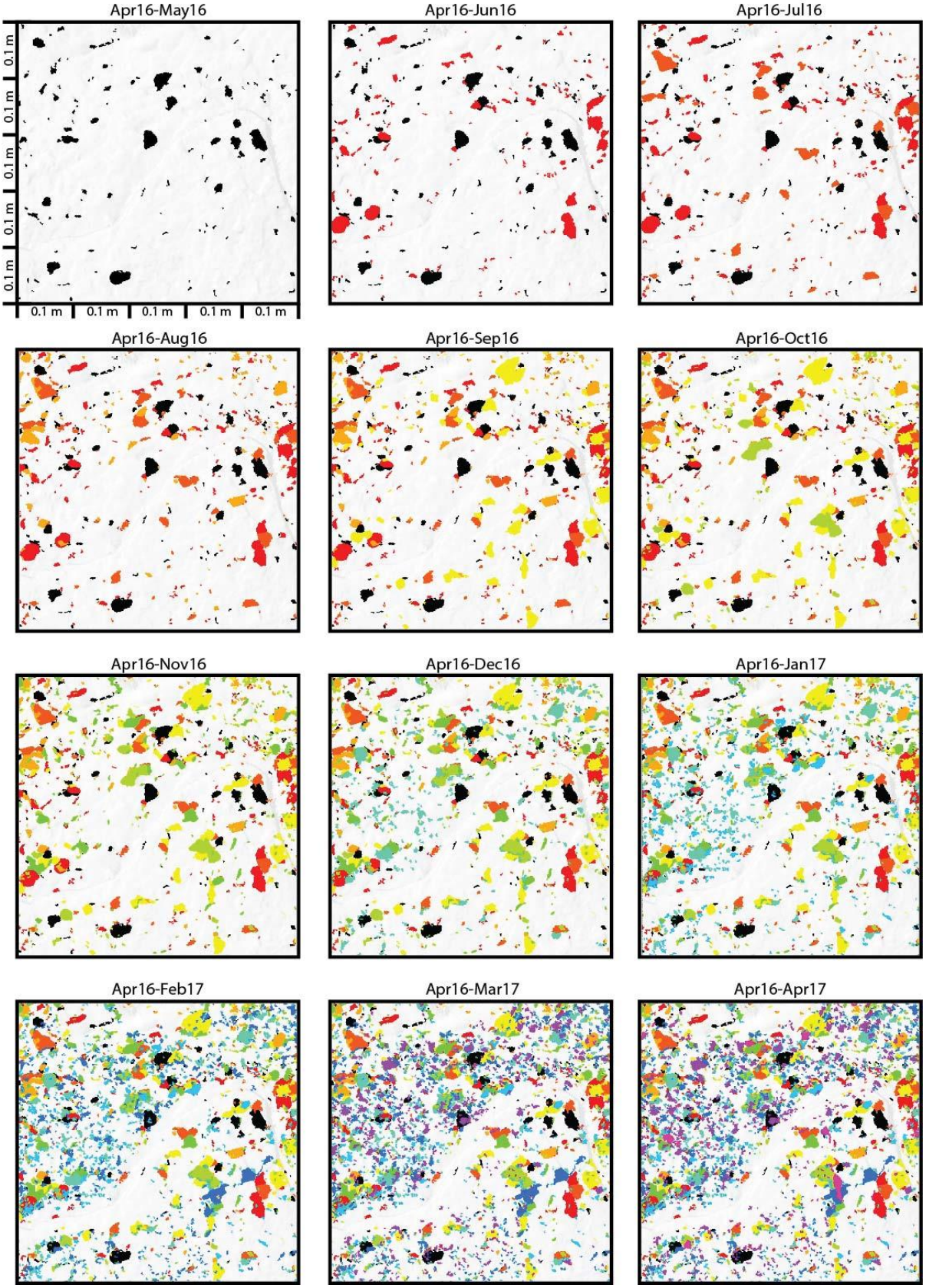
Site 9: Cumulative distribution of erosion



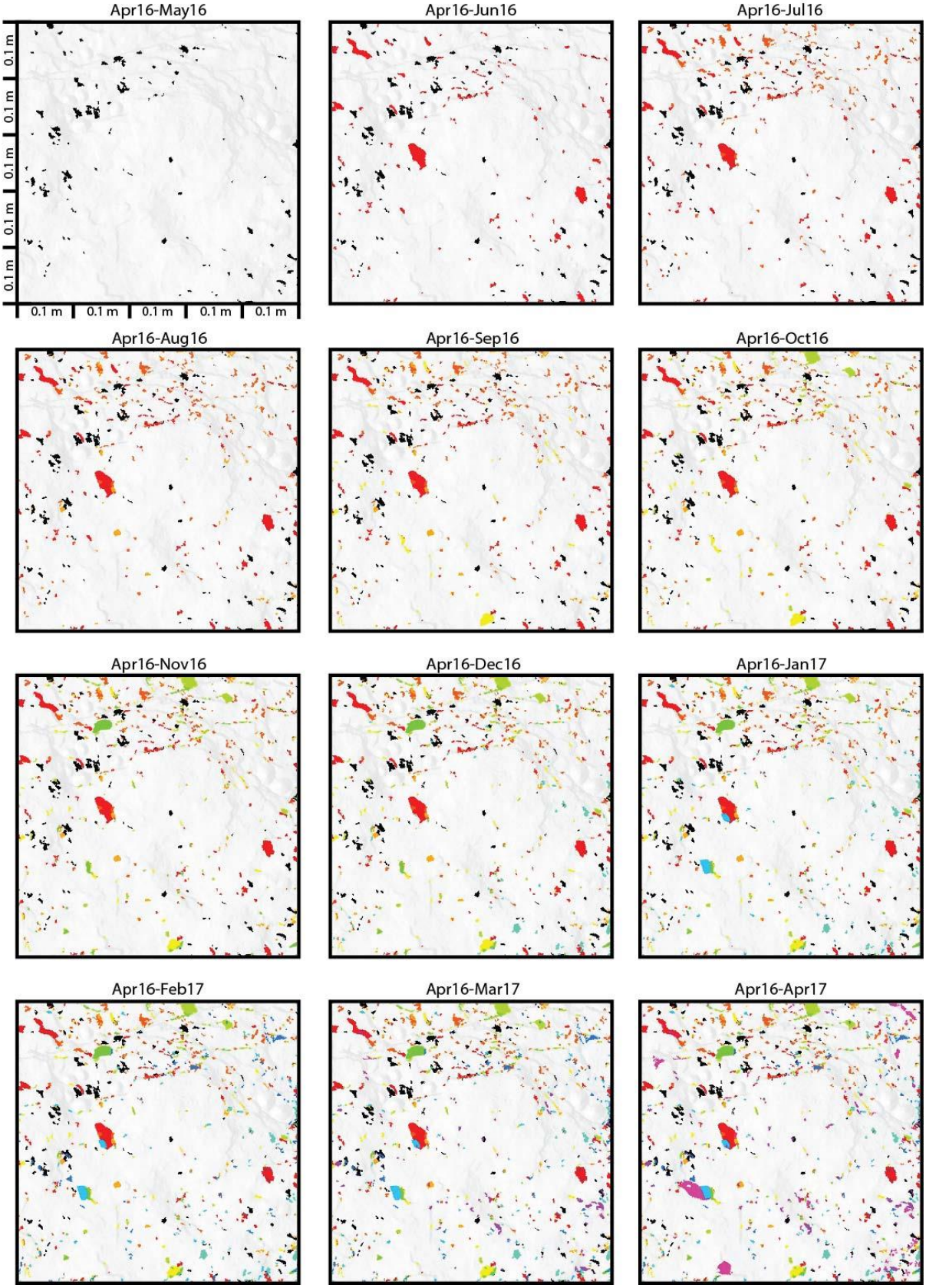
Site 10: Cumulative distribution of erosion



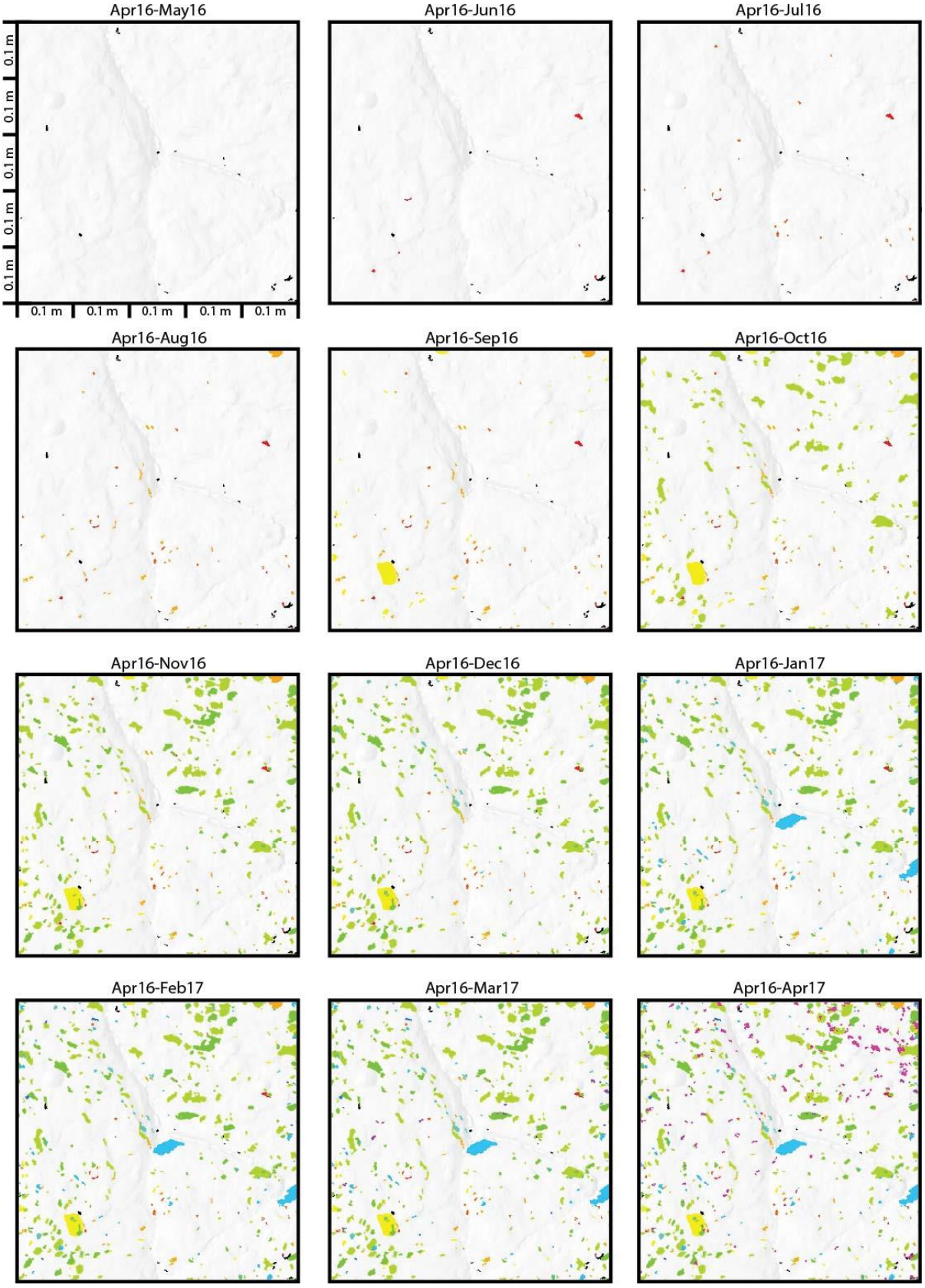
Site 11: Cumulative distribution of erosion



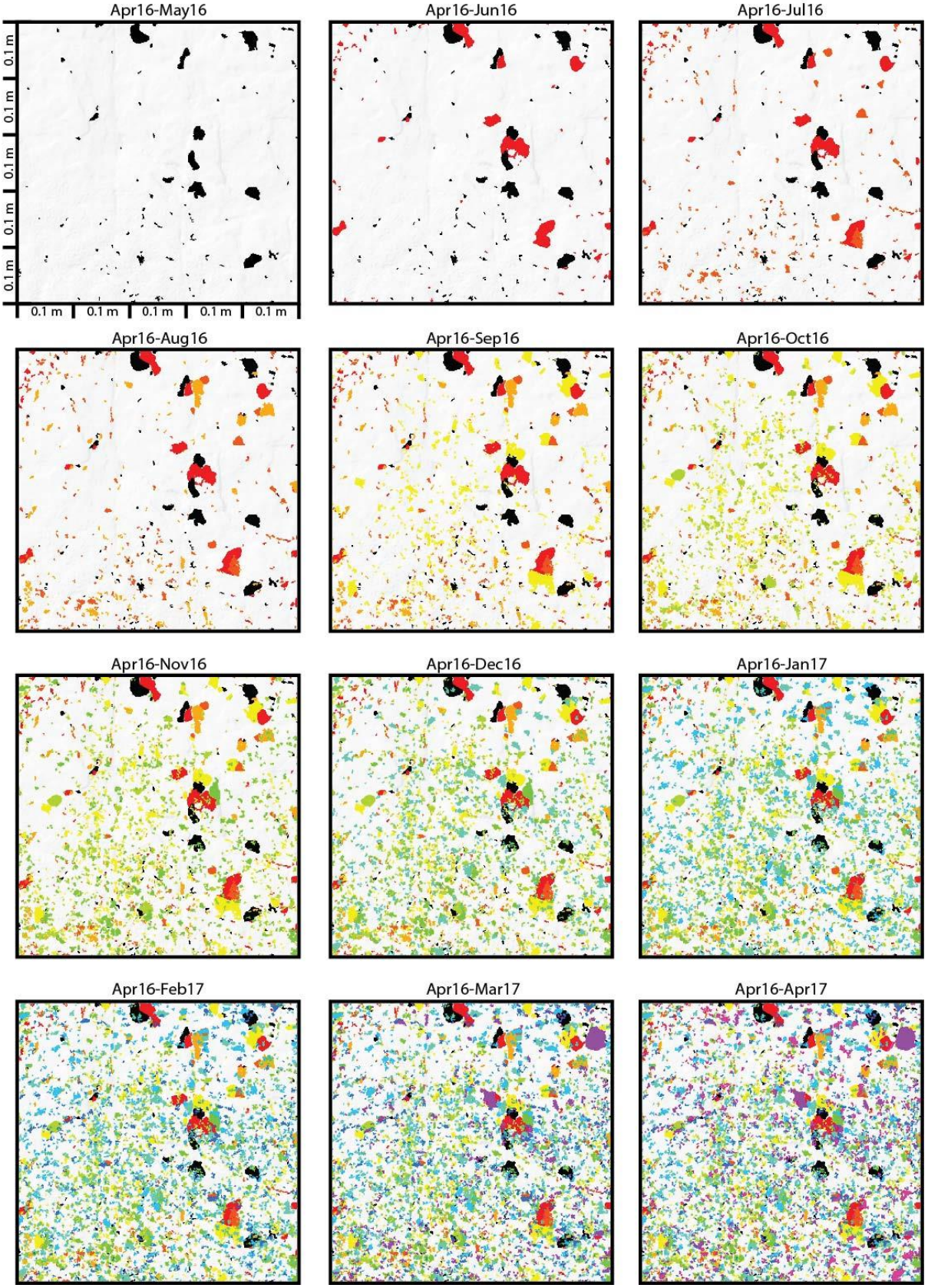
Site 12: Cumulative distribution of erosion



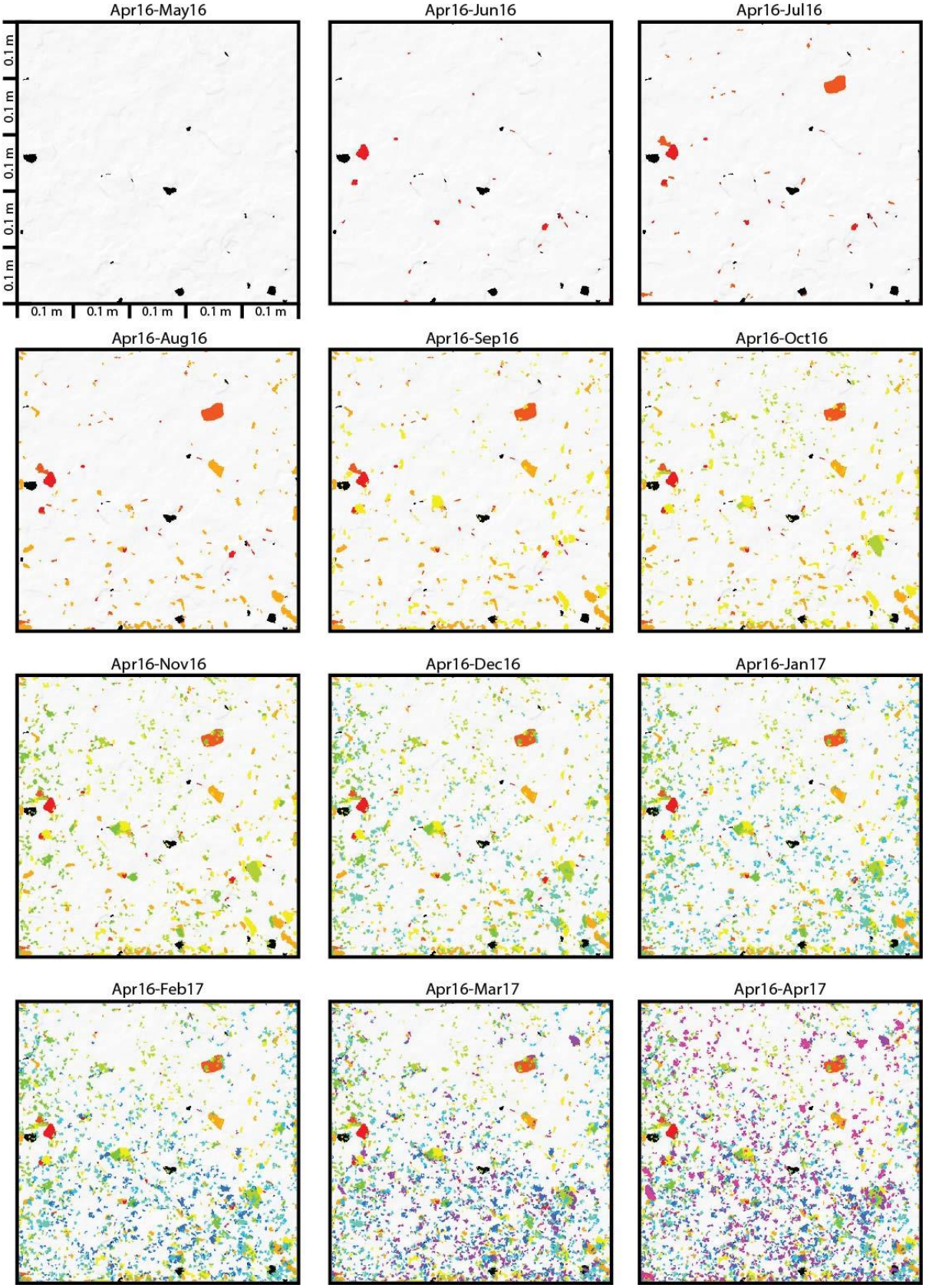
Site 13: Cumulative distribution of erosion



Site 14: Cumulative distribution of erosion

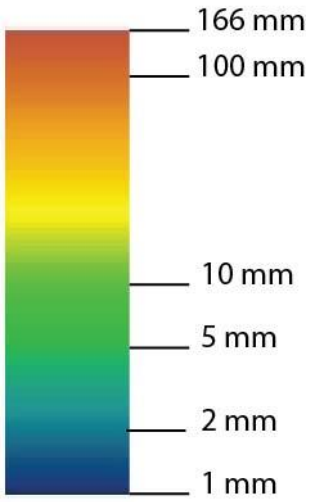


Site 15: Cumulative distribution of erosion

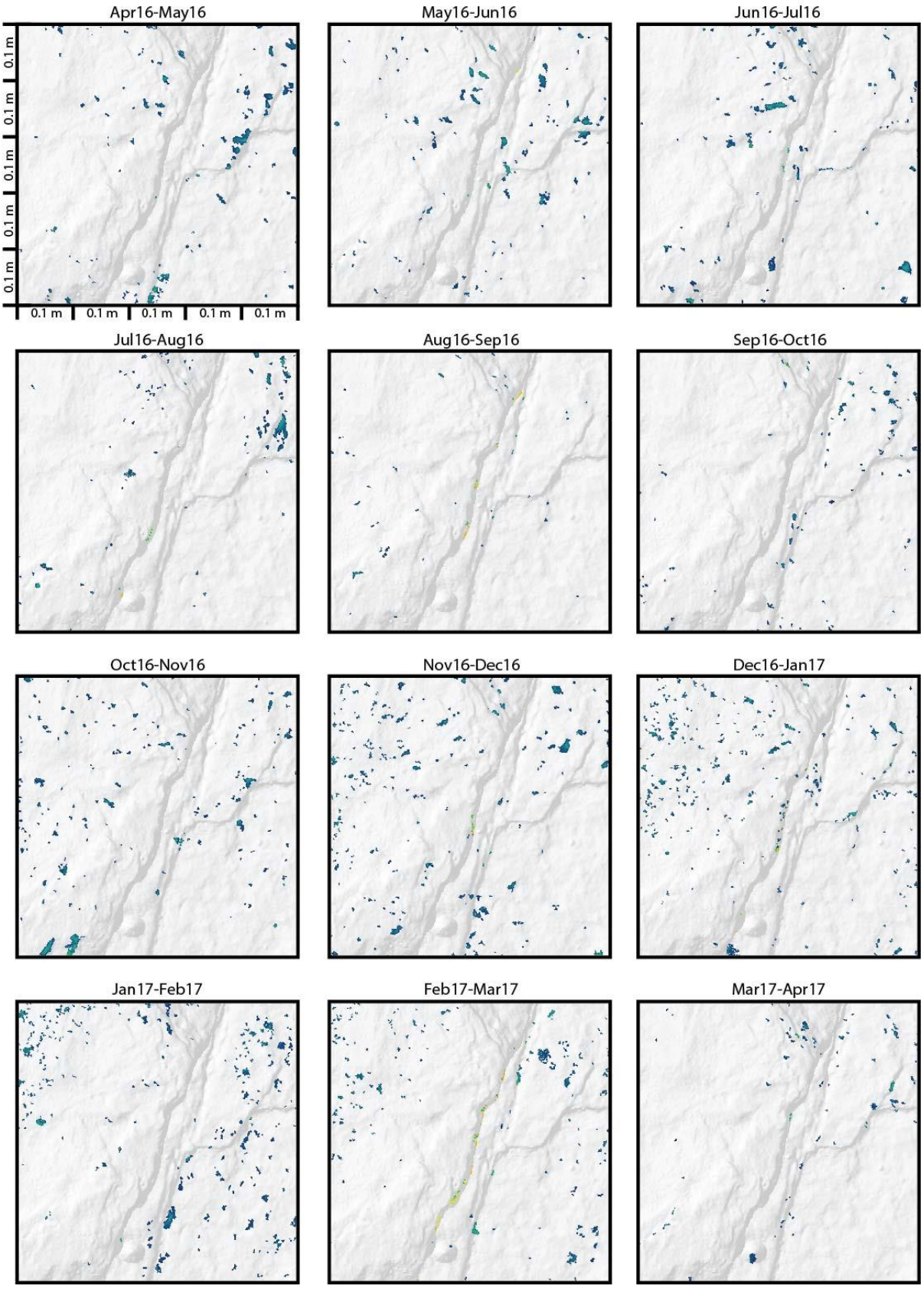


Appendix 6: Monthly erosion (depth) at each micro-erosion monitoring site.

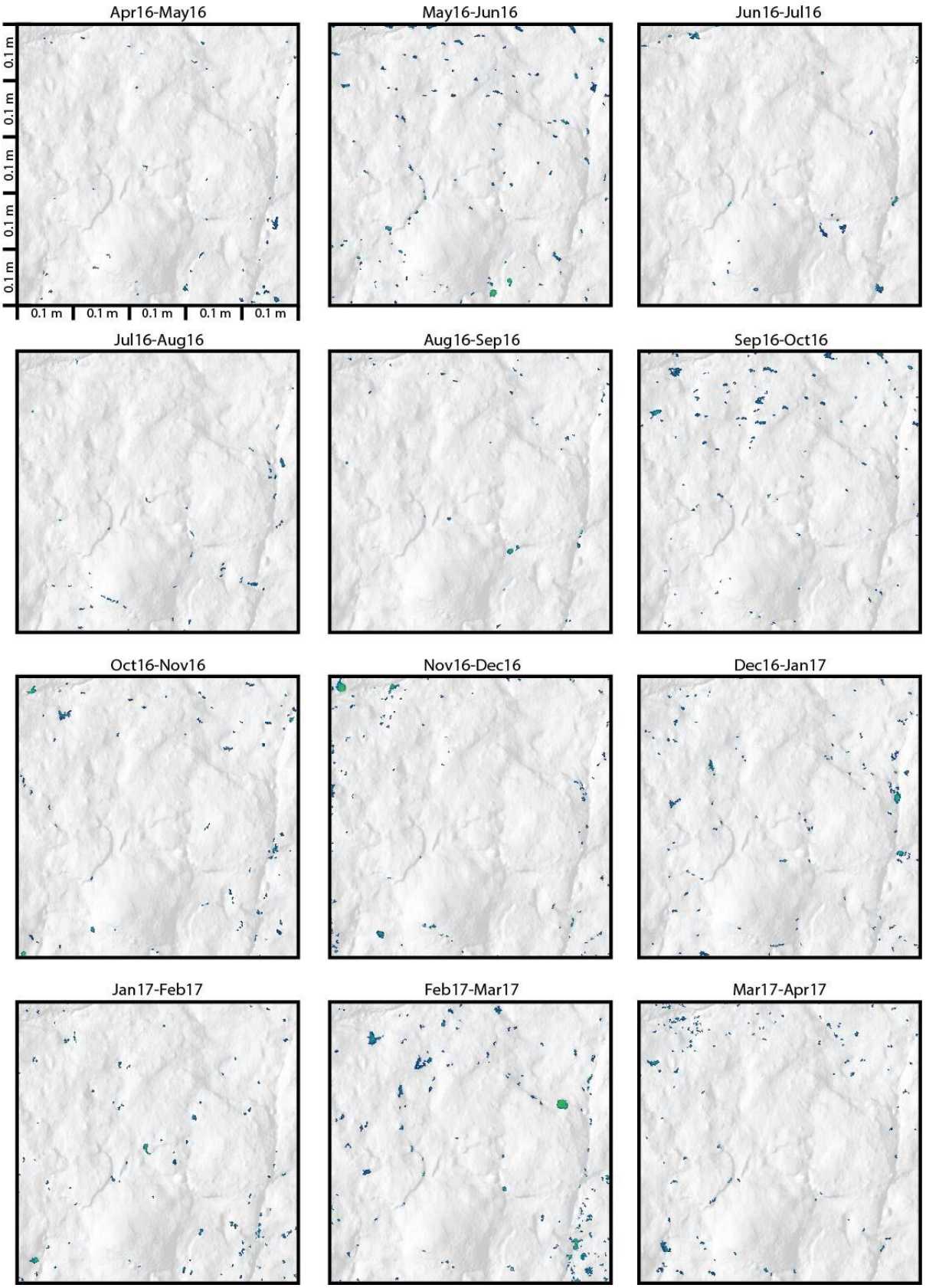
The background image is hillshade at 80% transparency created from the Apr'16 DEM. The same logarithmic scale bar displaying erosion depth is applied to all sites, as shown below.



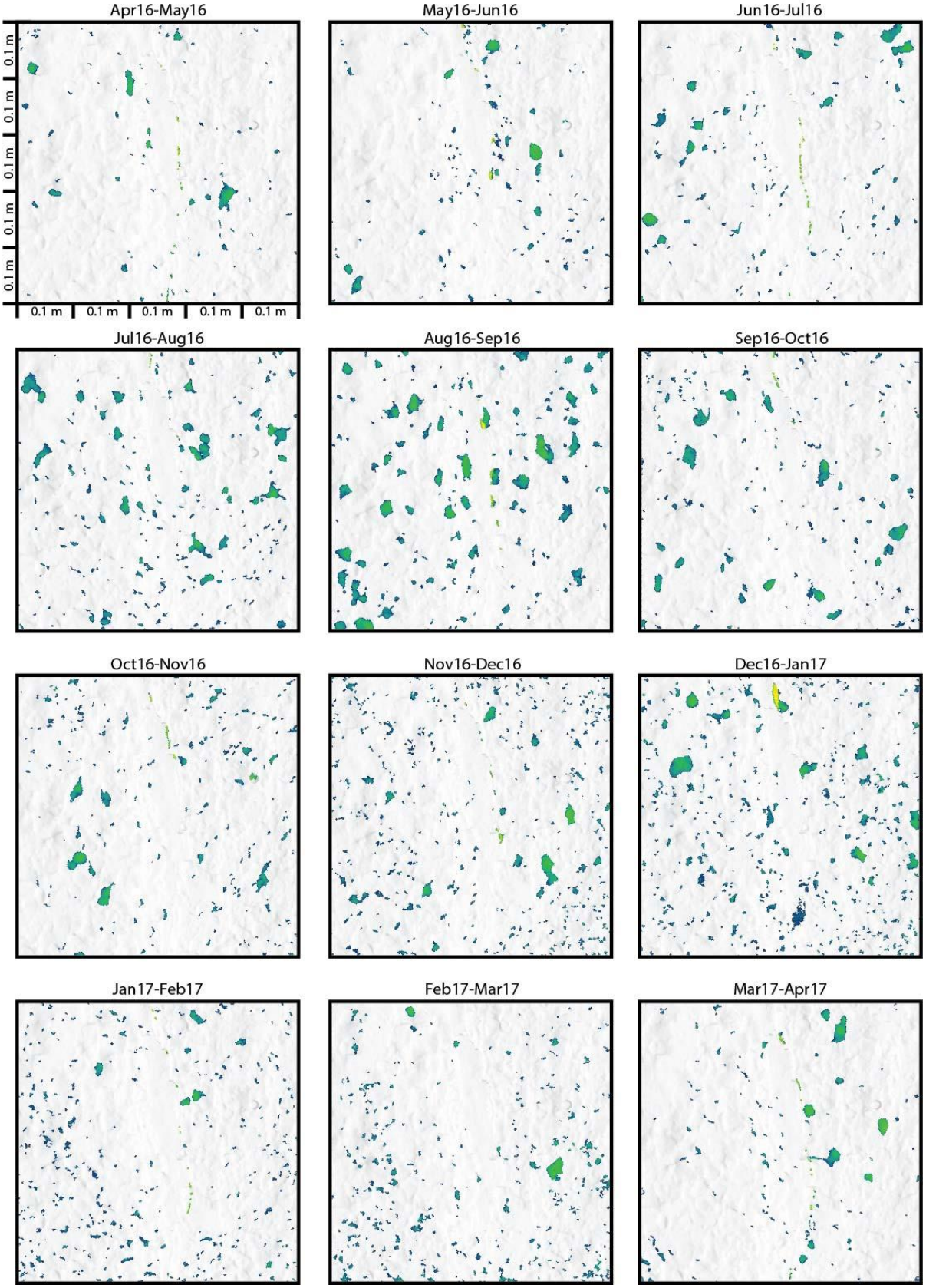
Site 1: Monthly erosion



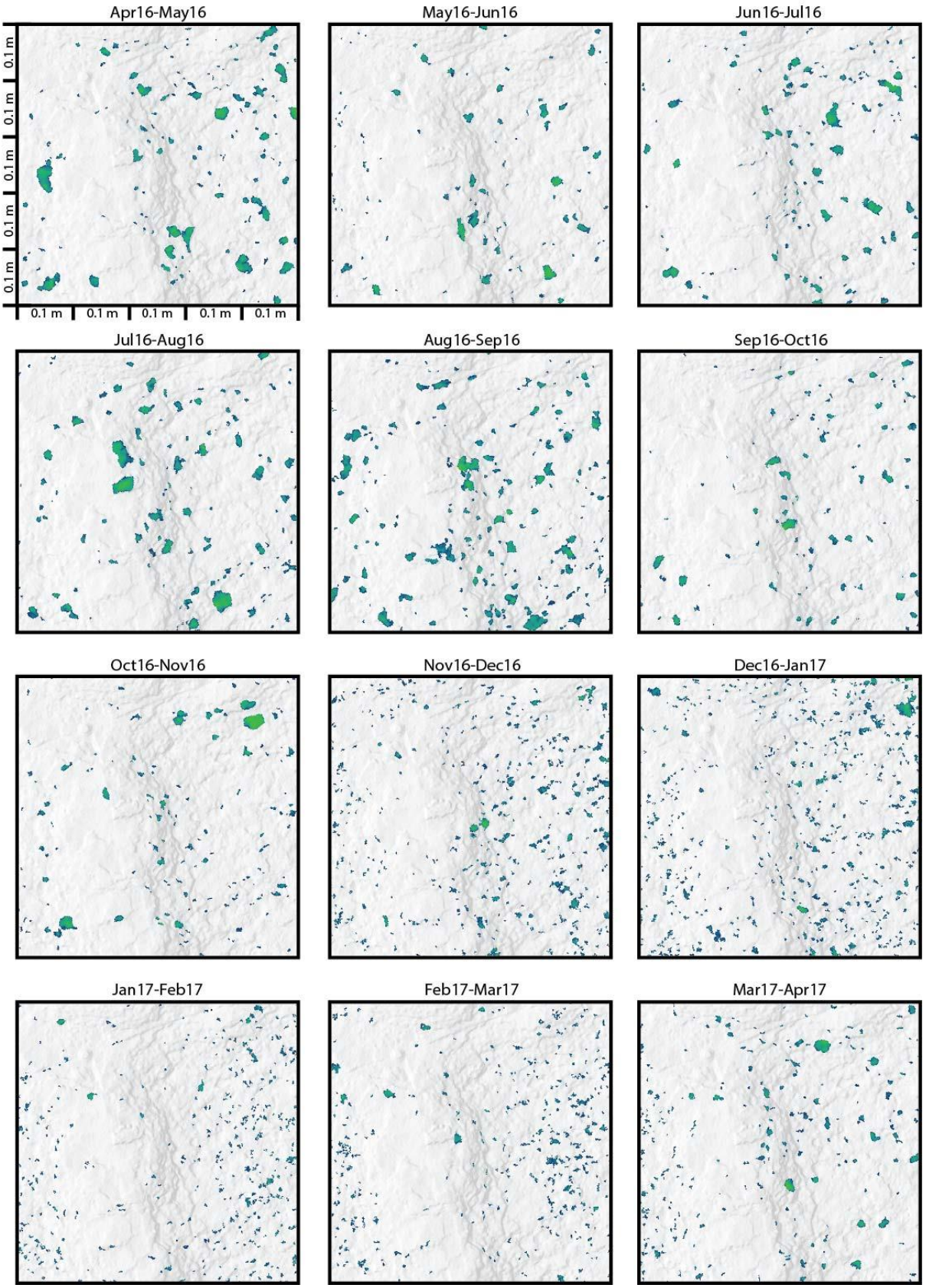
Site 2: Monthly erosion



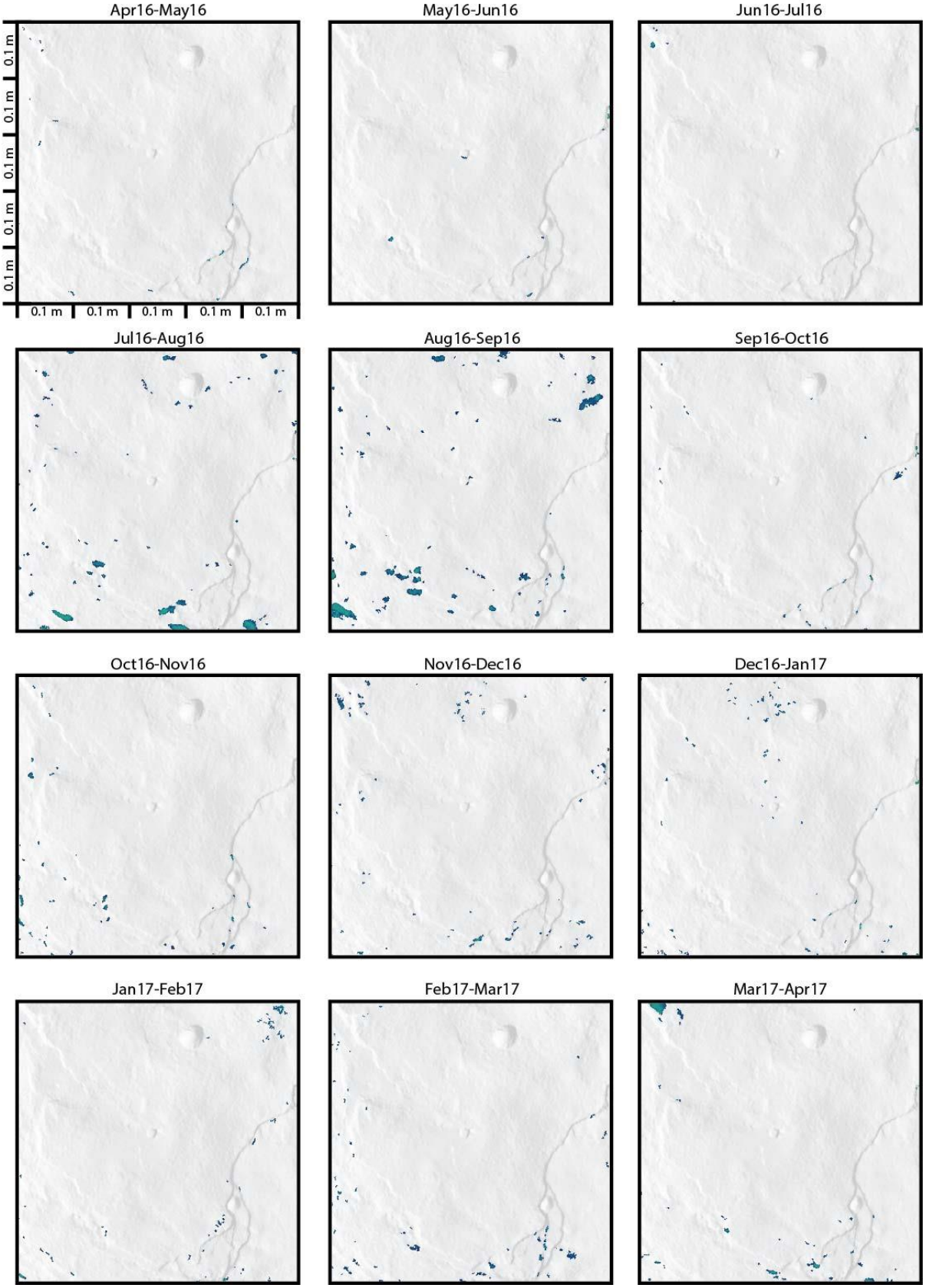
Site 3: Monthly erosion



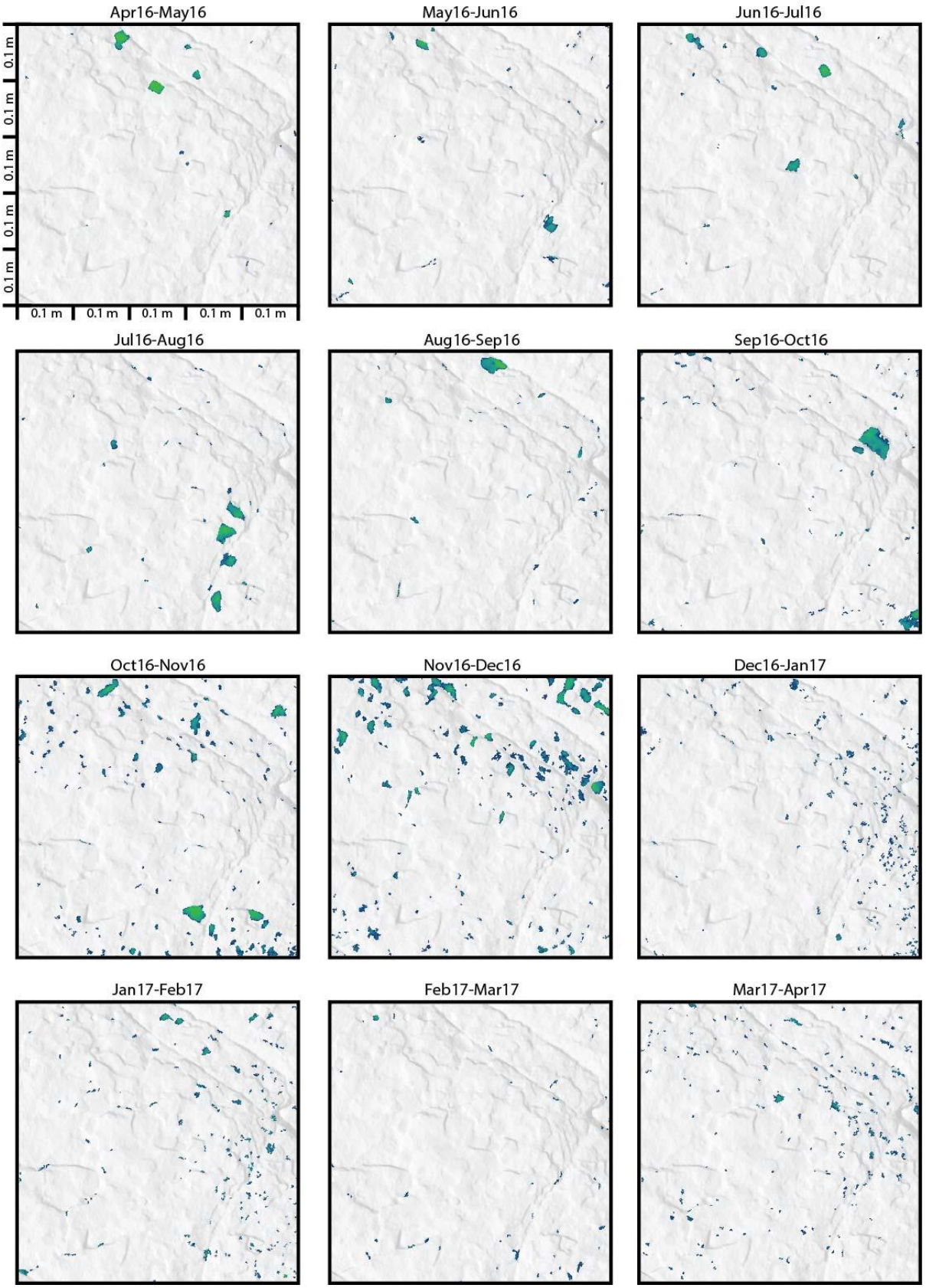
Site 4: Monthly erosion



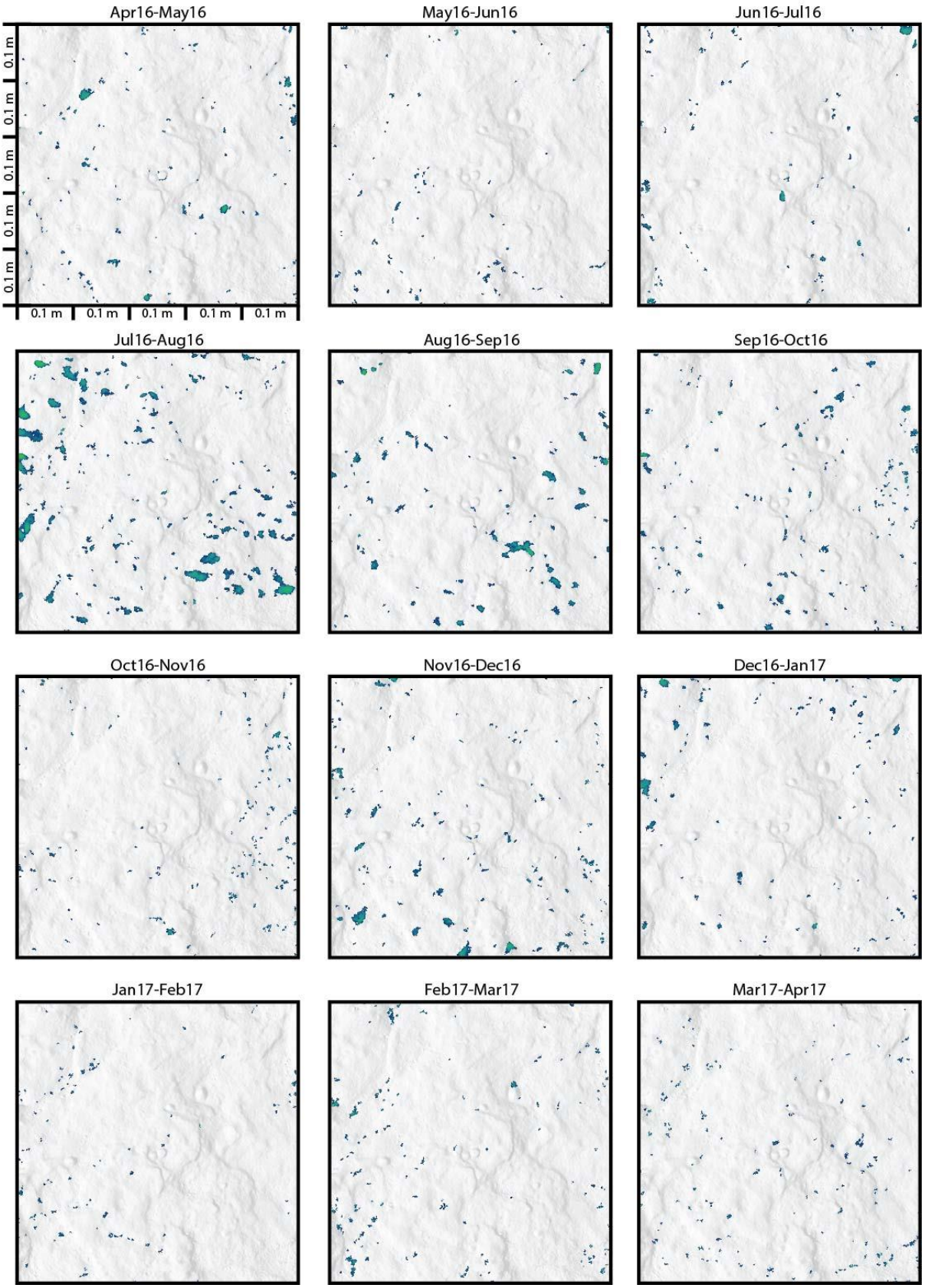
Site 5: Monthly erosion



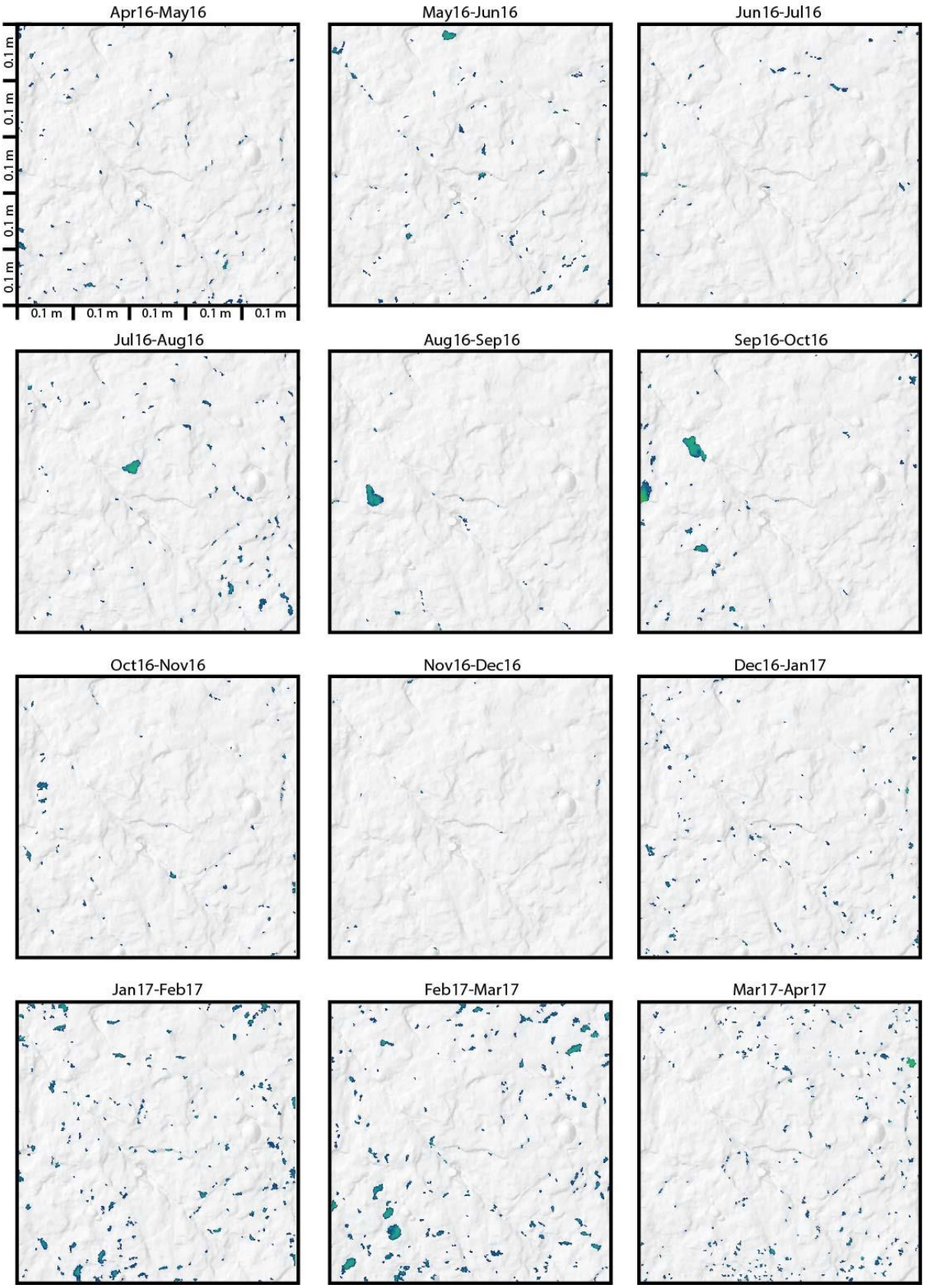
Site 6: Monthly erosion



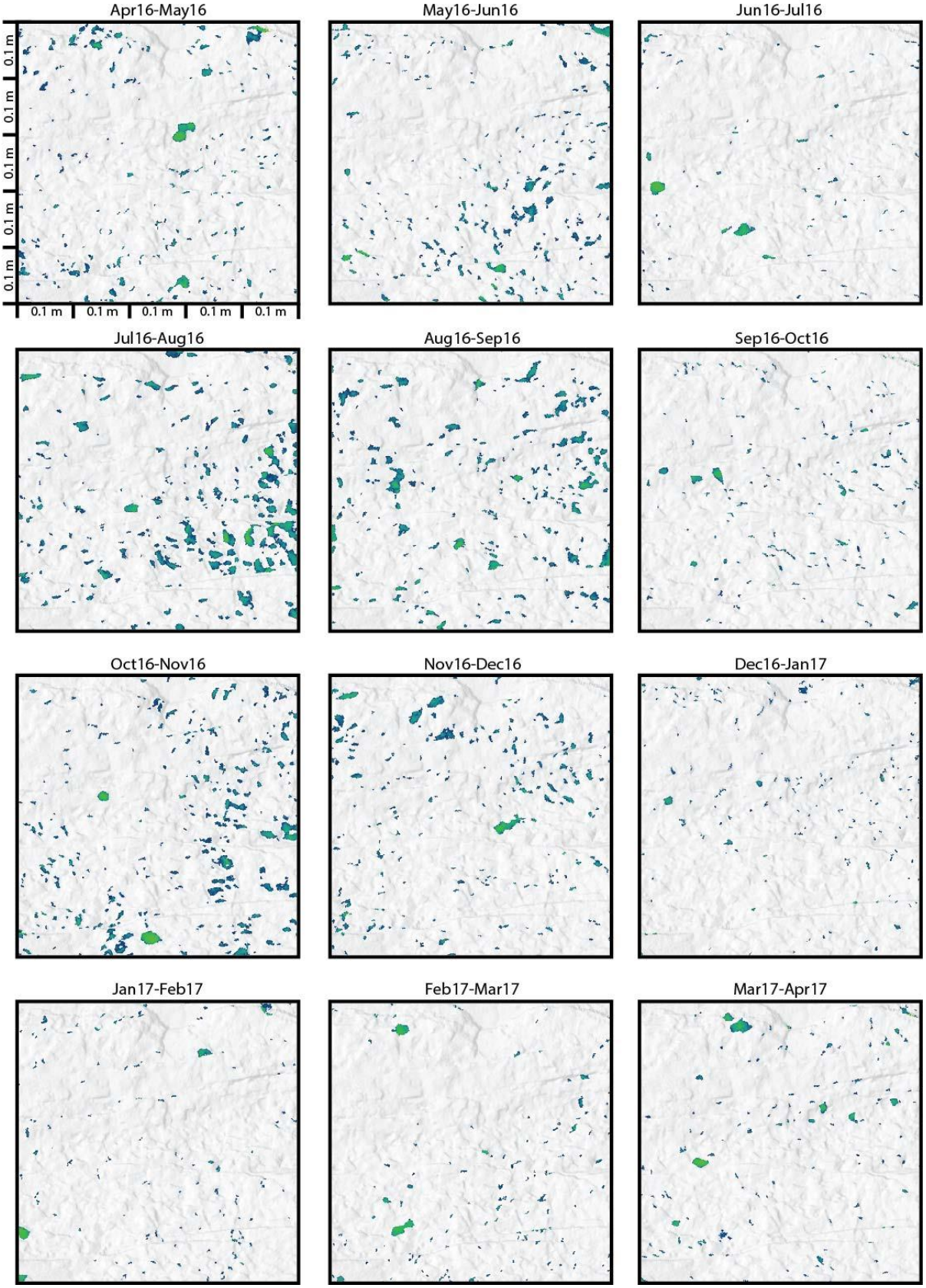
Site 7: Monthly erosion



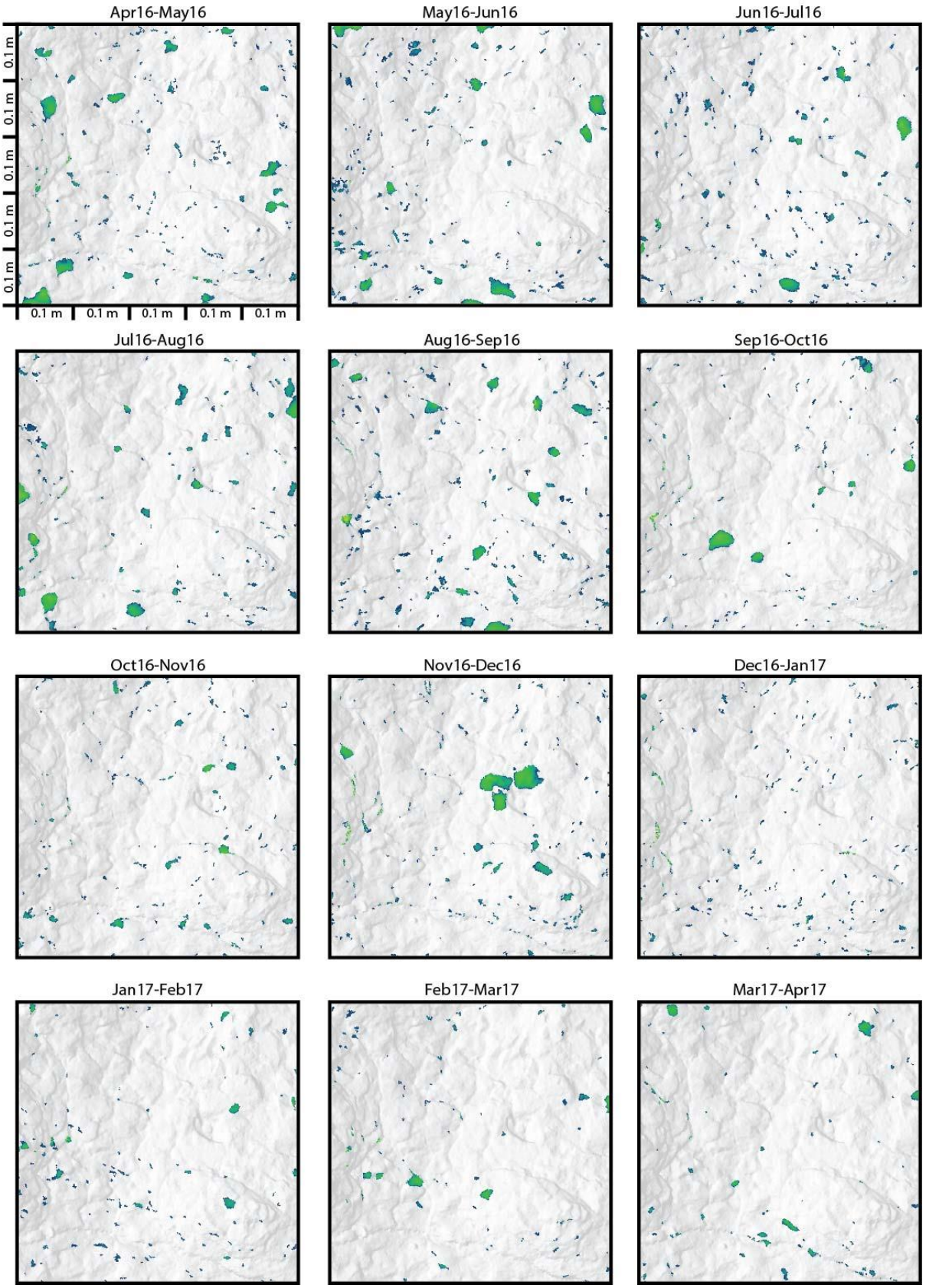
Site 8: Monthly erosion



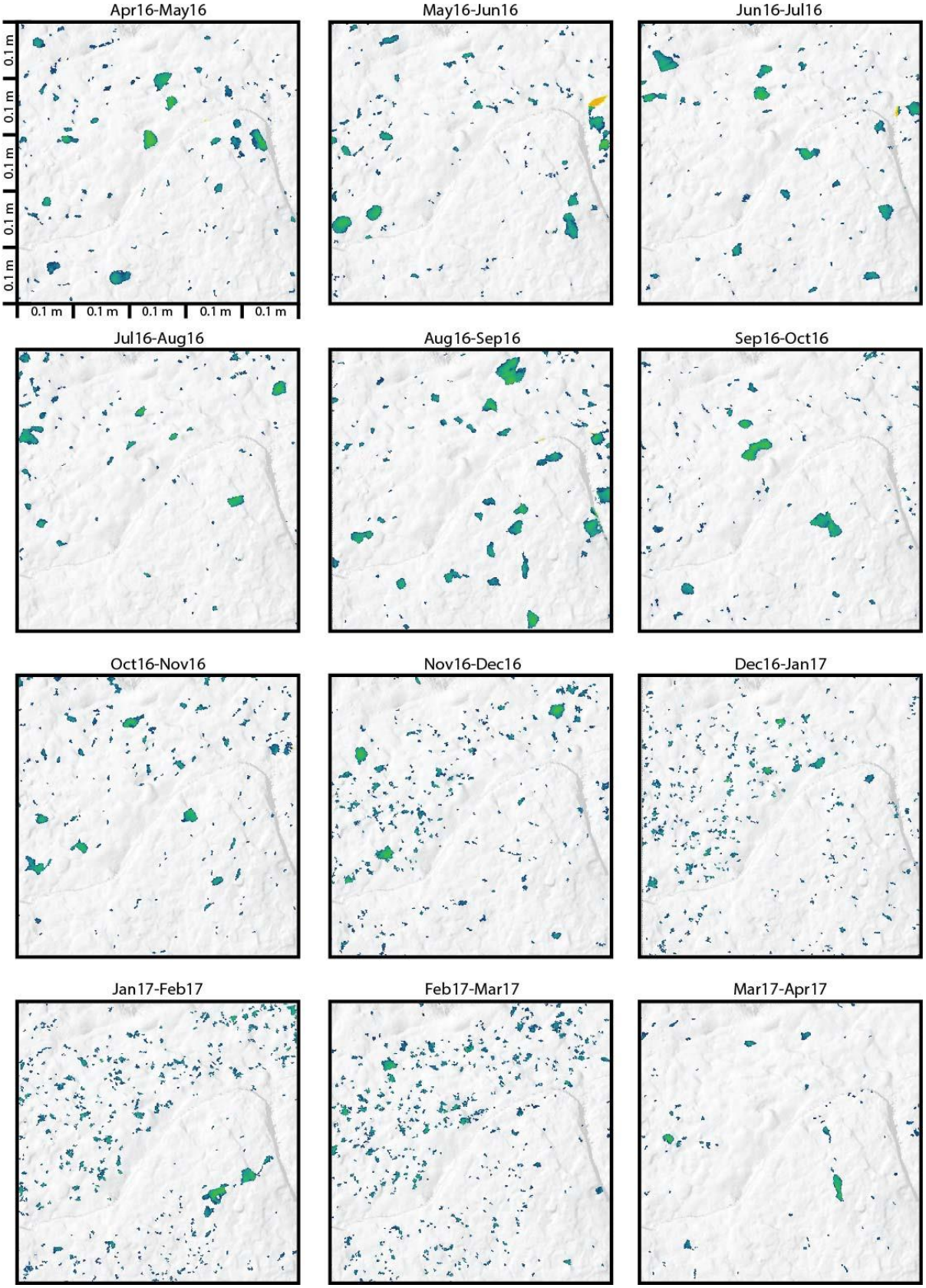
Site 9: Monthly erosion



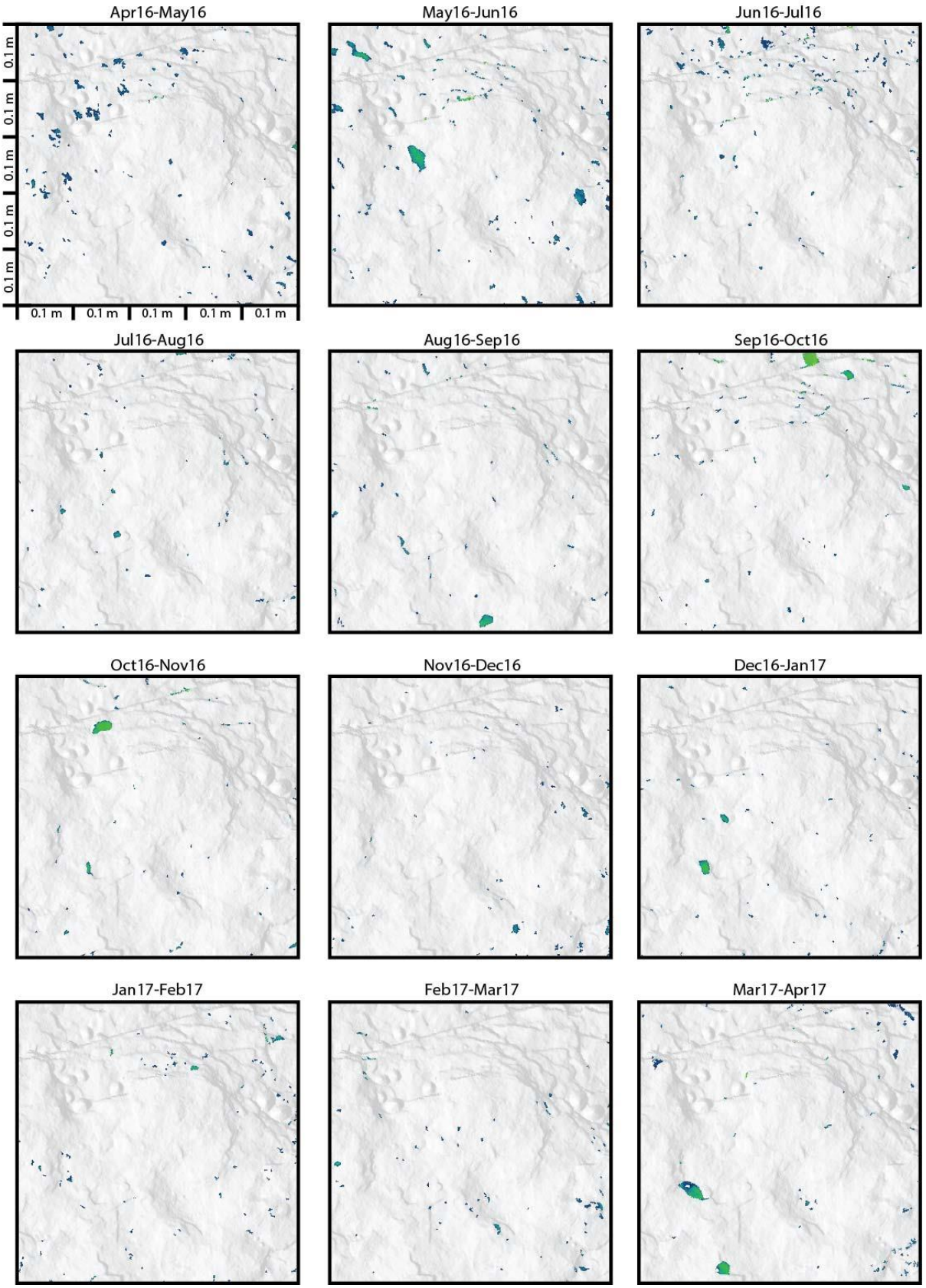
Site 10: Monthly erosion



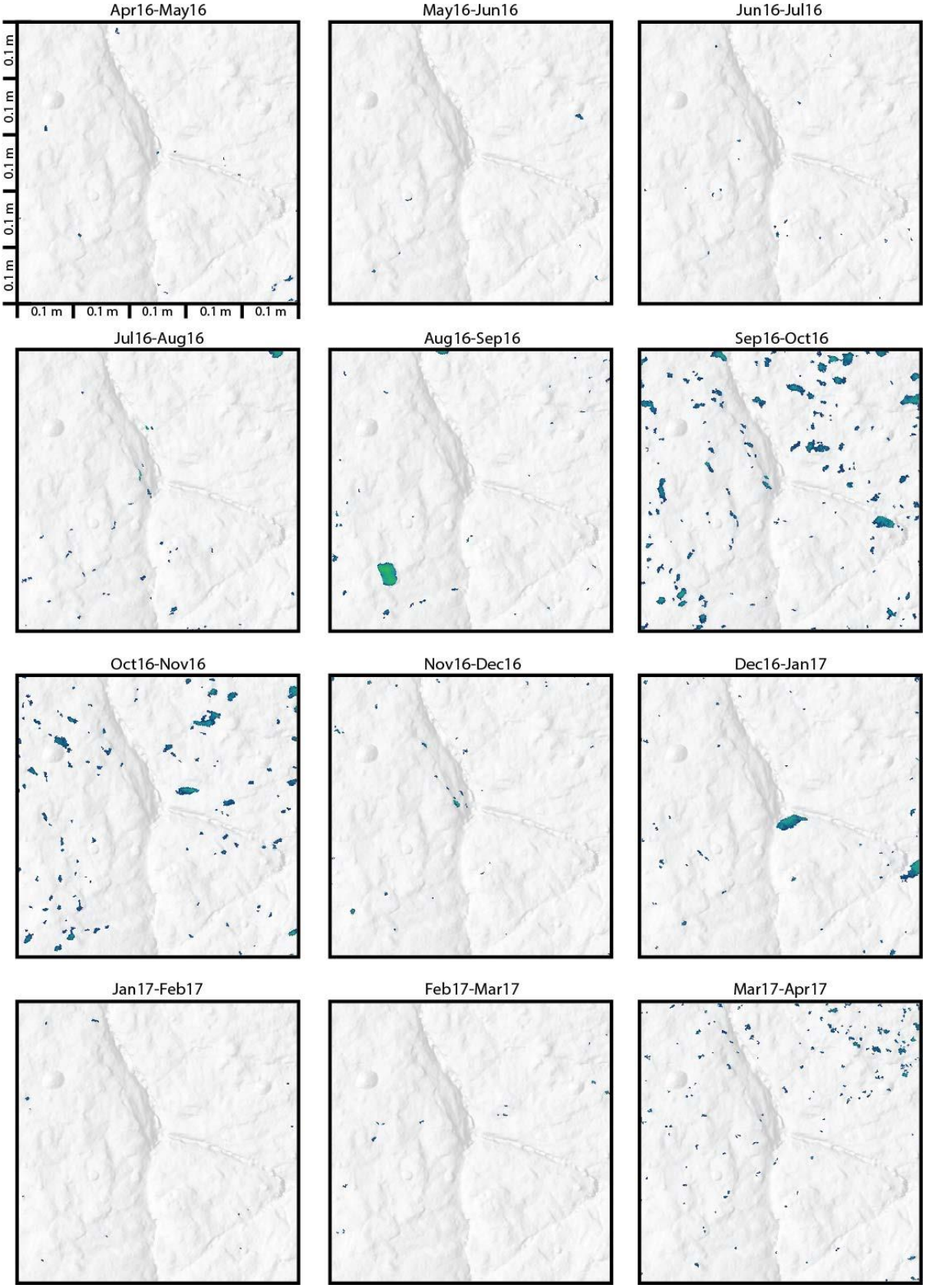
Site 11: Monthly erosion



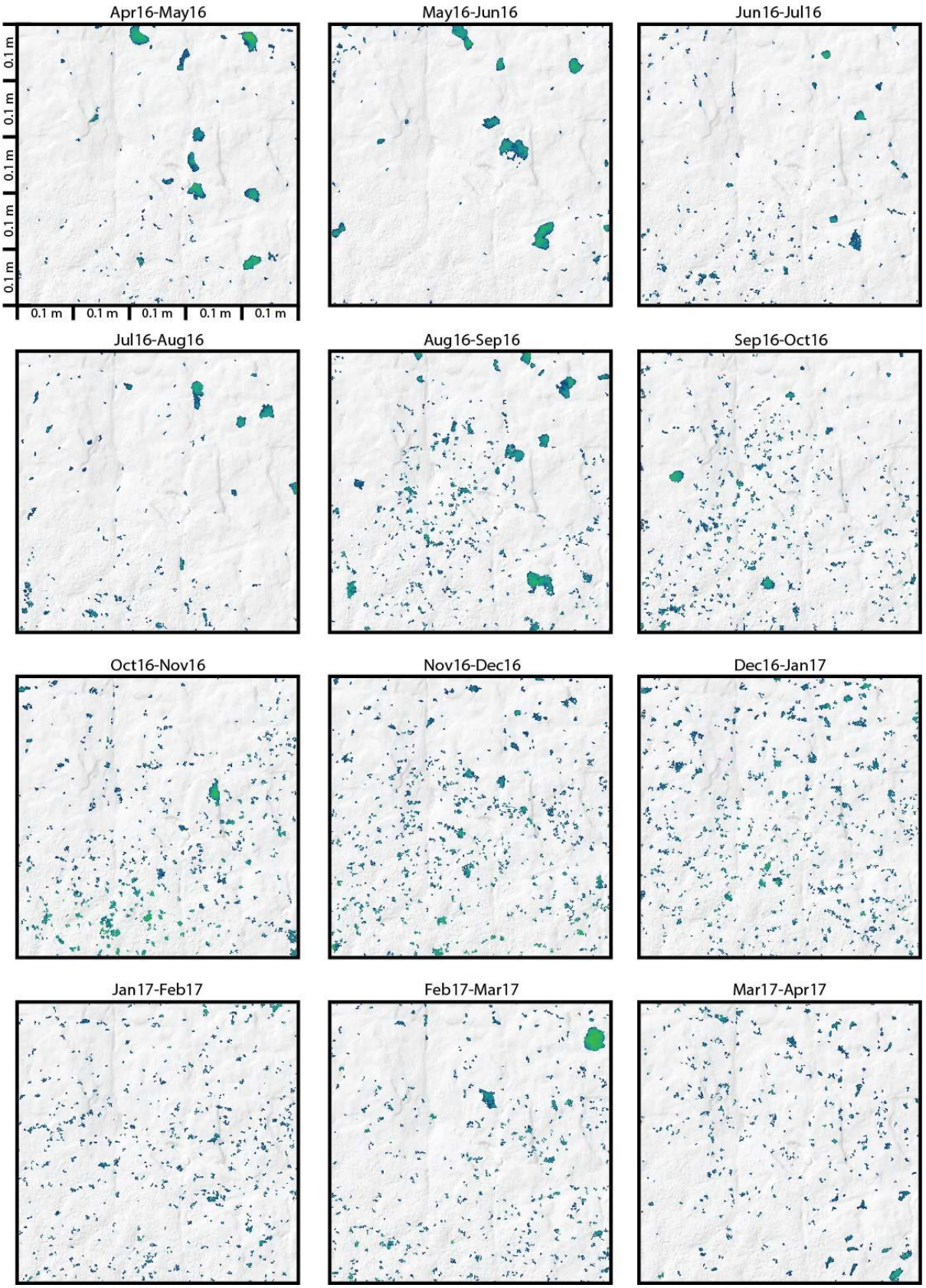
Site 12: Monthly erosion



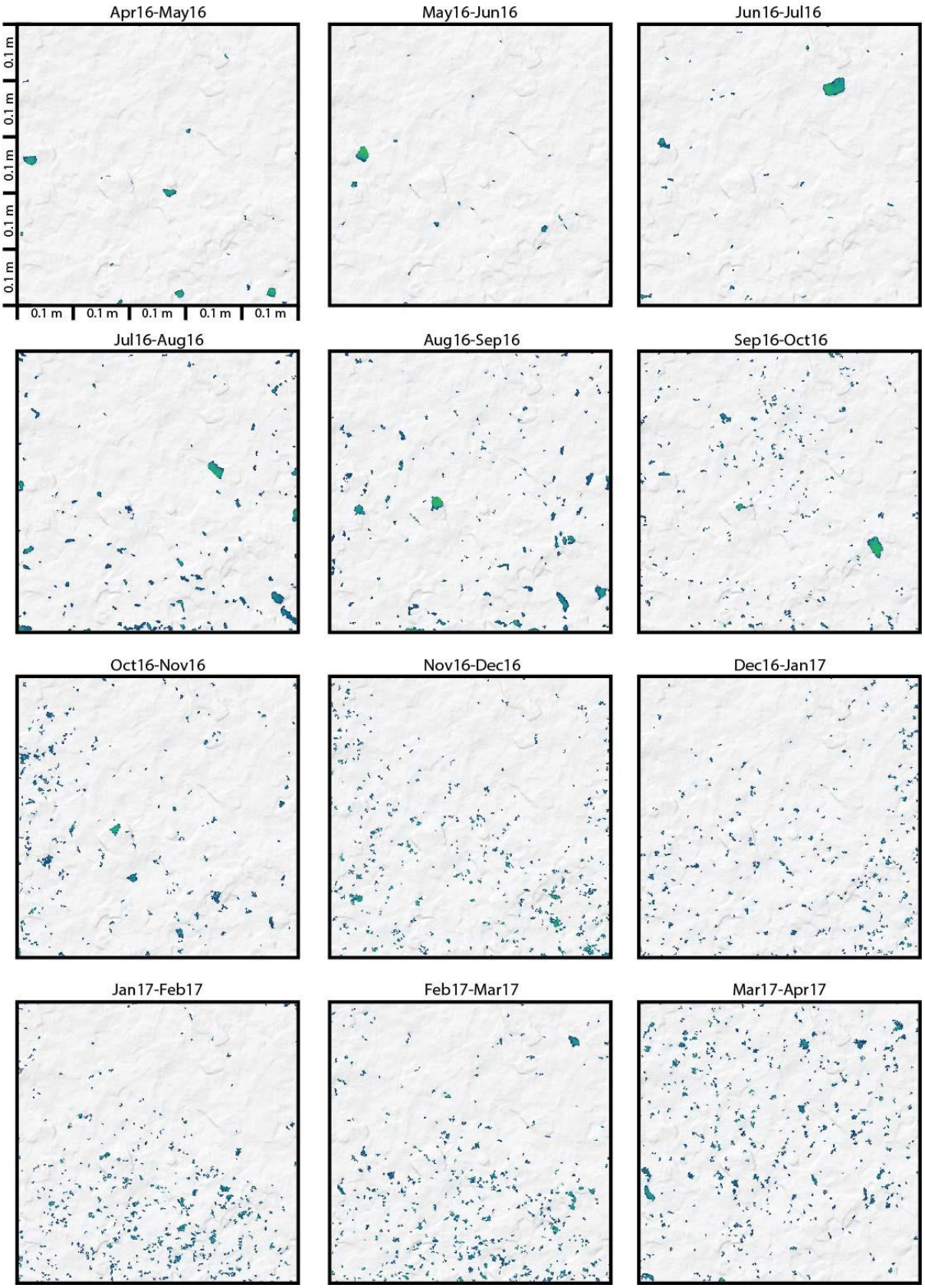
Site 13: Monthly erosion



Site 14: Monthly erosion

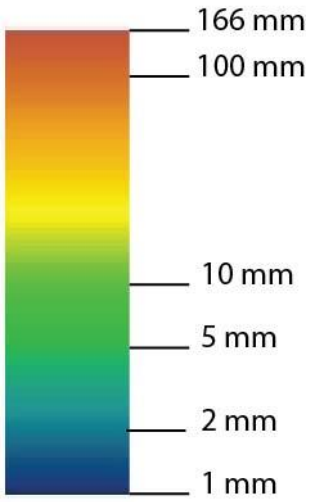


Site 15: Monthly erosion

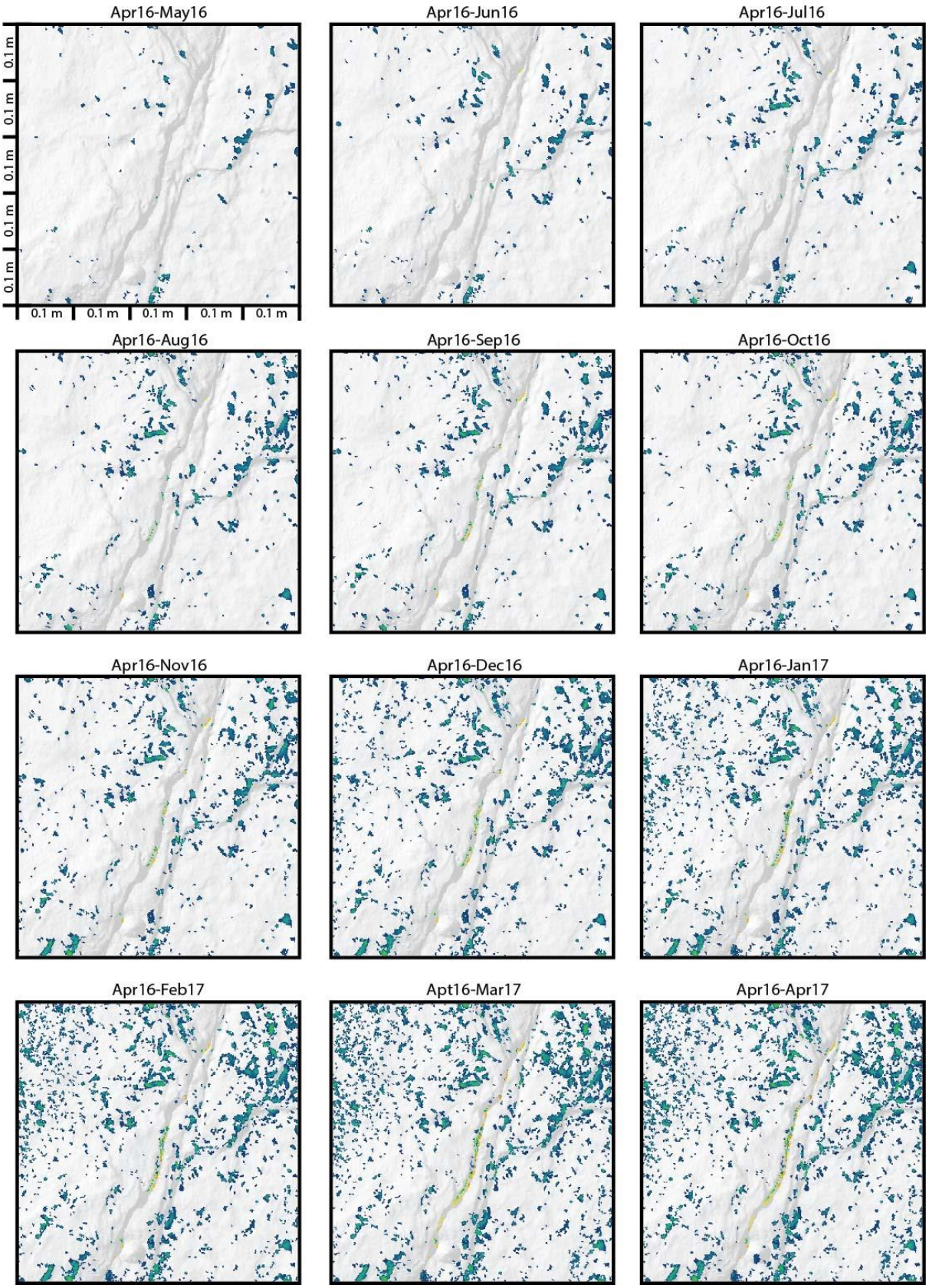


Appendix 7: Cumulative erosion (depth) at each micro-erosion monitoring site.

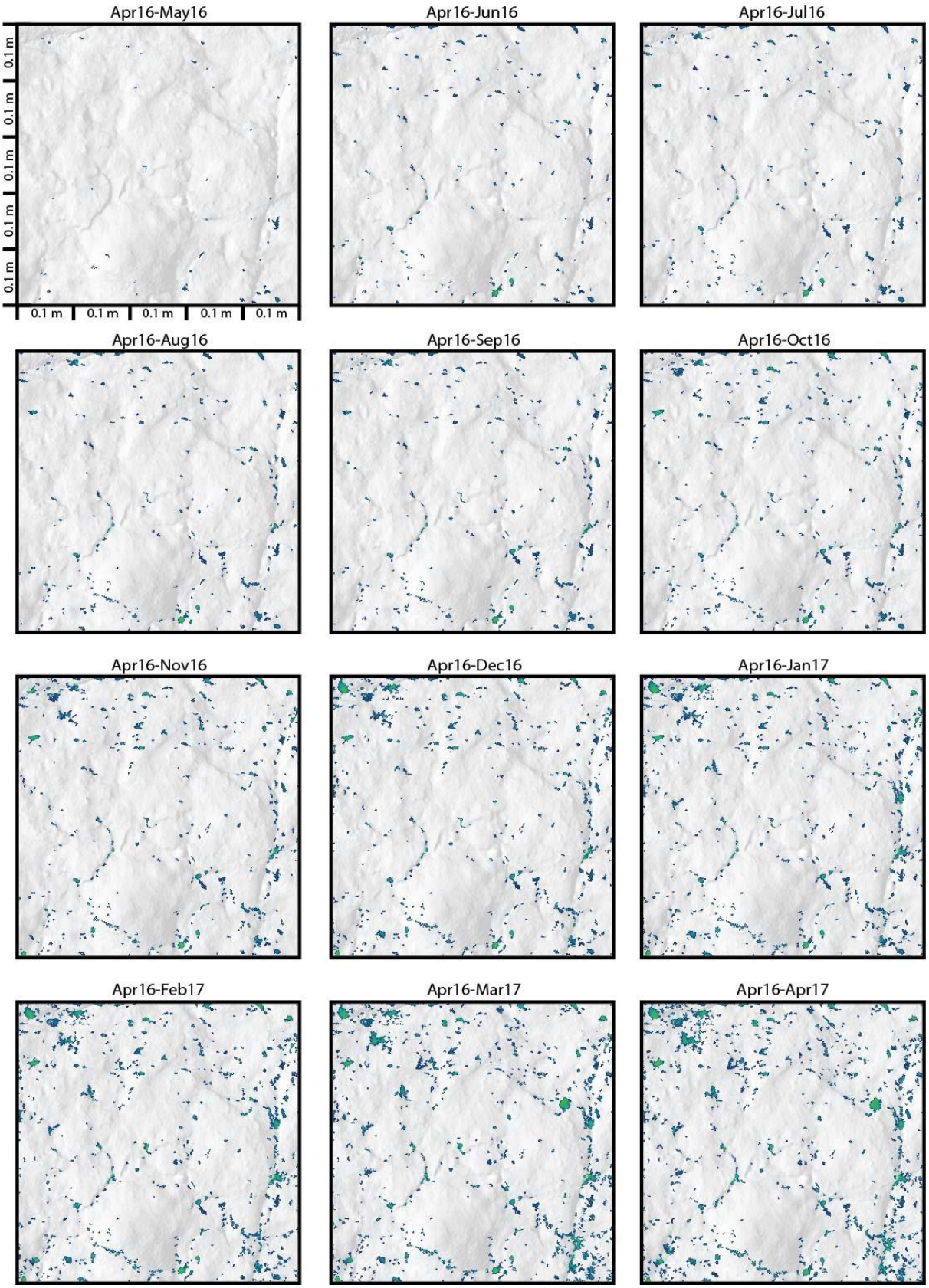
The background image is hillshade at 80% transparency created from the Apr'16 DEM. The same logarithmic scale bar is applied to all sites, as shown below.



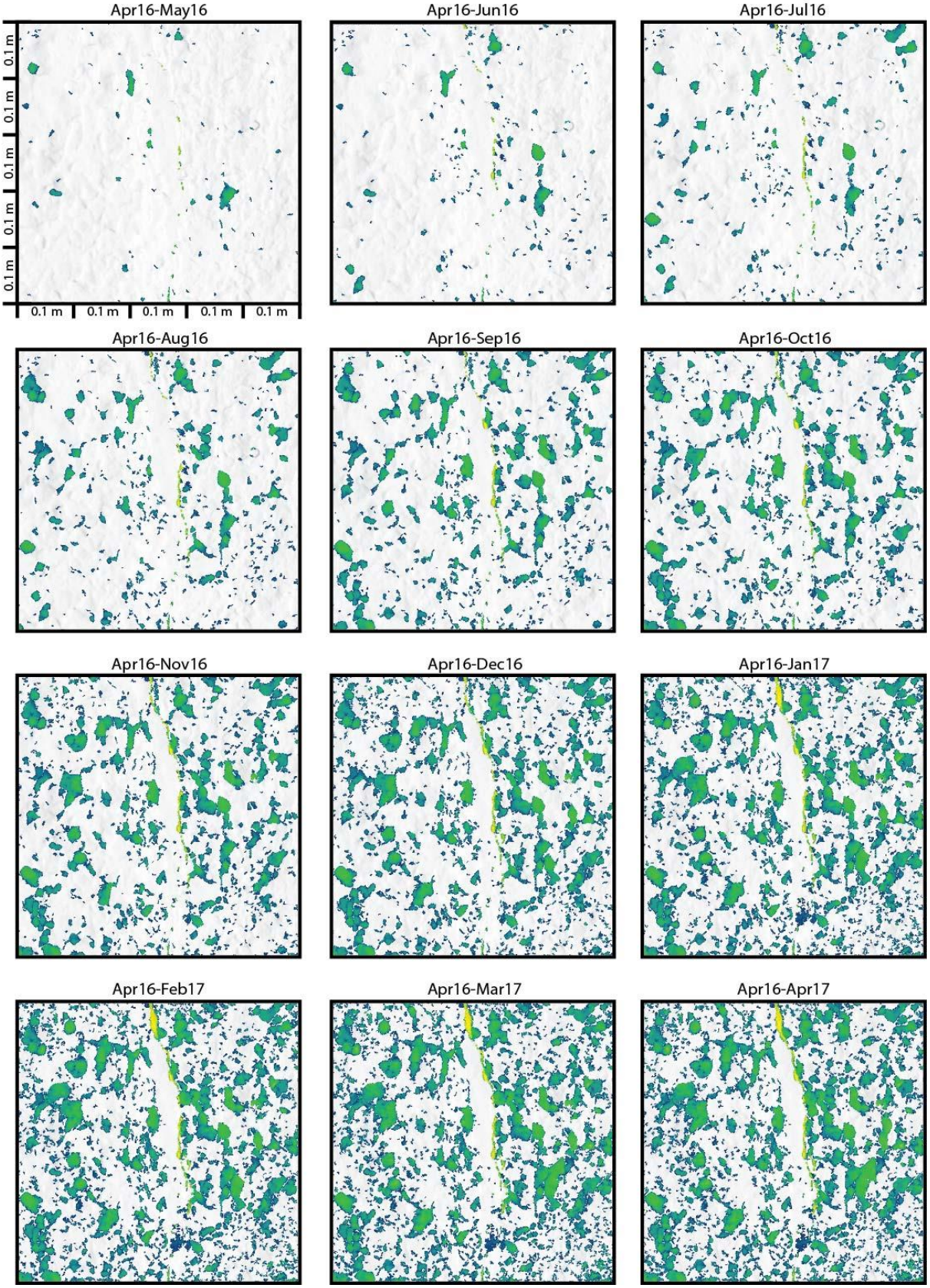
Site 1: Cumulative erosion



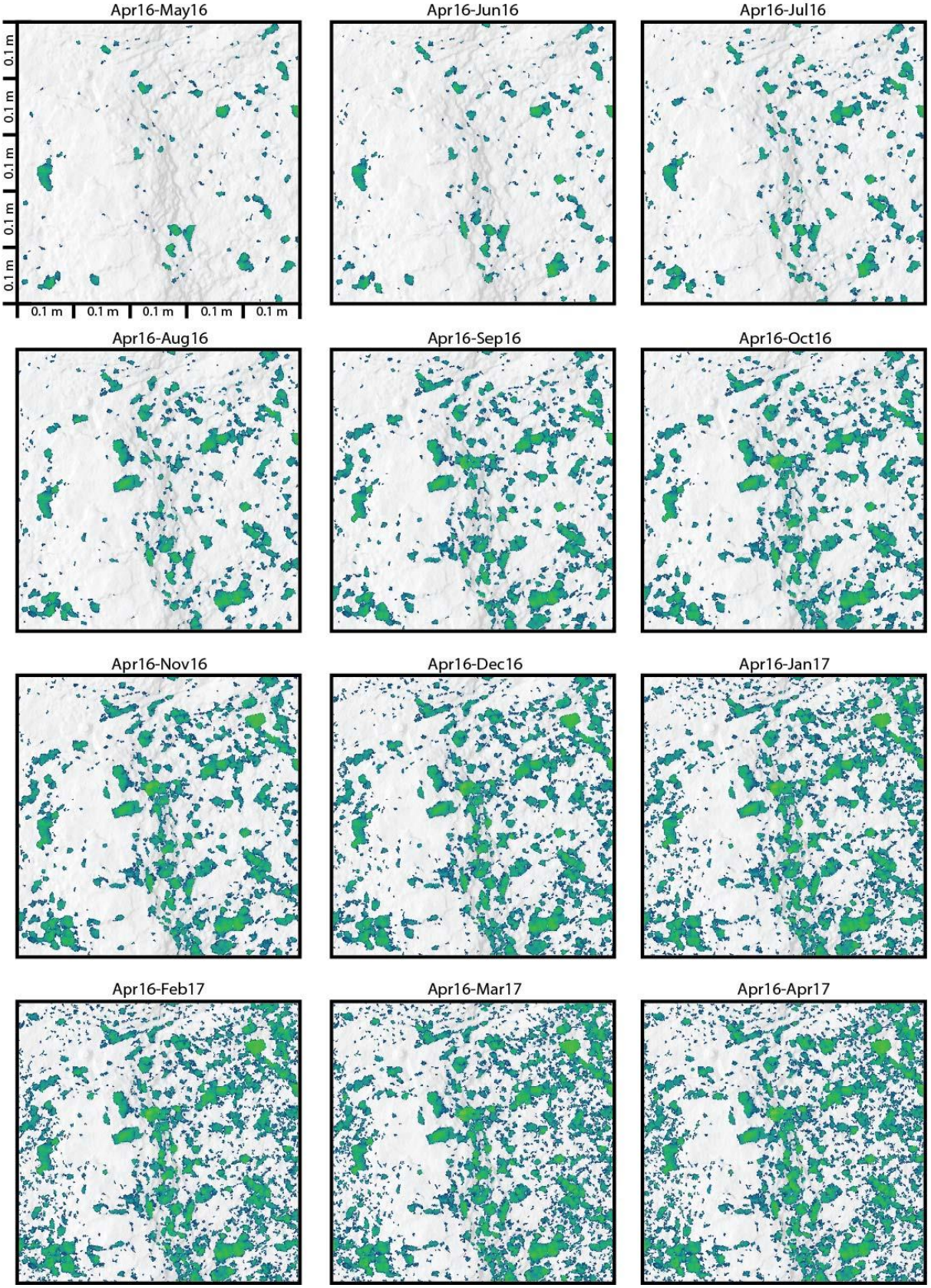
Site 2: Cumulative erosion



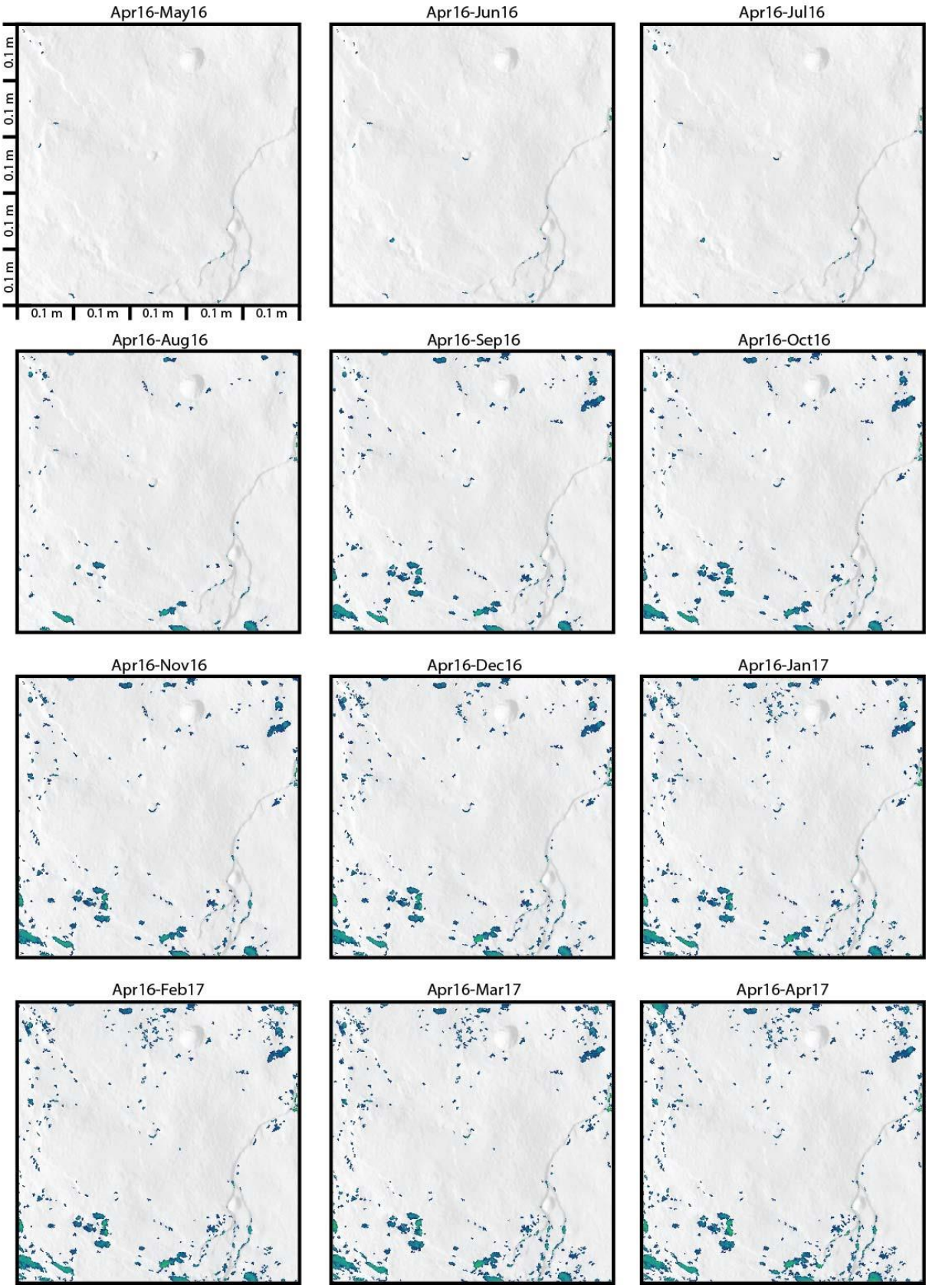
Site 3: Cumulative erosion



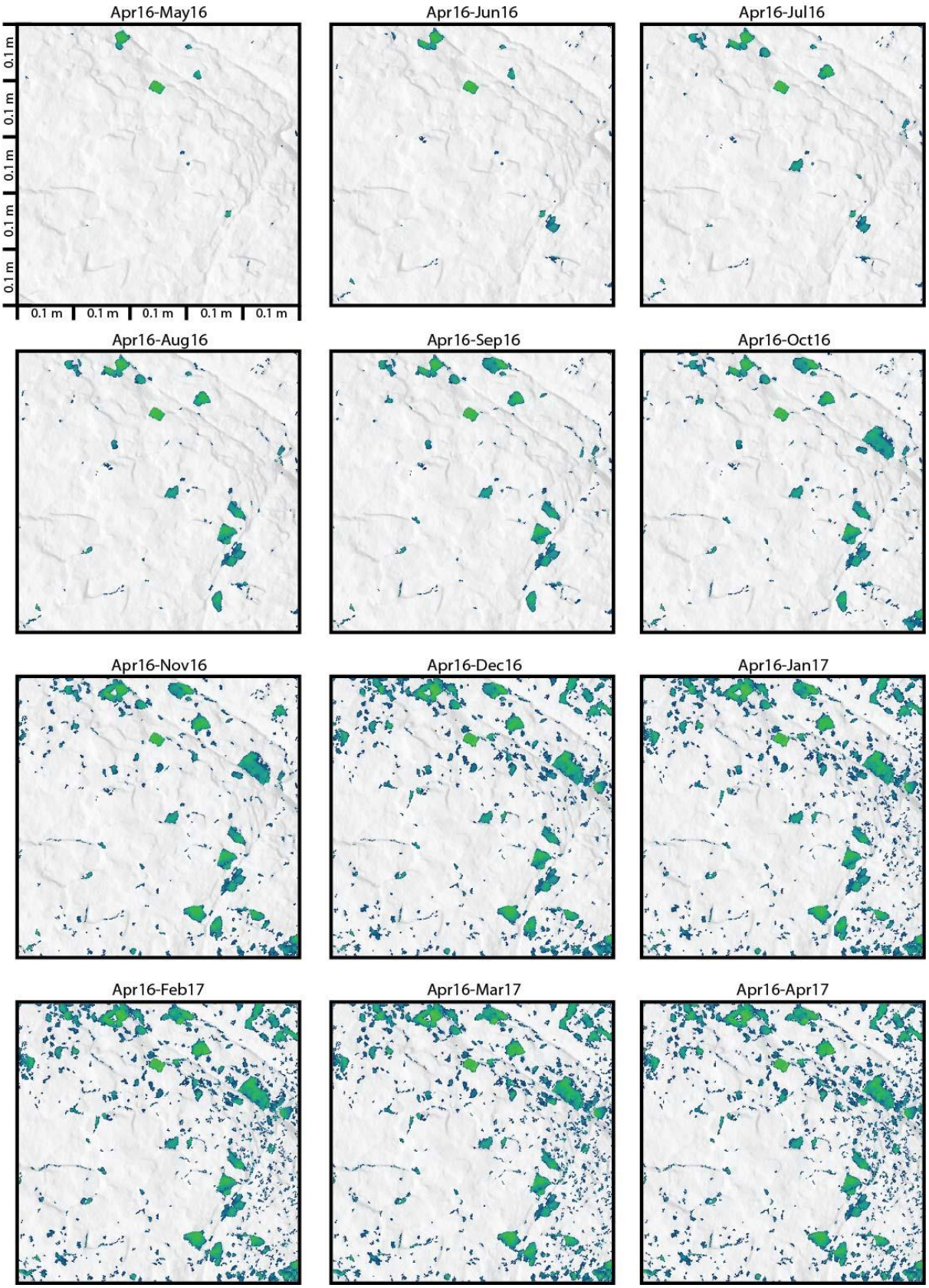
Site 4: Cumulative erosion



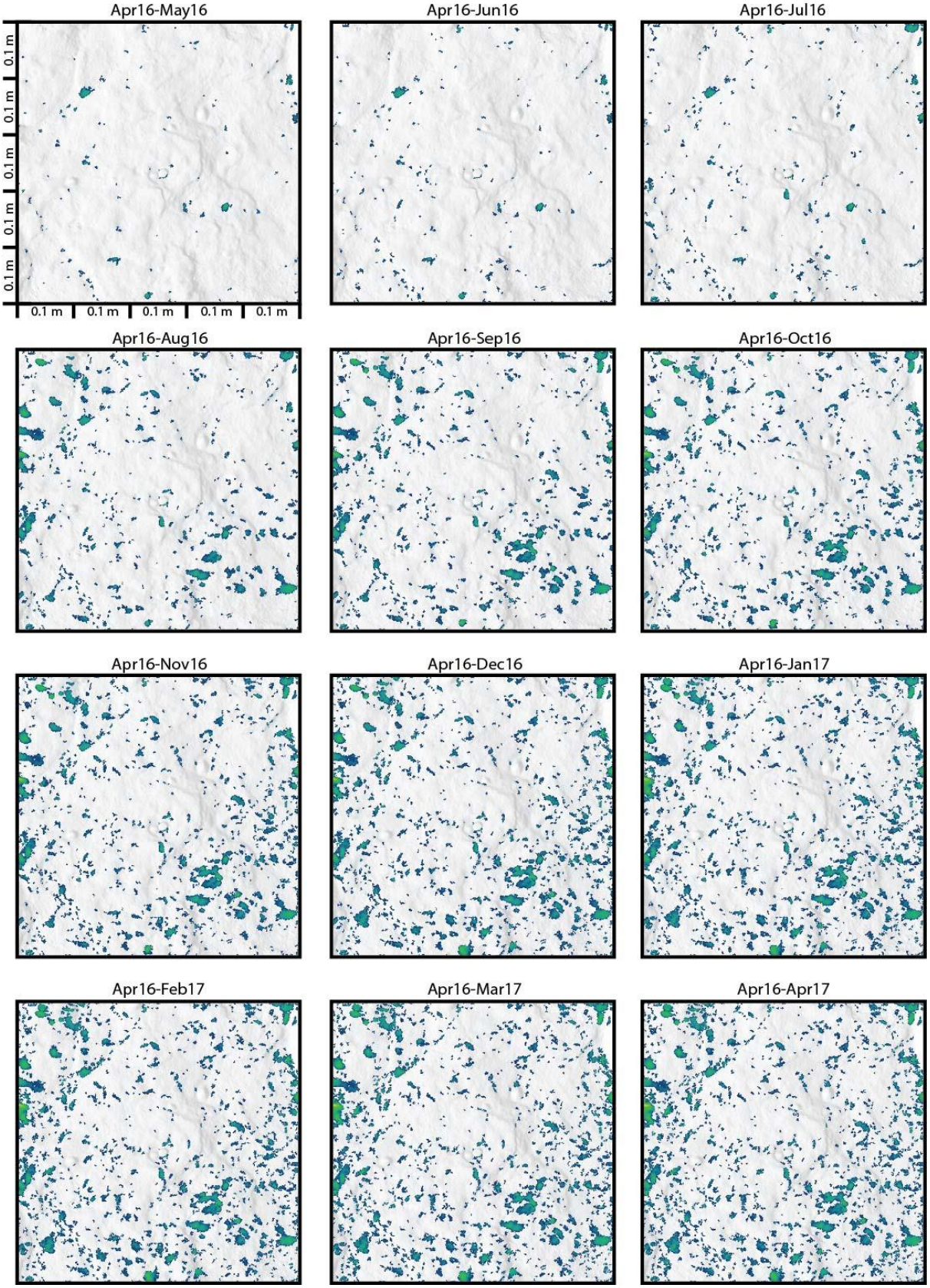
Site 5: Cumulative erosion



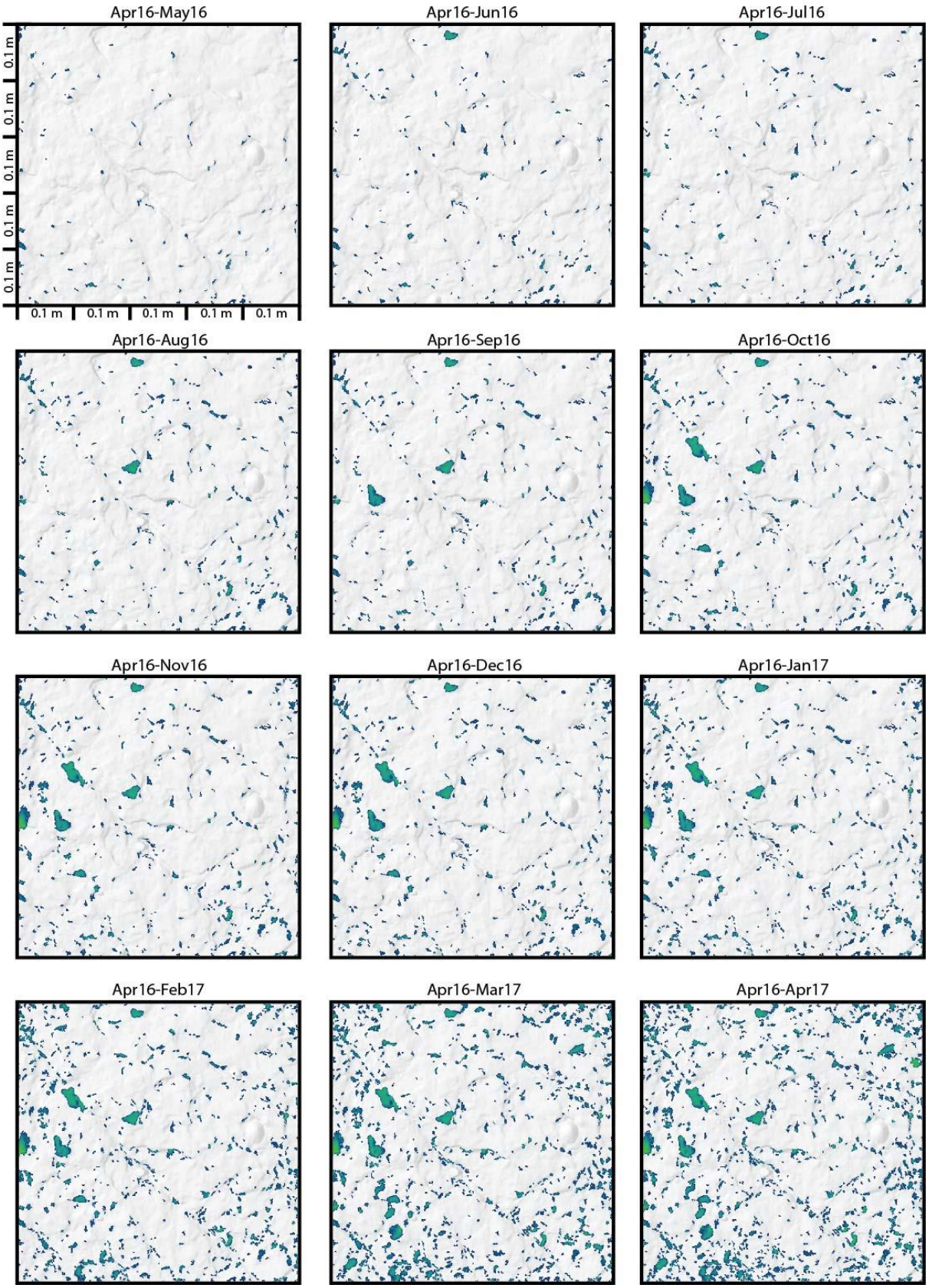
Site 6: Cumulative erosion



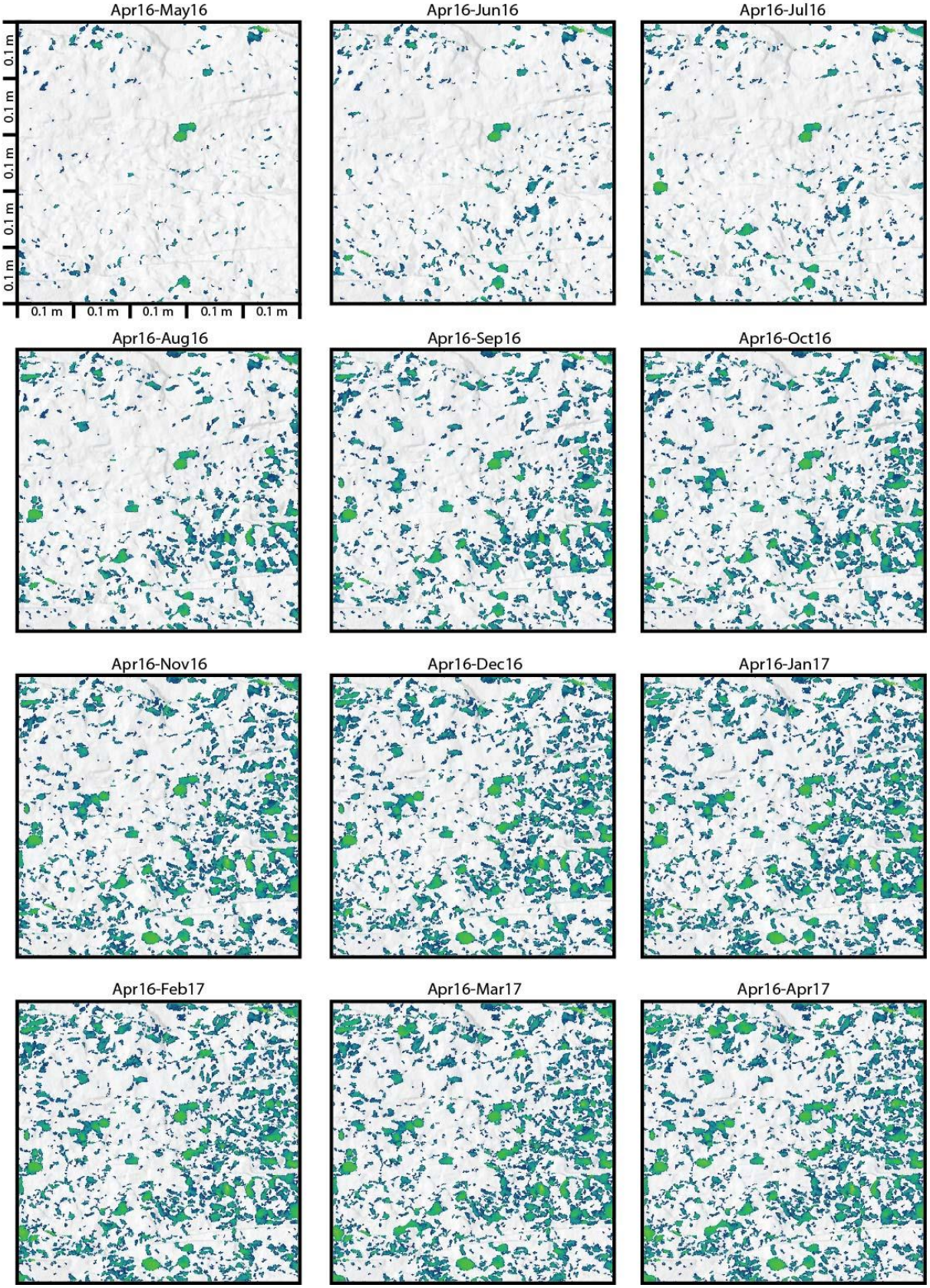
Site 7: Cumulative erosion



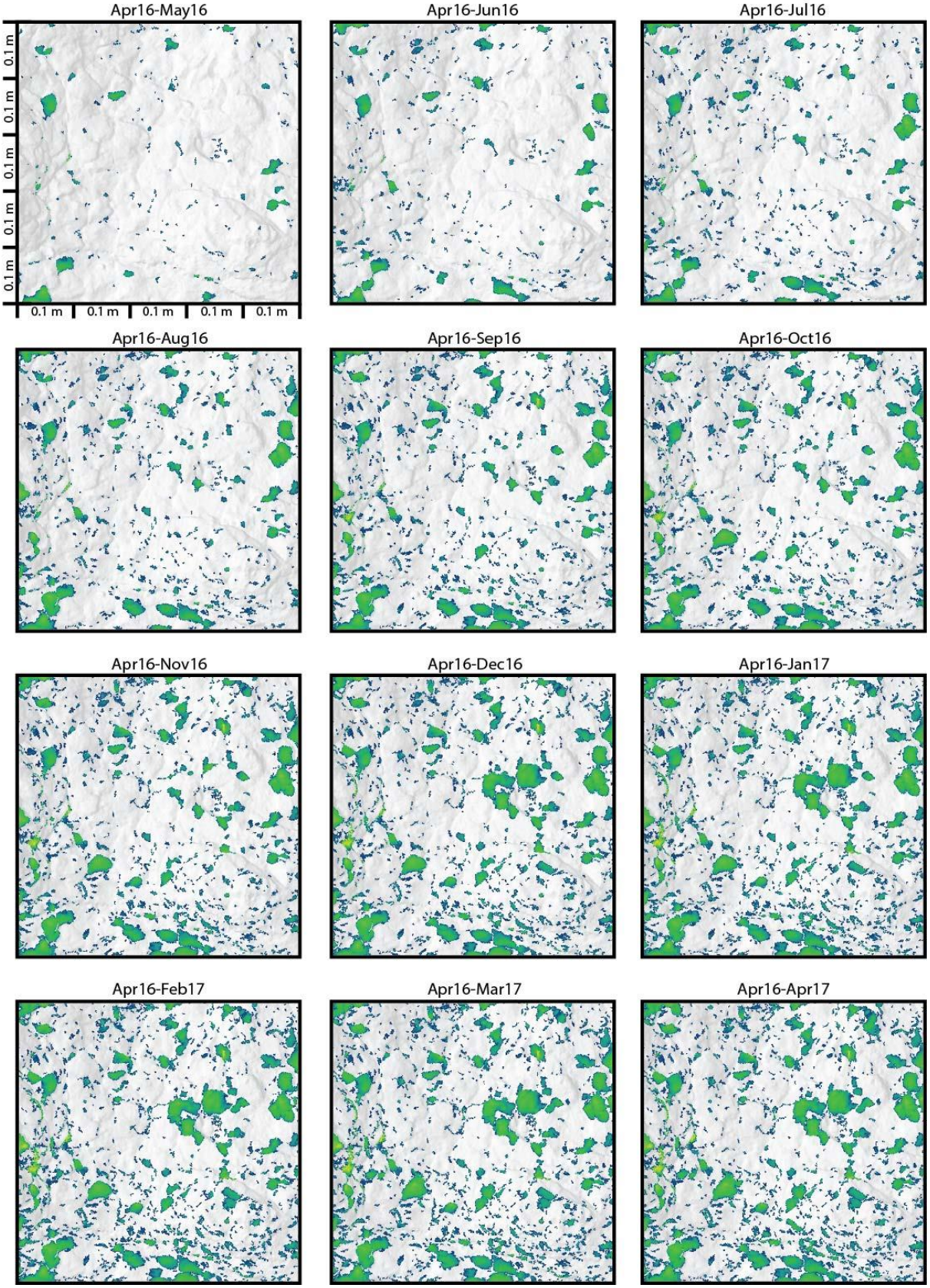
Site 8: Cumulative erosion



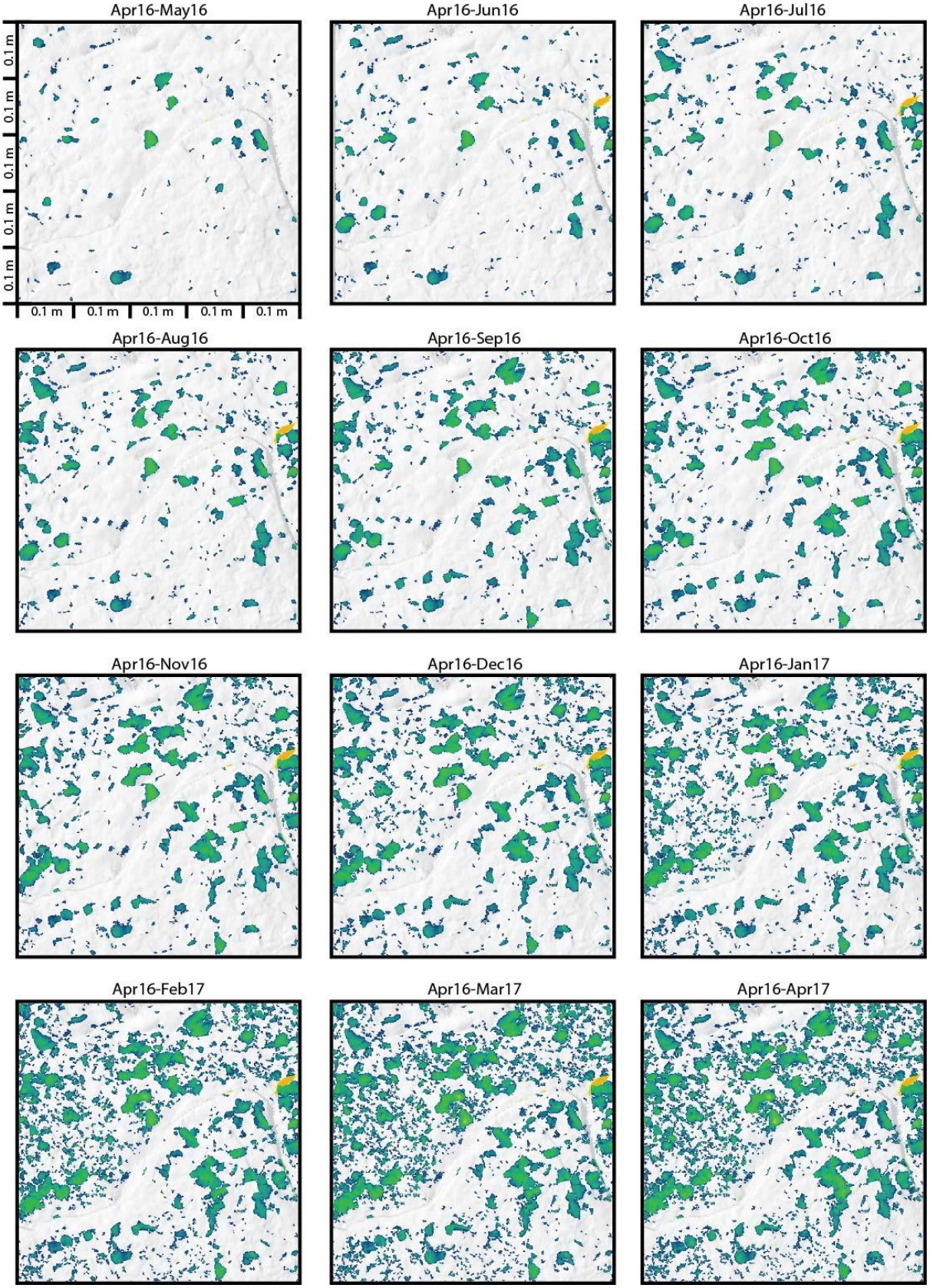
Site 9: Cumulative erosion



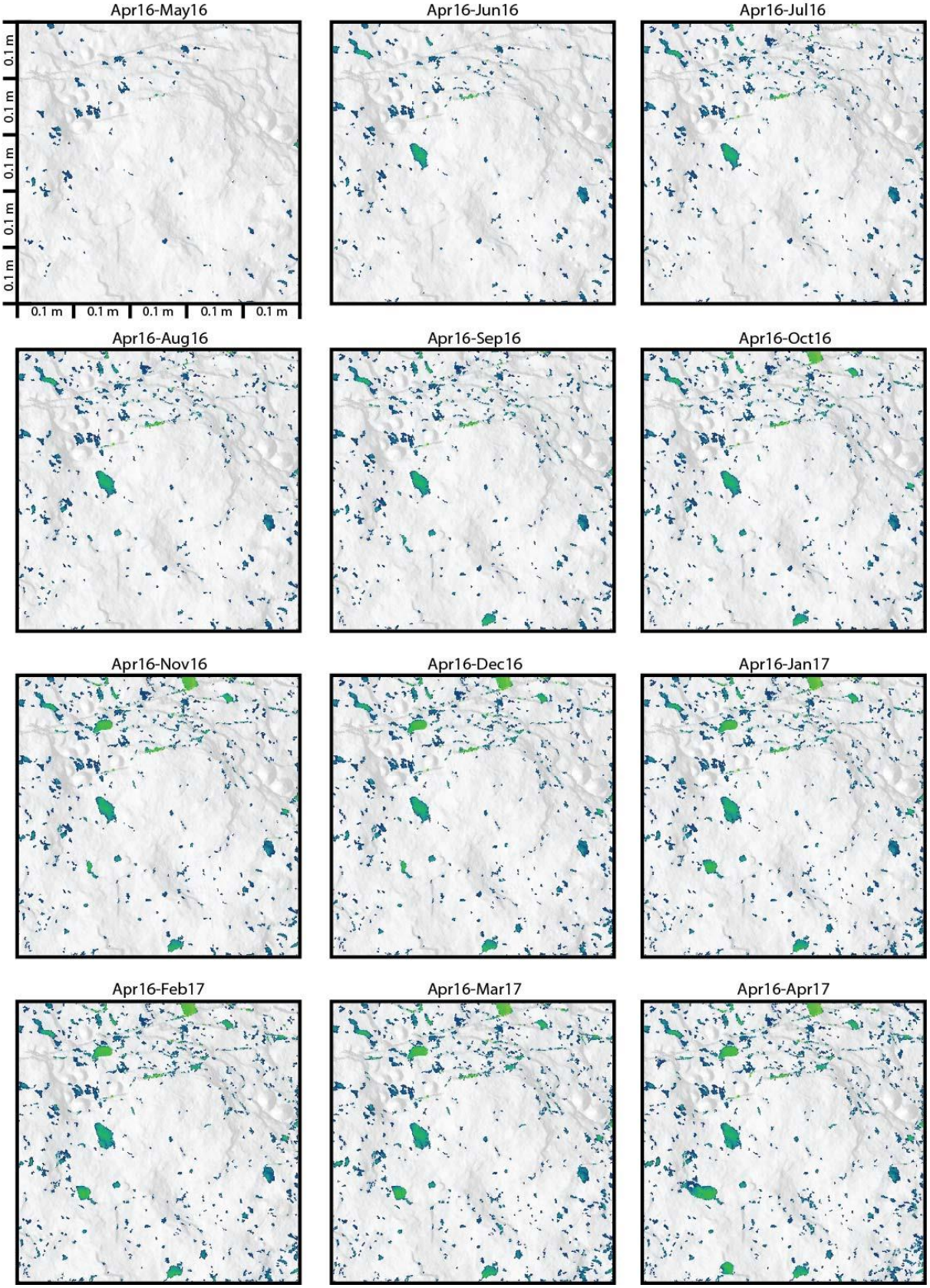
Site 10: Cumulative erosion



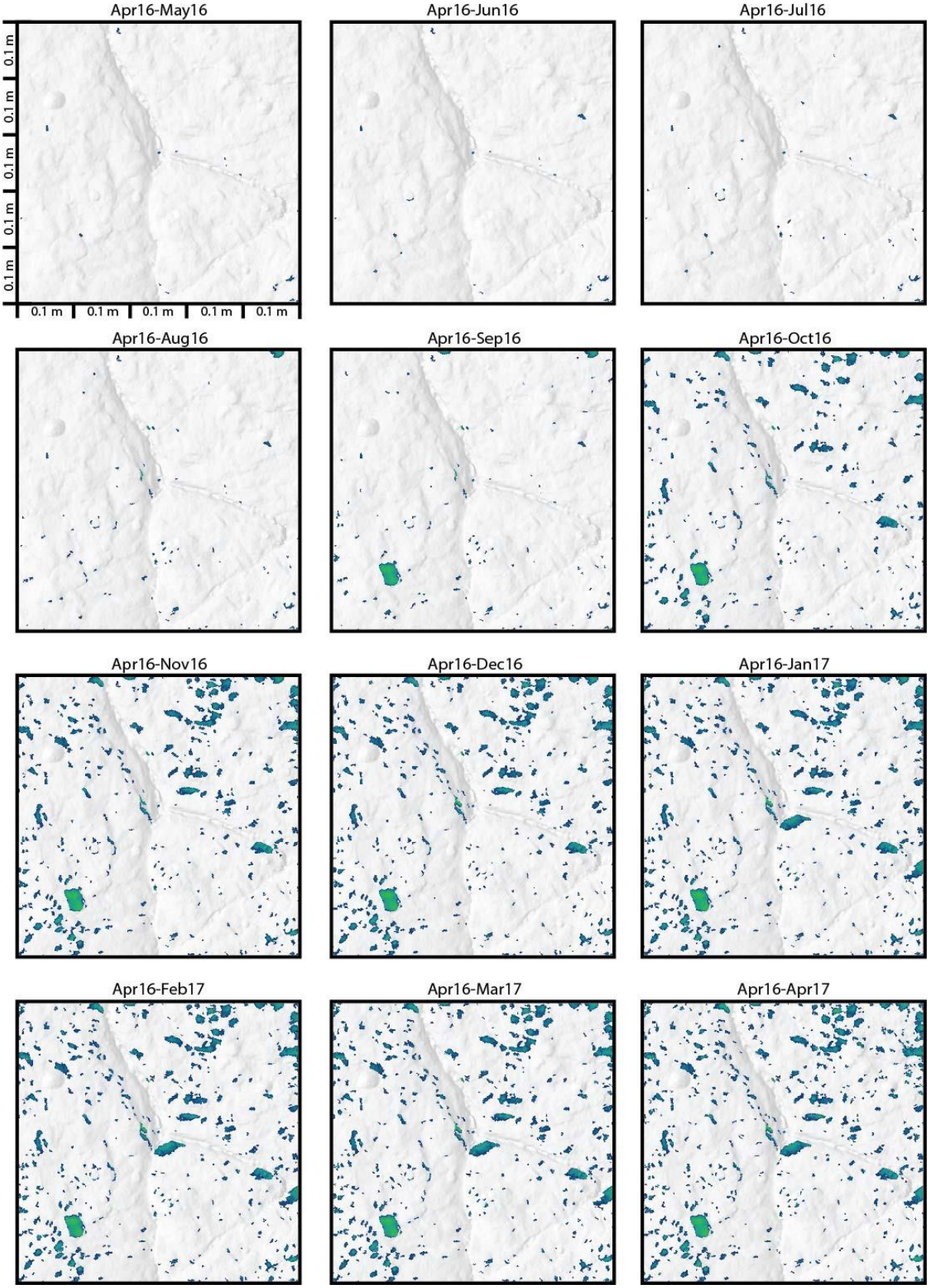
Site 11: Cumulative erosion



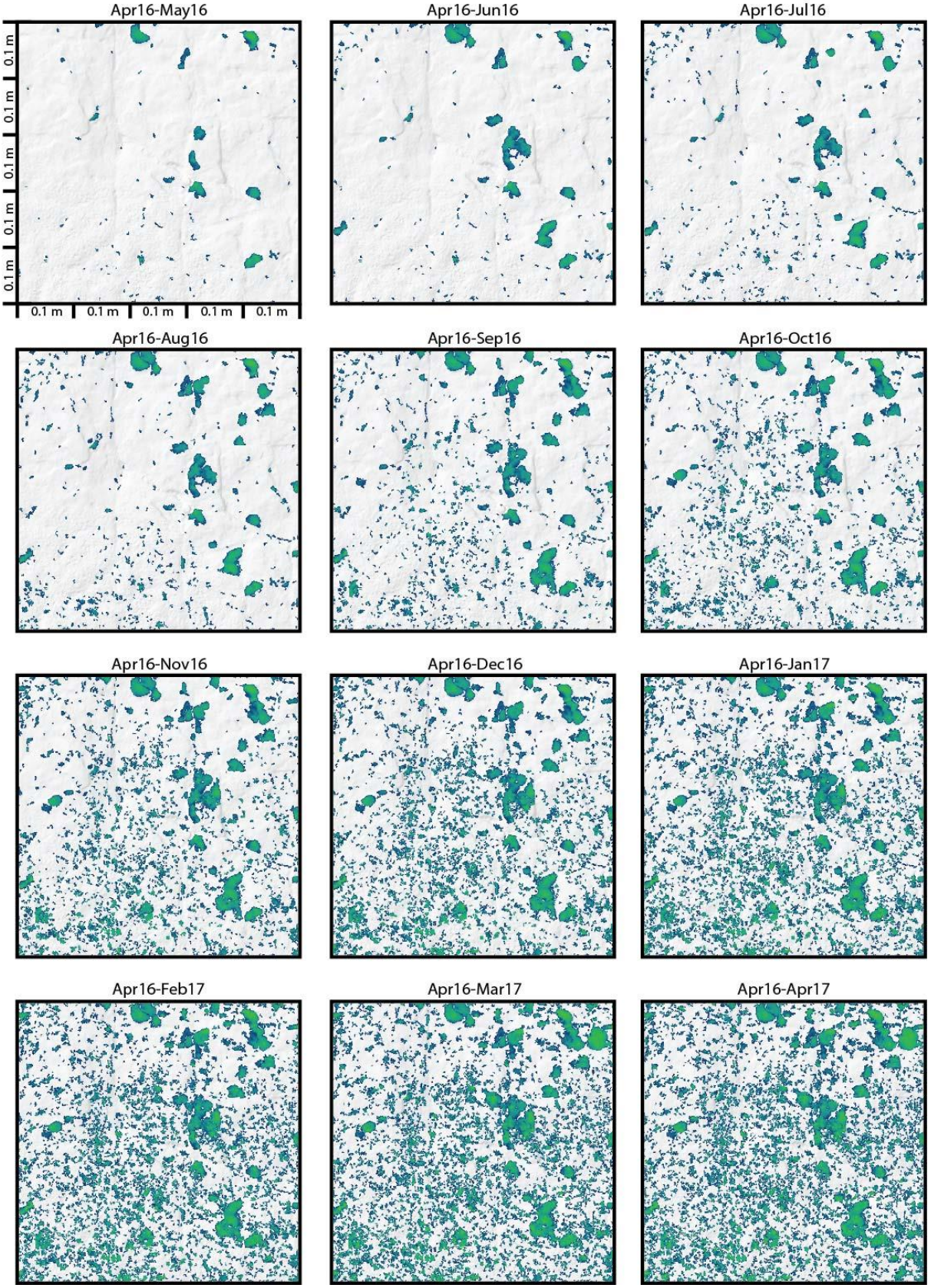
Site 12: Cumulative erosion



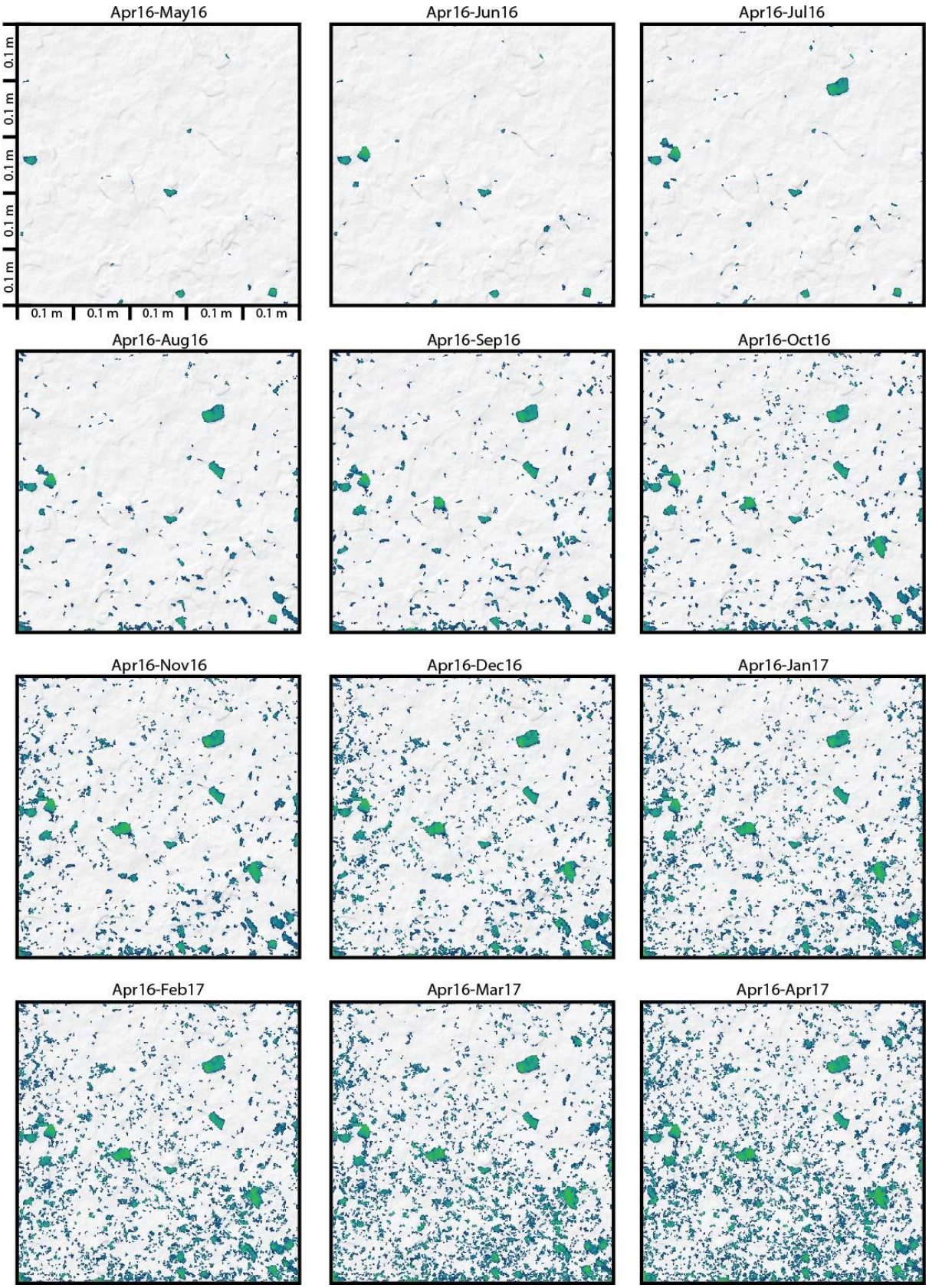
Site 13: Cumulative erosion



Site 14: Cumulative erosion



Site 15: Cumulative erosion



Appendix 8: Settings to process LiDAR-derived point clouds

1) RiSCAN PRO: *Multi-Station Adjustment*

Settings:

Step	Search radius (m)	Max tilt angle (°)	Min change error 1 (m)	Min change error 2 (m)
1	0.75	10	1	0.002
2	0.5	8	1	0.002
3	0.2	3	1	0.002

Position and orientation of LiDAR2016 was locked. MSA transformation of the remaining surveys:

Tile	Step	Standard deviation	Name	delta X	delta Y	delta Z	delta Roll	delta Pitch	delta Yaw
3	1	0.0742	LiDAR2014	-0.147	0.025	-0.036	-0.006	-0.014	-0.011
			LiDAR2015	-0.05	-0.031	0.036	-0.024	-0.007	-0.014
			LiDAR2017	-0.064	-0.014	-0.054	-0.006	0.004	0
	2	0.0545	LiDAR2014	-0.018	0.004	-0.022	0.012	0.008	-0.001
			LiDAR2015	0.009	0.001	-0.002	0.007	0.007	0.004
			LiDAR2017	0.02	-0.003	0.014	-0.005	0.002	0
	3	0.0307	LiDAR2014	0.091	-0.013	0.011	0.005	0.011	-0.005
			LiDAR2015	0.006	0.002	-0.007	0.007	0.007	0.004
			LiDAR2017	0.01	-0.012	0.015	-0.002	0	-0.01
4	1	0.0681	LiDAR2014	-0.013	-0.007	0.086	-0.044	0.008	0.004
			LiDAR2015	-0.008	-0.072	0.068	-0.045	0.007	-0.001
			LiDAR2017	-0.014	-0.039	0.024	-0.037	0.009	0.001
	2	0.0589	LiDAR2014	0.012	-0.006	-0.005	-0.001	-0.001	-0.002
			LiDAR2015	-0.001	0.01	-0.012	0.008	0	0.001
			LiDAR2017	0.001	-0.005	0.005	-0.001	0.001	0.001
	3	0.0385	LiDAR2014	0.01	-0.001	-0.009	-0.011	0.001	-0.001
			LiDAR2015	0.014	0.016	-0.018	-0.008	-0.001	-0.006
			LiDAR2017	0.007	0.013	-0.012	-0.004	0.001	0.001
5	1	0.0546	LiDAR2014	-0.09	0.031	0.03	-0.019	0.001	-0.015
			LiDAR2015	-0.033	-0.045	0.073	-0.028	0	-0.003
			LiDAR2017	-0.047	-0.046	0.035	-0.033	0.002	-0.004
	2	0.0487	LiDAR2014	-0.005	0.004	-0.004	0.002	-0.001	-0.004
			LiDAR2015	0.001	-0.01	0.003	0.001	-0.002	-0.002
			LiDAR2017	-0.002	0.014	-0.009	0.001	-0.002	-0.002
	3	0.03	LiDAR2014	-0.109	0.086	-0.014	0.001	-0.001	-0.001
			LiDAR2015	0	0.007	-0.032	0.01	-0.001	0.008
			LiDAR2017	0	-0.009	-0.019	-0.001	0.002	0.006
6	1	0.0481	LiDAR2014	-0.053	-0.032	0.021	-0.021	-0.004	0.002
			LiDAR2015	-0.041	-0.045	0.019	-0.019	0.002	-0.001
			LiDAR2017	-0.032	-0.018	0.011	-0.028	-0.006	0.001
	2	0.0435	LiDAR2014	0	0.003	-0.008	0.001	0.001	0.001
			LiDAR2015	-0.001	0.001	-0.002	0	-0.001	0
			LiDAR2017	-0.002	0.001	-0.001	0	-0.001	0
	3	0.0325	LiDAR2014	-0.022	-0.015	0	0.003	0.001	0.002
			LiDAR2015	-0.002	-0.003	-0.004	0.003	0.002	0.002
			LiDAR2017	-0.022	-0.008	-0.013	0.003	0.002	0.002
7	1	0.0565	LiDAR2014	-0.041	0.018	0.009	-0.018	-0.005	-0.002
			LiDAR2015	0.004	-0.018	0.037	-0.022	-0.006	-0.002
			LiDAR2017	-0.015	0.007	-0.012	-0.022	0.001	0.003
	2	0.0535	LiDAR2014	0.014	0.01	-0.011	0.003	0	-0.001
			LiDAR2015	0.009	0.006	-0.009	0.002	0.001	-0.001
			LiDAR2017	0.007	0.006	-0.011	0.002	0.001	-0.001
	3	0.0245	LiDAR2014	0.039	0.008	-0.021	0.005	0.004	0.002
			LiDAR2015	-0.008	0.013	-0.038	0.008	0	0
			LiDAR2017	0.029	-0.005	0	-0.004	-0.005	-0.002
8	1	0.0456	LiDAR2014	-0.04	0.01	0.036	-0.02	-0.001	-0.004
			LiDAR2015	0.009	-0.04	0.03	-0.025	0.008	0.001
			LiDAR2017	-0.025	-0.007	-0.031	-0.023	-0.002	-0.003

Tile	Step	Standard deviation	Name	delta X	delta Y	delta Z	delta Roll	delta Pitch	delta Yaw
	2	0.0393	LiDAR2014	0.004	0.001	-0.005	0.001	0	-0.001
			LiDAR2015	0.001	0.005	-0.001	0	0	-0.001
			LiDAR2017	-0.001	0.005	-0.003	0	-0.001	-0.001
	3	0.0262	LiDAR2014	-0.005	0.019	-0.012	0.002	-0.001	-0.002
			LiDAR2015	0.008	0.024	-0.002	0.001	-0.001	-0.002
			LiDAR2017	0.014	0.028	-0.001	0.001	-0.001	-0.005
	1	0.0576	LiDAR2014	-0.07	-0.018	0.08	-0.015	-0.013	-0.017
			LiDAR2015	-0.024	-0.024	0.061	-0.021	-0.002	-0.007
			LiDAR2017	-0.03	0.01	0.001	-0.009	0.003	0.001
9	2	0.0486	LiDAR2014	0.005	-0.001	-0.005	0.001	0.005	0.003
			LiDAR2015	-0.009	-0.006	0.002	-0.001	0.003	0.001
			LiDAR2017	-0.005	0	0.005	-0.001	0.002	0
	3	0.029	LiDAR2014	0.022	0.006	-0.021	0.005	0.001	0.004
			LiDAR2015	-0.012	0.011	-0.022	0.004	-0.003	0
			LiDAR2017	-0.005	0.004	0.005	0	-0.001	-0.001
	1	0.0563	LiDAR2014	-0.093	-0.006	0.035	-0.01	0.013	-0.004
			LiDAR2015	-0.049	-0.003	0.043	-0.017	0.013	-0.006
			LiDAR2017	-0.023	0.006	-0.031	-0.008	0.004	0
	2	0.047	LiDAR2014	0.016	0.005	-0.017	0.002	-0.007	-0.004
10			LiDAR2015	-0.003	0.002	-0.002	0	0	0
			LiDAR2017	0.002	0.003	-0.006	0.003	0.001	0.002
	3	0.036	LiDAR2014	-0.018	-0.016	0.005	-0.001	-0.002	0
			LiDAR2015	-0.013	-0.019	0.004	-0.001	-0.002	-0.002
			LiDAR2017	0.002	0.009	0	0.002	-0.003	0.001
	1	0.0567	LiDAR2014	-0.054	-0.033	0.072	-0.022	-0.004	-0.005
			LiDAR2015	-0.009	-0.014	0.034	-0.015	0.002	0.003
			LiDAR2017	-0.026	-0.018	0.008	-0.012	0.004	0
	2	0.0463	LiDAR2014	0.002	0.004	-0.015	0.003	0.001	0.002
11			LiDAR2015	-0.002	0.005	-0.008	0.002	-0.001	0.001
			LiDAR2017	-0.002	-0.002	0	0	0	0.001
	3	0.0345	LiDAR2014	-0.008	0.002	-0.018	0.005	0.004	0.002
			LiDAR2015	0.003	-0.009	-0.01	0.002	0.002	0.002
			LiDAR2017	-0.014	-0.002	-0.004	0	0	-0.002
	1	0.056	LiDAR2014	0.005	-0.036	0.108	-0.036	0.029	0.015
			LiDAR2015	-0.002	-0.015	0.054	-0.025	0.007	0
			LiDAR2017	-0.031	-0.005	0.036	-0.043	0.021	0.001
	2	0.0509	LiDAR2014	0.003	0.002	-0.013	0.002	-0.005	-0.002
12			LiDAR2015	0.003	0.005	-0.007	0.002	-0.001	-0.001
			LiDAR2017	0.003	0.002	-0.006	0.001	-0.002	-0.001
	3	0.0348	LiDAR2014	0.003	-0.005	-0.034	0.011	-0.014	-0.007
			LiDAR2015	-0.001	-0.002	-0.014	0.003	-0.004	-0.003
			LiDAR2017	0.003	-0.014	-0.009	0.001	-0.001	-0.003
	1	0.06	LiDAR2014	-0.018	-0.033	0.108	-0.045	0.012	-0.001
			LiDAR2015	-0.007	-0.035	0.113	-0.045	0.018	0.004
			LiDAR2017	-0.03	-0.019	0.004	-0.024	0.006	0
	2	0.0549	LiDAR2014	0.003	0.013	-0.032	0.011	0	0.001
13			LiDAR2015	0.001	0.013	-0.024	0.007	0	0
			LiDAR2017	0.006	0.016	-0.036	0.008	-0.005	-0.002
	3	0.0305	LiDAR2014	-0.003	0.004	-0.014	0.01	-0.002	0
			LiDAR2015	-0.006	0.01	-0.02	0.012	-0.006	-0.002
			LiDAR2017	0.007	-0.003	0.023	-0.007	0.004	0.002
	1	0.0844	LiDAR2014	-0.003	-0.038	0.102	-0.057	0.036	0.01
			LiDAR2015	-0.018	-0.068	0.091	-0.06	0.044	0.01
			LiDAR2017	-0.034	-0.007	-0.034	-0.033	0.01	-0.006
	2	0.0795	LiDAR2014	0.004	-0.005	-0.005	0.001	0.002	0.001
14			LiDAR2015	-0.005	-0.01	0.003	-0.004	0.004	0.001
			LiDAR2017	0.003	0.004	-0.004	0	0.004	0.002
	3	0.032	LiDAR2014	0.02	0.019	-0.041	0.023	-0.025	-0.012
			LiDAR2015	0.019	0.061	-0.078	0.046	-0.041	-0.013
			LiDAR2017	-0.006	-0.008	-0.004	0.003	0.003	0.007
	1	0.0539	LiDAR2014	0.002	-0.022	0.057	-0.054	-0.006	0.005
			LiDAR2015	-0.012	-0.08	0.028	-0.038	0.001	0
15			LiDAR2017	-0.009	-0.052	-0.012	-0.039	-0.006	0.007
	2	0.0454	LiDAR2014	0	0.007	-0.012	0.009	-0.002	-0.002
			LiDAR2015	-0.001	0.004	-0.008	0.008	-0.002	-0.002
			LiDAR2017	-0.004	0.003	-0.009	0.004	-0.003	-0.002

Tile	Step	Standard deviation	Name	delta X	delta Y	delta Z	delta Roll	delta Pitch	delta Yaw
	3	0.0308	LiDAR2014	0.009	0.019	-0.018	0.011	0.002	-0.003
			LiDAR2015	0.004	0.016	-0.01	0.007	0.002	-0.003
			LiDAR2017	0.001	-0.002	0.002	-0.003	0.001	0.003
16	1	0.0538	LiDAR2014	-0.032	-0.002	0.051	-0.022	0.003	-0.006
			LiDAR2015	-0.024	-0.068	0.024	-0.013	-0.001	-0.006
			LiDAR2017	-0.024	-0.037	0.001	-0.022	-0.001	-0.002
	2	0.046	LiDAR2014	0.002	-0.004	-0.001	0.002	0.001	-0.001
			LiDAR2015	0.005	0.003	-0.002	0.002	0.002	0.001
			LiDAR2017	-0.002	-0.004	0	0.001	0.001	-0.001
	3	0.0293	LiDAR2014	-0.002	0	-0.012	0.004	-0.001	-0.002
			LiDAR2015	0.001	0.007	-0.009	0.002	0.004	0.002
			LiDAR2017	-0.01	0.005	-0.01	0.002	0.001	-0.002
17	1	0.0502	LiDAR2014	-0.015	0.006	0.013	-0.011	0.013	-0.007
			LiDAR2015	0.006	-0.04	0.002	-0.012	0.014	-0.007
			LiDAR2017	-0.028	-0.011	-0.02	-0.014	0.007	0.002
	2	0.0399	LiDAR2014	0.002	-0.003	-0.002	0.001	-0.005	0
			LiDAR2015	0.003	0	-0.005	0.003	-0.007	-0.001
			LiDAR2017	0.003	0.001	-0.005	0.001	0	0.001
	3	0.0254	LiDAR2014	-0.008	0.013	-0.003	0.003	-0.003	0
			LiDAR2015	-0.005	0.017	-0.007	0.003	-0.005	-0.002
			LiDAR2017	-0.007	0.017	-0.008	0.002	-0.002	-0.005
18	1	0.058	LiDAR2014	-0.015	-0.055	0.068	-0.035	0.02	0.004
			LiDAR2015	-0.008	-0.088	0.058	-0.018	0.02	0.001
			LiDAR2017	-0.037	-0.052	0.035	-0.027	0.011	0.002
	2	0.0375	LiDAR2014	0	-0.012	-0.005	0.002	-0.003	0.002
			LiDAR2015	0.007	0.005	-0.016	0.004	-0.005	-0.001
			LiDAR2017	0.006	0.001	-0.008	0.001	-0.001	0
	3	0.0258	LiDAR2014	0.041	-0.018	-0.002	0.002	-0.002	0.003
			LiDAR2015	0.024	-0.004	-0.01	0.005	-0.003	-0.002
			LiDAR2017	0.027	0.008	-0.011	0.003	-0.002	-0.002
19	1	0.05	LiDAR2014	0.001	-0.023	0.048	-0.034	-0.011	-0.014
			LiDAR2015	-0.004	-0.11	0.045	-0.024	-0.012	-0.005
			LiDAR2017	-0.022	-0.042	0.01	-0.03	-0.004	-0.007
	2	0.039	LiDAR2014	0.003	0.001	-0.006	0.005	0.003	0.001
			LiDAR2015	-0.004	0.005	-0.006	0.006	0.004	0
			LiDAR2017	0	0.004	-0.004	0.003	0.001	0.002
	3	0.035	LiDAR2014	0.007	0.015	-0.014	0.003	0.007	0.004
			LiDAR2015	0.012	0.025	-0.012	0.005	0.005	0.002
			LiDAR2017	0.027	0.003	-0.007	0.003	0.003	0.001
20	1	0.0661	LiDAR2014	-0.075	-0.018	0.103	-0.024	0.037	-0.012
			LiDAR2015	-0.024	-0.086	0.056	-0.017	0.029	-0.009
			LiDAR2017	-0.033	-0.012	0.031	-0.002	0.028	0.001
	2	0.0571	LiDAR2014	0.005	0.022	-0.019	0.002	-0.005	-0.001
			LiDAR2015	0.009	0.001	-0.013	0.001	-0.002	0.003
			LiDAR2017	0.003	0.017	-0.01	-0.001	-0.002	-0.002
	3	0.029	LiDAR2014	0.025	0.024	-0.035	0.01	-0.014	0.003
			LiDAR2015	0.012	-0.005	-0.009	0.005	-0.005	0.006
			LiDAR2017	-0.02	0.011	-0.002	0	-0.003	-0.006
21	1	0.0823	LiDAR2014	-0.049	-0.025	0.182	-0.045	0.034	0.009
			LiDAR2015	-0.031	-0.046	0.134	-0.037	0.023	0.012
			LiDAR2017	-0.027	-0.028	0.041	-0.018	0.009	-0.005
	2	0.0706	LiDAR2014	-0.01	-0.014	-0.016	0.003	-0.005	-0.006
			LiDAR2015	-0.007	-0.004	-0.014	0.003	-0.002	-0.003
			LiDAR2017	0.004	0.004	-0.021	0.003	-0.006	-0.002
	3	0.0364	LiDAR2014	0.018	0.024	-0.067	0.021	-0.015	-0.007
			LiDAR2015	0.02	0.019	-0.043	0.02	-0.008	-0.006
			LiDAR2017	-0.026	-0.019	0.023	-0.001	0.006	-0.002
22	1	0.0832	LiDAR2014	0.003	0.025	0.08	-0.009	0.023	-0.002
			LiDAR2015	0.062	-0.006	0.108	-0.012	0.023	0.001
			LiDAR2017	-0.032	-0.018	0.019	-0.008	0.013	0
	2	0.0613	LiDAR2014	-0.036	-0.008	0.004	-0.002	-0.007	-0.004
			LiDAR2015	-0.011	0.001	-0.01	0	-0.008	-0.002
			LiDAR2017	-0.001	0.011	-0.007	0	-0.003	-0.001
	3	0.0302	LiDAR2014	-0.028	-0.012	-0.031	0.006	-0.006	-0.008
			LiDAR2015	-0.007	0	-0.041	0.006	-0.005	-0.005

Tile	Step	Standard deviation	Name	delta X	delta Y	delta Z	delta Roll	delta Pitch	delta Yaw
			LiDAR2017	-0.002	0.015	-0.01	0.002	-0.001	-0.001
23	1	0.0849	LiDAR2014	0	0.036	0.04	-0.022	0.002	-0.013
			LiDAR2015	-0.055	-0.156	0.16	-0.08	0.022	0.007
			LiDAR2017	-0.014	-0.02	0.029	-0.039	0.012	-0.004
	2	0.0698	LiDAR2014	-0.033	-0.005	-0.006	0.003	-0.002	0
			LiDAR2015	-0.003	-0.003	-0.007	0.004	-0.003	-0.004
			LiDAR2017	0	0	-0.001	0.001	-0.001	-0.002
	3	0.0319	LiDAR2014	-0.025	-0.042	0.007	0	0.002	0.013
			LiDAR2015	0.011	0.098	-0.107	0.052	-0.015	-0.009
			LiDAR2017	0.001	-0.004	-0.006	0.007	0.002	0.004
24	1	0.0786	LiDAR2014	-0.007	0.078	0.071	-0.023	0.013	0.005
			LiDAR2015	-0.019	-0.078	0.123	-0.034	0.041	0.013
			LiDAR2017	-0.028	-0.045	0.023	-0.028	0.022	0
	2	0.0599	LiDAR2014	0.008	-0.029	-0.008	0.003	0.002	0.001
			LiDAR2015	-0.011	-0.014	0.003	-0.007	-0.003	-0.008
			LiDAR2017	0.001	-0.001	0	-0.001	-0.001	-0.001
	3	0.0357	LiDAR2014	-0.029	-0.019	-0.011	0	-0.006	-0.009
			LiDAR2015	0.027	-0.006	-0.043	0.008	-0.016	-0.014
			LiDAR2017	0	-0.004	-0.009	-0.004	-0.003	-0.003
25	1	0.0847	LiDAR2014	-0.011	0.065	0.092	-0.013	0.03	-0.004
			LiDAR2015	-0.041	0.014	0.161	-0.023	0.036	-0.002
			LiDAR2017	-0.066	-0.018	0.075	-0.015	0.032	-0.004
	2	0.0701	LiDAR2014	-0.022	-0.022	0.001	-0.002	0	0.002
			LiDAR2015	0	-0.003	-0.014	0.002	0	0.002
			LiDAR2017	0.008	-0.001	-0.018	0.001	-0.002	0.001
	3	0.0439	LiDAR2014	0.014	-0.005	-0.029	0.006	-0.009	0.001
			LiDAR2015	0.026	0.002	-0.061	0.012	-0.015	0.004
			LiDAR2017	0.016	0.017	-0.027	0.004	-0.003	-0.002
26	1	0.0905	LiDAR2014	-0.046	-0.018	0.082	-0.005	0.006	-0.025
			LiDAR2015	0.024	-0.002	0.081	-0.002	0.014	-0.006
			LiDAR2017	-0.077	-0.011	0.029	-0.002	0.011	-0.008
	2	0.0655	LiDAR2014	-0.014	-0.002	0.002	-0.003	-0.006	-0.001
			LiDAR2015	-0.015	-0.009	-0.004	0	-0.002	-0.001
			LiDAR2017	0.015	0	-0.006	0.002	0.002	0.002
	3	0.0344	LiDAR2014	0.017	0.011	-0.003	-0.002	-0.007	0.007
			LiDAR2015	0.027	-0.006	-0.017	0.003	0	0.004
			LiDAR2017	0.051	-0.002	-0.014	0.001	0	0.006
27	1	0.1036	LiDAR2014	-0.021	0.065	0.031	-0.04	0.025	0.001
			LiDAR2015	-0.004	0.053	0.096	-0.034	0.018	-0.011
			LiDAR2017	-0.016	-0.027	0.025	-0.035	0.033	0.014
	2	0.0678	LiDAR2014	-0.019	-0.023	0.016	0.018	-0.011	0.004
			LiDAR2015	-0.006	-0.02	-0.003	0.013	-0.007	0.004
			LiDAR2017	-0.015	-0.005	-0.006	0.009	-0.012	-0.01
	3	0.0339	LiDAR2014	0.038	-0.058	-0.01	0.012	-0.006	-0.001
			LiDAR2015	0.055	0.03	-0.031	0.007	-0.008	-0.02
			LiDAR2017	0.005	-0.004	-0.009	0.005	-0.005	-0.005
28	1	0.065	LiDAR2014	-0.066	0.034	0.114	-0.036	0.004	0.007
			LiDAR2015	-0.082	-0.022	0.083	-0.021	0	0.002
			LiDAR2017	-0.038	-0.01	0.03	-0.033	-0.004	-0.001
	2	0.0517	LiDAR2014	0.017	-0.011	-0.01	-0.001	-0.001	-0.003
			LiDAR2015	0.021	-0.003	-0.005	0.001	-0.001	-0.001
			LiDAR2017	0.016	-0.007	0.004	-0.002	0.001	0.002
	3	0.0324	LiDAR2014	0.009	-0.017	-0.024	0.002	-0.002	-0.009
			LiDAR2015	0.022	0.005	-0.012	0.002	-0.001	-0.007
			LiDAR2017	0.01	-0.003	-0.011	0	0.001	-0.002
29	1	0.0675	LiDAR2014	-0.065	0.043	0.076	-0.026	-0.007	-0.003
			LiDAR2015	-0.001	-0.065	0.112	-0.034	-0.027	-0.015
			LiDAR2017	-0.019	0	0.005	-0.034	-0.016	0.001
	2	0.051	LiDAR2014	0.018	-0.013	-0.005	0	0.001	0.001
			LiDAR2015	-0.028	0.034	-0.038	0.005	0.015	0.004
			LiDAR2017	-0.004	0.004	-0.01	0.002	0	-0.002

Tile	Step	Standard deviation	Name	delta X	delta Y	delta Z	delta Roll	delta Pitch	delta Yaw
	3	0.0406	LiDAR2014	0.015	-0.028	0	0	0.004	-0.002
			LiDAR2015	0.001	-0.022	0.013	-0.002	0	0.001
			LiDAR2017	0.006	-0.018	0.014	-0.001	-0.006	-0.002
	1	0.0738	LiDAR2014	-0.057	0.023	0.154	-0.044	0	-0.015
			LiDAR2015	-0.055	-0.043	0.113	-0.039	0.002	-0.006
			LiDAR2017	-0.049	-0.013	0.021	-0.027	-0.009	-0.01
30	2	0.0579	LiDAR2014	0.012	-0.008	-0.006	-0.001	0.001	0.002
			LiDAR2015	0.003	0.004	-0.012	0.004	-0.001	-0.001
			LiDAR2017	0.008	0.002	-0.004	0.001	-0.001	-0.001
	3	0.0349	LiDAR2014	0.004	-0.004	-0.043	0.018	0	0
			LiDAR2015	-0.004	0.004	-0.025	0.014	0	-0.002
			LiDAR2017	0.018	-0.023	0.008	-0.005	0.007	0
	1	0.0609	LiDAR2014	-0.015	0.004	0.077	-0.005	-0.008	-0.004
			LiDAR2015	0.027	-0.05	0.059	-0.013	-0.013	-0.006
			LiDAR2017	0.002	-0.054	0.009	-0.012	-0.008	-0.001
	2	0.0451	LiDAR2014	0.001	-0.007	-0.007	0.001	-0.001	0.001
31			LiDAR2015	-0.007	0.001	-0.011	0.001	-0.001	-0.001
			LiDAR2017	0.005	-0.003	0.004	-0.001	-0.002	0.001
	3	0.0302	LiDAR2014	0.005	-0.012	0.005	0.001	0.004	0.005
			LiDAR2015	-0.021	0.001	-0.013	0.006	0.003	-0.002
			LiDAR2017	-0.008	0.005	-0.02	0.006	0.005	0.002
	1	0.0915	LiDAR2014	0.01	0.01	0.128	-0.01	0.015	0
			LiDAR2015	-0.009	-0.032	0.145	-0.012	0.043	0.005
			LiDAR2017	-0.034	-0.026	0.031	-0.006	0.014	0.002
	2	0.0581	LiDAR2014	-0.01	0	-0.023	0.003	-0.014	-0.001
32			LiDAR2015	0.004	0.031	-0.053	0.004	-0.032	-0.002
			LiDAR2017	0.003	0.007	-0.004	-0.001	-0.003	0
	3	0.0348	LiDAR2014	-0.008	-0.005	-0.021	0.005	-0.007	-0.001
			LiDAR2015	0.01	0.021	-0.037	0.007	-0.018	-0.002
			LiDAR2017	-0.002	0.016	-0.004	-0.001	-0.001	-0.001
	1	0.0634	LiDAR2014	-0.032	0.03	0.117	-0.01	0	0.001
			LiDAR2015	-0.009	-0.047	0.124	-0.027	0.003	-0.004
			LiDAR2017	-0.043	-0.043	0.036	-0.014	0.004	-0.001
	2	0.0467	LiDAR2014	0.001	-0.02	-0.006	-0.001	0	0.001
33			LiDAR2015	-0.01	0.007	-0.018	0.004	0	-0.001
			LiDAR2017	0.004	-0.004	0.001	-0.003	0.001	0
	3	0.0371	LiDAR2014	0.004	-0.014	0	0.001	0.001	-0.001
			LiDAR2015	0.012	0.007	-0.024	0.008	-0.002	0
			LiDAR2017	0.006	0.009	-0.009	0.003	0	0.002
	1	0.1012	LiDAR2014	0.009	0.037	0.143	-0.013	0.031	0.002
			LiDAR2015	-0.034	-0.034	0.184	-0.034	0.038	-0.015
			LiDAR2017	-0.021	-0.002	0.063	-0.023	0.018	-0.007
	2	0.06	LiDAR2014	-0.008	-0.008	-0.051	0.009	-0.023	-0.004
34			LiDAR2015	0.005	0.018	-0.037	0.008	-0.009	0.003
			LiDAR2017	0.012	0.009	-0.016	0.004	-0.002	0.003
	3	0.034	LiDAR2014	-0.039	-0.012	0	-0.002	-0.005	-0.004
			LiDAR2015	0.01	0.01	-0.052	0.015	-0.014	0.004
			LiDAR2017	-0.006	0.011	-0.01	0.002	-0.002	0
	1	0.0714	LiDAR2014	-0.009	0.059	0.08	0.003	-0.009	-0.009
			LiDAR2015	-0.024	-0.04	0.194	-0.042	0.041	-0.002
			LiDAR2017	-0.022	0.016	0.046	-0.017	0.009	-0.004
	2	0.0575	LiDAR2014	0	-0.011	-0.015	0.003	-0.006	-0.001
35			LiDAR2015	0.015	0.013	-0.021	0.007	-0.008	-0.001
			LiDAR2017	-0.009	-0.003	0.008	-0.002	0.001	0
	3	0.03	LiDAR2014	0	-0.029	0.018	0.001	0.007	0.004
			LiDAR2015	0.011	0.038	-0.073	0.02	-0.024	-0.001
			LiDAR2017	-0.001	-0.006	0.003	-0.001	0	0.001
	1	0.0919	LiDAR2014	-0.023	-0.047	0.205	-0.072	0.005	-0.003
			LiDAR2015	-0.053	-0.104	0.155	-0.077	0.009	-0.002
			LiDAR2017	-0.005	-0.006	0.032	-0.024	-0.003	-0.003
36	2	0.0613	LiDAR2014	-0.01	0.024	-0.055	0.029	-0.003	0
			LiDAR2015	0.003	0.067	-0.062	0.043	-0.006	-0.001
			LiDAR2017	0	-0.004	-0.009	0.004	0	0
	3	0.0347	LiDAR2014	-0.036	0.007	-0.047	0.016	-0.002	0

Tile	Step	Standard deviation	Name	delta X	delta Y	delta Z	delta Roll	delta Pitch	delta Yaw
			LiDAR2015	-0.005	0.032	-0.036	0.015	-0.005	0
			LiDAR2017	-0.004	-0.004	0.011	-0.006	0.003	0.002
			LiDAR2014	0.001	0.007	0.14	-0.018	0.023	0.006
	1	0.0628	LiDAR2015	-0.023	0.002	0.074	-0.011	0.017	0.013
			LiDAR2017	-0.005	-0.056	0.041	-0.009	0.015	-0.001
			LiDAR2014	0	-0.004	-0.013	0.001	-0.004	-0.002
37	2	0.0577	LiDAR2015	-0.002	-0.001	-0.007	0.001	-0.003	-0.001
			LiDAR2017	0.009	-0.004	-0.004	0	-0.001	0
			LiDAR2014	-0.099	0.068	-0.047	0.012	-0.016	0.001
	3	0.0276	LiDAR2015	-0.005	-0.005	-0.002	0.002	-0.004	-0.002
			LiDAR2017	0.069	-0.048	-0.007	0.001	-0.002	0.005
			LiDAR2014	-0.001	0.032	0.114	-0.004	-0.001	-0.008
	1	0.0666	LiDAR2015	0.01	0.031	0.067	-0.006	0.001	-0.006
			LiDAR2017	-0.031	-0.014	0.024	-0.005	0.007	-0.002
			LiDAR2014	-0.009	-0.011	-0.001	0.001	0.003	0.001
38	2	0.0549	LiDAR2015	-0.007	-0.002	-0.004	0.001	0.001	0
			LiDAR2017	0.001	-0.001	-0.005	0.001	-0.001	0
			LiDAR2014	-0.003	-0.004	-0.015	0.003	0	0.005
	3	0.0367	LiDAR2015	-0.004	-0.006	-0.008	0.002	0.001	0.003
			LiDAR2017	0.004	-0.001	-0.002	0.001	-0.001	0.003
			LiDAR2014	0	0	0	0	0	0
	1	0.0949	LiDAR2015	0	0	0	0	0	0
			LiDAR2017	-0.001	0.001	0.001	0	0	0
			LiDAR2014	-0.013	0	-0.039	0.001	-0.014	0.001
39	2	0.0622	LiDAR2015	-0.01	0.003	-0.023	0	-0.005	0.001
			LiDAR2017	-0.01	0	0.015	-0.001	0.002	-0.001
			LiDAR2014	-0.031	-0.014	-0.03	-0.004	-0.009	-0.003
	3	0.034	LiDAR2015	-0.008	-0.015	-0.017	-0.001	-0.003	0.004
			LiDAR2017	-0.03	-0.006	-0.002	-0.001	-0.001	-0.003
			LiDAR2014	-0.004	0.09	0.076	0.005	0.004	-0.017
	1	0.0784	LiDAR2015	-0.01	0.078	0.098	-0.005	0.006	-0.014
			LiDAR2017	-0.042	0.015	0.059	-0.001	0.017	0
			LiDAR2014	-0.013	-0.013	-0.005	-0.001	-0.002	-0.002
40	2	0.0584	LiDAR2015	-0.009	-0.003	-0.007	0	0	-0.003
			LiDAR2017	0.001	0.004	0	0	0.001	-0.001
			LiDAR2014	-0.008	-0.01	-0.006	-0.001	0.002	-0.003
	3	0.0223	LiDAR2015	-0.015	0.013	-0.013	0.003	0.005	-0.007
			LiDAR2017	-0.005	-0.007	-0.007	0.002	0.001	0.001

2) ENVI Classic: creation of DEMs from the point clouds

Universal settings:

Pixel size	0.25
Type	Floating point
Name	tileX_lidarY_dem.img (X=3:40; Y=14:17)

Tile-dependent settings:

	Upper left corner		Output size	
Tile	Easting (m)	Northing (m)	X (m)	Y (m)
3	471335	520392	610	610
4	471929	520380	515	645
5	472428	520342	515	730
6	472925	520344	520	755
7	473426	520346	520	710
8	473929	520342	650	660
9	474352	520223	685	740
10	474808	520005	685	810
11	475231	519831	685	825
12	475694	519536	655	720
13	476156	519293	685	630
14	476636	519157	575	650
15	477180	519098	525	590
16	477667	519207	535	600
17	478166	519283	315	650
18	478600	519046	800	675
19	478396	519224	570	655
20	478956	518834	655	900
21	479228	518346	765	855
22	479497	518009	670	940
23	479784	517467	925	580
24	480302	517312	810	750
25	480645	516883	795	835
26	480779	516490	670	960
27	480914	515784	720	615
28	481453	515685	690	605
29	482022	515878	585	785
30	482459	516001	600	745
31	482881	516413	500	900
32	483506	516216	565	995
33	483274	516323	590	775
34	483731	515682	630	910
35	484026	515230	675	745
36	484436	514872	835	555
37	484930	514809	785	715
38	485238	514396	775	735
39	485504	513987	695	825
40	485653	513455	595	740

Appendix 9: Across-shore occurrence of erosion

The proportion of the grid cells (0-1) which experienced erosion as a function of the distance from the cliff. The distance provided in column 1 represents the lower limit of the 1 m interval bins into which the cells were classified. For instance, distance '0' represents the cells which are located ≥ 0 and < 1 m from the cliff.

Type of cell	Type of erosion
Boulder	Boulder movement
Stepped	Erosion at steps
Non-stepped	Down-wearing

Distance from the cliff – lower limit (m)	Boulder movement	Erosion at steps	Down-wearing
0	0.5857	0.5298	0.4151
1	0.6387	0.4521	0.3674
2	0.6851	0.4274	0.3548
3	0.7008	0.4502	0.3744
4	0.7296	0.4134	0.3766
5	0.7497	0.4599	0.3717
6	0.7524	0.4394	0.3814
7	0.7646	0.4743	0.3863
8	0.7707	0.4913	0.3878
9	0.7820	0.5399	0.3937
10	0.7929	0.5531	0.4069
11	0.7885	0.5509	0.4001
12	0.7901	0.5813	0.3972
13	0.7816	0.5731	0.3901
14	0.7745	0.5865	0.3755
15	0.7772	0.5980	0.3700
16	0.7691	0.5852	0.3560
17	0.7599	0.5814	0.3412
18	0.7562	0.6130	0.3365
19	0.7619	0.6027	0.3279
20	0.7554	0.6004	0.3171
21	0.7556	0.5855	0.3107
22	0.7474	0.5775	0.3000
23	0.7429	0.5782	0.2901
24	0.7369	0.5894	0.2809
25	0.7382	0.5667	0.2814
26	0.7323	0.6024	0.2814
27	0.7365	0.6119	0.2772
28	0.7331	0.5967	0.2709
29	0.7289	0.5856	0.2639
30	0.7298	0.5954	0.2594
31	0.7258	0.5793	0.2550
32	0.7248	0.5729	0.2527
33	0.7245	0.5624	0.2441
34	0.7211	0.5785	0.2393
35	0.7245	0.5562	0.2306
36	0.7246	0.5378	0.2248
37	0.7195	0.5607	0.2169
38	0.7047	0.5533	0.2129
39	0.7067	0.5820	0.2113
40	0.7164	0.5938	0.2060
41	0.7145	0.5754	0.2073
42	0.7176	0.5181	0.2100
43	0.7119	0.5378	0.2042
44	0.7177	0.5473	0.2030
45	0.7126	0.5503	0.1997
46	0.7101	0.5577	0.1940
47	0.7070	0.5230	0.1865
48	0.7038	0.5673	0.1830
49	0.7196	0.5524	0.1815
50	0.7045	0.5348	0.1781
51	0.7031	0.5481	0.1710
52	0.7001	0.5425	0.1694
53	0.6997	0.5815	0.1657

Distance from the cliff – lower limit (m)	Boulder movement	Erosion at steps	Down-wearing
54	0.7010	0.5629	0.1680
55	0.7092	0.5652	0.1681
56	0.6966	0.5286	0.1648
57	0.6873	0.5238	0.1591
58	0.6811	0.5248	0.1606
59	0.6911	0.5408	0.1558
60	0.6859	0.4832	0.1581
61	0.6857	0.4698	0.1609
62	0.6784	0.4662	0.1609
63	0.6830	0.5156	0.1596
64	0.6850	0.4907	0.1583
65	0.6743	0.4569	0.1527
66	0.6796	0.4718	0.1510
67	0.6780	0.4916	0.1488
68	0.6717	0.4940	0.1431
69	0.6692	0.4711	0.1464
70	0.6670	0.4982	0.1389
71	0.6617	0.5334	0.1396
72	0.6532	0.5307	0.1379
73	0.6628	0.5201	0.1360
74	0.6624	0.5413	0.1386
75	0.6463	0.5077	0.1378
76	0.6567	0.5246	0.1379
77	0.6516	0.5224	0.1369
78	0.6540	0.5022	0.1373
79	0.6503	0.4578	0.1339
80	0.6540	0.4419	0.1300
81	0.6424	0.4873	0.1303
82	0.6413	0.5109	0.1343
83	0.6314	0.4919	0.1302
84	0.6416	0.4812	0.1215
85	0.6381	0.5049	0.1214
86	0.6212	0.4485	0.1188
87	0.6280	0.4467	0.1194
88	0.6250	0.4323	0.1184
89	0.6276	0.4216	0.1175
90	0.6189	0.4781	0.1186
91	0.6215	0.4832	0.1144
92	0.6167	0.4748	0.1160
93	0.6166	0.4463	0.1144
94	0.6102	0.4391	0.1145
95	0.6061	0.4432	0.1117
96	0.5999	0.4640	0.1108
97	0.5962	0.4721	0.1108
98	0.5823	0.4315	0.1110
99	0.5888	0.4038	0.1081
100	0.5983	0.4307	0.1064
101	0.6070	0.4088	0.1054
102	0.6026	0.3792	0.1047
103	0.5951	0.3983	0.1051
104	0.5901	0.3921	0.1070
105	0.5896	0.4026	0.1048
106	0.5808	0.3889	0.1037
107	0.5843	0.4328	0.1034
108	0.5860	0.3911	0.0985
109	0.5882	0.3916	0.0997
110	0.5775	0.4117	0.1022
111	0.5692	0.3975	0.1003
112	0.5695	0.3730	0.0997
113	0.5664	0.4047	0.0952
114	0.5691	0.3981	0.0956
115	0.5785	0.3899	0.0976
116	0.5631	0.4029	0.0949
117	0.5610	0.4072	0.0931
118	0.5550	0.4042	0.0878
119	0.5451	0.3774	0.0905
120	0.5437	0.3834	0.0887
121	0.5416	0.4416	0.0903
122	0.5202	0.4351	0.0884
123	0.5251	0.3889	0.0899
124	0.5391	0.4261	0.0877
125	0.5258	0.3800	0.0926
126	0.5143	0.3950	0.0900
127	0.4994	0.3651	0.0917
128	0.4995	0.3368	0.0901
129	0.5091	0.3290	0.0873
130	0.4914	0.3931	0.0870
131	0.5054	0.3651	0.0899
132	0.4794	0.3407	0.0877
133	0.5011	0.3859	0.0831
134	0.4798	0.3528	0.0821
135	0.4702	0.3575	0.0798
136	0.4759	0.3264	0.0822
137	0.4655	0.3531	0.0814
138	0.4494	0.3378	0.0808
139	0.4791	0.3582	0.0836

Distance from the cliff – lower limit (m)	Boulder movement	Erosion at steps	Down-wearing
140	0.4654	0.3208	0.0802
141	0.4552	0.3351	0.0824
142	0.4517	0.3838	0.0790
143	0.4642	0.2784	0.0795
144	0.4598	0.2590	0.0727
145	0.4366	0.2910	0.0745
146	0.4810	0.2809	0.0738
147	0.4492	0.2581	0.0720
148	0.4369	0.2908	0.0708
149	0.4447	0.2645	0.0681
150	0.4497	0.2634	0.0733
151	0.4631	0.2838	0.0729
152	0.4465	0.3003	0.0729
153	0.4639	0.2810	0.0725
154	0.4330	0.2862	0.0731
155	0.4456	0.2902	0.0731
156	0.4479	0.3263	0.0691
157	0.4256	0.2984	0.0752
158	0.4711	0.2590	0.0717
159	0.4790	0.2996	0.0747
160	0.4337	0.3457	0.0722
161	0.4525	0.3696	0.0741
162	0.4863	0.2774	0.0771
163	0.4493	0.2814	0.0752
164	0.4781	0.2888	0.0767
165	0.4700	0.3166	0.0722
166	0.4588	0.3071	0.0801
167	0.4487	0.3042	0.0729
168	0.4664	0.2640	0.0749
169	0.4248	0.3108	0.0758
170	0.4308	0.2264	0.0792
171	0.4590	0.2458	0.0783
172	0.4492	0.2749	0.0785
173	0.4425	0.3028	0.0738
174	0.4806	0.2966	0.0798
175	0.4355	0.3178	0.0766
176	0.4288	0.3548	0.0800
177	0.3777	0.3254	0.0789
178	0.3459	0.3270	0.0743
179	0.4137	0.2793	0.0763
180	0.4291	0.3040	0.0770
181	0.4404	0.2804	0.0828
182	0.3736	0.2817	0.0822
183	0.3540	0.2919	0.0817
184	0.3393	0.2548	0.0745
185	0.3991	0.2692	0.0731
186	0.4472	0.2139	0.0813
187	0.4587	0.2402	0.0815
188	0.3175	0.2261	0.0833
189	0.4036	0.2805	0.0809
190	0.3554	0.2965	0.0844
191	0.3634	0.2922	0.0843
192	0.3780	0.2419	0.0788
193	0.3649	0.2800	0.0773
194	0.3746	0.2535	0.0809
195	0.3763	0.2621	0.0736
196	0.3430	0.2437	0.0857
197	0.3807	0.1926	0.0829
198	0.3650	0.1532	0.0850
199	0.3418	0.2277	0.0831
200	0.3976	0.2366	0.0826
201	0.4211	0.3196	0.0843
202	0.4072	0.2966	0.0829
203	0.3296	0.2083	0.0804
204	0.3780	0.3085	0.0827
205	0.3673	0.3193	0.0853
206	0.3278	0.3333	0.0899
207	0.2814	0.2448	0.0855
208	0.3200	0.2700	0.0973
209	0.3723	0.2035	0.0936
210	0.4074	0.3028	0.0865
211	0.3971	0.2823	0.0911
212	0.3889	0.3305	0.0895
213	0.3924	0.3176	0.0917
214	0.3553	0.2959	0.0915
215	0.4150	0.2188	0.0808
216	0.3947	0.3662	0.0886
217	0.3294	0.1719	0.0755
218	0.3452	0.2400	0.0771
219	0.3894	0.1975	0.0784
220	0.3246	0.2558	0.0782
221	0.2118	0.3483	0.0726
222	0.3097	0.1731	0.0887
223	0.2868	0.2000	0.0822
224	0.2793	0.2836	0.0738
225	0.2800	0.4906	0.0779

Distance from the cliff – lower limit (m)	Boulder movement	Erosion at steps	Down-wearing
226	0.2346	0.3023	0.0781
227	0.3619	0.3200	0.0884
228	0.3855	0.2778	0.0807
229	0.4505	0.3065	0.0740
230	0.3095	0.1897	0.0770
231	0.3333	0.3030	0.0751
232	0.4624	0.3387	0.0699
233	0.3205	0.2346	0.0698
234	0.3478	0.3438	0.0804
235	0.3000	0.1967	0.0662
236	0.3204	0.2619	0.0703
237	0.3056	0.2727	0.0532
238	0.3333	0.3750	0.0692
239	0.3889	0.4138	0.0475
240	0.3483	0.3729	0.0724
241	0.2250	0.2826	0.0614
242	0.3452	0.1915	0.0576
243	0.2609	0.1852	0.0528
244	0.2258	0.0488	0.0573
245	0.1786	0.2500	0.0555
246	0.3571	0.3793	0.0561
247	0.4464	0.2830	0.0725
248	0.4915	0.2909	0.0725
249	0.4082	0.2329	0.0609
250	0.2500	0.3205	0.0622
251	0.2222	0.2381	0.0681
252	0.2683	0.1961	0.0685
253	0.3103	0.1220	0.0662
254	0.2222	0.1923	0.0716
255	0.3333	0.1818	0.0656
256	0.1379	0.1765	0.0729
257	0.3158	0.3617	0.0643
258	0.2414	0.2353	0.0768
259	0.2813	0.2500	0.0576
260	0.2000	0.1633	0.0709
261	0.2400	0.2576	0.0624
262	0.3125	0.2754	0.0787
263	0.2394	0.2239	0.0576
264	0.3235	0.2241	0.0719
265	0.2462	0.1563	0.0733
266	0.1176	0.1970	0.0629
267	0.3750	0.1692	0.0491
268	0.2222	0.1948	0.0647
269	0.3636	0.2099	0.0649
270	0.2222	0.2667	0.0670
271	0.2222	0.2333	0.0427
272	0.3478	0.2000	0.0628
273	0.1429	0.1556	0.0623
274	0.3333	0.1628	0.0638
275	0.3404	0.1233	0.0789
276	0.2603	0.2062	0.0866
277	0.2857	0.2039	0.1119
278	0.2169	0.1571	0.1086
279	0.2340	0.2071	0.0827
280	0.2545	0.2846	0.1304
281	0.2344	0.2069	0.1364
282	0.2000	0.2321	0.1147
283	0.2750	0.3182	0.1031
284	0.2051	0.2059	0.0892
285	0.1905	0.2143	0.0639
286	0.1795	0.2414	0.0896
287	0.3810	0.2000	0.1014
288	0.3333	0.1111	0.1071
289	0.3158	0.2143	0.0824
290	0.2222	0.2222	0.1144
291	0.3810	0.3684	0.1213
292	0.1538	0.2632	0.1002
293	0.2174	0.2500	0.1137
294	0.3714	0.2174	0.1236
295	0.2000	0.0909	0.1085
296	0.2174	0.2500	0.1123
297	0.1429	0.1200	0.0962
298	0.1429	0.2105	0.1104
299	0.0909	0.0952	0.0978
300	0.1176	0.2667	0.0769
301	0.3846	0.2400	0.0884
302	0.0714	0.3793	0.0731
303	0.1667	0.2121	0.0757
304	0.2500	0.1034	0.0833
305	0.2941	0.1071	0.0767
306	0.0870	0.0882	0.0823
307	0.1154	0.1556	0.0776
308	0.0357	0.1224	0.0719
309	0.1000	0.1026	0.0923
310	0.0833	0.0645	0.0746
311	0.1579	0.0968	0.0668

Distance from the cliff – lower limit (m)	Boulder movement	Erosion at steps	Down-wearing
312	0.1667	0.1176	0.0571
313	0.0370	0.1154	0.0626
314	0.2188	0.0000	0.0569
315	0.0667	0.0811	0.0675
316	0.0400	0.1750	0.0610
317	0.0000	0.1351	0.0513
318	0.2143	0.0769	0.0453
319	0.1176	0.0526	0.0787
320	0.0000	0.0968	0.0518
321	0.0000	0.1250	0.0637
322	0.1071	0.1061	0.0480
323	0.0909	0.1695	0.0443
324	0.1053	0.0980	0.0286
325	0.2000	0.0417	0.0506
326	0.0435	0.1026	0.0550
327	0.0588	0.0952	0.0281
328	0.1000	0.1000	0.0605
329	0.1250	0.0000	0.0345
330	0.1333	0.1351	0.0333

Distance from the cliff – lower limit (m)	Boulder movement	Erosion at steps	Down-wearing
331	0.0556	0.1081	0.0354
332	0.1538	0.0976	0.0162
333	0.2500	0.0000	0.0732
334	0.0000	0.1000	0.0502
335	0.1111	0.0000	0.0346
336	0.0000	0.0000	0.0276
337	0.0000	0.3333	0.0455
338	0.0000	0.0000	0.0577
339	0.0000	0.3333	0.0347
340	0.0000	0.0000	0.0255
341	0.0000	0.0000	0.0219
342	0.0000	0.0000	0.0263
343	0.0000	0.0000	0.0095
344	0.0000	0.0000	0.0588
345	0.0000	0.0000	0.0519
346	0.0000	0.0000	0.0500
347	0.0000	0.0000	0.1000
348	0.0000	0.1000	0.0000
349	0.0000	0.0000	0.0000

Appendix 10: MATLAB scripts used to predict cosmogenic ^{10}Be concentrations and reconstruct past cliff retreat rates.

Values highlighted in yellow indicate site-specific attributes that would need changing for application in other locations; and file names.

Script 1: Calculation of expected ^{10}Be concentrations across a shore platform under assumption of negligible platform erosion

```
%Script to calculate expected 10Be concentrations across a shore platform
%including topographic and water shielding, and geomagnetic scalar
%(it requires an input table with distances from cliff and elevations)
%ZMS 20/04/2018

close all
clear

be10=4.009;%10Be production [atoms/gr/yr]: Lifton et al 2014

%PLATFORM SPECIFICATIONS
pw=300;%platform width [m]
tt=7000;%total time [yr]
r=pw/tt;%cliff retreat rate [m/yr] (de Lange and Moon, 2005)
h=50;%cliff height [m]

data1=load('profile300elev.txt');%input table with distance from the cliff (c1) and elevation
(c2)
d=data1(:,1);%distance from cliff [m]
el=data1(:,2);%site elevation [m AOD]
et=tt/pw*d;%exposure time [yr]
et=round(et)';

figure(1) %coastal profile
plot(d,el)
axis([0 pw -2 4])
xlabel('Distance from the cliff [m]')
ylabel('Elevation [m AOD]')

%TOPOGRAPHIC SHIELDING: Dunne et al 1999
io=2.105572;%incident radiation [calculated from the Fmax equation]
m=2.3;%scalling coefficient
fmax=2*pi*io/(m+1);%max flux
theta=degtorad(70);%cliff inclination angle
dphi=degtorad(102);%subtended azimuth angle
dcl=h/tan(theta);%horizontal distance between the cliff toe and the cliff top
dfcumt=zeros(tt+1,pw+1);%missing flux at year t (1year=1row)
scumt=zeros(tt+1,pw+1); %topographic shielding factor at time t

for n=1:pw+1
    for t=1:(et(n)+1)%time [yr]
        theta = atan(h/(r*t+dcl));
        dfcumt(t+tt-et(n),n) = (io*dphi/(m+1))*(sin(theta))^(m+1);
        scumt(t+tt-et(n),n)=(fmax-dfcumt(t+tt-et(n),n))/fmax;
    end
end

scumtfinal=sum(scumt,1)./(et+1);%total topographic shielding factor across the platform

figure(2) %topographic shielding
plot(d,scumtfinal)
axis([0 pw 0.75 1])
xlabel('Distance from the cliff [m]')
ylabel('Topographic shielding, S_t_o_p_o')

%WATER SHIELDING
```

```
sealevel=load('sealevel.txt');% relative sea level for the last 7 kyr: Sturt et al 2013 (1
column only)
freq=load('frequency.txt');%occurrence of tides at 10 cm intervals between -4 and +4 m AOD:
British Oceanographic Data Centre; c1: occurrence count; c2: tidal duration [%]; c3:
elevation [m AOD]
ro=1.024;%water density [g/cm3]: Rosser et al 2010
lambda=160;%attenuation length [g/cm2]: Goethals et al 2009
fcumw=zeros(length(sealevel),pw+1);%expected flux at year t (1year=1row) (water shielding
only)
scumw=zeros(tt+1,pw+1);%water shielding factor at time t

for m=1:pw+1
    for t=1:(tt+1)
        elt=el(m)-sealevel(t);%site elevation [m AOD] at time t
        if t<tt+1-et(m)
            fcumw(t,m)=0;
            scumw(t,m)=0;
        else
            for n=1:length(freq)
                if elt>=freq(n,3)+0.05
                    fcumw(t,m)=fcumw(t,m)+fmax*freq(n,2)/100;
                elseif elt<freq(n,3)+0.05 && elt>=freq(n,3)-0.05
                    x=(freq(n,3)+0.05-elt)*100;%depth [cm]
                    fcumw(t,m)=fcumw(t,m)+fmax*freq(n,2)*((freq(n,3)+0.05-
elt)/0.1)/100+fmax*freq(n,2)*(1-(freq(n,3)+0.05-elt)/0.1)/100*exp(-ro*x/lambda);
                else
                    x=(freq(n,3)-0.05-elt)*100;
                    fcumw(t,m)=fcumw(t,m)+fmax*freq(n,2)/100*exp(-ro*x/lambda);
                end
            end
        end
    end
end

scumw=fcumw./fmax;
scumwfinal=sum(scumw,1)./(et+1);%total water shielding factor across the platform

figure(3) %water shielding
plot(d,scumwfinal)
axis([0 pw 0.4 1])
xlabel('Distance from the cliff [m]')
ylabel('Water shielding, S_w')

%GEOMAGNETICS: Lifton et al 2014
magn=load('geomagnetics2.txt');%c1: scalar value; c2: time [yr BP]

figure(4) %geomagnetic scalar
plot(magn(:,2),magn(:,1))
xlabel('Time [yr BP]')
ylabel('Geomagnetic scalar, S_g_m')

magn(:,1)=flipud(magn(:,1));
scumm=zeros(tt+1,pw+1);%geomagnetic scalar

for m=1:pw+1
    for t=1:(tt+1)
        if t<tt+1-et(m)
            scumm(t,m)=0;
        else
            scumm(t,m)=magn(t,1);
        end
    end
end

scummfinal=sum(scumm,1)./(et+1);%total geomagnetic scalar across the platform

%TOTAL CONCENTRATIONS
scumfinal=(scumtfinal.*scumwfinal).*scummfinal; %total shielding
be10total=be10*(et+1).*scumtfinal.*scumwfinal.*scummfinal; %total expected 10Be
concentrations

figure(5)%shielding/scalar factors for locations across the platform
plot(d,scumtfinal,d,scumwfinal,d,scummfinal,d,scumfinal)
xlabel('Distance from the cliff [m]')
ylabel('Shielding/scaling factors')
legend('Topographic','Water','Geomagnetic','Total')
```

```
figure(6)%expected 10Be concentrations or locations across the platform
plot(d,be10total)
xlabel('Distance from the cliff [m]')
ylabel('Expected ^1^0Be concentrations [at/g]')

output(:,1)=scumfinal;%total shielding
output(:,2)=be10total;%total expected 10Be concentrations
dlmwrite('profile300shield_concentrations.txt',output)
```

Script 2: Calculation of expected ^{10}Be concentrations at a single point with known elevation and distance from the cliff under assumption of negligible platform erosion

```
%Script to calculate expected 10Be concentrations at a single site with
%known elevation, distance from the cliff and platform total width
%ZMS 20/04/2018

close all
clear

be10=4.009;%10Be production [atoms/gr/yr]: Lifton et al 2014

%PLATFORM SPECIFICATIONS
pw=300;%platform width [m]
tt=7000;%total time [yr]
r=pw/tt;%recession rate [m/yr]
h=50;%cliff height [m]

%SITE SPECIFICATIONS
el=-1.27;%site elevation [m AOD]
d=298.58;%distance from cliff [m]
et=round(tt/pw*d);%exposure time [yr]

%TOPOGRAPHIC SHIELDING: Dunne et al 1999
io=2.105572;%incident radiation [calculated from the Fmax equation]
m=2.3;%scalling coefficient
fmax=2*pi*io/(m+1);%max flux
theta=degtorad(70);%cliff inclination angle
dphi=degtorad(102);%subtended azimuth angle
dcl=h/tan(theta);%horizontal distance between the cliff toe and the cliff top

dfcumt=zeros(tt+1,1);%missing flux at year t (1year=1row)
scumt=zeros(tt+1,1);%shielding factor at time t

for t=1:(et+1)%time [yr]
    theta = atan(h/(r*t+dcl));
    dfcumt(t+tt-et) = (io*dphi/(m+1))*(sin(theta))^(m+1);
    scumt(t+tt-et)=(fmax-dfcumt(t+tt-et))/fmax;
end

figure(1) %topographic shielding in time
plot(scumt)
axis([0 tt 0.75 1])
xlabel('Time [yr]')
ylabel('Topographic shielding, S_t_o_p_o')

%WATER SHIELDING
sealevel=load('sealevel.txt');% relative sea level for the last 7 kyr: Sturt et al 2013
freq=load('frequency.txt');%occurrence of tides at 10-cm intervals between -4 and +4 m AOD:
British Oceanographic Data Centre
ro=1.024;%water density [g/cm3]: Rosser et al 2010
lambda=160;%attenuation length [g/cm2]: Goethals et al 2009
fcumw=zeros(tt+1,1);%expected flux at year t (1year=1row) (water shielding only)
scumw=zeros(tt+1,1);%water shielding factor at time t

for t=1:(tt+1)
    elt=el-sealevel(t);%site elevation [m AOD] at time t
    if t<tt+1-et
        fcumw(t)=0;
        scumw(t)=0;
    else
        for n=1:length(freq)
            if elt>=freq(n,3)+0.05
                fcumw(t)=fcumw(t)+fmax*freq(n,2)/100;
            elseif elt<freq(n,3)+0.05 && elt>=freq(n,3)-0.05
                x=(freq(n,3)+0.05-elt)*100;%depth [cm]
```

```
                fcumw(t)=fcumw(t)+fmax*freq(n,2)*((freq(n,3)+0.05-
elt)/0.1)/100+fmax*freq(n,2)*(1-(freq(n,3)+0.05-elt)/0.1)/100*exp(-ro*x/lambda);
            else
                x=(freq(n,3)-0.05-elt)*100;
                fcumw(t)=fcumw(t)+fmax*freq(n,2)/100*exp(-ro*x/lambda);
            end
        end
    end
end

scumw=fcumw/fmax;

figure(2)%water shielding in time
plot(scumw)
axis([0 tt 0.3 1])
xlabel('Time [yr]')
ylabel('Water shielding, S_w')

%GEOMAGNETICS: Lifton et al 2014
magn=load('geomagnetics2.txt');
magn(:,1)=flipud(magn(:,1));

scumm=zeros(tt+1,1);%geomagnetics scalar

for t=1:(tt+1)
    if t<tt+1-et
        scumm(t)=0;
    else
        scumm(t)=magn(t,1);
    end
end

%TOTAL CONCENTRATIONS
et%exposure time
be10max=(et+1)*be10%unshielded concentrations
St=sum(scumt)/(et+1)%topographic shielding
Sw=sum(scumw)/(et+1)%water shielding
Sm=sum(scumm)/(et+1)%geomagnetic scalar
be10total=be10max*St*Sw*Sm%expected concentrations
```

Script 3: Calculation of the platform erosion scalar, S_{er}, for a simple platform profile with known width and slope under various assumptions about platform down-wearing

```
%Platform erosion scalar (down-wearing) for a simplified morphology
%platform = straight with known width and slope
%ZMS 20/04/2018

close all
clear

tt=7000;%total time [yr]
pw=300;%platform width [m]
slope=degtorad(0.4);%present slope [o]
dc=0:pw;%distance from the cliff [m]
texp=dc/pw*tt;%exposure time of the point [yr BP]
r1=pw/tt; %cliff retreat rate [m/yr]
ph=pw*tan(slope); %vertical range of platform [m]
phd=(pw-dc)*tan(slope); %elevation of each site [m]

%SCENARIO 1: erosion proportional to cliff retreat
down1=r1*tan(slope);%platform down-wearing rate [m/yr]
depth1=zeros(tt+1,pw+1);%depth at each time step [m]
scumed1=zeros(tt+1,pw+1);%platform erosion scalar at each time step

for t=0:tt
    wt=t*r1;%platform width at time t [m]
    for w=0:pw %distance from the cliff [m]
        if w>pw-wt;
            depth1(tt-t+1,w+1)=down1*(t-tt+texp(w+1));
            scumed1(tt-t+1,w+1)=exp(-depth1(tt-t+1,w+1)/1.3);
        end
    end
end

scumed1final=zeros(1,pw+1);
```

```
for w=0:pw
    scumed1final(w+1)=sum(scumed1(:,w+1))/nnz(scumed1(:,w+1)~=0);
end
scumed1final(1)=1;

%SCENARIO 2: erosion extrapolated from monitoring data: Robinson, 1977a
down2a=0.00133;%A - mean
down2b=0.0035;%B - mean+std

depth2a=zeros(tt+1,pw+1); %depth at each time step [m]
scumed2a=zeros(tt+1,pw+1); %shielding factor at time t
depth2b=zeros(tt+1,pw+1);
scumed2b=zeros(tt+1,pw+1);

for t=0:tt
    wt=t*r1;%width at time t [m]
    for w=0:pw %width
        if w>pw-wt;
            depth2a(tt-t+1,w+1)=down2a*(t-tt-1+texp(w+1));
            scumed2a(tt-t+1,w+1)=exp(-depth2a(tt-t+1,w+1)/1.3);
            depth2b(tt-t+1,w+1)=down2b*(t-tt-1+texp(w+1));
            if depth2b(tt-t+1,w+1)>ph-phd(w+1)
                depth2b(tt-t+1,w+1)=texp(w+1)*down2a;
            end
            scumed2b(tt-t+1,w+1)=exp(-depth2b(tt-t+1,w+1)/1.3);
        end
    end
end

scumed2afinal=zeros(1,pw+1);
for w=0:pw
    scumed2afinal(w+1)=sum(scumed2a(:,w+1))/nnz(scumed2a(:,w+1)~=0);
end
scumed2afinal(1)=1;

scumed2bfinal=zeros(1,pw+1);
for w=0:pw
    scumed2bfinal(w+1)=sum(scumed2b(:,w+1))/nnz(scumed2b(:,w+1)~=0);
end
scumed2bfinal(1)=1;

%SCENARIO 3: erosion decreases with platform widening
slopet=zeros(tt+1,1); %slope in time

for t=0:tt
    slopet(t+1)=atan(ph/(t*r1));
end
slopet(1)=degtorad(90);

depth3=zeros(tt+1,pw+1);%depth at each time step [m]
scumed3=zeros(tt+1,pw+1);%shielding factor at each time step

for t=0:tt
    wt=t*r1;%width at time t [m]
    for w=0:pw %width
        if w>pw-wt;
            depth3(tt-t+1,w+1)=tan(slopet(t+1))*(pw-dc(w+1))-phd(w+1);
            scumed3(tt-t+1,w+1)=exp(-depth3(tt-t+1,w+1)/1.3);
        end
    end
end

scumed3final=zeros(1,pw+1);
for w=0:pw
    scumed3final(w+1)=sum(scumed3(:,w+1))/nnz(scumed3(:,w+1)~=0);
end
scumed3final(1)=1;

table(1,:)=scumed1final;
table(2,:)=scumed2afinal;
table(3,:)=scumed2bfinal;
table(4,:)=scumed3final;

dlmwrite('depth_shield_300_04.txt',table)

figure(1)
plot(dc,table(1,:),dc,table(2,:),dc,table(3,:),dc,table(4,:))
```

```
axis([0 pw 0 1])
xlabel('Distance from the cliff [m]', 'FontSize', 10)
ylabel('Shielding factor, S_e_r', 'FontSize', 10)
legend('Scenario 1','Scenario 2A','Scenario 2B','Scenario 3')
```

Script 4: Application of the empirical platform down-wearing model under assumption of constant cliff retreat and stable seaward edge position

```
%Including the empirical platform down-wearing from Chapter 5 into the
%model of constant cliff retreat and stable position of the seaward edge
%ZMS 26/06/2018

close all
clear

toe=3.2;%HAT
sealevel=load('sealevel.txt');% relative sea level for the last 7 kyr: Sturt et al 2013
freq=load('frequency.txt');%occurrence of tides at 10-cm intervals between -4 and +4 m AOD:
British Oceanographic Data Centre

tt=7000;%total time [yr]
pw=300;%platform width [m]
dc=0:pw;%distance from the cliff [m]
texp=dc/pw*tt;%exposure of the point [yr BP]
r1=pw/tt; %cliff retreat rate [m/yr]

down=zeros(tt+1,pw+1);%platform down-wearing rate at each time step [m/yr]
elev=10*ones(tt+1,pw+1);%elevation of the surface (10 m cliff - abstract value)

for t=1:tt
    pwt=t*r1;%platform width at time t [m]
    for n=0:pw%distance from the cliff
        if texp(n+1)>=tt-t && elev(t,n+1)==10;
            elev(t+1,n+1)=toe+sealevel(t+1);
        elseif texp(n+1)>=tt-t && elev(t,n+1)~=10;
            el=elev(t,n+1)-sealevel(t+1);
            for m=1:length(freq)
                if el<freq(m,3)+0.05 && el>=freq(m,3)-0.05
                    tid=freq(m,2);
                    down(t+1,n+1)=-2.01+0.01*(pw-dc(n+1))+0.60*tid;
                    if down(t+1,n+1)<0
                        down(t+1,n+1)=0;
                    end
                end
            end
            elev(t+1,n+1)=elev(t,n+1)-down(t+1,n+1)/1000;
        end
    end
end

figure(1)%development of coastal cross-section
cc=jet(15);
for n=1:500:(tt+1)
    plot(dc,elev(n,:),'color',cc(0.002*(n - 1) + 1,:))
    hold on
end
hold off

ser_table=zeros(tt+1,pw+1);
for t=0:tt
    for n=0:pw
        surf=elev(tt+1,n+1);
        if elev(t+1,n+1)~=10
            ser_table(t+1,n+1)=exp((surf-elev(t+1,n+1))/1.3);
        end
    end
end

ser=zeros(1,pw+1);
for n=0:pw
    a=elev(:,n+1);
    b=elev(a~=10,(n+1));
    size2=size(b,1);
    ser(n+1)=sum(ser_table(:,n+1))/size2;
end
```

```
figure(2)%total across-shore platform erosion scalar
plot(dc, ser)

data1=load('profile300shield_concentrations.txt')';%total shielding (c1) and expected
concentrations (c2) for the real cross-section
be10total=data1(2,:);
be10ser=be10total.*ser;

figure(3)%total 10Be concnetrations
plot(dc,be10total,dc,be10ser)
```

Script 5: Exploring 60 scenarios of cliff retreat rates and patterns (stable, acceleration, deceleration) and platform down-wearing (parallel, platform widening, empirical)

```
%Modelling 10Be concentrations under differen assumptions about cliff
%retreat rates and platform erosion scenarios
%ZMS 2/07/2018

clear
close all

%PLATFORM MORPHOLOGY
data1=load('profile300elev.txt');%input table with distance from the cliff (c1) and elevation
(c2)
sel=data1(:,2);%site elevation [m AOD]
pw=300;%contemporary platform width [m]
tt=7000;%considered time [yr]
dc=0:pw;%distance from the cliff [m]
h=50;%cliff height [m]
slope=degtorad(0.4);%present slope [o]
ph=3.2+1.5;%platform vertical range [m]
slope2=atan(ph/pw);%slope [o] for platform widening scenario
phd=(pw-dc).*tan(slope2);%elevation of points above platfomr base
toe=3.2;%HAT [m AOD]
sealevel=load('sealevel.txt');% relative sea level for the last 7 kyr: Sturt et al 2013
freq=load('frequency.txt');%occurrence of tides at 10-cm intervals between -4 and +4 m AOD:
British Oceanographic Data Centre
be10=4.009;%Be production rate [atoms/gr/yr]: Lifton et al 2014

%CALCULATING EXPOSURE AGES
table=zeros(1,pw+1);
table_year=zeros(1,tt);%cliff position every year
table_down1=zeros(1,tt);%down-wearing every year

%PLATFORM DOWN-WAERING SCENARIOS
%1: erosion proportional to cliff retreat
scumer1final=zeros(60,pw+1);
%2: platform widening
depth2=zeros(tt,pw+1);%depth at each time step [m]
scumer2=zeros(tt,pw+1);%shielding factor at each time step
scumer2final=zeros(60,pw+1);%total shielding across the platform
%3: empirical (width kept at 300 m)
table_down3=zeros(tt,pw+1);%platform down-wearing rate at each time step [m/yr]
elev3=10*ones(tt,pw+1);%elevation of the surface (10 m cliff - abstract value)
depth3=zeros(tt,pw+1);%depth at each time step [m]
scumer3=zeros(tt,pw+1);%shielding factor at each time step
scumer3final=zeros(60,pw+1);%total shielding across the platform

year_count=1;
%CLIFF RETREAT SCENARIOS
%1: constant rates 0.0025:0.0025:0.05 m/yr
for n=0.0025:0.0025:0.05%present rates m/yr
    year=0;
    count=2;
    for m=1:200000%to make sure max value > 300
        year(count)=year(count-1)+n;%moving backwards
        count=count+1;
    end
    for k=0:pw;
        index=sum(year(:)<k+0.0001);
        table(round(n*400),k+1)=index;
    end
    table_year(year_count,:)=year(1:tt);
    for k=2:tt
```

```
        table_down1(year_count,k)=(year(k)-year(k-1))*tan(slope);
    end
    year_count=year_count+1;
    for k=1:tt
        if year(k)=='NaN'
            year_slope(k)='NaN'
        else
            year_slope(k)=atan(ph/(pw-year(k)+1));
            if year_slope(k)<0
                year_slope(k)=0;
            end
        end
    end
    for m1=1:size(depth2,1)
        for m2=1:size(depth2,2)
            if dc(m2)>year(m1)
                depth2(m1,m2)=tan(year_slope(m1))*(pw-dc(m2)+1)-phd(m2);
                scumer2(m1,m2)=exp(-depth2(m1,m2)/1.3);
            end
        end
    end
    for m1=1:size(scumer2,2)
        count_scumer2=0;
        for m2=1:size(scumer2,1)
            if scumer2(m2,m1)~=0
                count_scumer2=count_scumer2+1;
            end
            scumer2final(round(n*400),m1)=sum(scumer2(:,m1))/count_scumer2;
        end
    end
    for m1=0:pw
        for m2=size(elev3,1)-1:-1:1
            if dc(m1+1)>=year(m2)
                if elev3(m2+1,m1+1)==10;
                        elev3(m2,m1+1)=toe+sealevel(end-m2+1);
                else
                    count_dc=0;
                    for m3=1:dc(m1)
                        if m3~=10
                            count_dc=count_dc+1;
                        end
                    end
                    elt=elev3(m2+1,m1+1)-sealevel(end-m2+1);
                    for m=1:length(freq)
                        if elt<freq(m,3)+0.05 && elt>=freq(m,3)-0.05
                            tid=freq(m,2);
                            table_down3(m2+1,m1+1)=-2.01+0.01*(pw-count_dc+1)+0.60*tid;
                            if table_down3(m2+1,m1+1)<0
                                table_down3(m2+1,m1+1)=0;
                            end
                        end
                    end
                    elev3(m2,m1+1)=elev3(m2+1,m1+1)-table_down3(m2+1,m1+1)/1000;
                end
            end
        end
    end
    for m1=1:pw+1
        for m2=1:size(elev3,1)
            if elev3(m2,m1)~=10
                depth3(m2,m1)=abs(elev3(m2,m1)-elev3(1,m1));
                scumer3(m2,m1)=exp(-depth3(m2,m1)/1.3);
            end
        end
    end
    for m1=1:size(scumer3,2)
        count_scumer3=0;
        for m2=1:size(scumer3,1)
            if scumer3(m2,m1)~=0
                count_scumer3=count_scumer3+1;
            end
            scumer3final(round(n*400),m1)=sum(scumer3(:,m1))/count_scumer3;
        end
    end
end

nn=size(table,1);
```

```
year_count=size(table_year,1)+1;

%2: deceleration
for n=0.0025%present rates [m/yr]
   for p=0.000005:0.000005:0.0001%deceleration rate [m/yr]
       year=n;
       count=2;
       for m=1:200000%to make sure max value > pw
            year(count)=year(count-1)+m*p;%moving backwards
            count=count+1;
       end
        for k=0:pw;
            index=sum(year(:)<k+0.0000001);
            table(round(p*200000)+nn,k+1)=index;
        end
        table_year(year_count,:)=year(1:tt);
        for k=2:tt
            table_down1(year_count,k)=(year(k)-year(k-1))*tan(slope);
        end
        year_count=year_count+1;
        for k=1:tt
            if year(k)=='NaN'
                year_slope(k)='NaN'
            else
                year_slope(k)=atan(ph/(pw-year(k)+1));
                if year_slope(k)<0
                    year_slope(k)=0;
                end
            end
        end
        for m1=1:size(depth2,1)
            for m2=1:size(depth2,2)
                if dc(m2)>year(m1)
                    depth2(m1,m2)=tan(year_slope(m1))*(pw-dc(m2)+1)-phd(m2);
                    scumed2(m1,m2)=exp(-depth2(m1,m2)/1.3);
                end
            end
        end
        for m1=1:size(scumed2,2)
            count_scumed2=0;
            for m2=1:size(scumed2,1)
                if scumed2(m2,m1)~=0
                    count_scumed2=count_scumed2+1;
                end
                scumer2final(round(p*200000)+nn,m1)=sum(scumed2(:,m1))/count_scumed2;
            end
        end
        for m1=0:pw
            for m2=size(elev3,1)-1:-1:1
                if dc(m1+1)>=year(m2)
                    if elev3(m2+1,m1+1)==10;
                            elev3(m2,m1+1)=toe+sealevel(end-m2+1);
                    else
                        count_dc=0;
                        for m3=1:dc(m1)
                            if m3~=10
                                count_dc=count_dc+1;
                            end
                        end
                        el=elev3(m2+1,m1+1)-sealevel(end-m2+1);
                        for m=1:length(freq)
                            if el<freq(m,3)+0.05 && el>=freq(m,3)-0.05
                                tid=freq(m,2);
                                table_down3(m2+1,m1+1)=-2.01+0.01*(pw-count_dc+1)+0.60*tid;
                                if table_down3(m2+1,m1+1)<0
                                    table_down3(m2+1,m1+1)=0;
                                end
                            end
                        end
                        elev3(m2,m1+1)=elev3(m2+1,m1+1)-table_down3(m2+1,m1+1)/1000;
                    end
                end
            end
        end
        for m1=1:pw+1
            for m2=1:size(elev3,1)
                if elev3(m2,m1)~=10
```

```
                    depth3(m2,m1)=abs(elev3(m2,m1)-elev3(1,m1));
                    scumer3(m2,m1)=exp(-depth3(m2,m1)/1.3);
                end
            end
        end
        for m1=1:size(scumer3,2)
            count_scumer3=0;
            for m2=1:size(scumer3,1)
                if scumer3(m2,m1)~=0
                    count_scumer3=count_scumer3+1;
                end
                scumer3final(round(p*200000)+nn,m1)=sum(scumer3(:,m1))/count_scumer3;
            end
        end
    end
end

nn=size(table,1);
year_count=size(table_year,1)+1;

%3: acceleration
for n=0.05%present rates [m/yr] (Rosser et al., 2013)
   for p=0.000005:0.000005:0.0001%acceleration rate [m/yr]
       year=n;
       count=2;
       for m=1:200000%to make sure max value > 300
            year(count)=year(count-1)+n-m*p;%moving backwards
            if year(count)<=year(count-1)
                year(count)=year(count-1)+year(count-1)-year(count-2);
            end
            count=count+1;
       end
        for k=0:pw;
            index=sum(year(:)<k+0.000000001);
            table(round(p*200000)+nn,k+1)=index;
        end
        if size(year,2)>tt
            table_year(year_count,:)=year(1:tt);
            table_down1(year_count,:)=year(1:tt).*tan(slope);
            for k=2:tt
                table_down1(year_count,k)=(year(k)-year(k-1))*tan(slope);
            end
        else
            table_year(year_count,1:size(year,2))=year;
            table_down1(year_count,1:size(year,2))=year.*tan(slope);
            for k=2:tt
                table_down1(year_count,k)=(year(k)-year(k-1))*tan(slope);
            end
        end
        year_count=year_count+1;
        for k=1:tt
            if year(k)=='NaN'
                year_slope(k)='NaN'
            else
                year_slope(k)=atan(ph/(pw-year(k)+1));
                if year_slope(k)<0
                    year_slope(k)=0;
                end
            end
        end
        for m1=1:size(depth2,1)
            for m2=1:size(depth2,2)
                if dc(m2)>year(m1)
                    depth2(m1,m2)=tan(year_slope(m1))*(pw-dc(m2)+1)-phd(m2);
                    scumed2(m1,m2)=exp(-depth2(m1,m2)/1.3);
                end
            end
        end
        for m1=1:size(scumed2,2)
            count_scumed2=0;
            for m2=1:size(scumed2,1)
                if scumed2(m2,m1)~=0
                    count_scumed2=count_scumed2+1;
                end
                scumer2final(round(p*200000)+nn,m1)=sum(scumed2(:,m1))/count_scumed2;
            end
        end
```

```
        for m1=0:pw
            for m2=size(elev3,1)-1:-1:1
                if dc(m1+1)>=year(m2)
                    if elev3(m2+1,m1+1)==10;
                            elev3(m2,m1+1)=toe+sealevel(end-m2+1);
                    else
                        count_dc=0;
                        for m3=1:dc(m1)
                            if m3~=10
                                count_dc=count_dc+1;
                            end
                        end
                        el=elev3(m2+1,m1+1)-sealevel(end-m2+1);
                        for m=1:length(freq)
                            if el<freq(m,3)+0.05 && el>=freq(m,3)-0.05
                                tid=freq(m,2);
                                table_down3(m2,m1+1)=-2.01+0.01*(pw-count_dc+1)+0.60*tid;
                                if table_down3(m2,m1+1)<0
                                    table_down3(m2,m1+1)=0;
                                end
                            end
                        end
                        elev3(m2,m1+1)=elev3(m2+1,m1+1)-table_down3(m2,m1+1)/1000;
                    end
                end
            end
        end
        for m1=1:pw+1
            for m2=1:size(elev3,1)
                if elev3(m2,m1)~=10
                    depth3(m2,m1)=abs(elev3(m2,m1)-elev3(1,m1));
                    scumer3(m2,m1)=exp(-depth3(m2,m1)/1.3);
                end
            end
        end
        for m1=1:size(scumer3,2)
            count_scumer3=0;
            for m2=1:size(scumer3,1)
                if scumer3(m2,m1)>0
                    count_scumer3=count_scumer3+1;
                end
                scumer3final(round(p*200000)+nn,m1)=sum(scumer3(:,m1))/count_scumer3;
            end
        end
    end
end

table(:,1)=table(:,1).^0;
scumer2final(:,1)=ones;

for n=size(table,1):-1:1
    for m=size(table,2):-1:2
        if table(n,m)>tt
            table(n,m)=NaN;
        elseif abs(table(n,m)-table(n,m-1))<0.001
            table(n,m)=NaN;
        end
    end
end

table2=zeros(size(table));
table2(1:20,:)=table(40:-1:21,:);
table2(21:40,:)=table(1:20,:);
table2(41:60,:)=table(41:60,:);

cc=jet(60);
figure(1)
for n=1:size(table2,1)
    plot(dc,table2(n,:),'color',cc(n,:))
    hold on
end
hold off
axis([0 pw 0 tt])

down1b=zeros(size(table_down1));
down1b(1:20,:)=table_down1(40:-1:21,:);
down1b(21:40,:)=table_down1(1:20,:);
```

```
down1b(41:60,:)=table_down1(41:60,:);

for n=1:60
    depth1=zeros(tt,pw+1);
    scumer1=zeros(tt,pw+1);
    for d=1:pw+1
        if table2(n,d)~='NaN'
            if table2(n,d)<=tt
                for m=2:table2(n,d)
                    depth1(m,d)=depth1(m-1,d)+ down1b(n,m);
                    scumer1(m,d)=exp(-depth1(m,d)/1.3);
                end
            end
        end
    end
    for t=1:size(scumer1,2)
        if table2(n,t)== 'NaN'
            scumer1final(n,t)=0;
        else
            scumer1final(n,t)=sum(scumer1(:,t))/table2(n,t);
        end
    end
end

scumer1final(:,1)=ones;

figure(2)
for n=1:size(scumer1final,1)
    plot(dc,scumer1final(n,:),'color',cc(n,:))
    hold on
end
hold off

scumer2finalb=zeros(size(scumer2final));
scumer2finalb(1:20,:)=scumer2final(40:-1:21,:);
scumer2finalb(21:40,:)=scumer2final(1:20,:);
scumer2finalb(41:60,:)=scumer2final(41:60,:);

table2b=table2.^0;
scumer2finalb=scumer2finalb.*table2b;

figure(3)
for n=1:size(scumer2finalb,1)
    plot(dc,scumer2finalb(n,:),'color',cc(n,:))
    hold on
end
hold off

scumer3finalb=zeros(size(scumer3final));
scumer3finalb(1:20,:)=scumer3final(40:-1:21,:);
scumer3finalb(21:40,:)=scumer3final(1:20,:);
scumer3finalb(41:60,:)=scumer3final(41:60,:);

scumer3finalb=scumer3finalb.*table2b;

figure(4)
for n=1:size(scumer3finalb,1)
    plot(dc,scumer3finalb(n,:),'color',cc(n,:))
    hold on
end
hold off

%TOPOGRAPHIC SHIRELDING: Dunne et al 1999
io=2.105572;%incident radiation [calculated from the Fmax equation]
m=2.3;%scalling coefficient
fmax=2*pi*io/(m+1);%max flux
theta=degtorad(70);%cliff inclination angle
dphi=degtorad(102);%subtended azimuth angle
dcl=h/tan(theta);%horizontal distance between the cliff toe and the cliff top

scumtfinal=zeros(1,pw+1);%total topographic shielding factor across the platform

for s=1:60
    dfcumt=zeros(tt,pw+1);%missing flux at year t (1year=1row)
    scumt=zeros(tt,pw+1); %topographic shielding factor at time t
    for n=1:pw+1
        if table2(s,n)>0
```

```
            for t=1:table2(s,n)
                theta = atan(h/(table_year(s,t)+dcl));
                dfcumt(t+tt-table2(s,n),n) = (io*dphi/(m+1))*(sin(theta))^(m+1);
            end
        end

    end
    for z1=1:size(dfcumt,1)
        for z2=1:size(dfcumt,2)
            if dfcumt(z1,z2)~=0
                scumt(z1,z2)=(fmax-dfcumt(z1,z2))/fmax;
            end
        end
    end
    scumtfinal(s,:)=sum(scumt,1)./(table2(s,:));
end

figure(5) %topographic shielding
for n=1:60
    plot(dc,scumtfinal(n,:),'color',cc(n,:))
    hold on
end
hold off
axis([0 pw 0.75 1])
xlabel('Distance from the cliff [m]')
ylabel('Topographic shielding, S_t_o_p_o')

%WATER SHIELDING
sealevel=load('sealevel.txt');% relative sea level for the last 7 kyr: Sturt et al 2013 (1
column only)
freq=load('frequency.txt');%occurrence of tides at 10 cm intervals between -4 and +4 m AOD:
British Oceanographic Data Centre
%c1: occurrence count; c2: tidal duration [%]; c3: elevation [m AOD]

ro=1.024;%ro - water density [g/cm3]: Rosser et al 2010
lambda=160;%lambda - attenuation length [g/cm2]: Goethals et al 2009

for s=1:60
    fcumw=zeros(tt,pw+1);%expected flux at year t (1year=1row) (water shielding only)
    scumw=zeros(tt,pw+1);%water shielding factor at time t
    for m=1:pw+1
        for t=1:tt
            elt=sel(m)-sealevel(t);%site elevation [AOD] at time t
            if table2(s,m)>0
                if t<tt+1-table2(s,m)
                    fcumw(t,m)=0;
                    scumw(t,m)=0;
                else
                    for n=1:length(freq)
                        if elt>=freq(n,3)+0.05
                            fcumw(t,m)=fcumw(t,m)+fmax*freq(n,2)/100;
                        elseif elt<freq(n,3)+0.05 && elt>=freq(n,3)-0.05
                            x=(freq(n,3)+0.05-elt)*100;%depth [cm]
                            fcumw(t,m)=fcumw(t,m)+fmax*freq(n,2)*((freq(n,3)+0.05-
elt)/0.1)/100+fmax*freq(n,2)*(1-(freq(n,3)+0.05-elt)/0.1)/100*exp(-ro*x/lambda);
                        else
                            x=(freq(n,3)-0.05-elt)*100;
                            fcumw(t,m)=fcumw(t,m)+fmax*freq(n,2)/100*exp(-ro*x/lambda);
                        end
                    end
                end
            end
        end
    end
    for z1=1:size(fcumw,1)
        for z2=1:size(fcumw,2)
            if fcumw(z1,z2)~=0
                scumw(z1,z2)=fcumw(z1,z2)/fmax;
            end
        end
    end
    scumwfinal(s,:)=sum(scumw,1)./(table2(s,:));
end

figure(6) %water shielding
for n=1:size(scumwfinal,1)
    plot(dc,scumwfinal(n,:),'color',cc(n,:))
```

```
    hold on
end
hold off
axis([0 pw 0.3 1])
xlabel('Distance from the cliff [m]')
ylabel('Water shielding, S_w')

%GEOMAGNETIC SCALAR
magn=load('geomagnetics2.txt');%c1: scalar; c2: time [yr BP]
magn(:,1)=flipud(magn(:,1));
scumm=zeros(tt,pw+1);%geomagnetics scalar

for s=1:60
    for m=1:pw+1
        for t=1:tt
            if table2(s,m)>0
                if t<tt+1-table2(s,m)
                    scumm(t,m)=0;
                else
                    scumm(t,m)=magn(t,1);
                end
            end
        end
    end
    scummfinal(s,:)=sum(scumm,1)./table2(s,:);%total magnetic scalar across the platform
end

figure(7) %geomagnetics
for n=1:size(scummfinal,1)
    plot(dc,scummfinal(n,:),'color',cc(n,:))
    hold on
end
hold off
axis([0 pw 0.92 1.12])
xlabel('Distance from the cliff [m]')
ylabel('Geomagnetic scalar, S_g_m')
```